MESOSCALE CHARACTERISTICS OF THE TEXAS HIPLEX AREA DURING SUMMER 1977

LP-99

TDWR CONTRACTS NO. 14-80002 AND NO. 14-80039

Prepared by:

DEPARTMENT OF METEOROLOGY
COLLEGE OF GEOSCIENCES
TEXAS A&M UNIVERSITY
COLLEGE STATION, TEXAS

Prepared for:

TEXAS DEPARTMENT OF WATER RESOURCES
AUSTIN, TEXAS

Funded by:

DEPARTMENT OF THE INTERIOR, BUREAU OF RECLAMATION
TEXAS DEPARTMENT OF WATER RESOURCES

May 1979
Reprinted April 1981

MESOSCALE CHARACTERISTICS OF THE TEXAS HIPLEX AREA DURING SUMMER 1977

James R. Scoggins, Gregory S. Wilson, and Steven F. Williams
Department of Meteorology
College of Geosciences
Texas A&M University
College Station, Texas 77843

May 1979
Reprinted April 1981

Final Report
TDWR Contract Nos. 14-80002 and 14-80039

Availability Unlimited

Prepared for
Texas Department of Water Resources
Austin, Texas

Funded by
Department of the Interior, Bureau of Reclamation, and the
State of Texas through the Texas Department of Water Resources

TDWR
LP-99

MESOSCALE CHARACTERISTICS OF THE TEXAS HIPLEX AREA DURING SUMMER 1977

by

James R. Scoggins, Gregory S. Wilson, and Steven F. Williams
Department of Meteorology
College of Geosciences
Texas A&M University
College Station, Texas 77843

ABSTRACT

This report contains an analysis for 19 days on which mesoscale meteorological data were obtained in the Texas HIPLEX area during the period June 1 to July 10, 1977. Rawinsonde soundings were made at 3-h intervals between 1500 and 0300 GMT on 16 of the 19 days at Midland, Robert Lee, Post, and Big Spring. Surface data consisting of 10-min average values of temperature, humidity, pressure, and wind direction and speed were available from 17 stations for all 19 days. In addition, data were available from the National Weather Service radar at Midland.

The data were analyzed and results presented for each day separately. In addition, composite analyses of selected surface variables and atmospheric energetics are presented. Variables considered in the surface analysis include temperature, mixing ratio, velocity divergence, vertical motion, vertical flux of moisture, moisture divergence, equivalent potential temperature, vorticity, sea level pressure, and pressure change. Charts of analyzed fields determined from data placed on a 15-km grid are compared with radar data coded on a similar grid. Variables considered in the upper-air analysis include mass divergence, vertical motion, moisture divergence, and budgets of latent heat energy, kinetic energy, and water vapor. Composite analyses are presented for the surface and upper-air variables as a function of convective activity.

The results show pronounced interactions between the environment and convective activity. Marked changes in nearly all surface and upper-air variables occur in association with convective activity. The analysis of individual days as well as the composite analyses suggest that surface processes indicated by moisture divergence, vertical flux of moisture, and vertical motion are important in the formation and maintenance of convective clouds. The importance of these same variables also is reflected in the upper-air analyses as well as energy processes and time changes.

No attempt is made to reach definitive scientific conclusions because of the relatively small number of days for which data are available. However, the results are conclusive in terms of demonstrating the value of mesoscale research in the overall problem of developing the technology for systematic rainfall enhancement. Also, the results confirm those obtained from the 1976 mesoscale data.

Key Words

Mesoscale analysis
Moisture divergence
Vertical motion
Vorticity
Energy budget
Moisture budget
Surface analysis
Kinematic parameters
Energetics
Time changes
Meteorological data
Winds

ACKNOWLEDGMENTS

The authors gratefully acknowledge the assistance of Ms. Doreen Westwood and Mrs. Nine-Min Cheng for preparation of the figures, Ms. Betty Seymour for assisting with the composite surface analysis, and Mrs. Karen Hood for typing and assembling the manuscript. Also, the guidance and council provided by Mr. Robert Riggio, Mr. John Carr, and Dr. Herbert Grubb of the Texas Department of Water Resources during this research is greatly appreciated.

This research was funded by the Bureau of Reclamation, Department of the Interior, and the State of Texas through the Texas Department of Water Resources under TDWR Contract Nos. 14-80002 and 14-80039.

TABLE OF CONTENTS

TABLE OF CONTENTS (CONTINUED)

TABLE OF CONTENTS (CONTINUED)

TABLE OF CONTENTS (CONTINUED)

TABLE OF CONTENTS (CONTINUED)

LIST OF FIGURES

1. INTRODUCTION

A mesoscale experiment was conducted during the summers of 1976, 1977, and 1978 as part of the Texas HIPLEX program. The primary objective of these experiments is to investigate interactions between convective clouds and their environment for the purpose of better understanding environmental conditions related to the initiation, growth, and other aspects of convective clouds in the semiarid region of West Texas. A report was prepared (Scoggins, et al. 1978) which presents a case study analysis for each of fifteen days, as well as a composite surface analysis and average conditions of atmospheric energetics during times with and without convective activity, for data collected during the summer of 1976. The present report contains a similar analysis of mesoscale data collected on nineteen days during the summer of 1977. Case studies are presented for the nineteen days and in a matter almost identical to those for the 1976 data. The surface analysis has been extended to include surface pressure and pressure change fields, and a section has been added on the average moisture processes as a function of convective activity.

It is not the purpose of this report to attempt to present a comprehensive interpretation of results for each case study, but rather to present an analysis with sufficient depth to permit the interpretation and integration of mesoscale conditions in other phases of the research such as radar analysis, satellite analysis, and the analysis of aircraft data. When the analysis of enough case studies become available to permit meaningful stratification of the results by convective regime, models will be formulated and greater in-depth interpretation presented of the mesoscale conditions accompaning the convective activity.

This report contains a description of the mesoscale experiment for 1977, a brief discussion of data and processing procedures, methods of data analysis, results for each case study day, a composite analysis of surface data, average conditions of upper-level kinematic and atmospheric energetics during times with and without convective activity, and average moisture processes as a function of convective activity. A standard format was used in the presentation of results to facilitate the retrieval of information for any desired day as well as for making comparisons between days. Also, direct comparisons may be made with results for 1976.

The computational procedures for the analysis of the surface data were identical to those employed in the analysis of the 1976 data, but the procedures for analysis of the sounding data was changed somewhat. These

changes did not alter the results in a noticeable way. The purpose of the changes was to reduce computer costs. The computational procedures used are presented in Section 4.

2. THE MESOSCALE EXPERIMENT

The mesoscale experiment conducted in 1977 was bounded approximately by Midland-Garden City-Robert Lee-Colorado City-Snyder-Post-Lamesa-Big Spring-Midland as was the experiment conducted in 1976. All data, both surface and atmospheric soundings, were taken within this area which encompassed the CRMWD cloud seeding target area.

2.1 Surface Measurements

A network of ten special surface stations was in operation during the entire period of the 1977 mesoscale experiment. The location of the stations is shown in Fig. 2.1. The instrumentation at each station consisted of a

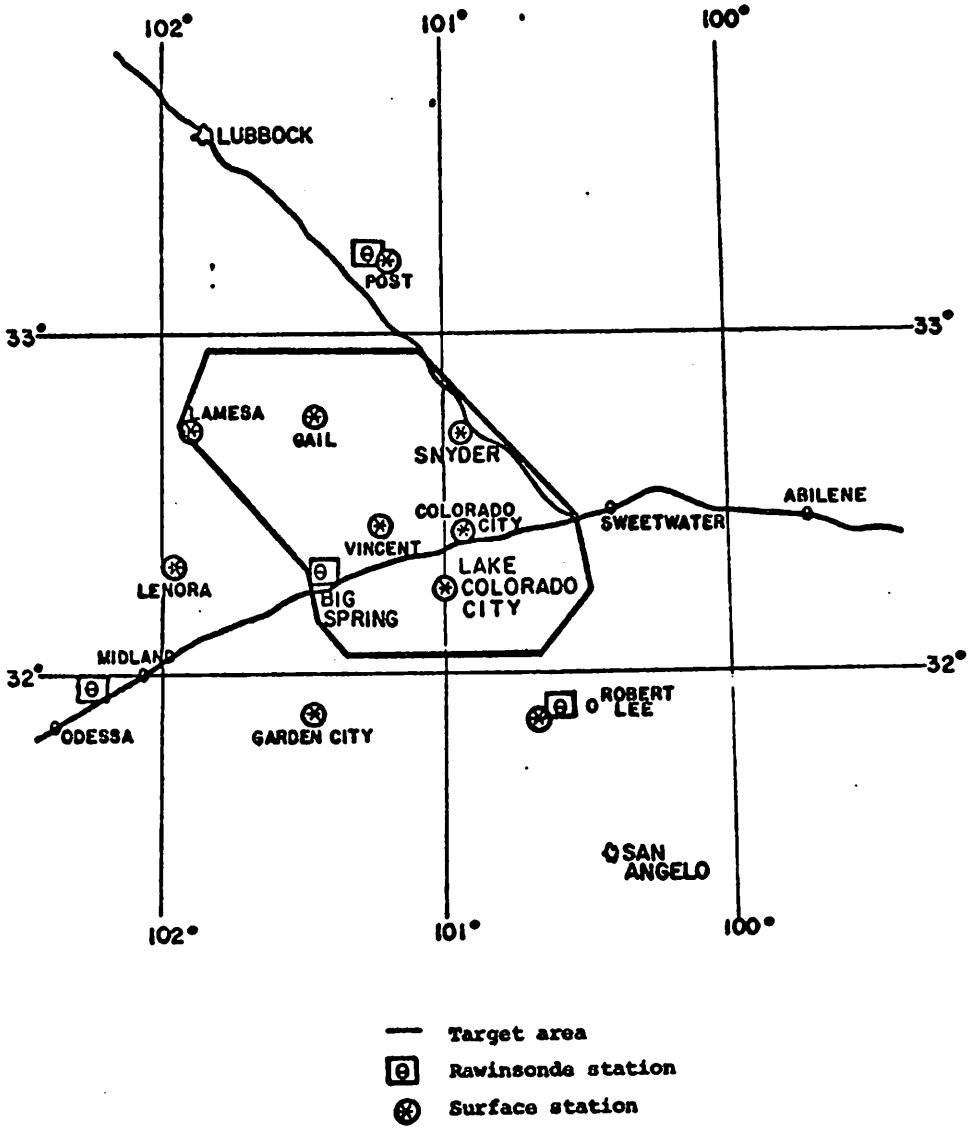

Fig. 2.1 Target area and locations of special surface and rawinsonde stations.

hygrothermograph for measurements of temperature and relative humidity, a microbarograph for measuring pressure, and an MRI automatic weather station for measuring wind direction and speed as well as temperature. A standard-type instrument shelter was used at each station to house the hygrothermograph and microbarograph. The instruments were calibrated routinely at 2- or 3-day intervals during the entire experimental period. The hygrothermograph data were checked by use of a sling psychrometer, and the microbarograph data by use of an aneroid barometer that was checked against a National Weather Service barometer at Midland. The accuracy of the wind data could not be checked to the same extent that the thermodynamic data were checked, but it could be determined whether or not the equipment was functioning properly.

2.2 Upper Air Measurements

Atmospheric soundings were made at 4 locations including Midland, Post, Robert Lee, and Big Spring. These locations are shown in Fig. 2.1. Arrangements were made with the National Weather Service for the purchase of soundings for Midland. The Colorado River Municipal Water District operated the sounding station at Big Spring, and Texas A&M University operated those at Post and Robert Lee. All stations used the same type of radiosonde.

An RD-65 rawinsonde set was used at Big Spring, while GMD-1b units were used at the other locations.

2.3 Radar

An M-33 radar located at Snyder, Texas, and operated by Meteorology Research, Inc. was dedicated to the task of obtaining radar data for all convective echoes over the Texas HIPLEX area during the mesoscale experiment. Excellent data were obtained in digital form for all mesoscale days.

The National Weather Service radar at Midland was operated continuously by National Weather Service personnel during the entire experiment, and a copy of PPI overlays and the radar operator logs were made available for our use. The data were coded and used in this report to locate convective echoes. Studies which require precise radar information should utilize the M-33 data.

2.4 Rainfall

Rainfall measurements were made at approximately 150 locations during the entire experimental period. There were approximately 40 recording raingages with the remainder being fence post gages. Since

these data are not used in this report no further discussion of the data will be provided.

2.5 Other

Surface data were obtained from five locations in addition to the ten special surface stations discussed in Section 2.1 above. The five stations included Reese AFB (Lubbock), Midland, Webb AFB (Big Spring), San Angelo, and Dyess AFB (Abilene). These data were obtained from teletype data for each hour on the hour which coincides with the measurement schedule for the ten special surface stations. All teletype and facsimile data consisting of routine observations and charts prepared by the National Weather Service were obtained from the Texas A&M University weather station and archived for future reference and use. In addition, complete surface observations and regularly scheduled rawinsonde releases made by National Weather Service personnel at Midland were obtained.

3. DATA

3.1 Processing Procedures

3.1.1 Surface

All data collected at the ten special surface stations were recorded on strip charts continuously as a function of time. Ten-minute average values of temperature, relative humidity, pressure, and wind direction and speed were extracted from the strip charts each hour on the hour. These data were keypunched, checked and cross-checked for errors and corrections made as necessary, and placed on magnetic tape for subsequent analysis.

3.1.2 Soundings

All atmospheric soundings made as part of the mesoscale program were processed by two methods. The method developed by the Bureau of Reclamation is based on criteria for determining significant points in a sounding. The soundings including baseline data were coded and placed on magnetic tape, and processed on the Bureau of Reclamation computer in Denver following the field program.

The second method used to process the soundings was a method developed at Texas A&M University as part of NASA's Atmospheric Variability Experiments in which data are extracted from the sounding records for every pressure contact and later interpolated to 25-mb intervals. The contact data provides the greatest accuracy and resolution possible for the rawinsonde system, while the 25-mb data generally provides more resolution than the significant point data provided by the Bureau of Reclamation method. The significant point method is essentially the same as used by the National Weather Service and is adequate for most purposes.

Data for the soundings processed at Texas A&M University were placed on magnetic tape and a data report prepared (Scoggins, 1977). The 25-mb data were used in the analysis presented in this report.

3.1.3 National Weather Service Radar

Radar data obtained from the National Weather Service station at Midland consisted of the operators log and PPI overlays at approximately 20-min intervals during periods when significant convective activity existed. Information was provided on areal extent of the echoes, movement, intensity, and height. The PPI charts were digitized by overlaying a grid and coding the echoes for each grid point as a function of height. If an echo appeared within one half a grid distance from a grid point,

a code was assigned to that grid point of either 1, 2, or 3. A code of 1 represents an echo whose height did not exceed 6.1 km (20,000 ft), a 2 was used for echoes whose height was between 6.1 and 9.1 km (20,000 and 30,000 ft), while a 3 was used to denote an echo exceeding an altitude of 9.1 km (30,000 ft). These data were keypunched and used in this report to locate convective echoes.

3.2 Data Inventory for 1977

Surface data were collected each day during the period May 31-July 12, 1977, while sounding data were collected on 16 days during this period. Some instrumentation difficulties were encountered which resulted in the loss of some surface and sounding data. A complete description and presentation of all surface and sounding data were presented by Scoggins (1977). Results are presented in this report for all days on which consecutive soundings were made at all four stations as well as a number of days when only surface data were obtained.

4. METHODS OF DATA ANALYSIS

4.1 Gridding of Data

An objective analysis scheme developed by Barnes (1964) was used to interpolate the HIPLEX surface data to an 18 x 18 grid (Fig. 4.1.1) with approximately a 16-km spacing between grid points. The analysis scheme operates by making successive corrections to a "first guess field" (usually a constant value over the network) and results in a Fourier representation of the variables after gridding. Each grid point in the array was also assigned a terrain height from a standard topographic map and an analysis of the terrain (hundreds of feet) is also shown in Fig. 4.1.1.

In addition to the HIPLEX mesoscale surface stations (two letter station identifiers), data from surrounding National Weather Service and Air Force stations (three letter station identifiers) were used in the surface analyses (stations shown in Fig. 4.1.1). Only the four rawinsondes (Midland, Big Spring, Robert Lee, and Post) were used in the upper air analyses but these data were not gridded. The four basic variables objectively analyzed onto the grid surface were temperature, mixing ratio, and the "u" and "v" wind components. All other surface parameters were computed from these basic fields.

The "scanning radius" of influence around each input station was specified for the objective analysis program based upon the station spacing at the surface. The final gridded fields contained features and systems consistent with the spatial and temporal resolution of the input data. A comparison between these fields and carefully hand analyzed fields was used to "fine tune" the gridding program.

4.2 Surface

The basic meteorological variables were objectively gridded onto the 18 x 18 array each hour of every day for 43 consecutive days starting May 31, 1977 and ending July 12, 1977. These gridded variables were used to approximate the parameters that follow by using centered difference computations over two grid distances and applied to the center point.

4.2.1 Velocity Divergence

Surface wind velocity divergence was calculated using the expression

$$\vec{\nabla}_2 \cdot \vec{\nabla}_2 = \frac{\partial u}{\partial x} + \frac{\partial v}{\partial y} \approx \frac{u_2 - u_1}{2\Delta x} + \frac{v_2 - v_1}{2\Delta y}$$

where it is understood that all expressions refer to surface variables and

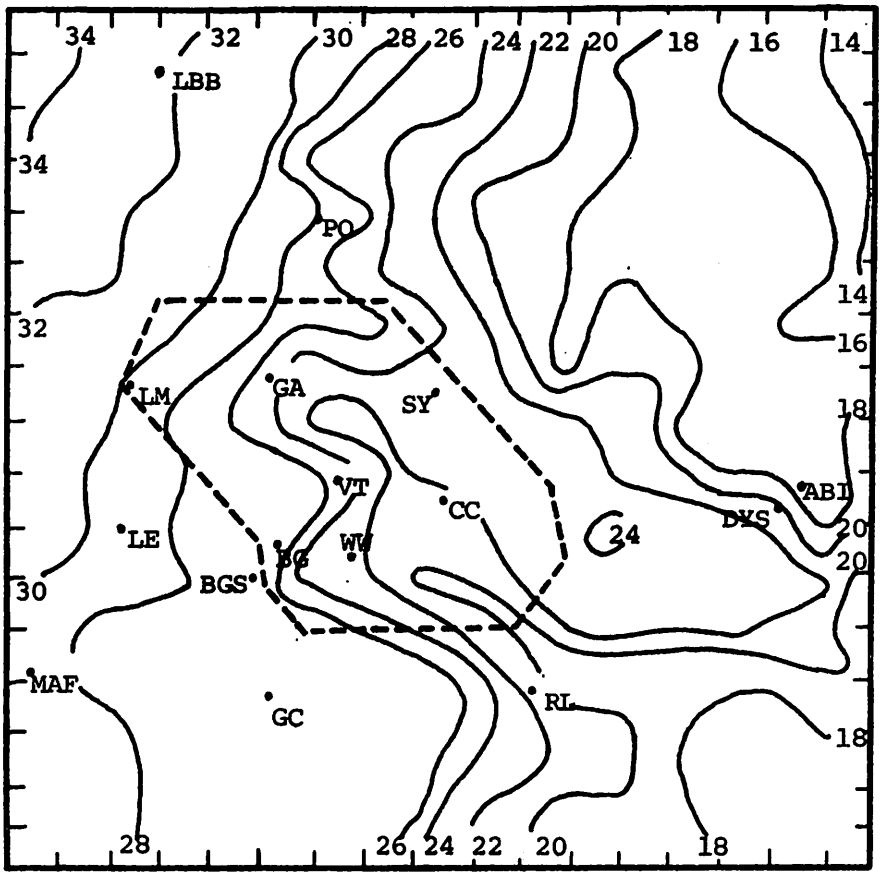

Fig. 4.1.1 Analysis of terrain heights (hundreds of feet) drawn from computer-gridded data. The grid is indicated by tick marks.

have their usual meteorological meanings. The subscripts "1" and "2" are grid point values surrounding the "center point" and in the positive direction, respectively, and $\Delta x=\Delta y=16$ km.

4.2.2 Moisture Divergence

Surface moisture divergence was computed by use of the expression

$$\vec{\nabla}_2 \cdot q\vec{v}_2 = \frac{\partial(qu)}{\partial x} + \frac{\partial(qv)}{\partial y} \simeq \frac{q_2u_2 - q_1u_1}{2\Delta x} + \frac{q_2v_2 - q_1v_1}{2\Delta x} .$$

The subscripts have the same meaning as above, and all computed values were applied to the center point.

4.2.3 Vertical Motion

In computing vertical motion 50 mb above the surface, both terrain-induced vertical motion and velocity divergence of the surface wind were considered. By assuming the surface wind field as representative of the

mean wind through a 50-mb deep layer above the surface, the equation of continuity in pressure coordinates

$$\vec{\nabla}_2 \cdot \vec{V}_2 = - \frac{\partial \omega}{\partial p}$$

can be integrated from the surface to the top of the 50-mb layer to give the vertical motion through the top of the layer. Thus,

$$\omega_{(P_s - 50\ mb)} = \omega_{P_s} + \int_{(P_s - 50\ mb)}^{P_s} (\vec{\nabla}_2 \cdot \vec{V}_2)\, dp$$

where $\omega = \frac{dp}{dt}$ and P_s is the surface pressure. The magnitude of ω_{P_s} can be approximated by the terrain-induced vertical motion

$$w_T = u\left(\frac{\partial h}{\partial x}\right) + v\left(\frac{\partial h}{\partial y}\right) \simeq \frac{u(h_2 - h_1)}{2\Delta x} + \frac{v(h_2 - h_1)}{2\Delta y}$$

where h is the terrain height. For the range of surface temperatures and pressures in the Texas HIPLEX area

$$w_T(cm\ s^{-1}) = -\omega_{P_s}(\mu b\ s^{-1}).$$

Therefore, the resultant vertical motion at 50 mb above the surface was calculated using the expression

$$\omega_{(P_s - 50\ mb)} = -w_T + (\vec{\nabla}_2 \cdot \vec{V}_2)\Delta p$$

where Δp = 50 mb.

4.2.4 Vertical Flux of Moisture

The vertical flux of moisture is given by the product of the vertical velocity 50 mb above the ground (cm s^{-1}), the surface mixing ratio, and air density. Units are g $cm^{-2} s^{-1}$.

4.2.5 Vorticity

The vorticity of the surface wind was calculated using the expression

$$\vec{\nabla}_2 \times \vec{V}_2 = \frac{\partial v}{\partial x} - \frac{\partial u}{\partial y} \simeq \frac{v_2 - v_1}{2\Delta x} - \frac{u_2 - u_1}{2\Delta y}$$

where subscripts have the same meaning as before.

4.3 Upper-Level Kinematic Parameters

The data analysis procedures used for the 1977 data are somewhat different

from those used in 1976 but the end product is the same. The final result for the upper-level kinematic calculations is still a single vertical profile of a given parameter representing the average environmental conditions over the network bounded by the triangle from Midland (MAF) to Post (PO) to Robert Lee (RL). Test comparisons between kinematic calculations made on 1976 data using both data analysis techniques showed only negligible differences.

4.3.1 Horizontal Velocity Divergence

For a given time period and pressure surface, the horizontal velocity divergence was computed by use of the expression

$$\vec{\nabla}_p \cdot \vec{v}_2 = \frac{1}{A}\frac{dA}{dt} \simeq \frac{1}{\bar{A}}\frac{\Delta A}{\Delta t}$$

where A is the horizontal triangular area determined from the three rawinsonde balloon locations (MAF, PO, and RL) projected onto a constant pressure surface, $\bar{A}$ is the average area of the triangle between two pressure surfaces 50 mb apart, and ΔA is the change of triangular area that occurs as the balloons move through a pressure layer 50 mb thick in time Δt.

4.3.2 Horizontal Moisture and Mass Divergence

Horizontal moisture and mass divergence were determined using the vector identity

$$\vec{\nabla}_p \cdot C\vec{v}_2 = \vec{v}_2 \cdot \vec{\nabla}_p C + C\vec{\nabla}_p \cdot \vec{v}_2$$

(1) (2) (3)

where C is any scalar. For moisture and mass divergence, q (mixing ratio) and ρ (air density) were used in place of C. Then term 2 was computed by the centered finite difference formula

$$\vec{v}_2 \cdot \vec{\nabla}_p C = u\frac{\partial C}{\partial x} + v\frac{\partial C}{\partial y} \simeq \bar{u}\frac{(C_2 - C_1)}{\Delta x} + \bar{v}\frac{(C_2 - C_1)}{\Delta y}$$

where $\bar{u}$ and $\bar{v}$ are the average wind components over the network along a pressure surface and $\frac{C_2 - C_1}{\Delta x}$ and $\frac{C_2 - C_1}{\Delta y}$ are the horizontal vector components of the gradient of C in the "x" and "y" directions, respectively. Term 3 was calculated by multiplying C (an average for the pressure surface) by the horizontal velocity divergence computed previously. Since the velocity divergence represents a 50-mb layer mean value, term 2 was actually computed

as a mean horizontal advection by averaging data from three 25-mb data levels constituting the 50-mb layer used in the velocity divergence calculation.

4.3.3 Vertical Motion

Vertical motion was computed on constant pressure surfaces using the formula

$$(\omega_p)_k = \omega_s + \sum^{k} \overline{(\vec{V}_p \cdot \vec{V}_2)}_k (\Delta p)$$

where $(\omega_p)_k$ is vertical velocity on a constant pressure surface k, ω_s is the vertical velocity at the ground (set to "0"), $\overline{(\vec{V}_p \cdot \vec{V}_2)}_k$ is the 50-mb layer mean divergence below layer k, and Δp = 50 mb.

4.4 Energetics

4.4.1 Total Energy Budget

The budget of total energy (kinetic, internal, and gravitational potential) per unit volume is given by

$$\rho \frac{dQ}{dt} = \frac{\partial}{\partial t} \rho \left(\frac{V^2}{2} + gz + c_v T\right) + \vec{\nabla} \cdot \rho \vec{V} \left(\frac{V^2}{2} + gz + c_p T\right) + \frac{\partial}{\partial p} \rho \omega \left(\frac{V^2}{2} + gz + c_p T\right) - \rho \vec{V} \cdot \vec{F}.$$

In this equation $\frac{V^2}{2}$ is kinetic energy, gz the gravitational potential energy, $c_v T$ the internal energy, $c_p T$ the enthalpy or sensible heat, $\vec{F}$ the frictional force, all per unit mass, and Q the heat added by diabatic processes. Other symbols have the standard meteorological meanings.

The above equation written in integral form in the x, y, p, t system is

$$\frac{1}{g} \int \frac{dQ}{dt} dV = \frac{1}{g} \int \frac{\partial}{\partial t} \left(\frac{V^2}{2} + gz + c_v T\right) dV + \frac{1}{g} \int \vec{\nabla} \cdot \left(\frac{V^2}{2} + gz + c_p T\right) \vec{V} \, dV + \frac{1}{g} \int \frac{\partial}{\partial p} \left(\frac{V^2}{2} + gz + c_p T\right) \omega \, dV - \frac{1}{g} \int \vec{V} \cdot \vec{F} \, dV.$$

This is the form of the equation evaluated in this research.

Diabatic heating can be evaluated from the first law of thermodynamics

in the form

$$\frac{dQ}{dt} = c_p \frac{\partial T}{\partial t} + c_p \vec{V} \cdot \vec{\nabla} T + \left(c_p \frac{\partial T}{\partial p} - \alpha\right)\omega.$$

The net effect of the various forms of diabatic heating such as evaporation/condensation, radiation, and sensible heat transfer is obtained from this equation in integral form.

4.4.2 Latent Heat Energy Budget

The budget of latent heat energy is given by

$$\frac{\partial}{\partial t}(\rho L q) + \vec{\nabla} \cdot (\rho L q \vec{V}) + \frac{\partial}{\partial p}(\rho L q \omega) = R$$

where L is the latent heat of vaporization and q is specific humidity. All other symbols have their usual meaning. The term on the right of this equation represents evaporation and/or condensation and energy processes that cannot be resolved in time and/or space using the available input data and computational procedures. Since this term is computed as a residual, some error from the remaining terms is included as well. The sign of the residual in the above equation was changed from the 1976 analysis (Scoggins et al; 1978). This change in sign has been taken into account in the interpretation of the residual.

The integral form of the latent heat energy budget in the x, y, p, t system is

$$\frac{1}{g} \int \frac{\partial}{\partial t}(Lq)\, dV + \frac{1}{g} \int \vec{\nabla} \cdot (Lq) \vec{V} dV + \frac{1}{g} \int \frac{\partial}{\partial p}(Lq\omega) = \int R dV$$

which is the form of the equation evaluated in this research.

4.4.3 Computational Procedures

The above equations were integrated vertically to obtain the energy balance of each atmospheric layer. The friction term in the first equation was not evaluated in this study. Values of all other terms were computed as averages per unit volume through a depth of 50 mb and horizontally covering the area bounded by the MAF-PO-RL triangle. A description of the method of computing vertical motion has been given earlier in this report. Terms were evaluated at the surface and at 50-mb intervals from 850 mb to 100 mb. Vertical integration was performed over 50-mb intervals except in the lowest layer which extended from the surface (about 920 mb) to 850 mb. The trapezoidal

rule was used for integration purposes.

4.4.4 Interpretation of Results

Accuracy of the energy budget terms is an important consideration. Again, it is difficult to estimate accuracy without introducing errors in the input data and observing the results. While this has not been done so far, values of the energy budget terms show reasonable vertical consistency and time continuity. Recent results by Vincent and Chang (1975) and Kornegay and Vincent (1976) indicated that random errors in input data do not affect seriously the results of synoptic-scale kinetic energy studies.

Kung and Tsui (1975) described the interpretation which should be given to energy budgets obtained from subsynoptic-scale data. They noted that energy processes can be strongly influenced by the presence of nearby convective cells but that features due to the larger scales of motion are not filtered out. They suggested that the type of energy budgets computed in this study "should be taken as the energy budget computed with sub-synoptic-scale network data."

The hydrostatic assumption, used in computing radiosonde data, is a potential source of distortion during times of convective activity. A few sondes are thought to have entered severe updrafts or downdrafts during the Texas HIPLEX 1977 program and have been identified for use in data analysis and interpretation.

4.5 Water Vapor Budget

The equation for the continuity of water substance can be expressed as

$$\int \frac{\partial(q\rho a)}{\partial t} dV + \int (q\rho_a V_n) dS + \int (q\rho_a \omega) dA = R$$

where:

q is mixing ratio,

ρ_a is density of the air,

V_n is the component of the horizontal velocity that is normal to the surface S,

ω is vertical velocity,

V is volume,

A is the horizontal area, and

R is a residual representing the sources and sinks of moisture (evaporation, condensation, precipitation, and turbulent flux of moisture through the boundaries).

The terms in this equation from left to right represent: The local rate-of-change or the net gain or loss of water vapor within the volume; the transport of water vapor through the lateral boundaries; the transport of water vapor through the vertical boundaries; and the residual. All terms in this equation except the residual were evaluated at 50-mb intervals over the triangle formed by Robert Lee-Post-Midland.

4.6 Composite Surface Analysis

The analyses of surface variables for each day and hour were stratified by several criteria to determine relationships between each variable and radar echoes. Variables considered were velocity divergence, moisture divergence, vertical motion 50 mb above the surface, and the vertical flux of moisture 50 mb above the surface. Contingency tables and frequency distributions were prepared for various categories of convective echoes.

5. RESULTS

In this section, figures are labeled in either Central Daylight Time (CDT) or Greenwich Mean Time (GMT), although GMT is used in the text. GMT is obtained by adding five hours to CDT.

5.1 1 June 1977

5.1.1 Radar

Radar charts for this day are shown in Fig. 5.1.1.1. Echoes with tops less than 6.1 km (20K ft) were observed at the first two observation times in the southeast corner of the area. No echoes were observed during the remainder of the period.

5.1.2 Surface

Radar charts (Fig. 5.1.1.1) show echoes with tops less than 6.1 km (20K ft) moving from the area by 1700 GMT. Surface temperature fields (Fig. 5.1.2.1), associated with observed radar echoes, show a region of cool air which moderates in time due to the effects of surface heating and mixing. A pattern of high surface mixing ratio (Fig. 5.1.2.2) develops over the southeastern corner of the network at 0200 GMT, which is also reflected by the surface equivalent potential temperature (Fig. 5.1.2.3). A check of the original data at Colorado City was made to insure the validity of these results.

Terrain-induced vertical motion (Fig. 5.1.2.4) remained small, with a negligible contribution to the kinematic vertical velocity computed from surface velocity divergence (Fig. 5.1.2.5). Vertical motion 50 mb above the surface (Fig. 5.1.2.6), surface moisture divergence (Fig. 5.1.2.7), and vertical flux of moisture 50 mb above the surface (Fig. 5.1.2.8) all show definite changes in their patterns associated with the observed echoes. Large centers of convergence at the surface correlates with vertical motions aloft. Following the movement of the echoes, fields of surface vorticity (Fig. 5.1.2.9) show several anticyclonic centers which diminish in time. A center of low sea level pressure (Fig. 5.1.2.10) is also associated with the movement of these echoes, which is also reflected in the surface pressure change (Fig. 5.1.2.11). Pressure changes for the remainder of the day are small.

5.1.3 Upper-Level Kinematic Parameters

Mass convergence below 700 mb at 1800 GMT was followed by mass divergence for all remaining periods through 0300 GMT (Fig. 5.1.3.1) as light

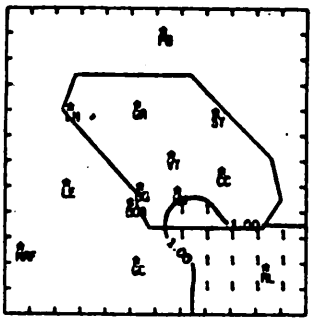

RADAR 6/1 /77 1000 CDT

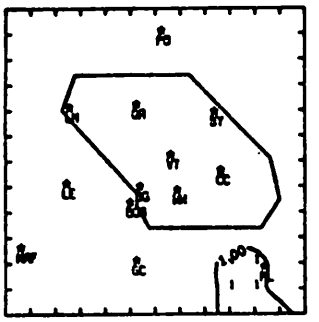

RADAR 6/1 /77 1100 CDT

NO ECHOES

RADAR 6/1 /77 1200 CDT

NO ECHOES

RADAR 6/1 /77 1300 CDT

NO ECHOES

RADAR 6/1 /77 1400 CDT

NO ECHOES

RADAR 6/1 /77 1500 CDT

NO ECHOES

RADAR 6/1 /77 1600 CDT

NO ECHOES

RADAR 6/1 /77 1700 CDT

NO ECHOES

RADAR 6/1 /77 1800 CDT

NO ECHOES

RADAR 6/1 /77 1900 CDT

NO ECHOES

RADAR 6/1 /77 2000 CDT

NO ECHOES

RADAR 6/1 /77 2100 CDT

NO ECHOES

RADAR 6/1 /77 2200 CDT

Fig. 5.1.1.1 Radar echoes for 1 June 1977.

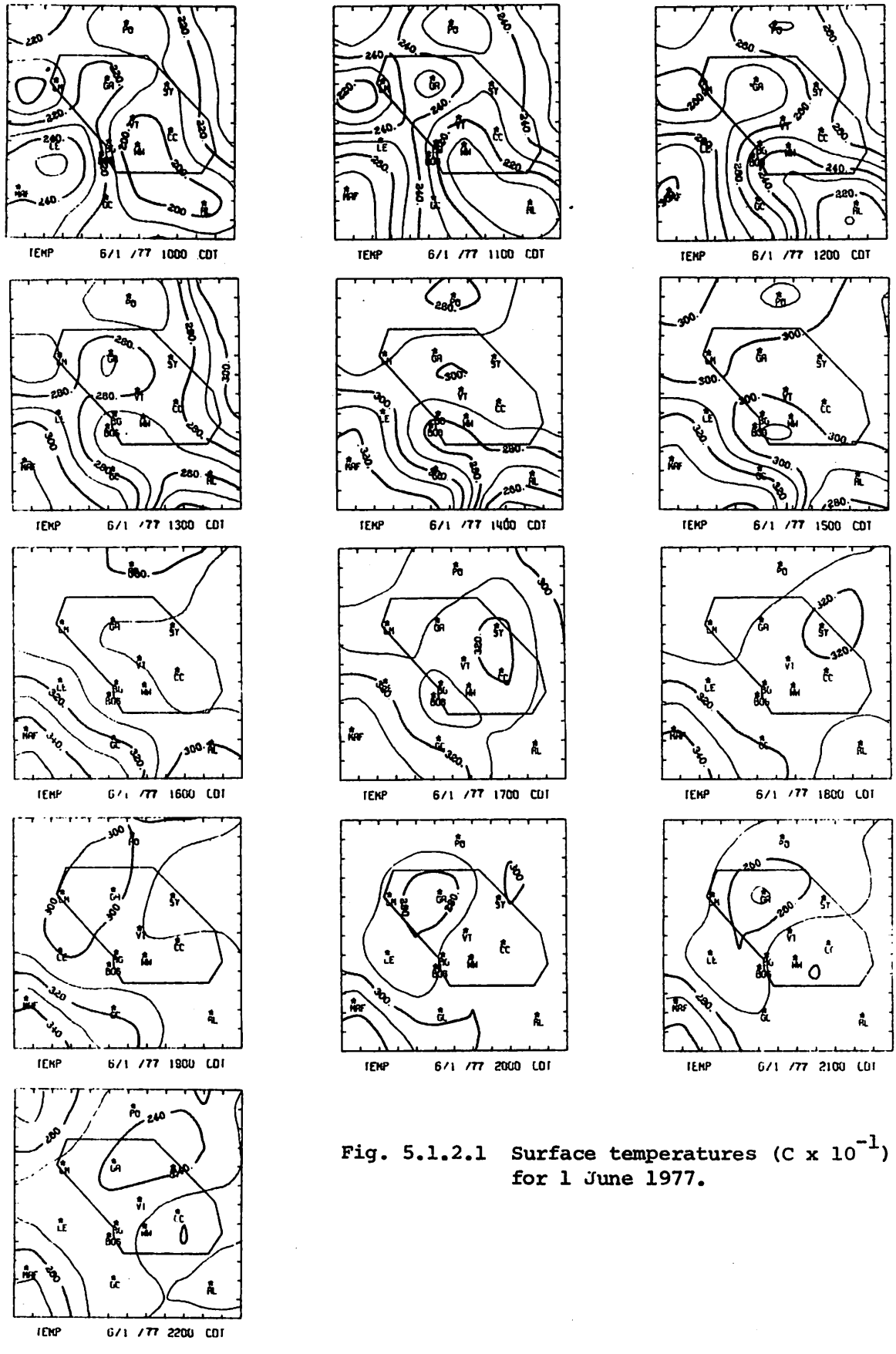

Fig. 5.1.2.1 Surface temperatures (C x 10^{-1}) for 1 June 1977.

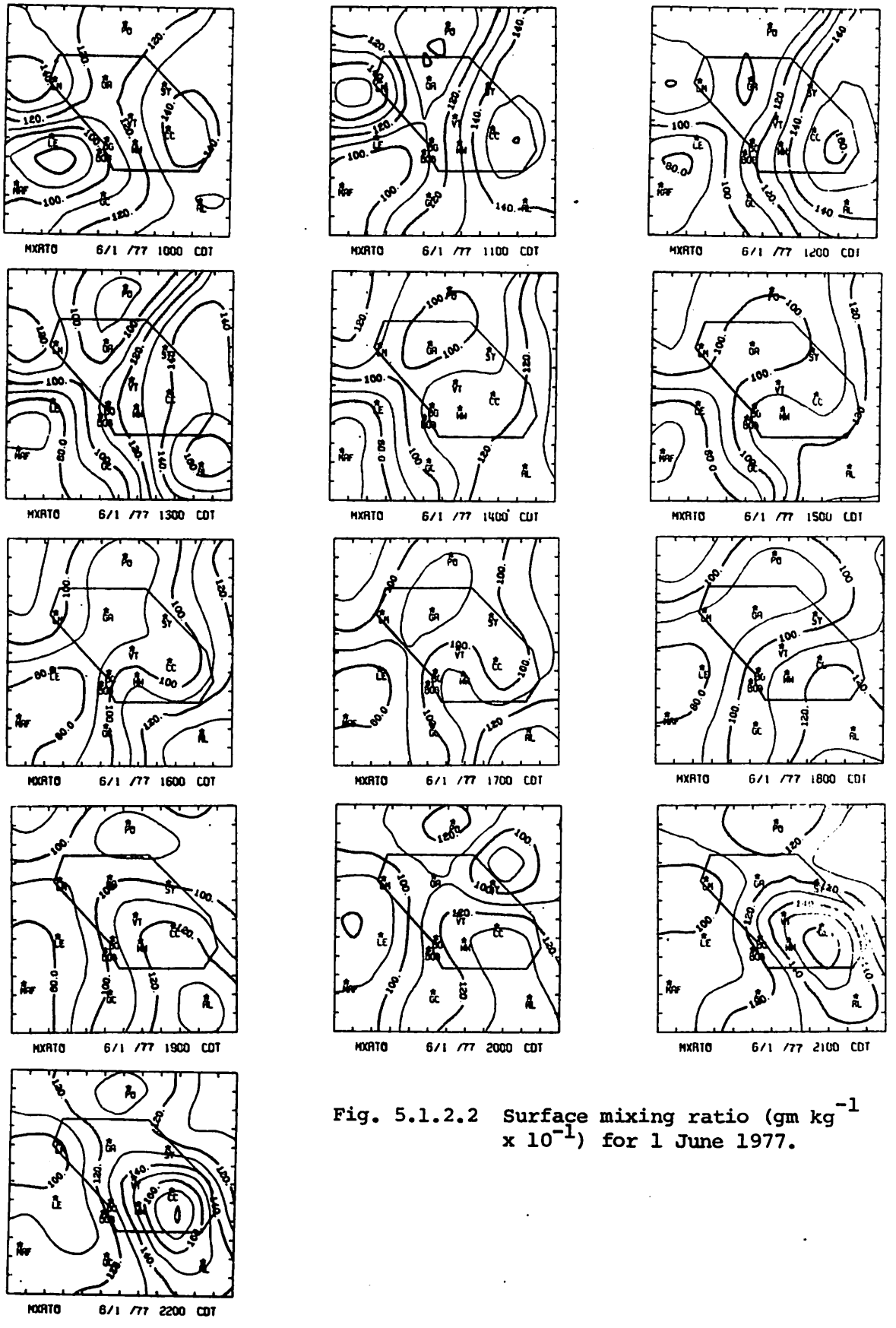

Fig. 5.1.2.2 Surface mixing ratio (gm kg^{-1} x 10^{-1}) for 1 June 1977.

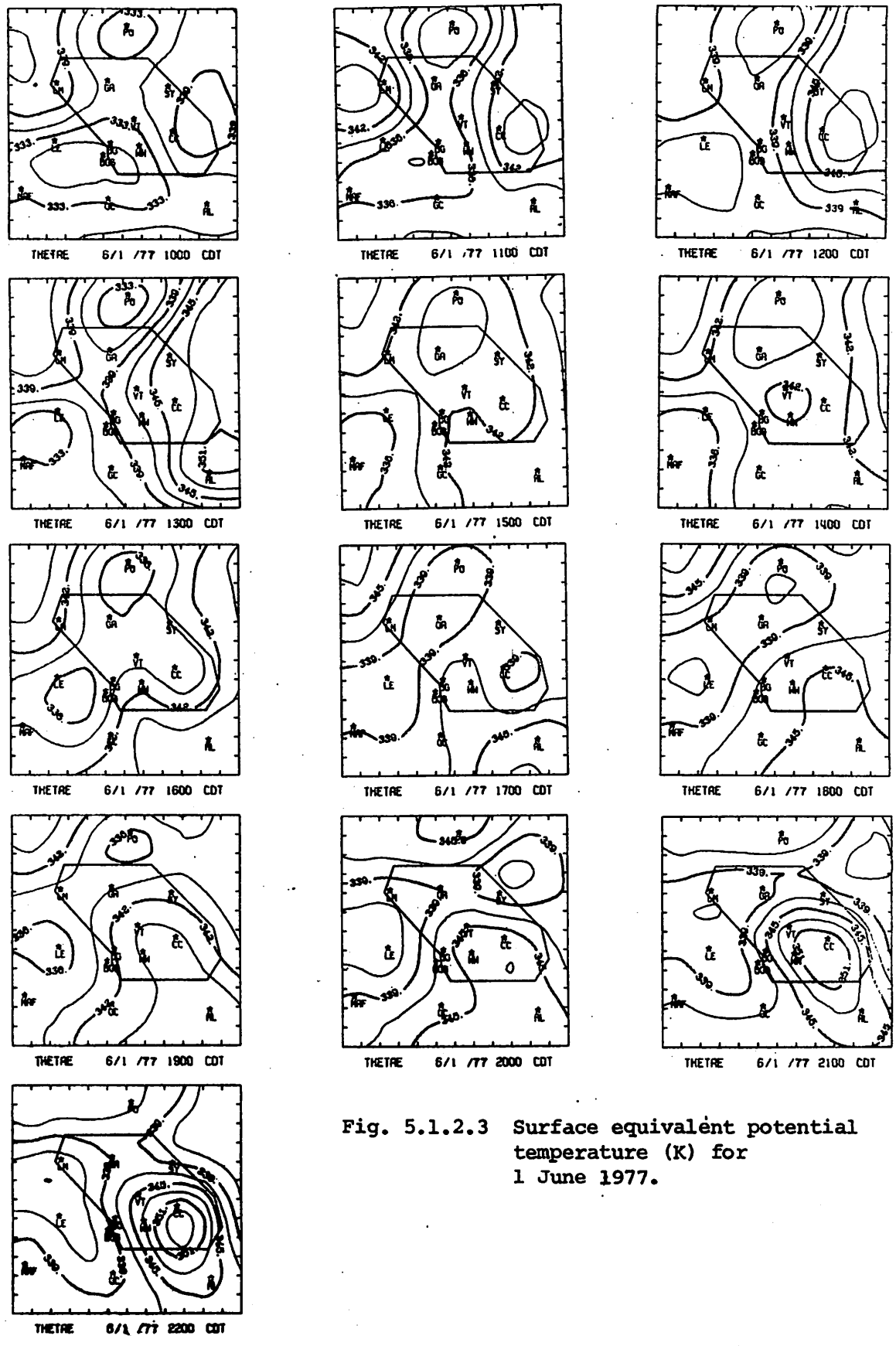

Fig. 5.1.2.3 Surface equivalent potential temperature (K) for 1 June 1977.

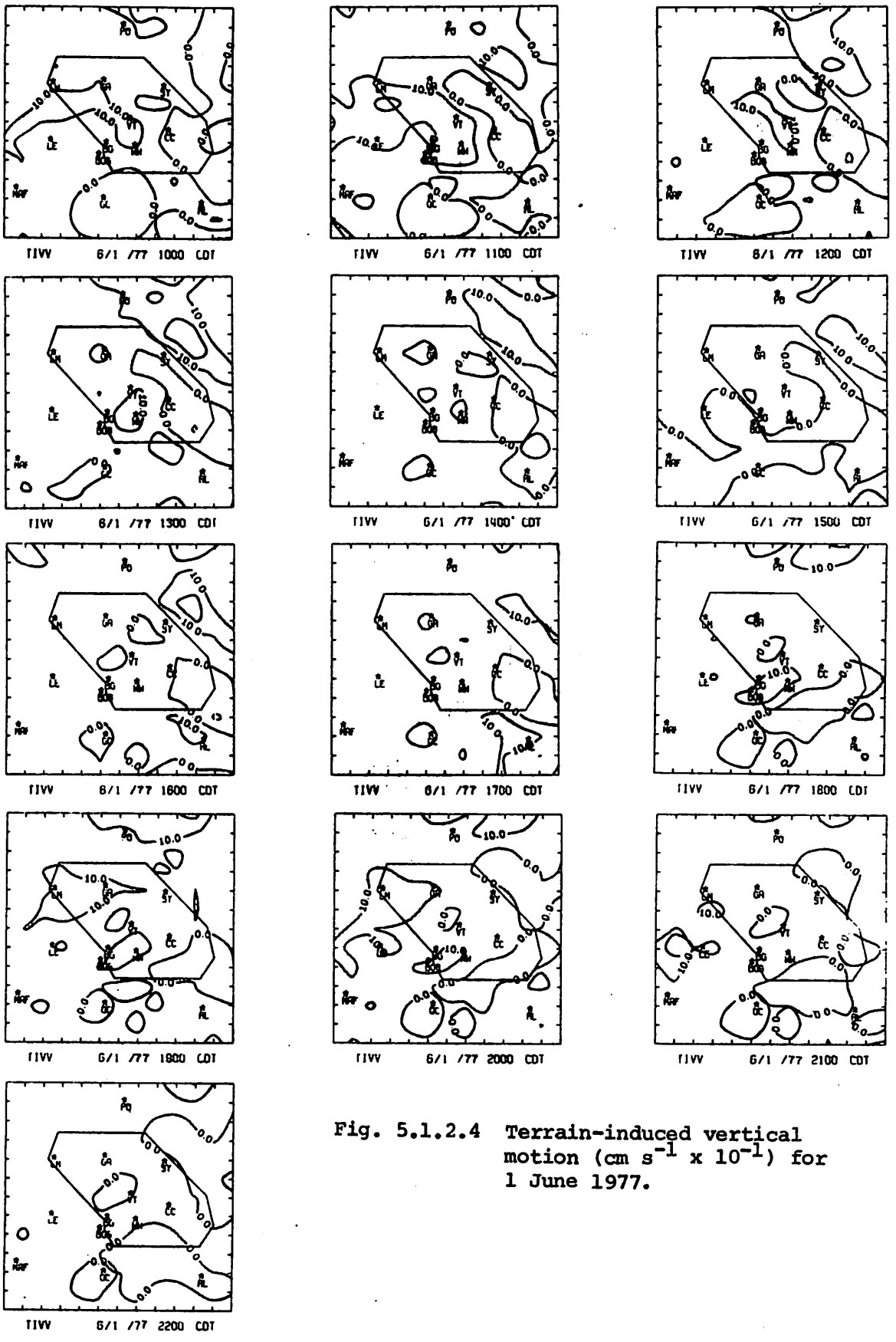

Fig. 5.1.2.4 Terrain-induced vertical motion (cm s^{-1} x 10^{-1}) for 1 June 1977.

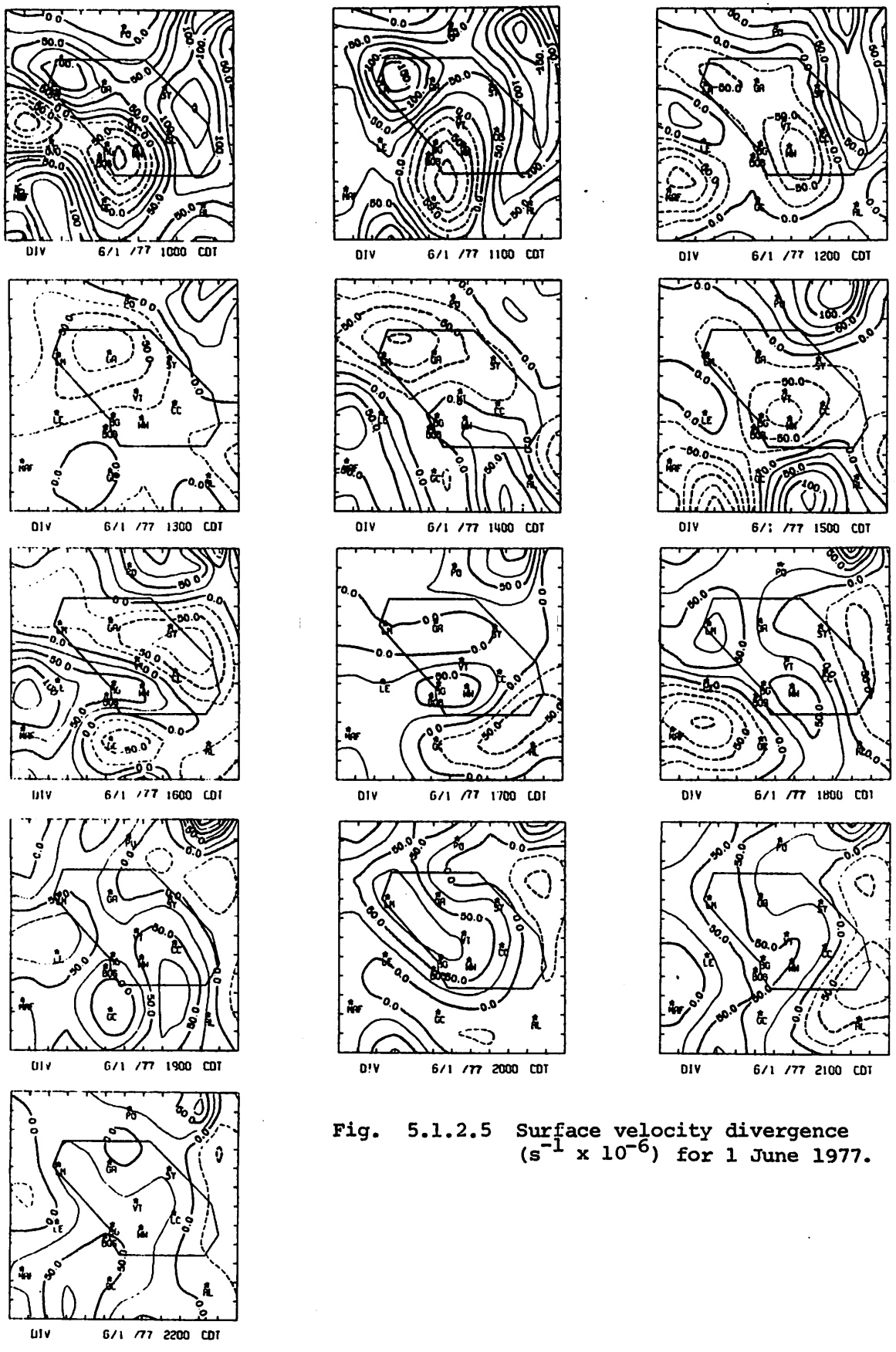

Fig. 5.1.2.5 Surface velocity divergence ($s^{-1} \times 10^{-6}$) for 1 June 1977.

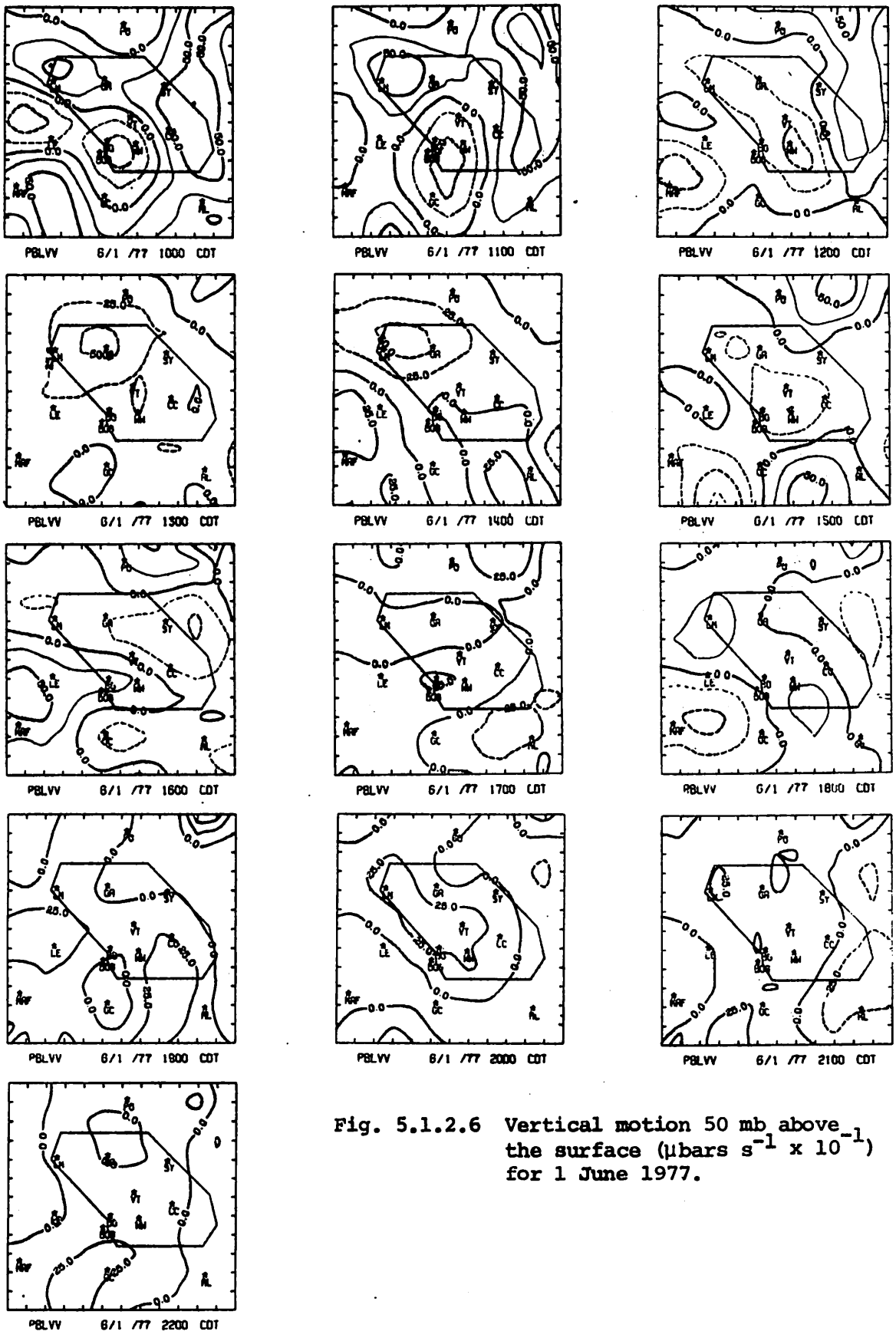

Fig. 5.1.2.6 Vertical motion 50 mb above the surface (μbars s^{-1} x 10^{-1}) for 1 June 1977.

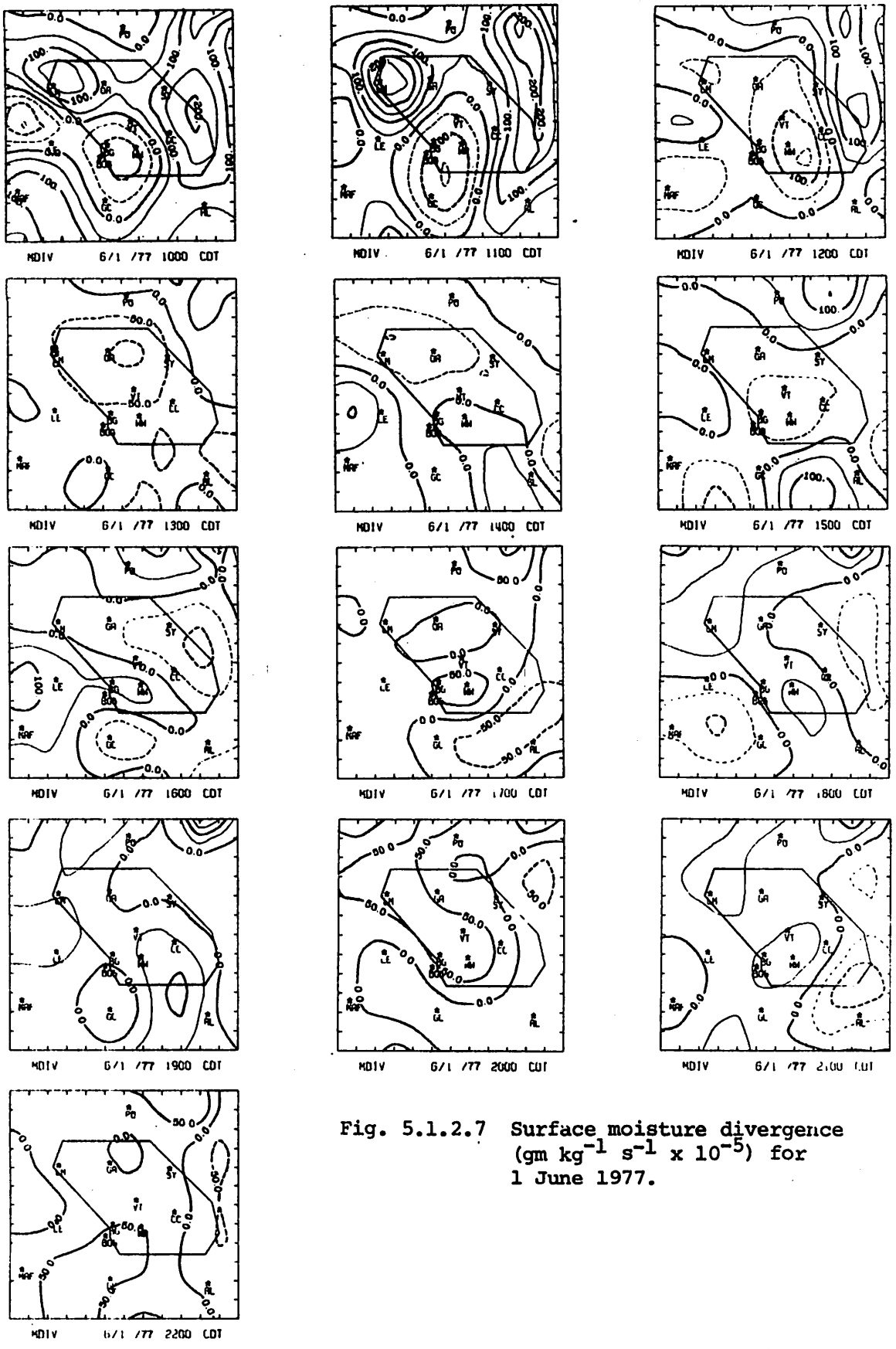

Fig. 5.1.2.7 Surface moisture divergence (gm kg^{-1} s^{-1} x 10^{-5}) for 1 June 1977.

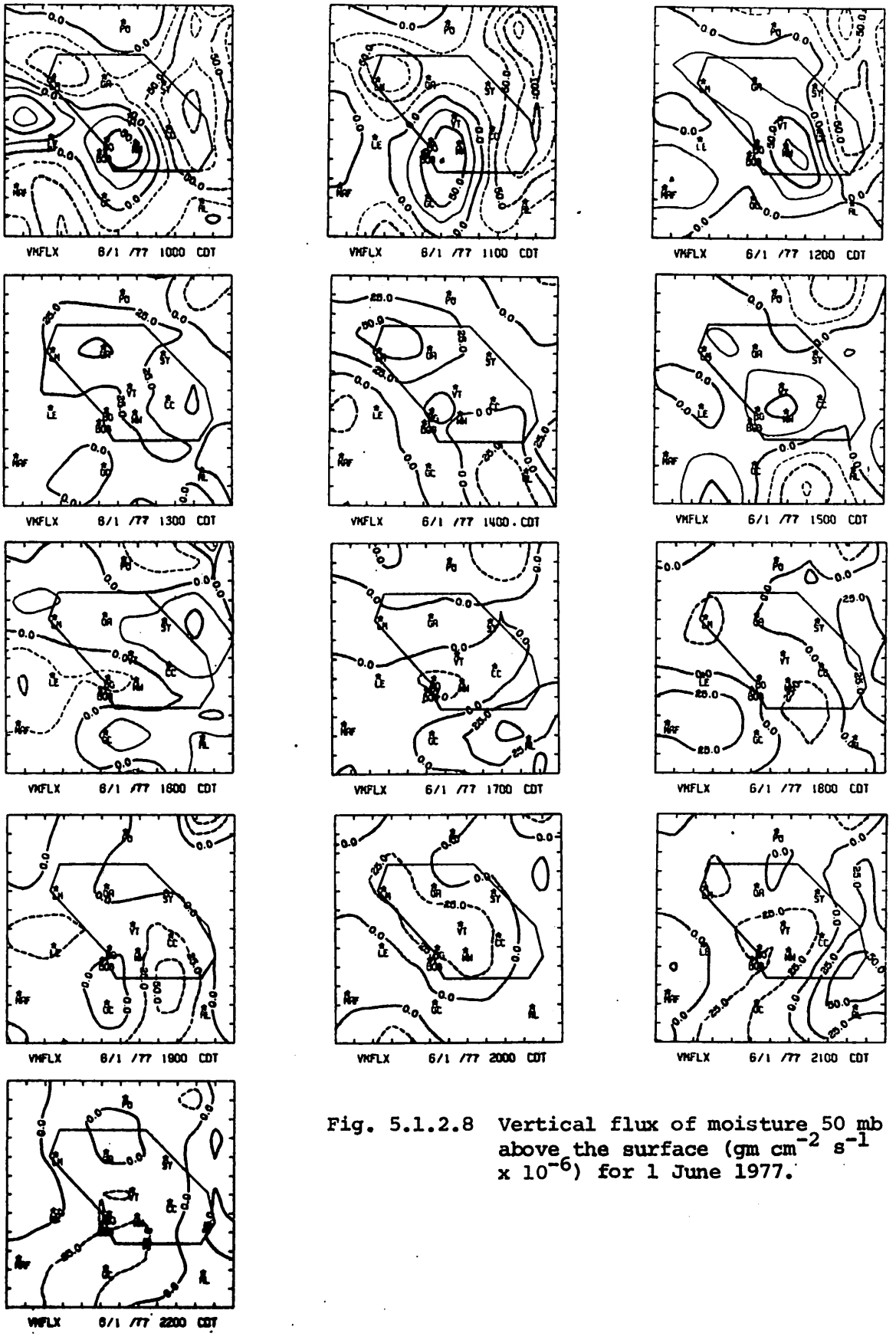

Fig. 5.1.2.8 Vertical flux of moisture 50 mb above the surface (gm cm^{-2} s^{-1} x 10^{-6}) for 1 June 1977.

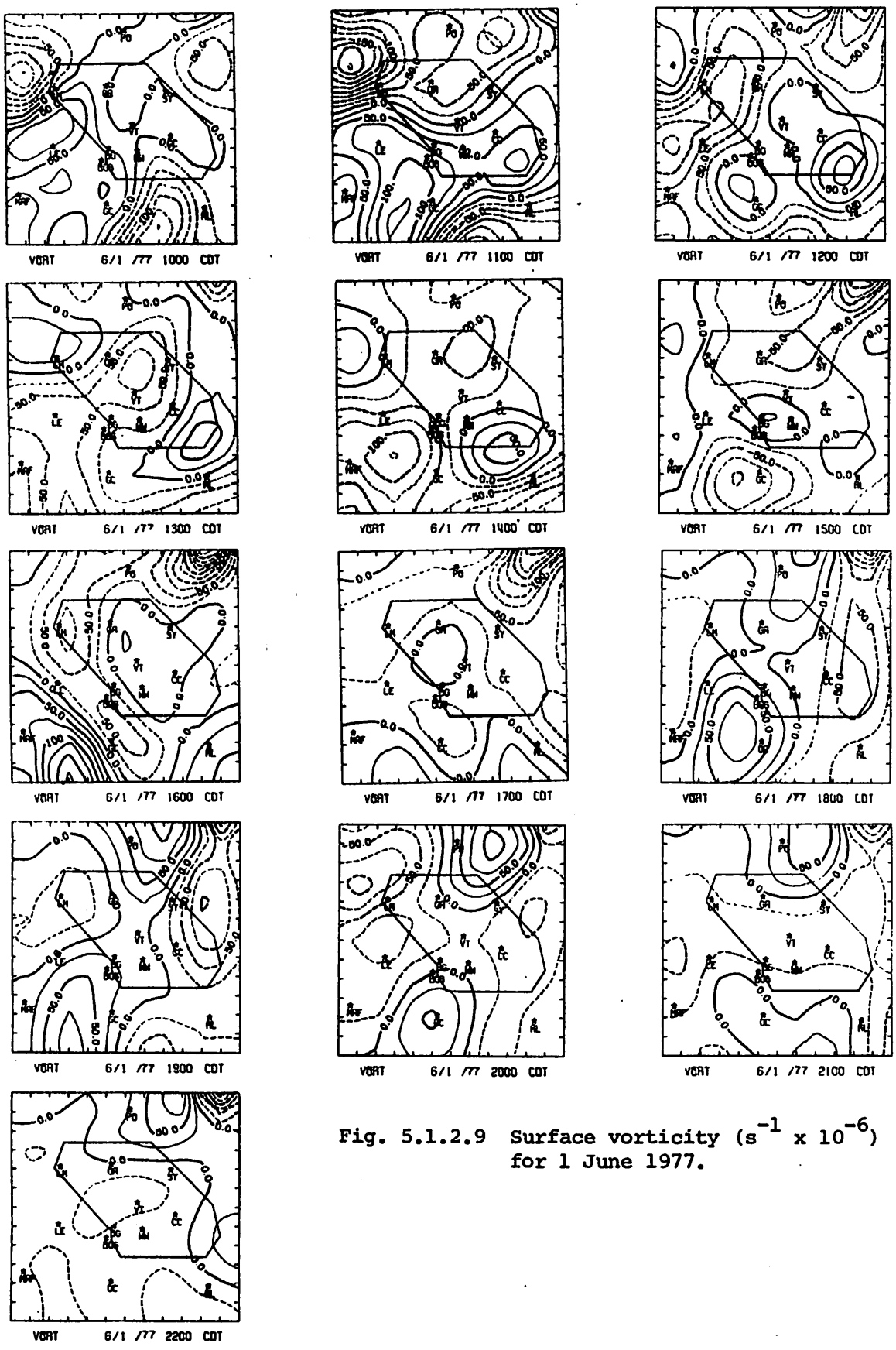

Fig. 5.1.2.9 Surface vorticity ($s^{-1} \times 10^{-6}$) for 1 June 1977.

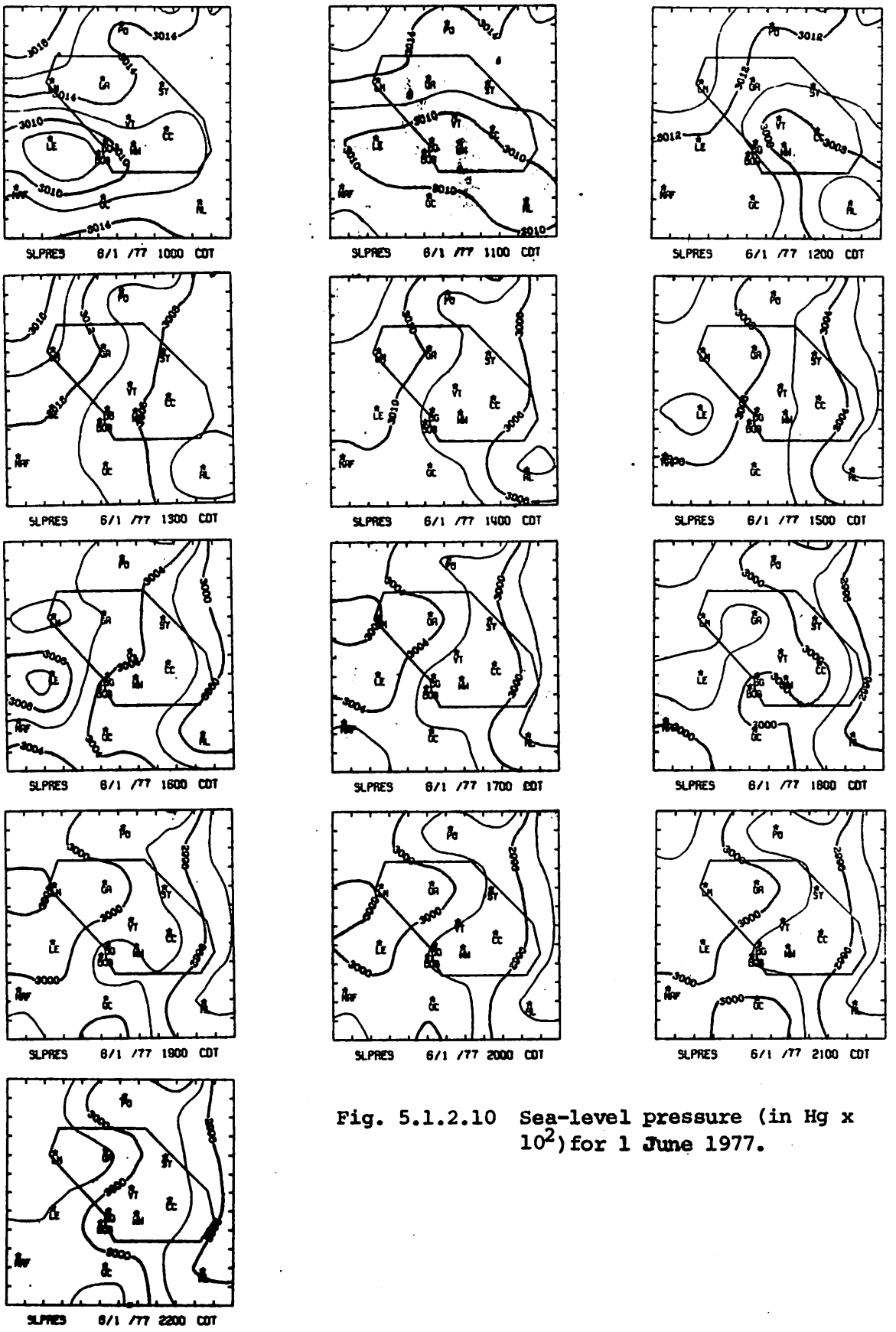

Fig. 5.1.2.10 Sea-level pressure (in Hg x 10^2) for 1 June 1977.

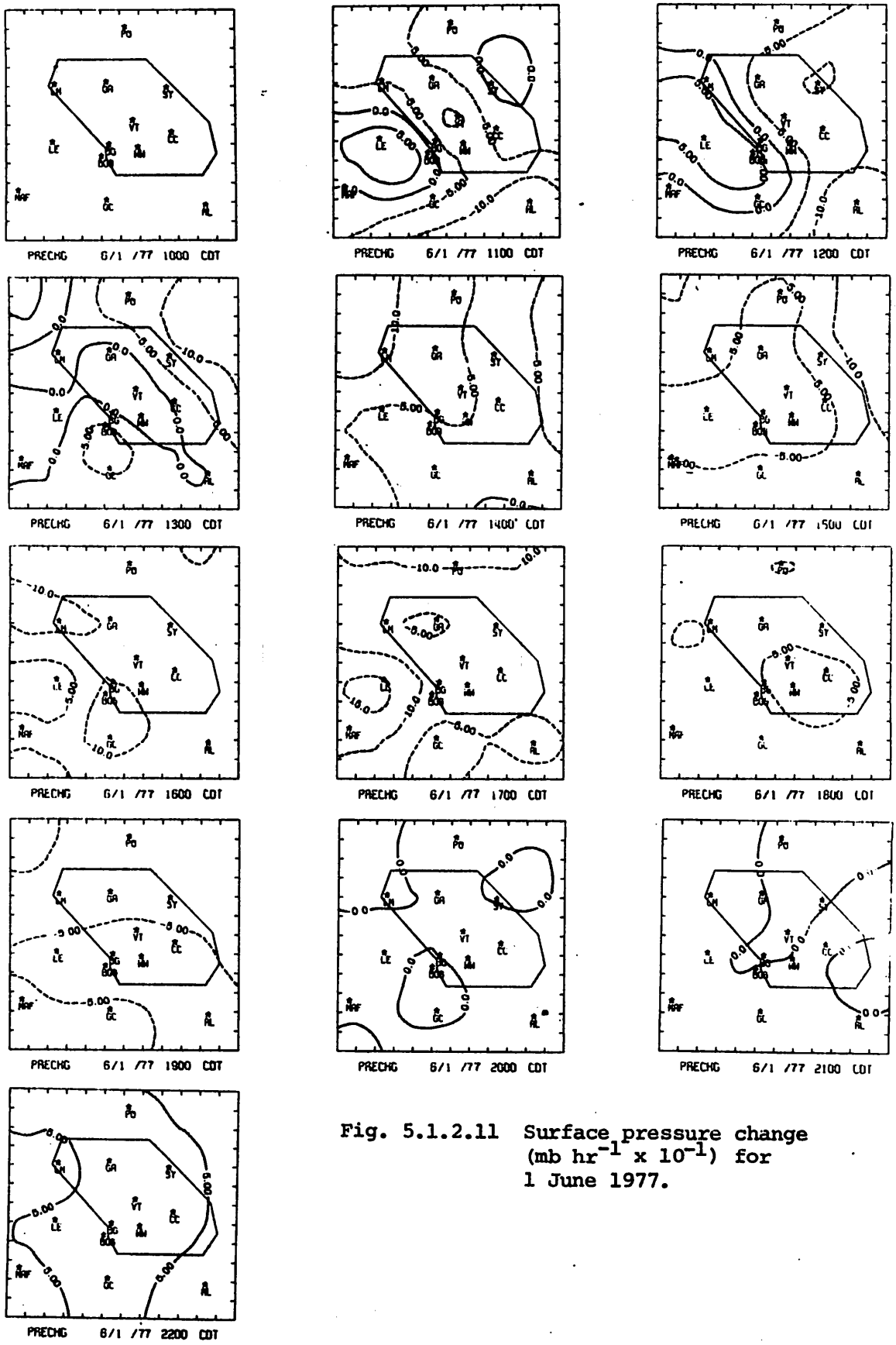

Fig. 5.1.2.11 Surface pressure change (mb hr^{-1} x 10^{-1}) for 1 June 1977.

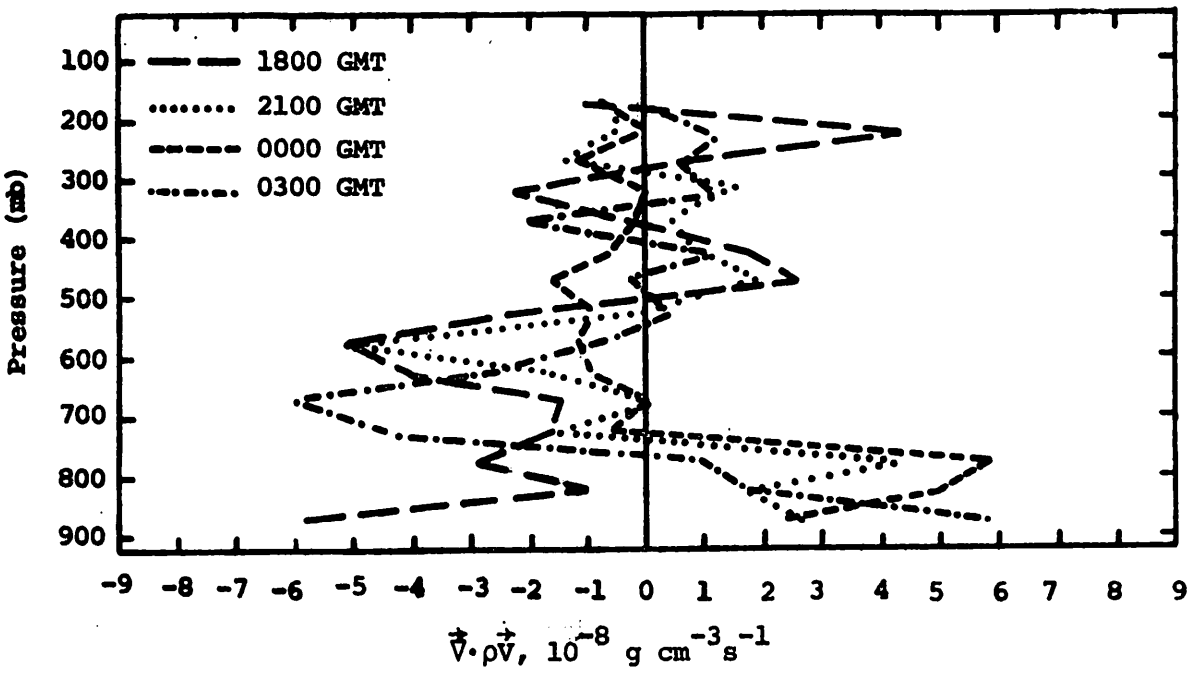

Fig. 5.1.3.1 Vertical profiles of mass divergence on 1 June 1977.

precipitation, observed before 1800 GMT, dissipated and no echoes developed through 0300 GMT. Mass convergence was present between 700 and 500 mb throughout the day and mass divergence was significant above 500 mb only at 1800 GMT.

Downward vertical velocities are the predominant feature in Fig. 5.1.3.2 except at 1800 GMT when strong upward values are present at all levels. The shift from upward to downward vertical velocities after 1800 GMT corresponds nicely to the dissipation of precipitation after 1800 GMT.

Moisture divergence occurred below 700 mb at all times except 1800 GMT when weak moisture convergence was observed (Fig. 5.1.3.3). Significant moisture convergence above 700 mb occurred at 1800 GMT and 0300 GMT between 700 and 400 mb. Relatively weak moisture convergence at 1800 GMT between 800 and 400 mb occurred when light precipitation was dissipating.

5.1.4 Energetics

Significant changes are observed in the budget of latent heat energy between 1800 GMT and 0300 GMT which was a period of rapid dissipation of precipitation. Net horizontal inflow of latent heat energy, extending from the surface up to 500 mb at 1800 GMT, is rapidly replaced by net horizontal outflow below 700 mb after 1800 GMT (Fig. 5.1.4.1). Vertical flux divergence of latent heat energy below 700 mb and flux convergence above to 300 mb at 1800 GMT is associated with an upward transport of latent energy into

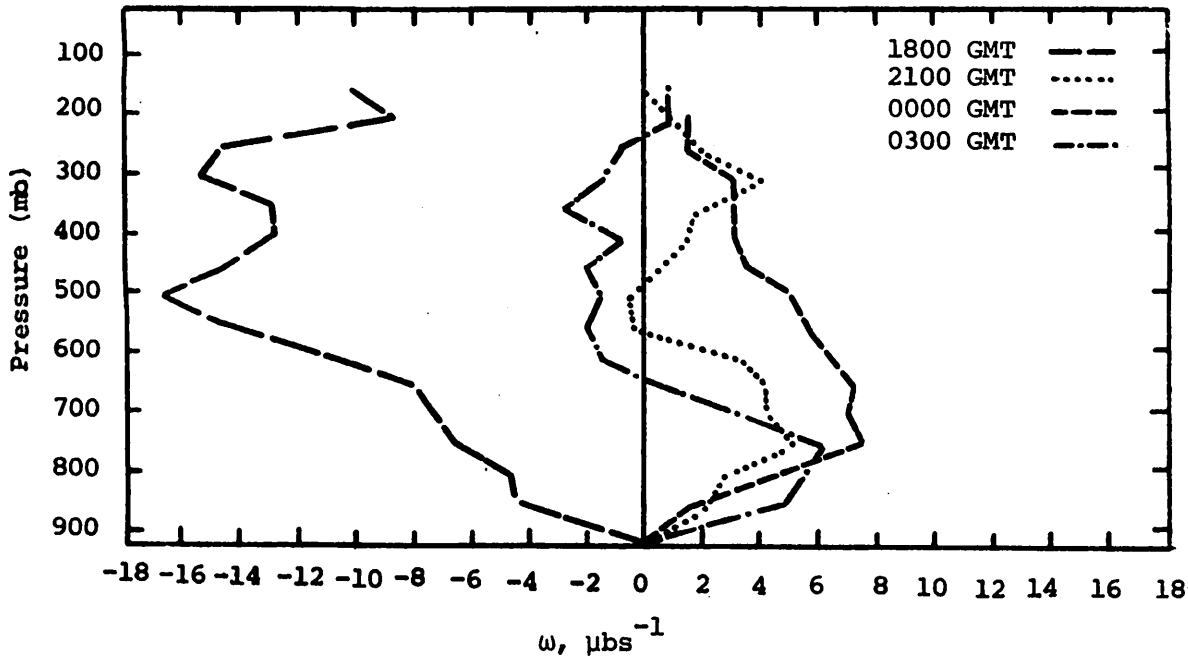

Fig. 5.1.3.2 Vertical profiles of vertical motion on 1 June 1977.

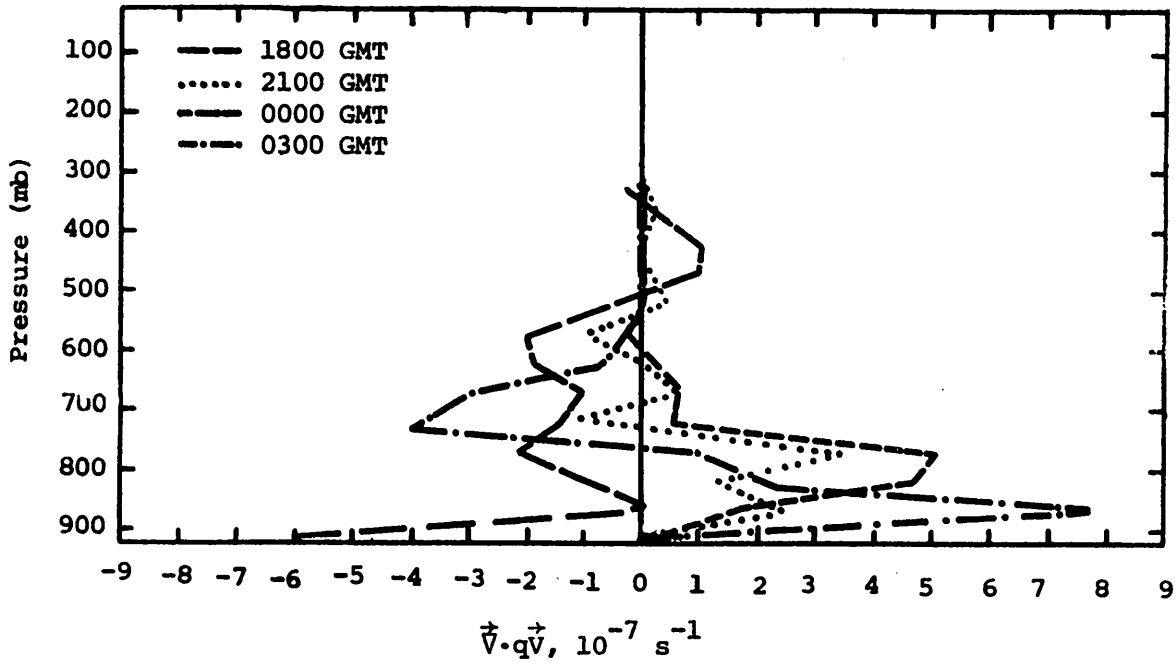

Fig. 5.1.3.3 Vertical profiles of moisture divergence on 1 June 1977.

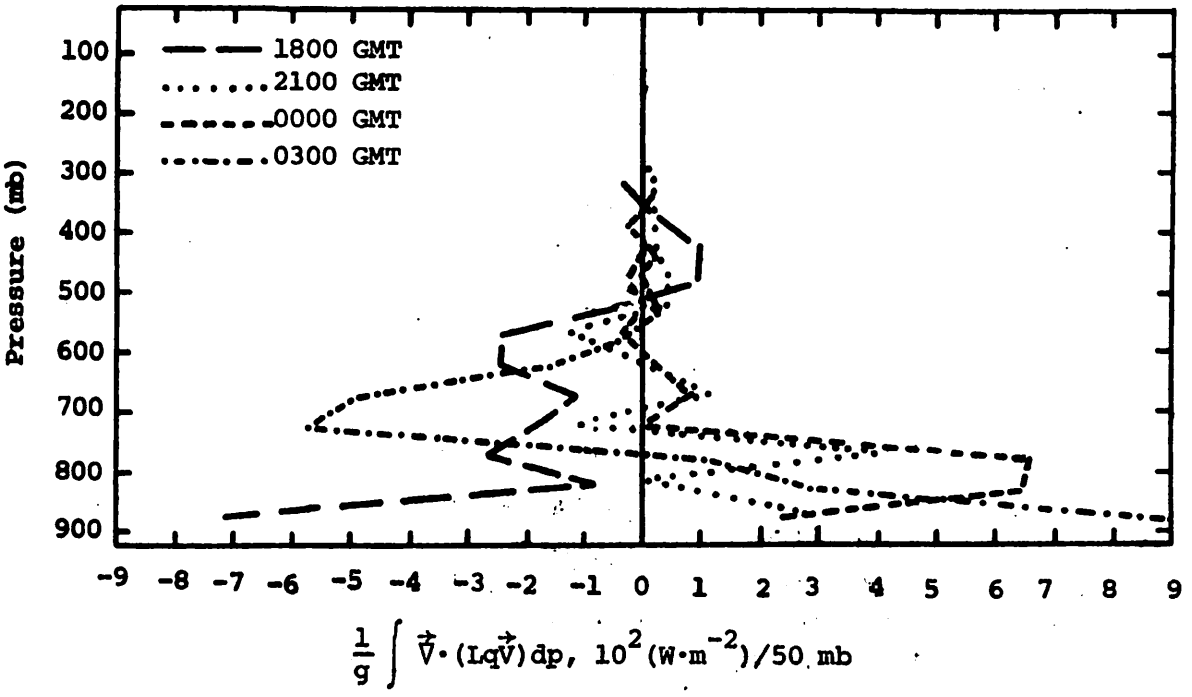

Fig. 5.1.4.1 Vertical profiles of the horizontal flux of latent heat energy on 1 June 1977.

the middle troposphere (Fig. 5.1.4.2). The reverse occurs after 1800 GMT as downward vertical velocities are associated with a net vertical flux convergence of latent heat energy below 700 mb and flux divergence above as downward transport of latent energy occurred. Local changes in latent heat energy were positive below 700, and negative between 700 and 300 mb only at 1800 and 2100 GMT (Fig. 5.1.4.3).

Figure 5.1.4.4 shows the vertical distribution of the residual of the latent heat energy equation (-R plotted). Positive values generally indicate condensation of liquid water or a loss of latent energy while negative values indicate evaporation of liquid water or a gain of latent energy. However, unresolved circulations created by small mesoscale (especially thunderstorms) and microscale systems plus error are also included in R so that a complete explanation of the term is difficult. The positive values at 1800 GMT are associated with loss of latent energy and environmental heating as condensation is occurring (especially in the mid-levels) within the upward vertical velocity field. Subsidence occurred afterwards and negative values were calculated as evaporation of precipitation and clouds increased the latent heat energy content and cooled the environment. This pattern is consistent with the dissipation of precipitation during the day and general improvement of weather conditions after 1800 GMT.

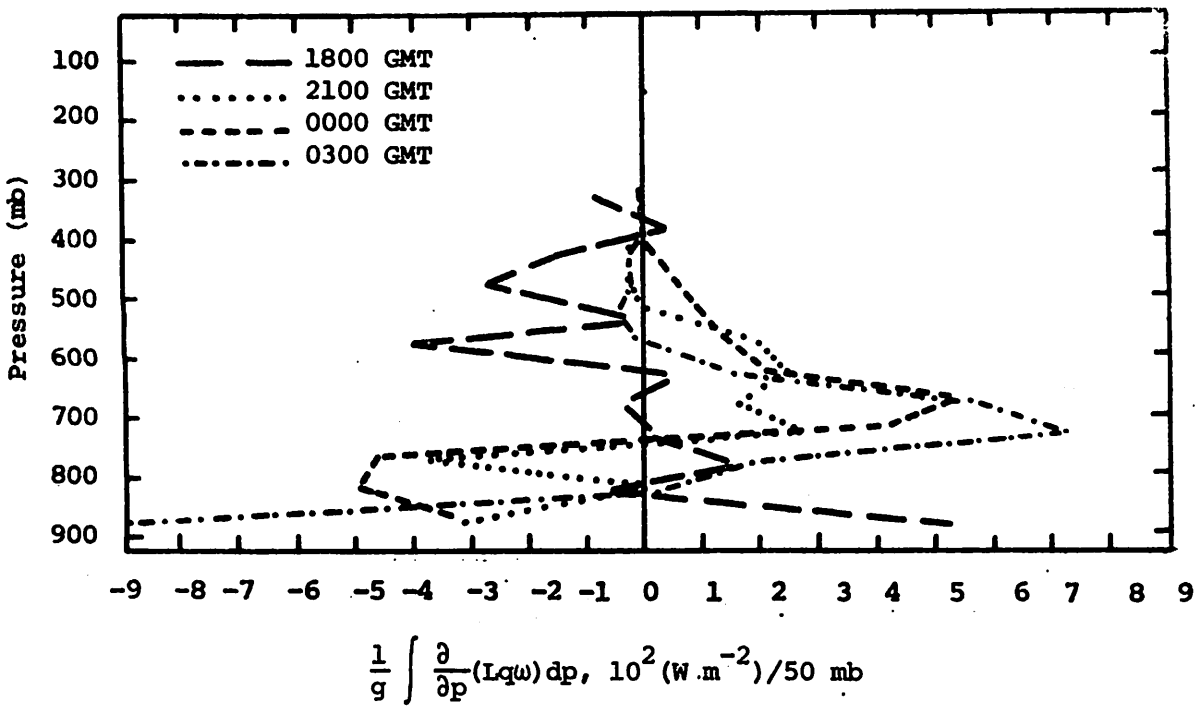

Fig. 5.1.4.2 Vertical profiles of the vertical flux of latent heat energy on 1 June 1977.

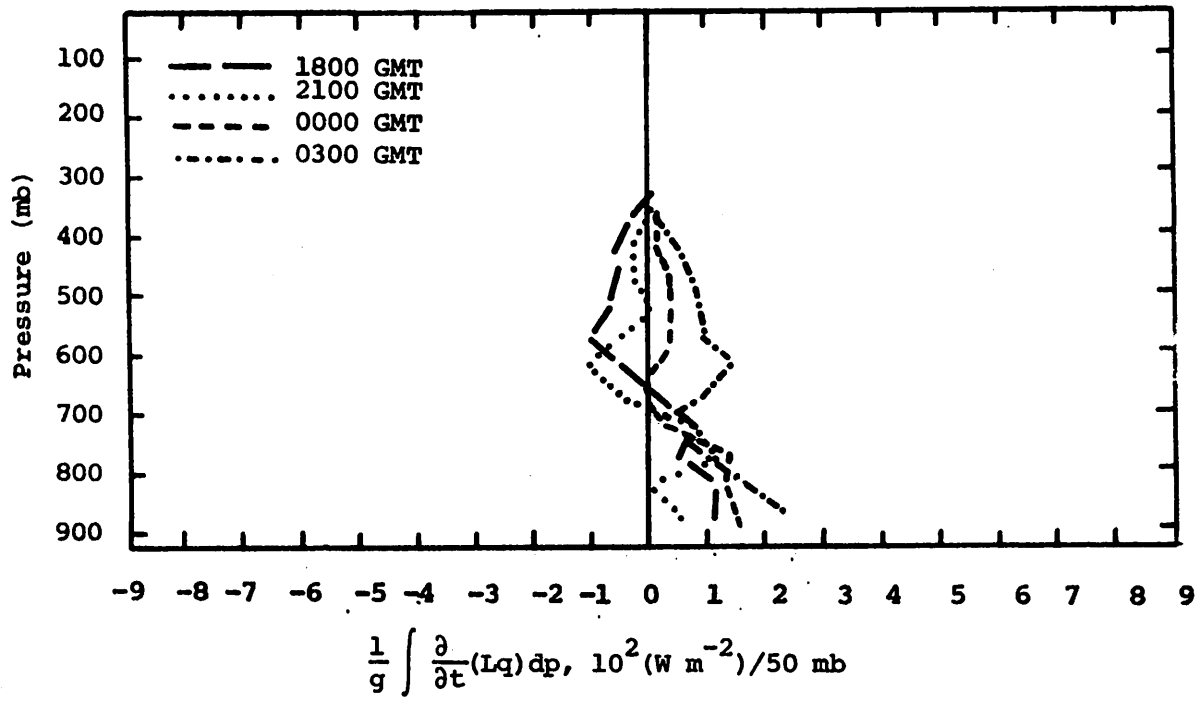

Fig. 5.1.4.3 Vertical profiles of the local change of latent heat energy on 1 June 1977.

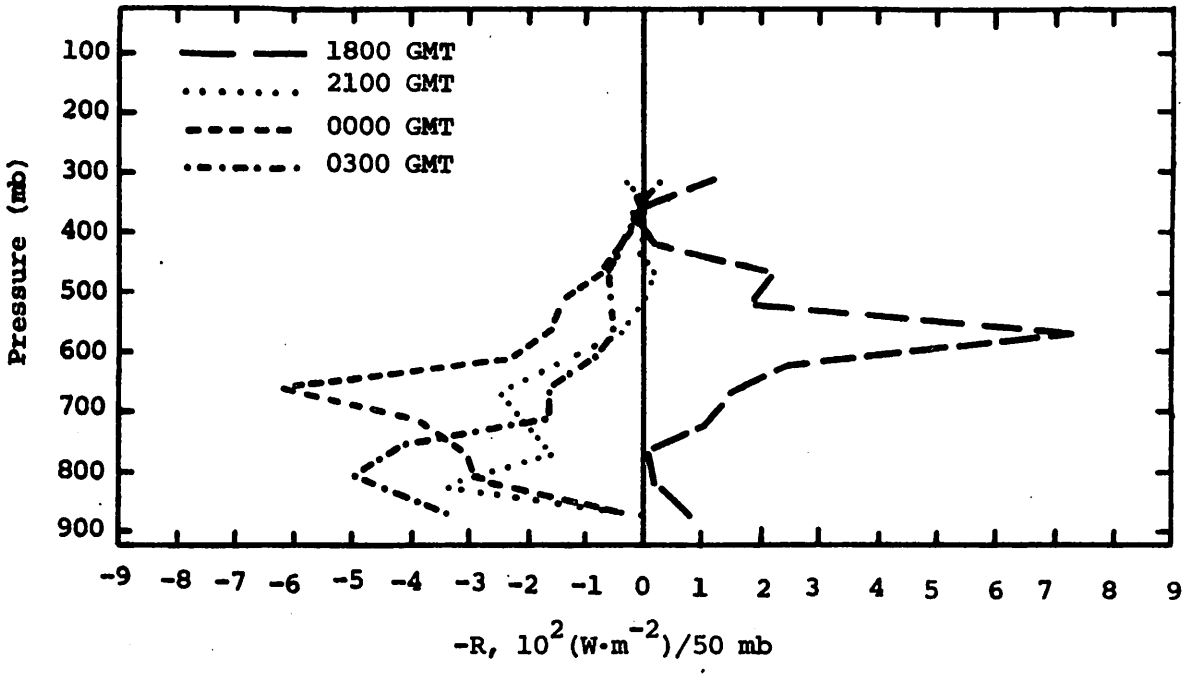

Fig. 5.1.4.4 Vertical profile of the residual of the latent heat energy equation on 1 June 1977.

Figure 5.1.4.5 shows the vertical profiles of diabatic heating (including the effects of condensation/evaporation, radiation, and unresolved circulations). Heating (positive values) was calculated at all levels at 1800 GMT consistent with the condensation and latent heat release seen previously. Generally, diabatic effects caused by radiational heating and cooling (especially below 800 mb) and diabatic cooling from evaporation were small after 1800 GMT.

Figures 5.1.4.6 and 5.1.4.7 show the horizontal and vertical flux divergence profiles, respectively, for kinetic energy. Net horizontal outflow was large only at 1800 GMT between 300 and 200 mb, while vertical flux convergence occurred between 500 and 300 mb and flux divergence was present above. Kinetic energy was being transported upwards and outwards in the mid- and upper-troposphere. After 1800 GMT the magnitude of each term became small except at 200 mb where both positive and negative flux divergence of kinetic energy occurred.

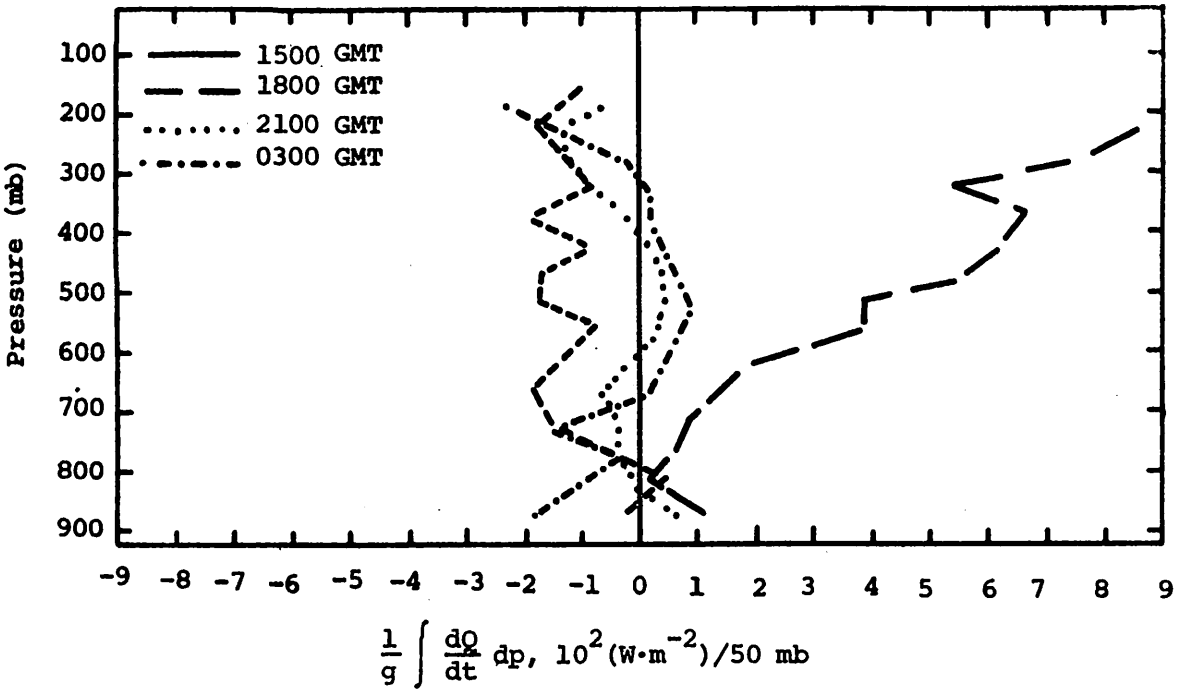

Fig. 5.1.4.5 Vertical profiles of diabatic heating computed from the first law of thermodynamics on 1 June 1977.

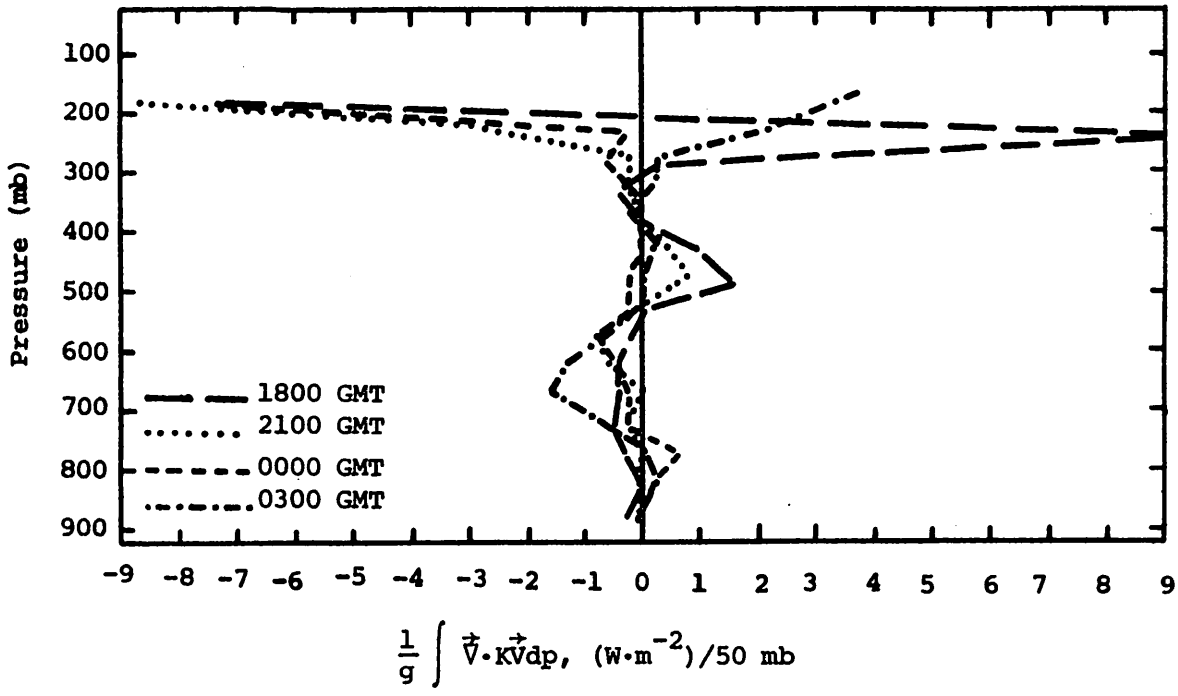

Fig. 5.1.4.6 Vertical profiles of the horizontal flux of kinetic energy on 1 June 1977.

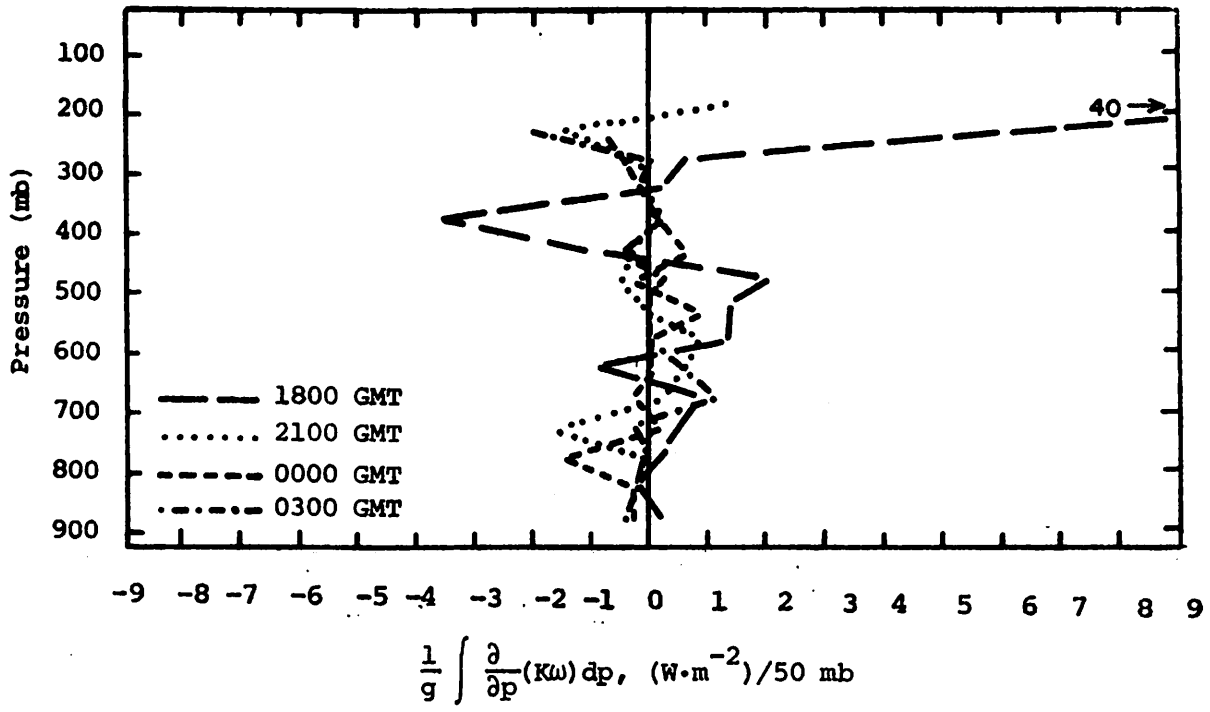

Fig. 5.1.4.7 Vertical profiles of the vertical flux of kinetic energy on 1 June 1977.

5.1.5 Water Vapor Budget

Radar charts (Fig. 5.1.1.1) show light convection located over the Southeast portion of the Texas HIPLEX area at 1500 GMT. This activity moved out by 1600 GMT, with no other echoes observed throughout the day.

Figure 5.1.5.1 shows vertical profiles of the net horizontal transport of water vapor. These profiles generally show a net inflow in layers up to 500 mb, and a net outflow in layers above. The 2100 GMT profile, however, shows a net outflow in most layers. A strong net outflow is also seen at 0000 and 0300 GMT for the lowest layers.

Figure 5.1.5.2 shows profiles of the net vertical transport of water vapor. The 1800 GMT profile shows moisture stratification in a series of layers between 750 and 500 mb. Such a stratification produces adjacent moist-dry layers, which eventually leads to vertical mixing. Profiles for 2100, 0000 and 0300 GMT all show a net outflow that reaches a maximum around 700 mb.

Figure 5.1.5.3 shows profiles of the vertical transport of water vapor through constant pressure surfaces. These profiles generally show a strong downward transport after 1800 GMT. Largest values are seen around 750 mb at 2100 and 0000 GMT. This is shown by a net inflow in lower layers for these times in Fig. 5.1.5.2. At 0300 GMT, upward transport is observed in layers above 650 mb.

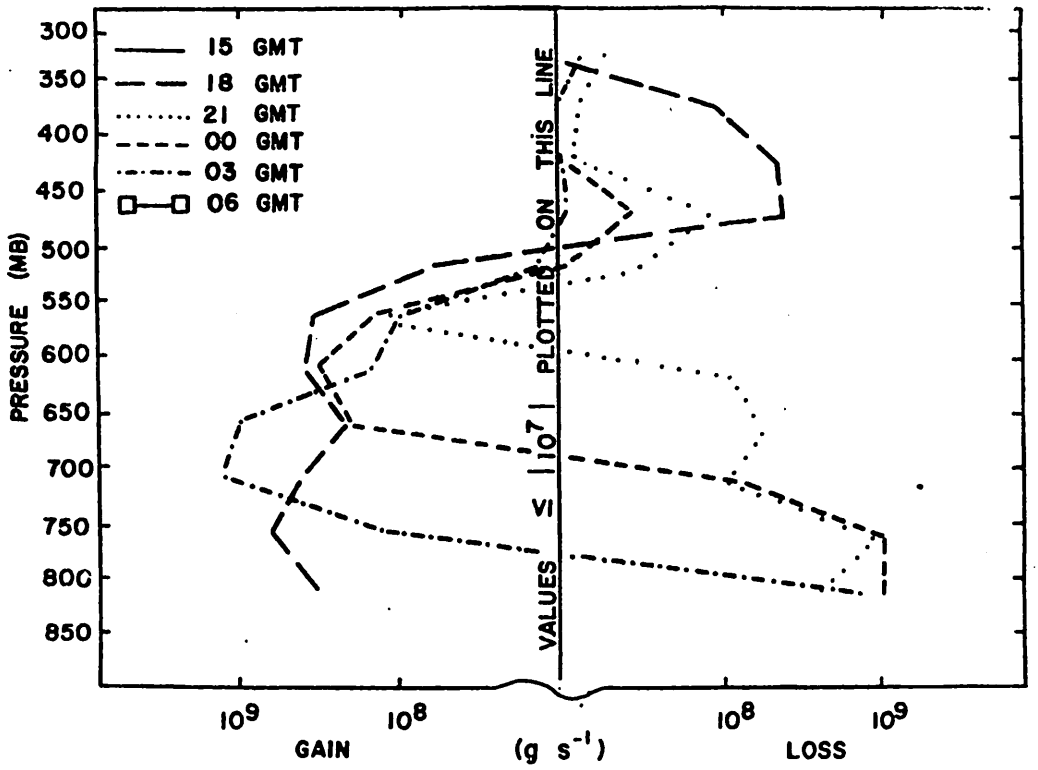

Fig. 5.1.5.1 Net horizontal transport of water vapor through boundaries of 50-mb layers (gm s^{-1}) over the Texas HIPLEX area for 1 June 1977.

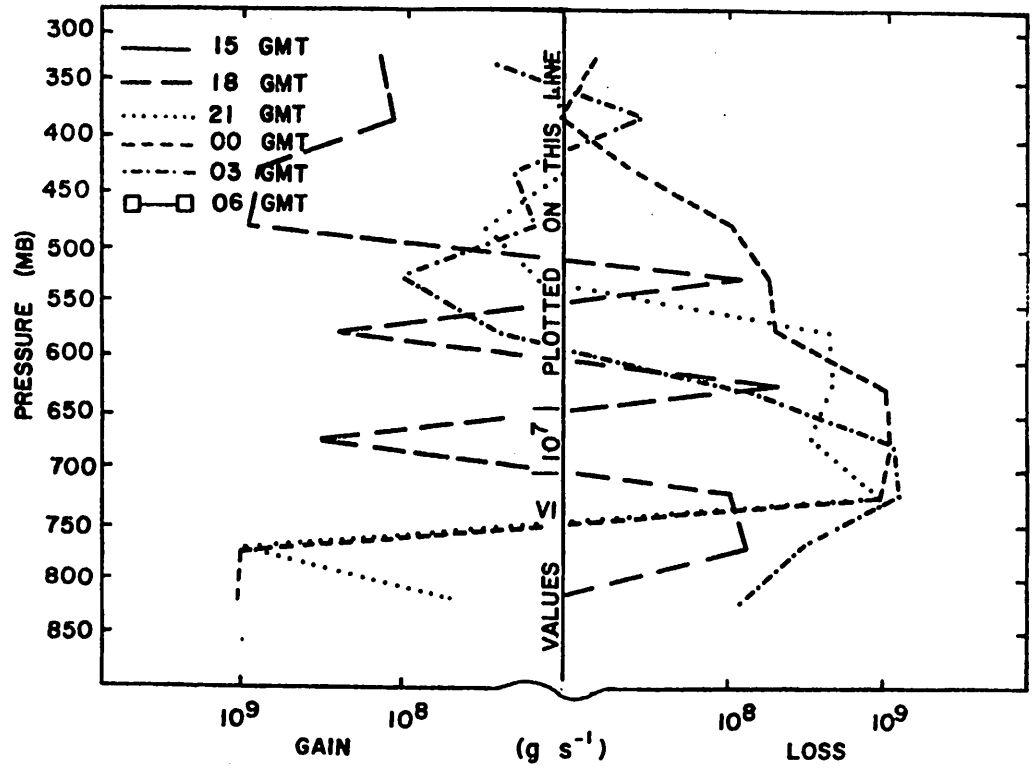

Fig. 5.1.5.2 Net vertical transport of water vapor through boundaries of 50-mb layers (gm s^{-1}) over the Texas HIPLEX area for 1 June 1977.

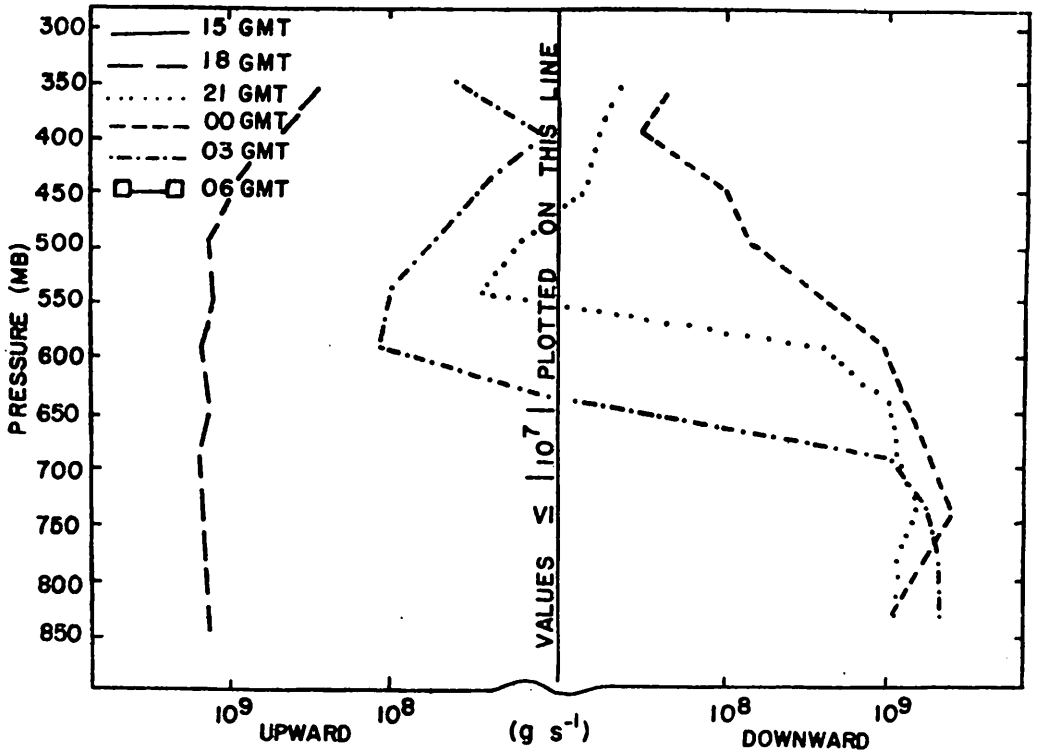

Fig. 5.1.5.3 Vertical transport of water vapor through constant pressure surfaces (gm s^{-1}) over the Texas HIPLEX area for 1 June 1977.

Figure 5.1.5.4 shows vertical profiles of the net combined horizontal and vertical transport of water vapor. Although no convection is observed over the Texas HIPLEX area at 1800 GMT, a net inflow is seen in most layers. Profiles at 2100 and 0000 GMT show a strong net outflow, and closely resemble one another. At 0300 GMT, a net inflow is observed in layers between 650 and 400 mb.

Figure 5.1.5.5 shows vertical profiles of the total mass of water vapor. A large amount of water vapor is observed in layers above 650 mb at 1800 GMT. Although water vapor increases with time in lower layers (i.e. up to 725 mb), it decreases with time in layers between 725 and 450 mb. The 2100 GMT profile shows an increase of water vapor with height at 400 mb. This characteristic was also seen to occur on days containing no significant activity in 1976 (Scoggins, et al., 1978).

Figure 5.1.5.6 shows profiles of the local rate of change in the mass of water vapor. These profiles generally show a gain in lower layers, and a loss aloft. Such a trend can also be seen in Fig. 5.1.5.5. A large decrease can be seen in upper layers between 1800-2100 GMT. This drying aloft seems to be characteristic of times following convection.

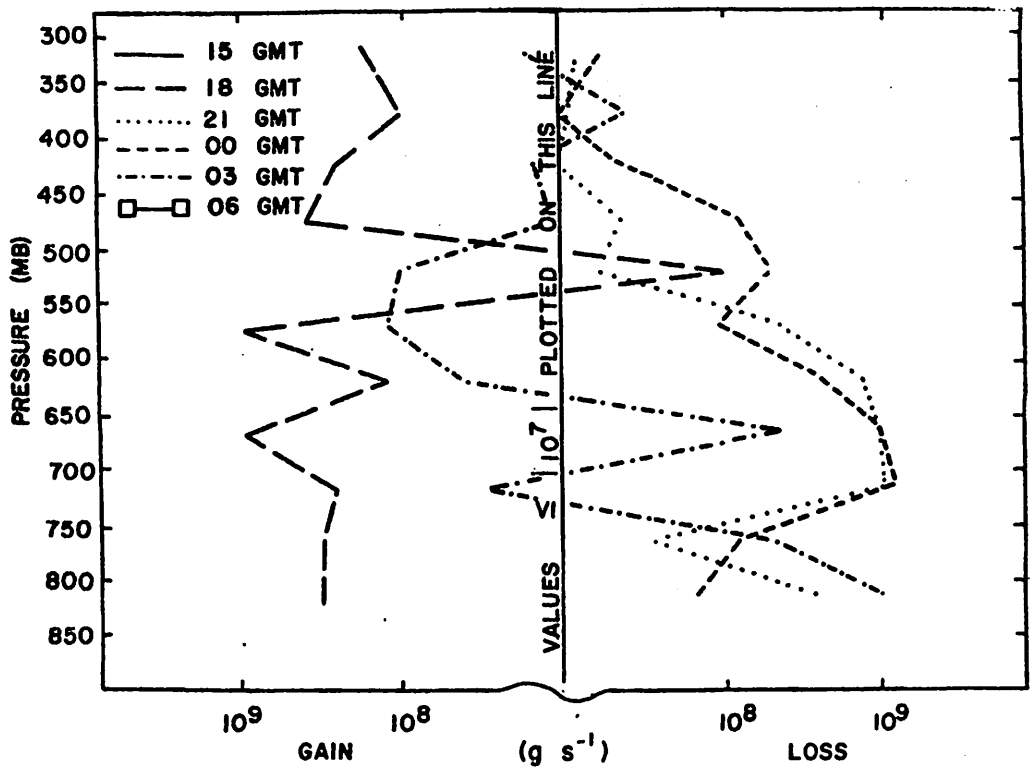

Fig. 5.1.5.4 Combined net horizontal and vertical transport of water vapor through boundaries of 50-mb layers (gm s^{-1}) over the Texas HIPLEX area for 1 June 1977.

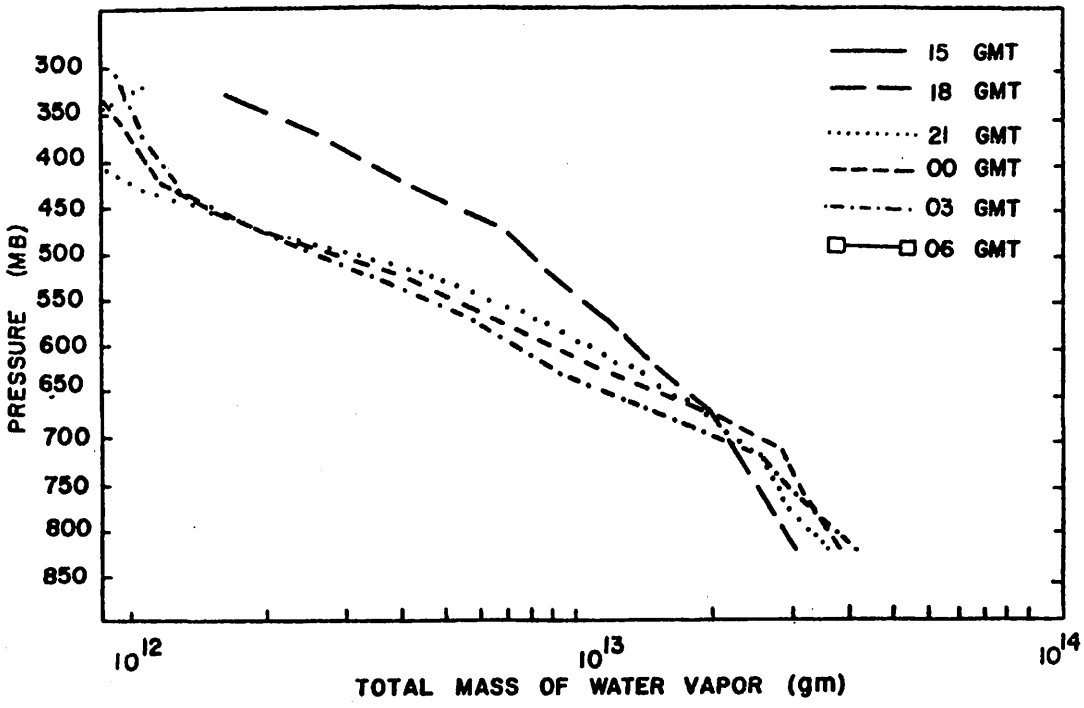

Fig. 5.1.5.5 Total mass of water vapor in layers 50 mb deep (gm) over the Texas HIPLEX area for 1 June 1977.

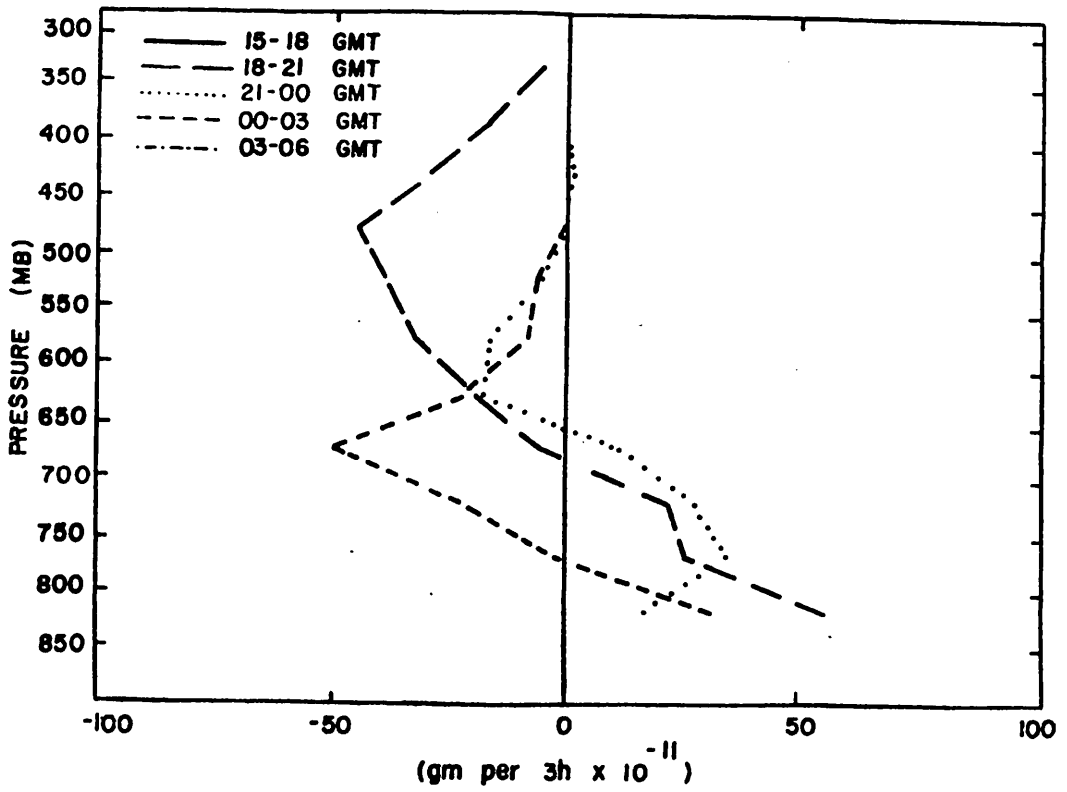

Fig. 5.1.5.6 Local rate-of-change in total mass of water vapor (gm per 3h x 10^{-11}) over the Texas HIPLEX area for 1 June 1977.

5.2 7 June 1977

5.2.1 Radar

No radar echoes were observed on this day.

5.2.2 Surface

No consistent patterns or large variations can be seen in surface temperature (Fig. 5.2.2.1), surface mixing ratio (Fig. 5.2.2.2), or surface equivalent potential temperature (Fig. 5.2.2.3), other than possibly diurnal effects. Values of terrain-induced vertical motion (Fig. 5.2.2.4) decreased in magnitude with time throughout the day, but maintained similar patterns. Several large centers, especially northeast of Snyder, show values of 2 cm s^{-1}. Irregular positive surface velocity divergence patterns (Fig. 5.2.2.5) were observed at most times in association with downward vertical motion 50 mb above the surface (Fig. 5.2.2.6). Surface moisture divergence (Fig. 5.2.2.7) remained small and variable which was reflected by surface mixing ratio (Fig. 5.2.2.2), and vertical flux of moisture 50 mb above the surface (Fig. 5.2.2.8). Surface vorticity fields (Fig. 5.2.2.9) show small alternating cyclonic and anticyclonic centers, decreasing to near zero by 0100 GMT. Sea level pressure patterns (Fig. 5.2.2.10) remain consistent,

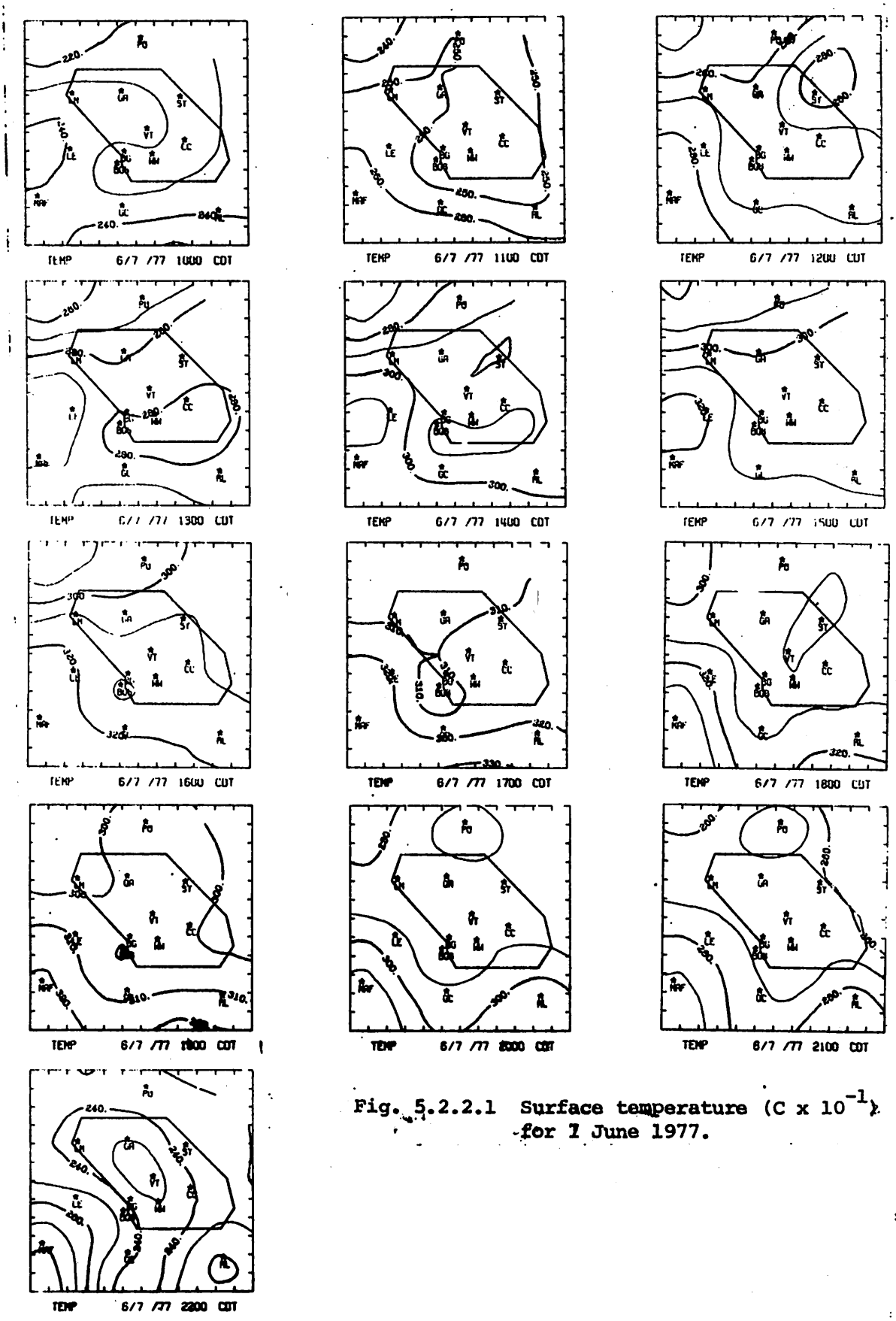

Fig. 5.2.2.1 Surface temperature (C x 10^{-1}) for 7 June 1977.

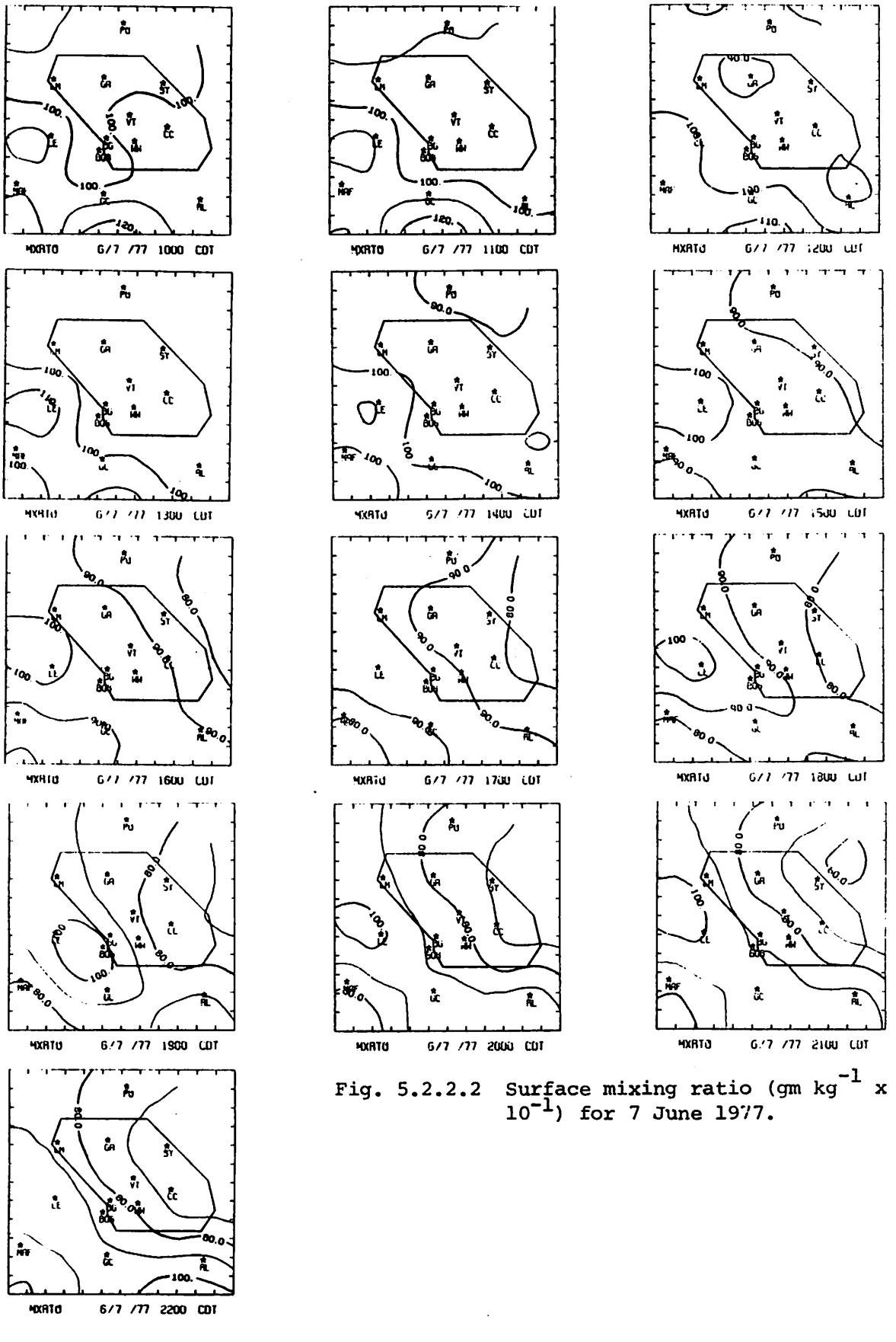

Fig. 5.2.2.2 Surface mixing ratio (gm kg^{-1} x 10^{-1}) for 7 June 1977.

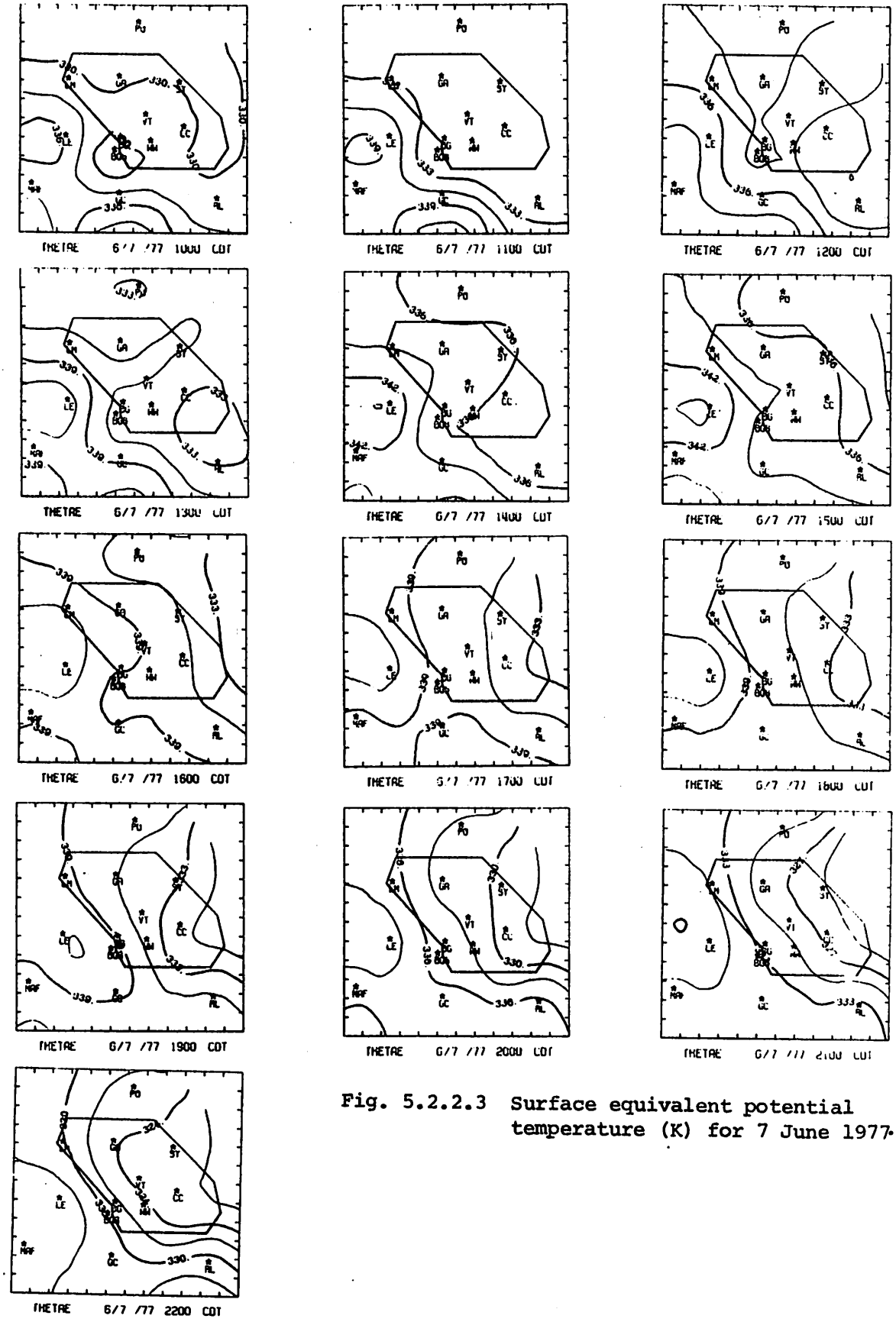

Fig. 5.2.2.3 Surface equivalent potential temperature (K) for 7 June 1977.

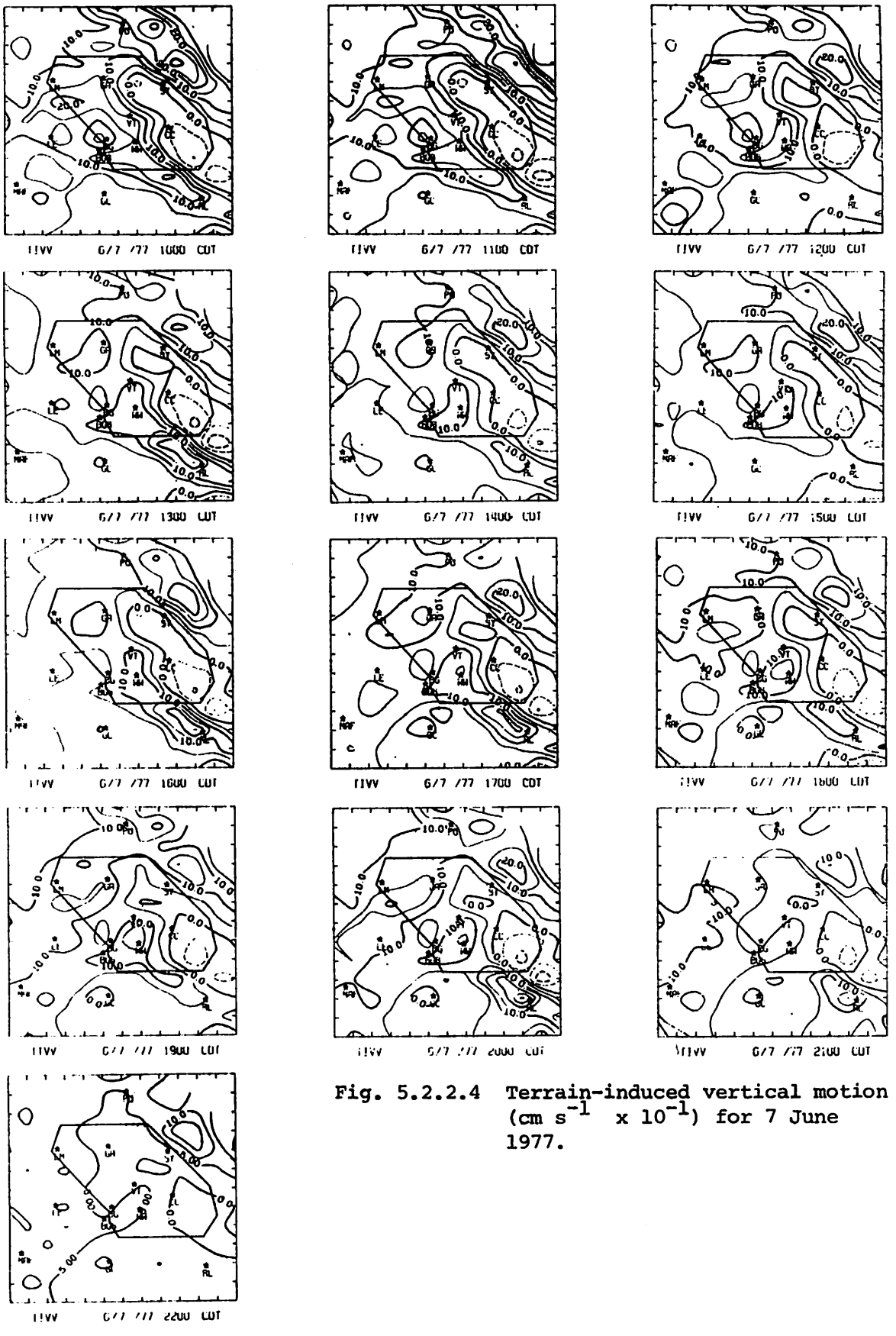

Fig. 5.2.2.4 Terrain-induced vertical motion (cm s^{-1} x 10^{-1}) for 7 June 1977.

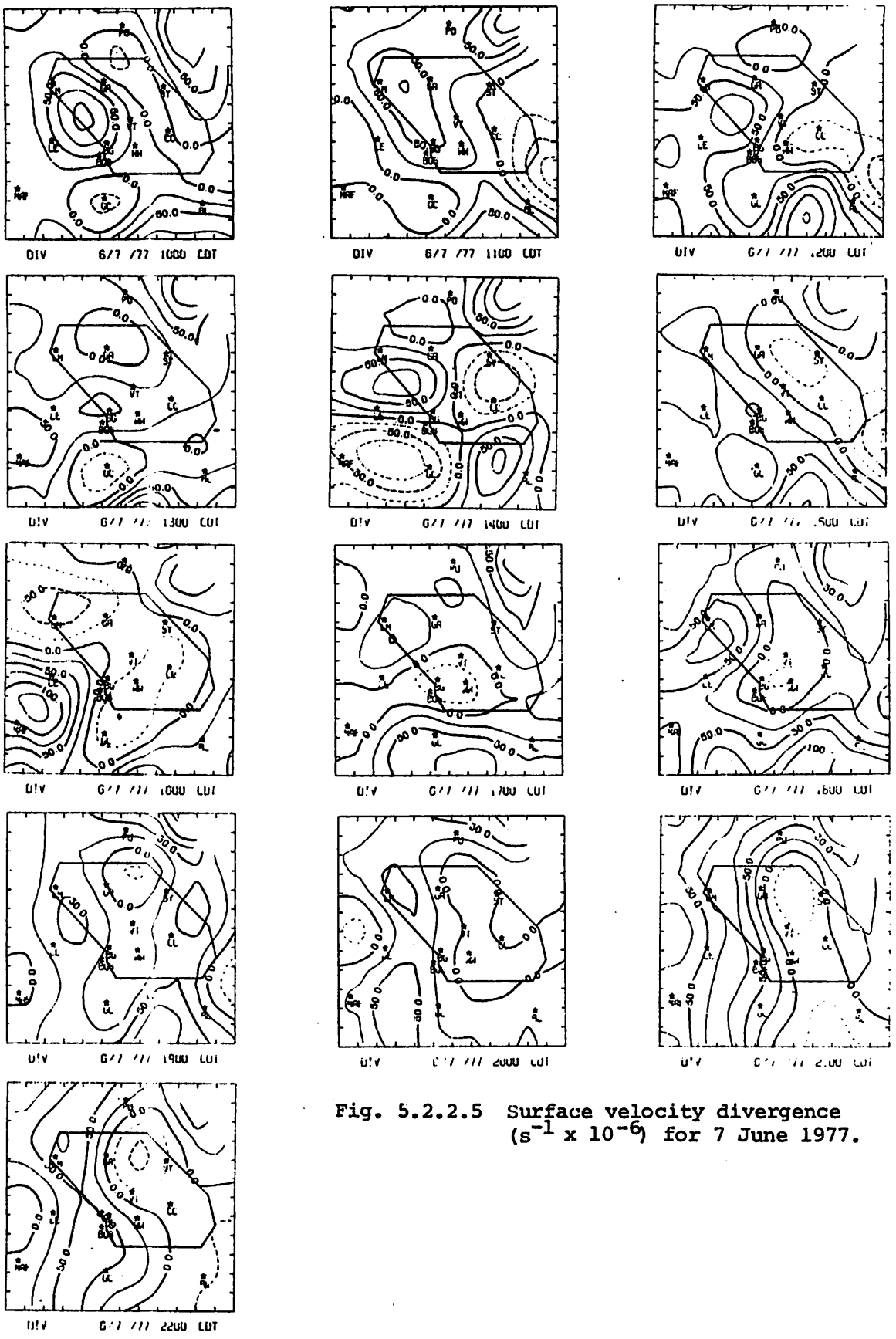

Fig. 5.2.2.5 Surface velocity divergence (s^{-1} x 10^{-6}) for 7 June 1977.

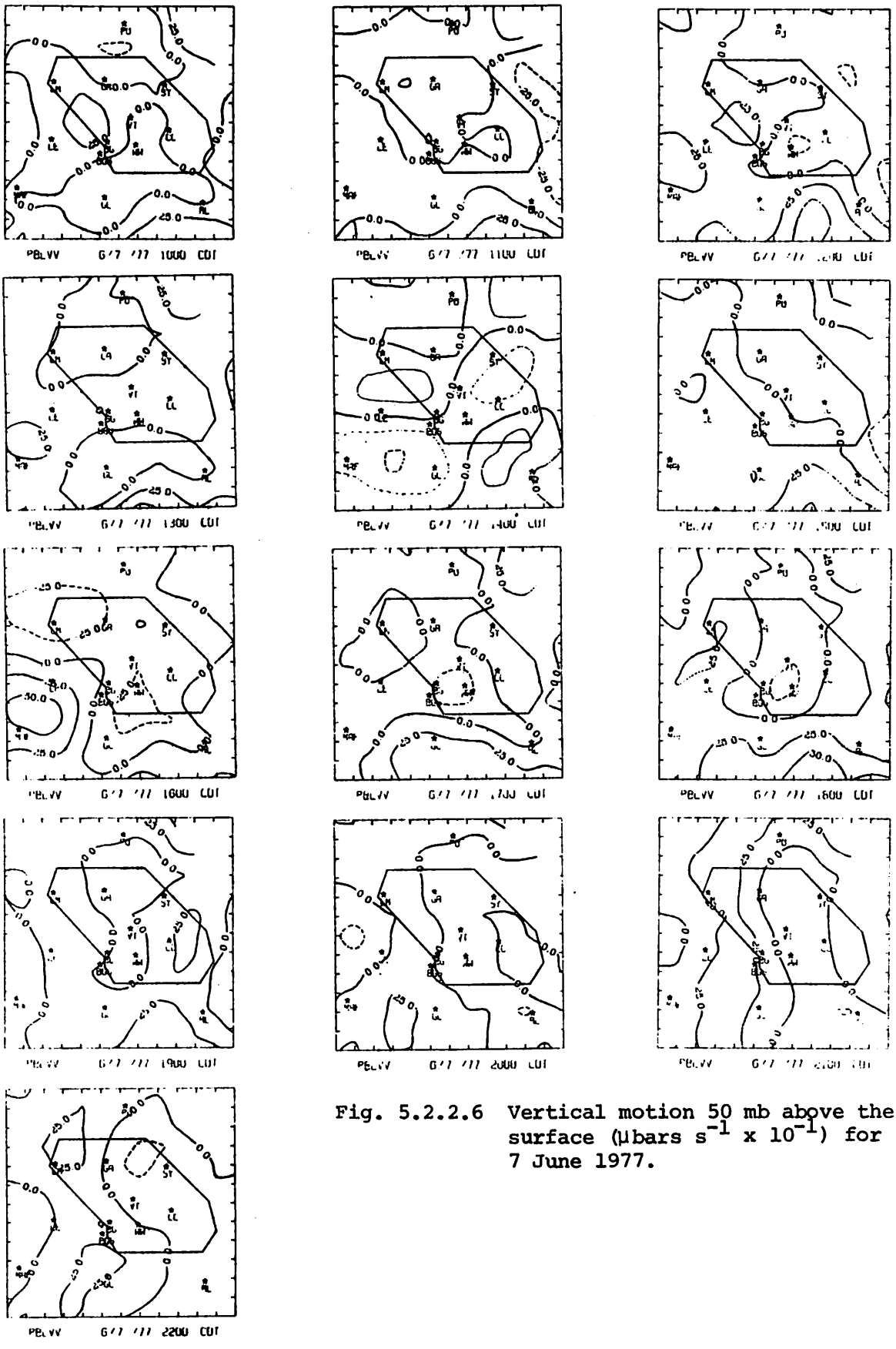

Fig. 5.2.2.6 Vertical motion 50 mb above the surface (μbars s^{-1} x 10^{-1}) for 7 June 1977.

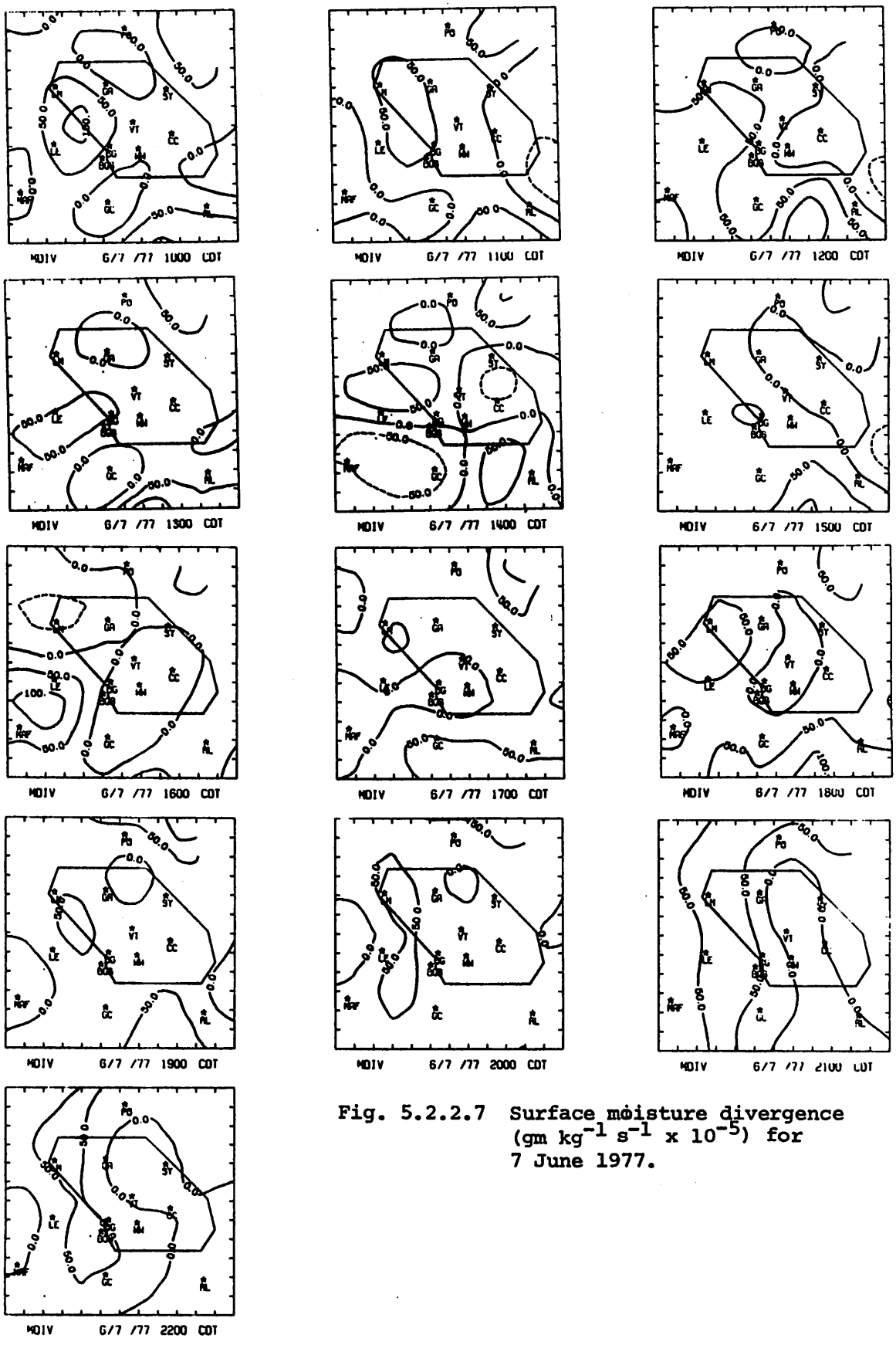

Fig. 5.2.2.7 Surface moisture divergence (gm kg^{-1} s^{-1} x 10^{-5}) for 7 June 1977.

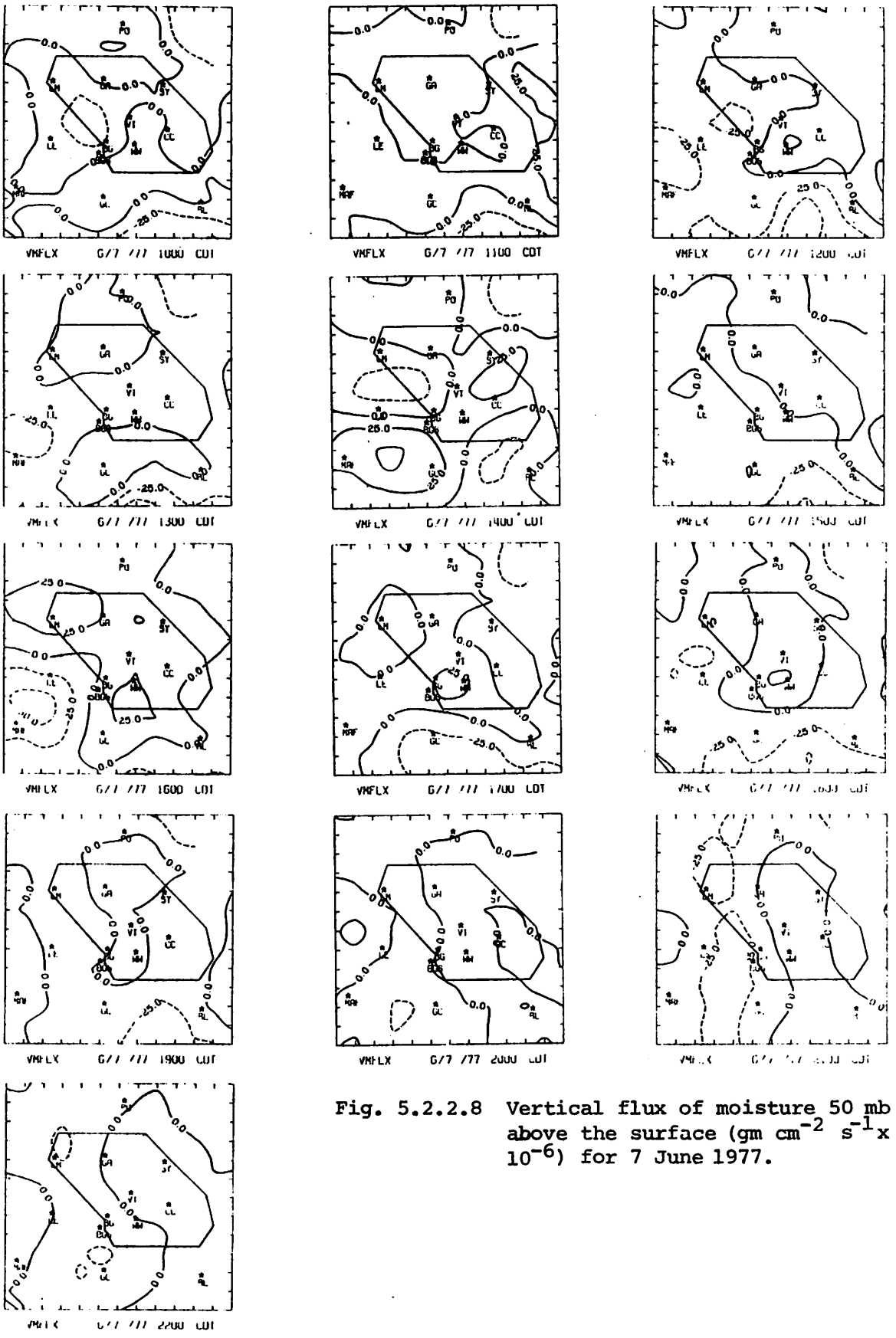

Fig. 5.2.2.8 Vertical flux of moisture 50 mb above the surface (gm cm^{-2} s^{-1} x 10^{-6}) for 7 June 1977.

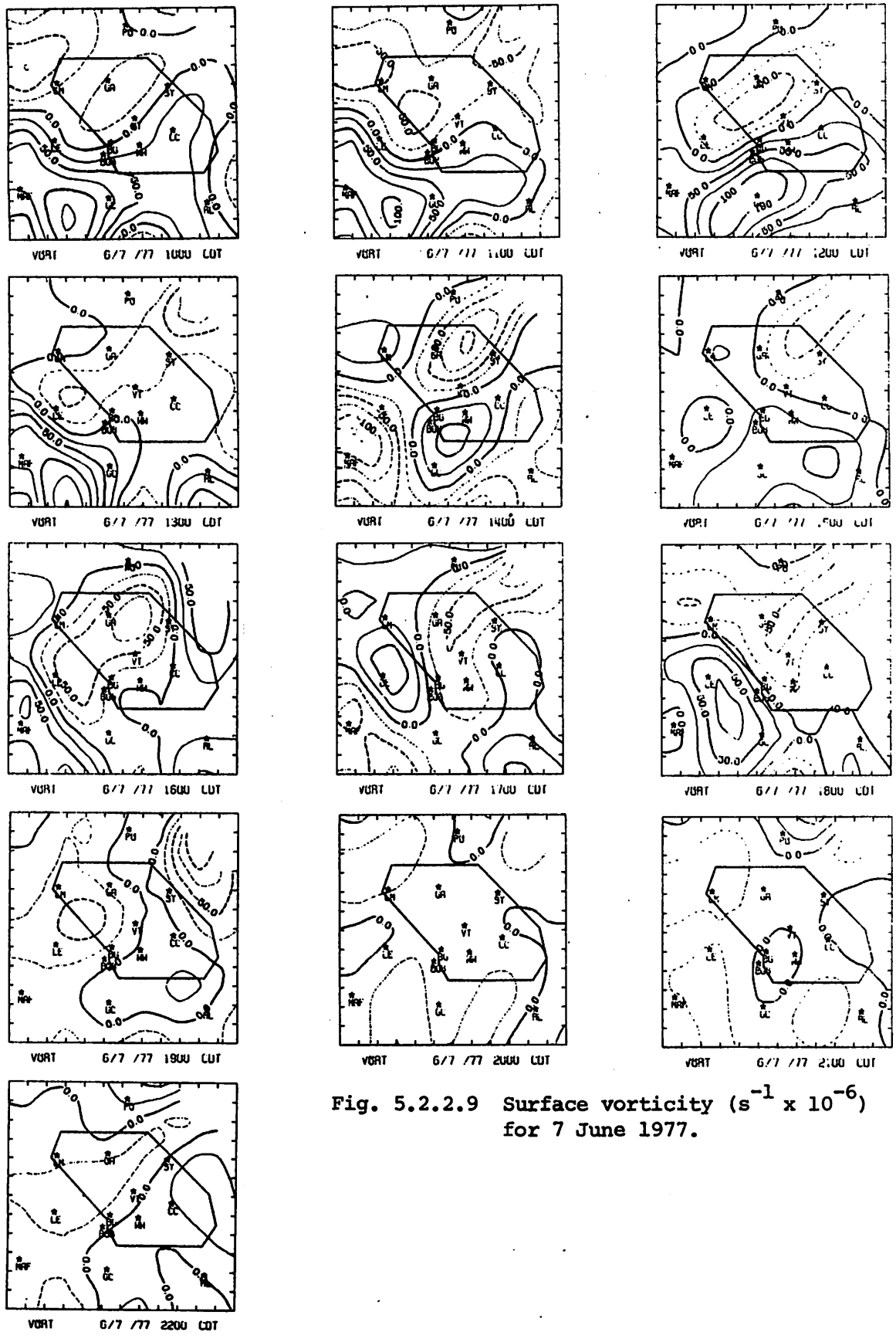

Fig. 5.2.2.9 Surface vorticity ($s^{-1} \times 10^{-6}$) for 7 June 1977.

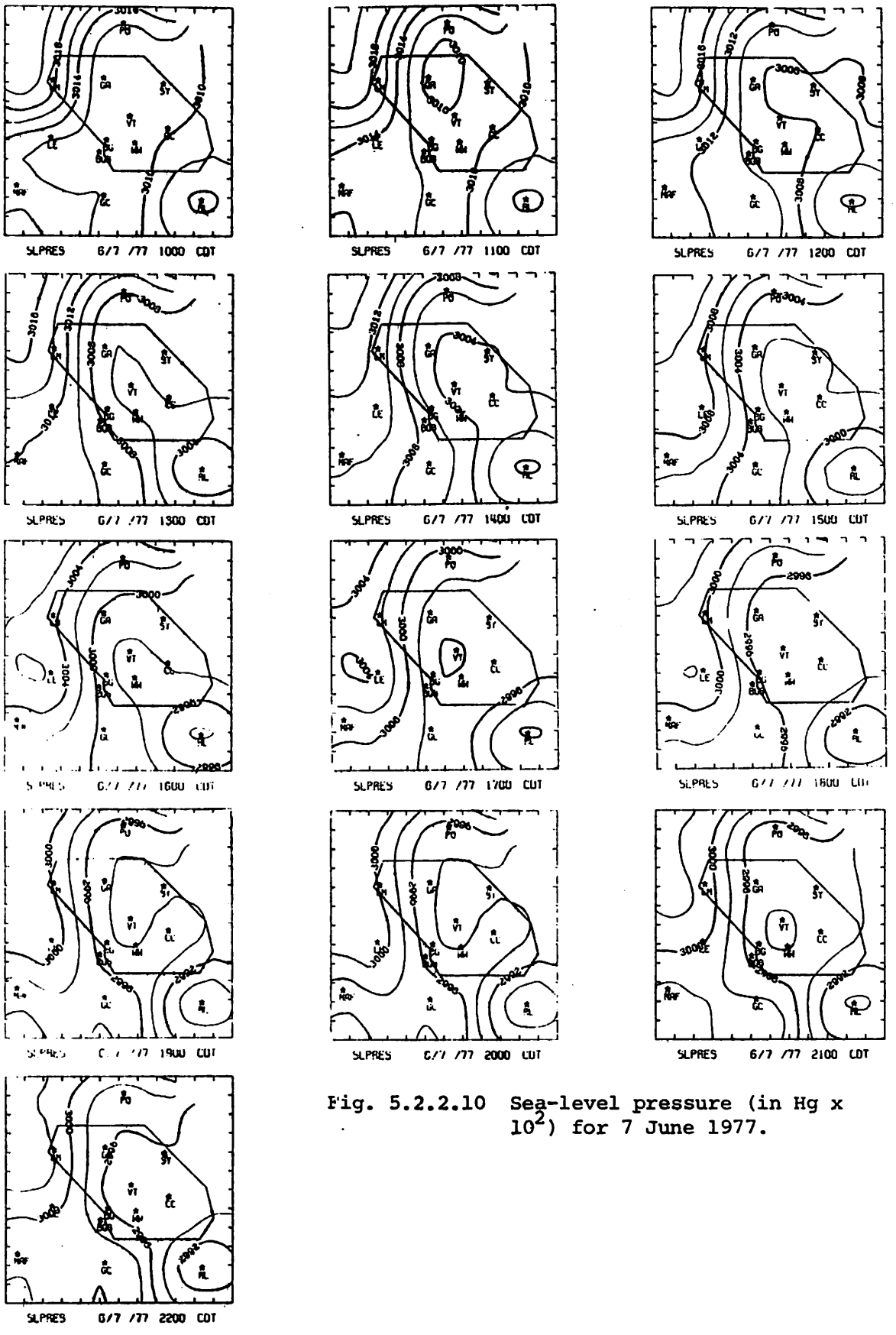

Fig. 5.2.2.10 Sea-level pressure (in Hg x 10^2) for 7 June 1977.

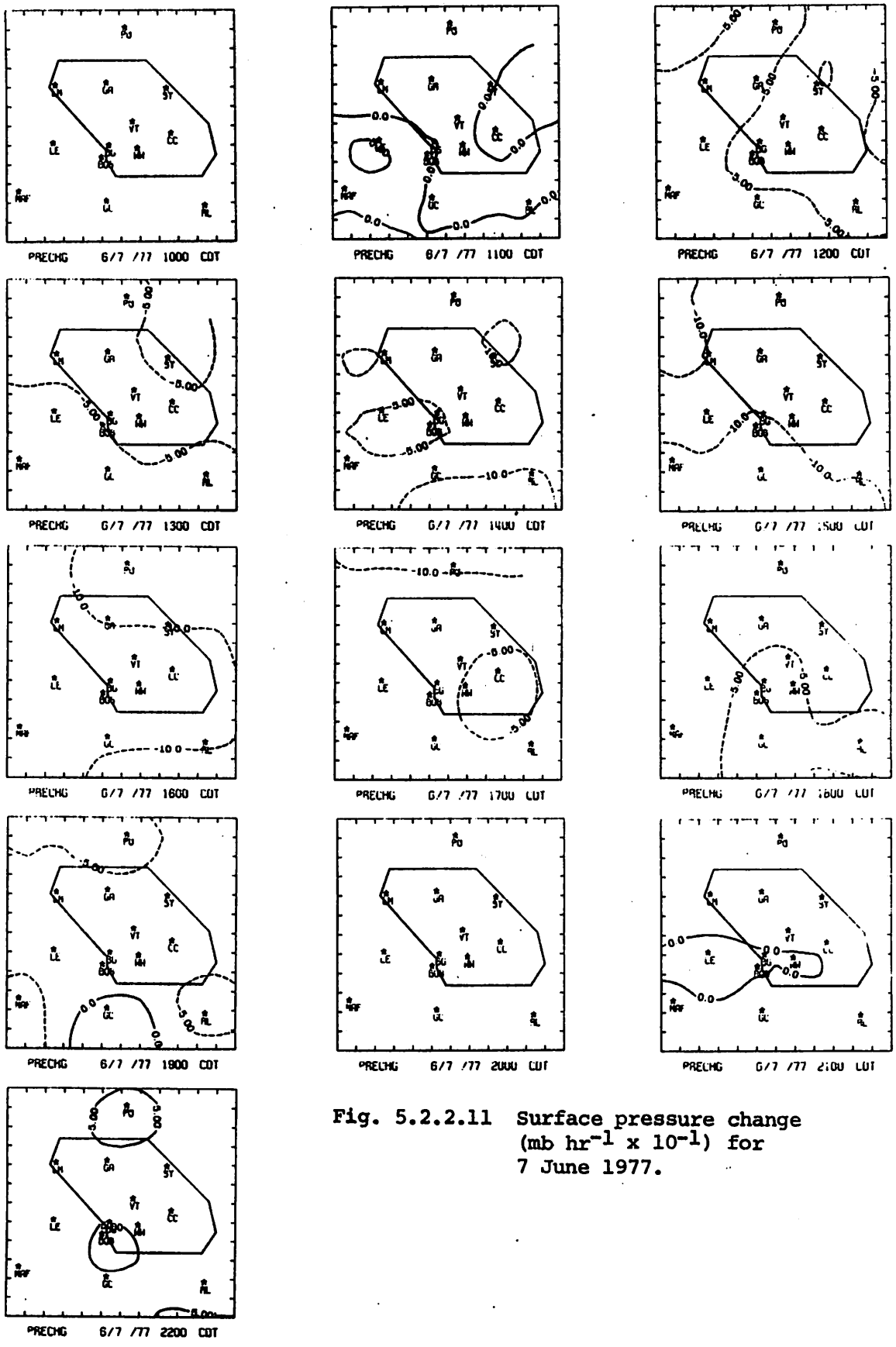

Fig. 5.2.2.11 Surface pressure change (mb hr^{-1} x 10^{-1}) for 7 June 1977.

showing a general decrease of pressure from west to east. Surface pressure changes (Fig. 5.2.2.11) are small throughout the day.

5.2.3 Upper-Level Kinematic Parameters

Mass convergence below 700 mb at 1500 GMT changes to mass divergence at 1800 and 2100 GMT, while mass convergence dominated the layer between 700 and 500 mb at all times (Fig. 5.2.3.1). Above 500 mb magnitudes of mass divergence were relatively small throughout the day.

Vertical velocity changes from upward at all levels at 1500 GMT to downward below 500 mb at 1800 GMT to strong downward at all levels at 2100 GMT (Fig. 5.2.3.2). The pattern is likely associated with the dissipation of mid-level cloudiness and rainshowers (just north of the network) between 1500 and 2100 GMT.

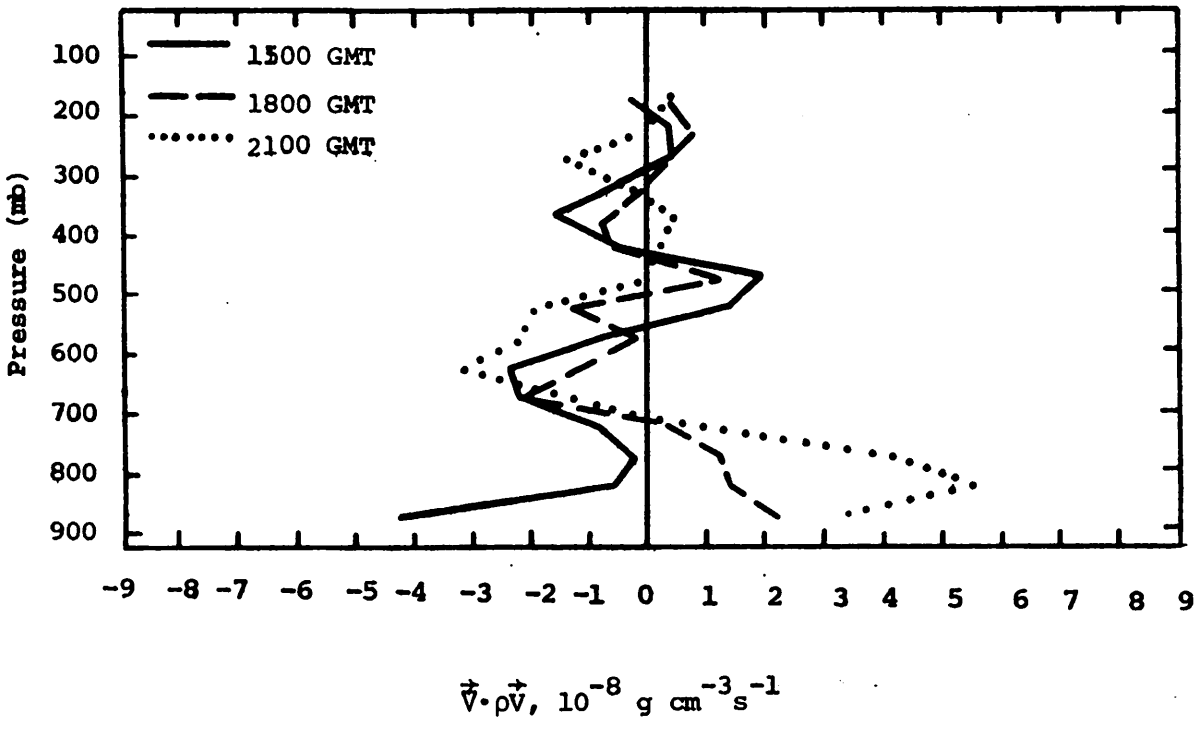

Fig. 5.2.3.1 Vertical profiles of mass divergence on 7 June 1977.

Horizontal moisture convergence at 1500 GMT is progressively replaced by larger values of horizontal moisture divergence below 700 mb between 1500 and 2100 GMT (Fig. 5.2.3.3). Small magnitudes of horizontal moisture divergence were calculated at all times above 600 mb.

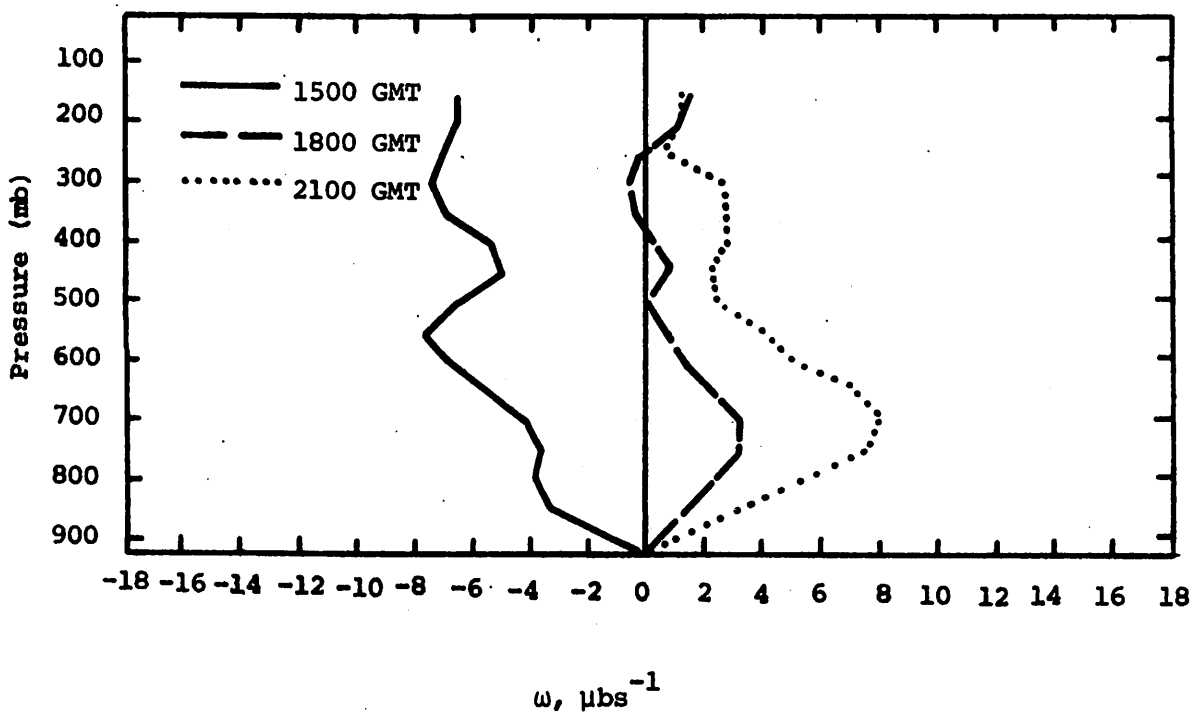

Fig. 5.2.3.2 Vertical profiles of vertical motion on 7 June 1977.

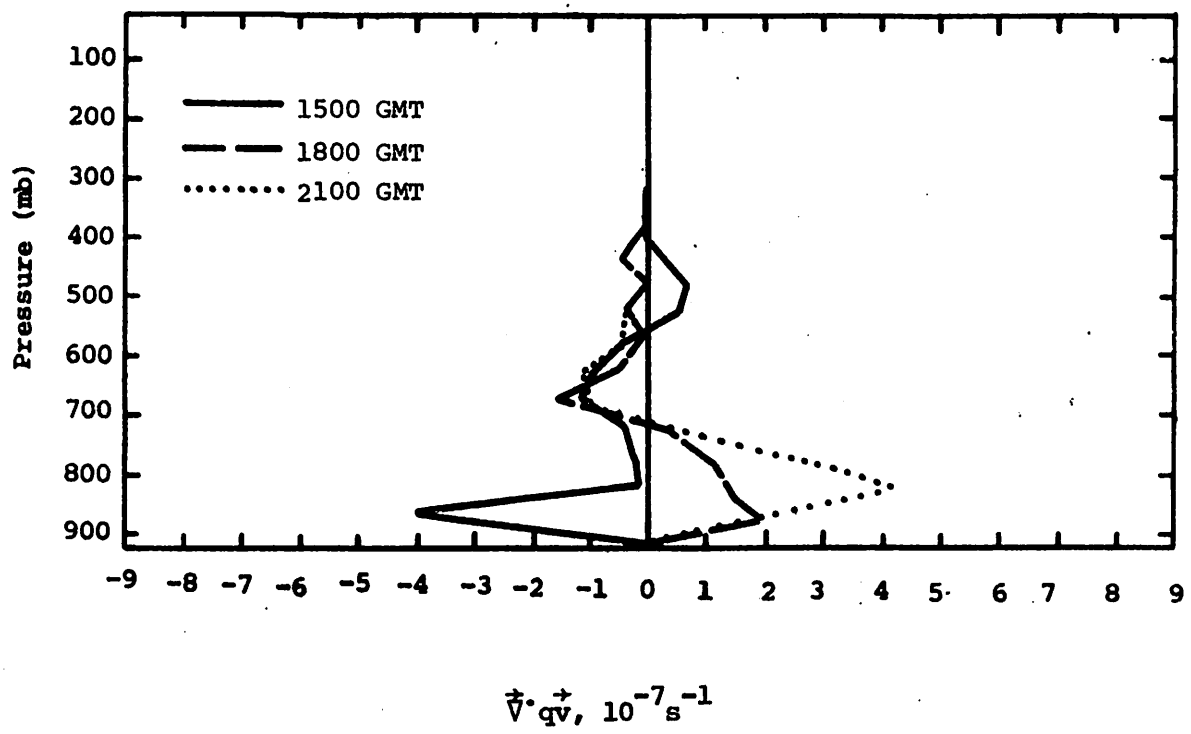

Fig. 5.2.3.3 Vertical profiles of moisture divergence on 7 June 1977.

5.2.4 Energetics

Horizontal inflow of latent heat energy is replaced by outflow between 1500 and 1800 GMT below 700 mb, while weak inflow occurred at all times between 700 and 500 mb (Fig. 5.2.4.1). Vertical flux divergence of latent heat energy below 800 mb changes to flux convergence above 800 mb at 1500 GMT as upward vertical velocities produce a net transport of latent energy from the low- to mid-levels where cloudiness was observed (Fig. 5.2.4.2). After 1500 GMT downward vertical velocities were associated with low-level vertical flux convergence and mid-level flux divergence of latent heat energy as water vapor is transported from the middle- to lower-troposphere and cloudiness and precipitation diminished. Local changes in latent heat energy were small at all times during the day (Fig. 5.2.4.3).

Losses of latent heat energy (positive values of -R) at 1500 GMT coincide with cloudiness and precipitation that were heating the environment through the release of latent heat (Fig. 5.2.4.4). After 1500 GMT, -R values are generally negative at all levels as evaporation of cloud water and light precipitation was cooling the environment and increasing the latent heat content of air over the network.

Diabatic heating profiles shown in Fig. 5.2.4.5 are fairly consistent with the residual from the latent heat budget. Diabatic heating above 800 mb at 1500 GMT is replaced by cooling by 2100 GMT in association with the rapid dissipation of cloudiness and precipitation during this period. Diabatic heating below 800 mb at all times is probably caused by radiational surface heating and the turbulent mixing of this heat in the planetary boundary layer.

Both the horizontal and vertical flux divergence profiles of kinetic energy (Figs. 5.2.4.6 and 5.2.4.7) show no noticeably important features at any time period.

5.2.5 Water Vapor Budget

Some sounding data were missing which made it impossible to determine local change. Therefore, results are not presented.

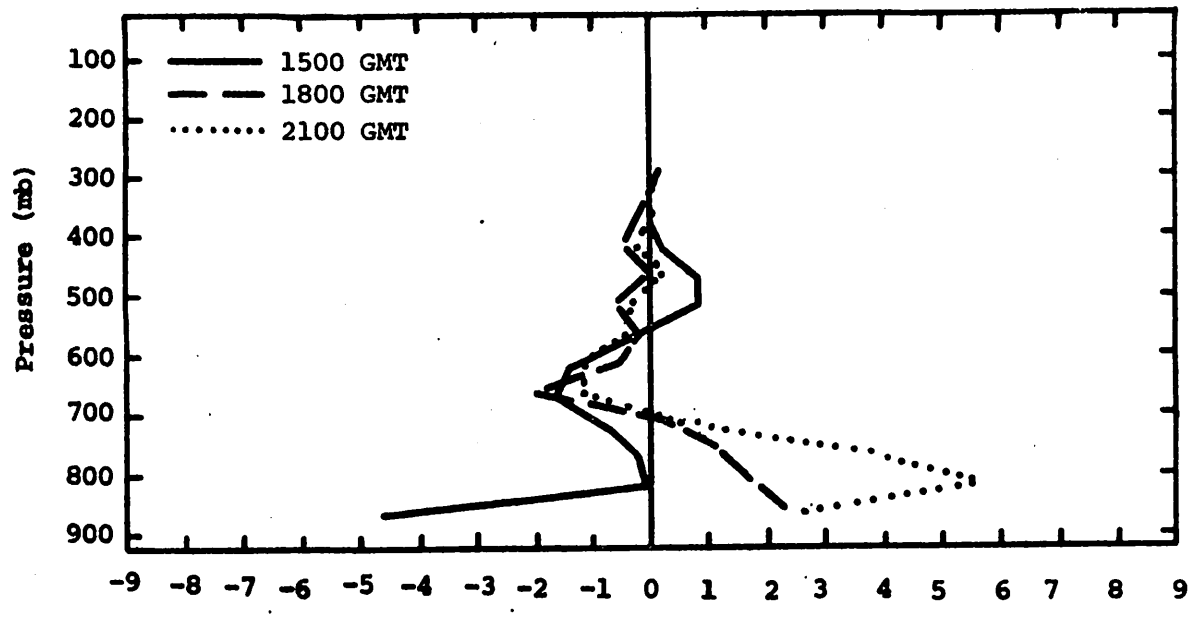

$$\frac{1}{g}\int \vec{\nabla}\cdot(Lq\vec{V})\,dp,\ 10^2(W\cdot m^{-2})/50\ mb$$

Fig. 5.2.4.1 Vertical profiles of the horizontal flux of latent heat energy on 7 June 1977.

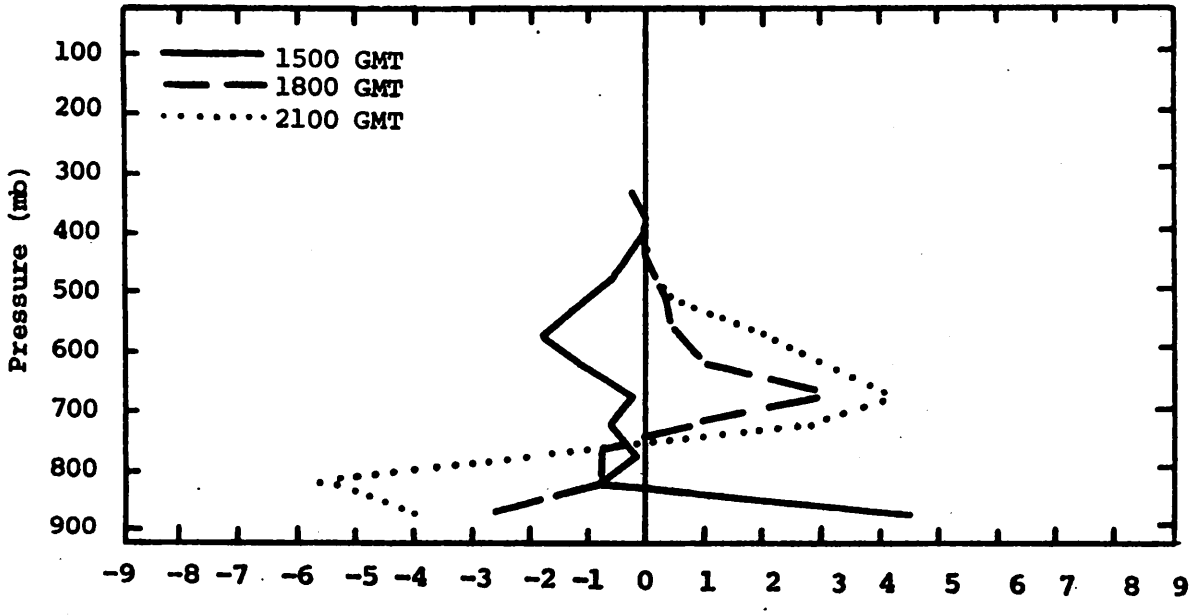

$$\frac{1}{g}\int\frac{\partial}{\partial p}(Lq\omega)\,dp,\ 10^2(W\ m^{-2})/50\ mb$$

Fig. 5.2.4.2 Vertical profiles of the vertical flux of latent heat energy on 7 June 1977.

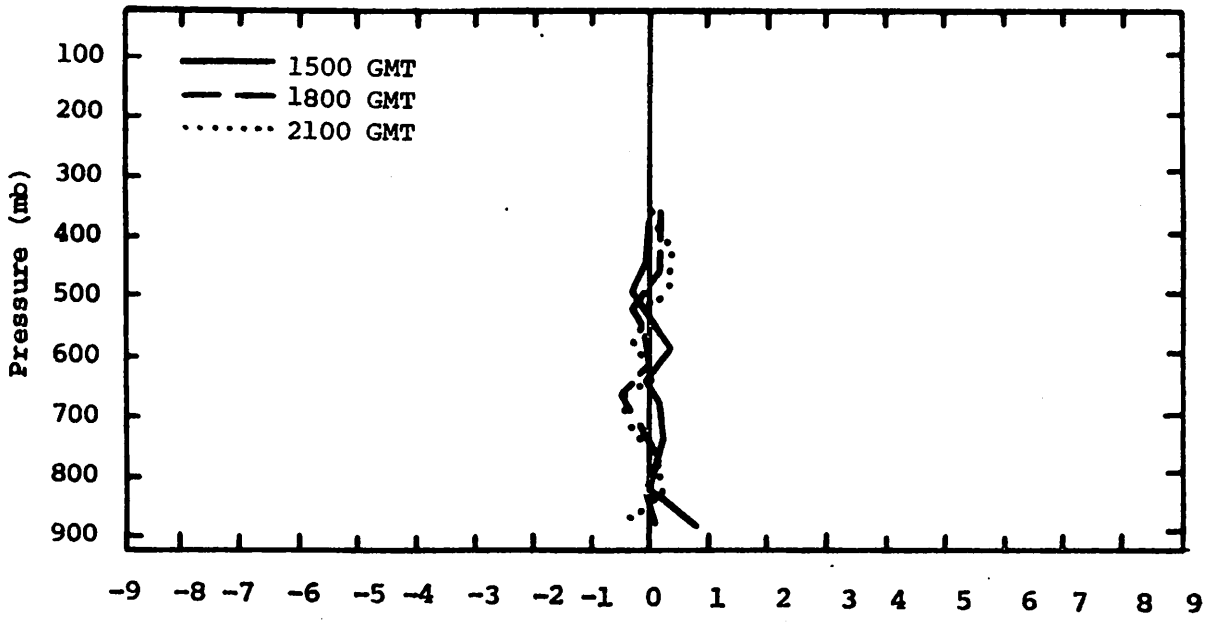

Fig. 5.2.4.3 Vertical profiles of the local change of latent heat energy on 7 June 1977.

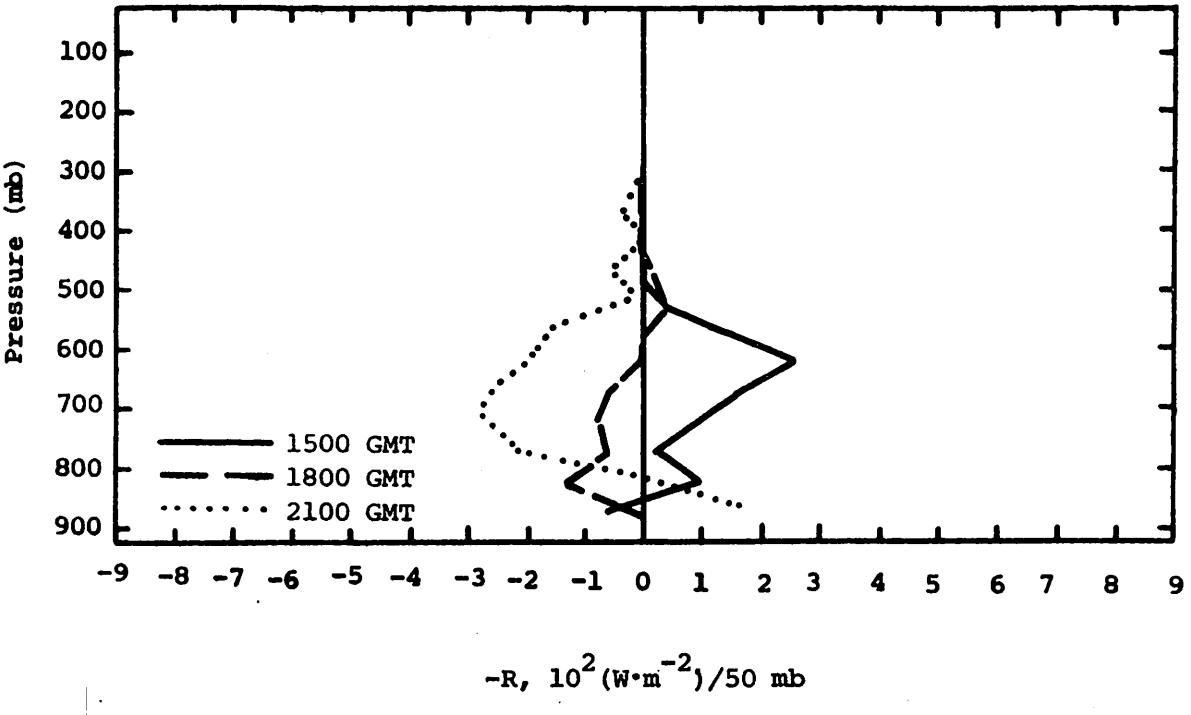

Fig. 5.2.4.4 Vertical profile of the residual of the latent heat energy equation on 7 June 1977.

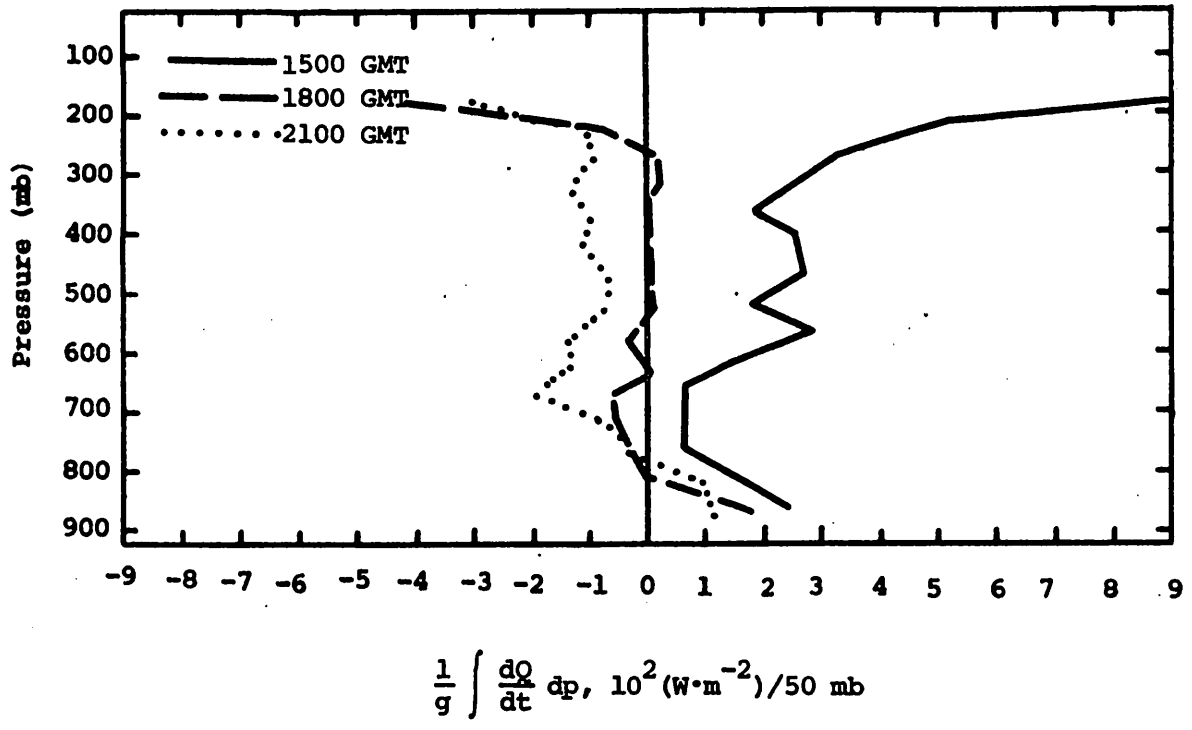

Fig. 5.2.4.5 Vertical profiles of diabatic heating computed from the first law of thermodynamics on 7 June 1977.

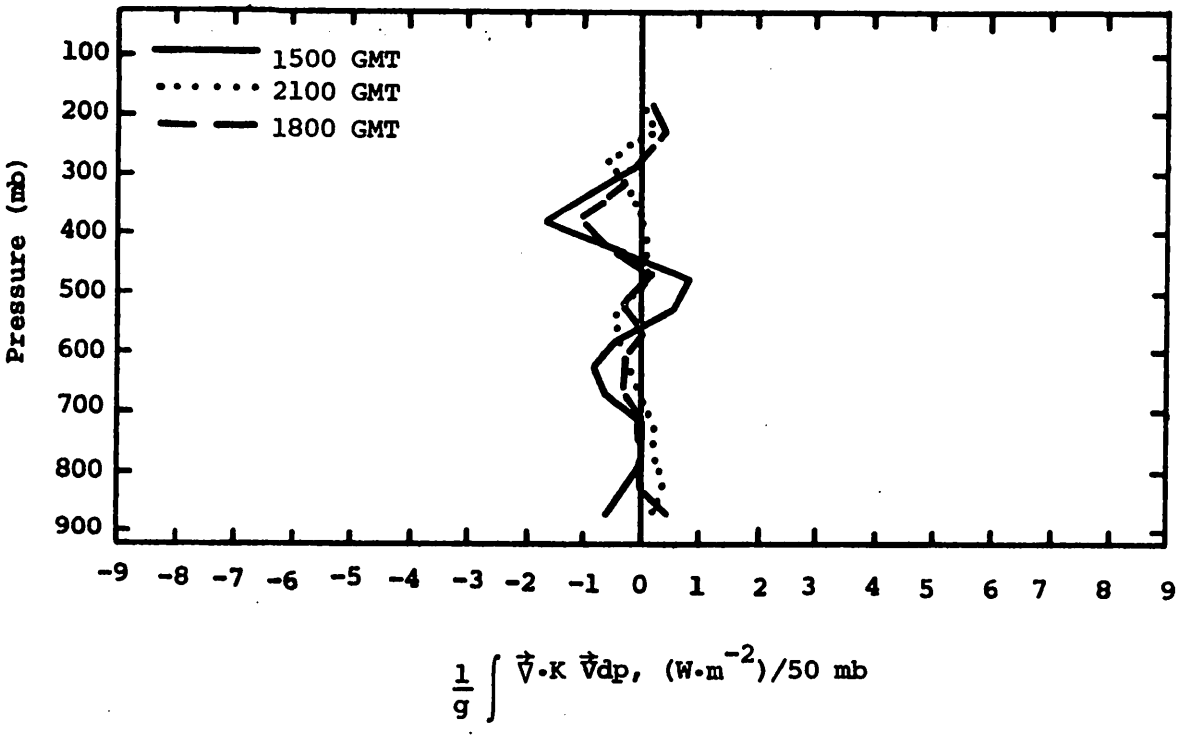

Fig. 5.2.4.6 Vertical profiles of the horizontal flux of kinetic energy on 7 June 1977.

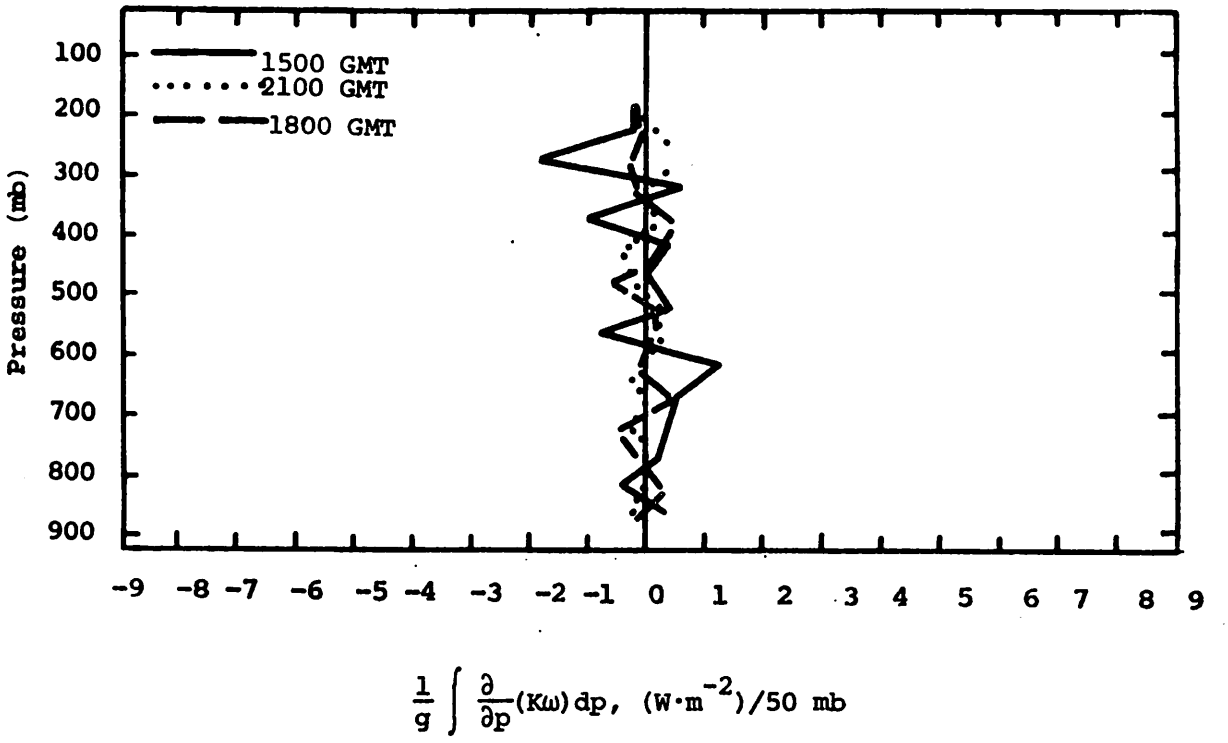

Fig. 5.2.4.7 Vertical profiles of the vertical flux of kinetic energy on 7 June 1977.

5.3 9 June 1977

5.3.1 Radar

Radar charts for this day are shown in Fig. 5.3.1.1. Echoes were observed beginning at 2000 GMT and persisted throughout the day, primarily over the northwestern part of the area. Tops of the echoes were generally less than 6.1 km (20K ft) except for the last two times when the tops exceeded 9.1 km (30K ft). The principal area of convective activity was located outside the HIPLEX area toward the northwest.

5.3.2 Surface

Although patterns of surface temperature (Fig. 5.3.2.1) are strongly influenced by surface heating, a strong temperature minimum is associated with the thunderstorm from 0200 to 0300 GMT. A temperature drop of approximately 10°C at the surface occurred as a result of the storm (see Fig. 5.3.1.1). Values of surface mixing ratio (Fig. 5.3.2.2) were observed to increase in this area along with values of surface equivalent potential temperature (Fig. 5.3.2.3). Prior to 0200 GMT when less intense echoes were observed, these fields varied in time, but showed no significant patterns or increases. Terrain-induced vertical motions (Fig. 5.3.2.4) remained nearly constant, showing no significant contribution to the kinematic

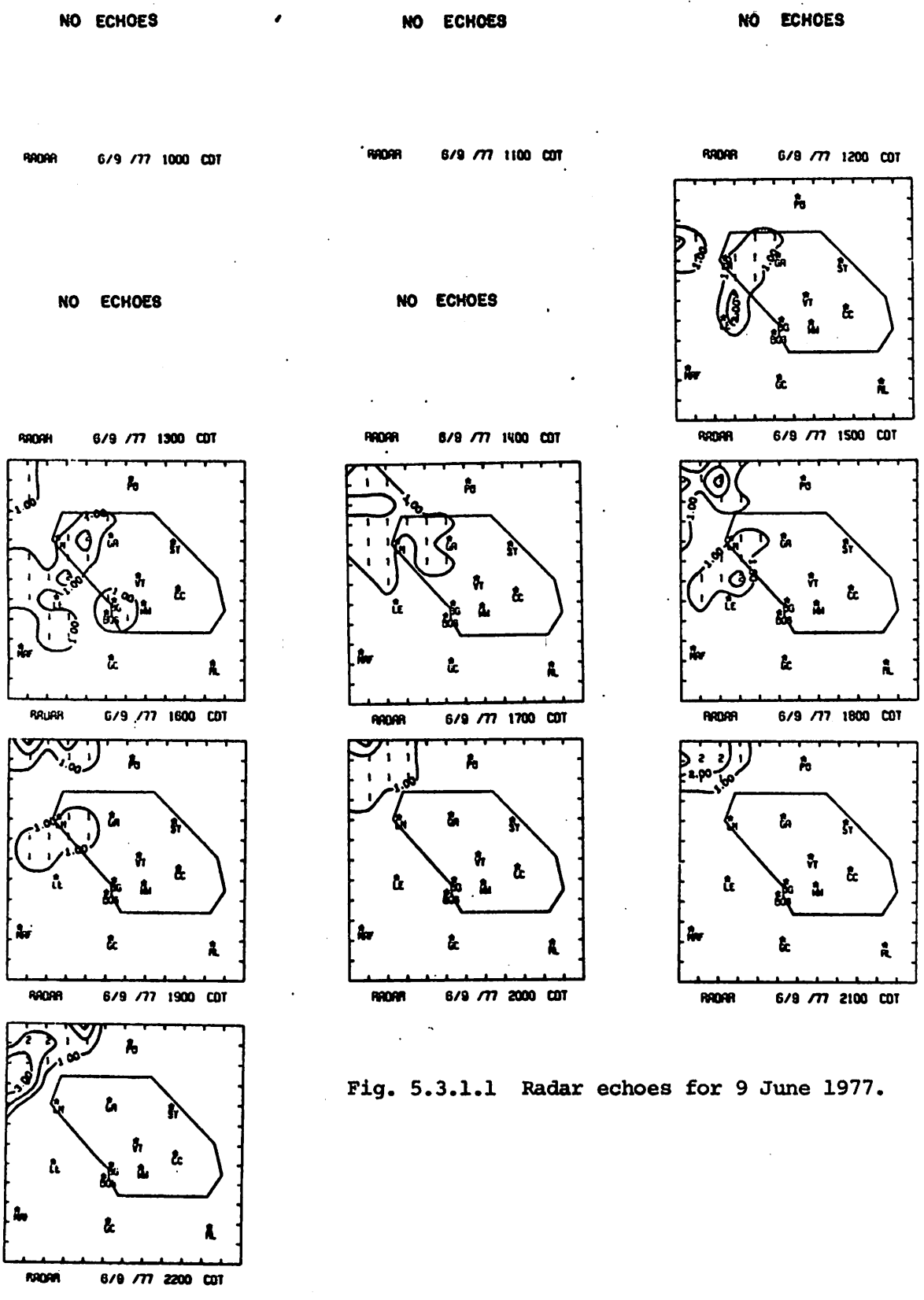

Fig. 5.3.1.1 Radar echoes for 9 June 1977.

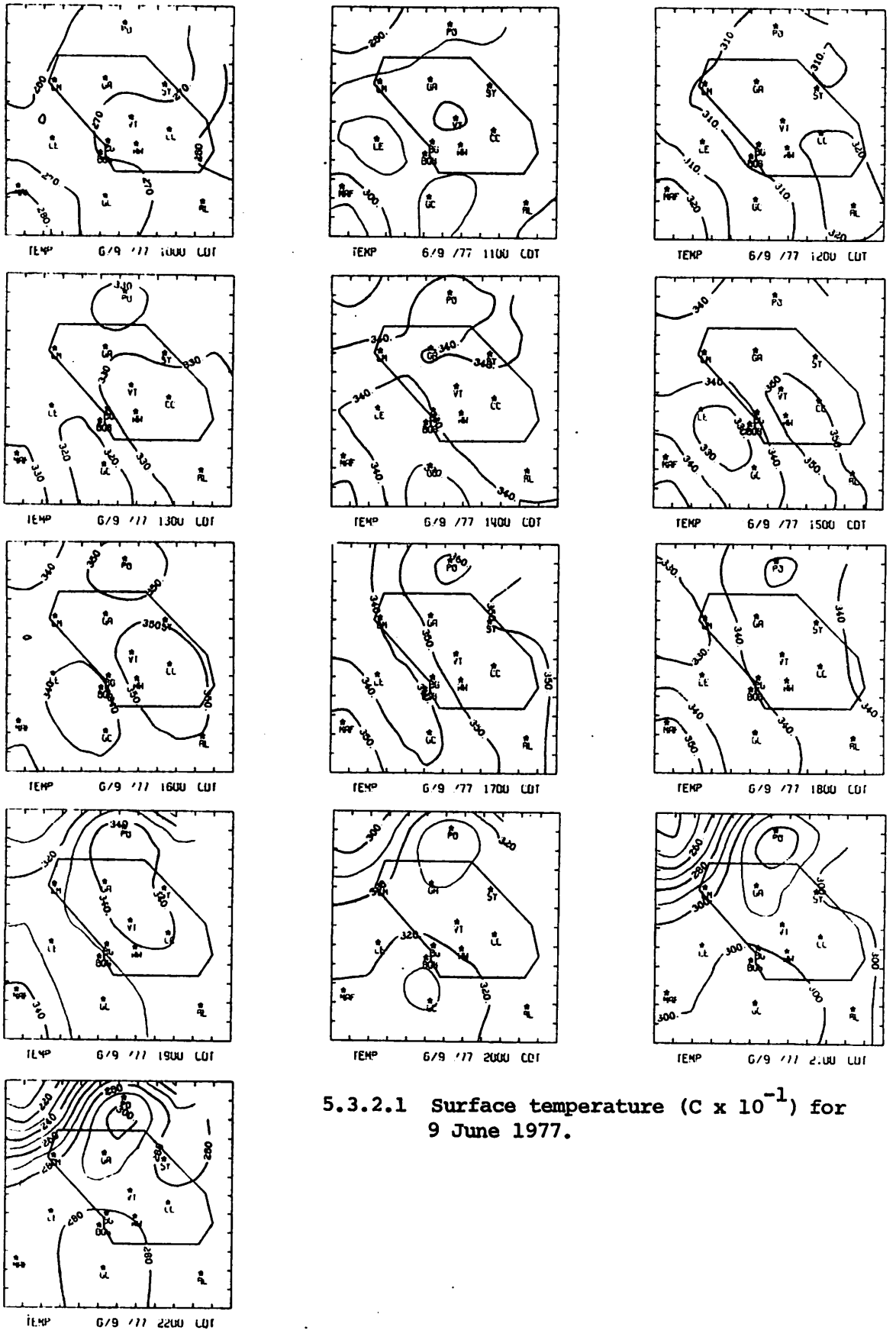

5.3.2.1 Surface temperature (C x 10^{-1}) for 9 June 1977.

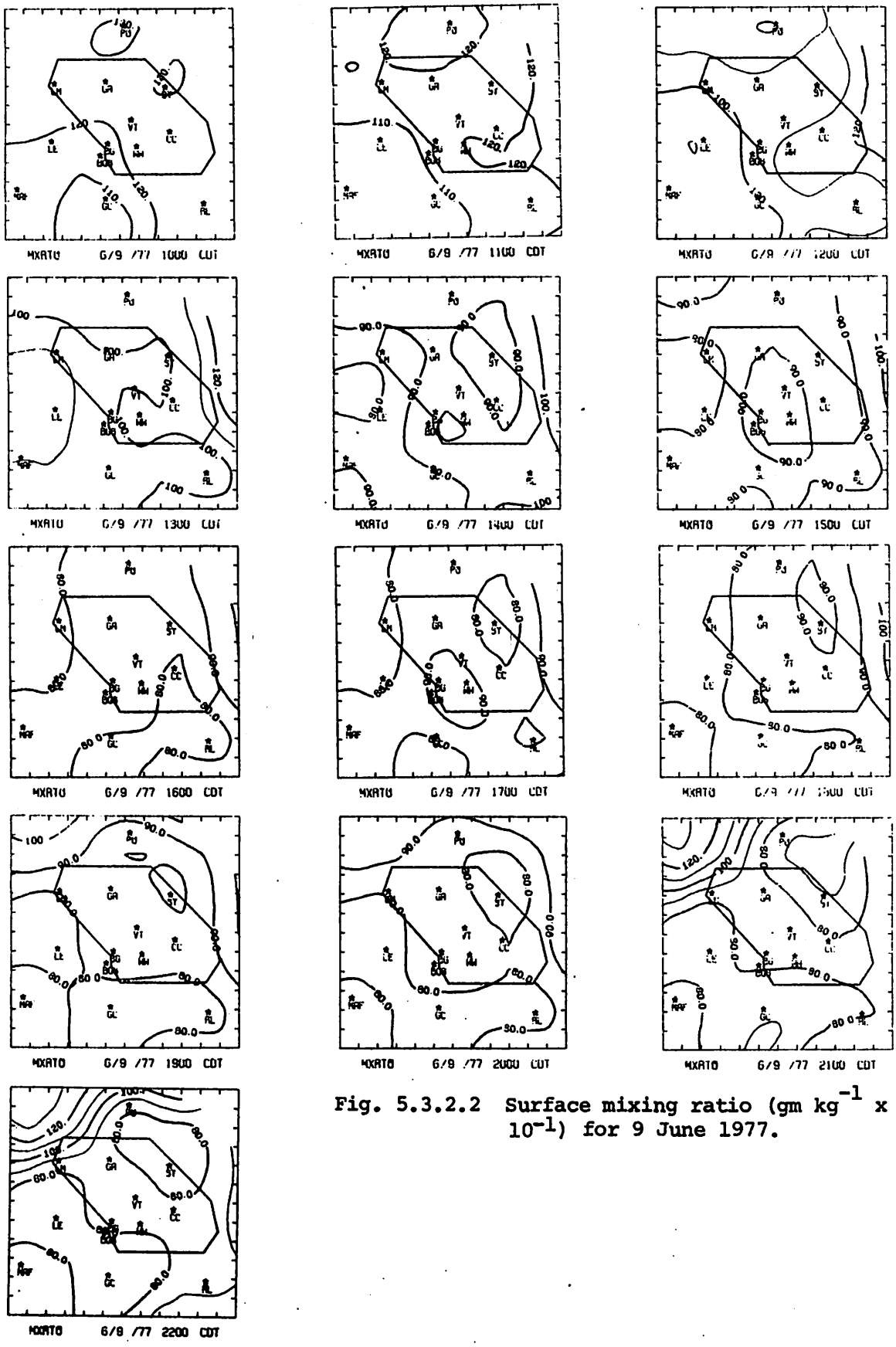

Fig. 5.3.2.2 Surface mixing ratio (gm kg^{-1} x 10^{-1}) for 9 June 1977.

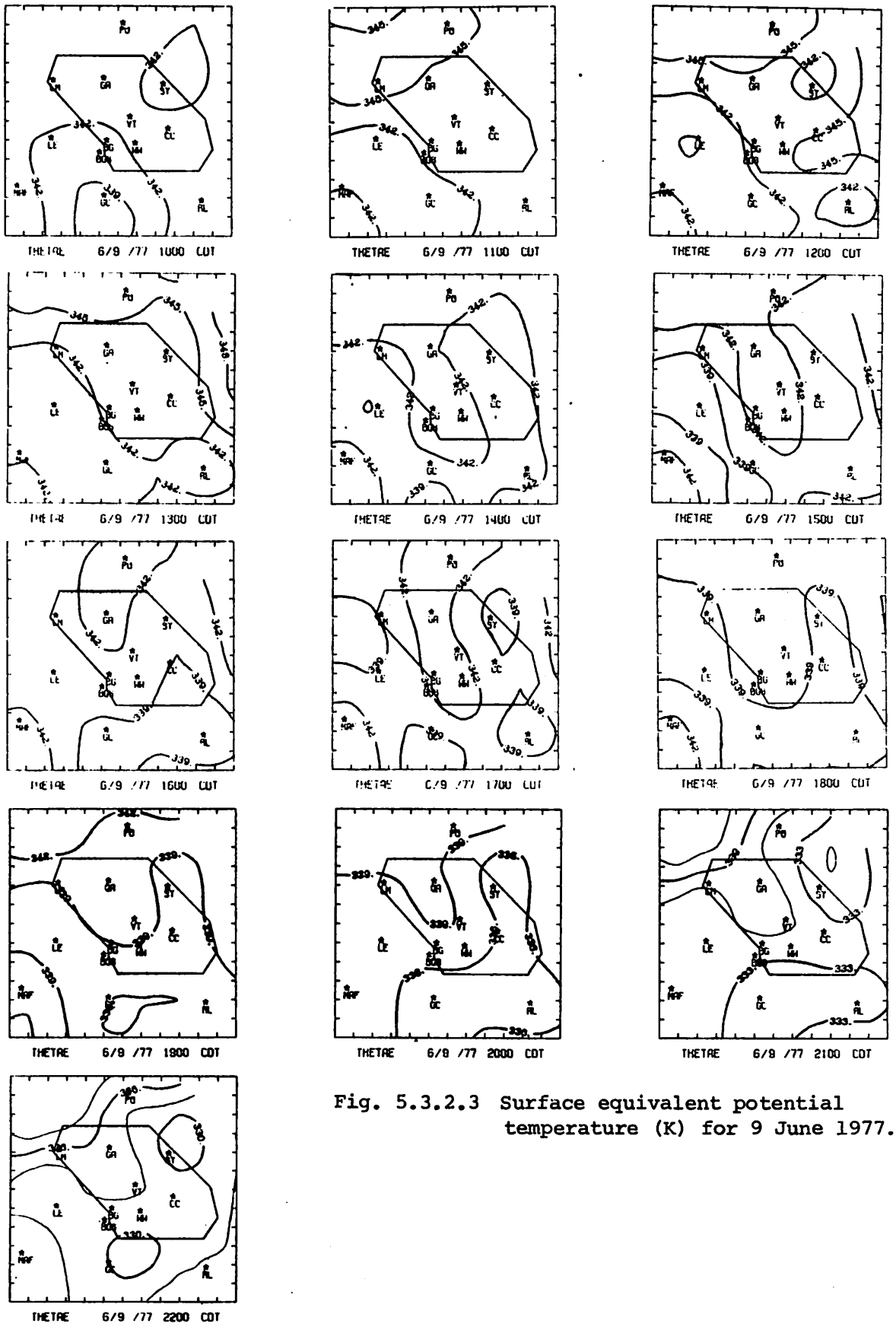

Fig. 5.3.2.3 Surface equivalent potential temperature (K) for 9 June 1977.

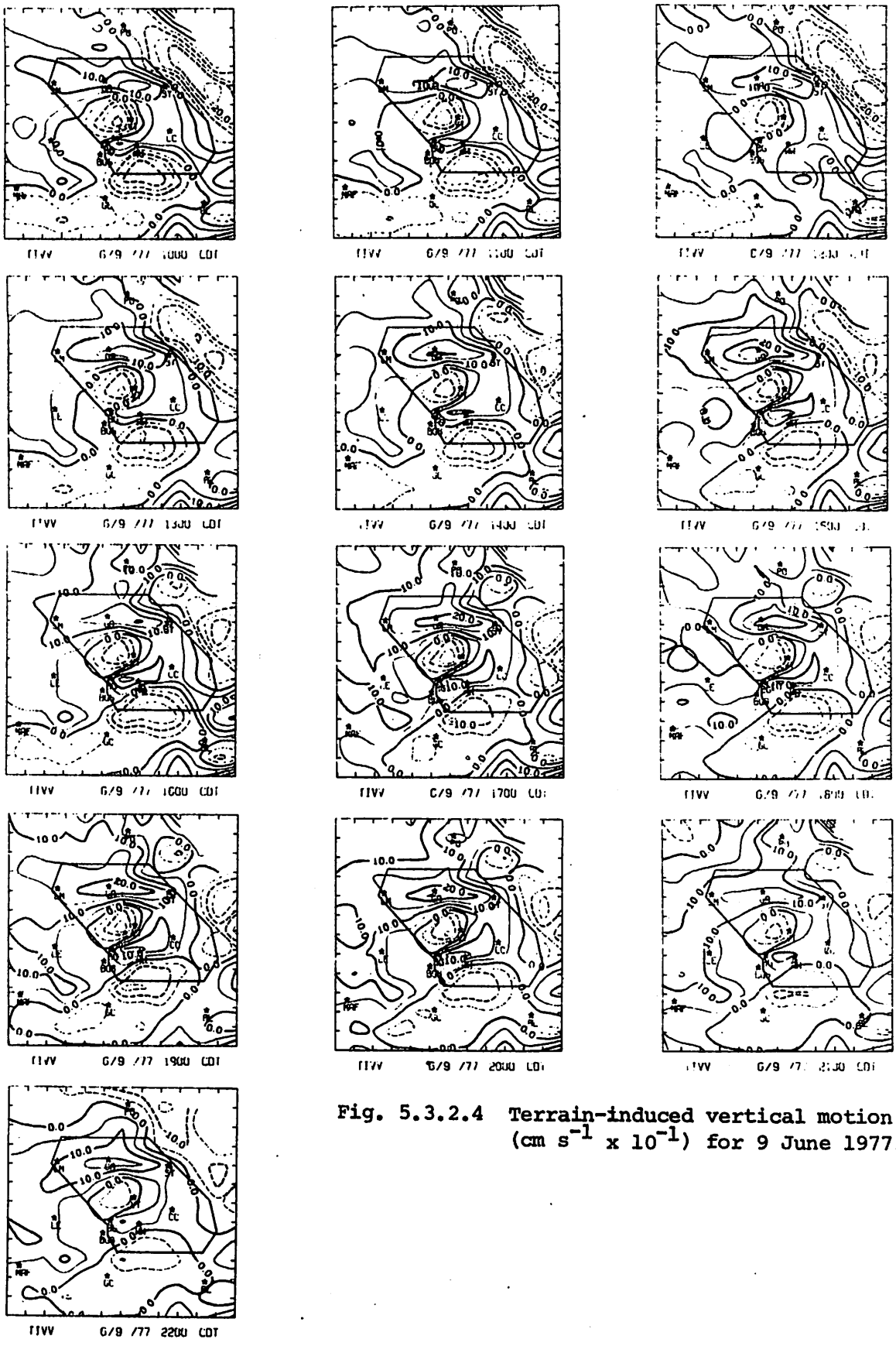

Fig. 5.3.2.4 Terrain-induced vertical motion (cm s^{-1} x 10^{-1}) for 9 June 1977.

vertical motions in the vicinity of convective activity.

Large values of surface velocity divergence (Fig. 5.3.2.5) were observed prior to convective activity, especially in the eastern part of the area. Strong surface velocity convergence correlates well with individual echoes, reaching a maximum at 0200 GMT. A direct relationship between the magnitude of the surface velocity convergence and the echo intensity can be seen. These centers of convergence precede the advance of the storm. Upward vertical motions 50 mb above the surface (Fig. 5.3.2.6), surface moisture divergence (Fig. 5.3.2.7), and vertical flux of moisture 50 mb above the surface (Fig. 5.3.2.8) all correlate well with the surface velocity divergence fields. Strongest upward vertical motion, and vertical moisture flux are found under echoes of strongest intensity. Values become small or negligible elsewhere.

Although large variations in surface vorticity (Fig. 5.3.2.9) exist, little correlation with convective activity is evident. A region of pronounced vorticity over the center of the area occurs at 1700 GMT, which is also reflected by the surface velocity divergence pattern (Fig. 5.3.2.5). This pattern changes by 1800 GMT, showing no relationship to the presence of radar echoes. Sea level pressure patterns (Fig. 5.3.2.10) remain similar with a cell of low pressure located over the center of the network. Negligible surface pressure changes (Fig. 5.3.2.11) exist until 0200 GMT when the influence of the thunderstorm's downdraft increases the surface pressure.

5.3.3 Upper-Level Kinematic Parameters

Mass divergence is the predominent feature in the vertical profiles of horizontal mass divergence at all times and levels except at 2100 GMT and 0000 GMT when mass convergence was computed below 700 mb (Fig. 5.3.3.1). The mass convergence in the lower levels between 2100 and 0000 GMT coincides with thunderstorm formation that occurred over the network. Precipitation had diminished by 0300 GMT when mass divergence was present within the planetary boundary layer.

The vertical velocity profiles show a complete reversal in sign during the day consistent with precipitation formation and dissipation (Fig. 5.3.3.2). Downward vertical velocities at most levels before 2100 GMT are replaced by large upward values by 0000 GMT which quickly change to subsidence at most levels by 0300 GMT.

Horizontal moisture divergence below 800 mb at 1800 GMT changes to

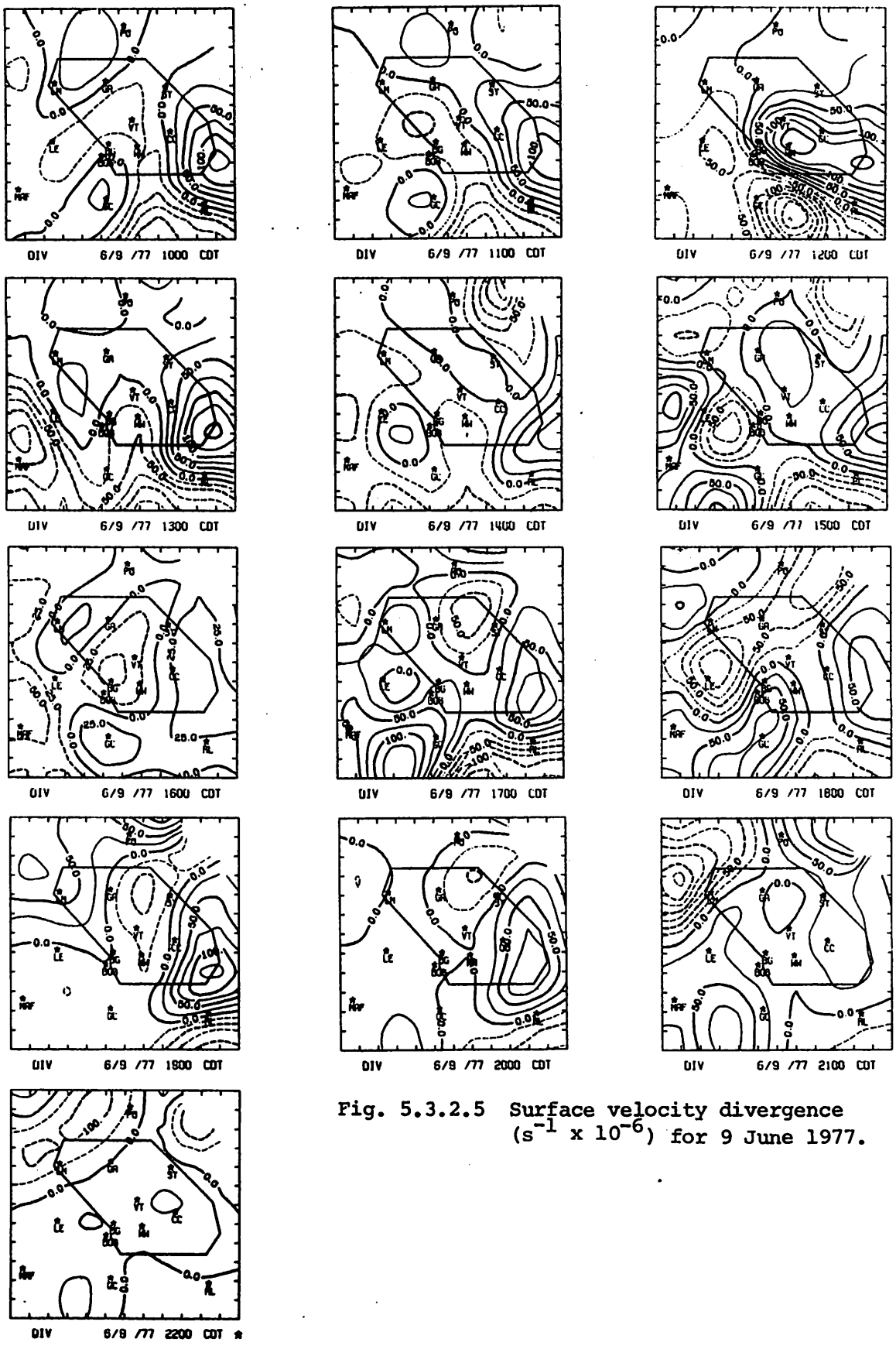

Fig. 5.3.2.5 Surface velocity divergence (s^{-1} x 10^{-6}) for 9 June 1977.

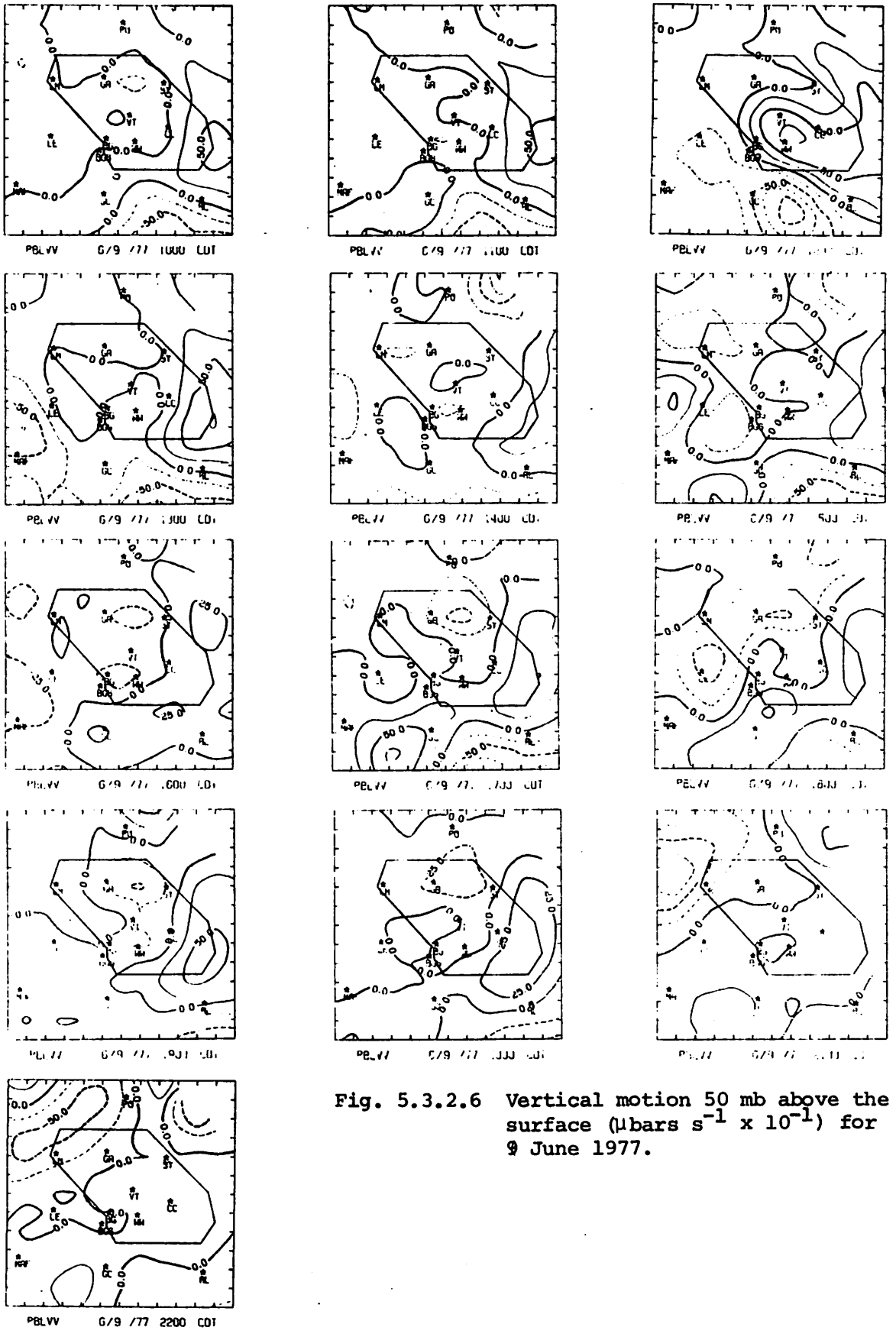

Fig. 5.3.2.6 Vertical motion 50 mb above the surface (μbars s^{-1} x 10^{-1}) for 9 June 1977.

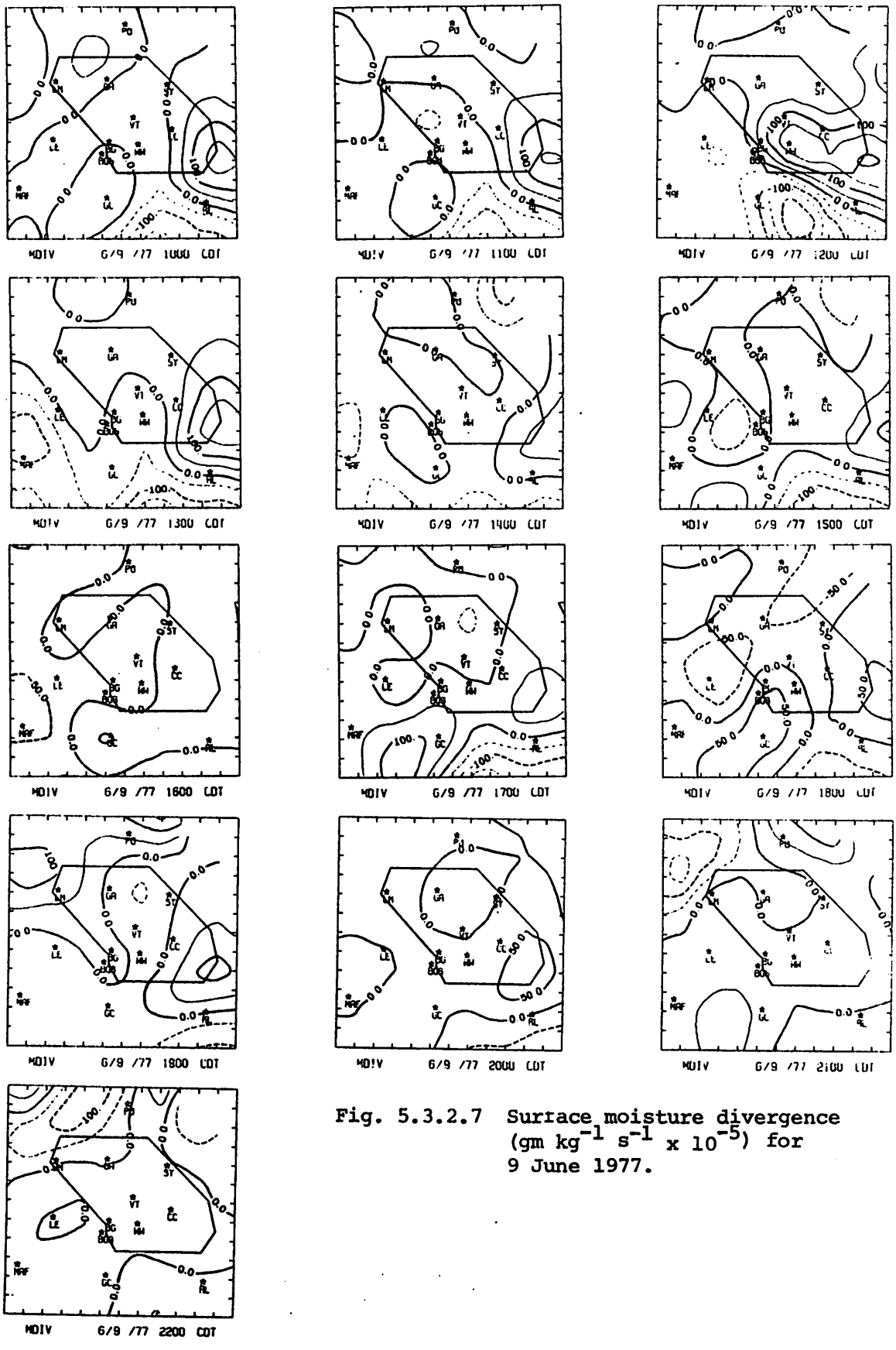

Fig. 5.3.2.7 Surface moisture divergence (gm kg^{-1} s^{-1} x 10^{-5}) for 9 June 1977.

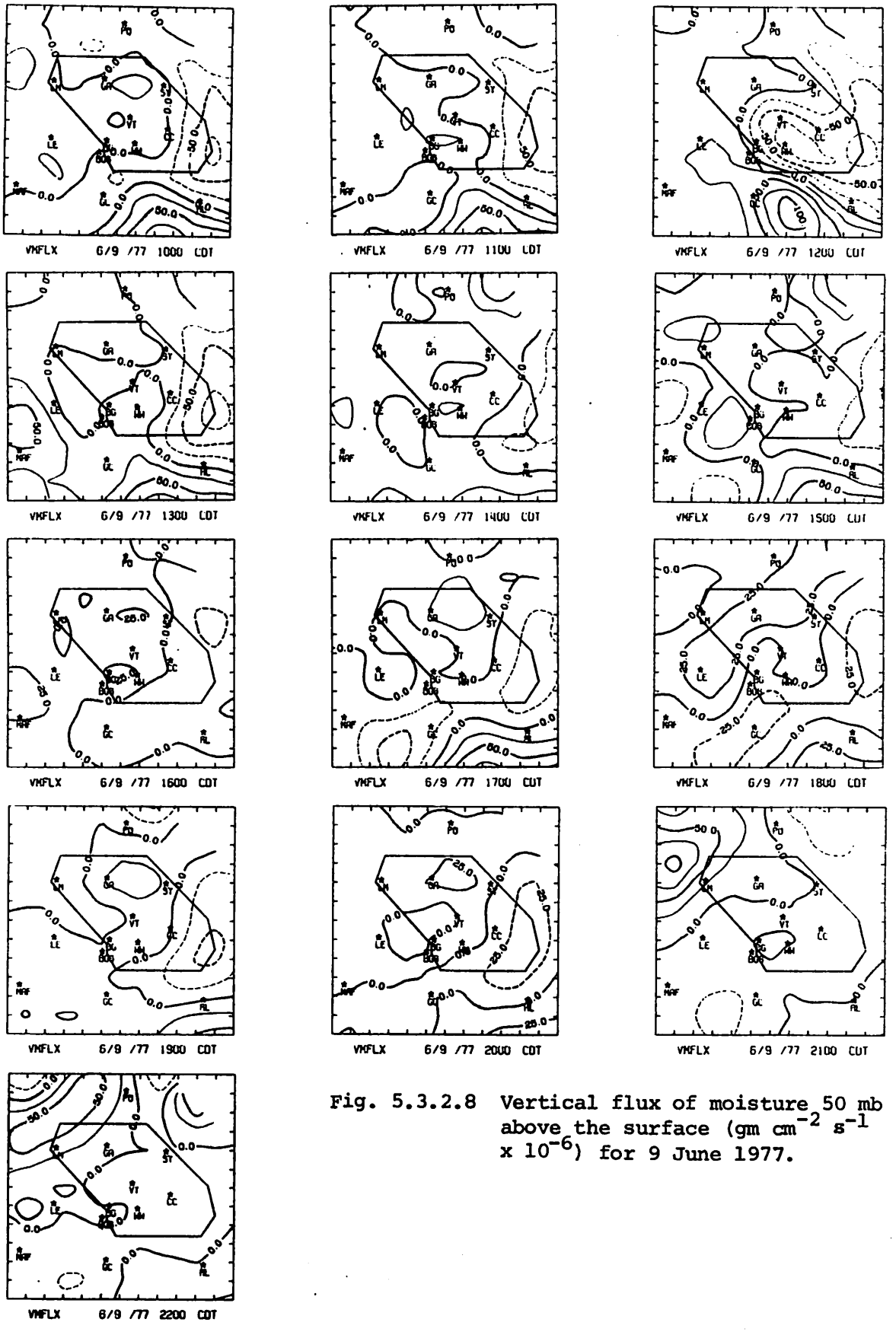

Fig. 5.3.2.8 Vertical flux of moisture 50 mb above the surface (gm cm^{-2} s^{-1} x 10^{-6}) for 9 June 1977.

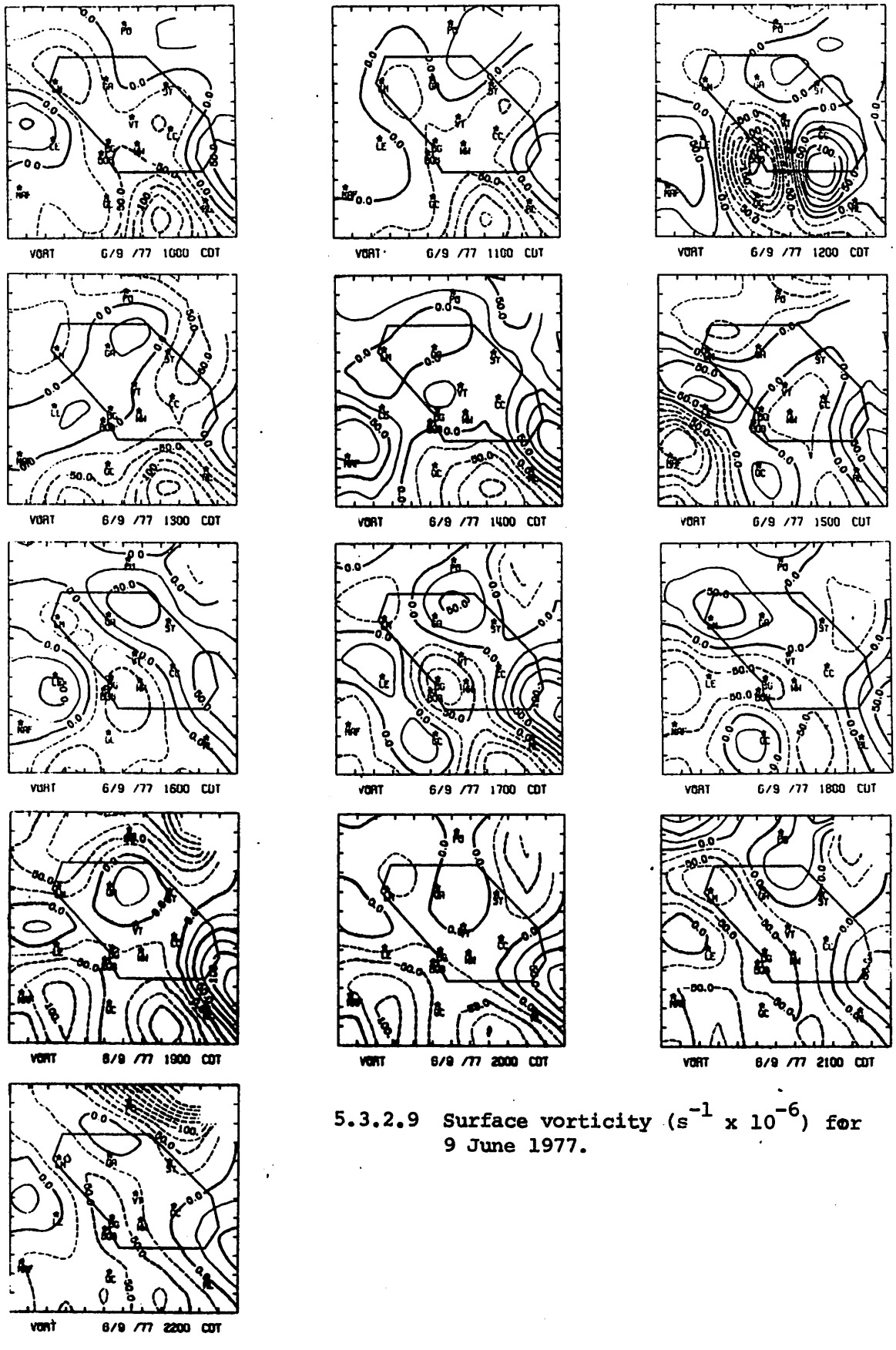

5.3.2.9 Surface vorticity ($s^{-1} \times 10^{-6}$) for 9 June 1977.

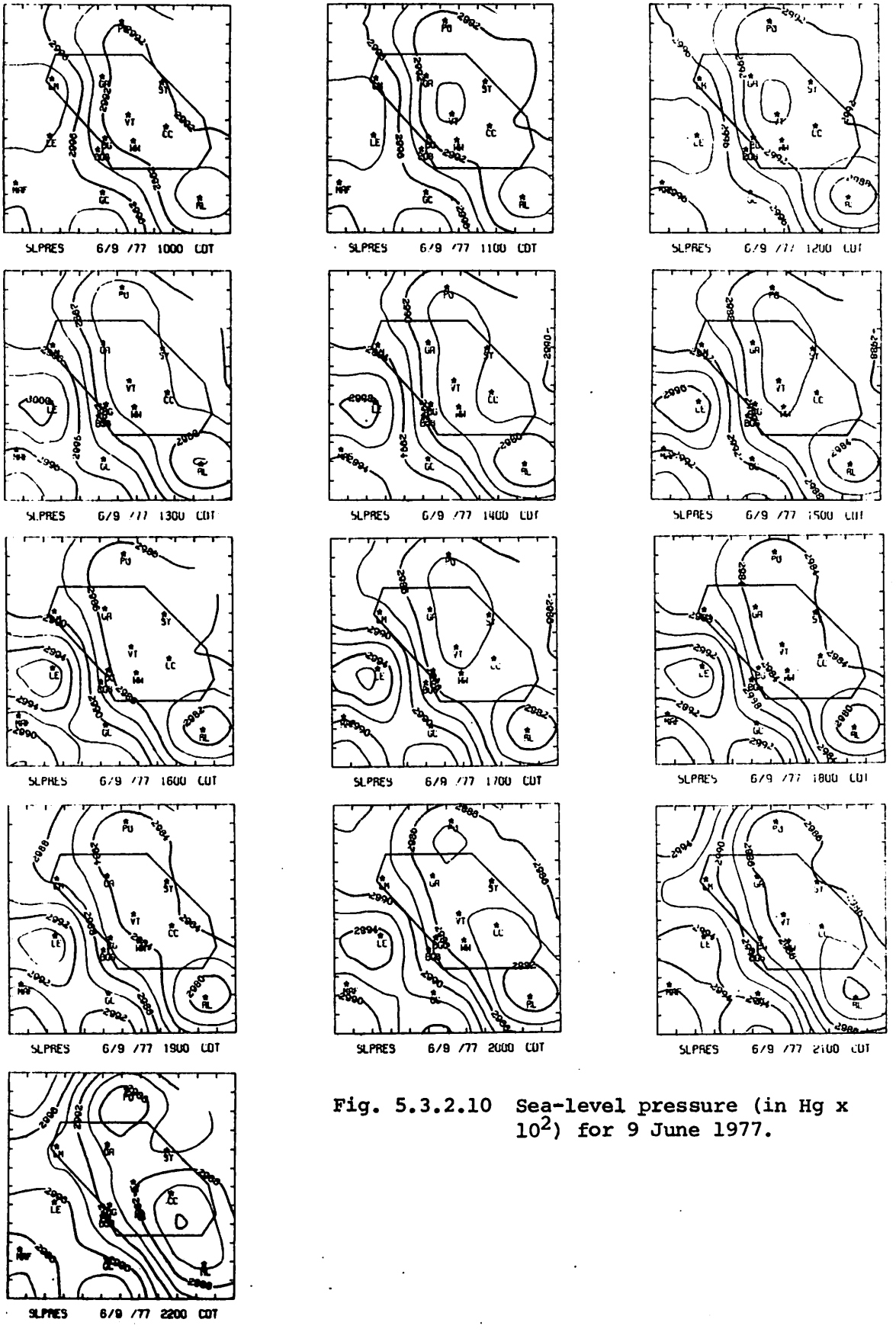

Fig. 5.3.2.10 Sea-level pressure (in Hg x 10^2) for 9 June 1977.

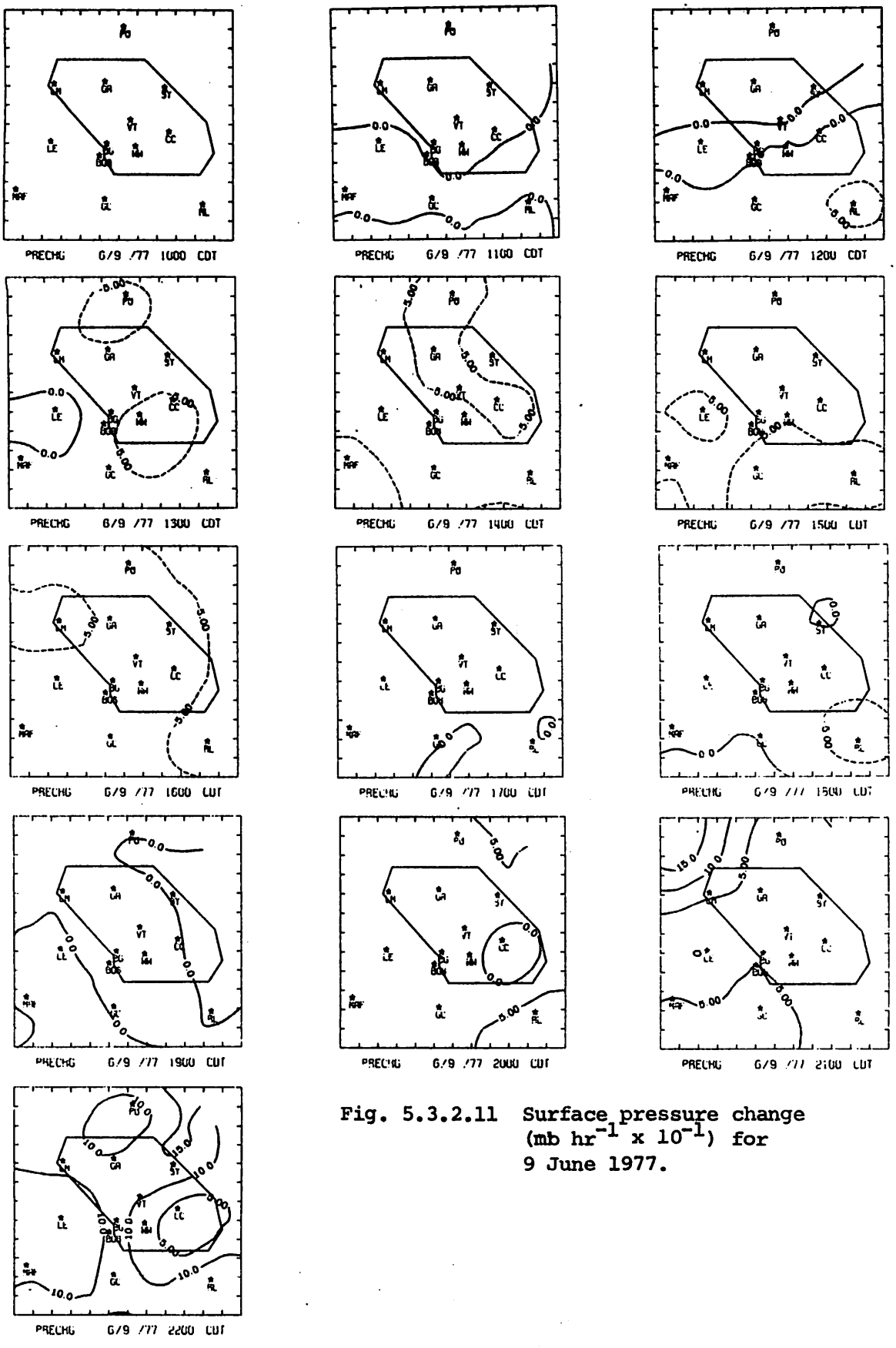

Fig. 5.3.2.11 Surface pressure change (mb hr^{-1} x 10^{-1}) for 9 June 1977.

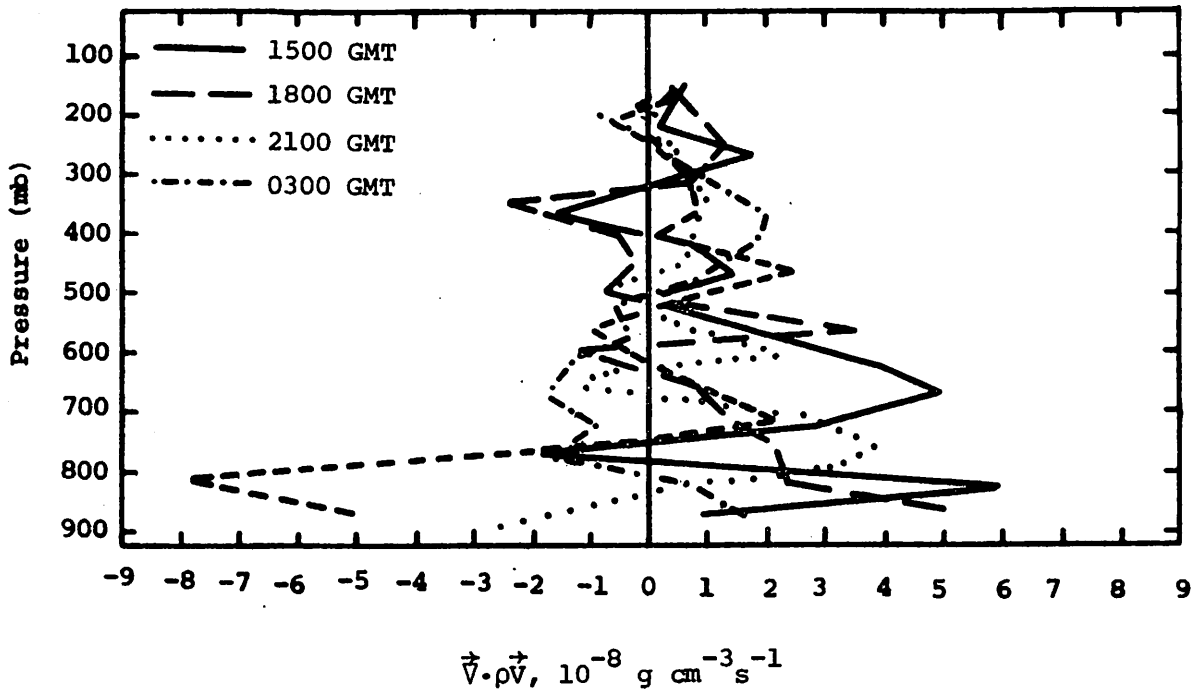

Fig. 5.3.3.1 Vertical profiles of mass divergence on 9 June 1977.

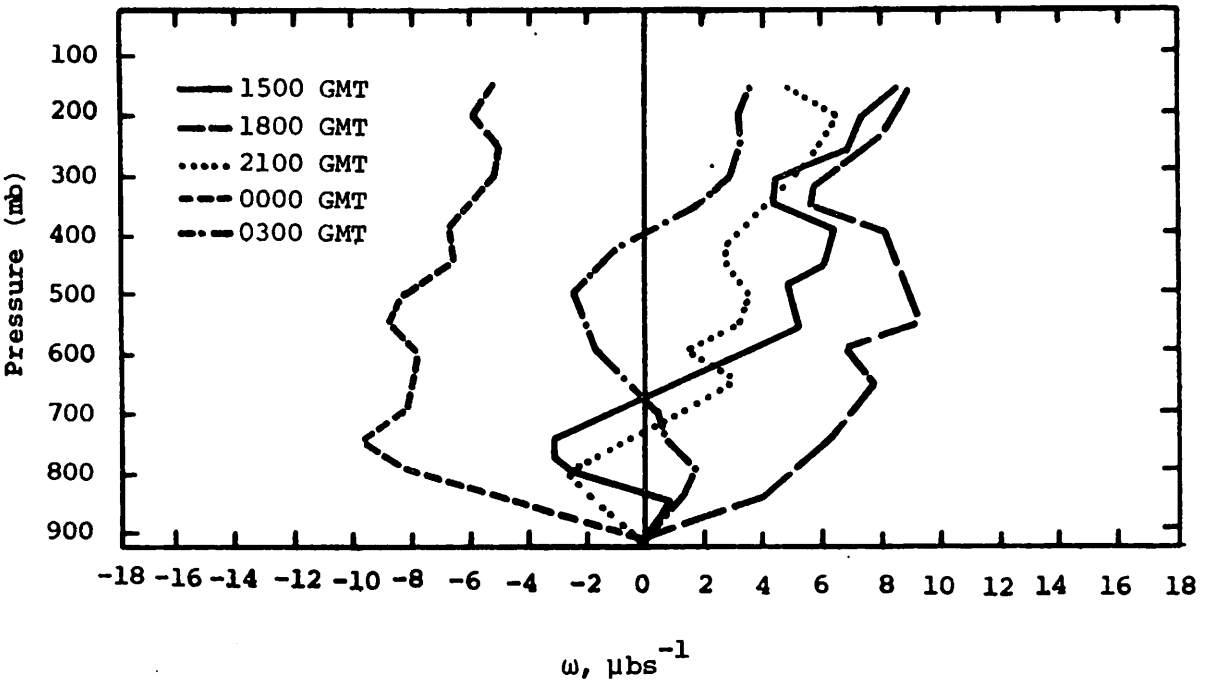

Fig. 5.3.3.2 Vertical profiles of vertical motion on 9 June 1977.

strong convergence by 0000 GMT and then to divergence again by 0300 GMT (Fig. 5.3.3.3). Magnitudes of the horizontal mass divergence are generally small at all times and all levels above 700 mb.

5.3.4 Energetics

Large horizontal inflow of latent heat energy below 800 mb at 1500 GMT changes to strong outflow at 1800 GMT and then returns to strong inflow by 0000 GMT as thunderstorm formation occurs (Fig. 5.3.4.1). By 0300 GMT the thunderstorms had dissipated and net horizontal outflow of latent energy was calculated. During times of thunderstorm activity (2100 and 0000 GMT) horizontal outflow of latent energy was present between 800 and 500 mb which was replaced by inflow after thunderstorm dissipation at 0300 GMT. Vertical flux divergence of latent heat energy occurred below 700 mb at 1500 GMT, 2100 GMT, and 0000 GMT and reversed to flux convergence at these times between 700 and 500 mb (Fig. 5.3.4.2) as latent heat was transported from lower levels to the mid-troposphere and to the upper-troposphere by 0000 GMT. Both before and after the thunderstorms, latent heat was being transported downward from the mid- to lower-troposphere as vertical flux divergence was computed between 700 and 500 mb and flux convergence occurred below. Local changes of latent heat energy were positive at most levels and times consistent with the formation of precipitation (Fig. 5.3.4.3) and remained positive both before and after thunderstorm development. Large positive values at 0300 GMT below 700 mb are possibly associated with the approach from the northwest of a strong line of thunderstorms that later moved into the network.

The residual term from the latent heat budget shows gains of latent energy (-R negative) at most levels before and during thunderstorm formation as the environment is possibly cooled by evaporation and removal of sensible heat energy (Fig. 5.3.4.4). At 0000 GMT, losses of latent energy (-R positive) occurred as condensation developed in the mid- and upper-troposphere, consistent with thunderstorm existence. At 0300 GMT the residual terms return to "near zero" values at most levels.

The diabatic heating profiles (Fig. 5.3.4.5) show time variations consistent in sign with the residual of the latent heat budget. Diabatic cooling at most levels above 700 mb is replaced by heating at 0000 GMT and returns to small values at most levels by 0300 GMT. Diabatic heating occurred below 800 mb between 1500 and 2100 GMT coincident with radiational warming of daytime and cooling was calculated after 0000 GMT following sunset.

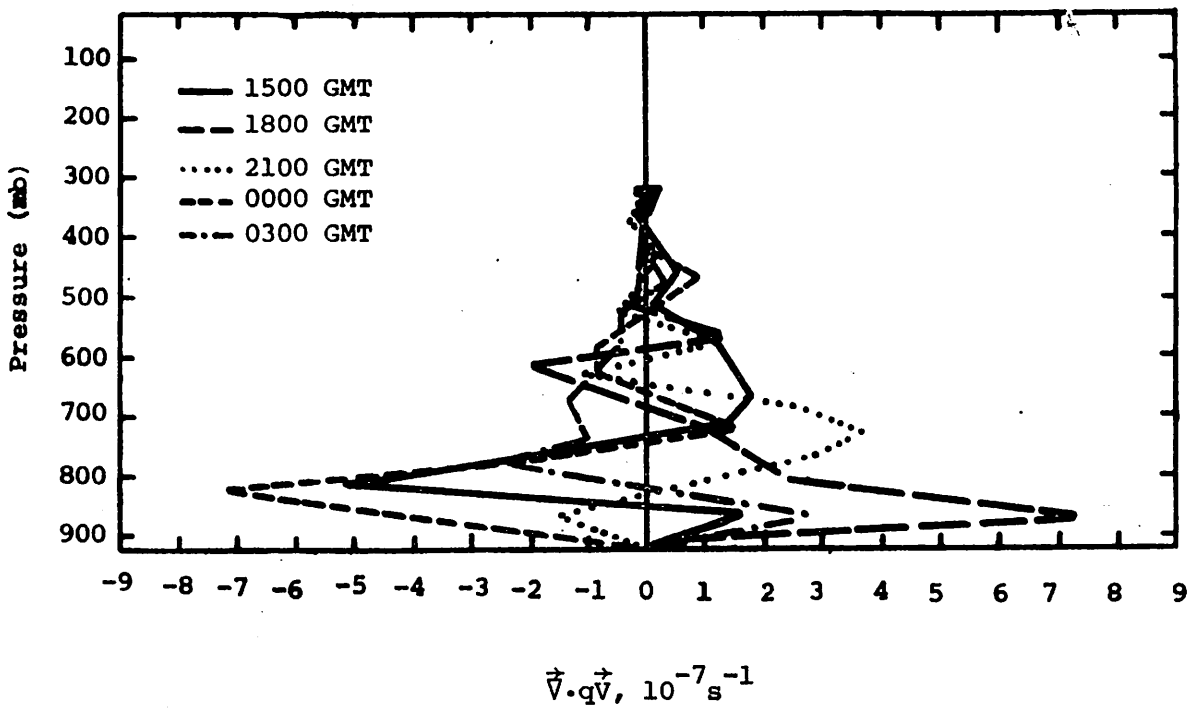

Fig. 5.3.3.3 Vertical profiles of moisture divergence on 9 June 1977.

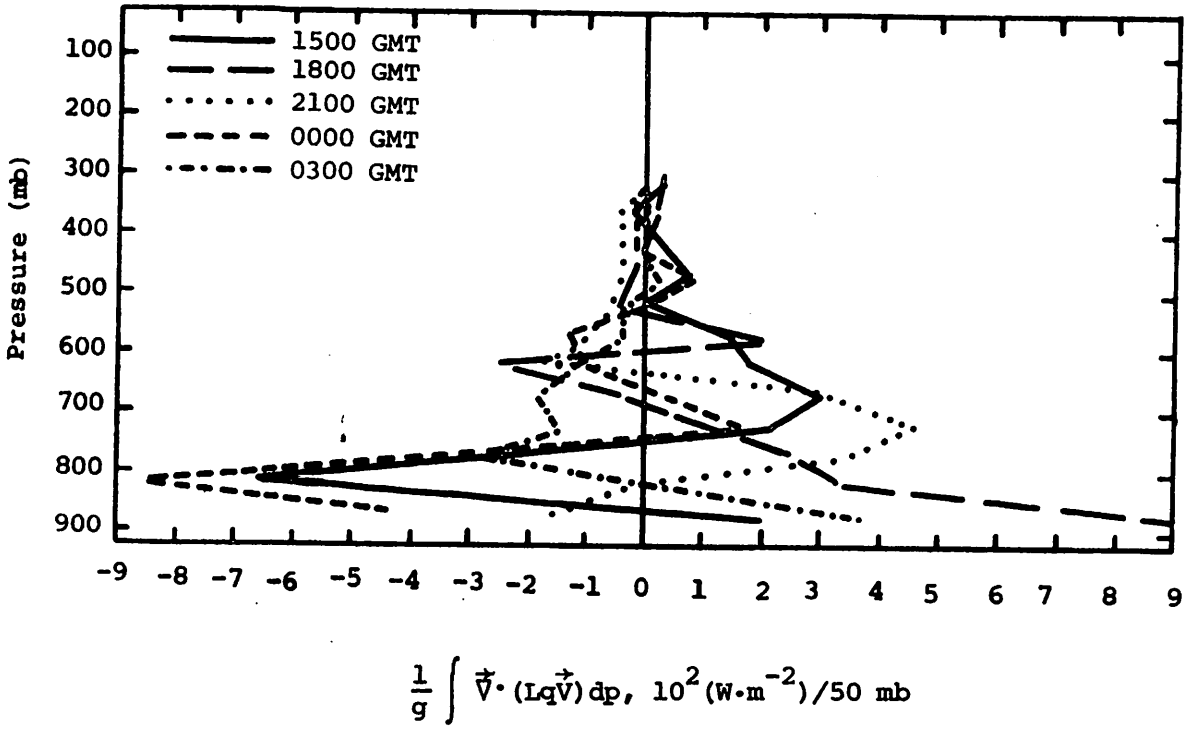

Fig. 5.3.4.1 Vertical profiles of the horizontal flux of latent heat energy on 9 June 1977.

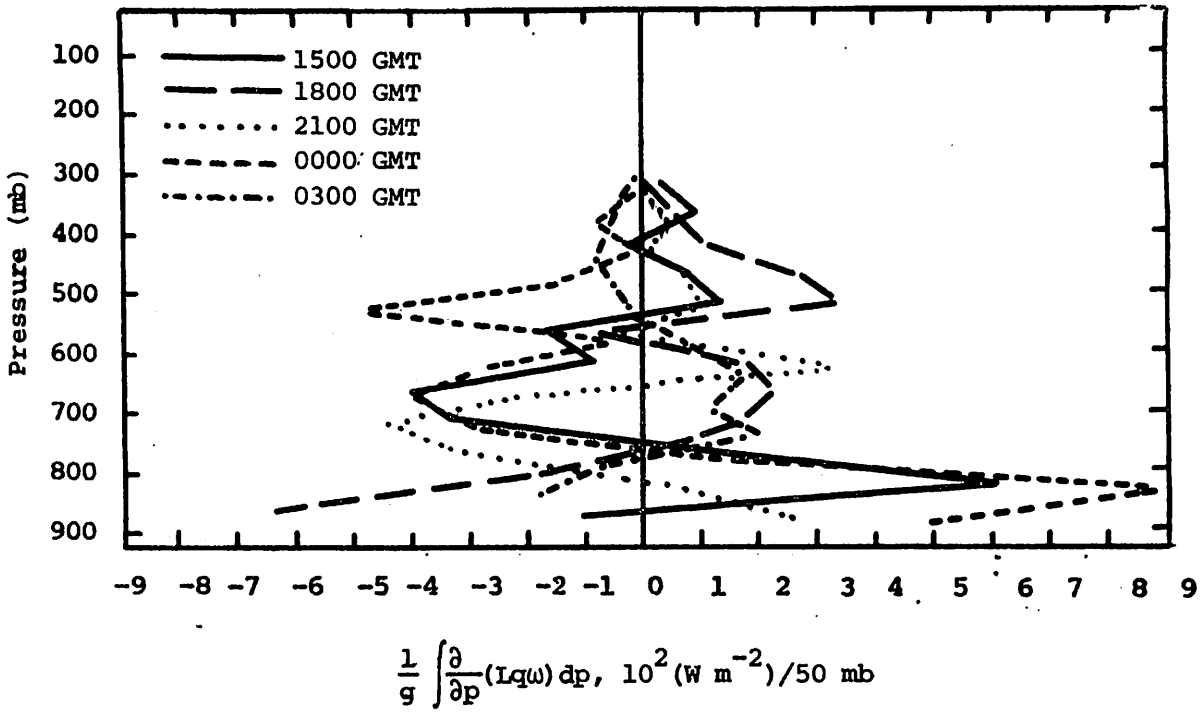

Fig. 5.3.4.2 Vertical profiles of the vertical flux of latent heat energy on 9 June 1977.

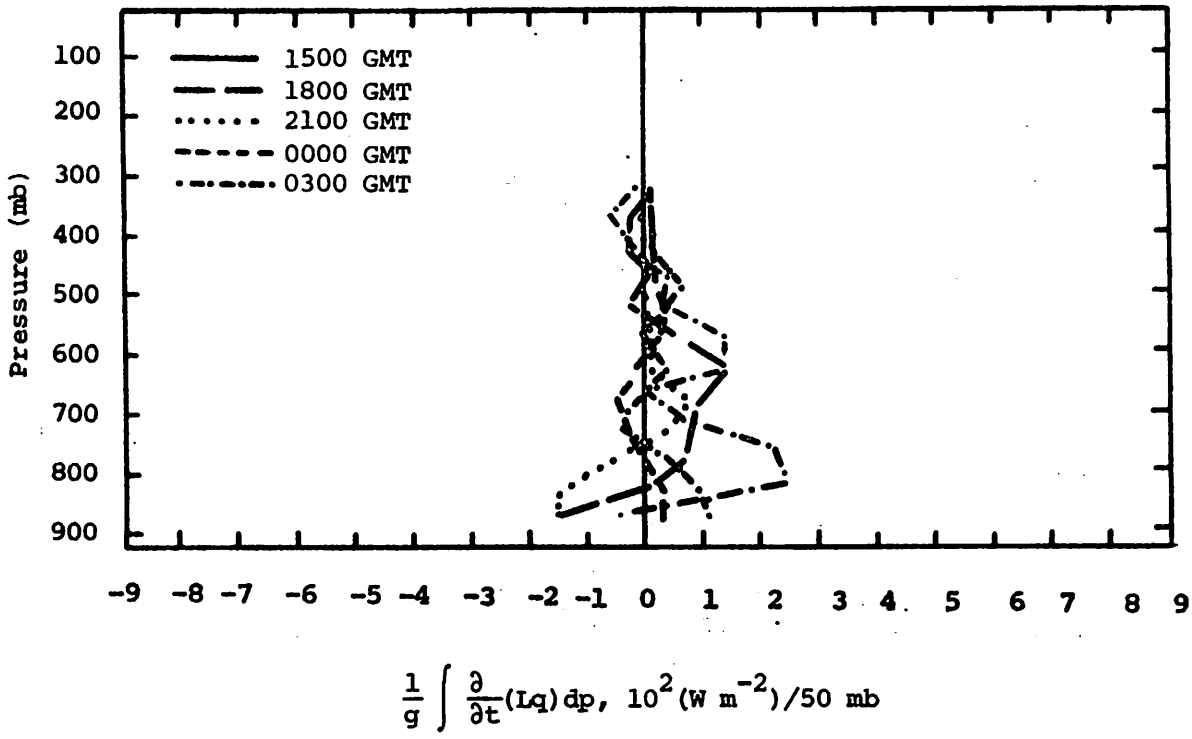

Fig. 5.3.4.3 Vertical profiles of the local change of latent heat energy on 9 June 1977.

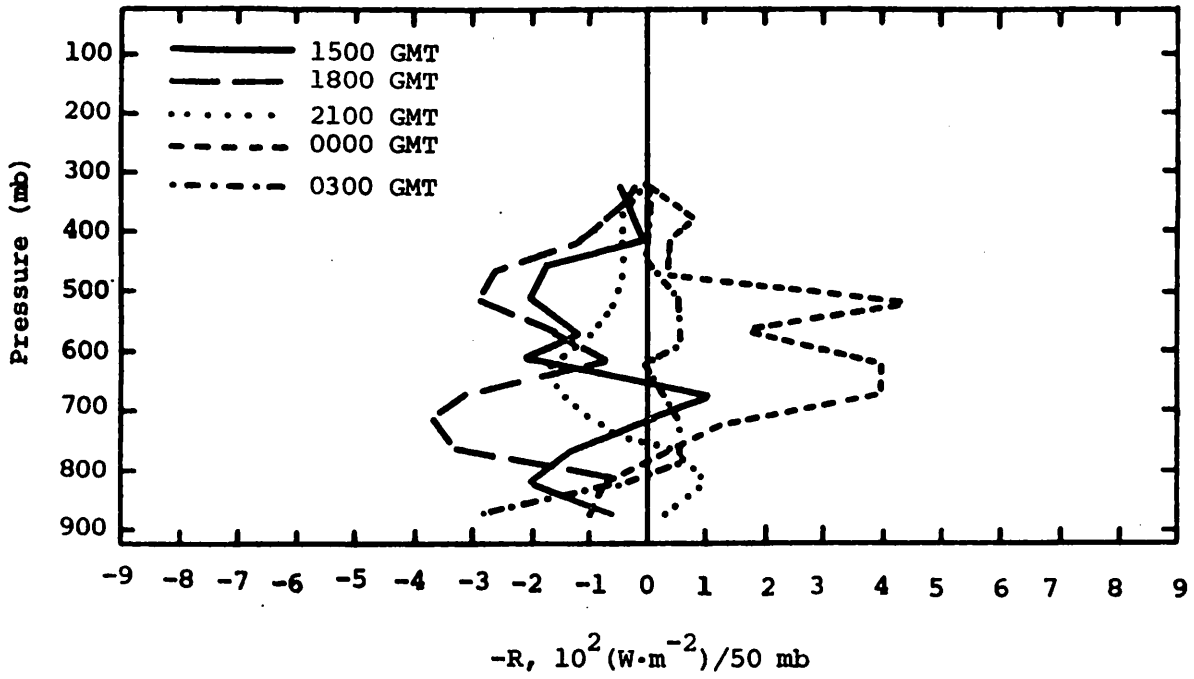

Fig. 5.3.4.4 Vertical profile of the residual of the latent heat energy equation on 9 June 1977.

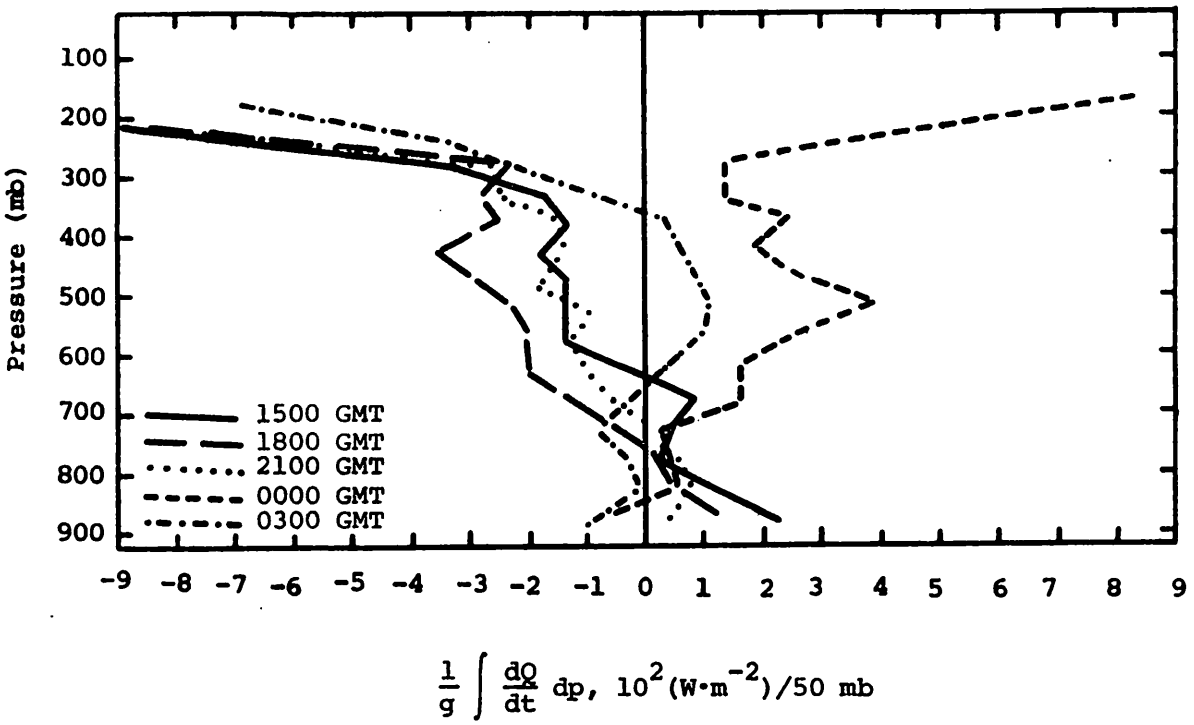

Fig. 5.3.4.5 Vertical profiles of diabatic heating computed from the first law of thermodynamics on 9 June 1977.

Horizontal flux divergence of kinetic energy occurred at most levels throughout the day except at 1500 GMT and 0000 GMT when flux convergence occurred in lower and upper levels (Fig. 5.3.4.6). Vertical flux divergence profiles of kinetic energy (Fig. 5.3.4.7) showed convergence between 700 and 500 mb and divergence between 500 and 300 mb before thunderstorm formation as kinetic energy was transported from the upper- to mid-troposphere. After 1800 GMT the profiles were vertically erratic and hard to interpret except above 300 mb where vertical flux convergence was large.

5.3.5 Water Vapor Budget

Radar charts show no activity over the Texas HIPLEX area until 2000 GMT. At this time, several isolated cells, varying in intensity, enter and move through the area.

Figure 5.3.5.1 shows vertical profiles of the net horizontal transport of water vapor. These profiles vary both spatially and temporally, which may be attributed to the scattered pattern of these isolated cells. At 0300 GMT, several echoes with tops exceeding 9.1 km (30K ft) move into the area. This can be seen by a large net inflow for most layers in the 0300 GMT profile.

Figure 5.3.5.2 shows profiles of net vertical transport of water vapor. Again, as in Figure 5.3.5.1, these profiles vary in space and time. The 0300 GMT profile shows a net inflow for layers above 600 mb, and a net outflow in layers below. This "storage" of water vapor seems to be a characteristic of heavy convection, and has also been observed in the analysis of 1976 data.

Figure 5.3.5.3 shows profiles of vertical transport of water vapor through constant pressure surfaces. Again, large spatial and temporal variations are observed. Strong upward transport of water vapor is present at 0000 GMT and in layers above 650 mb at 0300 GMT, prior to heavy convection.

Figure 5.3.5.4 shows profiles of the combined net horizontal and vertical transport of water vapor. Profiles prior to 0000 GMT generally show a net inflow in the lowest layers and a net outflow aloft. At 0000 GMT when strong convection approaches the network, a net inflow occurred in most layers in the 0000 and 0300 GMT profiles. However, the greatest inflow of water vapor is observed at 0000 GMT, prior to the appearance of the strongest

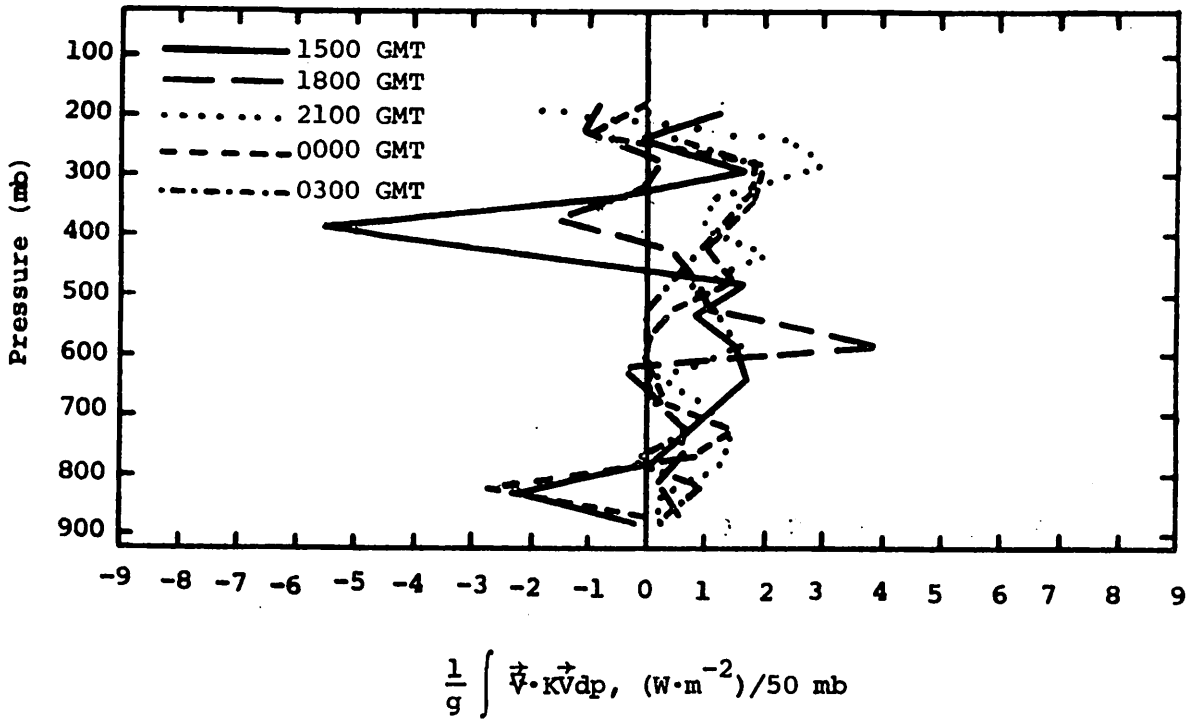

Fig. 5.3.4.6 Vertical profiles of the horizontal flux of kinetic energy on 9 June 1977.

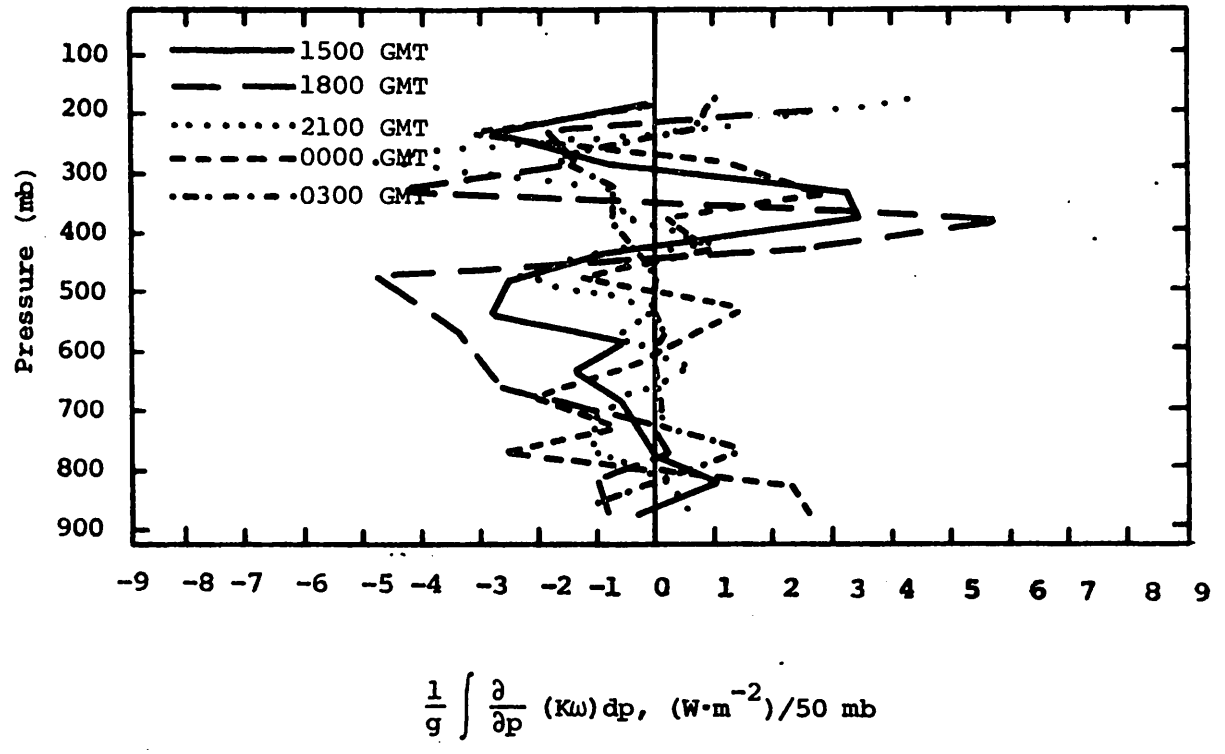

Fig. 5.3.4.7 Vertical profiles of the vertical flux of kinetic energy on 9 June 1977.

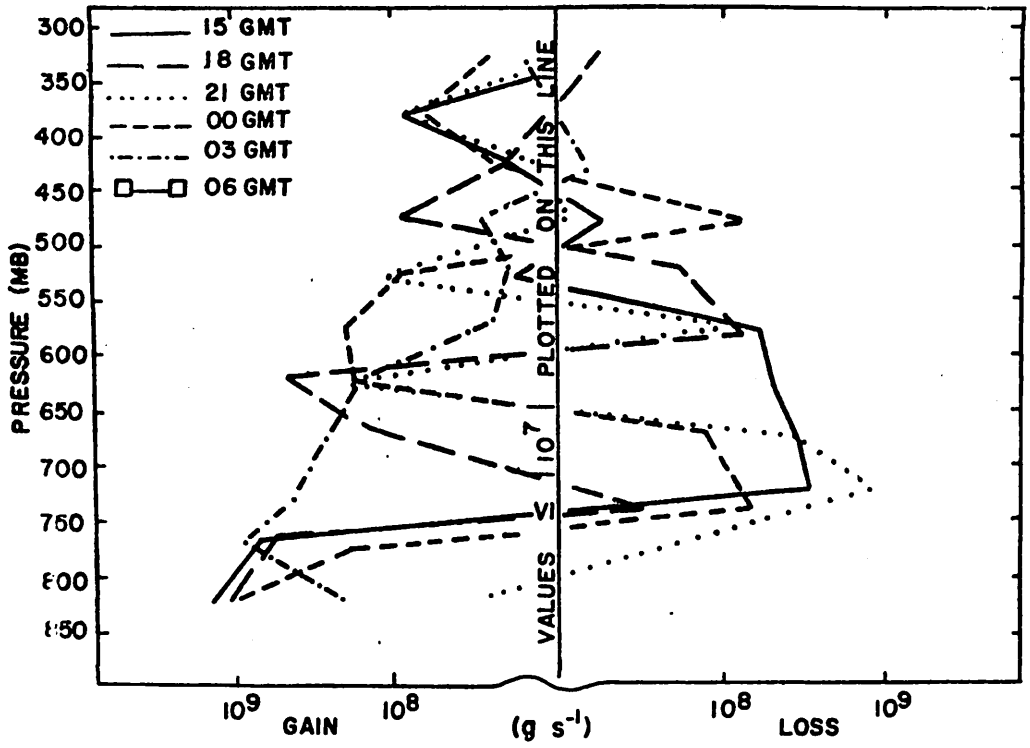

Fig. 5.3.5.1 Net horizontal transport of water vapor through boundaries of 50-mb layers (gm s^{-1}) over the Texas HIPLEX area for 9 June 1977.

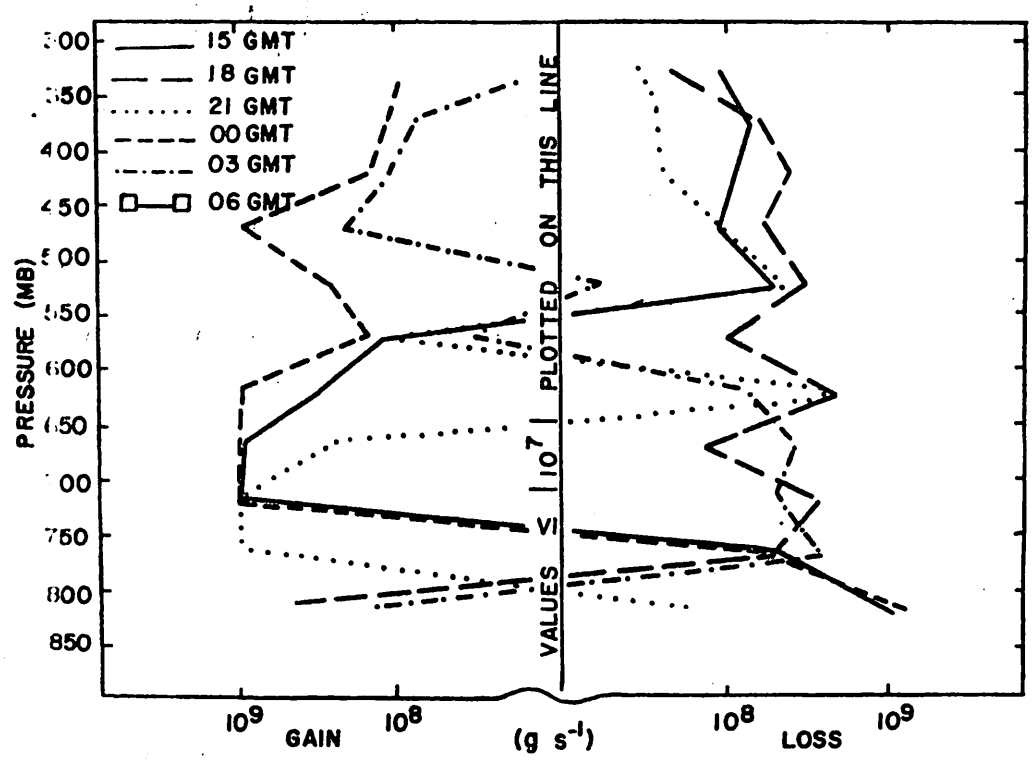

Fig. 5.3.5.2 Net vertical transport of water vapor through boundaries of 50-mb layers (gm s^{-1}) over the Texas HIPLEX area for 9 June 1977.

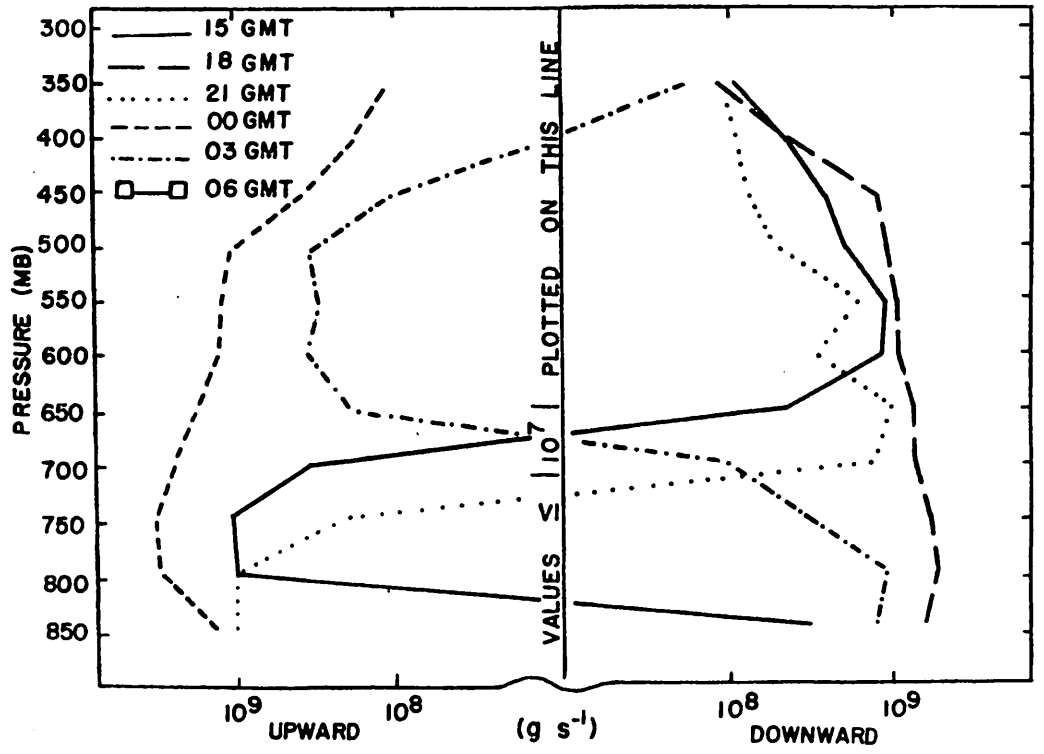

Fig. 5.3.5.3 Vertical transport of water vapor through constant pressure surfaces (gm s^{-1}) over the Texas HIPLEX area for 9 June 1977.

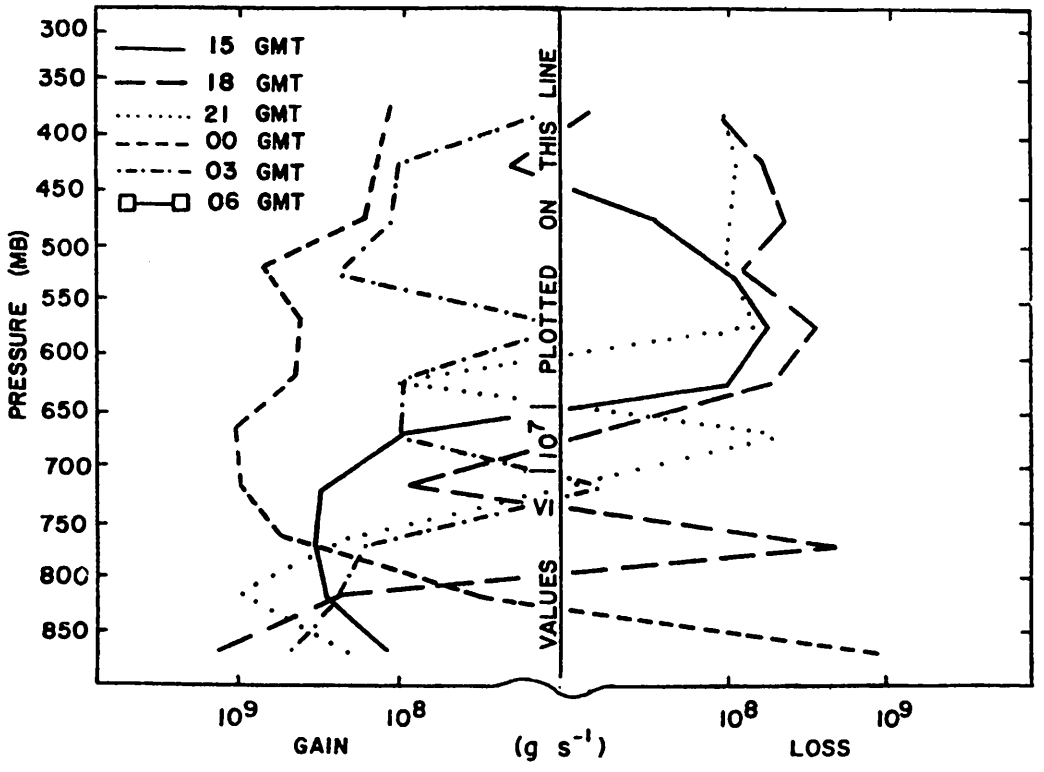

Fig. 5.3.5.4 Combined net horizontal and vertical transport of water vapor through boundaries of 50-mb layers (gm s^{-1}) over the Texas HIPLEX area for 9 June 1977.

echoes.

Figure 5.3.5.5 shows vertical profiles of the total mass of water vapor. These profiles remain nearly constant with time. However, the increase with time of water vapor in most layers prior to heavy convection at 0300 GMT can be seen.

Figure 5.3.5.6 shows vertical profiles of the local rate-of-change in the mass of water vapor with the appearance of the first echo at 2000 GMT. A large gain in water vapor is observed up to 500 mb. From 2100 to 0000 GMT, a gain occurred in most layers, reaching a maximum between 600 to 400 mb. This increase is shown in Figure 5.3.5.3, where strong vertical motion at 0000 GMT transports this water vapor to upper layers. This transport continues through 0300 GMT, where a net loss is seen in layers between 750 and 650 mb.

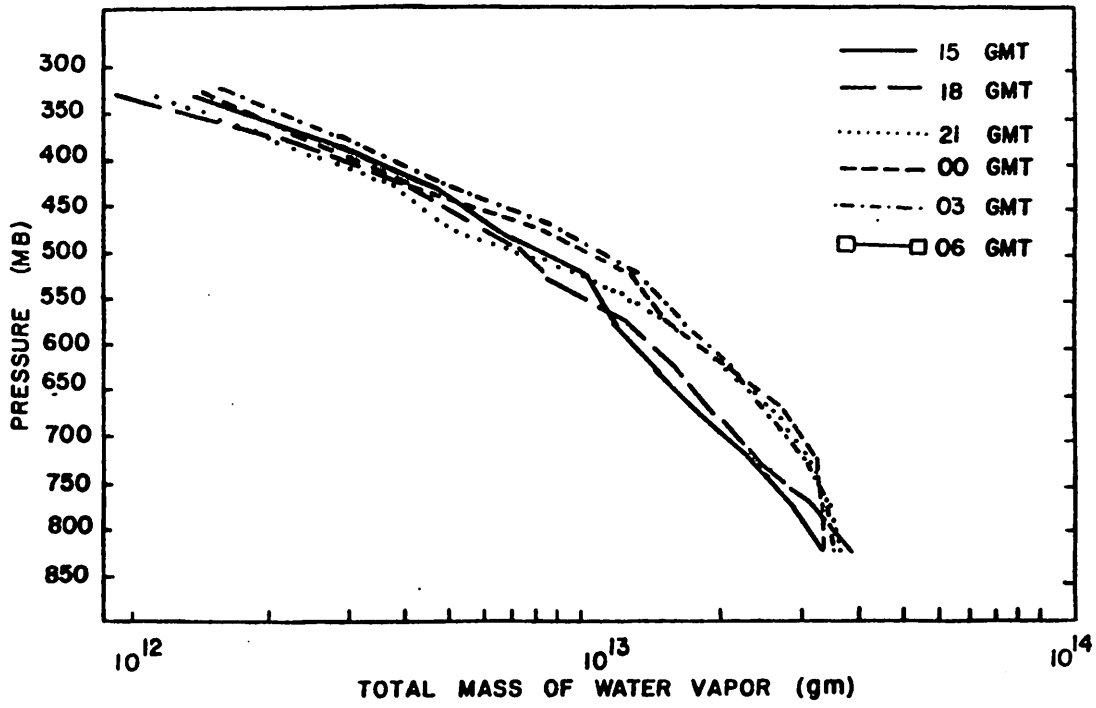

Fig. 5.3.5.5 Total mass of water vapor in layers 50 mb deep (gm) over the Texas HIPLEX area for 9 June 1977.

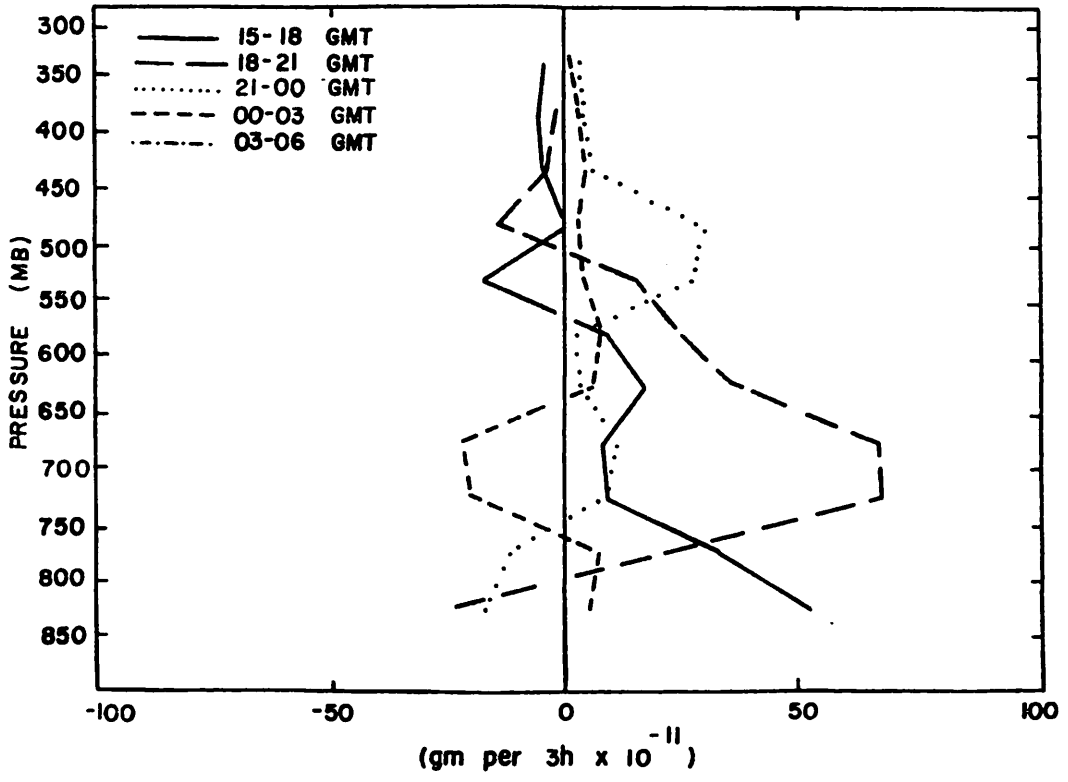

Fig. 5.3.5.6 Local rate-of-change in total mass of water vapor (gm per 3h x 10^{-11}) over the Texas HIPLEX area for 9 June 1977.

5.4 10 June 1977

5.4.1 Radar

Radar echoes were observed on this day beginning at 2100 GMT (Fig. 5.4.1.1). Between 2200 and 0200 GMT an echo with tops exceeding 9.1 km (30K ft) persisted over the northwest part of the target area. Little movement of the echo is indicated during this period, and by 0300 GMT the top of the echo had lowered and the echo was apparently dissipating.

5.4.2 Surface

Surface temperature fields (Fig. 5.4.2.1) show the effect of surface heating prior to the onset of convective activity at 2100 GMT. The thunderstorm's influence upon surface temperatures is first observed at 0200 GMT, during the dissipating stages of the storm. A region of minimum temperature, decreasing with time, occurs west of the storm.

Higher values of mixing ratio (Fig. 5.4.2.2) are observed prior to convective activity northwest of Lamesa. An increase in surface mixing ratio is also seen during the dissipating stages of the thunderstorm. This maximum increase occurs in the same region of minimum surface temperature (Fig. 5.4.2.1). Significant changes in surface equivalent potential temperature (Fig. 5.4.2.3) correspond with surface mixing ratio.

Terrain-induced vertical motion fields (Fig. 5.4.2.4) show a large temporal change, decreasing in magnitude. Prior to convective activity, large downward terrain-induced vertical motion exceeding 2 cm s^{-1} was observed northeast of Snyder. During convection, terrain-induced vertical motion approaches zero, showing a negligible contribution to kinematic vertical velocity.

Surface velocity divergence (Fig. 5.4.2.5) is observed prior to convective activity, especially in the eastern part of the area. At 0100 GMT, pronounced areas of strong surface convergence and divergence existed. During dissipation, surface velocity divergence decreased to nearly zero by 0300 GMT. Vertical motion 50 mb above the surface (Fig. 5.4.2.6) indicates strong downward motion north of the thunderstorm, and upward motion to the south which decreased to near zero by 0300 GMT.

Surface moisture divergence (Fig. 5.4.2.7) and vertical flux of moisture 50 mb above the surface (Fig. 5.4.2.8) also show similar

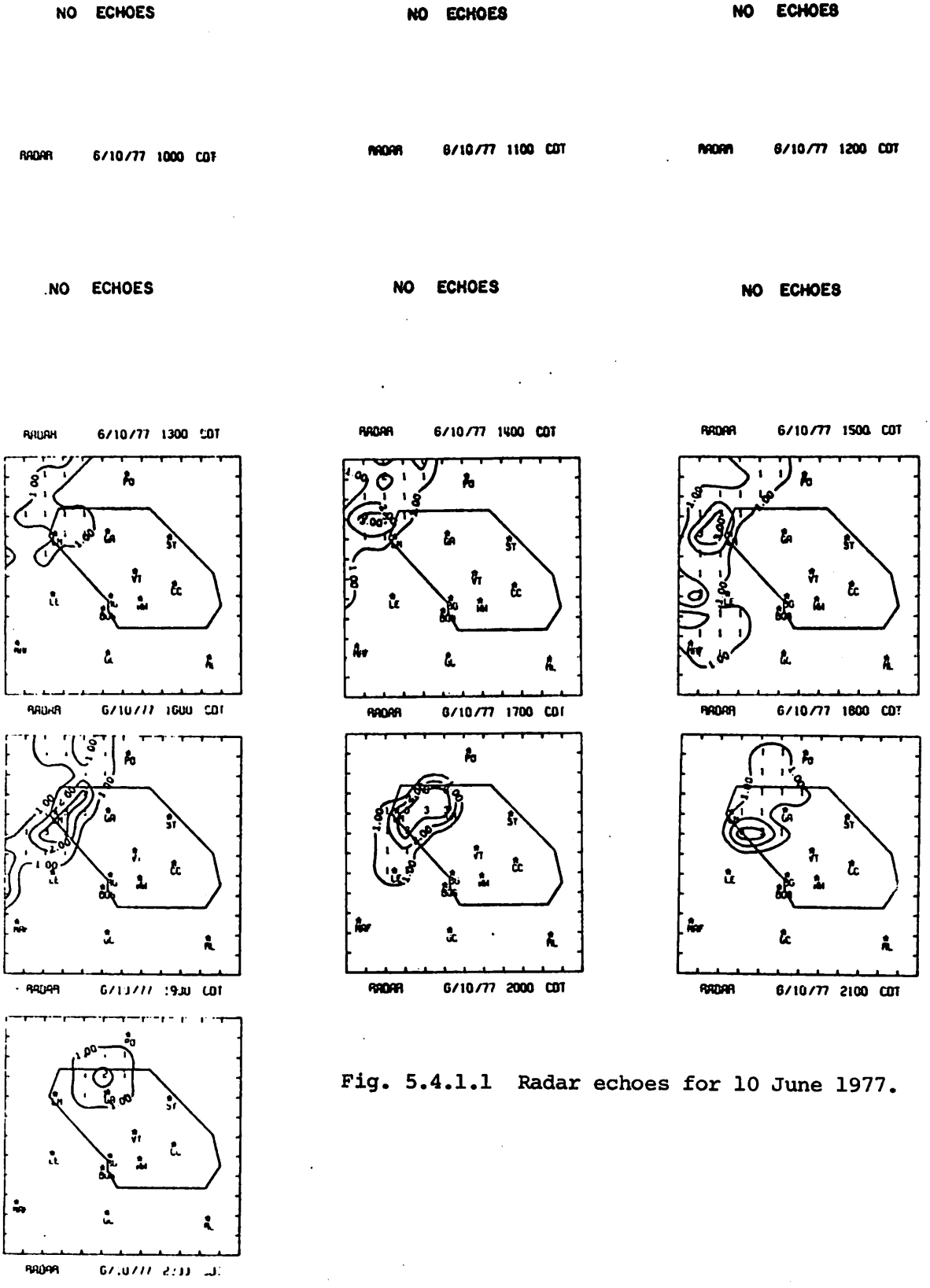

Fig. 5.4.1.1 Radar echoes for 10 June 1977.

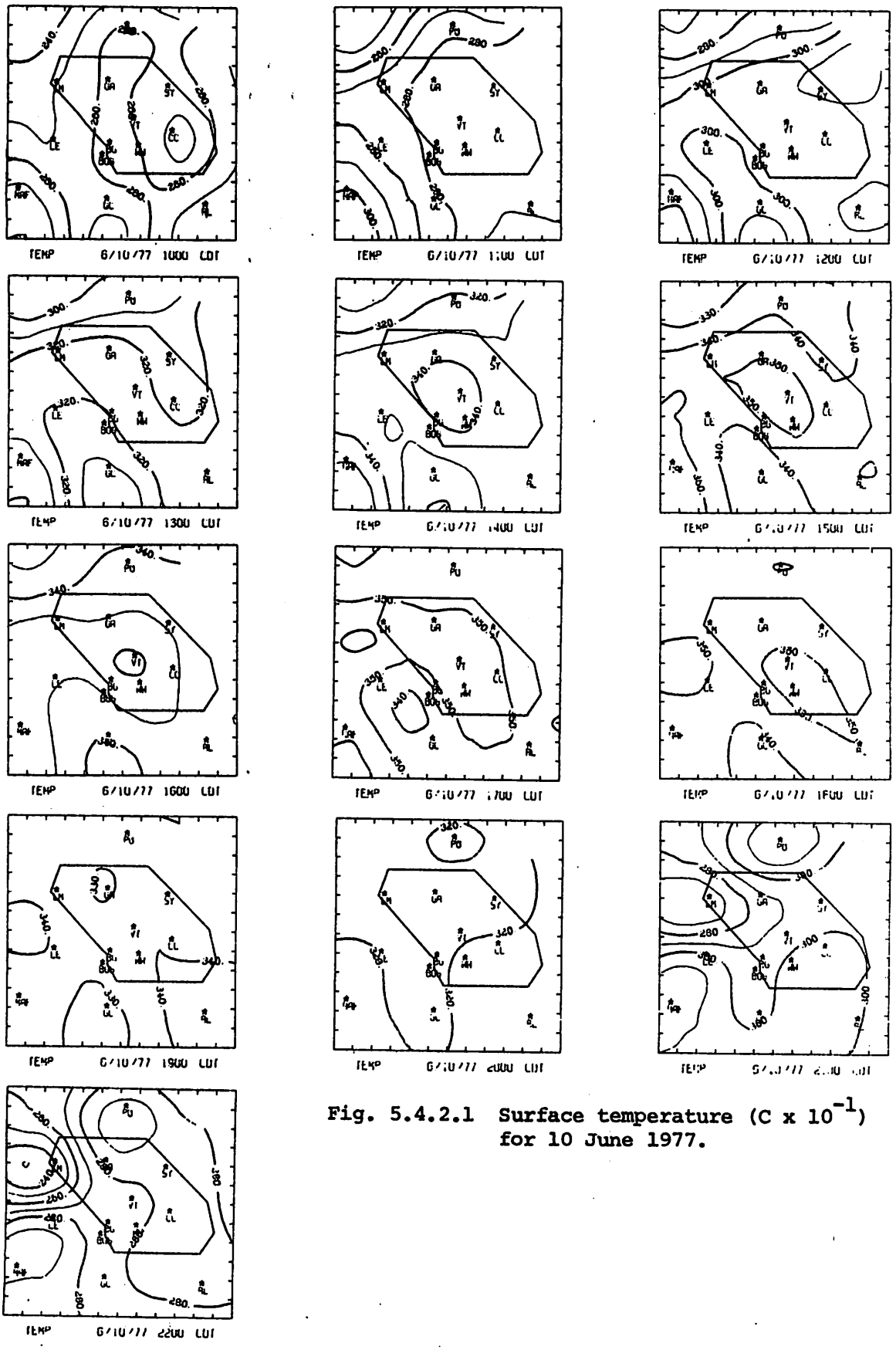

Fig. 5.4.2.1 Surface temperature (C x 10^{-1}) for 10 June 1977.

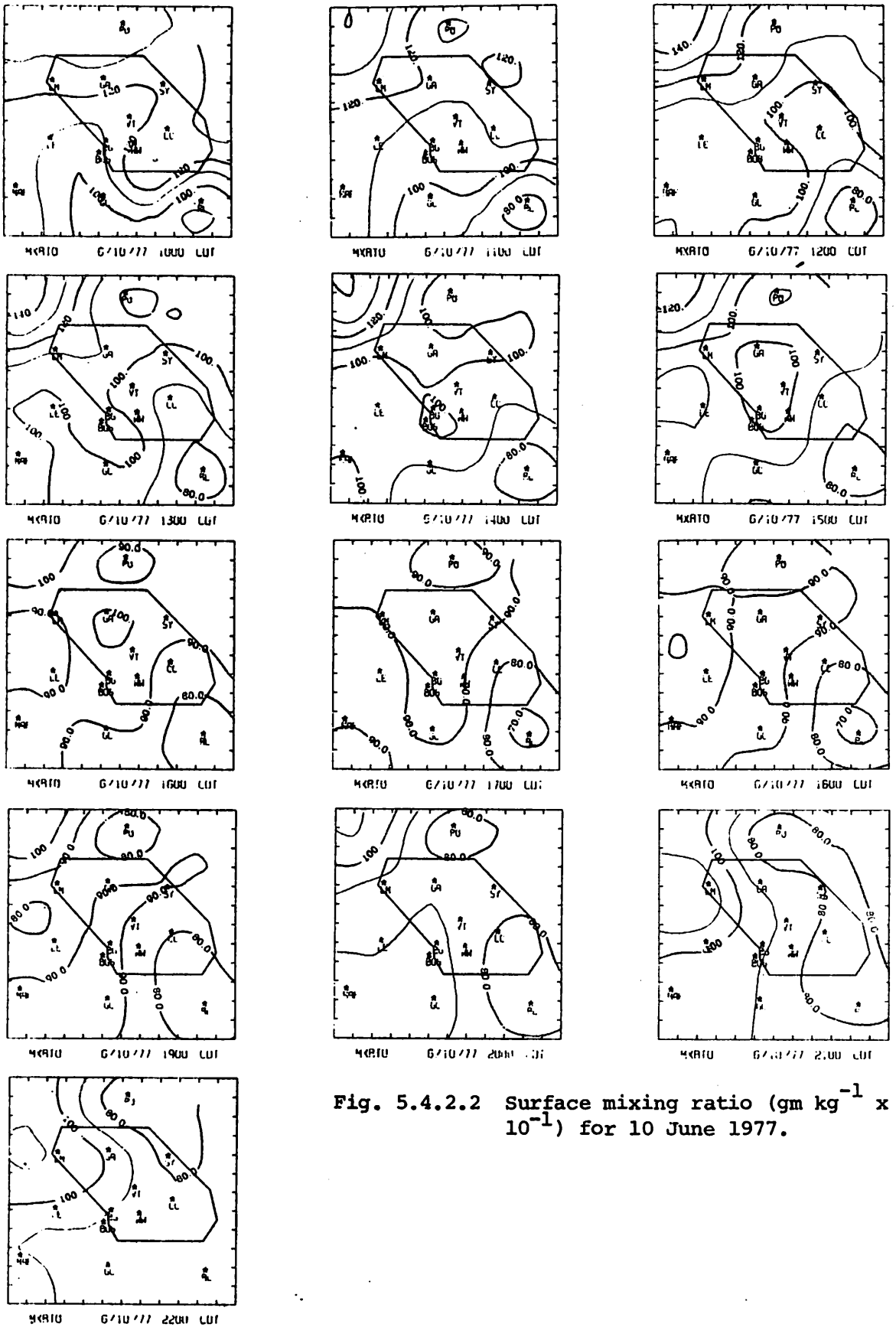

Fig. 5.4.2.2 Surface mixing ratio (gm kg^{-1} x 10^{-1}) for 10 June 1977.

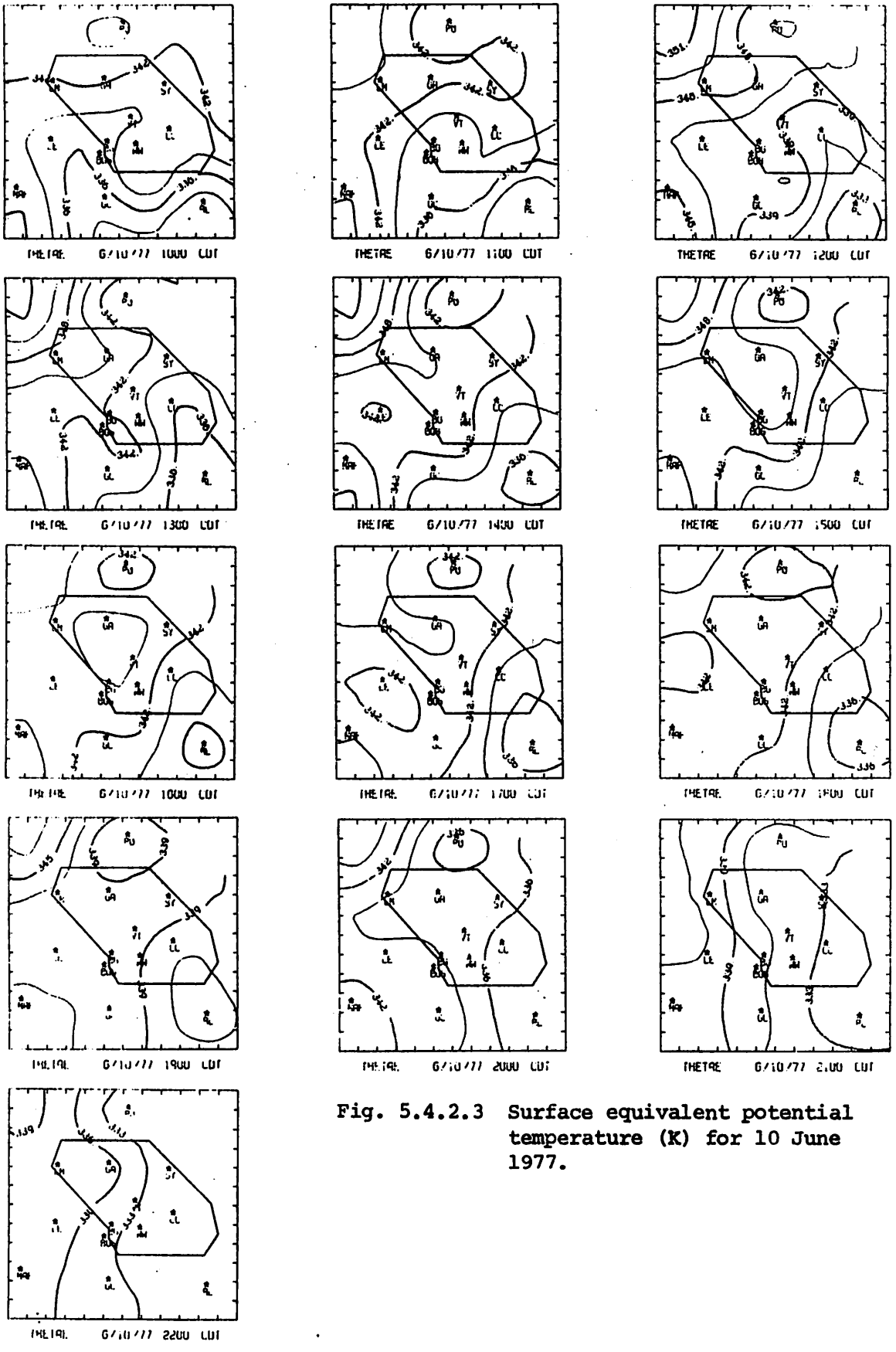

Fig. 5.4.2.3 Surface equivalent potential temperature (K) for 10 June 1977.

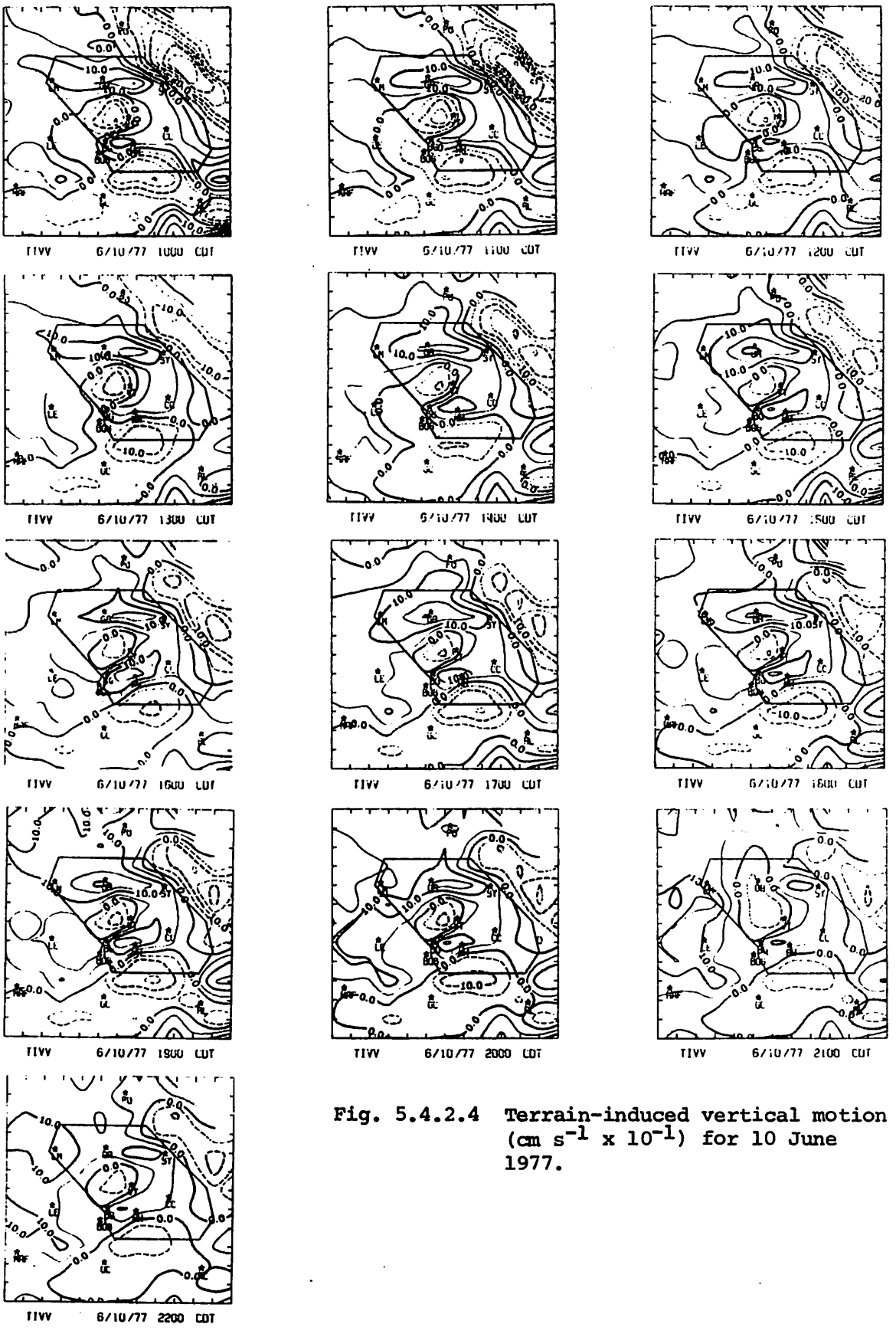

Fig. 5.4.2.4 Terrain-induced vertical motion (cm s^{-1} x 10^{-1}) for 10 June 1977.

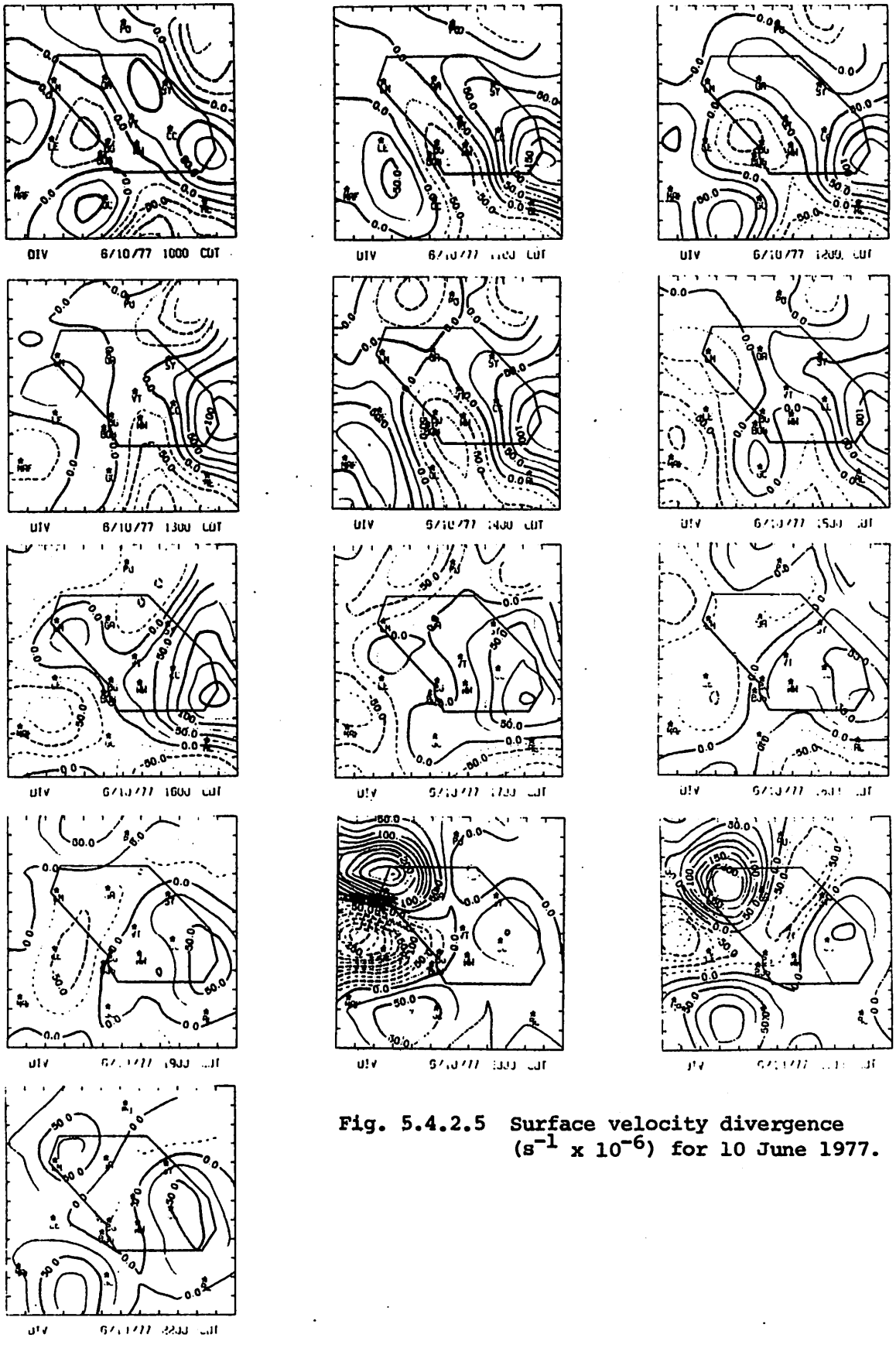

Fig. 5.4.2.5 Surface velocity divergence (s^{-1} x 10^{-6}) for 10 June 1977.

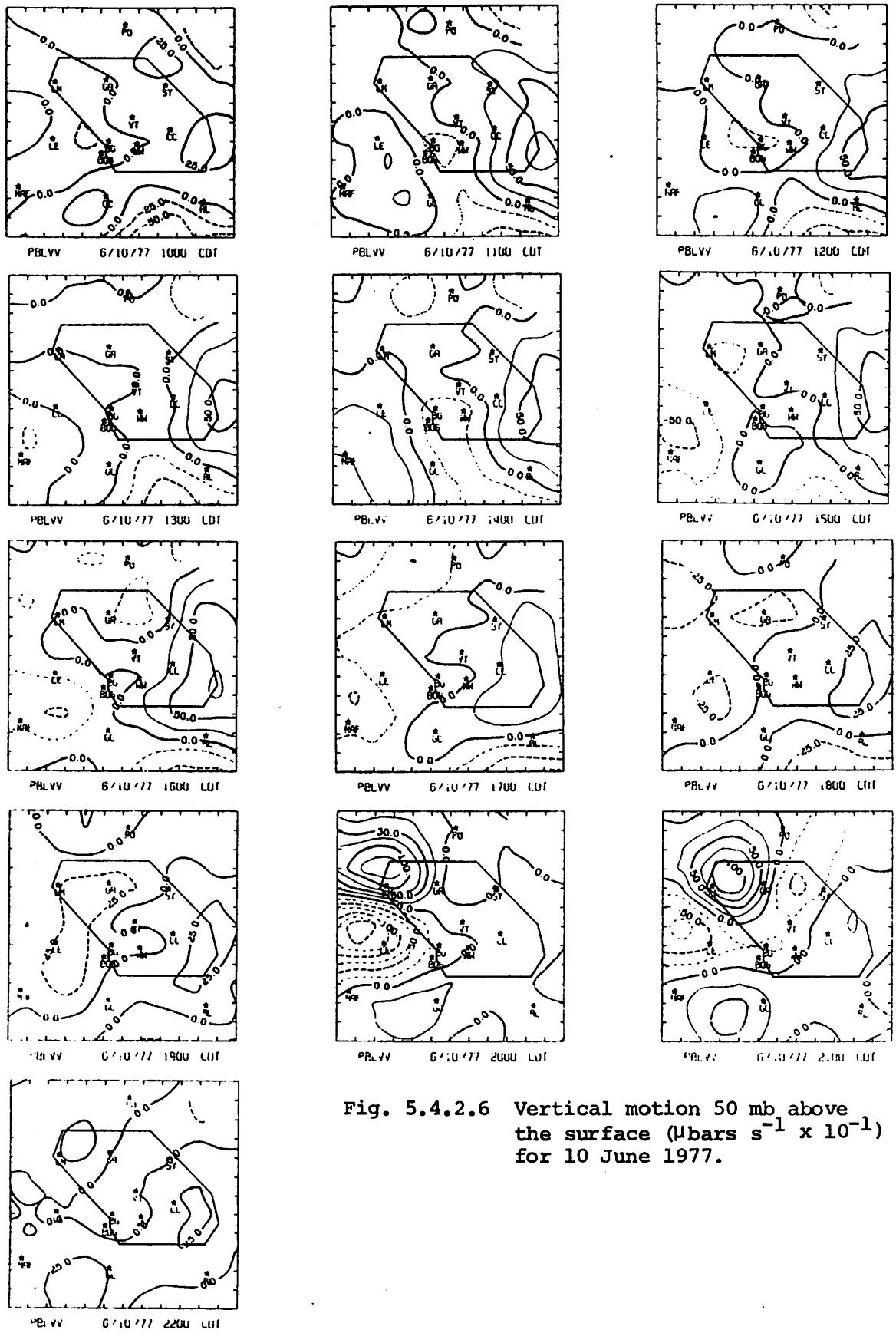

Fig. 5.4.2.6 Vertical motion 50 mb above the surface (μbars s^{-1} x 10^{-1}) for 10 June 1977.

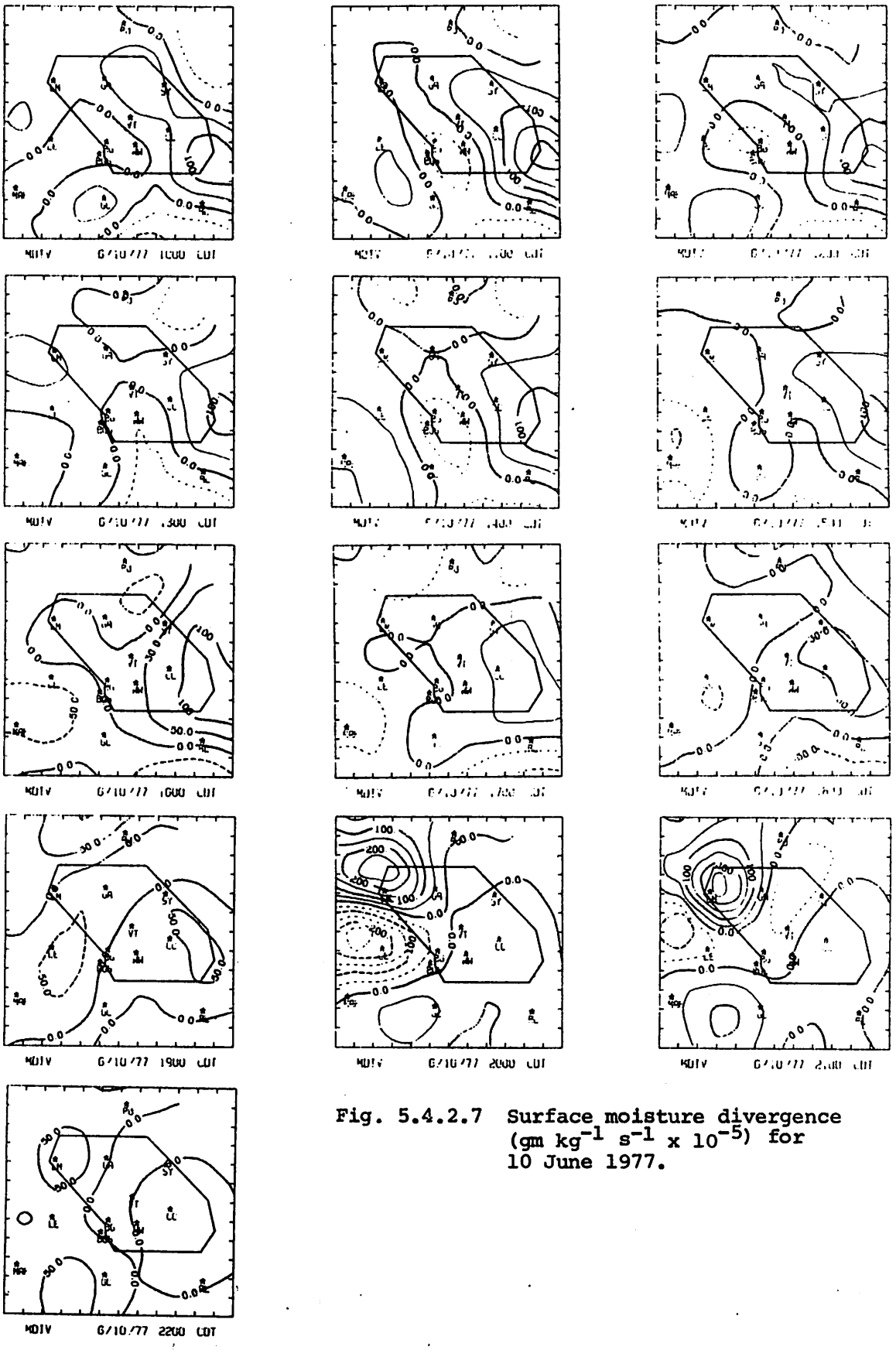

Fig. 5.4.2.7 Surface moisture divergence (gm kg^{-1} s^{-1} x 10^{-5}) for 10 June 1977.

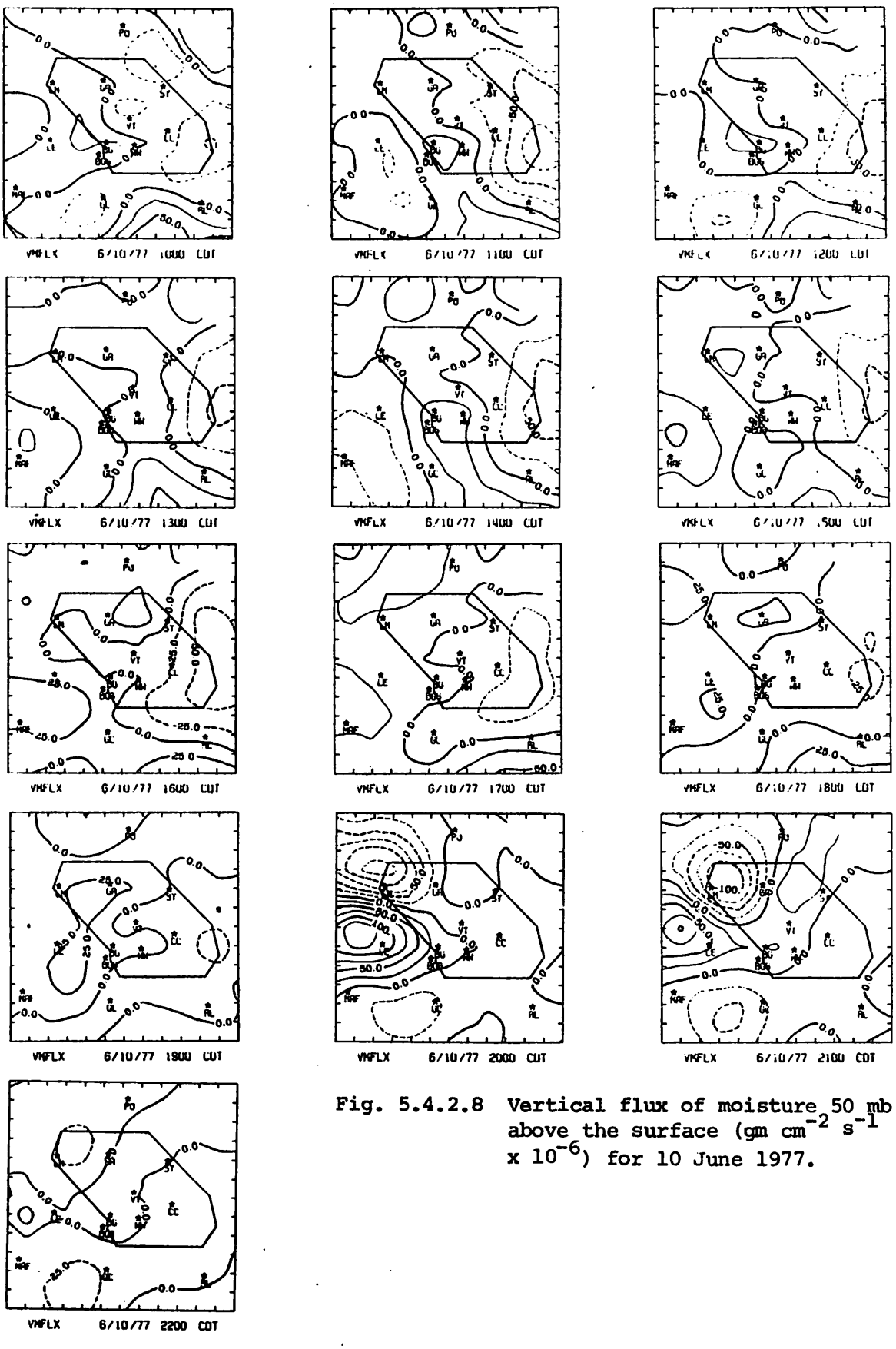

Fig. 5.4.2.8 Vertical flux of moisture 50 mb above the surface (gm cm^{-2} s^{-1} x 10^{-6}) for 10 June 1977.

patterns associated with surface velocity divergence and vertical motion 50 mb above the surface. Increased divergence and downward motion are both correlated with the dissipation of the echo (Fig. 5.4.1.1). Fields of surface vorticity (Fig. 5.4.2.9) show a decrease in cyclonic rotation during dissipation. Anticyclonic rotation occurred below the echo at 0300 GMT.

Sea level pressure patterns (Fig. 5.4.2.10) show a region of low pressure over the southeastern corner of the area. No effect of convective activity is reflected in sea level pressure. Surface pressure changes (Fig. 5.4.2.11) remained small throughout the day. The large pressure changes observed at 0200 and 0300 GMT were due to a plotting error at Garden City, so that no pressure change actually existed.

5.5 11 June 1977

5.5.1 Radar

Charts of radar echoes presented in Figure 5.5.1.1 show that no echoes were observed prior to 0000 GMT. By 0100 GMT an echo with tops exceeding 9.1 km (30K ft) entered the northwest corner of the area. This was the leading edge of a line with a northeast-southwest orientation which extended lengthwise across the entire area and moved toward the southeast. By 0300 GMT the line had moved well into the area with at least two cells with tops exceeding 9.1 km (30K ft). What appears to be the major cell is located near Lamesa at this time.

5.5.2 Surface

Surface temperature patterns (Fig. 5.5.2.1) show little change until the approach of the line of convective activity at 0000 GMT. A temperature drop of 15°C at the surface occurred as a result of this line. This region of minimum temperature is located directly under the strongest echo in the line. Although surface mixing ratios (Fig. 5.5.2.2) are also observed to increase in this region, a decrease in surface equivalent potential temperature (Fig. 5.5.2.3) occurred due to the large temperature decrease observed in Figure 5.5.2.1. A small center of maximum surface equivalent potential temperature exists over the center of the area that is reflected in values of the surface mixing ratio.

Changes in terrain-induced vertical motion (Fig. 5.5.2.4) occurred, but the magnitudes were small especially during times of convection. Surface velocity divergence (Fig. 5.5.2.5), remained variable until the approach of

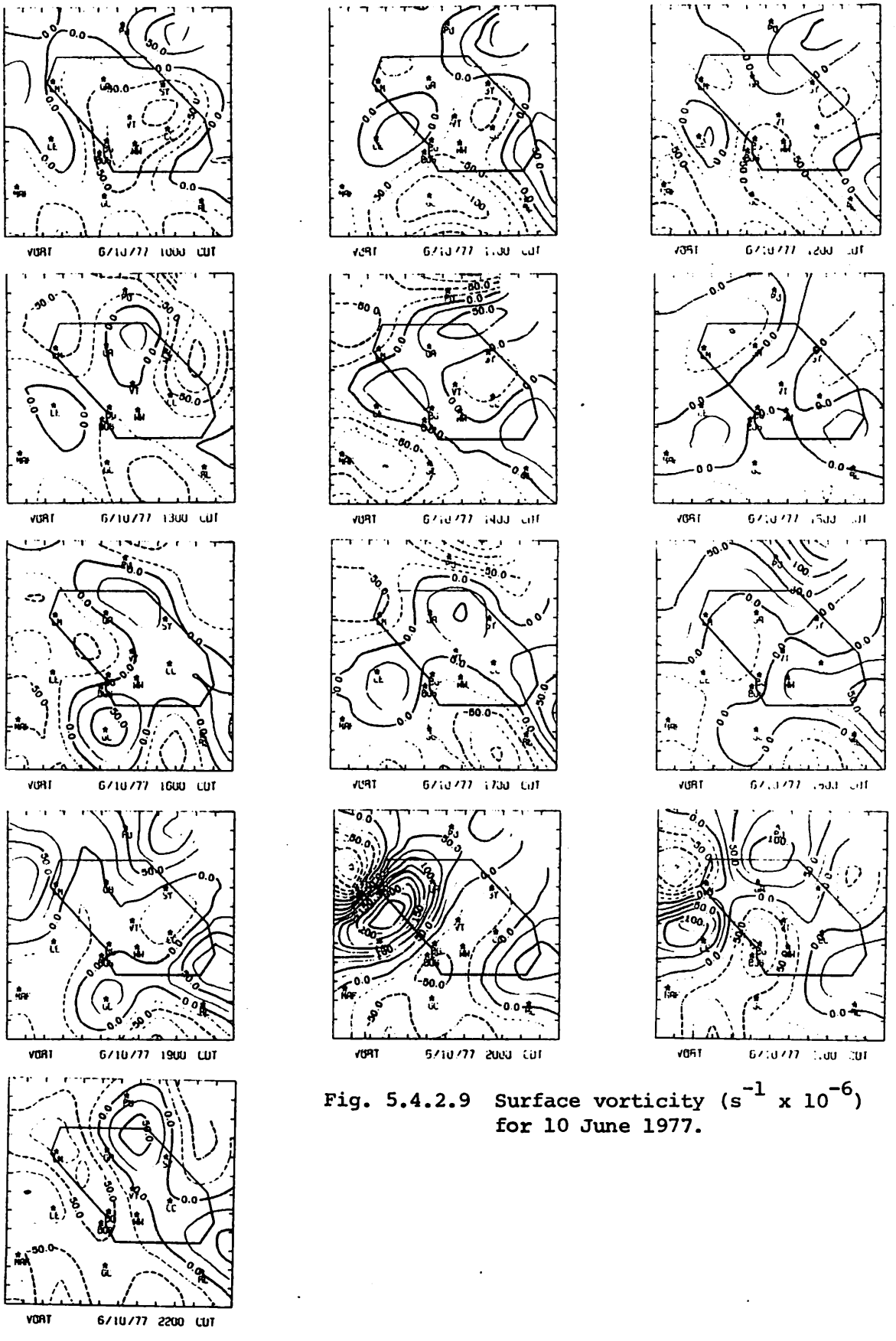

Fig. 5.4.2.9 Surface vorticity (s^{-1} x 10^{-6}) for 10 June 1977.

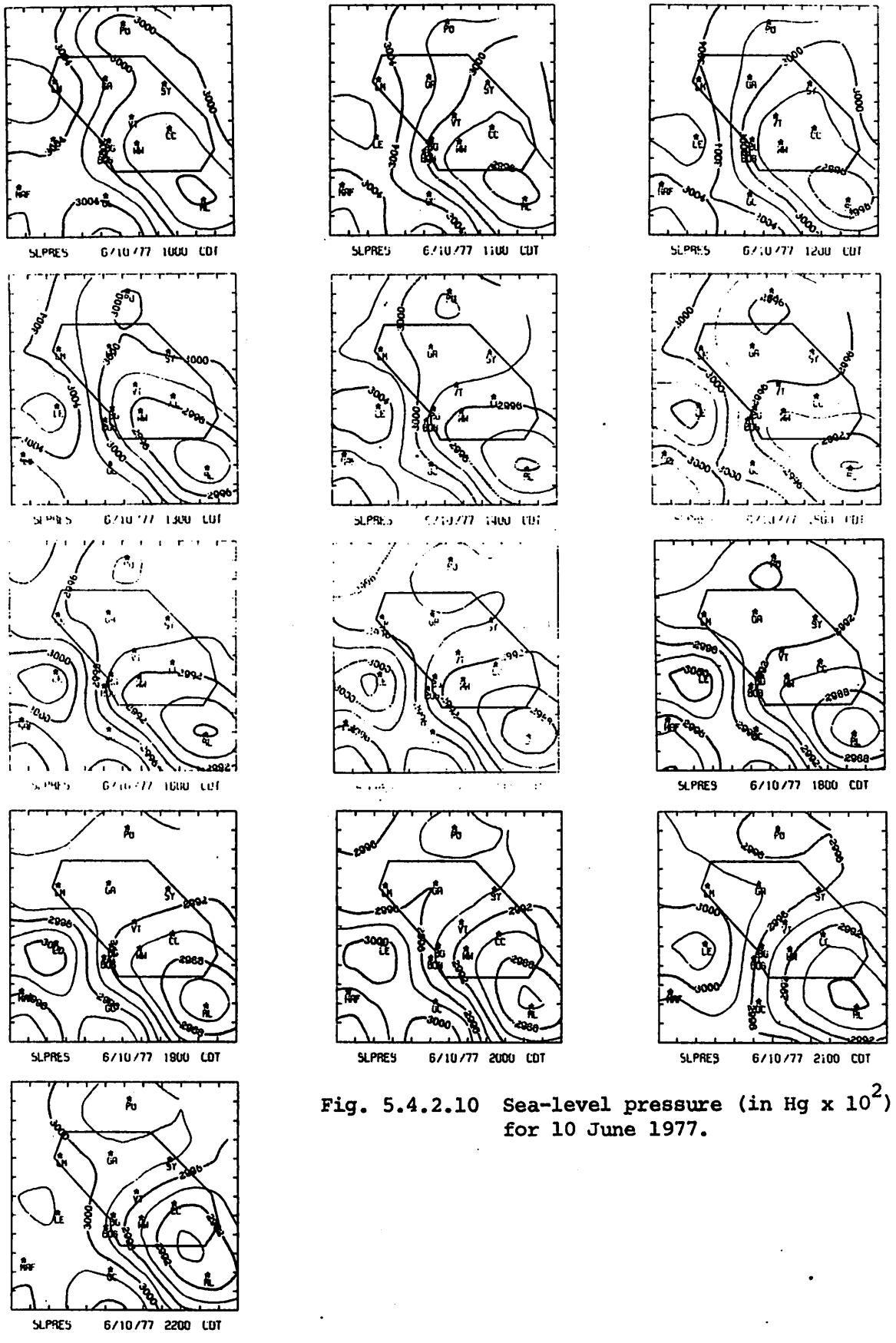

Fig. 5.4.2.10 Sea-level pressure (in Hg x 10^2) for 10 June 1977.

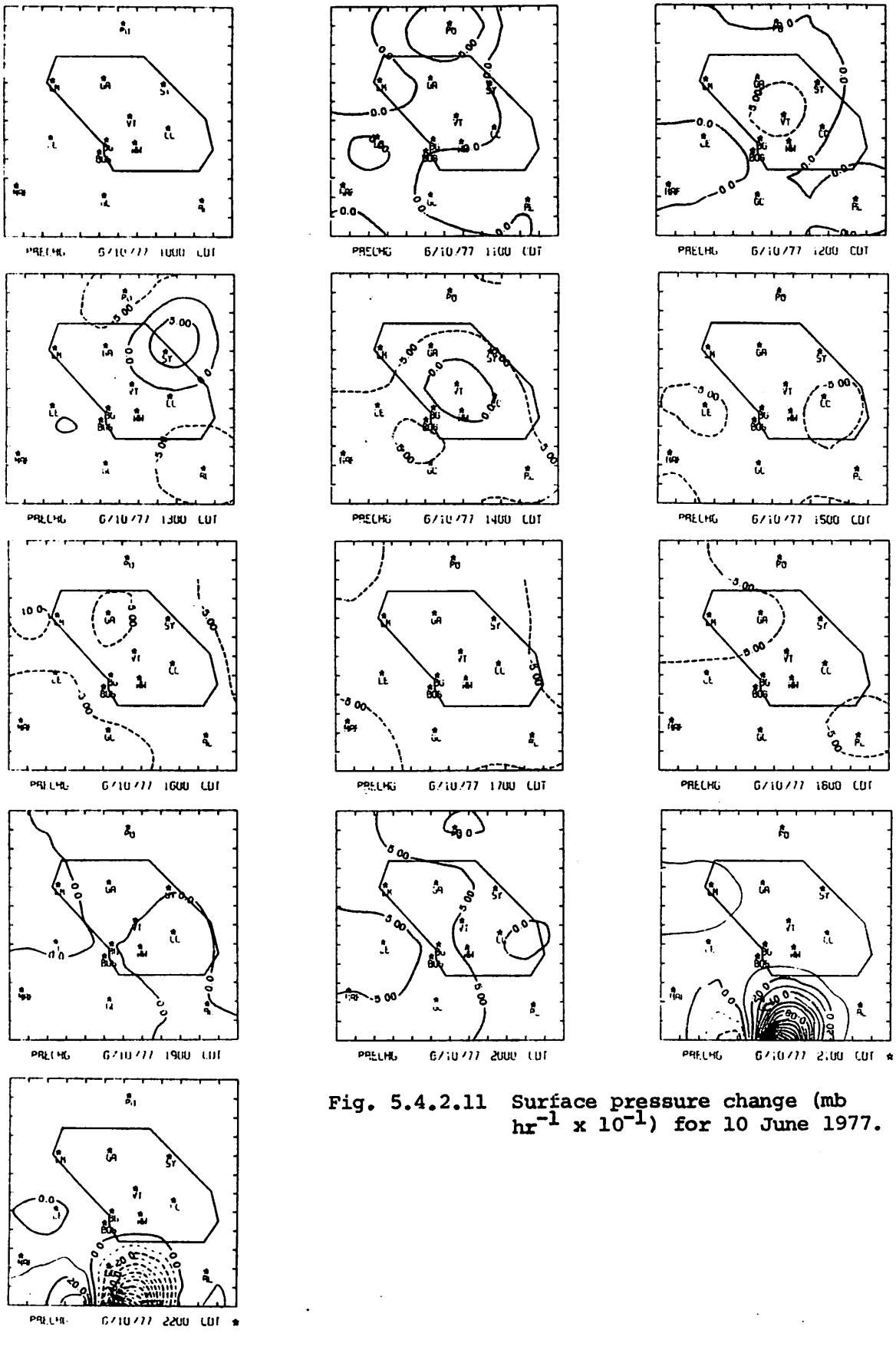

Fig. 5.4.2.11 Surface pressure change (mb hr^{-1} x 10^{-1}) for 10 June 1977.

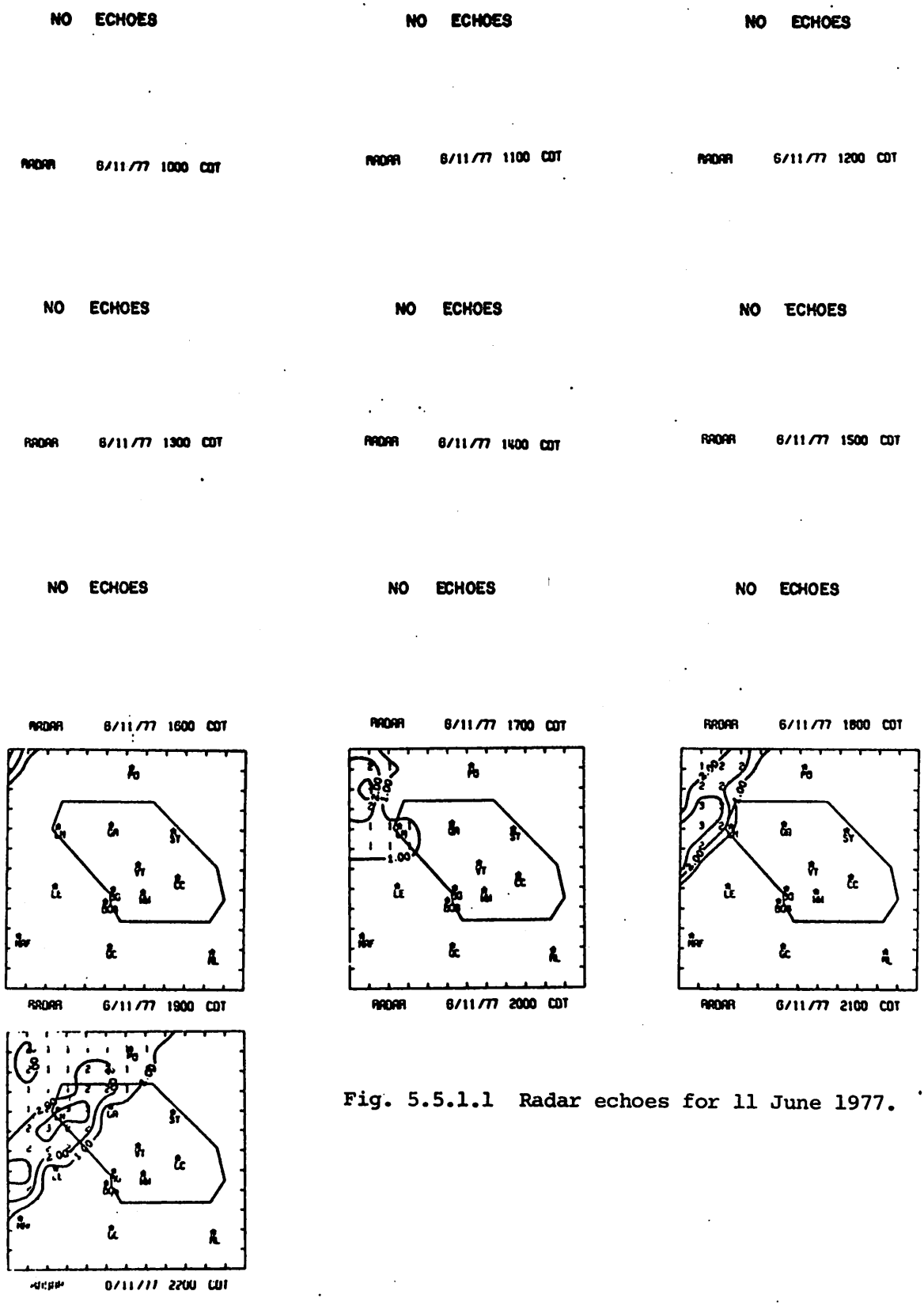

Fig. 5.5.1.1 Radar echoes for 11 June 1977.

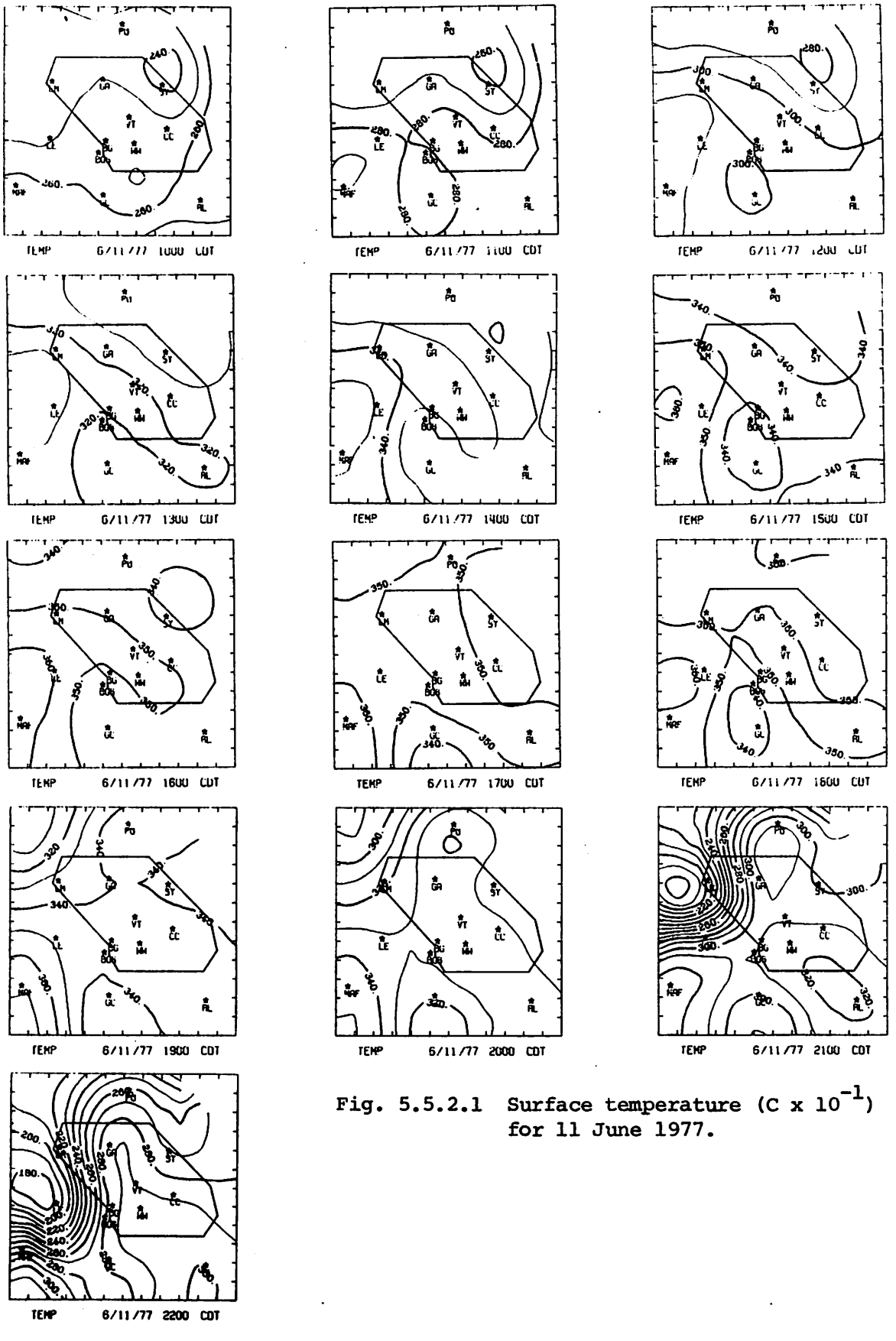

Fig. 5.5.2.1 Surface temperature (C x 10^{-1}) for 11 June 1977.

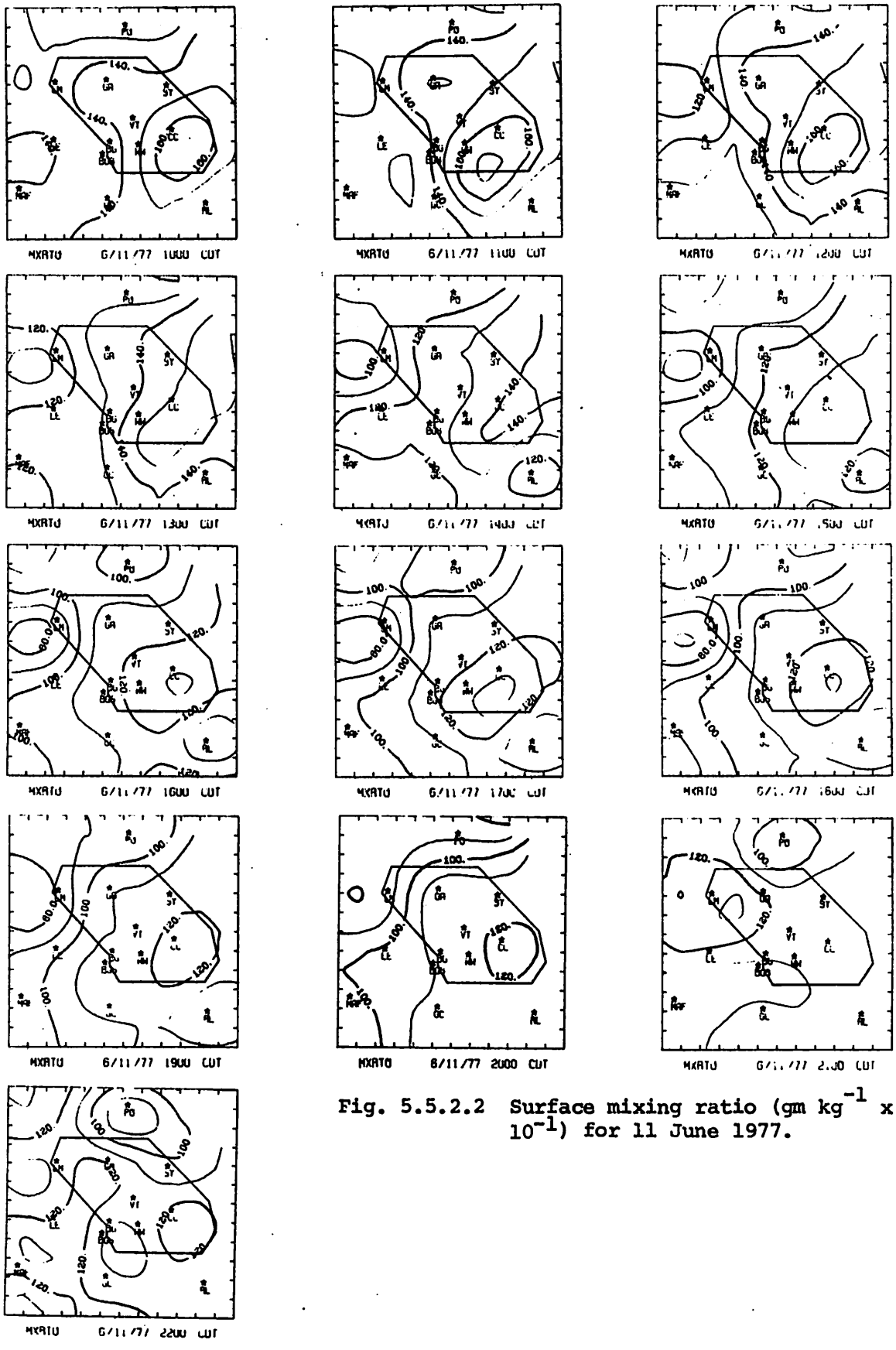

Fig. 5.5.2.2 Surface mixing ratio (gm kg^{-1} x 10^{-1}) for 11 June 1977.

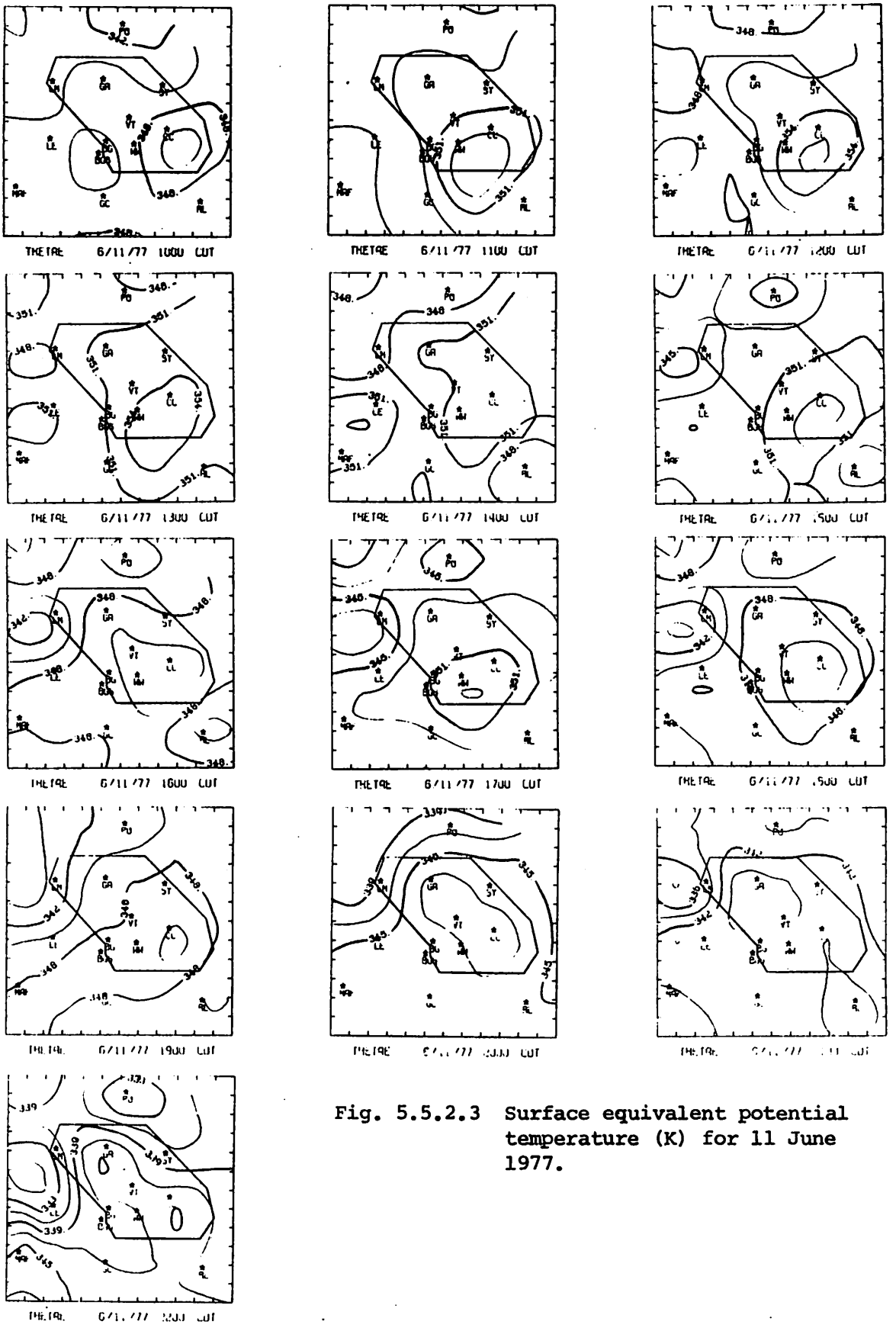

Fig. 5.5.2.3 Surface equivalent potential temperature (K) for 11 June 1977.

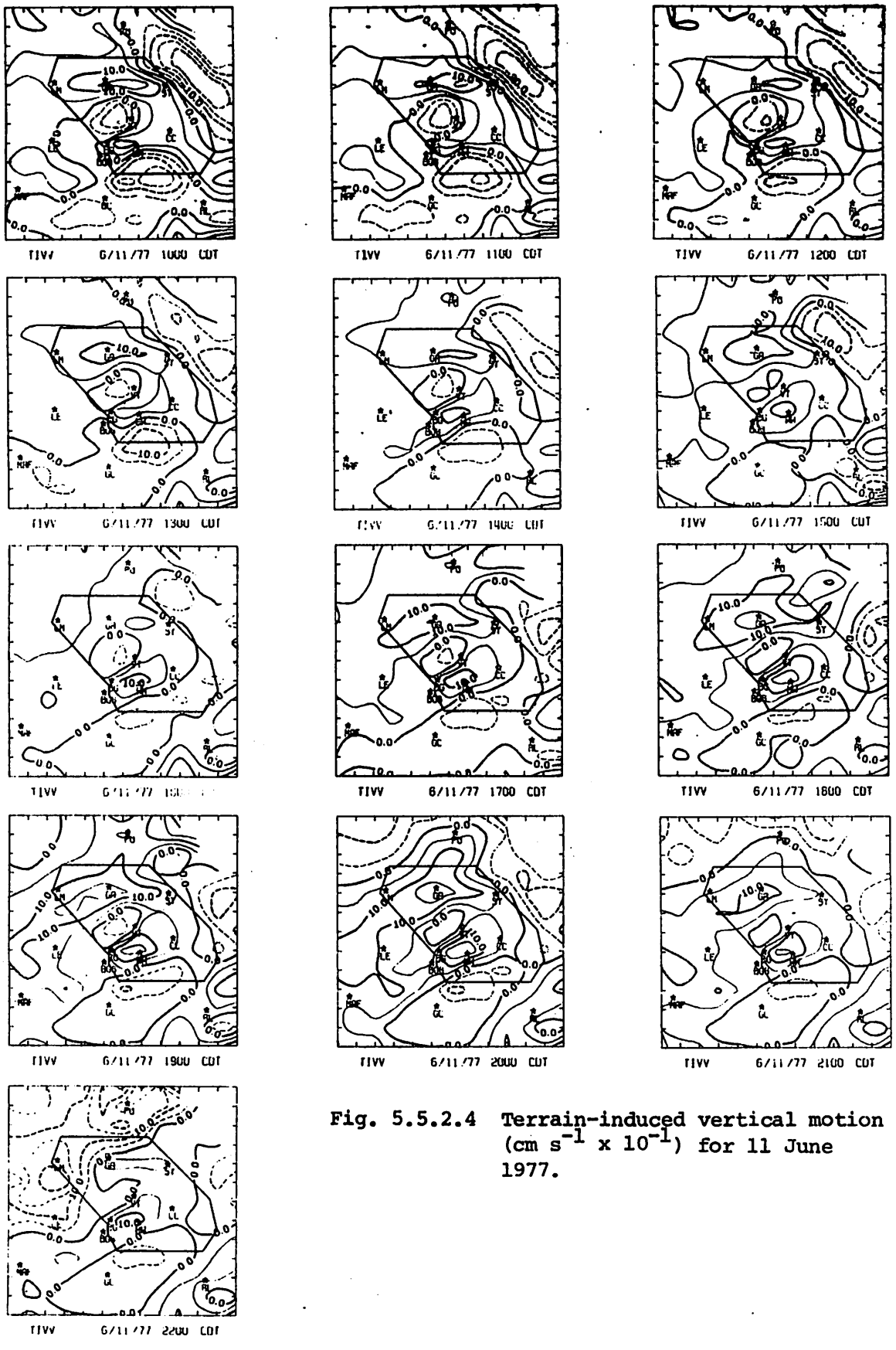

Fig. 5.5.2.4 Terrain-induced vertical motion (cm s^{-1} x 10^{-1}) for 11 June 1977.

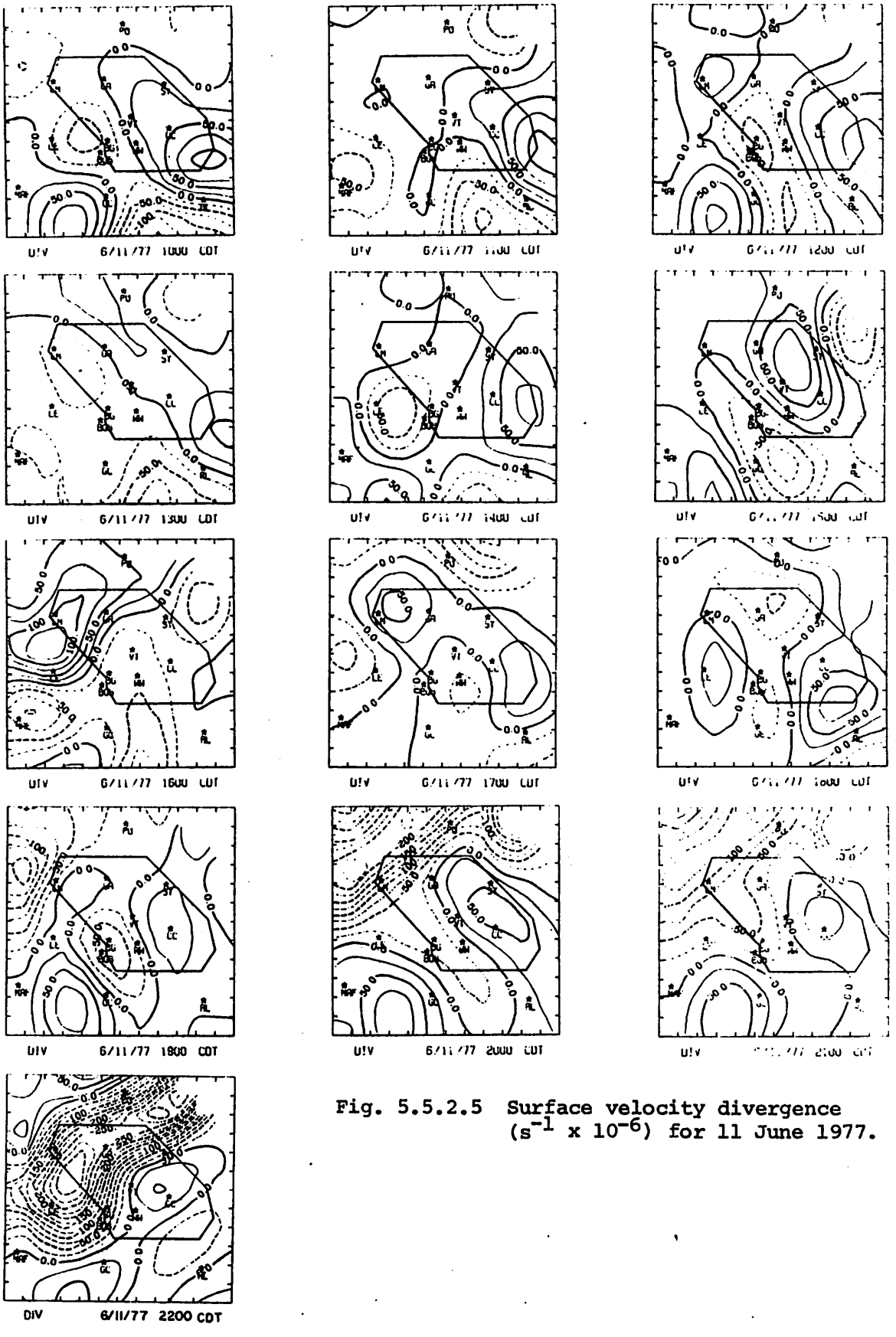

Fig. 5.5.2.5 Surface velocity divergence (s^{-1} x 10^{-6}) for 11 June 1977.

the squall line. A strong region of surface velocity convergence is seen at 0000 GMT and precedes the advance of the squall line. These strong surface velocity convergent fields are associated with strong upward vertical motion 50 mb above the surface (Fig. 5.5.2.6). Little vertical motion is observed prior to the advance of the squall line, but reaches a maximum of over 10 μbars s^{-1} at 0300 GMT. The transport of moisture in this region is reflected by surface moisture convergence patterns (Fig. 5.5.2.7) and vertical flux of moisture 50 mb above the surface (Fig. 5.5.2.8). In each case the convergence of moisture at the surface, and subsequent transport aloft, occurred at the leading edge of the squall line.

Patterns of surface vorticity (Fig. 5.5.2.9) were disorganized and discontinuous prior to the advance of the squall line. Strong regions of cyclonic and anticyclonic rotation were observed to be associated with the squall line. These alternating patterns of surface vorticity show a region of surface velocity convergence (Fig. 5.5.2.5). However, the largest center of positive vorticity is correlated with the strongest echo.

Sea level pressure (Fig. 5.5.2.10) patterns remain undisturbed prior to the squall line advance, with a center of low pressure located over Robert Lee. Surface pressure change (Fig. 5.5.2.11) remains small prior to the squall line advance. Surface pressure increases occur at 0100 GMT and reach a maximum below the strongest echo at 0300 GMT of over 3 mb hr^{-1}.

5.5.3 Upper-Level Kinematic Parameters

Mass divergence dominated the vertical profiles of horizontal mass divergence during the two available time periods of data (Fig. 5.5.3.1) (wind data were missing on three soundings at Post). Vertical velocities were downward at all levels at 1500 GMT and generally close to zero at 1800 GMT consistent with no radar-observed precipitation (Fig. 5.5.3.2). Horizontal moisture divergence below 700 mb at 1500 GMT changes to convergence at 1800 GMT, and values above 700 mb were near zero at both time periods (Fig. 5.5.3.3).

5.5.4 Energetics

The only significant feature seen in the vertical profiles of the horizontal flux divergence of latent heat energy (Fig. 5.5.4.1) is the rapid change from outflow at 1500 GMT to inflow at 1800 GMT below 700 mb.

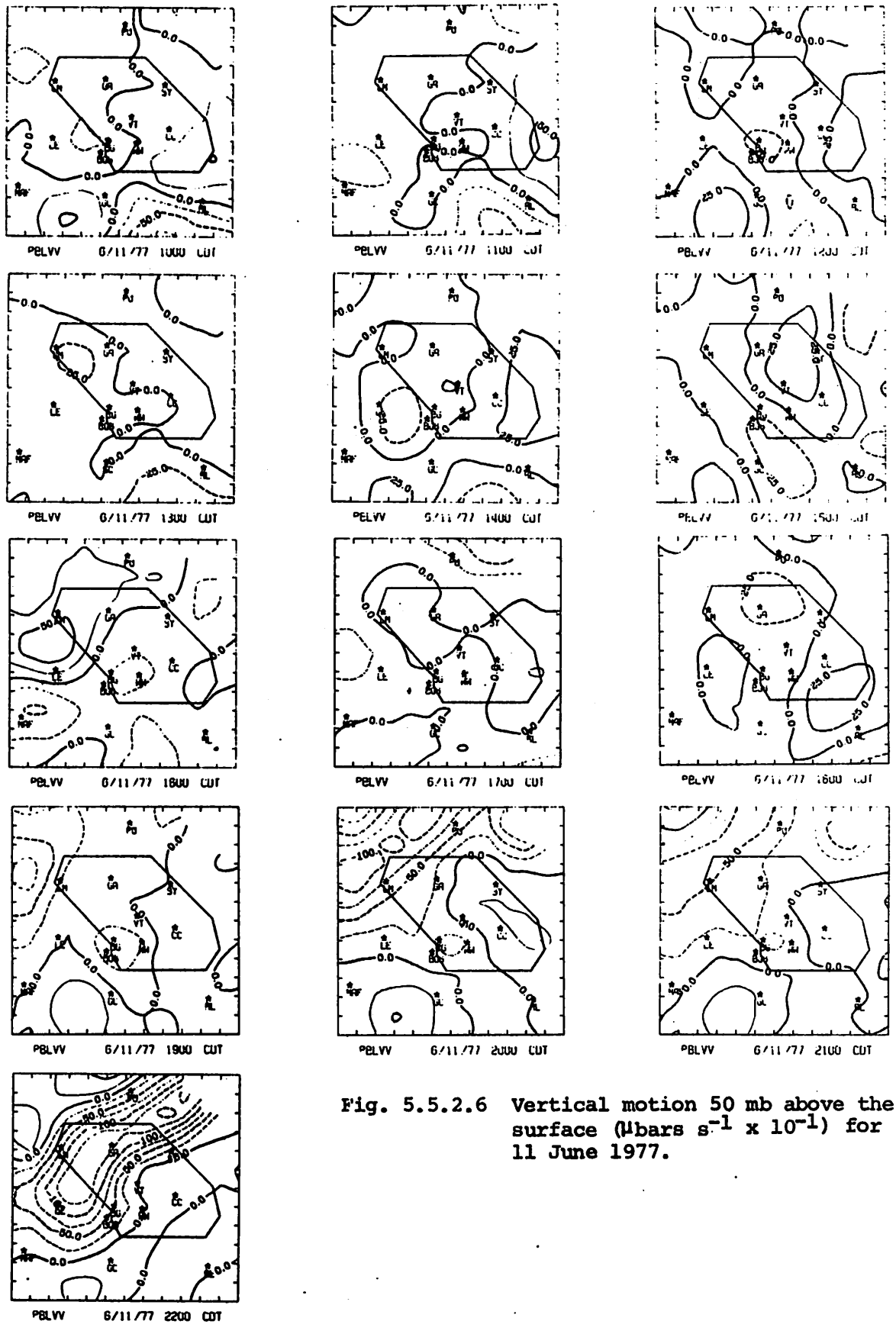

Fig. 5.5.2.6 Vertical motion 50 mb above the surface (μbars s^{-1} x 10^{-1}) for 11 June 1977.

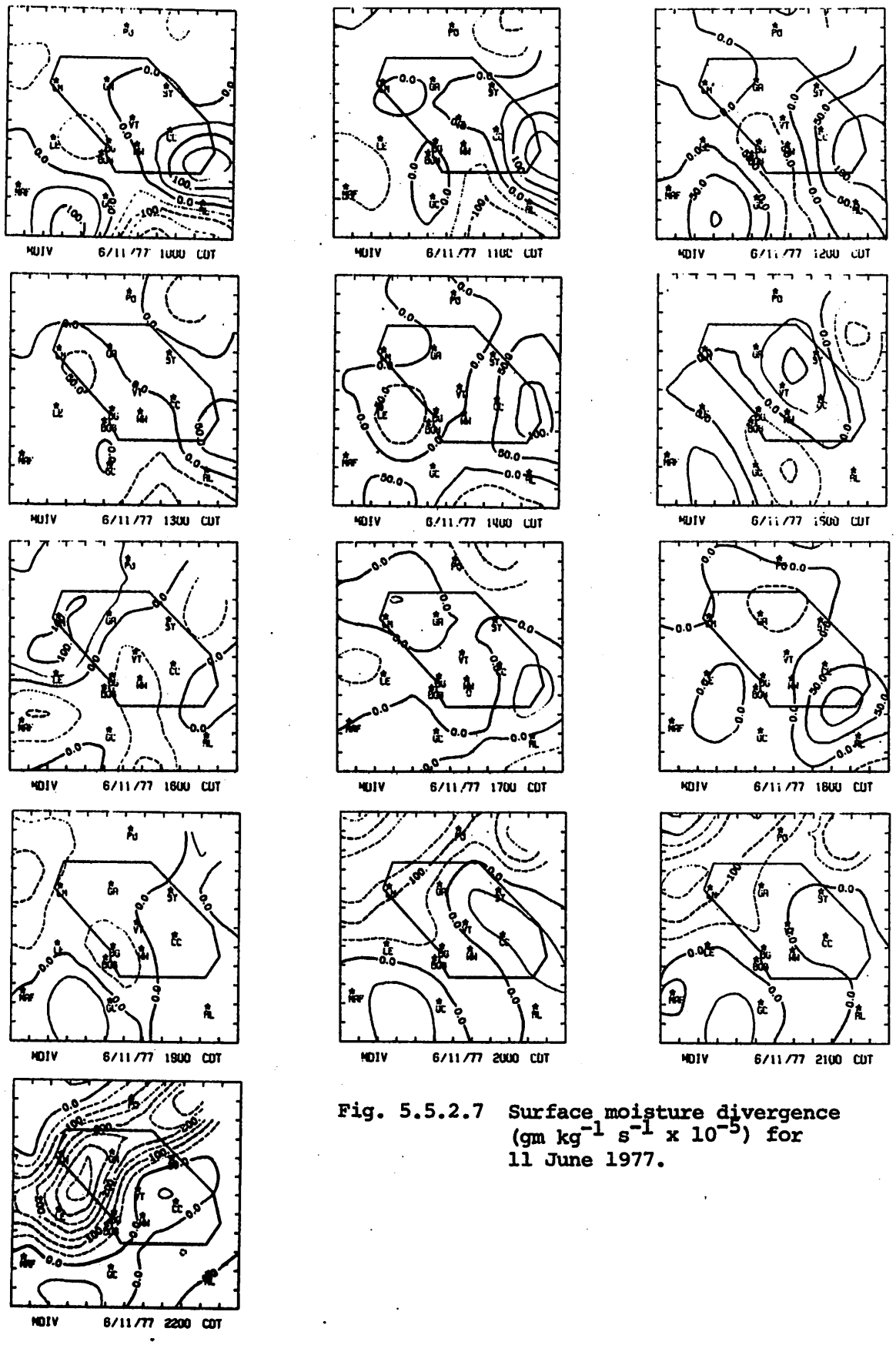

Fig. 5.5.2.7 Surface moisture divergence (gm kg^{-1} s^{-1} x 10^{-5}) for 11 June 1977.

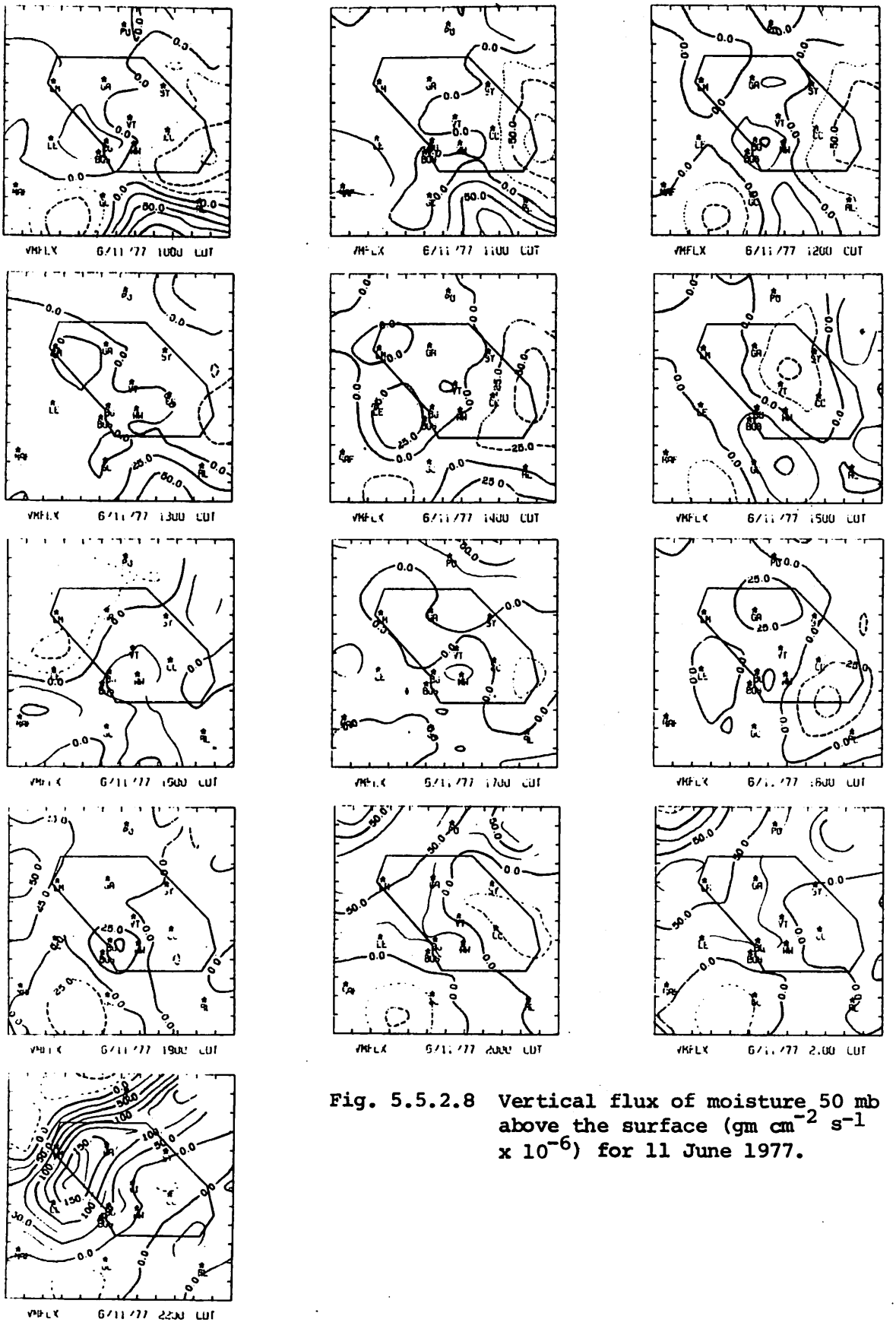

Fig. 5.5.2.8 Vertical flux of moisture 50 mb above the surface (gm cm^{-2} s^{-1} x 10^{-6}) for 11 June 1977.

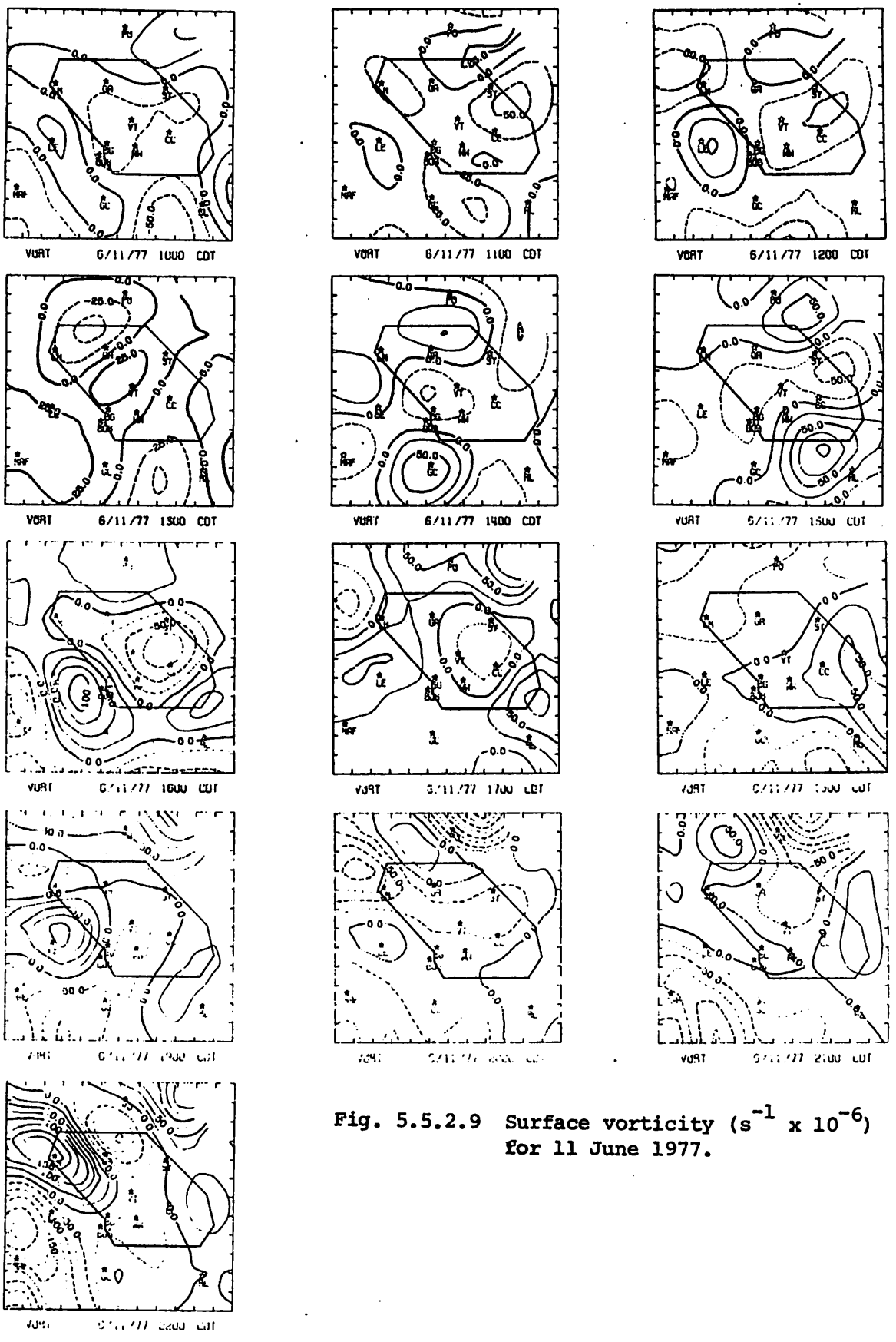

Fig. 5.5.2.9 Surface vorticity (s^{-1} x 10^{-6}) for 11 June 1977.

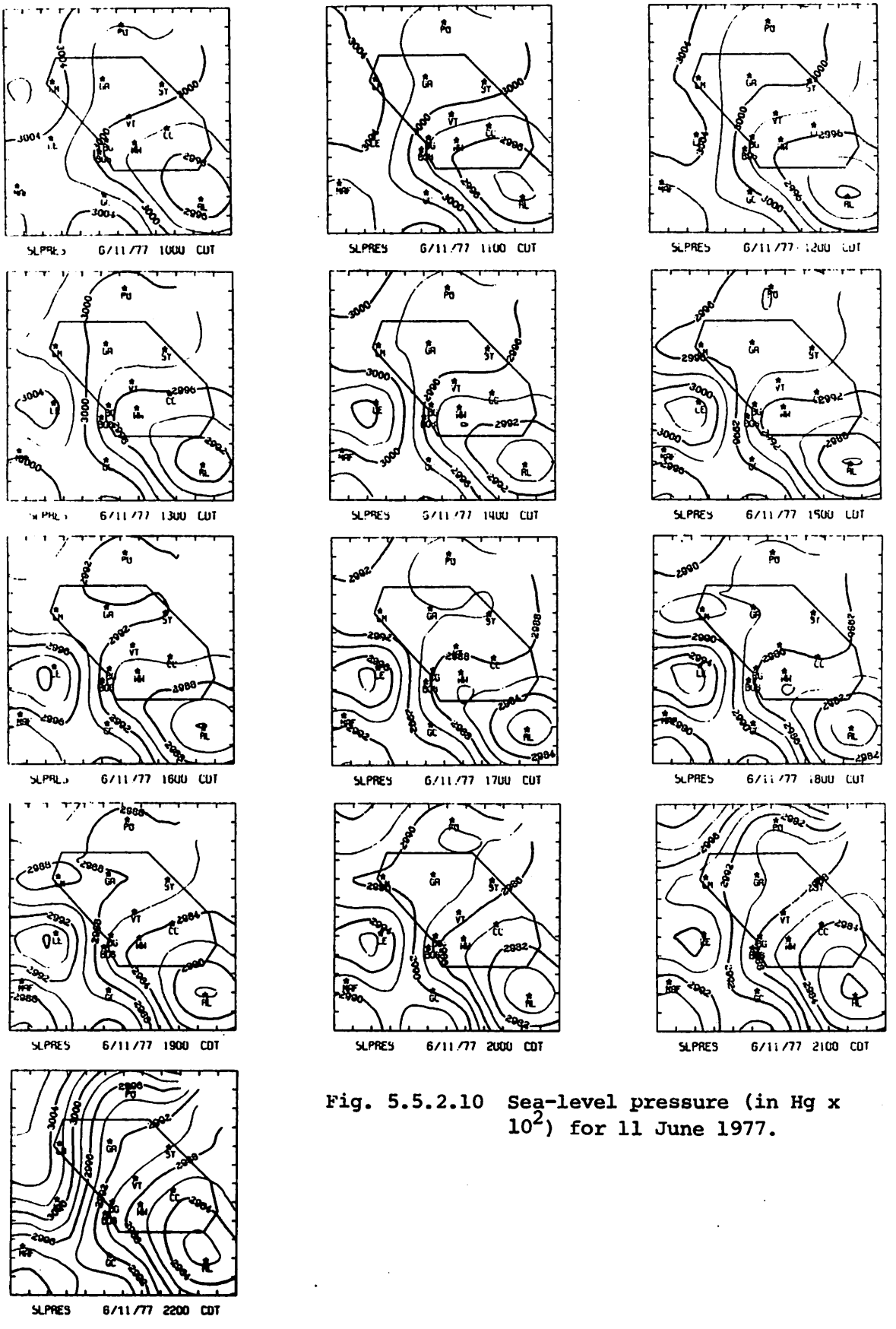

Fig. 5.5.2.10 Sea-level pressure (in Hg x 10^2) for 11 June 1977.

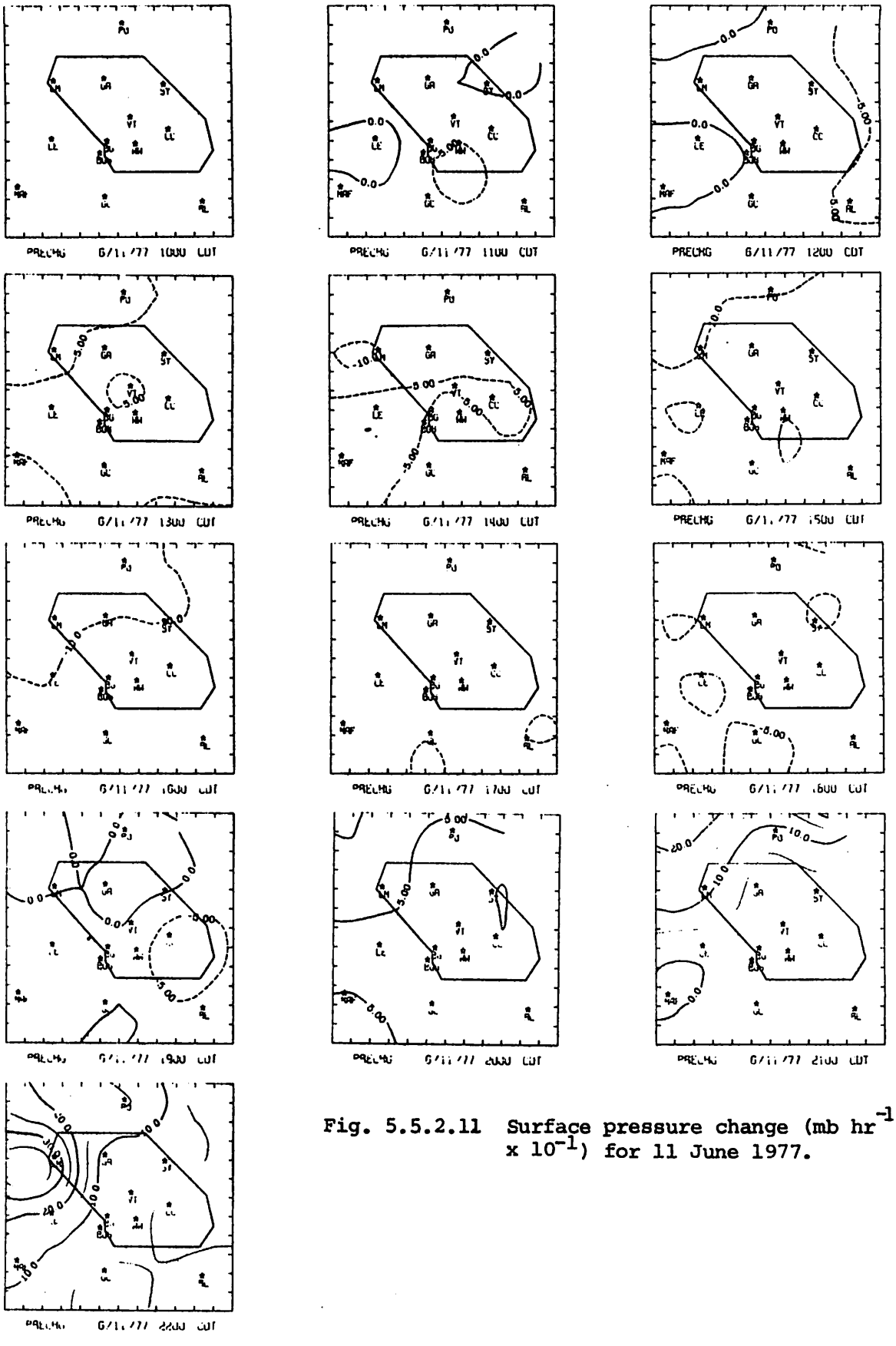

Fig. 5.5.2.11 Surface pressure change (mb hr^{-1} x 10^{-1}) for 11 June 1977.

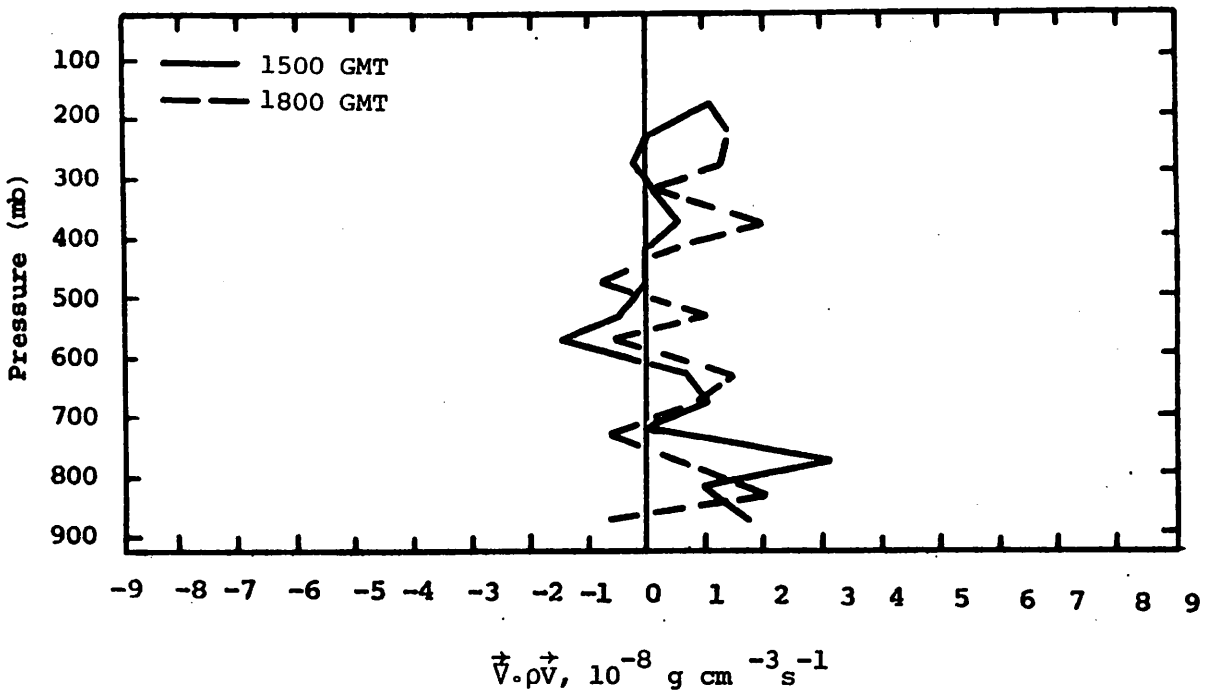

Fig. 5.5.3.1 Vertical profiles of mass divergence on 11 June 1977.

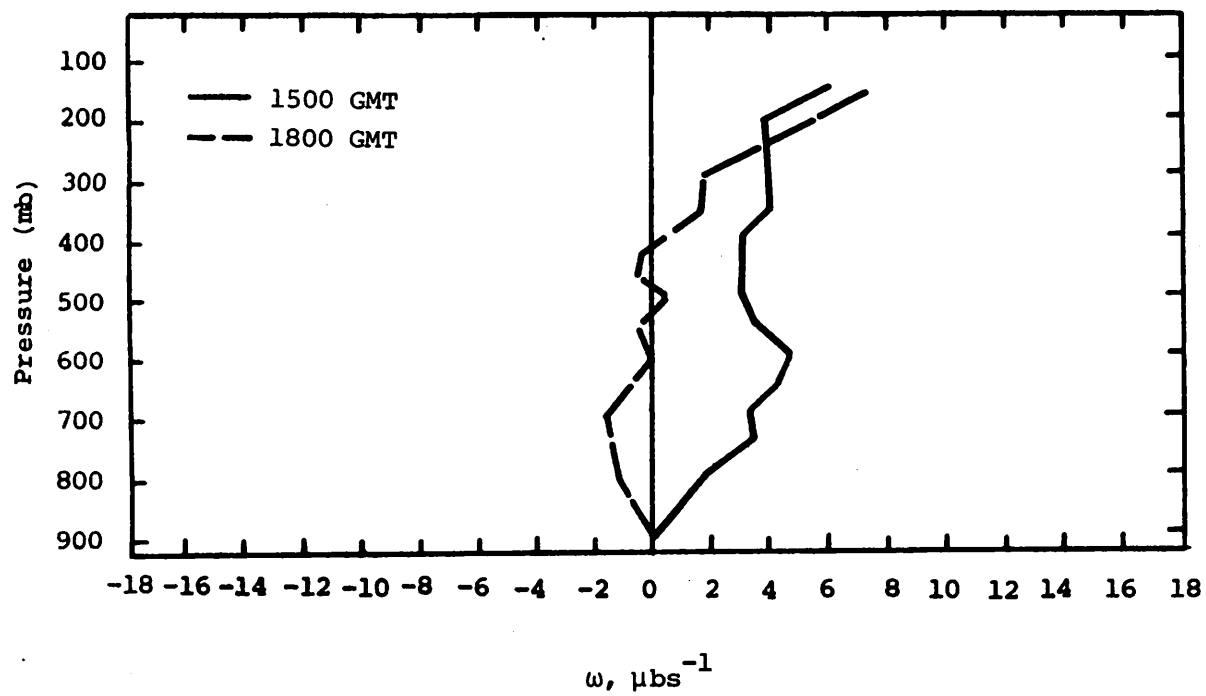

Fig. 5.5.3.2 Vertical profiles of vertical motion on 11 June 1977.

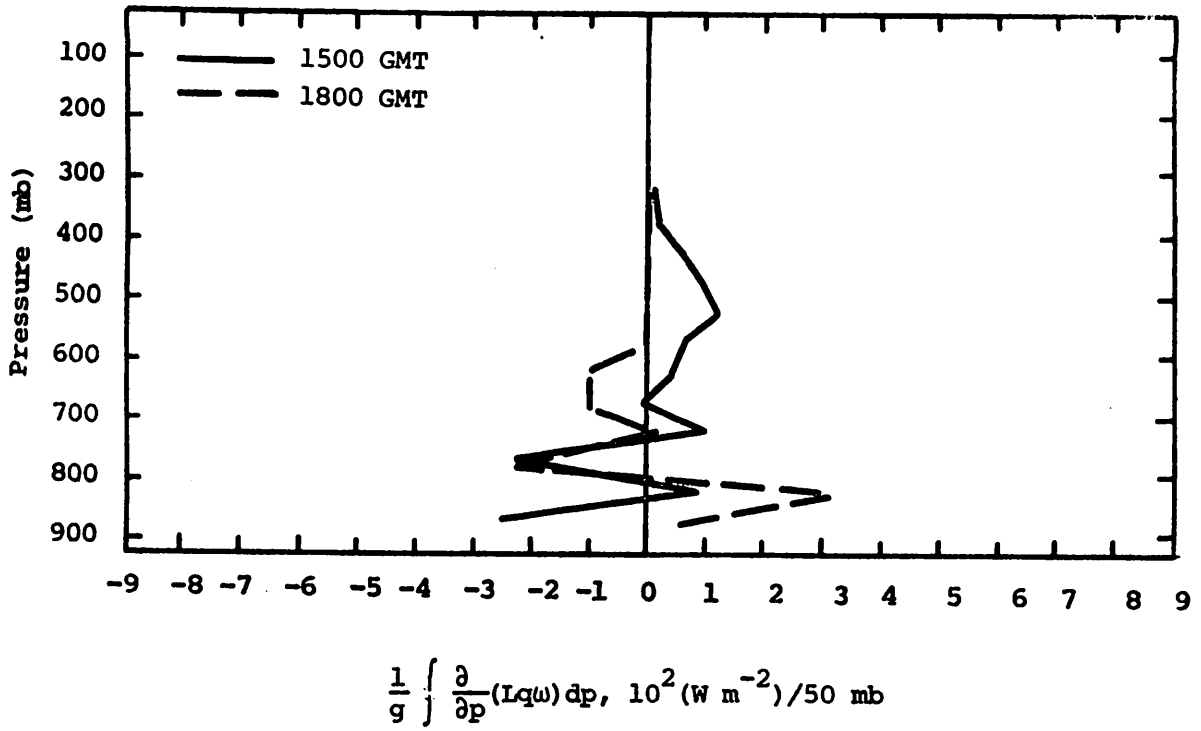

Fig. 5.5.4.2 Vertical profiles of the vertical flux of latent heat energy on 11 June 1977.

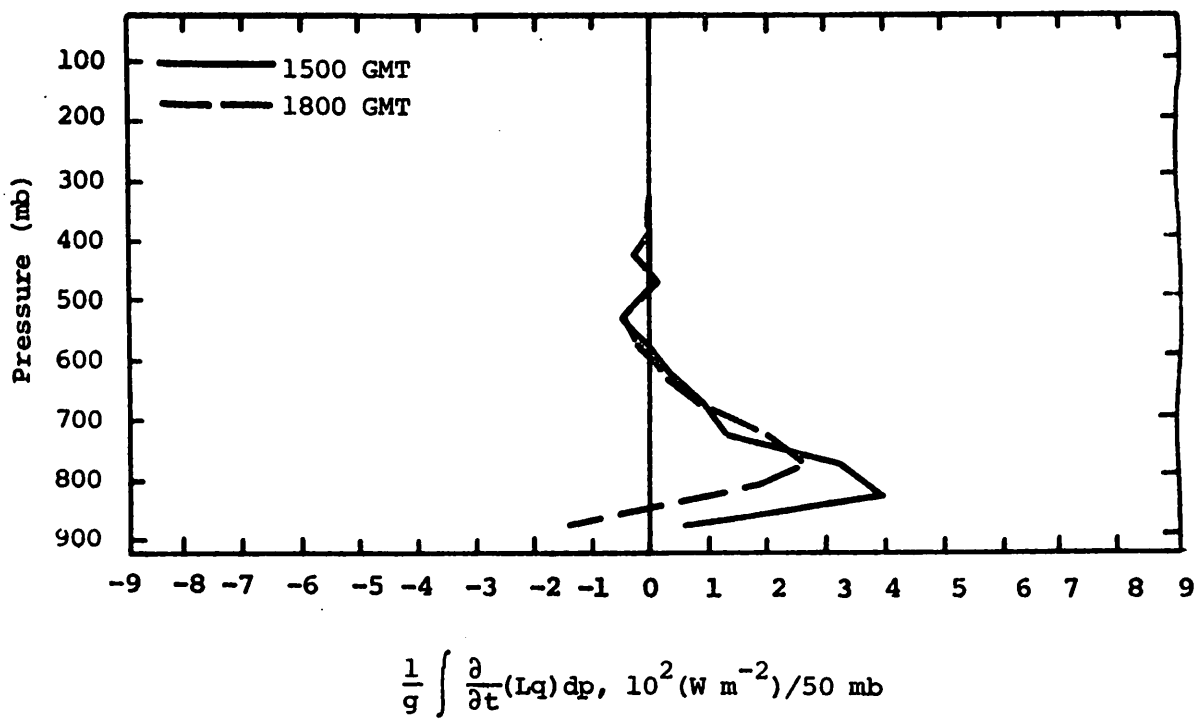

Fig. 5.5.4.3 Vertical profiles of the local change of latent heat energy on 11 June 1977.

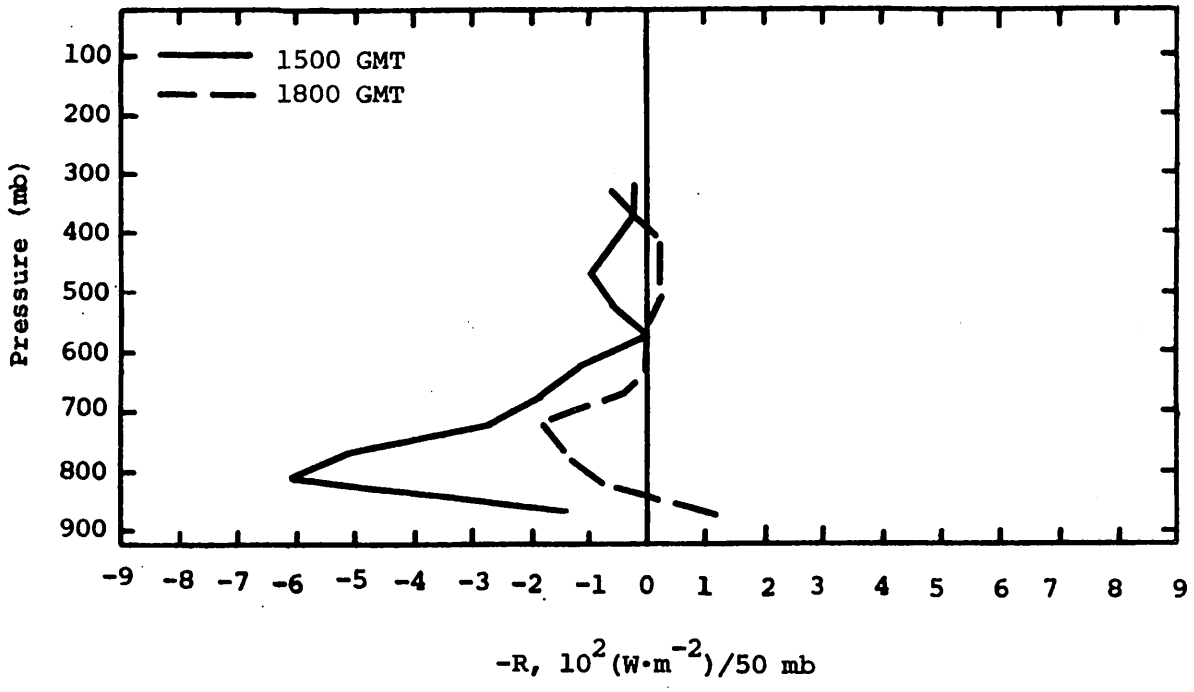

Fig. 5.5.4.4 Vertical profile of the residual of the latent heat energy equation on 11 June 1977.

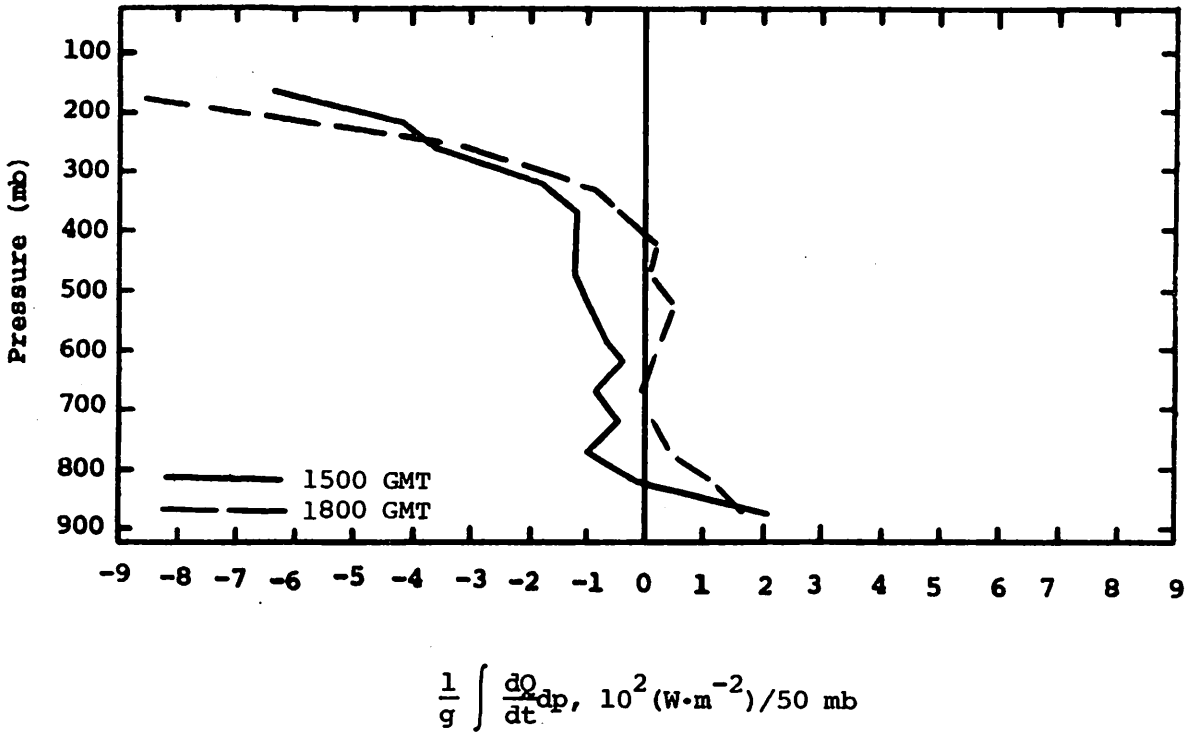

Fig. 5.5.4.5 Vertical profiles of diabatic heating computed from the first law of thermodynamics on 11 June 1977.

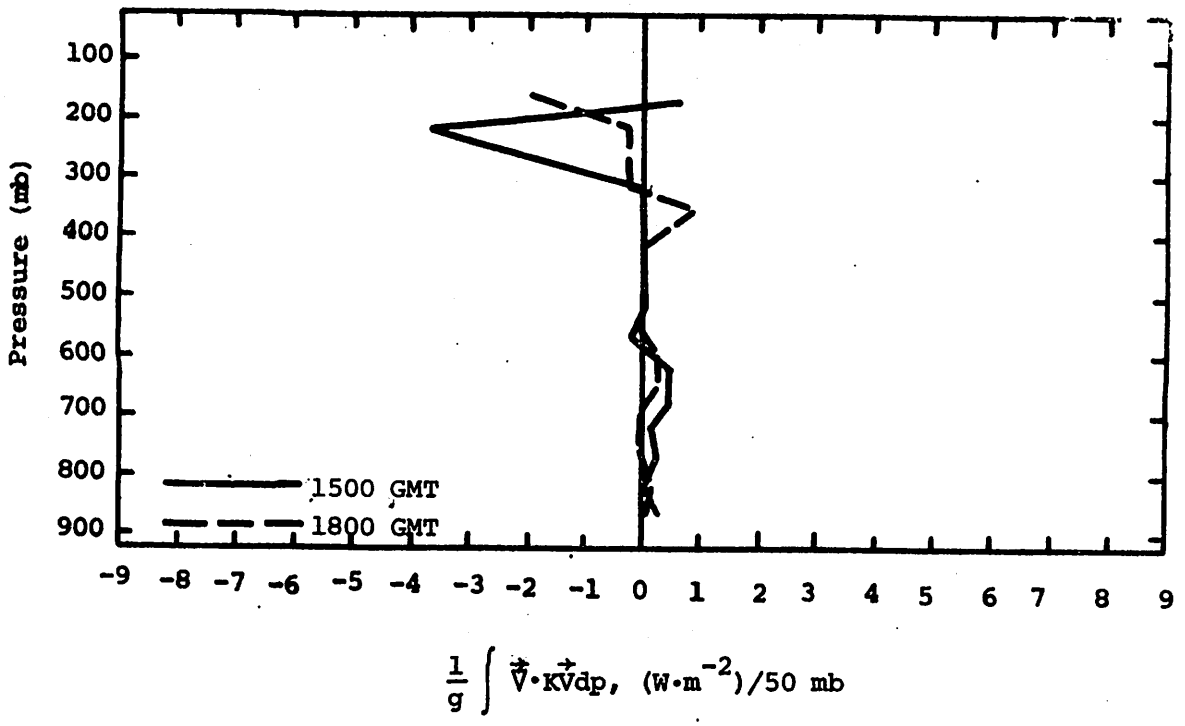

Fig. 5.5.4.6 Vertical profiles of the horizontal flux of kinetic energy on 11 June 1977.

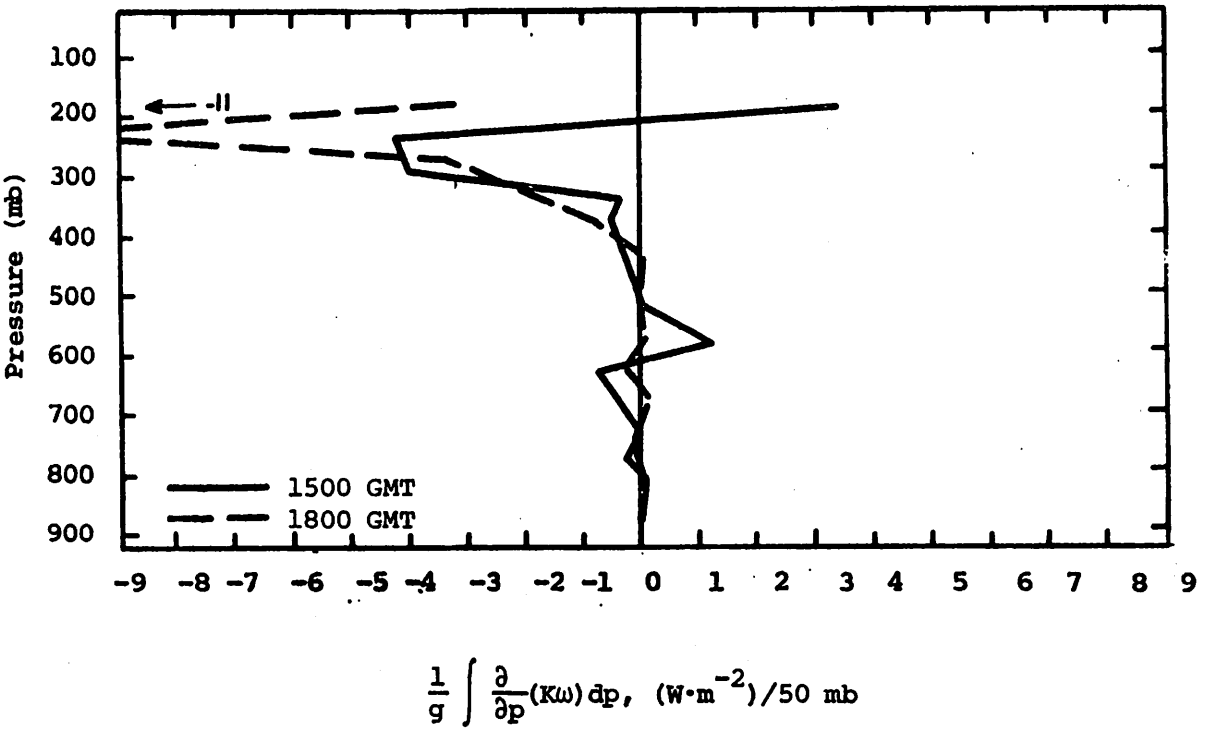

Fig. 5.5.4.7 Vertical profiles of the vertical flux of kinetic energy on 11 June 1977.

5.6 13 June 1977

5.6.1 Radar

Radar echoes observed on this day are shown in Figure 5.6.1.1. There were no echoes observed prior to 0300 GMT when a cell with tops exceeding 9.1 km (30K ft) was located in the north-central part of the area (over Post) just north of the target area. This cell moved southward to near the center of the target area by 0400 GMT and began to dissipate shortly thereafter. Only remnants of the storm remained by 0600 GMT with tops below 6.1 km (20K ft).

5.6.2 Surface

Fields of surface temperature (Fig. 5.6.2.1) show a center of minimum temperature over Snyder, which dissipated due to surface heating and mixing. The effects of the thunderstorm are evident at Post as indicated by a decrease in temperature at 0300 GMT. Values of surface mixing ratio (Fig. 5.6.2.2) do not vary much in time but generally show higher values to the east of the network. A slight increase in surface mixing ratio is observed over Post prior to the arrival of the storm.

Surface equivalent potential temperature fields (Fig. 5.6.2.2) closely resemble patterns of surface mixing ratio with a center of low values between Lamesa and Lenorah. The effect of the thunderstorm can also be seen by a 15°C temperature drop at Post.

Values of terrain-induced vertical motion increase with time with maximum upward values observed in the region of the convective activity at 0300 GMT. These values combine with strong surface velocity convergence (Fig. 5.6.2.5) to produce strong upward vertical motion 50 mb above the surface (Fig. 5.6.2.6) preceding the storm.

Fields of surface moisture convergence (Fig. 5.6.2.7) and vertical flux of moisture 50 mb above the surface (Fig. 5.6.2.8) show the accumulation and upward transport of moisture associated with the storm. Figures 5.6.2.5 through 5.6.2.8 also show a region of convergence and upward motion over the center of the network at 1600 GMT which later dissipated. Patterns of surface vorticity (Fig. 5.6.2.9) were highly variable throughout the day, but centers of positive vorticity correlate with centers of maximum convergence. Values of $3.5 \times 10^{-4} s^{-1}$ were observed in association with the thunderstorm at 0300 GMT.

Sea level pressure patterns (Fig. 5.6.2.10) remained nearly constant throughout the day except for the influence of the thunderstorm at 0300

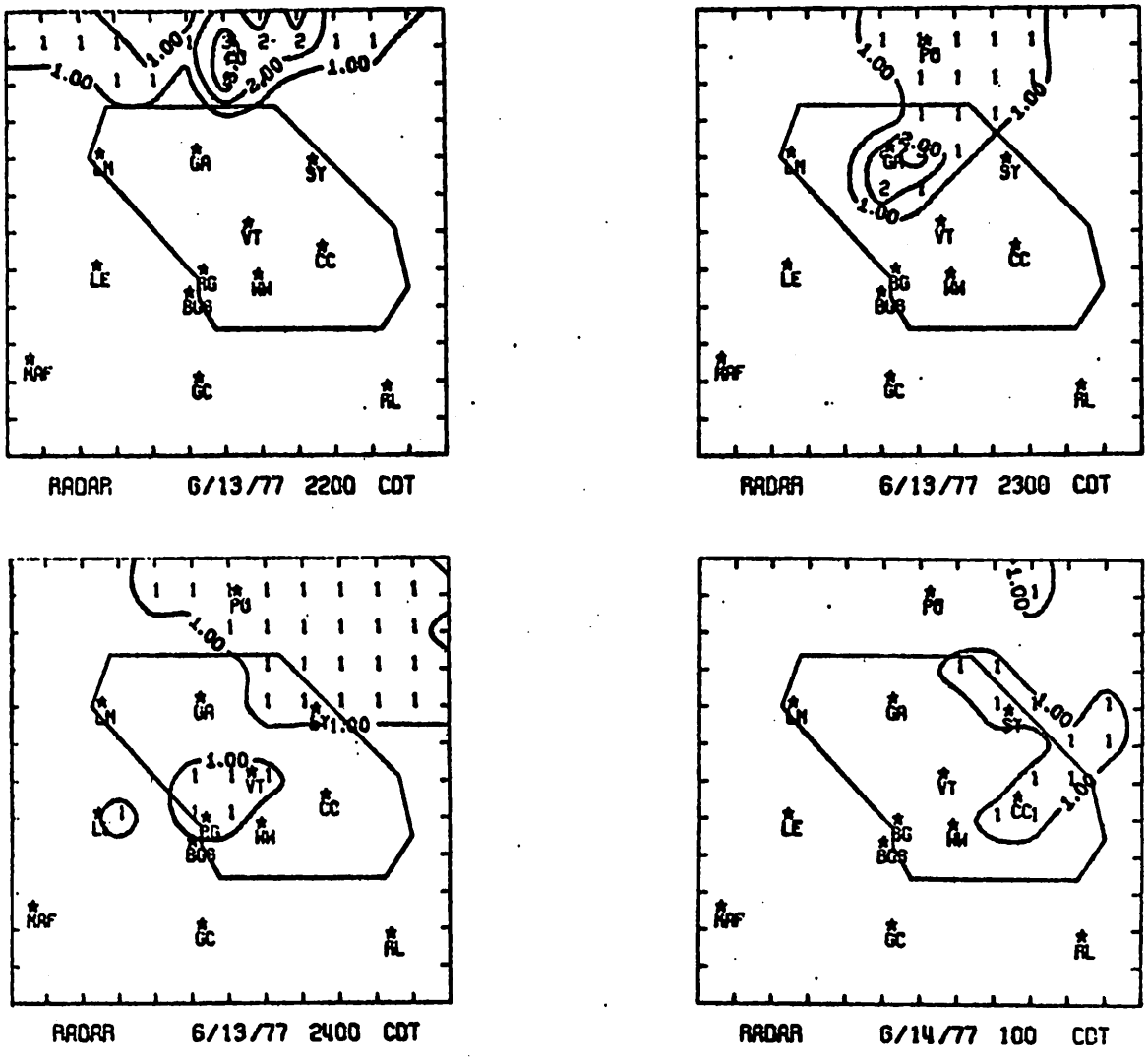

No echoes were observed on June 13 prior to 2200 CDT; echo coverage extended to 0100 CDT on June 14 to cover period for which soundings were made.

Fig. 5.6.1.1 Radar echoes for 13 June 1977.

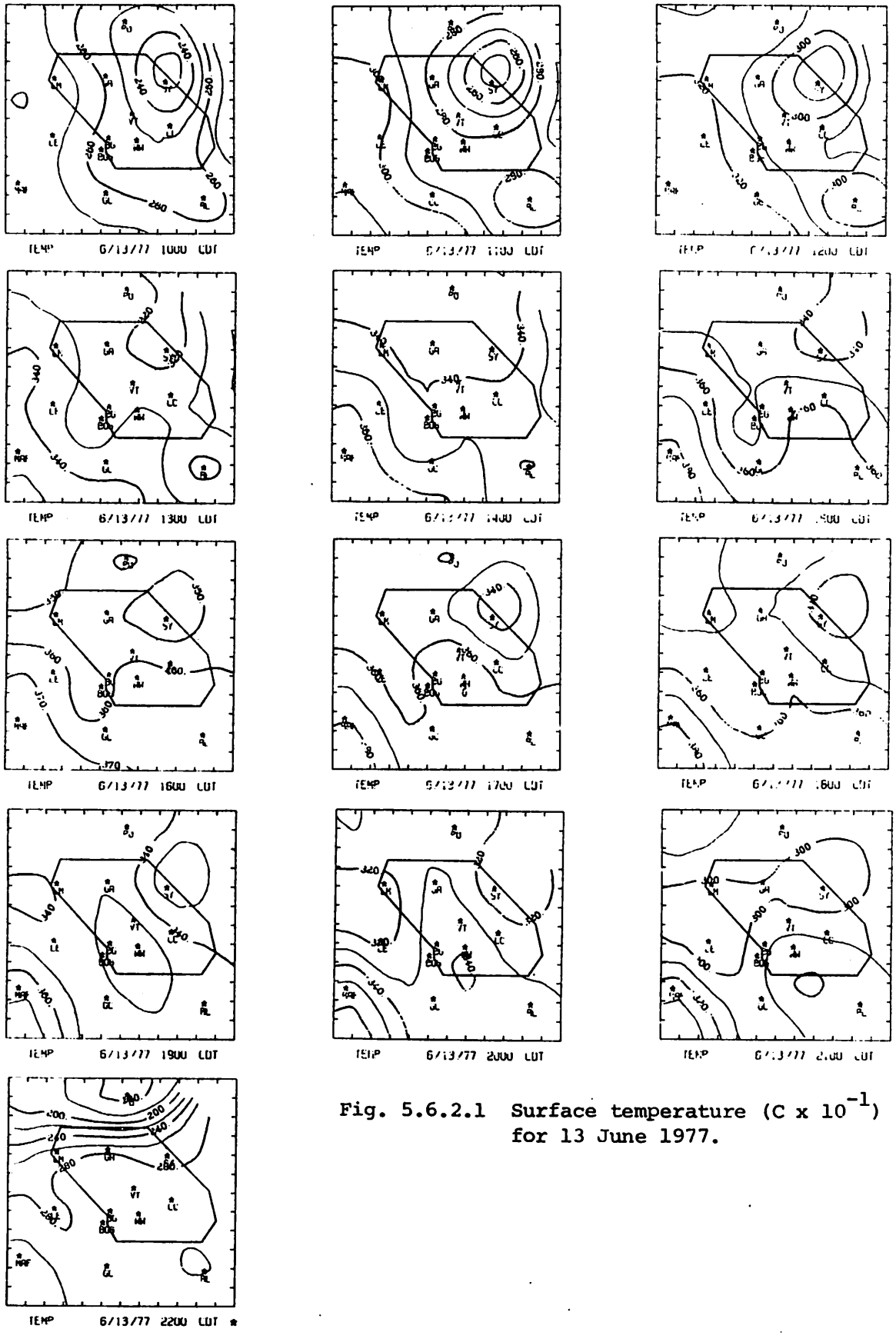

Fig. 5.6.2.1 Surface temperature (C x 10^{-1}) for 13 June 1977.

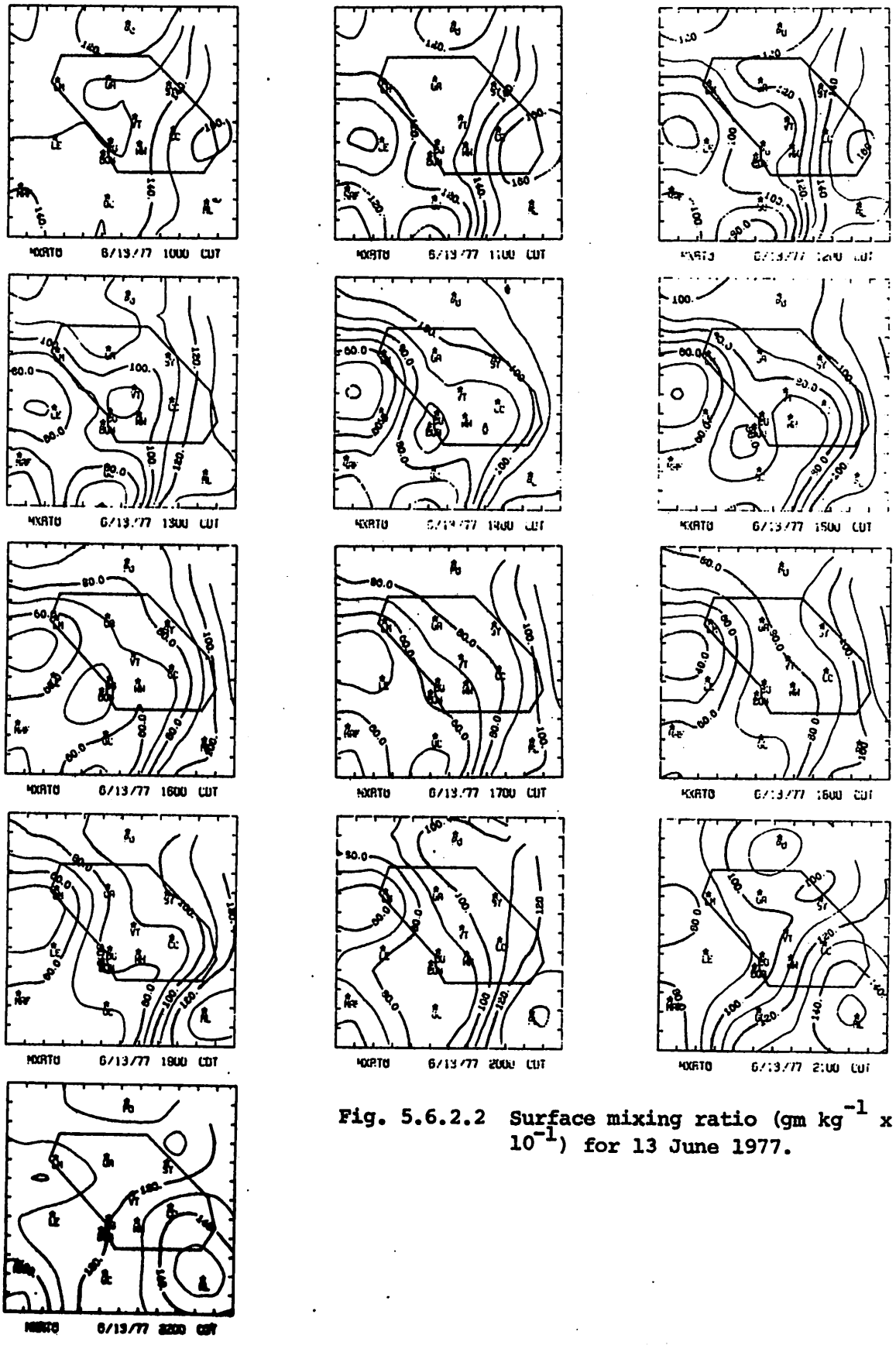

Fig. 5.6.2.2 Surface mixing ratio (gm kg^{-1} x 10^{-1}) for 13 June 1977.

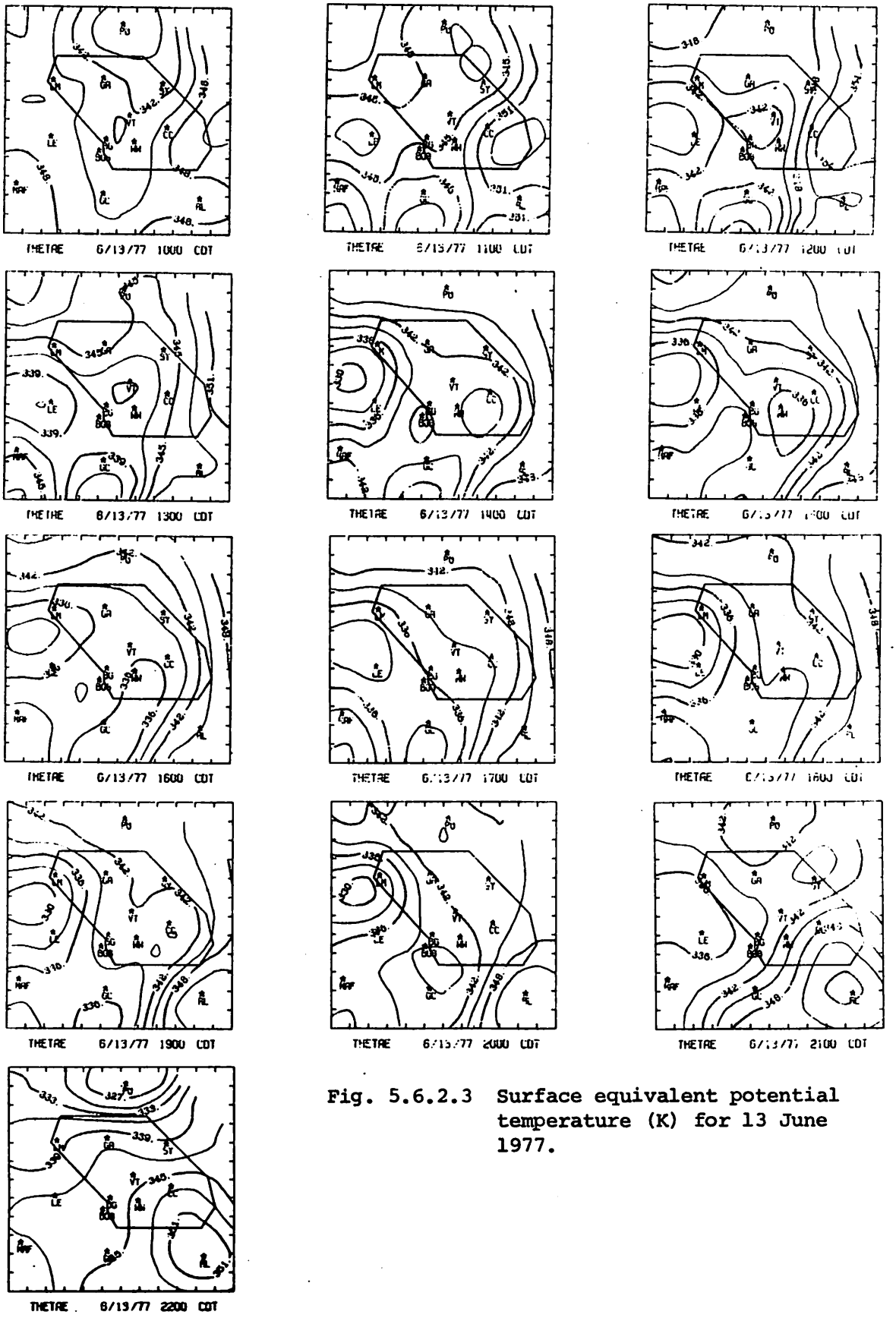

Fig. 5.6.2.3 Surface equivalent potential temperature (K) for 13 June 1977.

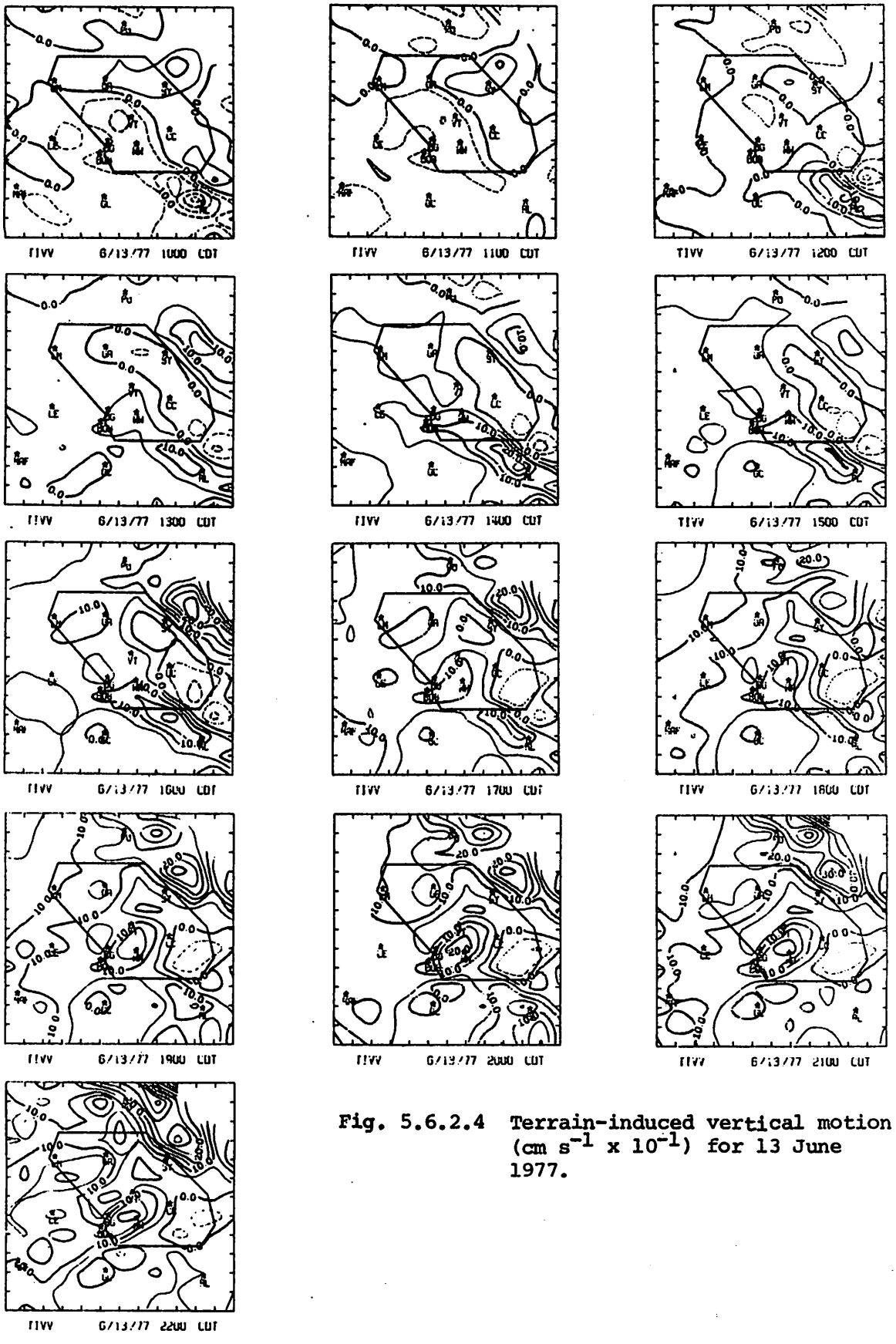

Fig. 5.6.2.4 Terrain-induced vertical motion (cm s^{-1} x 10^{-1}) for 13 June 1977.

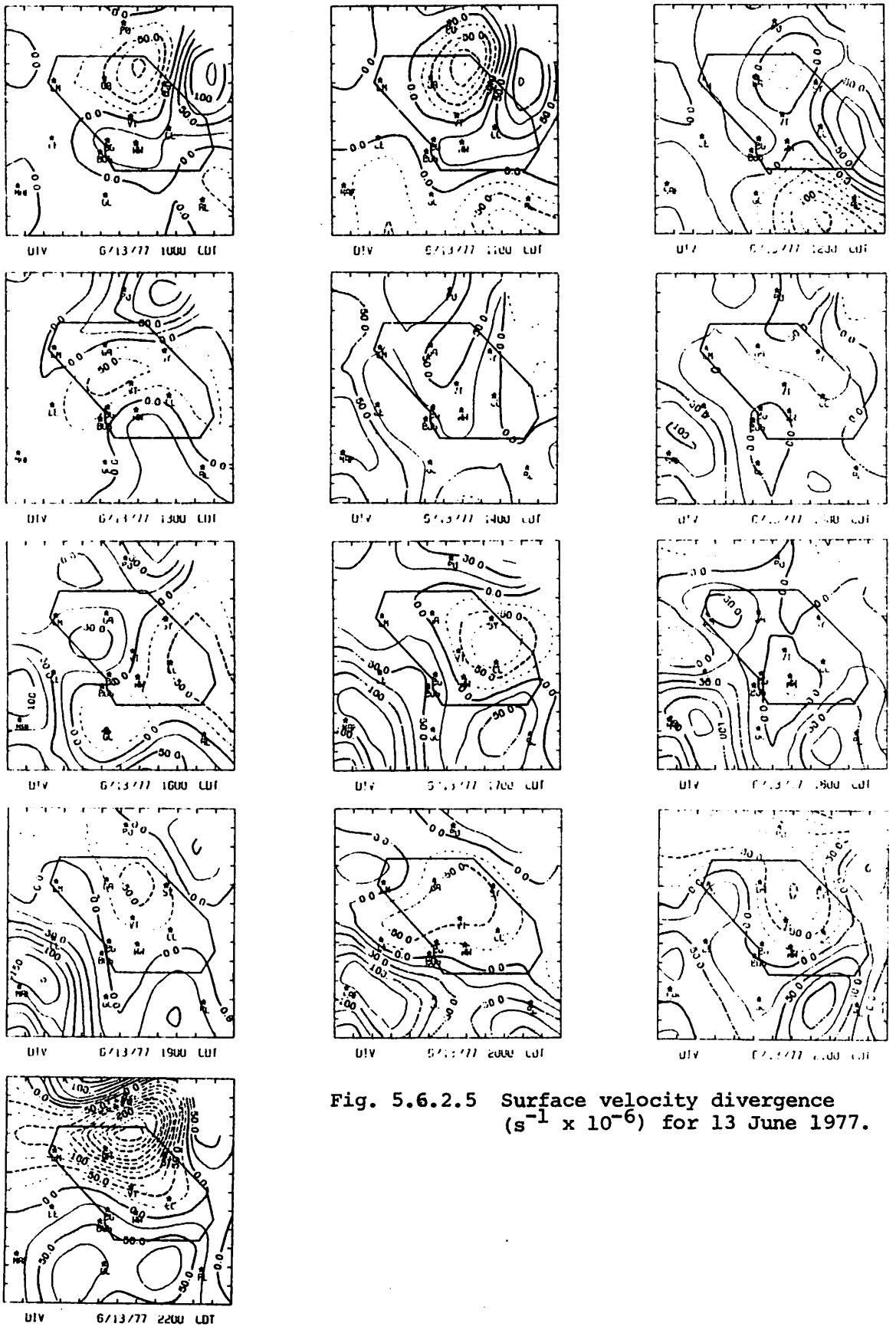

Fig. 5.6.2.5 Surface velocity divergence (s^{-1} x 10^{-6}) for 13 June 1977.

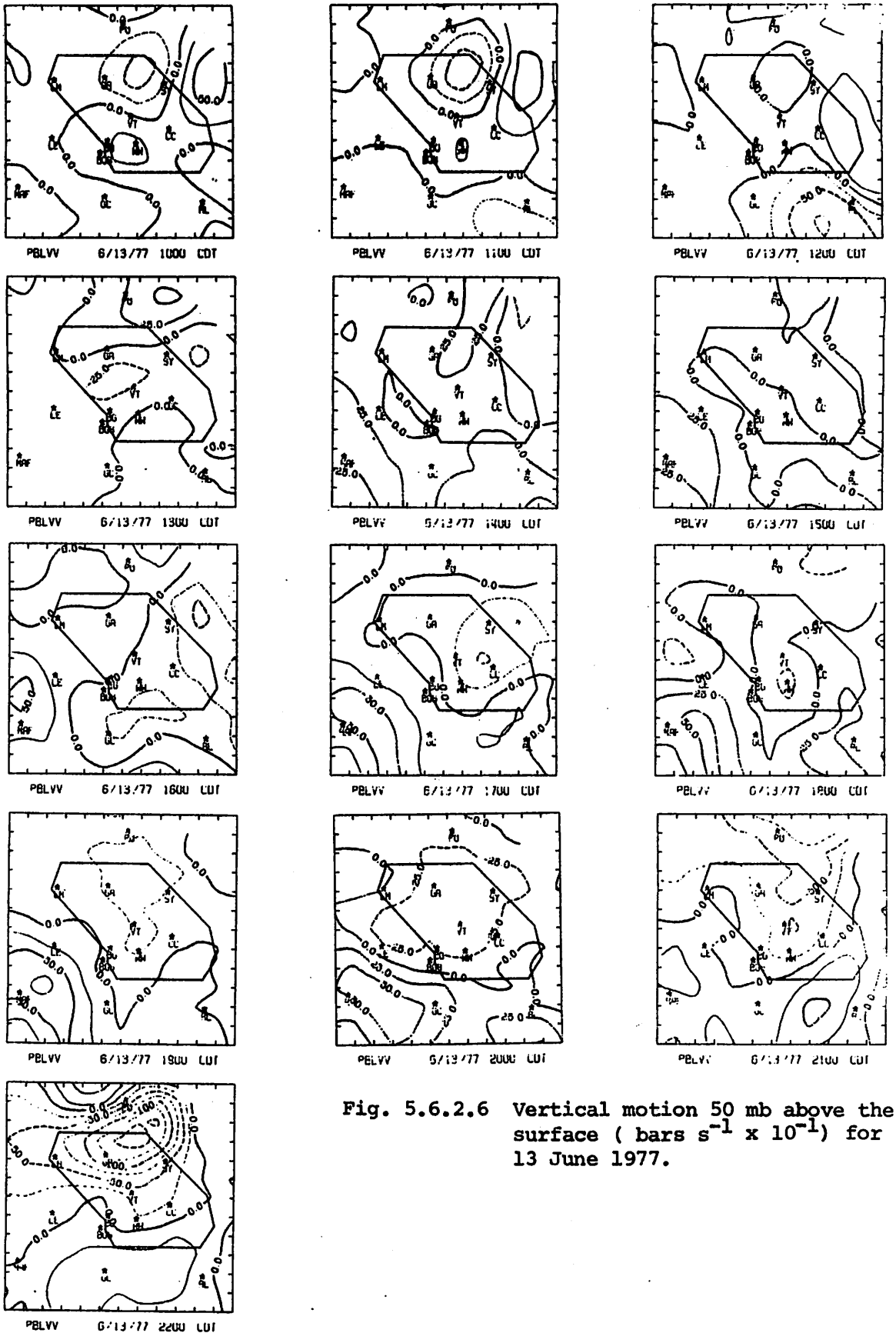

Fig. 5.6.2.6 Vertical motion 50 mb above the surface (bars s^{-1} x 10^{-1}) for 13 June 1977.

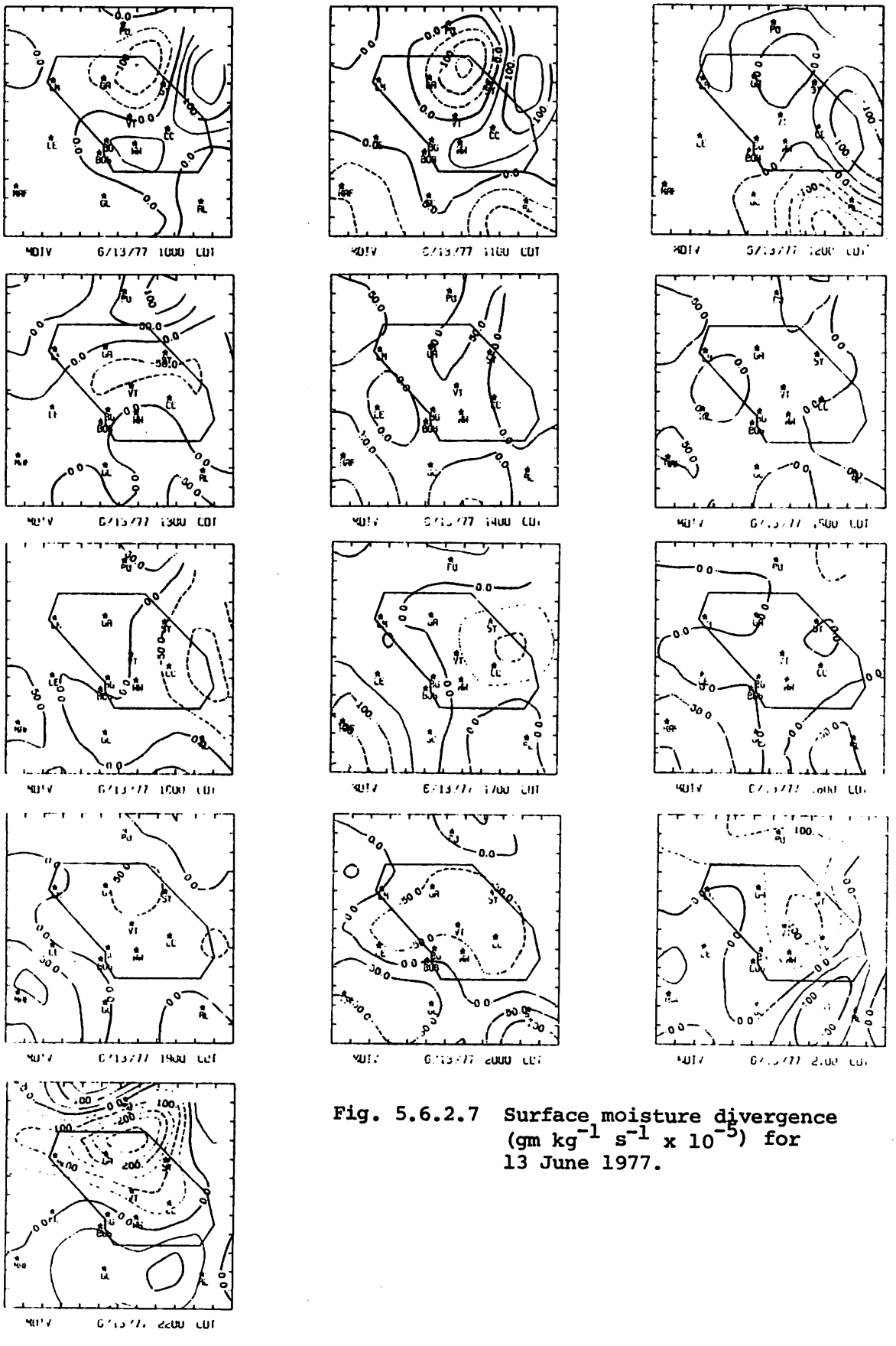

Fig. 5.6.2.7 Surface moisture divergence (gm kg^{-1} s^{-1} x 10^{-5}) for 13 June 1977.

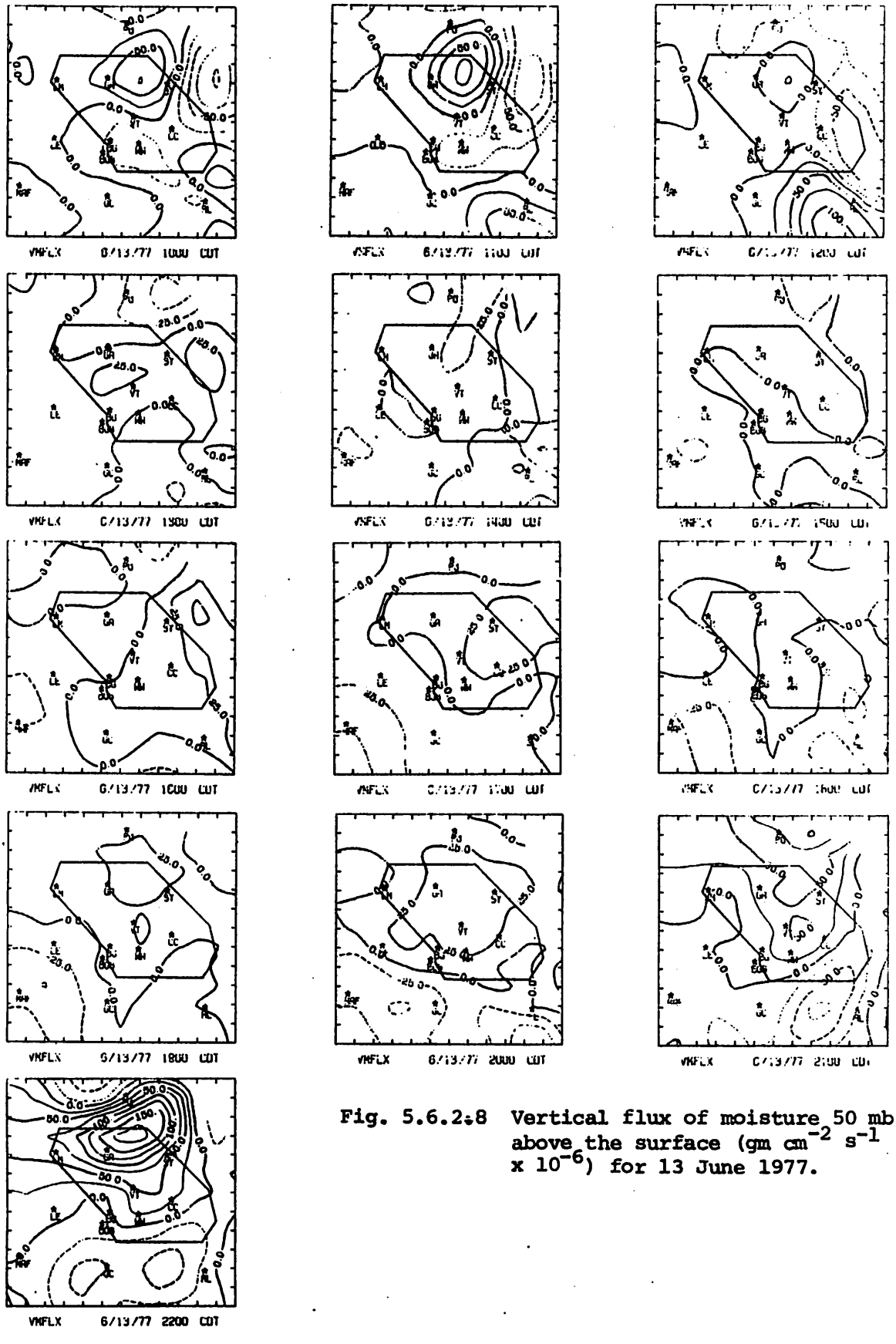

Fig. 5.6.2.8 Vertical flux of moisture 50 mb above the surface (gm cm^{-2} s^{-1} x 10^{-6}) for 13 June 1977.

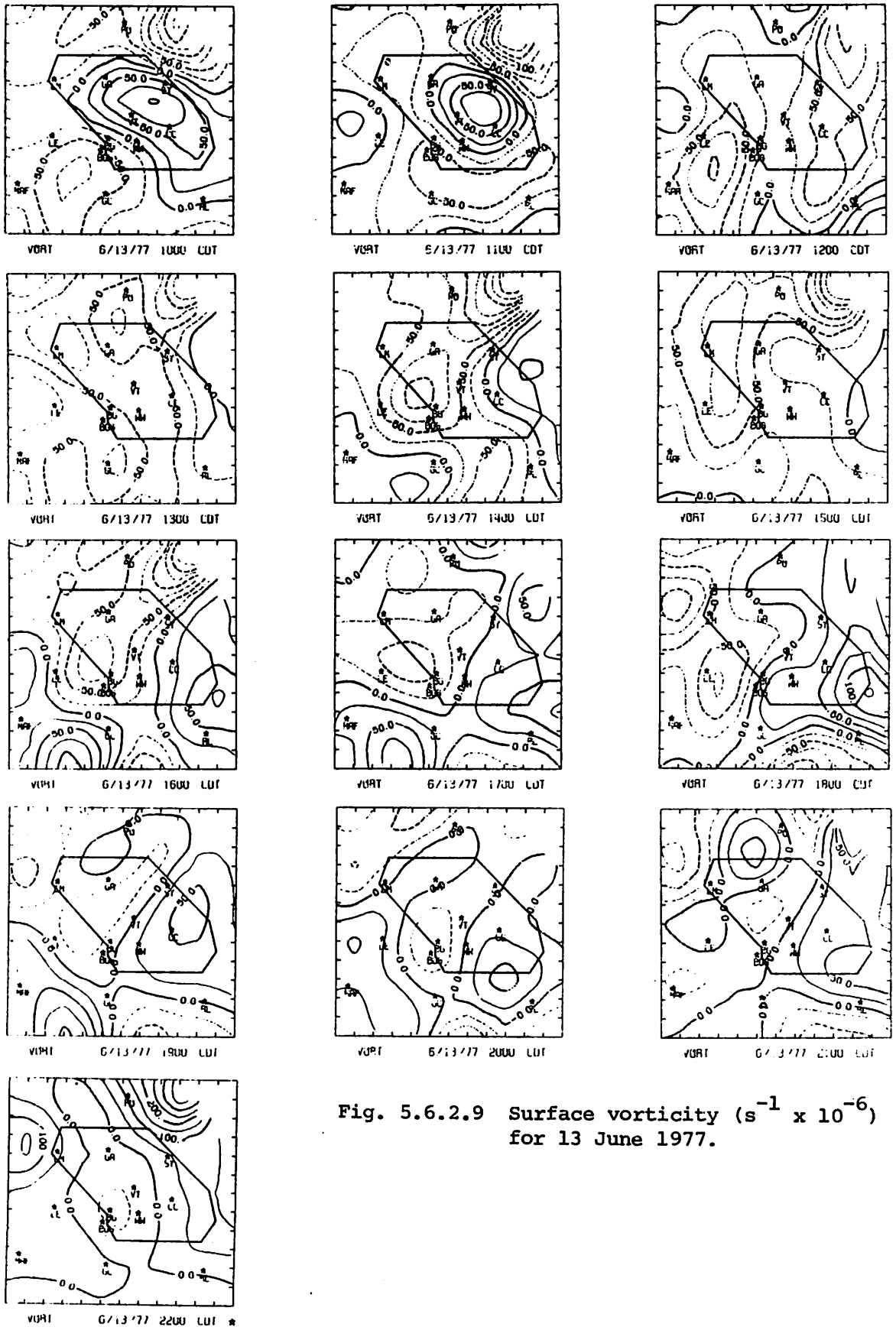

Fig. 5.6.2.9 Surface vorticity (s^{-1} x 10^{-6}) for 13 June 1977.

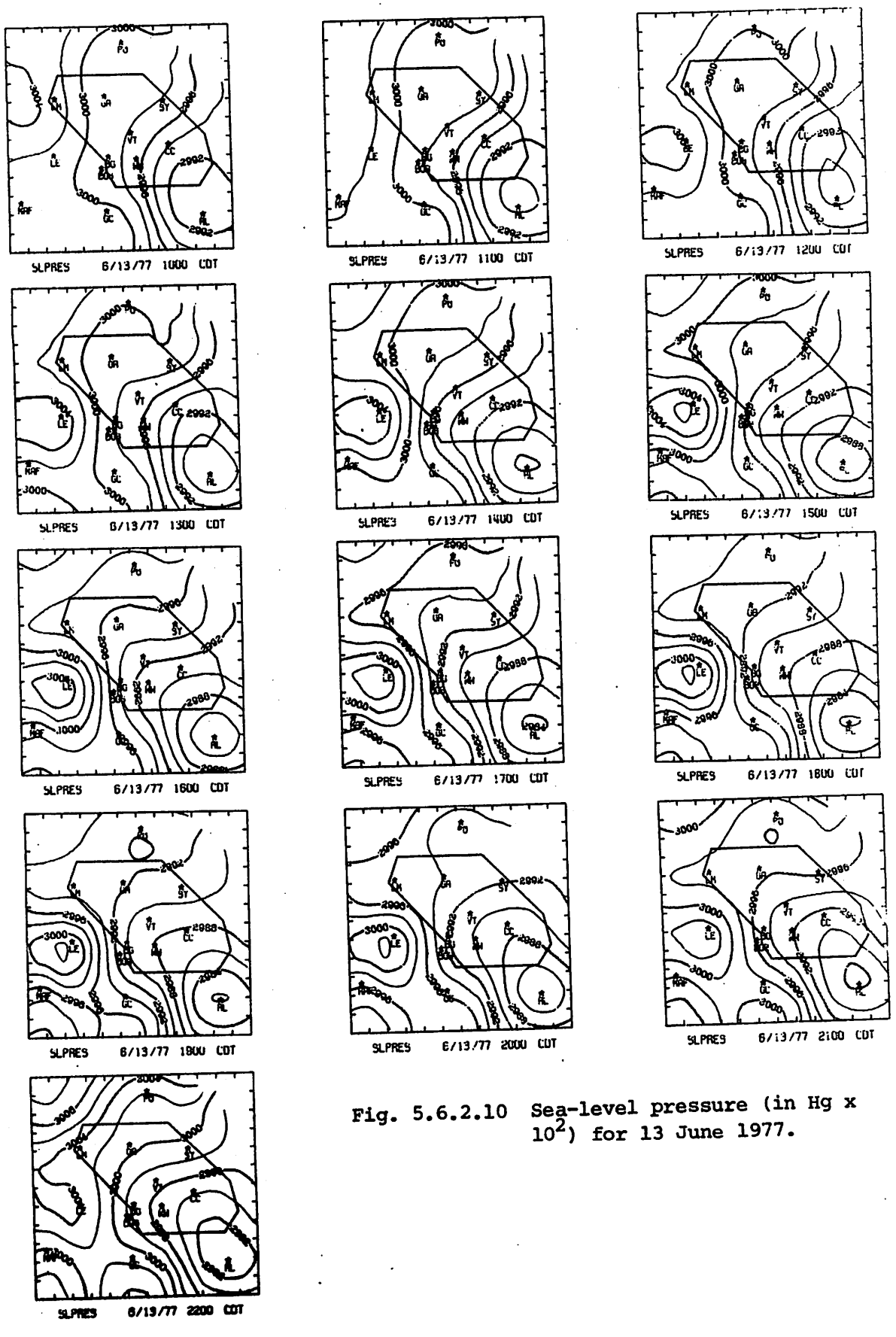

Fig. 5.6.2.10 Sea-level pressure (in Hg x 10^2) for 13 June 1977.

GMT. This is reflected in the surface pressure change (Fig. 5.6.2.11). Pressure increases correlate with temperature decreases in the vicinity of the storm. A large pressure increase at 1700 GMT is due to missing data at Walsh-Watts and resulted from the data processing methods.

5.6.3 Upper-Level Kinematic Parameters

Large and rapid changes in the vertical profiles of horizontal mass divergence (Fig. 5.6.3.1) occurred during the day as a line of strong thunderstorms moved over the network and dissipated between 0300 and 0600 GMT. Mass divergence below 800 mb changes to convergence after 1800 GMT and maximizes at 0300 GMT just before thunderstorms formed over the network. Dissipation of activity by 0600 GMT is accompanied by large mass divergence in the lower levels. Between 700 and 500 mb mass convergence changes to divergence before storm formation and returns to strong convergence during dissipation of the activity. Vertical velocities are downward or near zero at all levels before 0000 GMT but change to upward below 700 mb at 0000 and 0300 GMT before and during storm formation (Fig. 5.6.3.2). Vertical velocities are strong downward below 600 mb and upward aloft during storm dissipation, indicating the possible effects of thunderstorm downdrafts on the environment vertical velocity field close to the ground.

Horizontal moisture divergence profiles (Fig. 5.6.3.3) showed only small and "near zero" values at all levels before 0000 GMT. Between 0000 and 0300 GMT strong moisture convergence developed below 800 mb and moisture divergence aloft coincident with convective storm formation over the network. With storm dissipation, very strong moisture divergence occurred below 700 mb with convergence between 700 and 300 mb.

5.6.4 Energetics

Horizontal flux divergence of latent heat energy was small at all levels before 0000 GMT when strong inflow developed below 800 mb and strong outflow occurred between 800 and 500 mb during storm development (Fig. 5.6.4.1). After storm dissipation, large horizontal outflow occurred immediately below large inflow in the low and middle troposphere, respectively. The vertical flux divergence calculations (Fig. 5.6.4.2) showed low-level divergence of latent heat energy before and during storm development between 0000 and 0300 GMT, and large convergence during dissipation at 0600 GMT. The reverse occurred in mid levels during this 6-h period as latent heat energy is transported from low- to mid-levels between 0000 and 0300 GMT, and transported back into low levels at 0600 GMT.

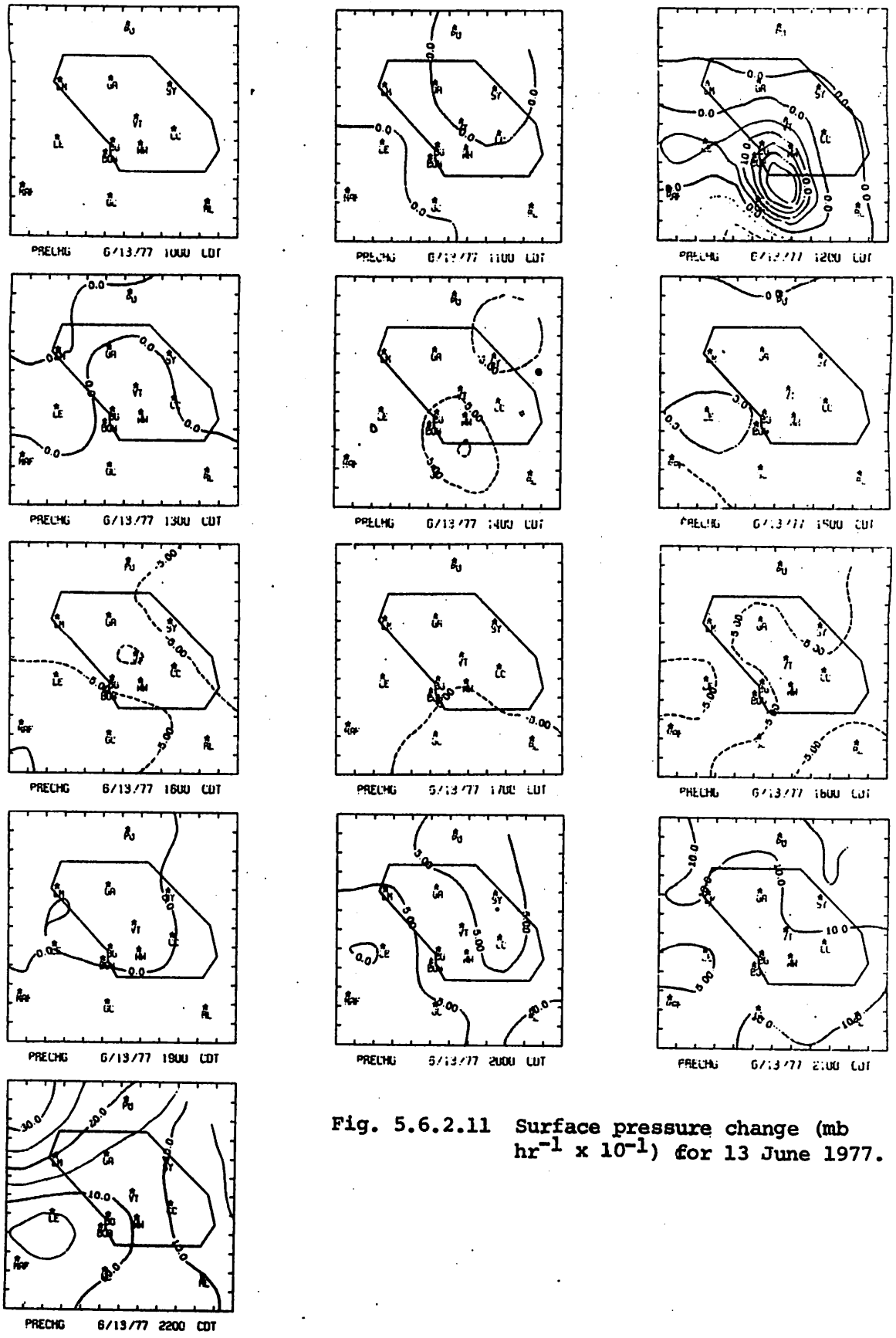

Fig. 5.6.2.11 Surface pressure change (mb hr^{-1} x 10^{-1}) for 13 June 1977.

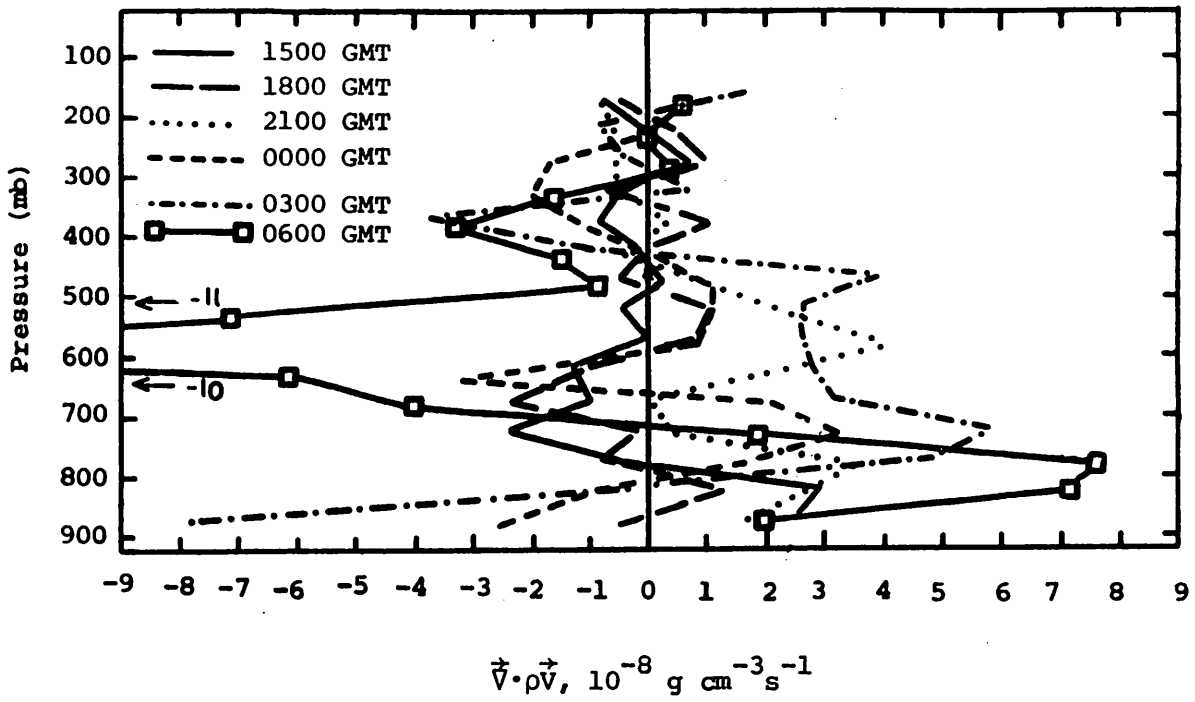

Fig. 5.6.3.1 Vertical profiles of mass divergence on 13 June 1977.

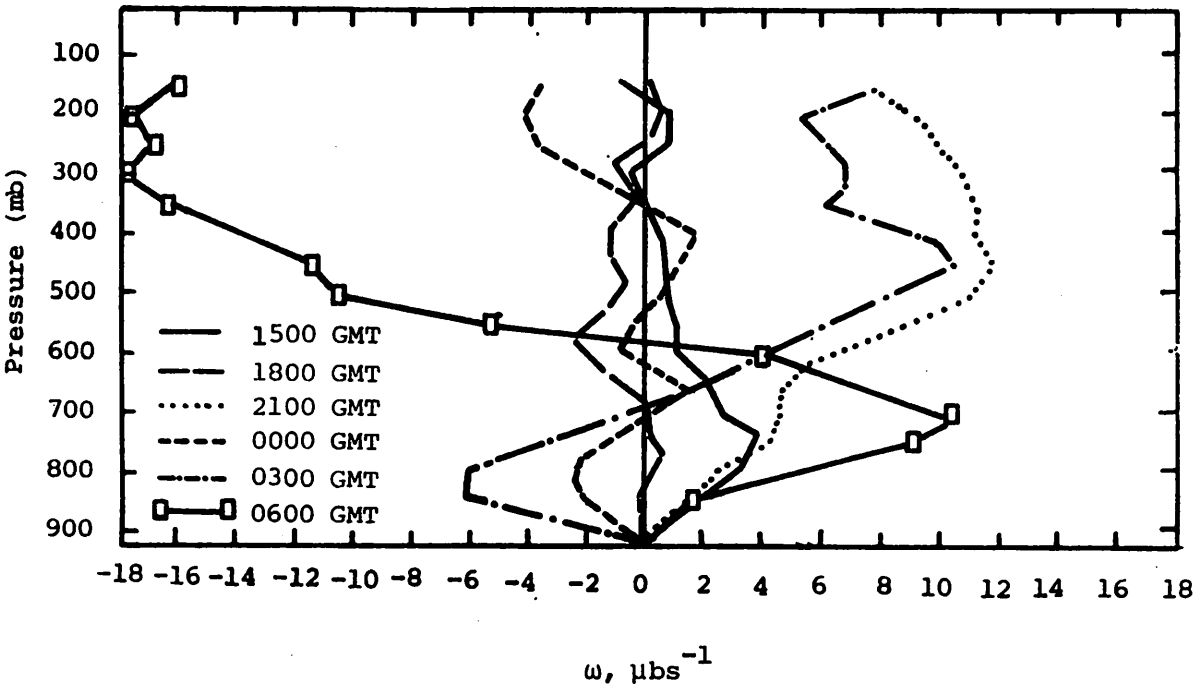

Fig. 5.6.3.2 Vertical profiles of vertical motion on 13 June 1977.

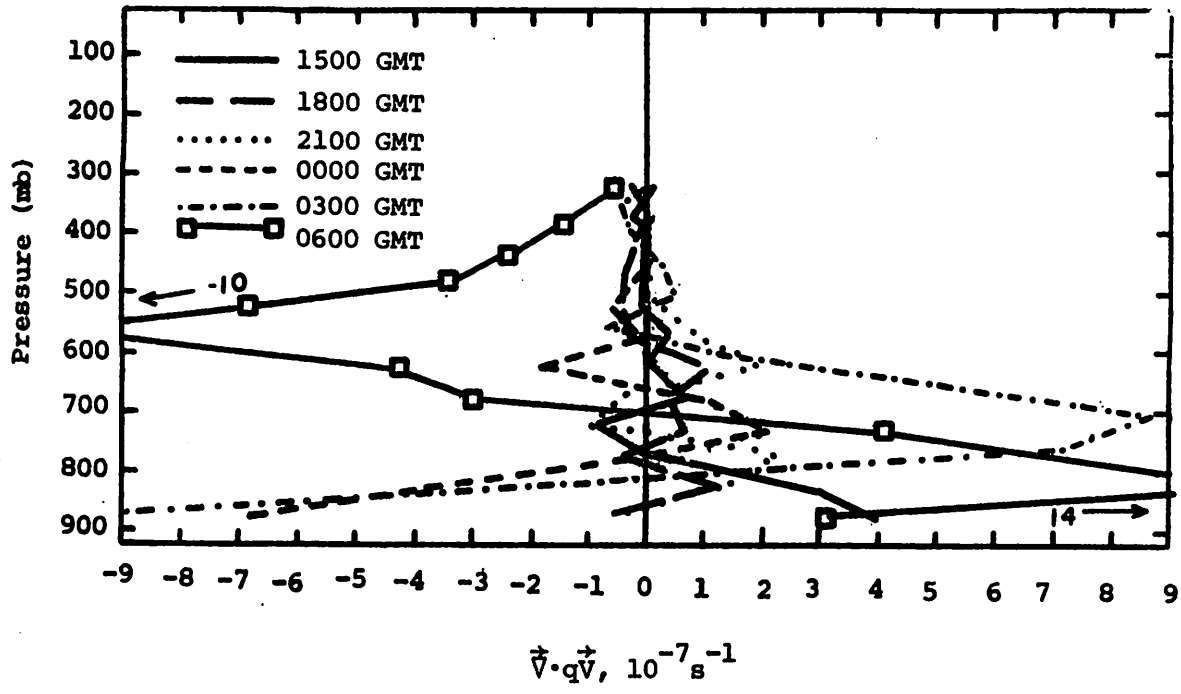

Fig. 5.6.3.3 Vertical profiles of moisture divergence on 13 June 1977.

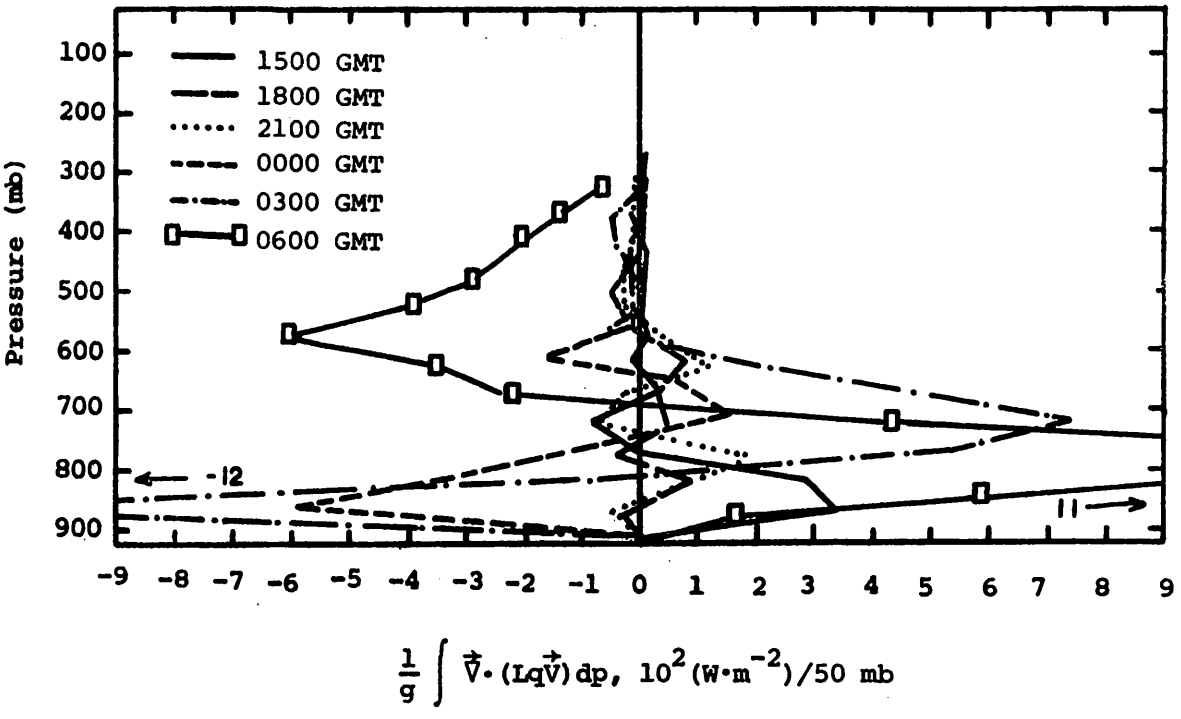

Fig. 5.6.4.1 Vertical profiles of the horizontal flux of latent heat energy on 13 June 1977.

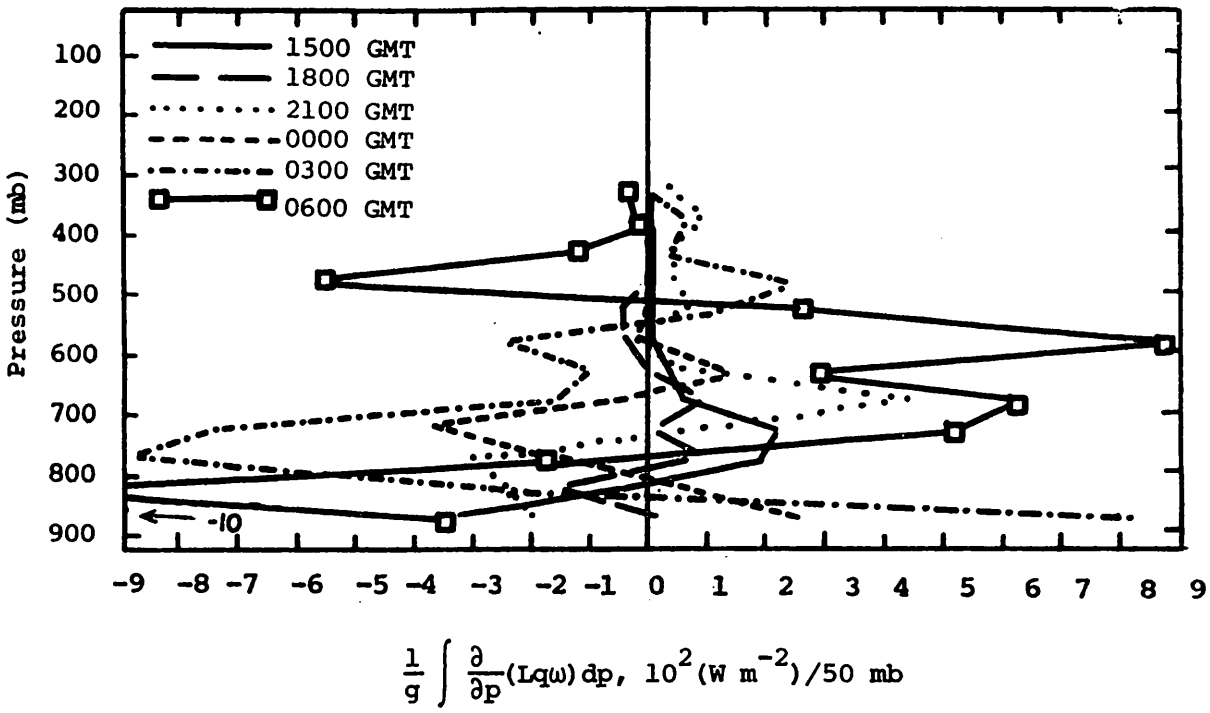

Fig. 5.6.4.2 Vertical profiles of the vertical flux of latent heat energy on 13 June 1977.

Local changes of latent heat energy are positive at most levels and times during the day (Fig. 5.6.4.3), especially in lower levels before storm development. The residual in the latent heat budget equation (-R) shows gains (negative -R values) at most times between 800 and 600 mb and losses below (Fig. 5.6.4.4). This distribution is not consistent with cloud formation (producing positive -R values and environment heating) that occurred during the day around the 700-mb layer. Since a dry adiabatic lapse rate developed between the surface and 700 mb before storm formation (0000 GMT), turbulent flux divergence of latent heat energy was possibly responsible for creating losses in latent heat content (positive -R values) in lower levels and turbulent flux convergence created large negative -R value (increasing water vapor and latent heat content) in mid levels. Large negative values of -R are probably associated with evaporation of precipitation at 0600 GMT. Condensation with environmental heating was calculated above 600 mb as latent heat was realized within thunderstorms and transported into the environment during storm dissipation.

Diabatic heating (Fig. 5.6.4.5) profiles show warming occurring in lower layers consistent with radiational and turbulent heating in the boundary layer. At 0600 GMT the diabatic heating profile is very similar to the -R curve with cooling in low levels from evaporation and heating

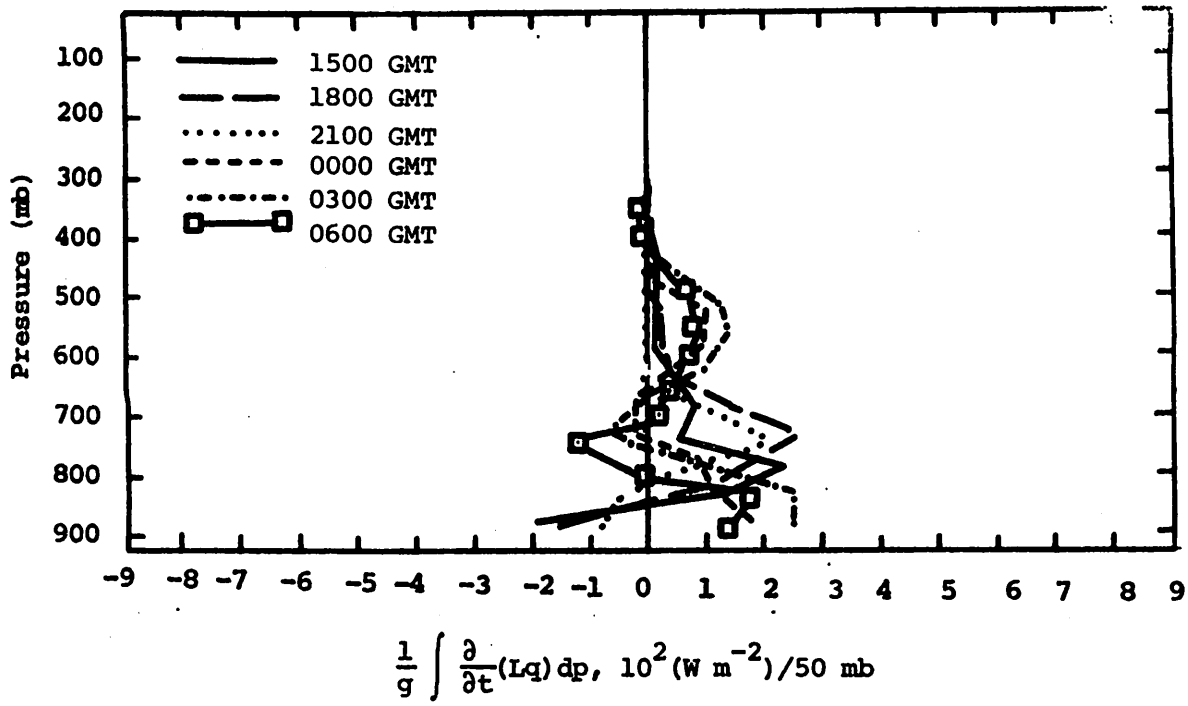

Fig. 5.6.4.3 Vertical profiles of the local change of latent heat energy on 13 June 1977.

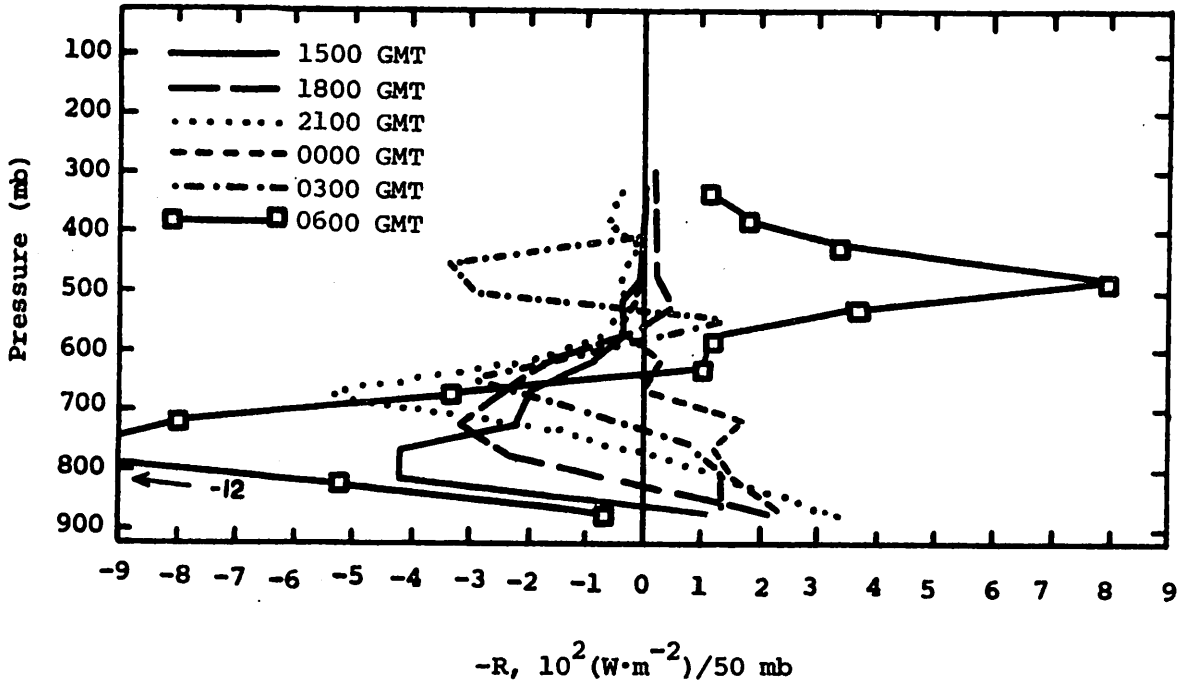

Fig. 5.6.4.4 Vertical profile of the residual of the latent heat energy equation on 13 June 1977.

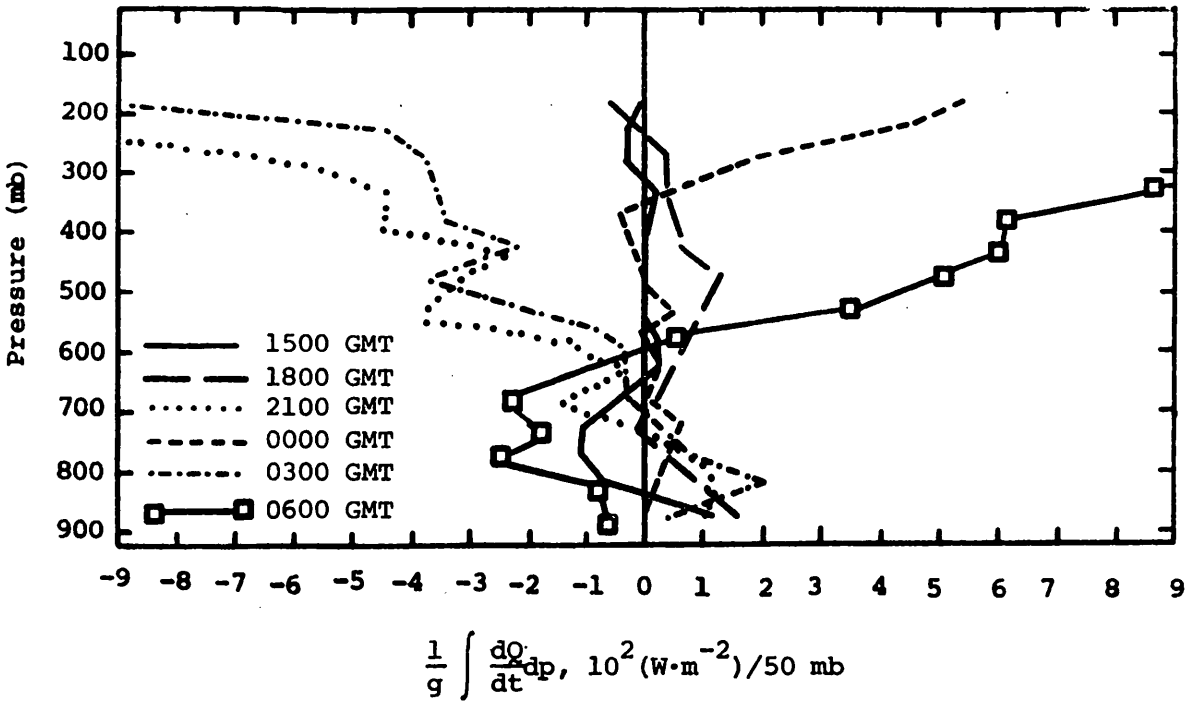

Fig. 5.6.4.5 Vertical profiles of diabatic heating computed from the first law of thermodynamics on 13 June 1977.

aloft from condensation.

Horizontal and vertical flux divergence profiles for kinetic energy (Figs. 5.6.4.6 and 5.6.4.7) contain no noticeably important features until 0300 and 0600 GMT when strong horizontal flux divergence was computed below 700 mb, and strong convergence was present aloft. Vertical flux convergence was present below 700 mb with strong flux divergence aloft except at 300 mb at 0600 GMT when strong flux convergence was present.

5.6.5 Water Vapor Budget

Figure 5.6.1.1 shows that no radar echoes were observed over the Texas HIPLEX area prior to 0300 GMT. An isolated cell moved over the area at 0300 GMT and began dissipating after 0400 GMT.

Figure 5.6.5.1 shows vertical profiles of the net horizontal transport of water vapor. Profiles prior to 0000 GMT generally show a strong net outflow in layers below 550 mb and a net inflow aloft. As activity approaches and enters the network at 0300 GMT, this net inflow aloft increases. At 0600 GMT a strong net inflow occurred in all layers above 700 mb.

Figure 5.6.5.2 shows profiles of net vertical transport of water vapor. These profiles generally show a net inflow in lower layers and a net outflow aloft that increases during times of convection.

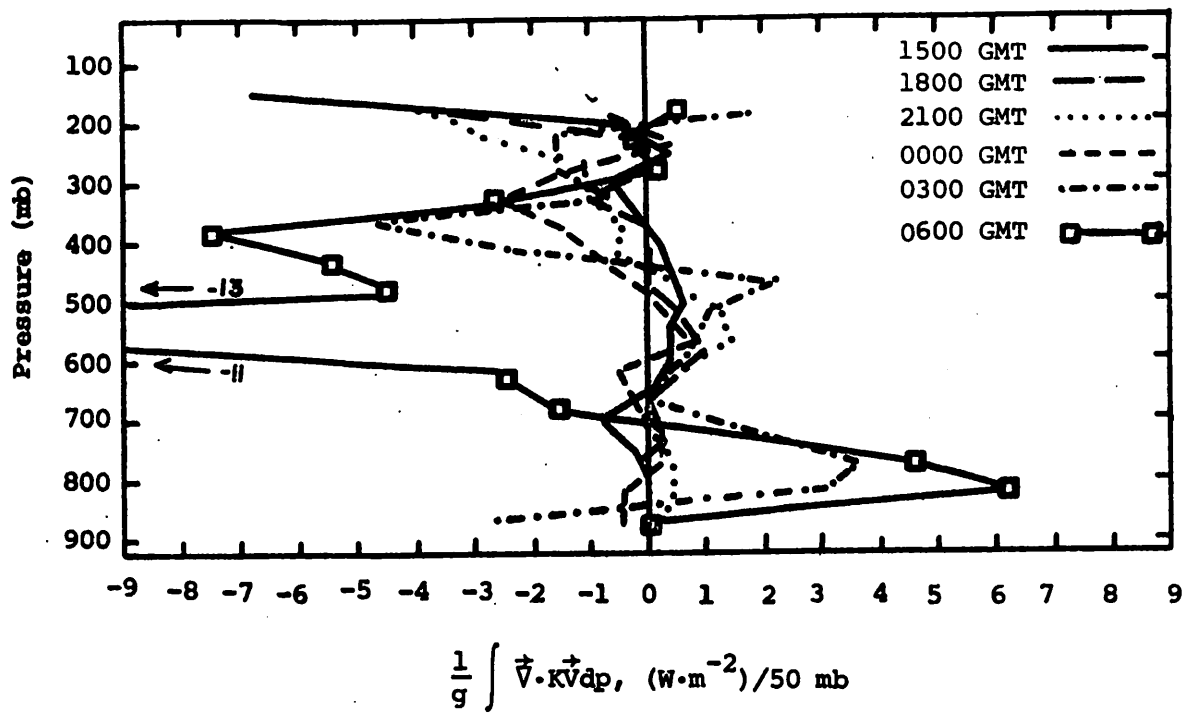

Fig. 5.6.4.6 Vertical profiles of the horizontal flux of kinetic energy on 13 June 1977.

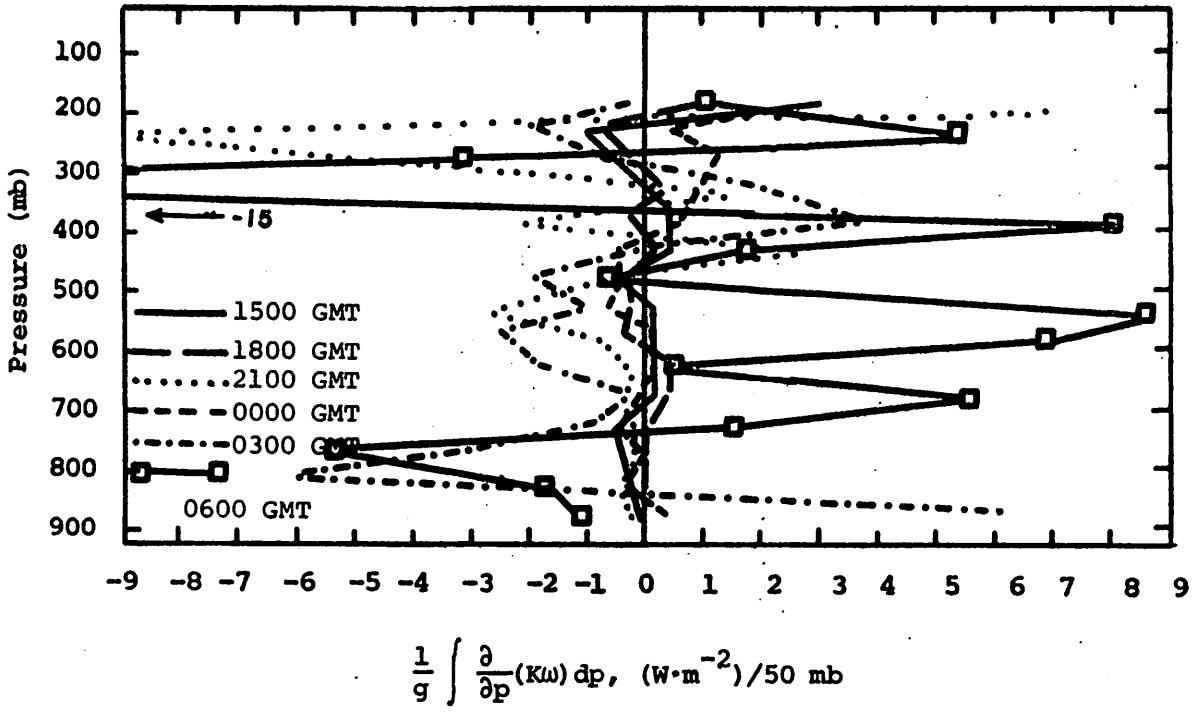

Fig. 5.6.4.7 Vertical profiles of the vertical flux of kinetic energy on 13 June 1977.

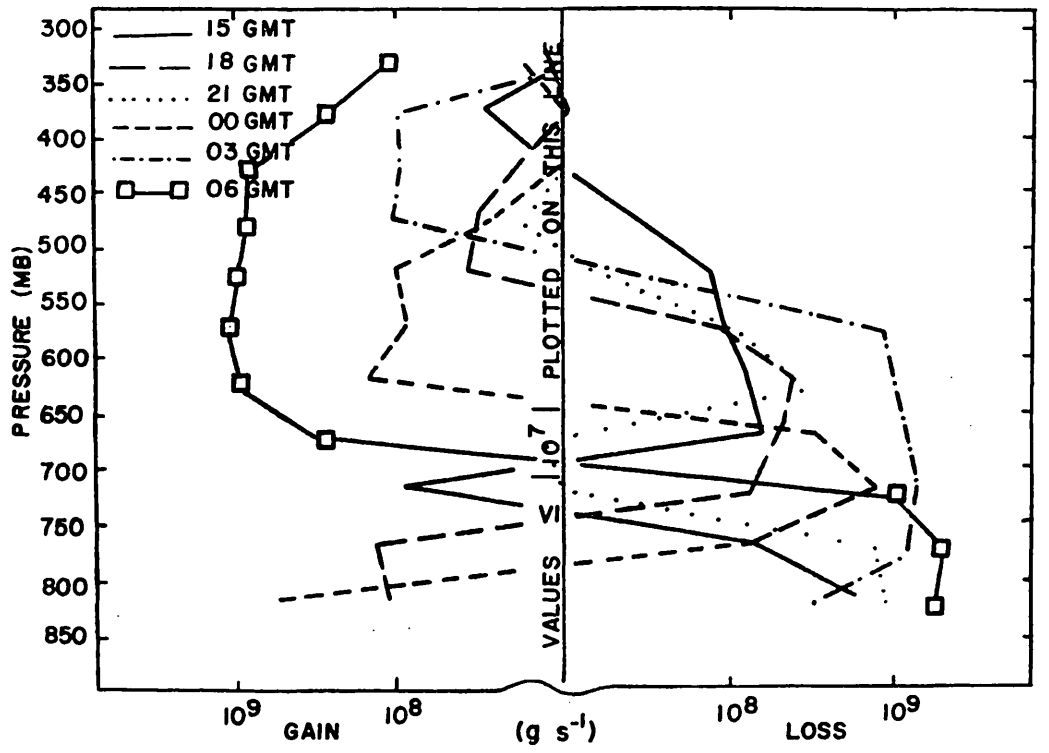

Fig. 5.6.5.1 Net horizontal transport of water vapor through boundaries of 50-mb layers (gm s^{-1}) over the Texas HIPLEX area for 13 June 1977.

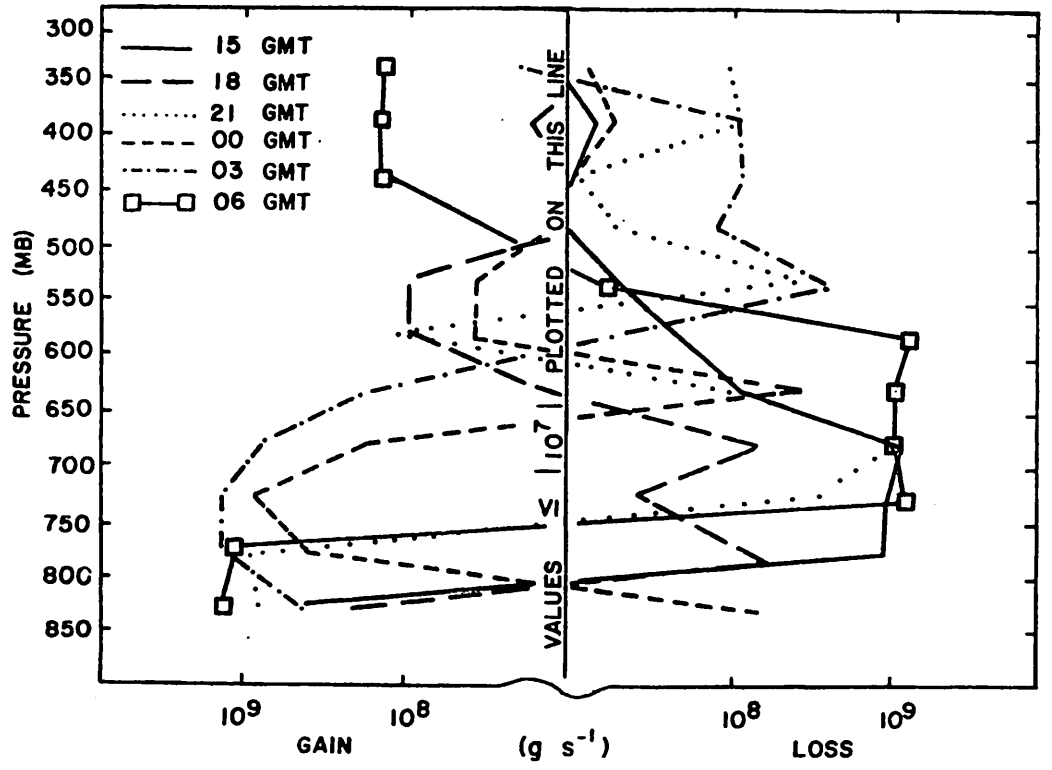

Fig. 5.6.5.2 Net vertical transport of water vapor through boundaries of 50-mb layers (gm s^{-1}) over the Texas HIPLEX area for 13 June 1977.

Figure 5.6.5.3 shows profiles of the vertical transport of water vapor through constant pressure surfaces. These profiles show large spatial and temporal variations which also are shown in Figure 5.6.5.2. However, prior to the heavy activity at 0300 GMT, strong upward transport occurred up to 700 mb. During dissipation at 0600 GMT, downward transport was present in these layers.

Figure 5.6.5.4 shows profiles of the combined net horizontal and vertical transport of water vapor. Although these profiles vary in space and time, a general net outflow in lower layers, and a net inflow in upper layers occurred, especially during times of convection.

Figure 5.6.5.5 shows vertical profiles of the total mass of water vapor. These profiles again vary in time. However, the greatest values of water vapor occur during times of convection in most layers, especially between 600 and 500 mb.

Figure 5.6.5.6 shows vertical profiles of the local rate-of-change in the total mass of water vapor. Although large temporal variations are observed, increases of water vapor prior to convection occurred. During convection, between 0300 and 0600 GMT, a large loss is observed up to 550 mb. This may be attributed to strong upward transport at 0300 GMT in Figure 5.6.5.3 and to condensation of water vapor into liquid water in these layers. The maximum loss occurred near 700 mb.

5.7 20 June 1977

5.7.1 Radar

No echoes of any consequence were observed prior to 0200 GMT when a large area of precipitation approached the HIPLEX area from the northwest (Fig. 5.7.1.1). This echo area contained two cells with tops exceeding 9.1 km (30K ft) with the highest echo tops oriented along a northeast-southwest line over Lamesa at 0300 GMT.

5.7.2 Surface

Surface temperature fields (Fig. 5.7.2.1) show only changes due to surface heating prior to the convective activity observed at 0200 GMT. A temperature drop of 10°C is associated with this line, and values of minimum temperature are found in regions of strongest echoes. Values of surface mixing ratio (Fig. 5.7.2.2) remain high over the area throughout the day with no appreciable change associated with the advancing line. Fields of surface equivalent potential temperature (Fig. 5.7.2.3) show

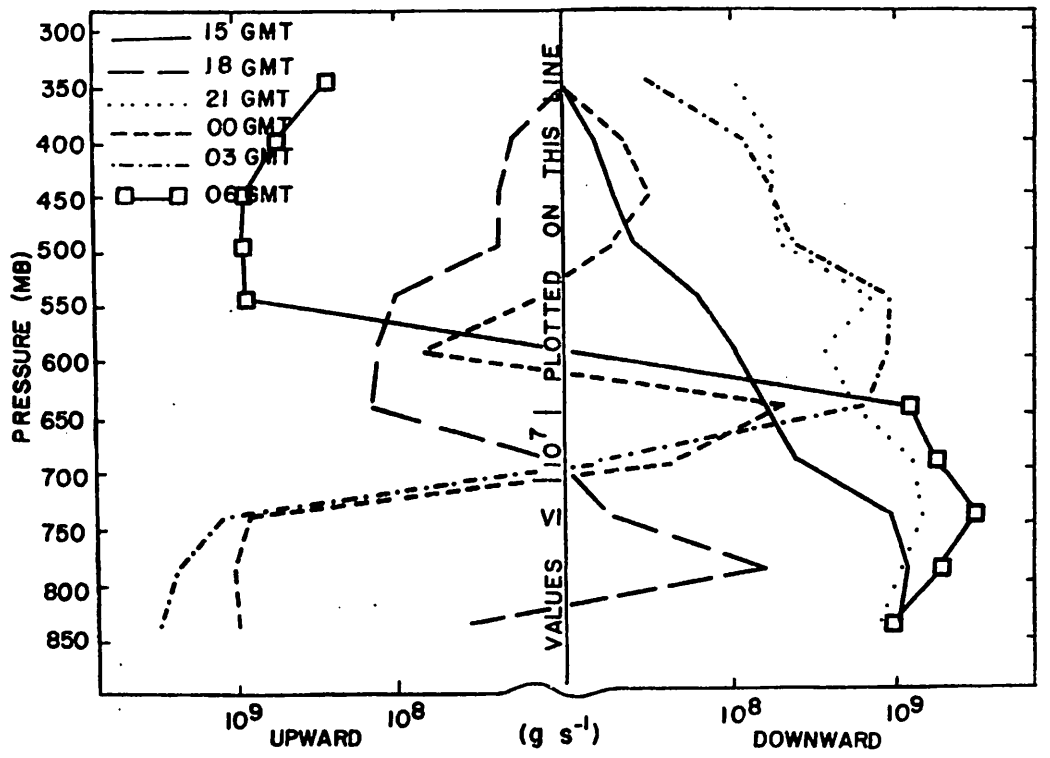

Fig. 5.6.5.3 Vertical transport of water vapor through constant pressure surfaces (gm s^{-1}) over the Texas HIPLEX area for 13 June 1977.

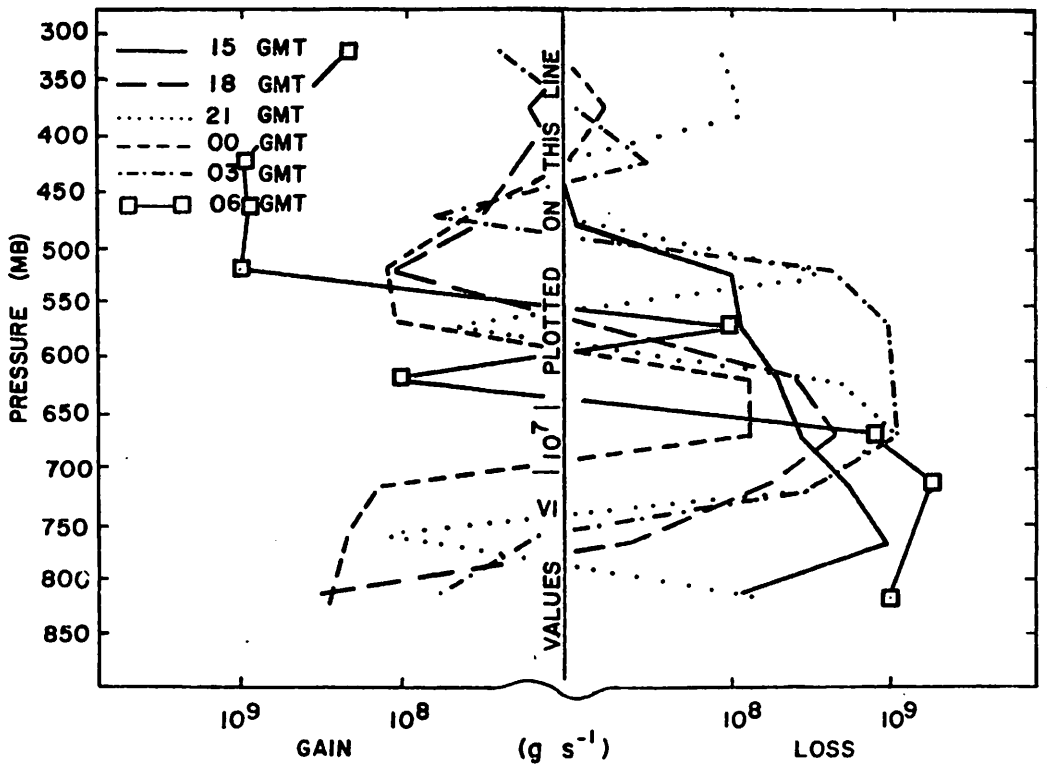

Fig. 5.6.5.4 Combined net horizontal and vertical transport of water vapor through boundaries of 50-mb layers (gm s^{-1}) over the Texas HIPLEX area for 13 June 1977.

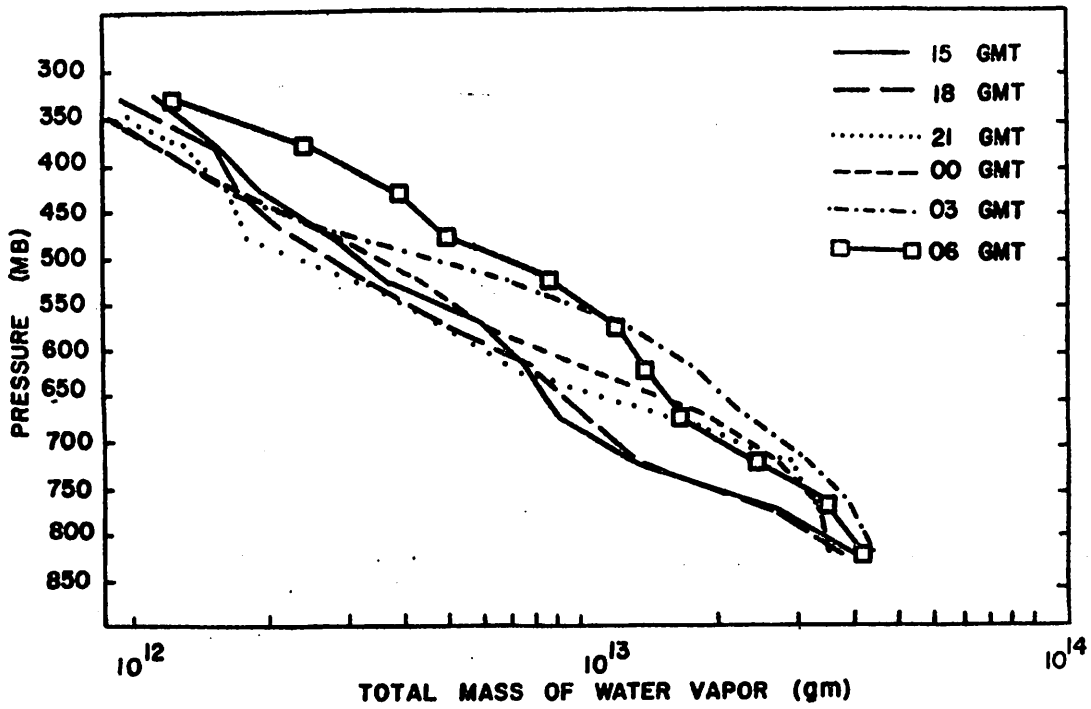

Fig. 5.6.5.5 Total mass of water vapor in layers 50 mb deep (gm) over the Texas HIPLEX area for 13 June 1977.

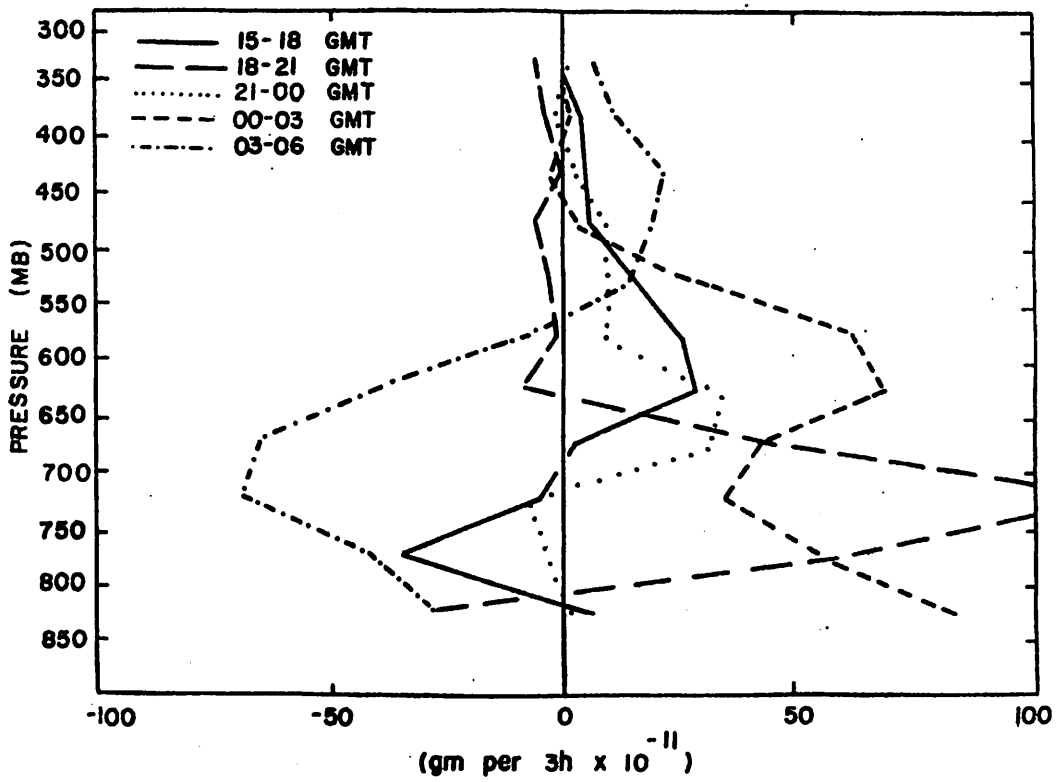

Fig. 5.6.5.6 Local rate-of-change in total mass of water vapor (gm per 3h x 10^{-11}) over the Texas HIPLEX area for 13 June 1977.

NO ECHOES

RADAR 6/20/77 1000 CDT

NO ECHOES

RADAR 6/20/77 1100 CDT

NO ECHOES

RADAR 6/20/77 1200 CDT

NO ECHOES

RADAR 6/20/77 1300 CDT

NO ECHOES

RADAR 6/20/77 1400 CDT

NO ECHOES

RADAR 6/20/77 1500 CDT

NO ECHOES

RADAR 6/20/77 1600 CDT

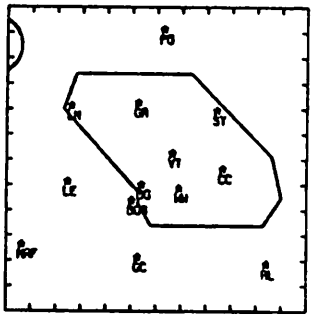

RADAR 6/20/77 1700 CDT

NO ECHOES

RADAR 6/20/77 1800 CDT

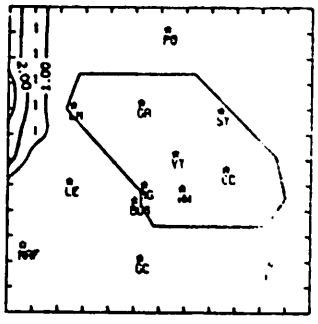

RADAR 6/20/77 1900 CDT

NO ECHOES

RADAR 6/20/77 2000 CDT

RADAR 6/20/77 2100 CDT

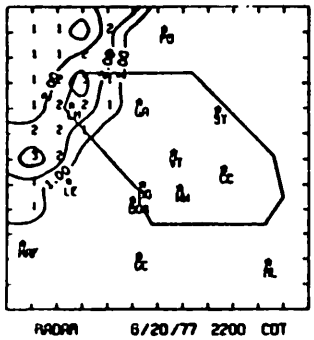

RADAR 6/20/77 2200 CDT

Fig. 5.7.1.1 Radar echoes for 20 June 1977.

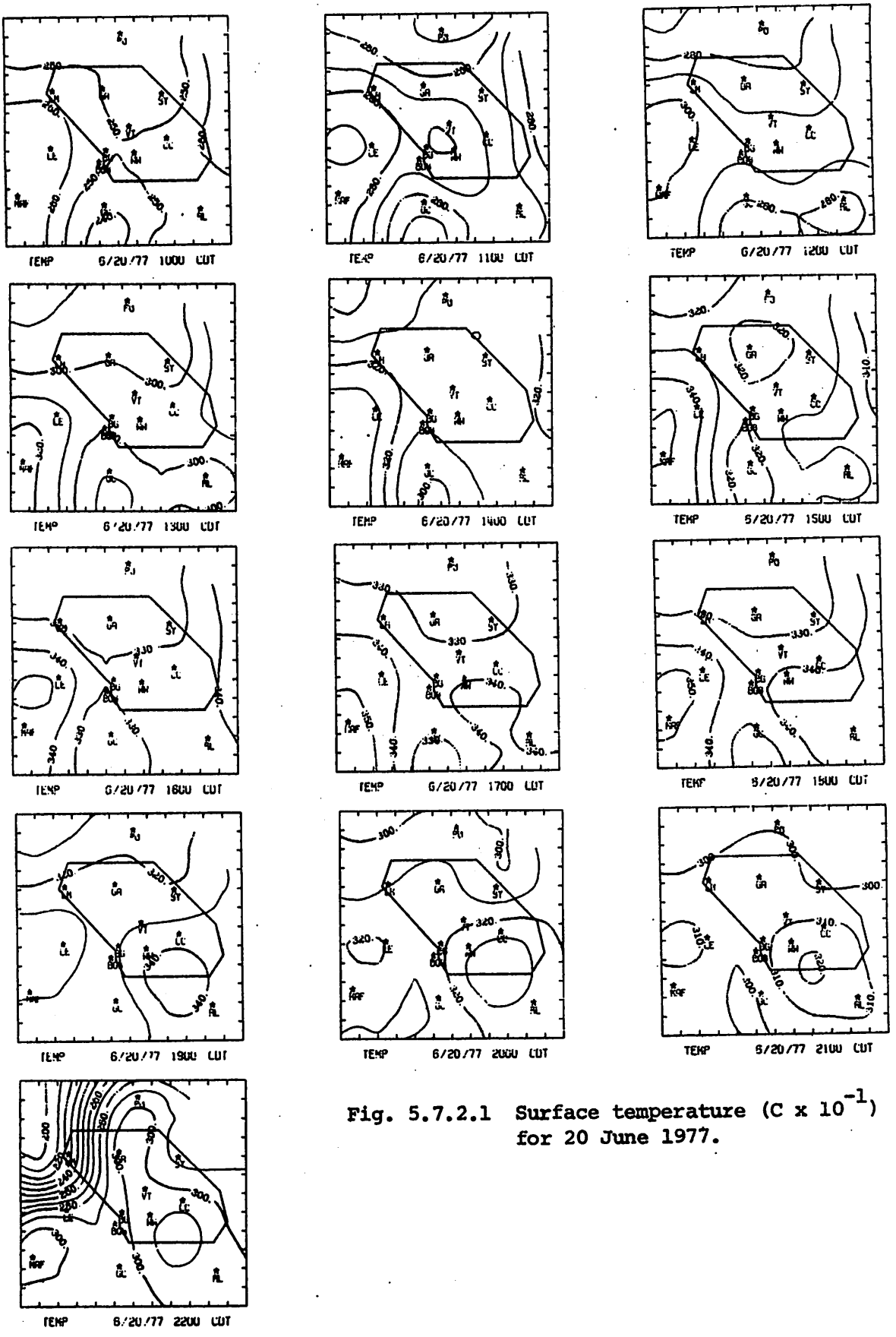

Fig. 5.7.2.1 Surface temperature (C x 10^{-1}) for 20 June 1977.

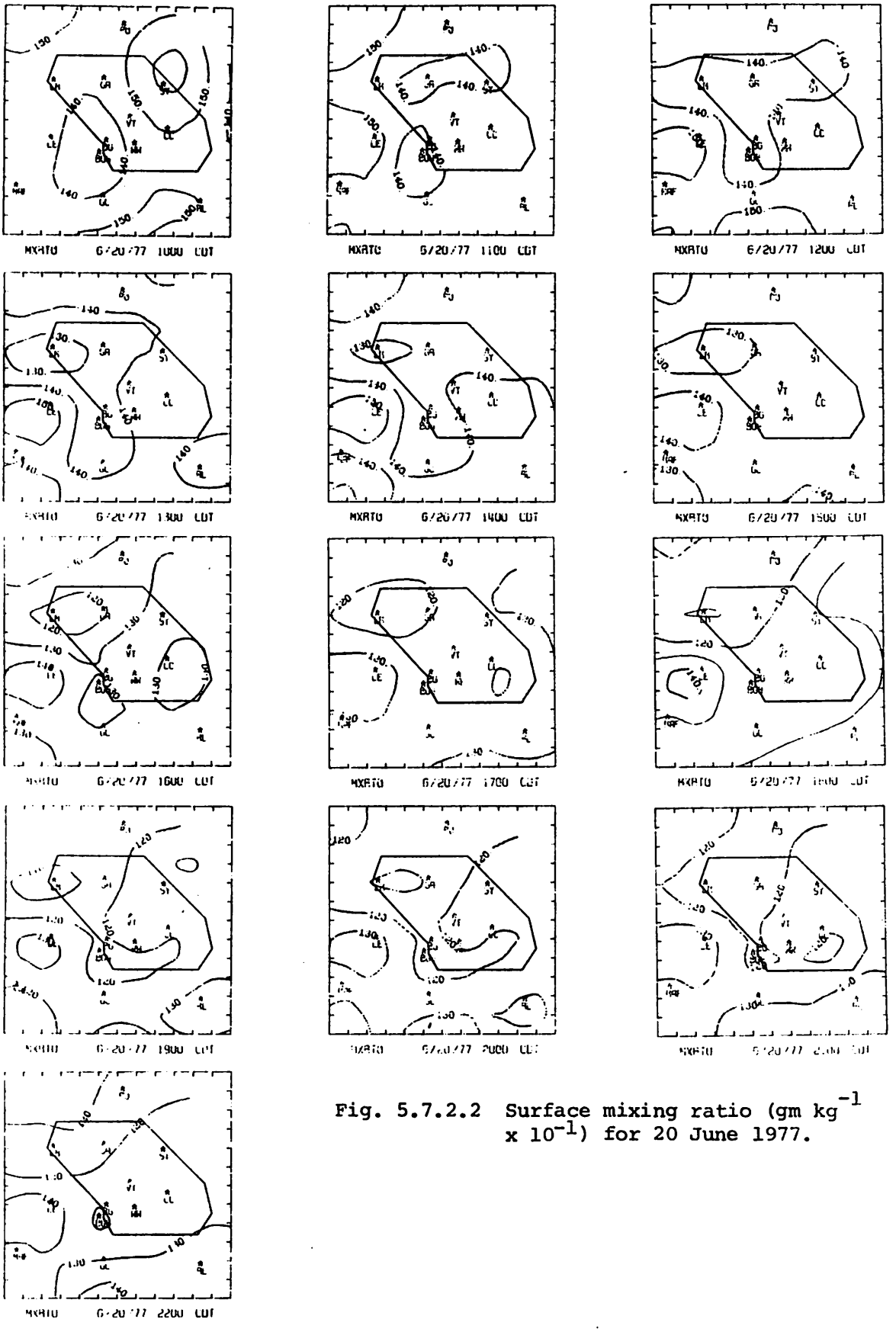

Fig. 5.7.2.2 Surface mixing ratio (gm kg^{-1} x 10^{-1}) for 20 June 1977.

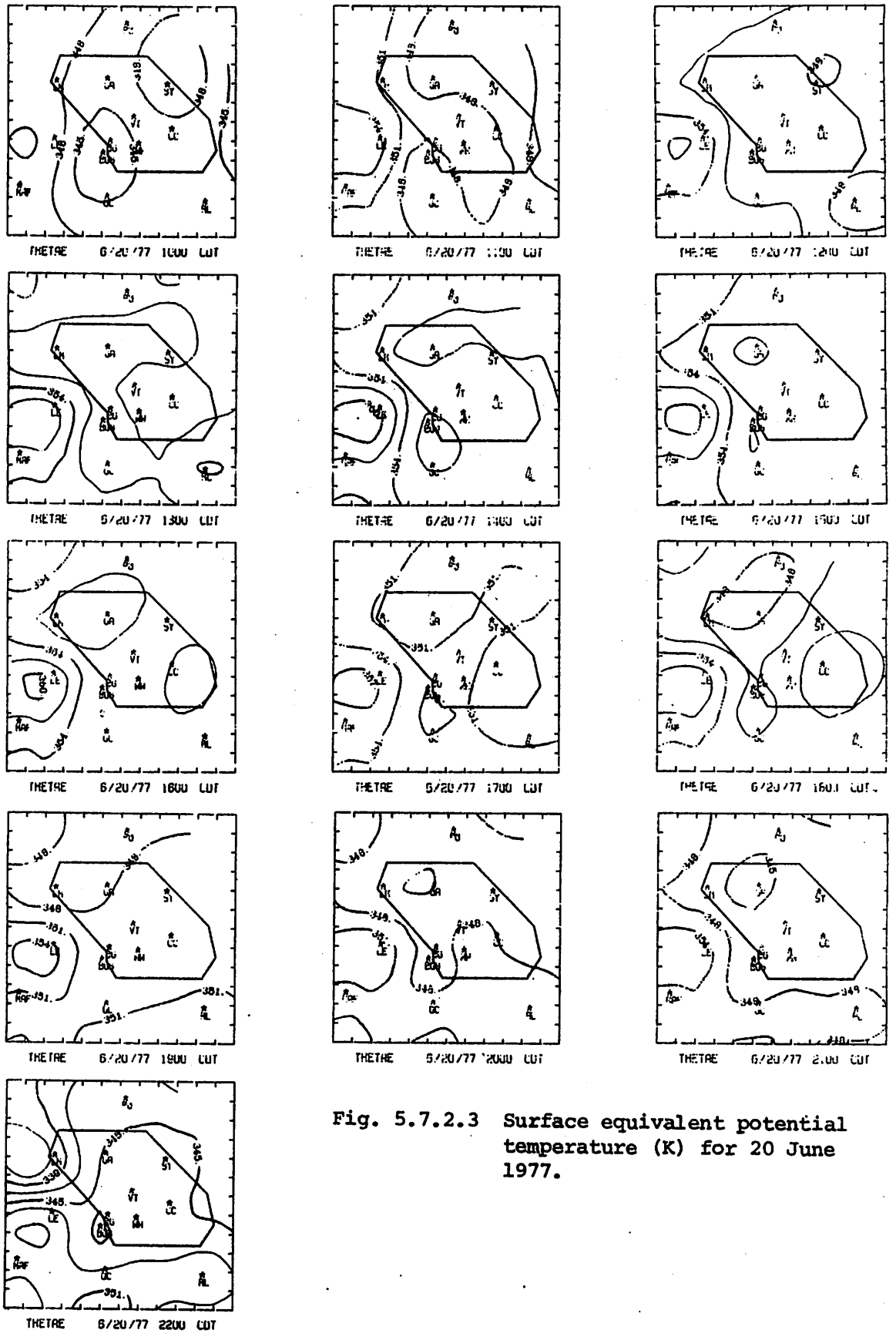

Fig. 5.7.2.3 Surface equivalent potential temperature (K) for 20 June 1977.

little variation prior to 0300 GMT. A decrease in surface equivalent potential temperature observed in areas of convection is due to the surface temperature minimum reflected in Figure 5.7.2.1.

Terrain-induced vertical motion (Fig. 5.7.2.4) shows little temporal change prior to the line at 0300 GMT. Downward motion exceeding 2 cm s^{-1} occurred in areas of strongest convection. Areas of pronounced surface velocity divergence (Fig. 5.7.2.5) occurred prior to the convective activity especially in the eastern regions of the area. Systematic patterns of surface velocity convergence, upward vertical motion 50 mb above the surface (Fig. 5.7.2.6), surface moisture convergence (Fig. 5.7.2.7), and upward vertical flux of moisture 50 mb above the surface (Fig. 5.7.2.8) occurred prior to the convective activity. Cyclonic rotation (Fig. 5.7.2.9) is observed prior to convective activity in eastern regions of the network. These patterns become more pronounced with time, but show no indication of convection until 0300 GMT.

Low sea-level pressure (Fig. 5.7.2.10) is situated over the center of the network with little temporal change prior to convective activity (Fig. 5.7.2.11). Pressure increases are observed preceding the advance of the squall line at 0100 GMT. A large pressure increase occurred over the center of the network at 0100 GMT which cannot be adequately explained by the resolution of the data available.

5.8 21 June 1977

5.8.1 Radar

The radar charts in Figure 5.8.1.1 show an isolated cell at 1600 and 1700 GMT south to southeast of Lamesa. Following these times no echoes were observed until 0100 GMT (data were missing at 2200, 2300, and 0000 GMT). Echoes with several cells exceeding a height of 9.1 km (30K ft) and covering a large fraction of the HIPLEX area were observed at 0100 through 0300 GMT. Two large cells were present, one south of Post at 0200 GMT and the other south of Big Spring at 0300 GMT.

5.8.2 Surface

Temperature fields (Fig. 5.8.2.1) show the temperature gradient associated with lines of echoes (Fig. 5.8.1.1), especially associated with the strong convection. The influence of the isolated cell at 1600 GMT results in a temperature minimum over Big Spring, Vincent, and Snyder. The largest temperature minimum is associated with the area of strongest echoes. The warmest temperature occurs over the southeastern region where

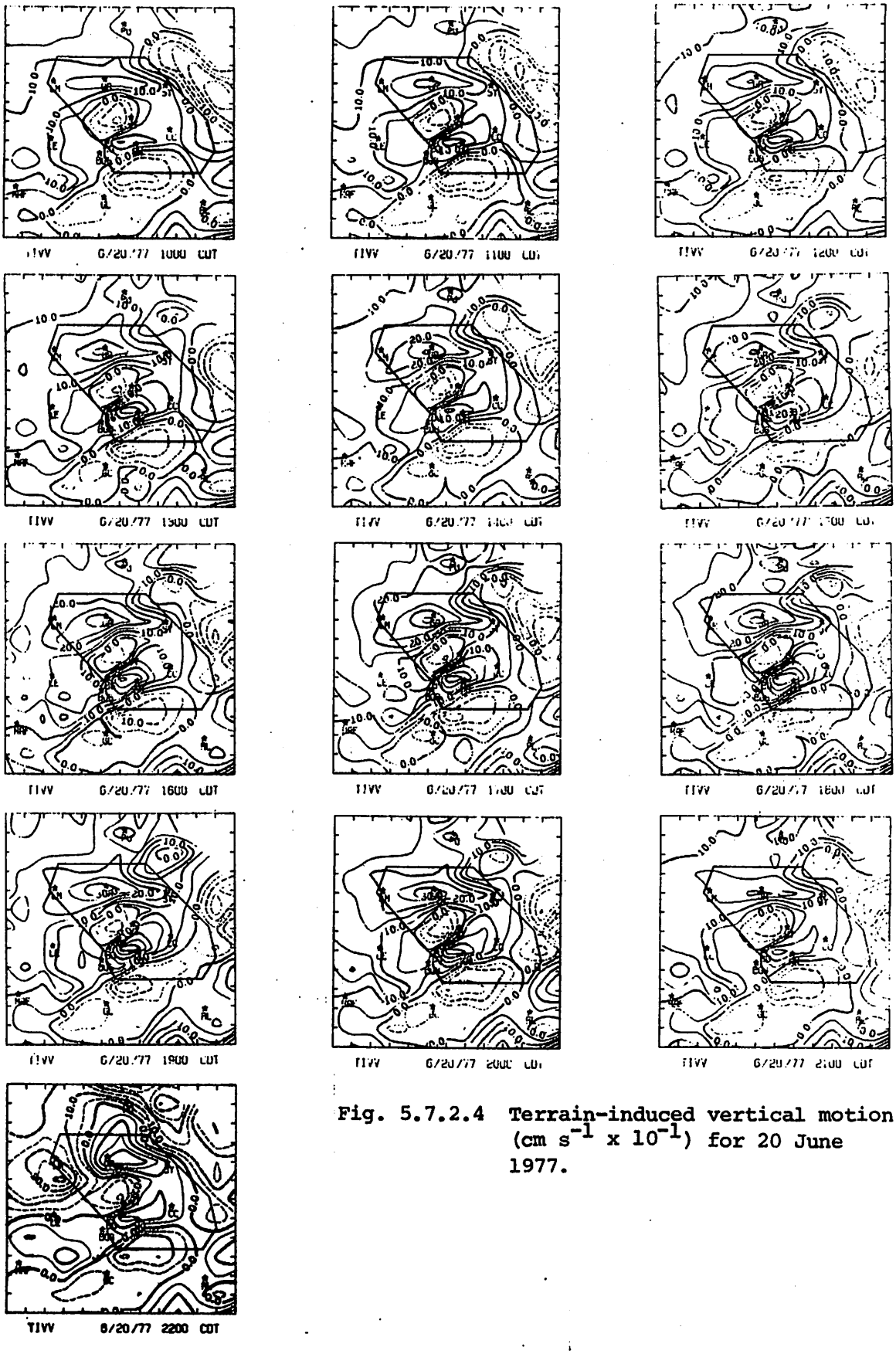

Fig. 5.7.2.4 Terrain-induced vertical motion (cm s^{-1} x 10^{-1}) for 20 June 1977.

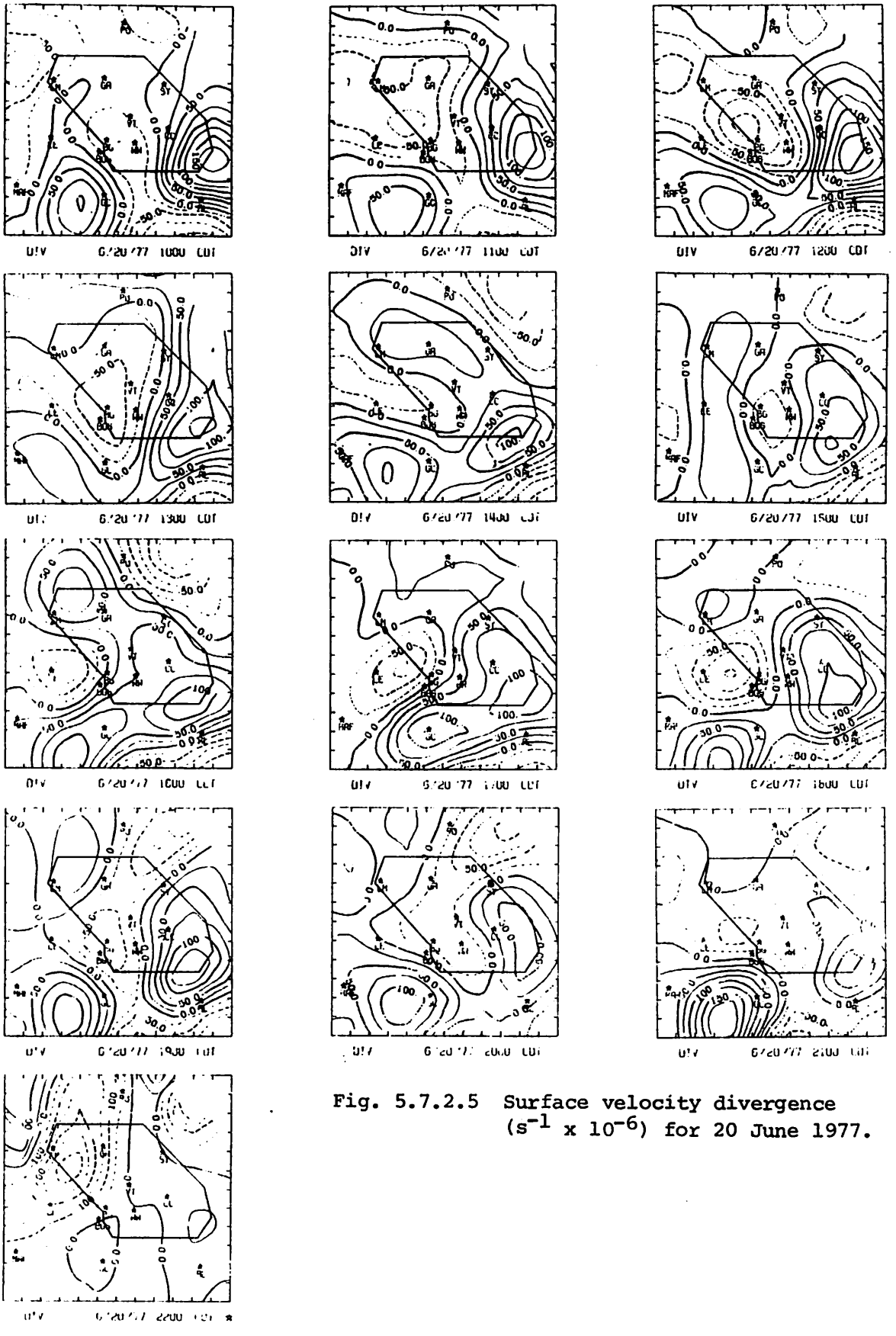

Fig. 5.7.2.5 Surface velocity divergence (s^{-1} x 10^{-6}) for 20 June 1977.

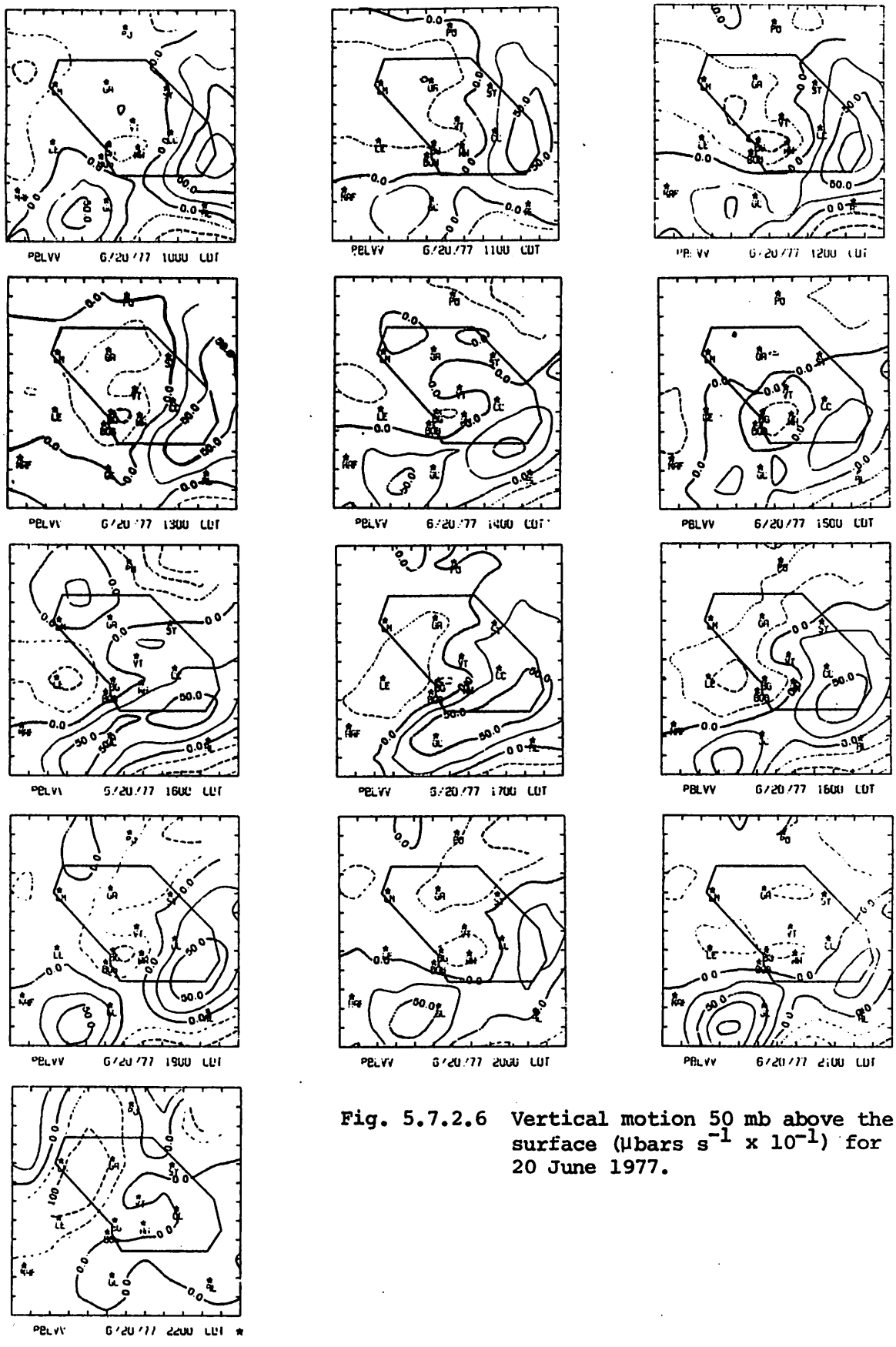

Fig. 5.7.2.6 Vertical motion 50 mb above the surface (μbars s^{-1} x 10^{-1}) for 20 June 1977.

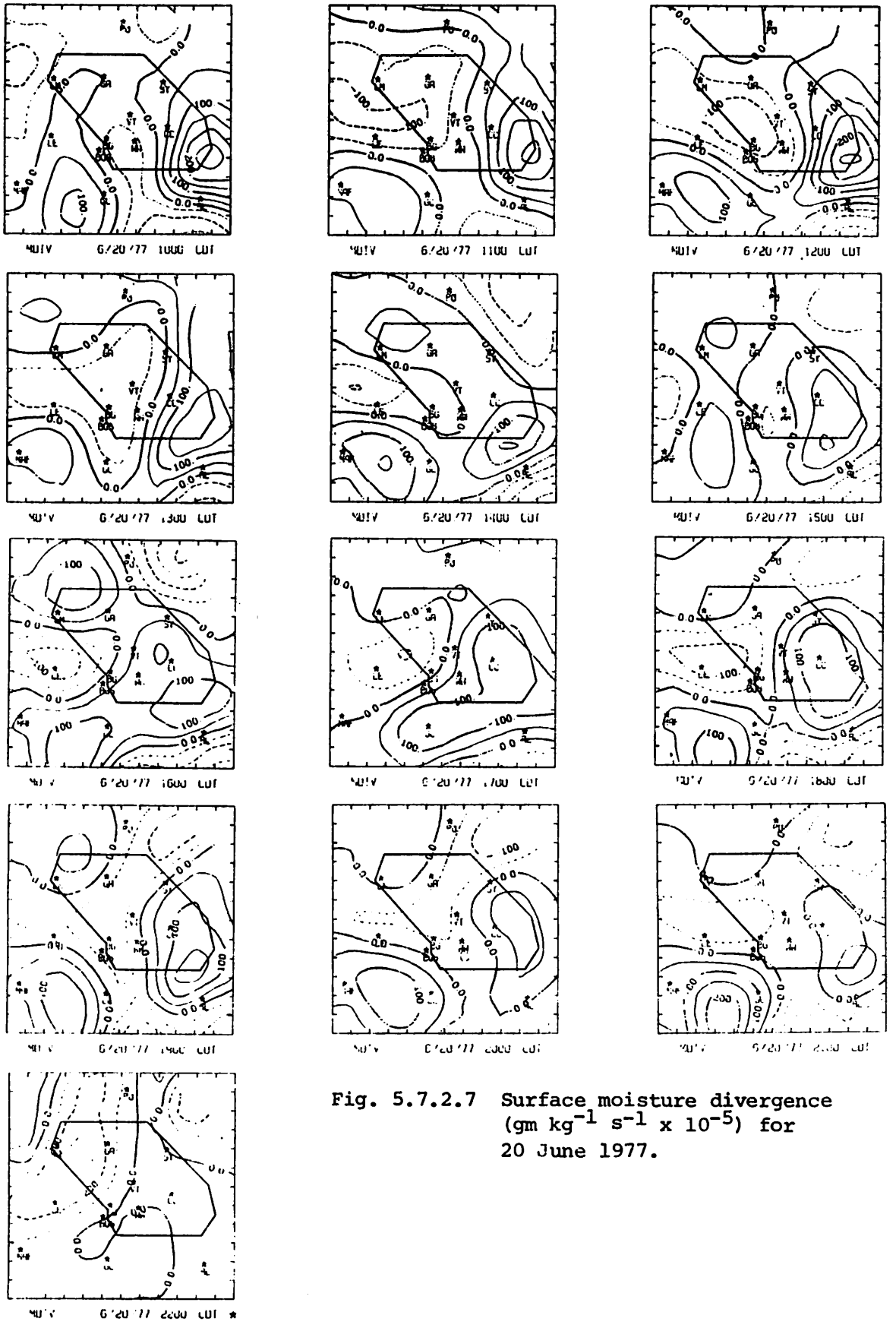

Fig. 5.7.2.7 Surface moisture divergence (gm kg^{-1} s^{-1} x 10^{-5}) for 20 June 1977.

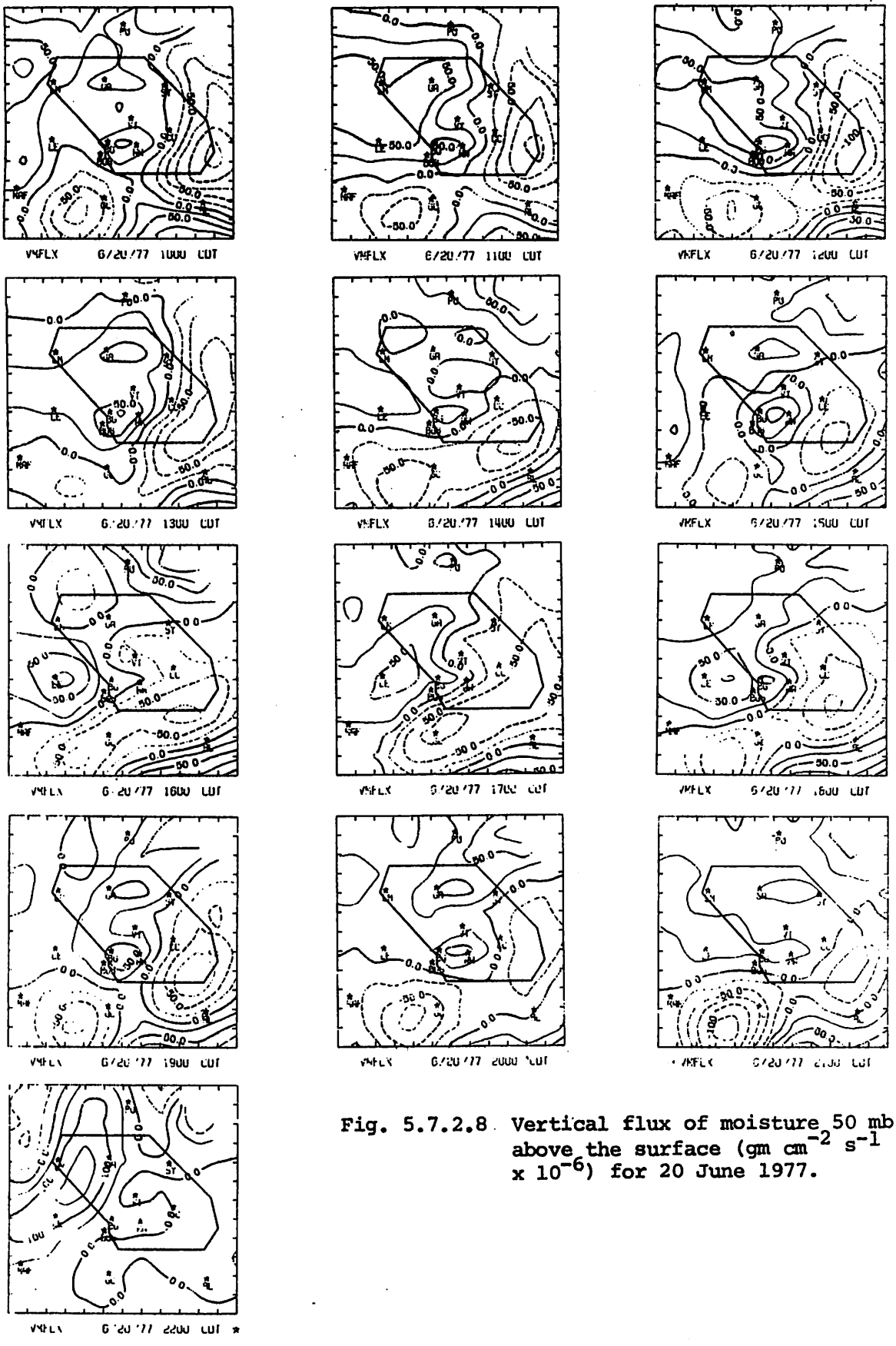

Fig. 5.7.2.8 Vertical flux of moisture 50 mb above the surface (gm cm^{-2} s^{-1} x 10^{-6}) for 20 June 1977.

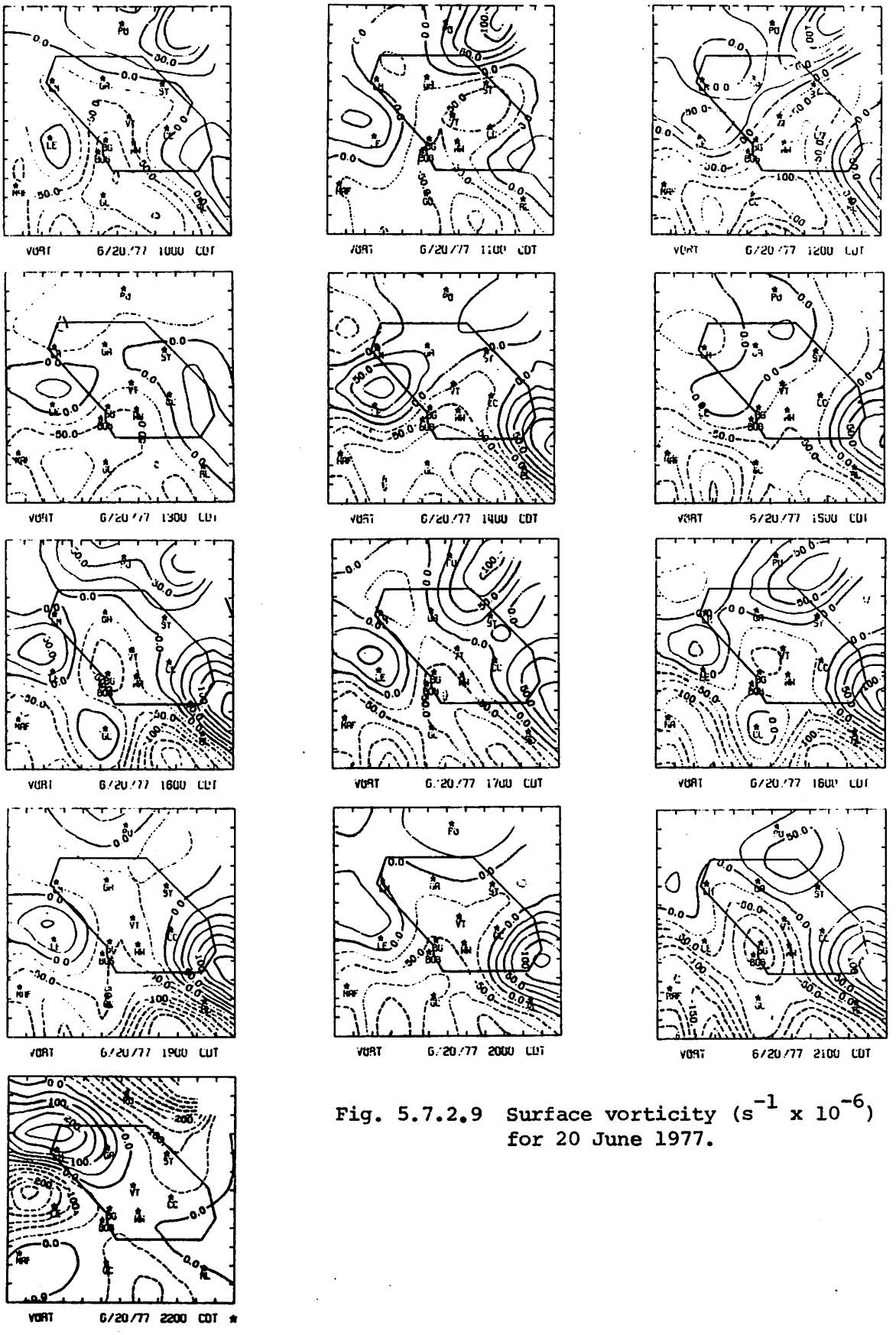

Fig. 5.7.2.9 Surface vorticity (s^{-1} x 10^{-6}) for 20 June 1977.

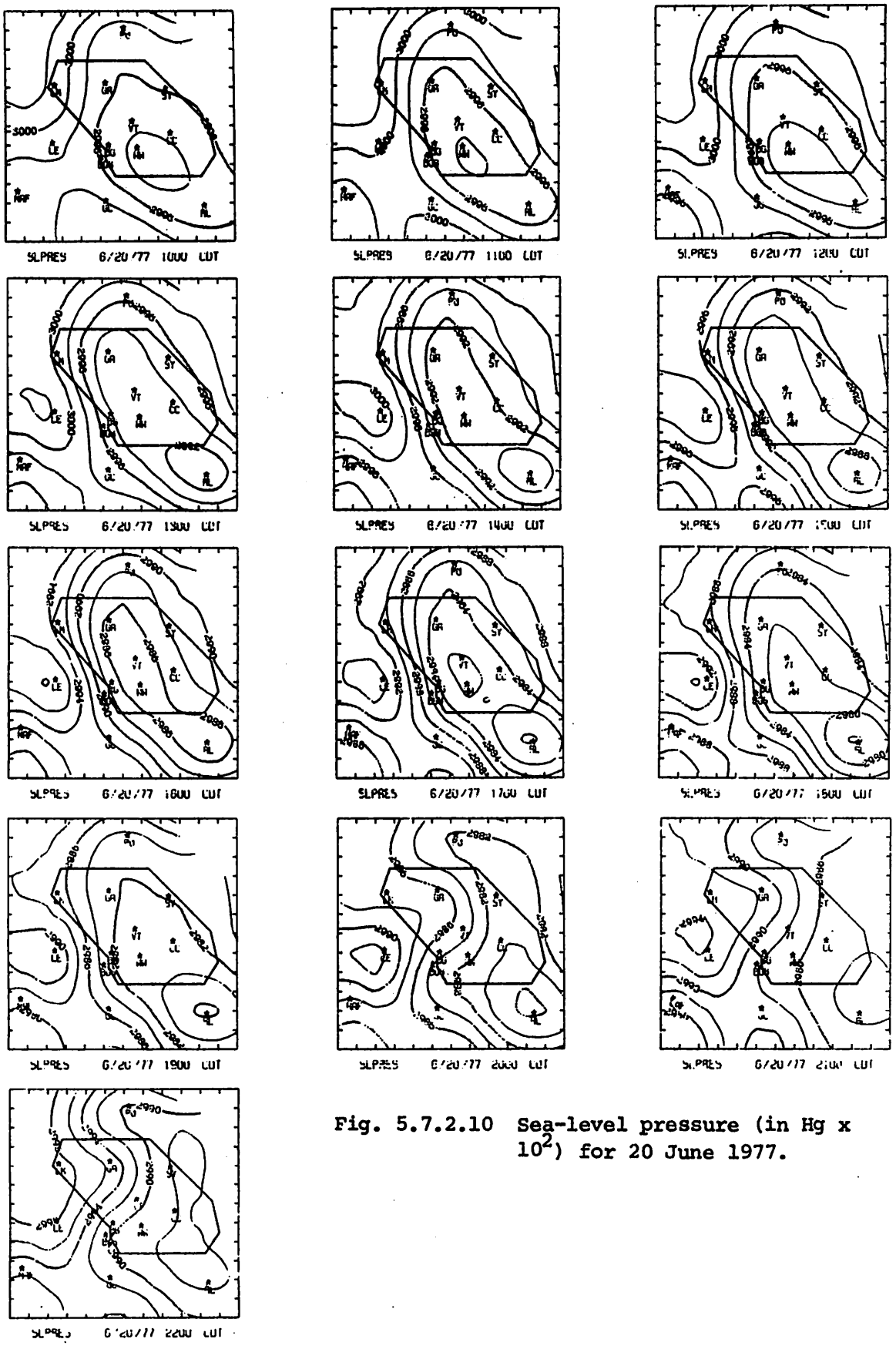

Fig. 5.7.2.10 Sea-level pressure (in Hg x 10^2) for 20 June 1977.

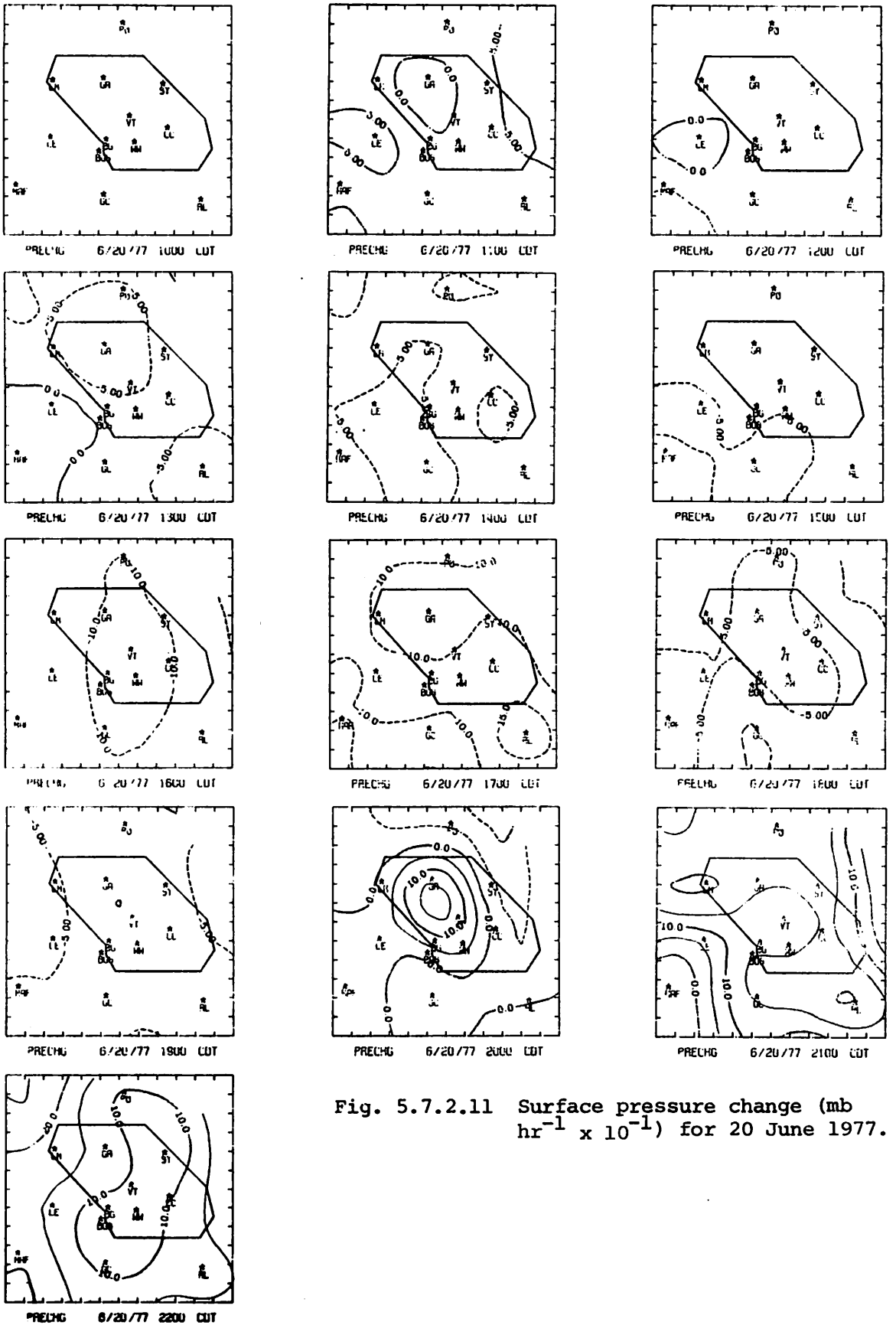

Fig. 5.7.2.11 Surface pressure change (mb hr^{-1} x 10^{-1}) for 20 June 1977.

NO ECHOES

RADAR 6/21/77 1000 CDT

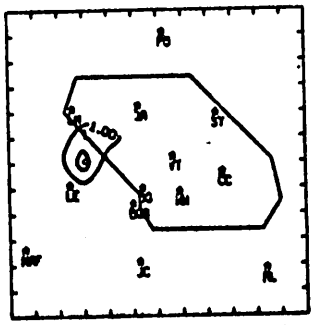

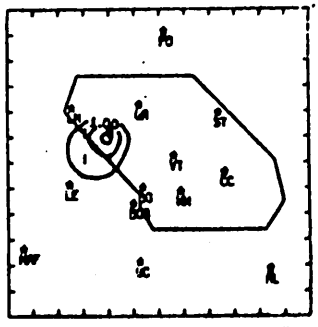

NO ECHOES

RADAR 6/21/77 1300 CDT

NO ECHOES

RADAR 6/21/77 1400 CDT

NO ECHOES

RADAR 6/21/77 1500 CDT

NO ECHOES

RADAR 6/21/77 1600 CDT

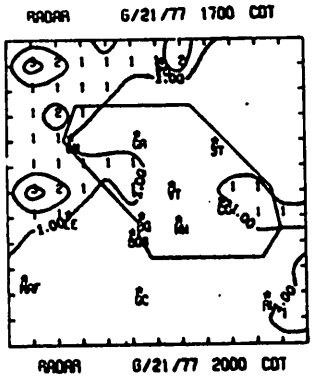

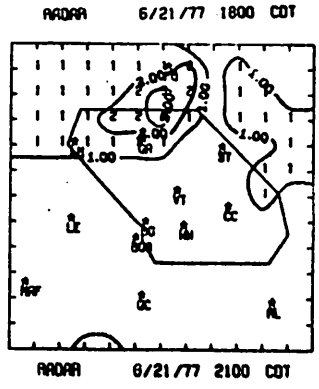

NO ECHOES

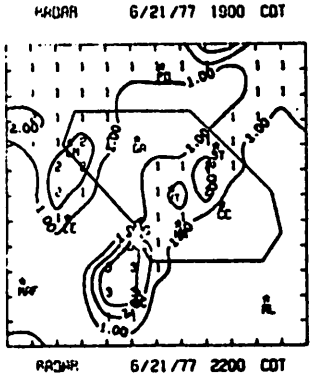

Fig. 5.8.1.1 Radar echoes for 21 June 1977.

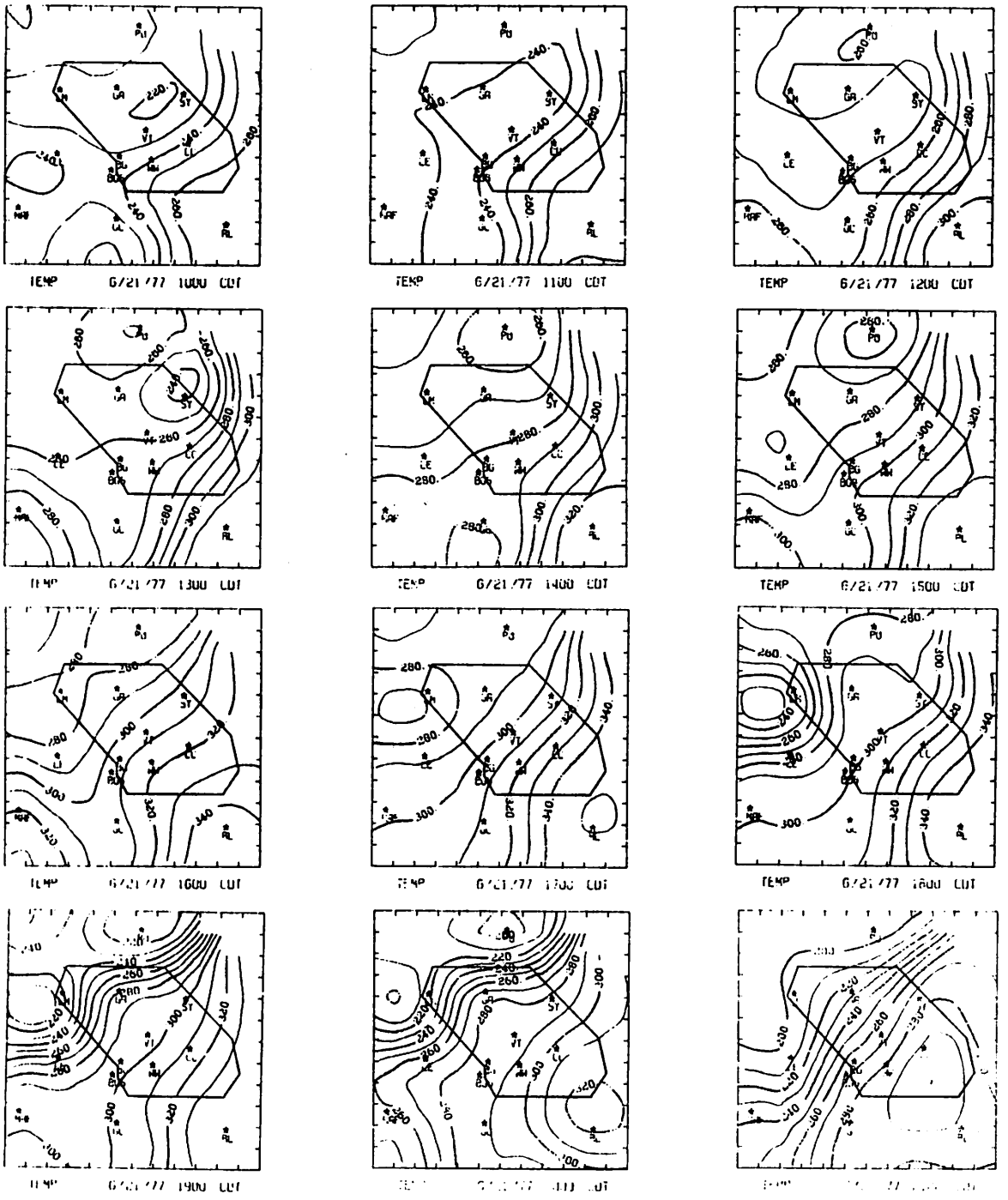

Fig. 5.8.2.1 Surface temperature (C x 10^{-1}) for 21 June 1977.

cloud coverage is a minimum throughout the day. Values of surface mixing ratio (Fig. 5.8.2.2) remain high throughout the day with organized patterns associated with convective activity especially at 0300 GMT. These patterns are associated with fields of surface equivalent potential temperature (Fig. 5.8.2.3) especially in areas of temperature minima.

The magnitude of terrain-induced vertical motion (Fig. 5.8.2.4) decreased with time due to lower windspeeds observed following 0100 GMT so that small contributions of terrain-induced vertical motion are made to the kinematic vertical velocity during strong convection. Strong centers of surface velocity convergence (Fig. 5.8.2.5) were associated with the lines of echoes. The area of strongest convergence was associated with the strongest echo. Large values of upward vertical motion 50 mb above the surface (Fig. 5.8.2.6) were also associated with this line, but show negligible vertical motion prior to the convective activity.

Centers with large magnitudes of surface moisture convergence (Fig. 5.8.2.7) and upward vertical flux of moisture 50 mb above the surface (Fig. 5.8.2.8) occurred in areas preceding the strongest echoes. Surface vorticity maps (Fig. 5.8.2.9) show areas of strong cyclonic rotation in the vicinity of strong echoes. A region of anticyclonic rotation occurred in the southern region of the network throughout the day.

Sea level pressure (Fig. 5.8.2.10) generally decreases to the east, and shows little variation with time until the squall lines approached (Fig. 5.8.2.11). An increase in surface pressure at 2300 GMT and a subsequent decrease near Gail at 0000 GMT are due to missing data at Gail. Increases of surface pressure at 0100 through 0300 GMT resulted from the cold downdraft (Fig. 5.8.2.1).

5.8.3 Upper-Level Kinematic Parameters

Horizontal mass convergence was present below 800 mb both before and after 1930 GMT when mass divergence occurred (Fig. 5.8.3.1). This pattern corresponds well with dissipation of moderate thunderstorm activity before 1930 GMT and regeneration of more intense activity before 0000 GMT. Mass divergence generally occurred at all times and levels above 600 mb. Time variations in the vertical velocity profiles (Fig. 5.8.3.2) reveal upward vertical velocities below 500 mb before 1930 GMT, downward motion between 1930 and 2100 GMT, and upward motion again at 0000 GMT, a

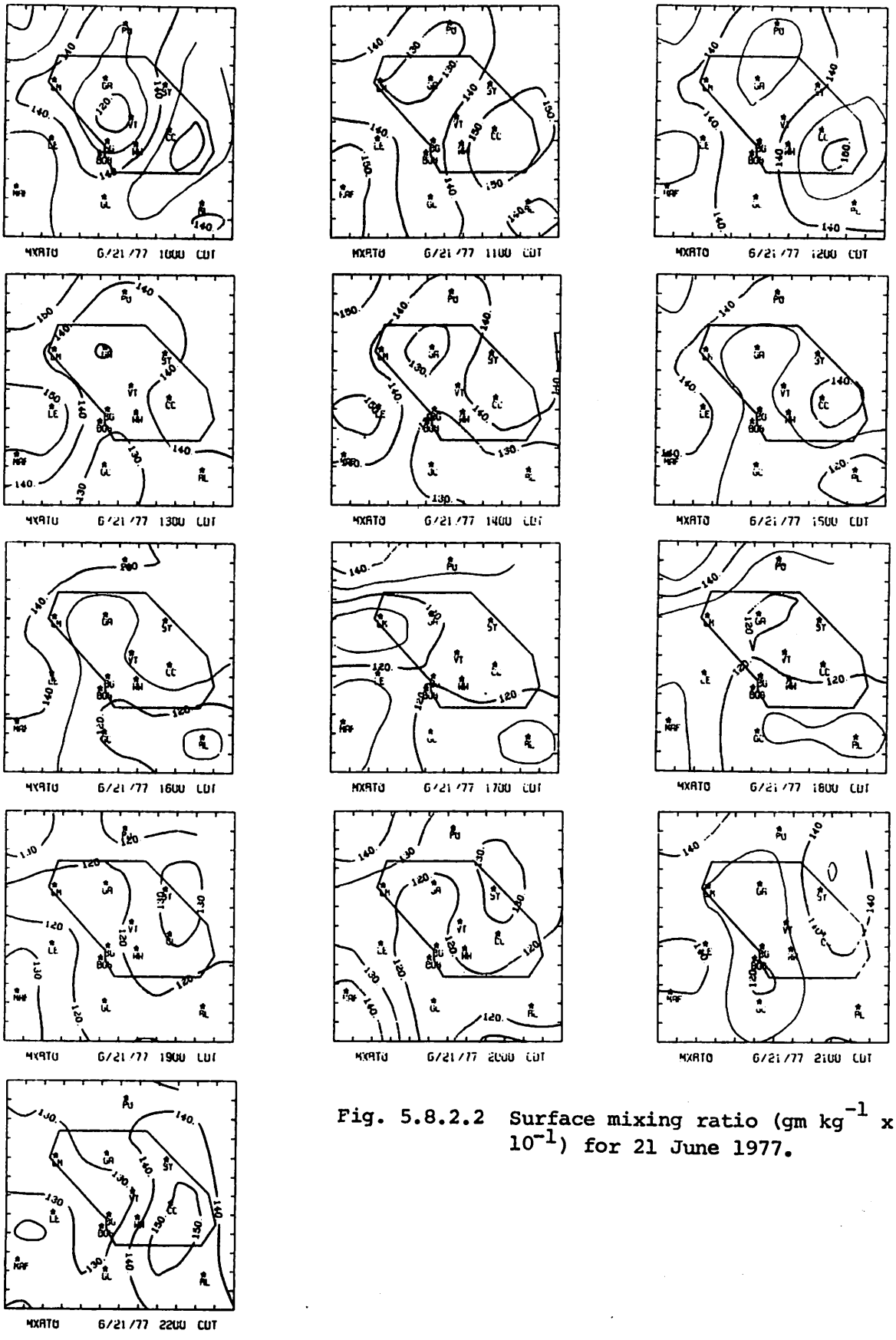

Fig. 5.8.2.2 Surface mixing ratio (gm kg^{-1} x 10^{-1}) for 21 June 1977.

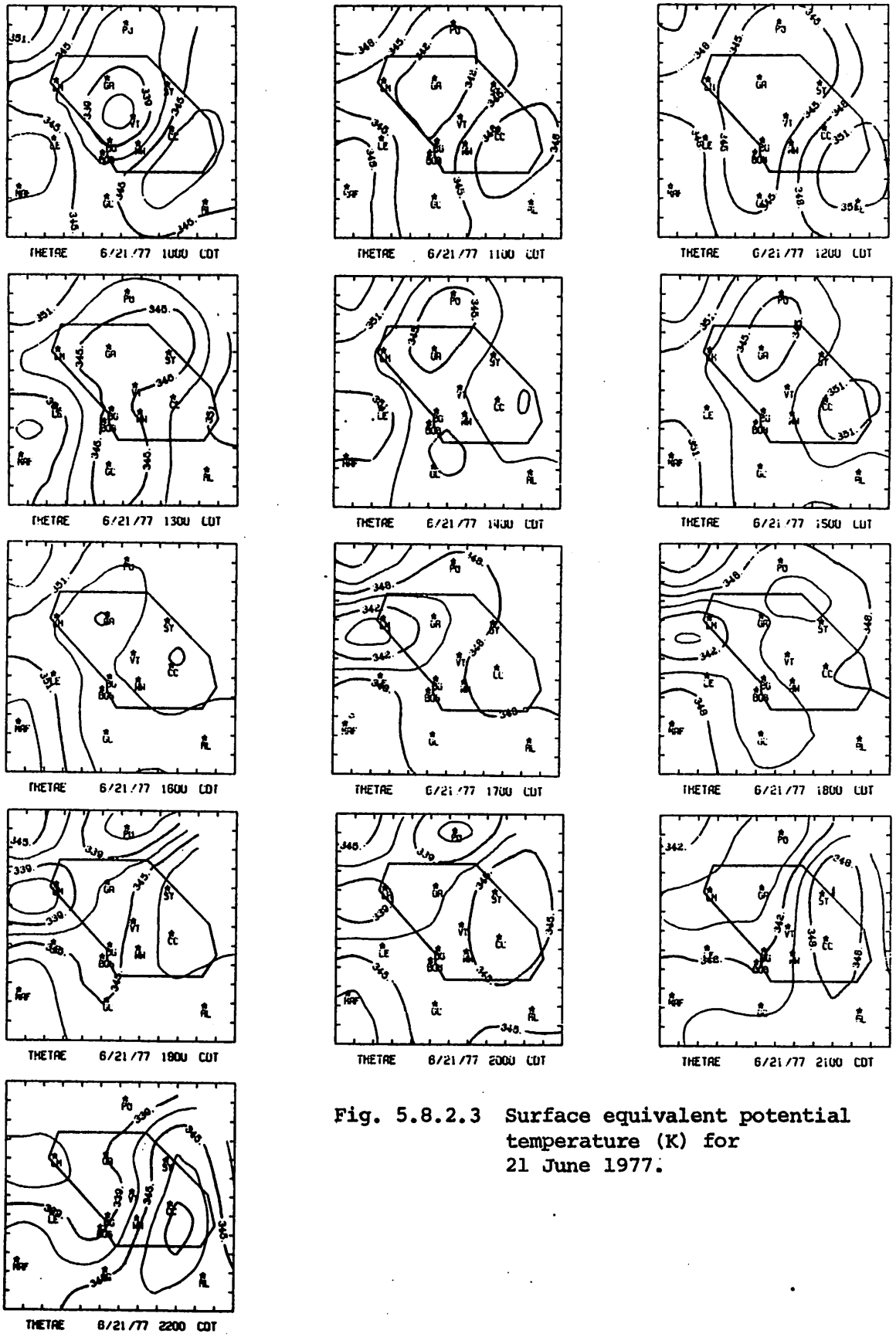

Fig. 5.8.2.3 Surface equivalent potential temperature (K) for 21 June 1977.

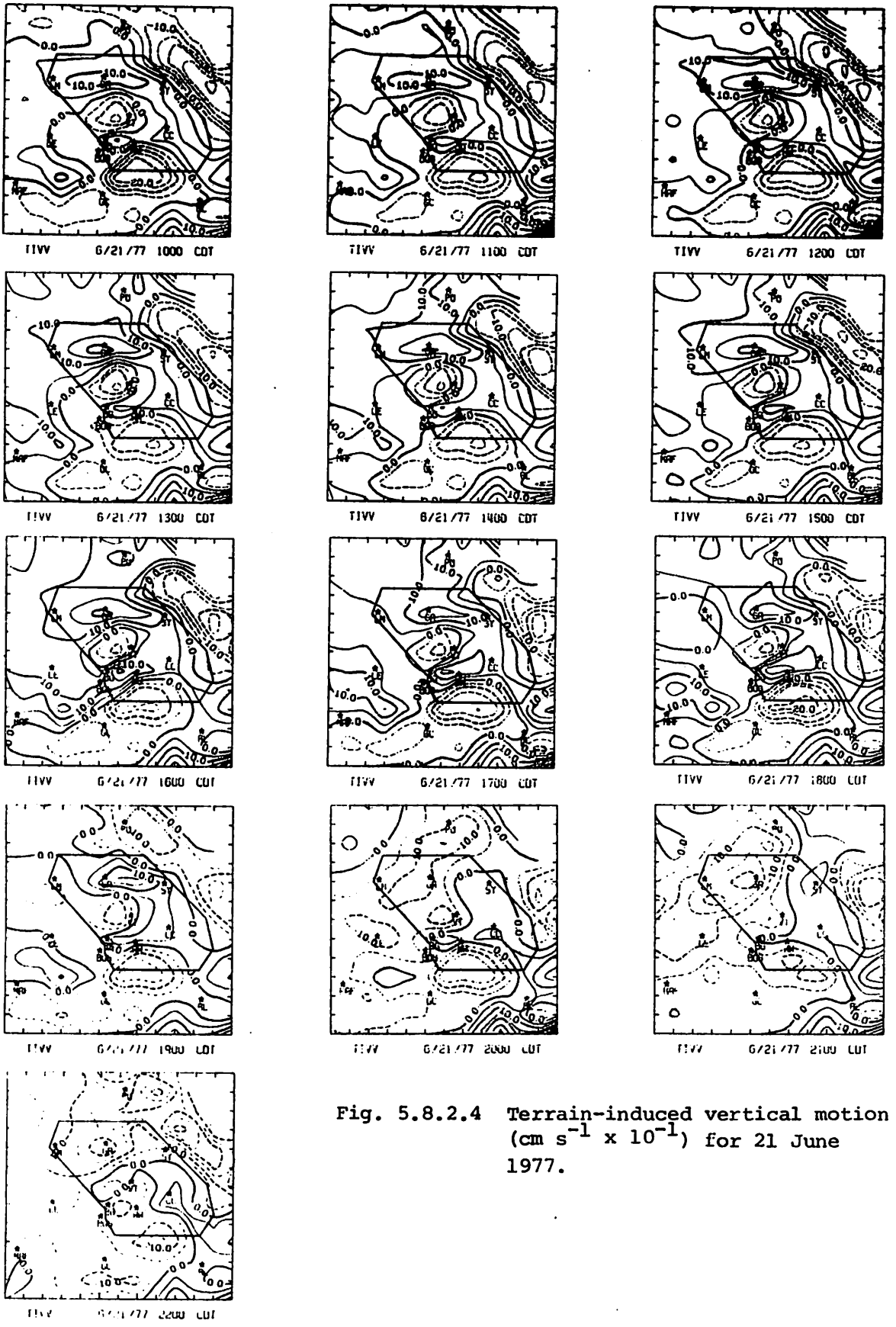

Fig. 5.8.2.4 Terrain-induced vertical motion (cm s^{-1} x 10^{-1}) for 21 June 1977.

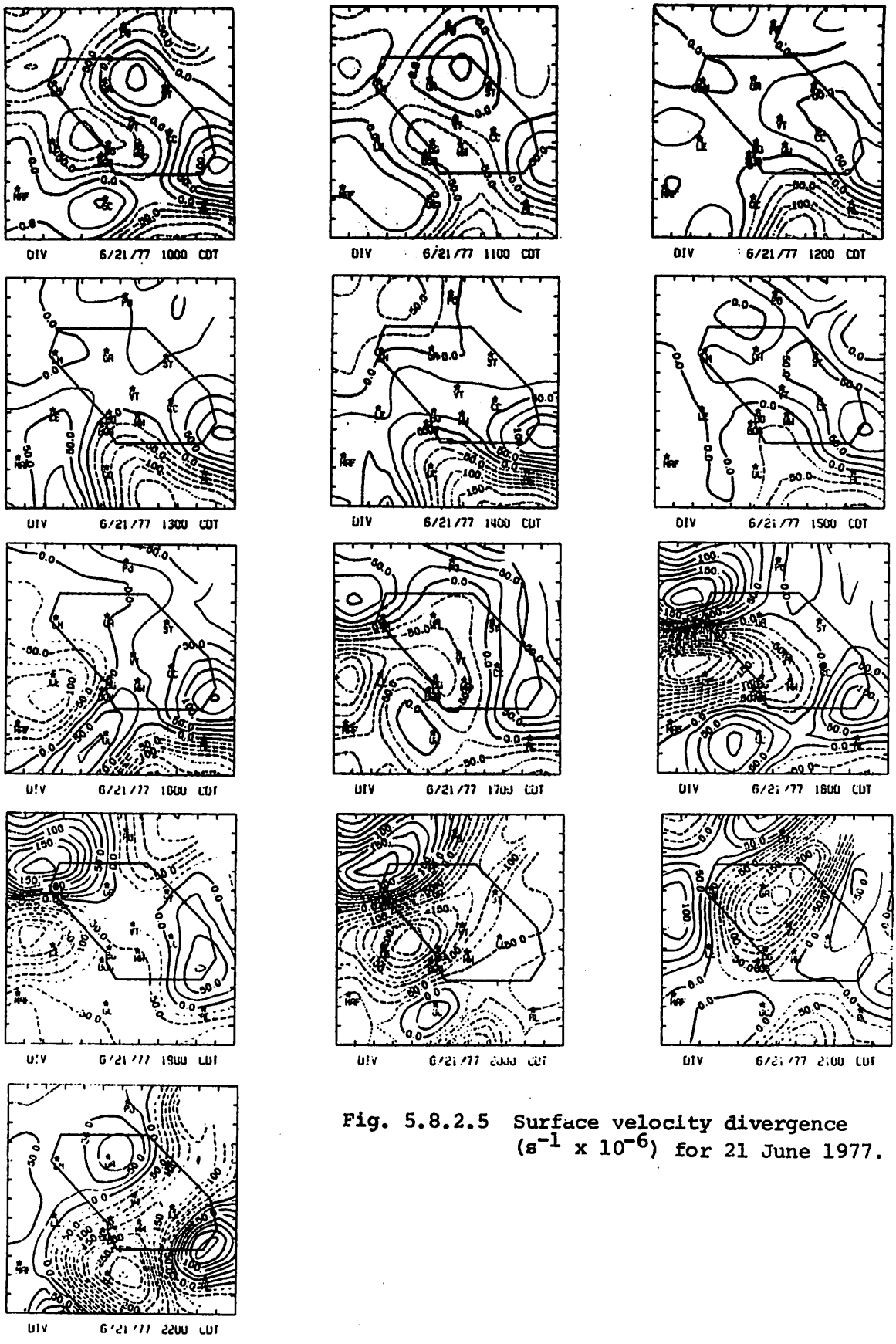

Fig. 5.8.2.5 Surface velocity divergence (s^{-1} x 10^{-6}) for 21 June 1977.

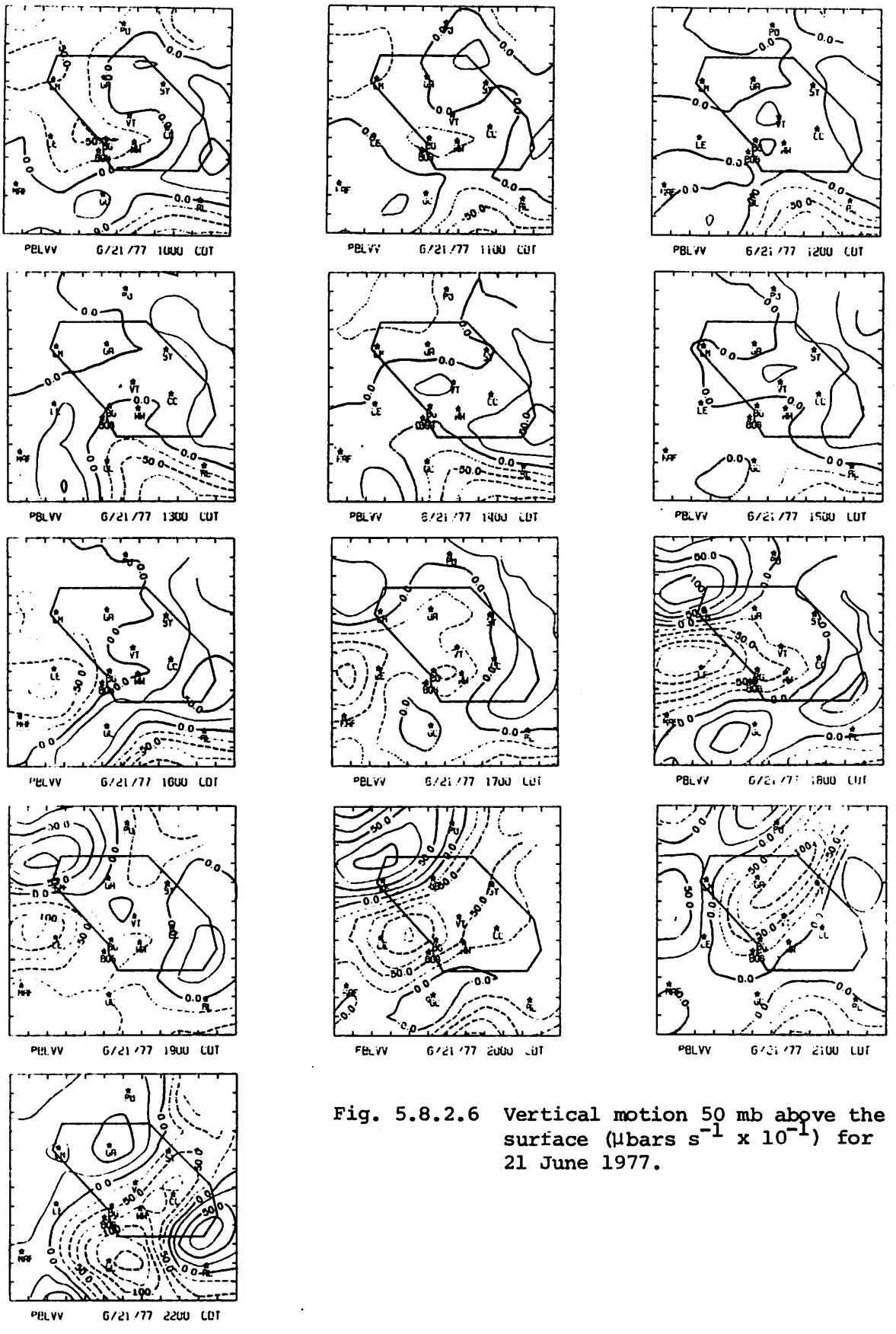

Fig. 5.8.2.6 Vertical motion 50 mb above the surface (μbars s^{-1} x 10^{-1}) for 21 June 1977.

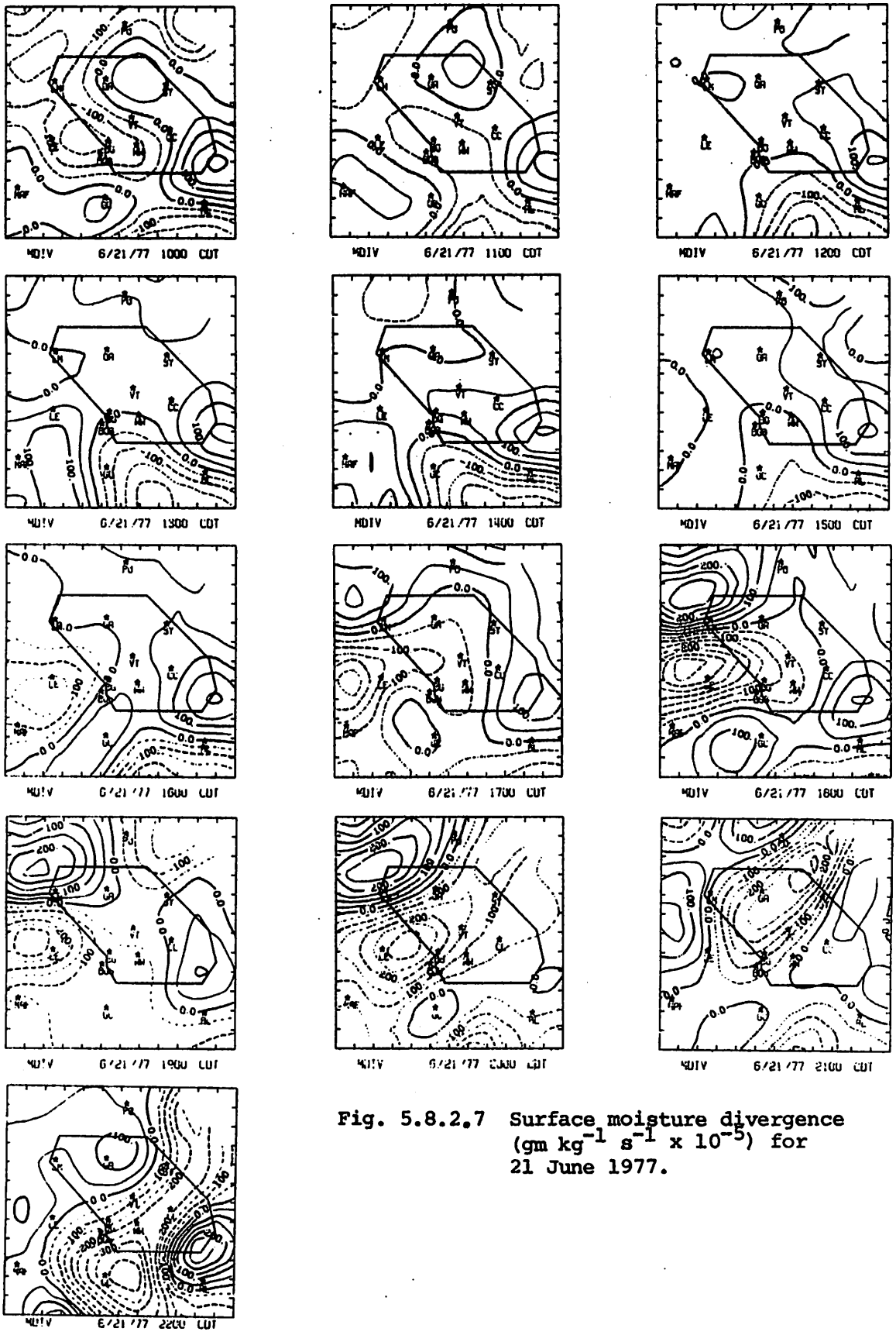

Fig. 5.8.2.7 Surface moisture divergence (gm kg^{-1} s^{-1} x 10^{-5}) for 21 June 1977.

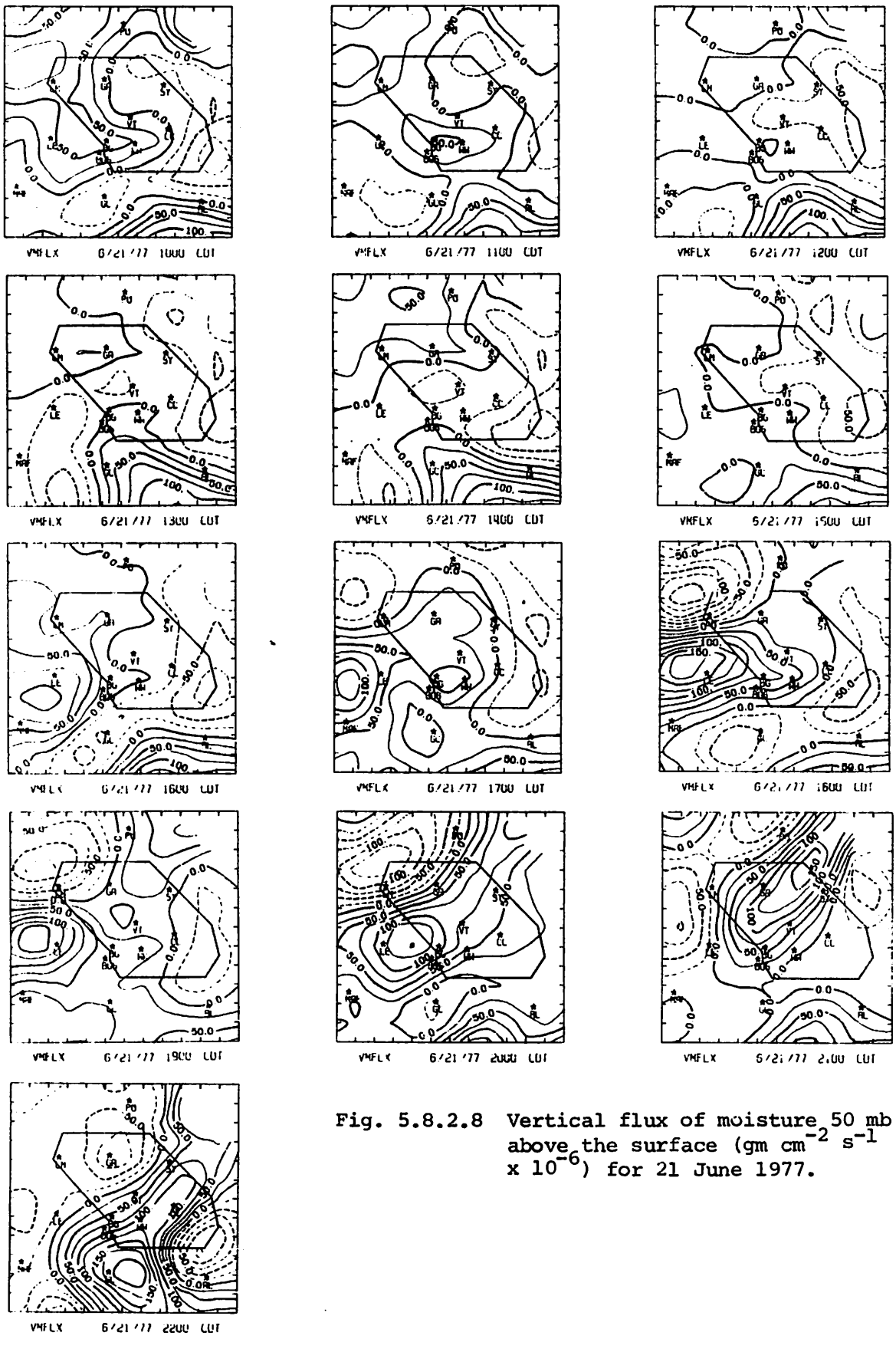

Fig. 5.8.2.8 Vertical flux of moisture 50 mb above the surface (gm cm^{-2} s^{-1} x 10^{-6}) for 21 June 1977.

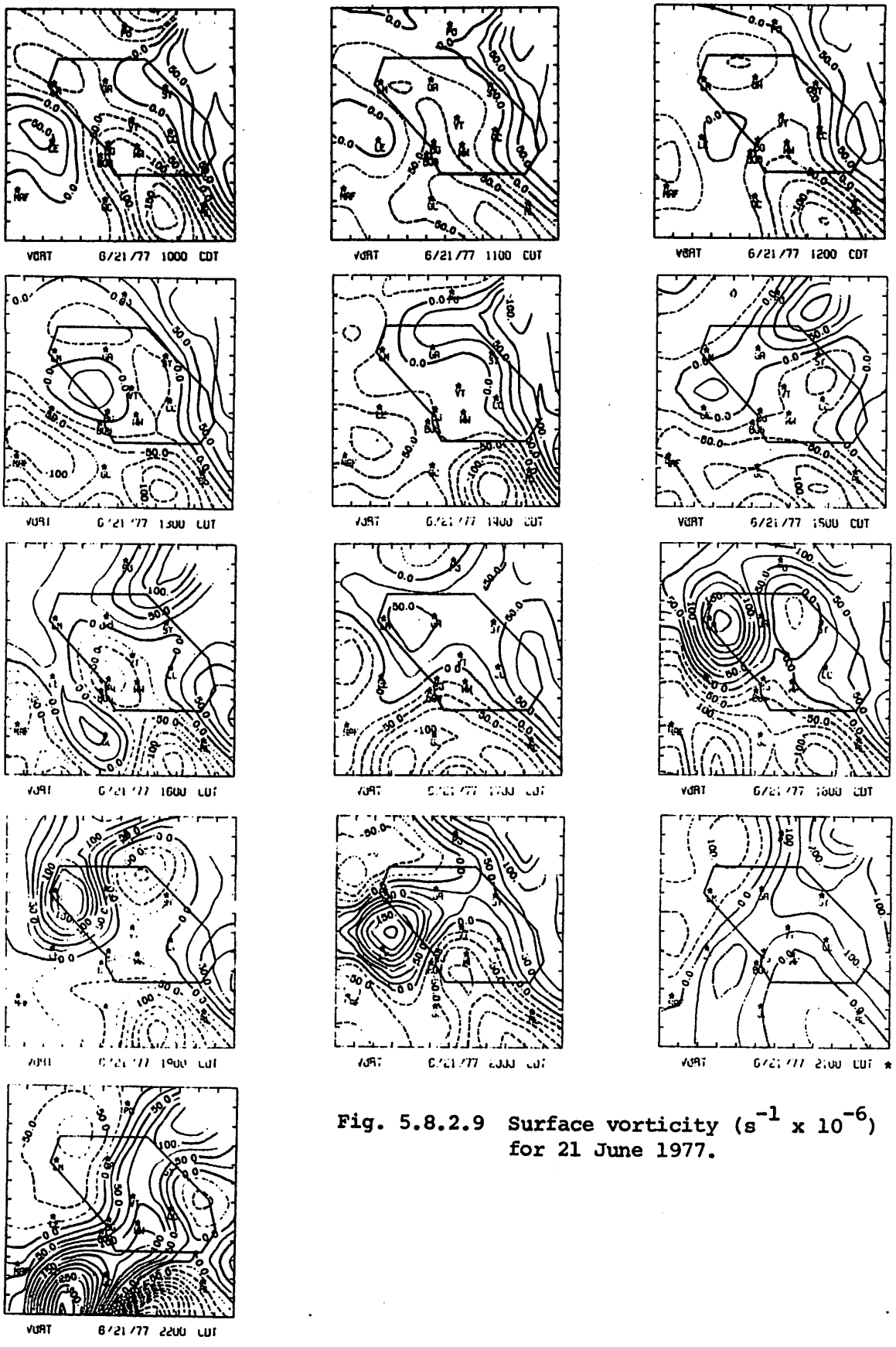

Fig. 5.8.2.9 Surface vorticity (s^{-1} x 10^{-6}) for 21 June 1977.

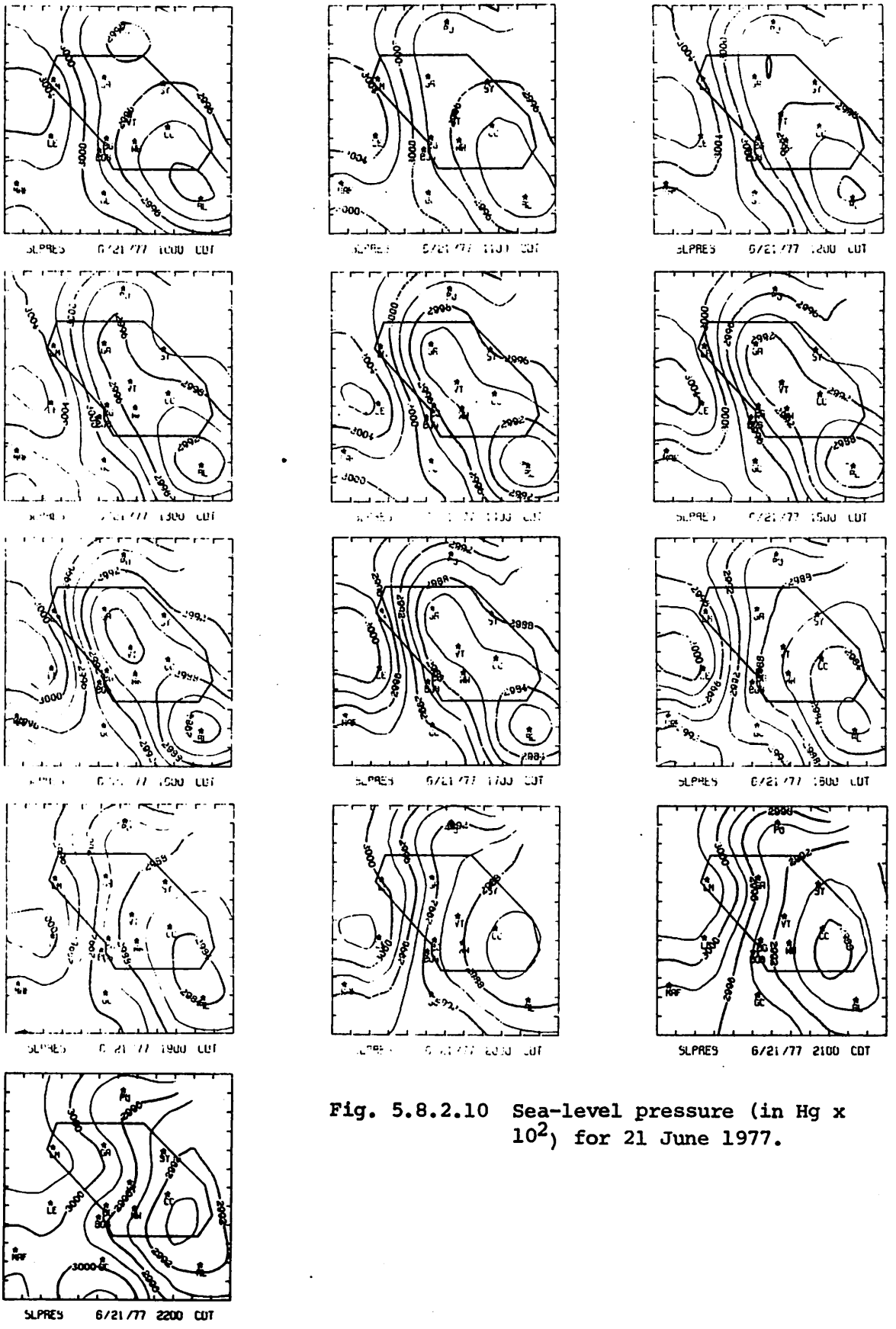

Fig. 5.8.2.10 Sea-level pressure (in Hg x 10^2) for 21 June 1977.

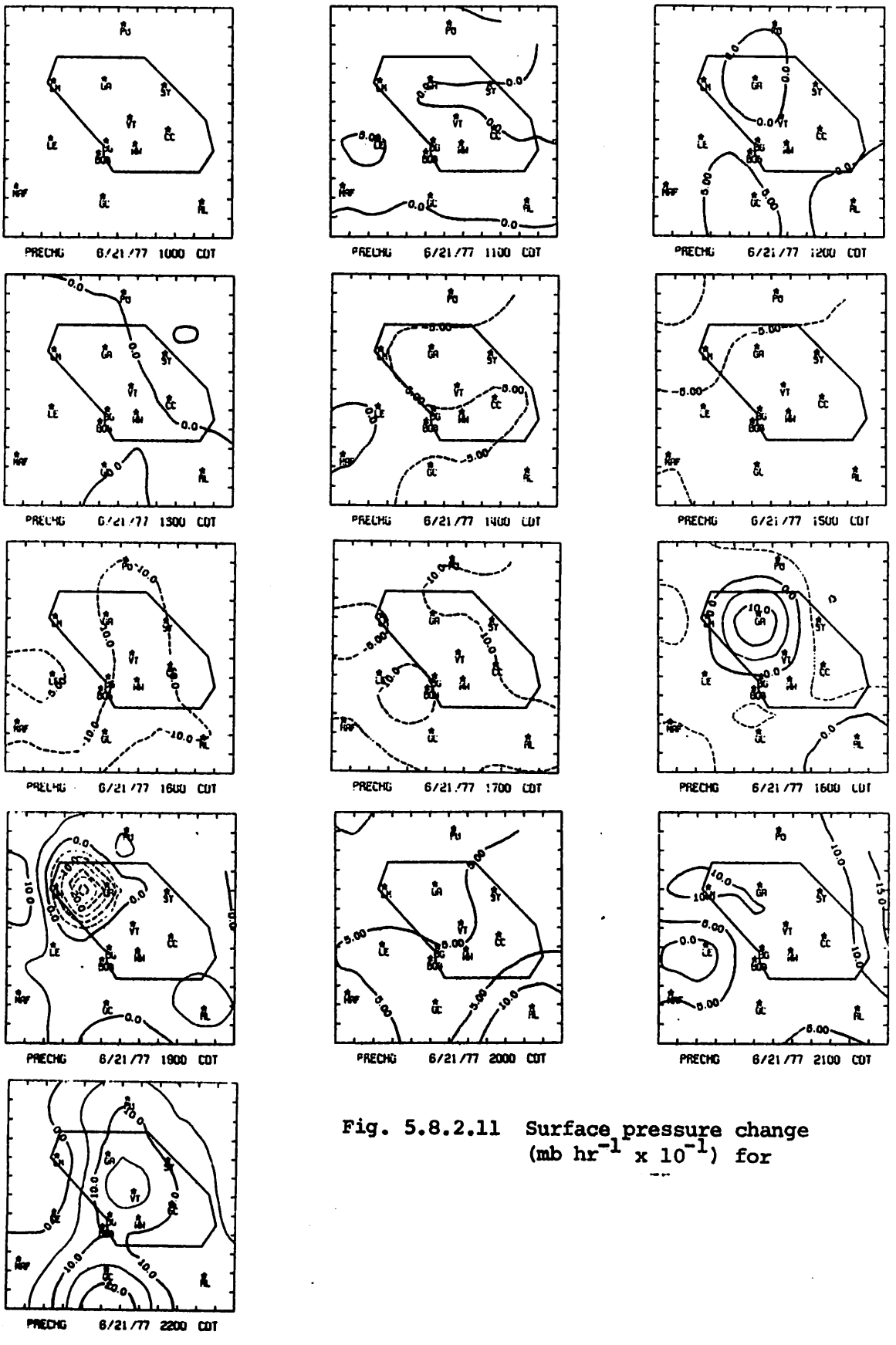

Fig. 5.8.2.11 Surface pressure change (mb hr^{-1} x 10^{-1}) for

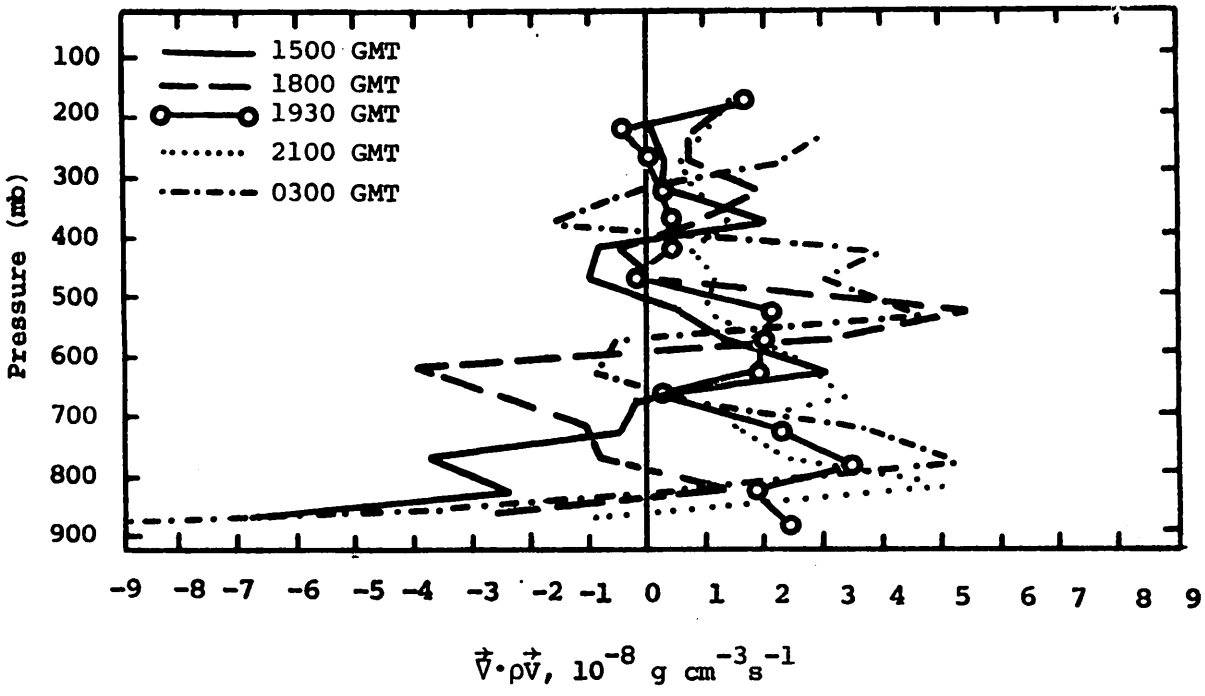

Fig. 5.8.3.1 Vertical profiles of mass divergence on 21 June 1977.

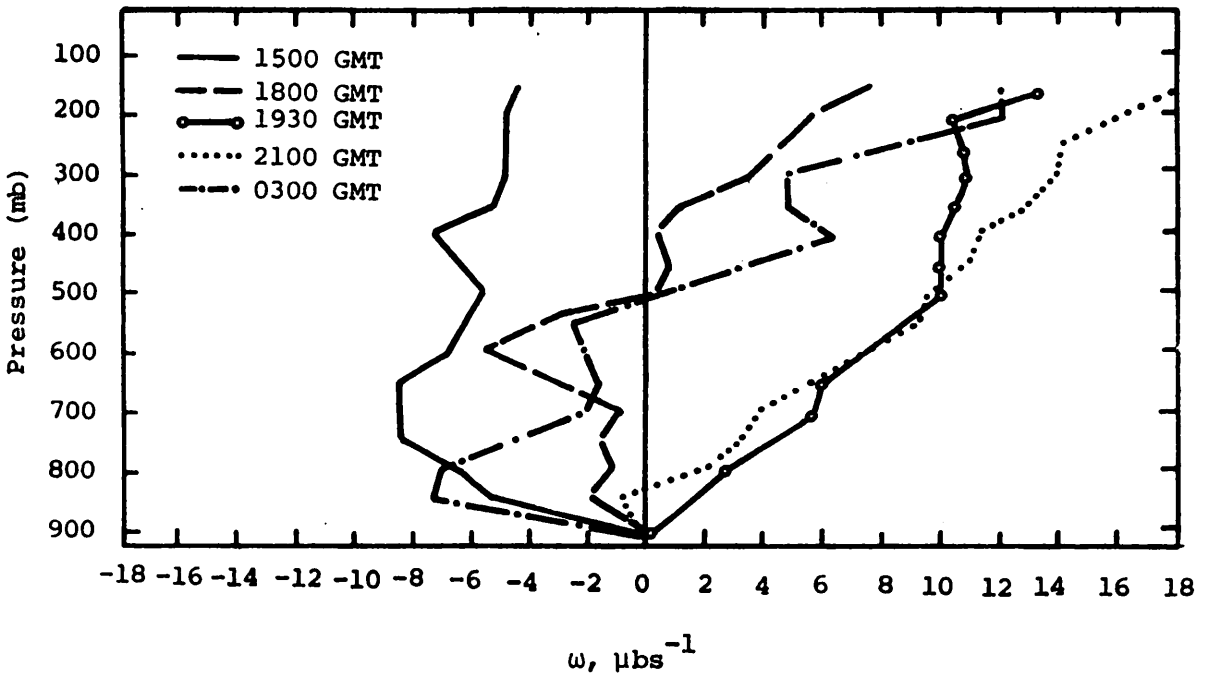

Fig. 5.8.3.2 Vertical profiles of vertical motion on 21 June 1977.

pattern that follows nicely the observed precipitation activity. Below 700 mb horizontal moisture convergence (Fig. 5.8.3.3) changes to divergence after 1800 GMT and returns to convergence again at 0000 GMT, again following precipitation development and dissipation as expected.

5.8.4 Energetics

The horizontal flux divergence profiles of latent heat energy (Fig. 5.8.4.1) show a rapid reversal from net inflow to outflow in lower layers between 1800 and 1930 GMT when activity dissipated. Vertical flux divergence of latent heat in lower layers before 1930 GMT changes to convergence at 1930 GMT as the net upward transport of latent heat changes to a downward transport with storm dissipation and subsidence at 1930 GMT (Fig. 5.8.4.2). Local changes of latent heat energy (Fig. 5.8.4.3) are generally small except at 1930 GMT when large positive values are likely associated with evaporation of clouds and precipitation when the activity dissipated.

The residual profiles of the latent heat budget (Fig. 5.8.4.4) show positive -R values switching to negative values between 1500 and 1930 GMT. This pattern is consistent with environmental heating (positive -R values and losses of latent heat energy through condensation) changing to environmental cooling (negative -R values and gains of latent heat energy through evaporation) as activity dissipated at 1930 GMT.

Diabatic heating profiles show essentially the same time variation in the pattern of total environmental heating (Fig. 5.8.4.5), indicating that condensation/evaporation was probably the dominant diabatic process responsible for the profile pattern. Diabatic heating changes to cooling between 1500 and 1930 GMT as thunderstorms dissipate over the network.

The horizontal flux divergence profiles of kinetic energy (Fig. 5.8.4.6) generally show flux divergence at most levels and times, especially at mid and upper layers. The vertical flux divergence profiles (Fig. 5.8.4.7) were vertically erratic and generally showed increasing flux convergence of kinetic energy with height.

5.8.5 Water Vapor Budget

Figure 5.8.5.1 shows profiles of net horizontal transport of water vapor. A net inflow below 700 mb, coupled with a maximum net outflow at 600 mb is seen at 1500 GMT. By 1800 GMT, this net inflow in lower layers increases with height, showing strong net inflow for most layers. At 2100 GMT, a large net outflow is again observed at 600 mb, as well as in lower layers. This trend reverses when the line of heavy thunderstorms moved

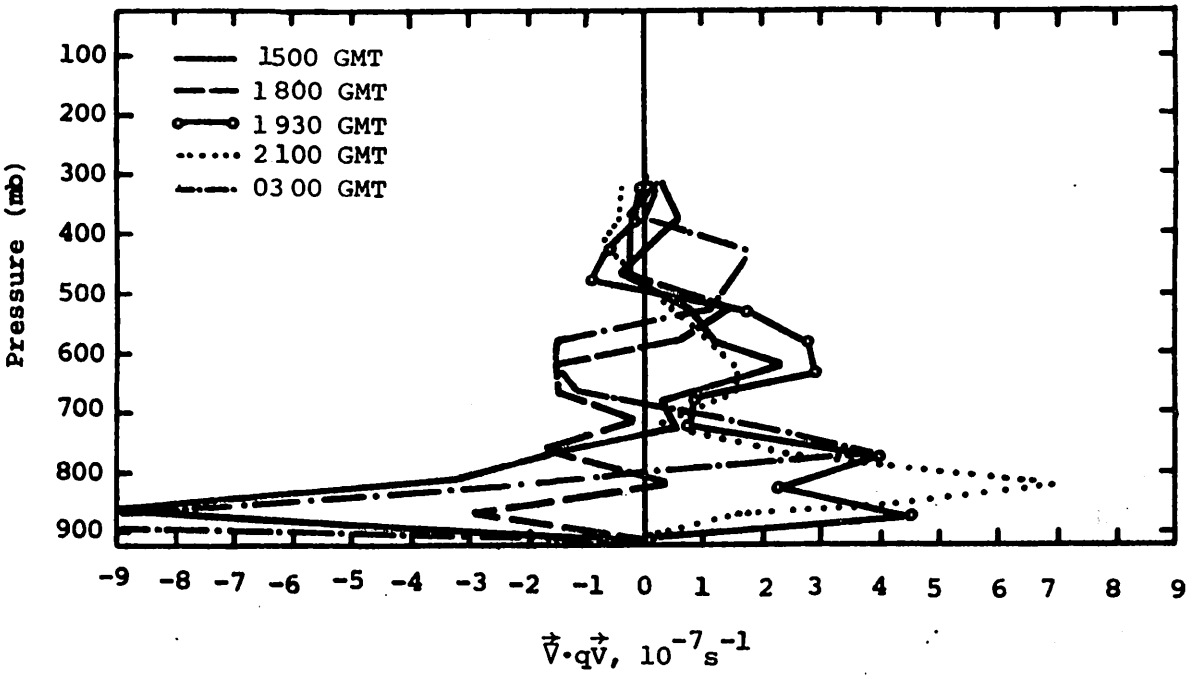

Fig. 5.8.3.3 Vertical profiles of moisture divergence on 21 June 1977.

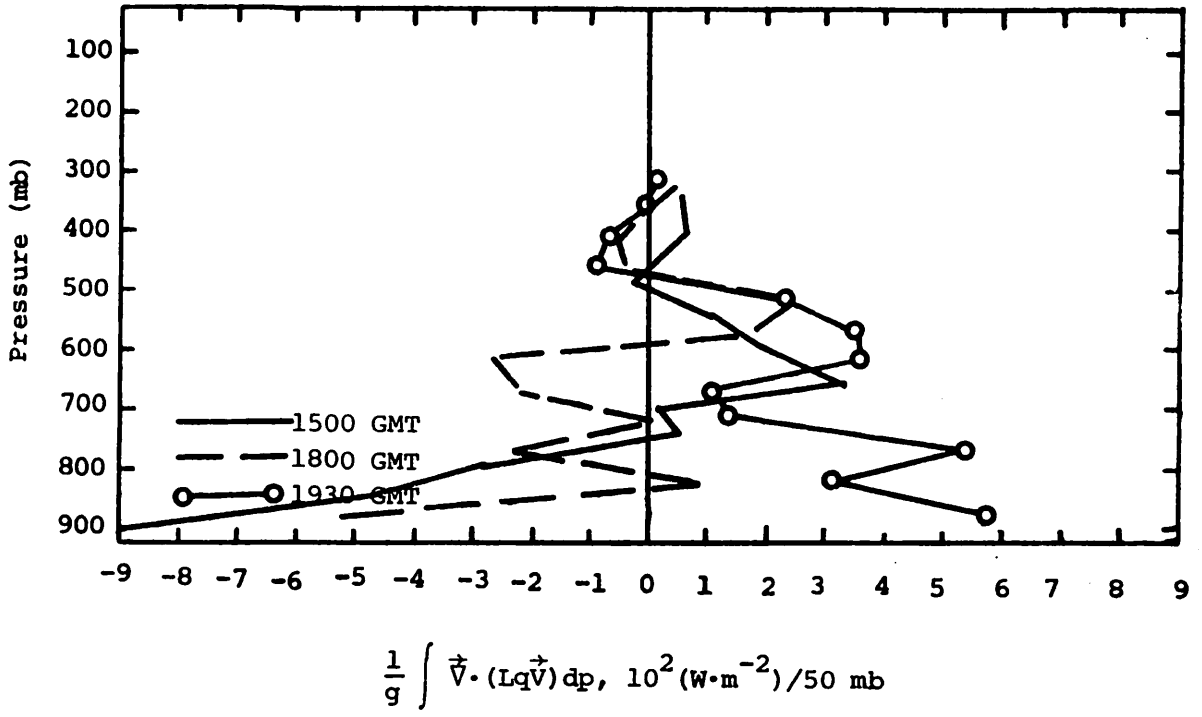

Fig. 5.8.4.1 Vertical profiles of the horizontal flux of latent heat energy on 21 June 1977.

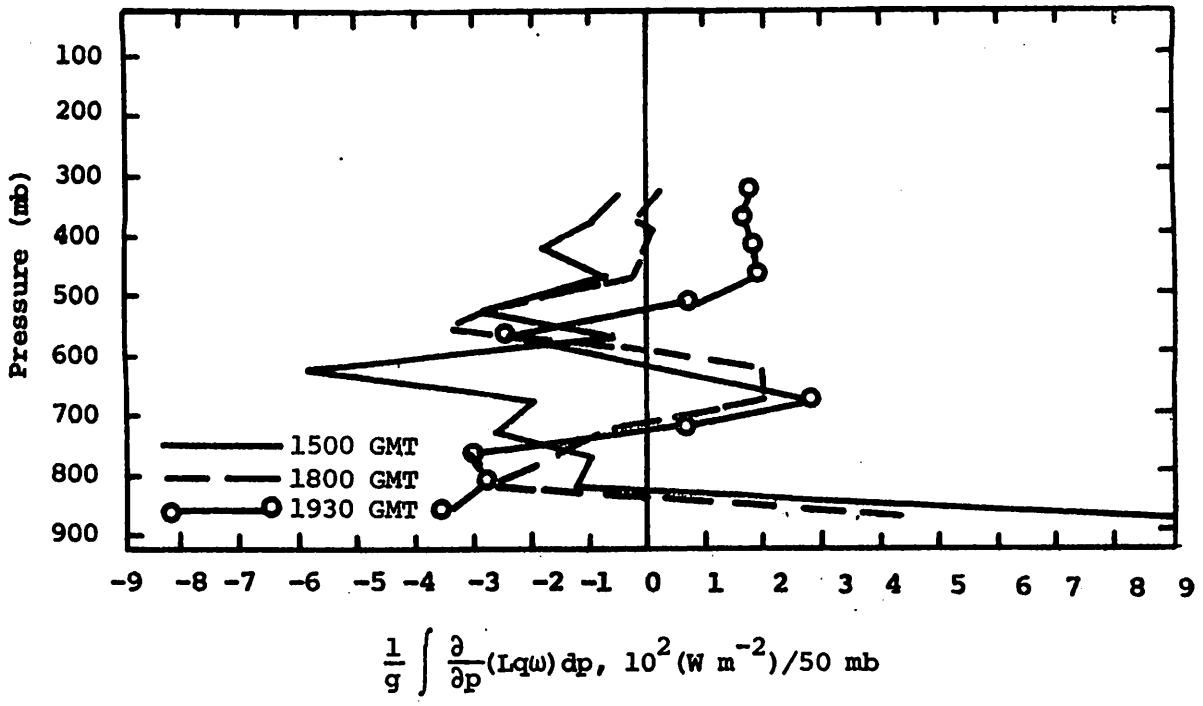

Fig. 5.8.4.2 Vertical profiles of the vertical flux of latent heat energy on 21 June 1977.

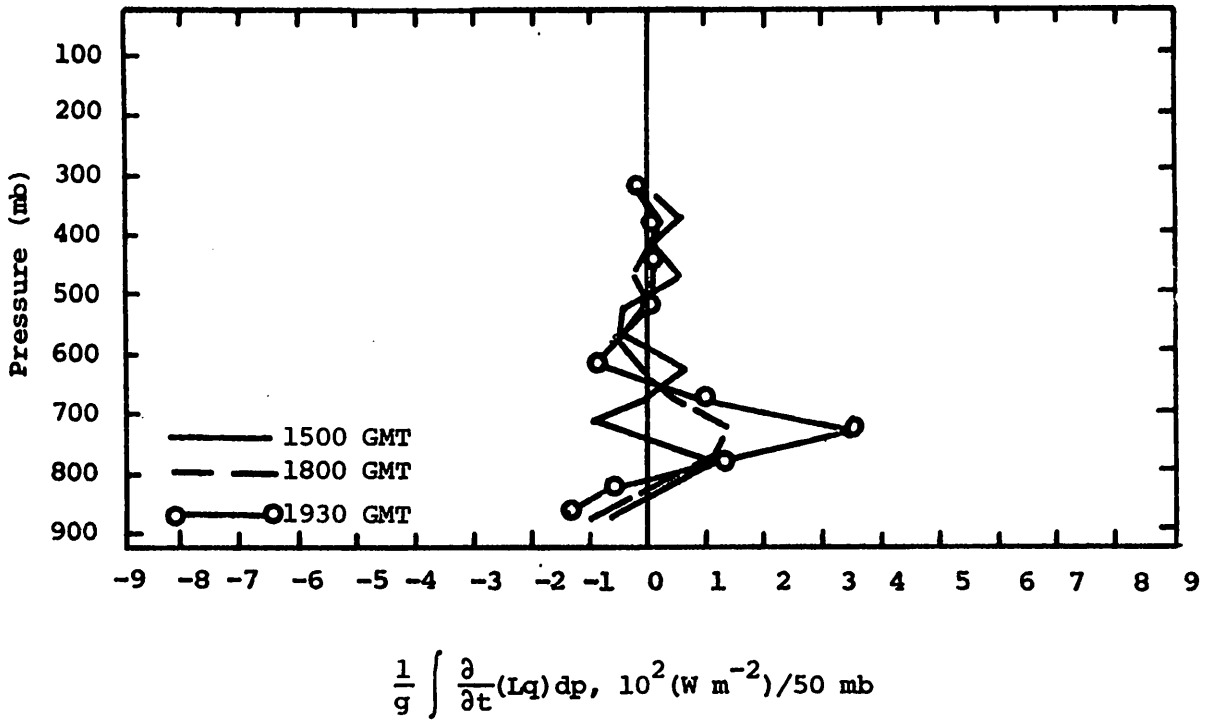

Fig. 5.8.4.3 Vertical profiles of the local change of latent heat energy on 21 June 1977.

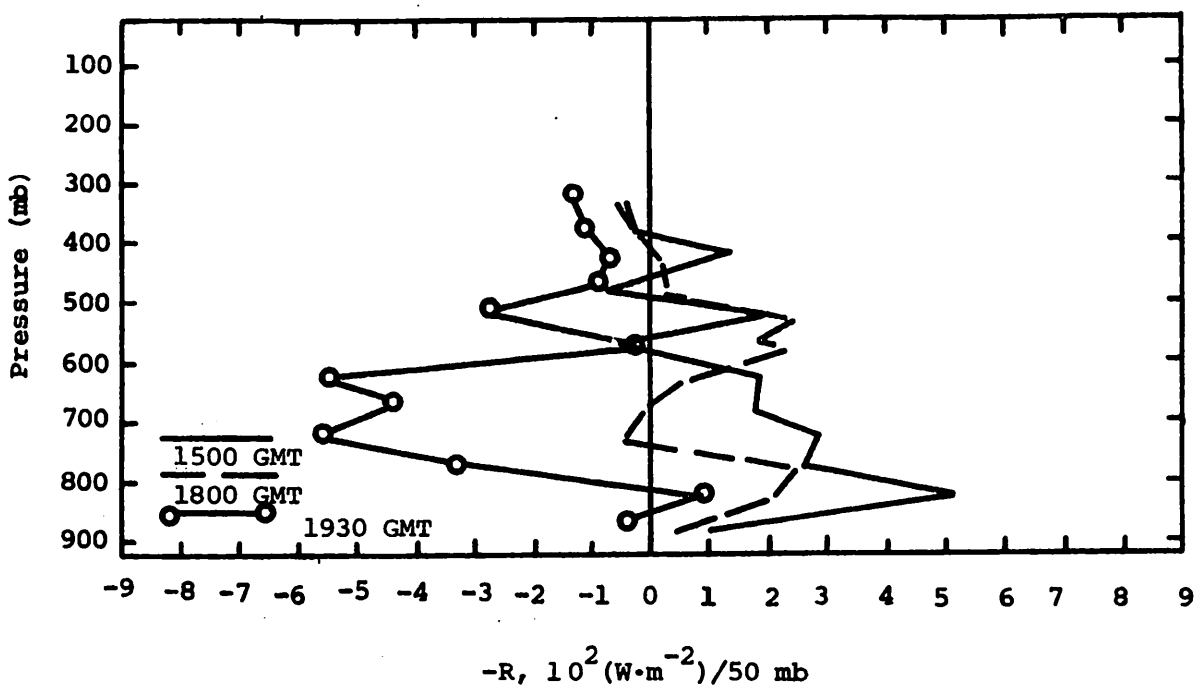

Fig. 5.8.4.4 Vertical profile of the residual of the latent heat energy equation on 21 June 1977.

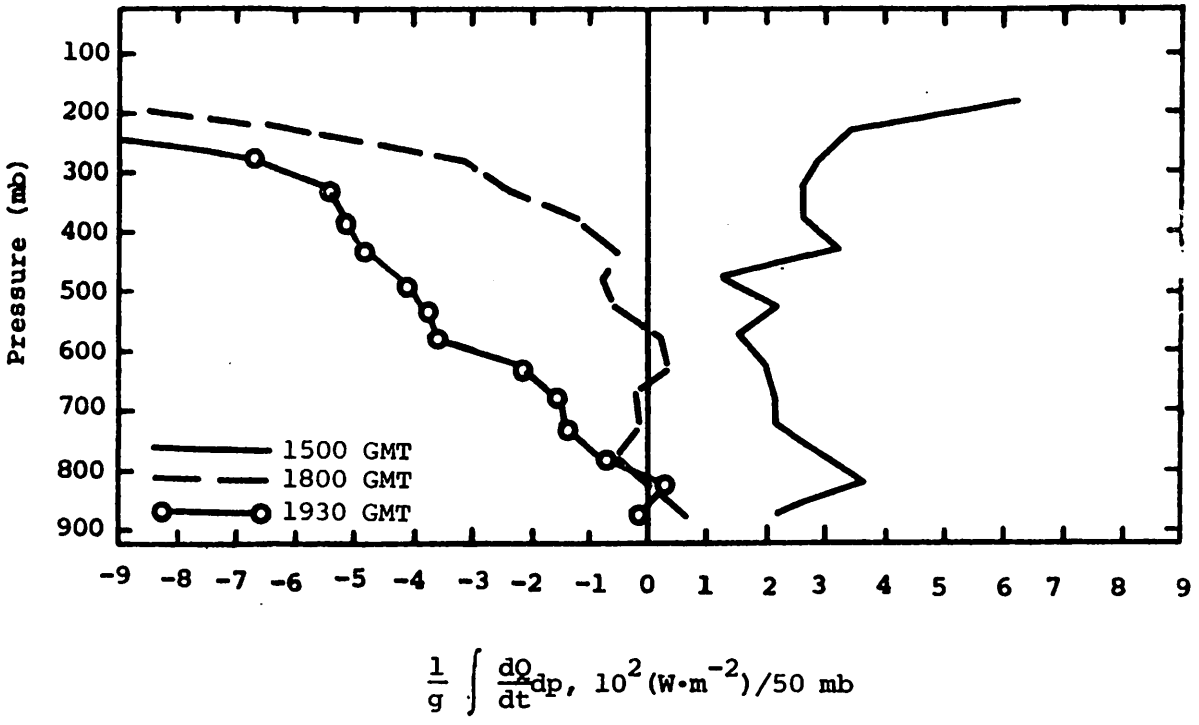

Fig. 5.8.4.5 Vertical profiles of diabatic heating computed from the first law of thermodynamics on 21 June 1977.

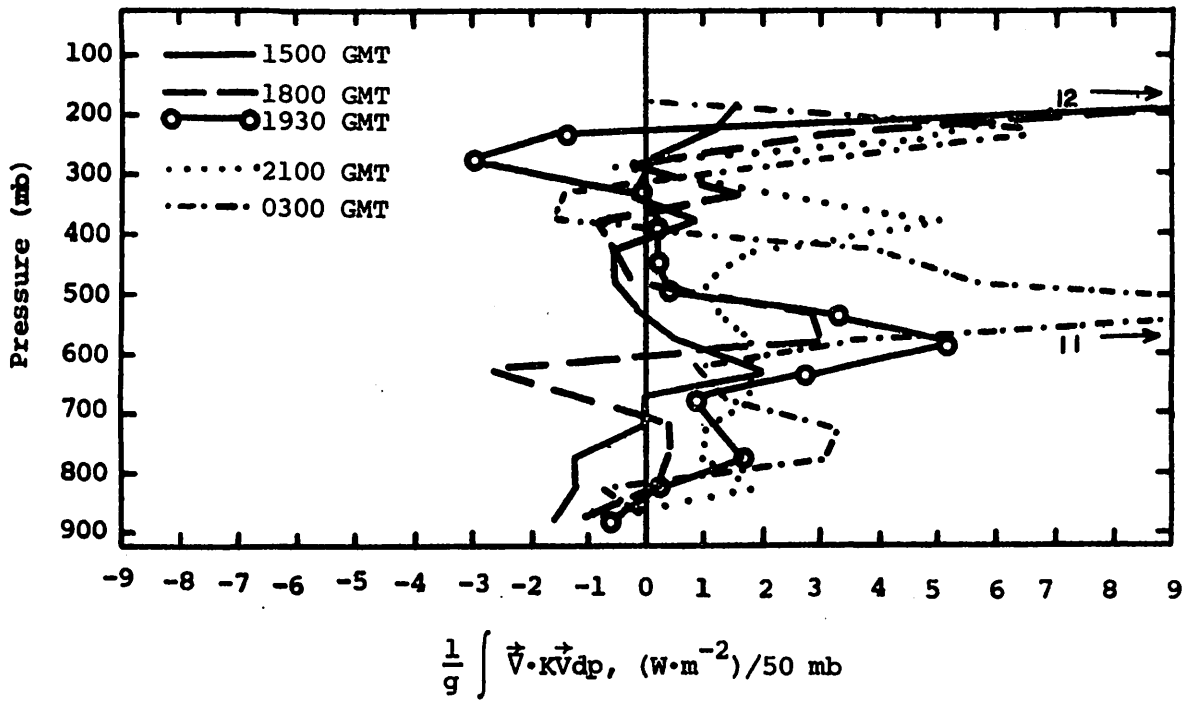

Fig. 5.8.4.6 Vertical profiles of the horizontal flux of kinetic energy on 21 June 1977.

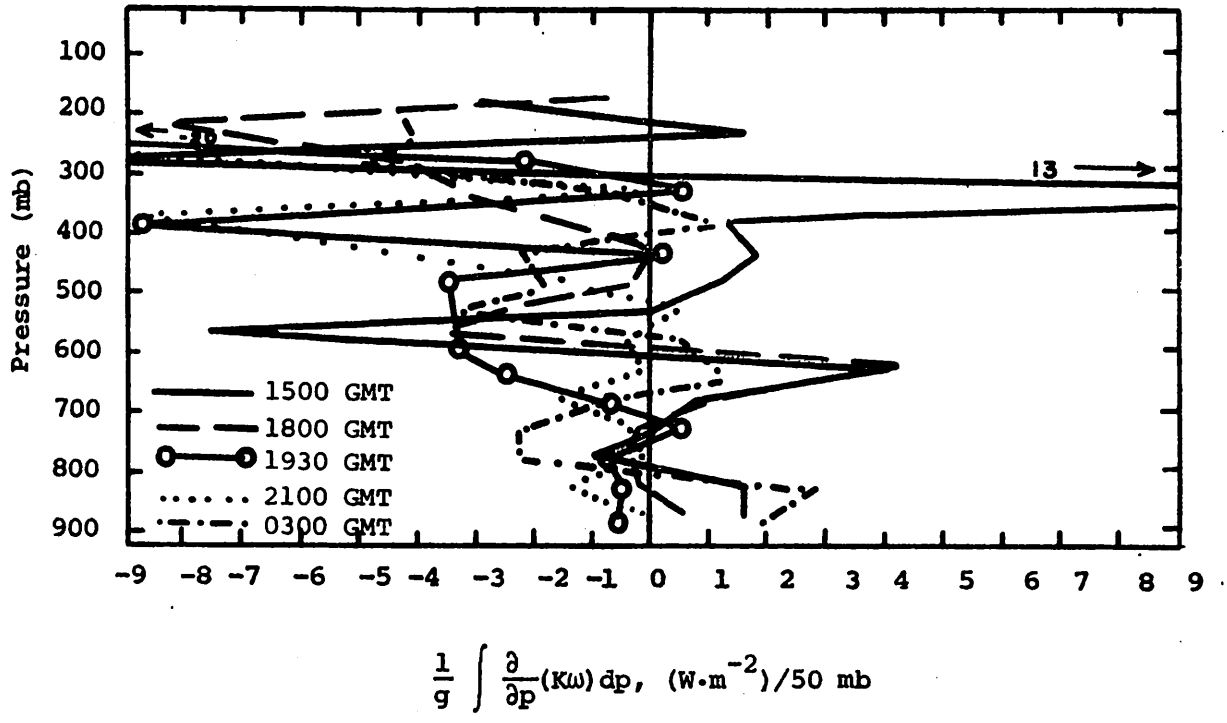

Fig. 5.8.4.7 Vertical profiles of the vertical flux of kinetic energy on 21 June 1977.

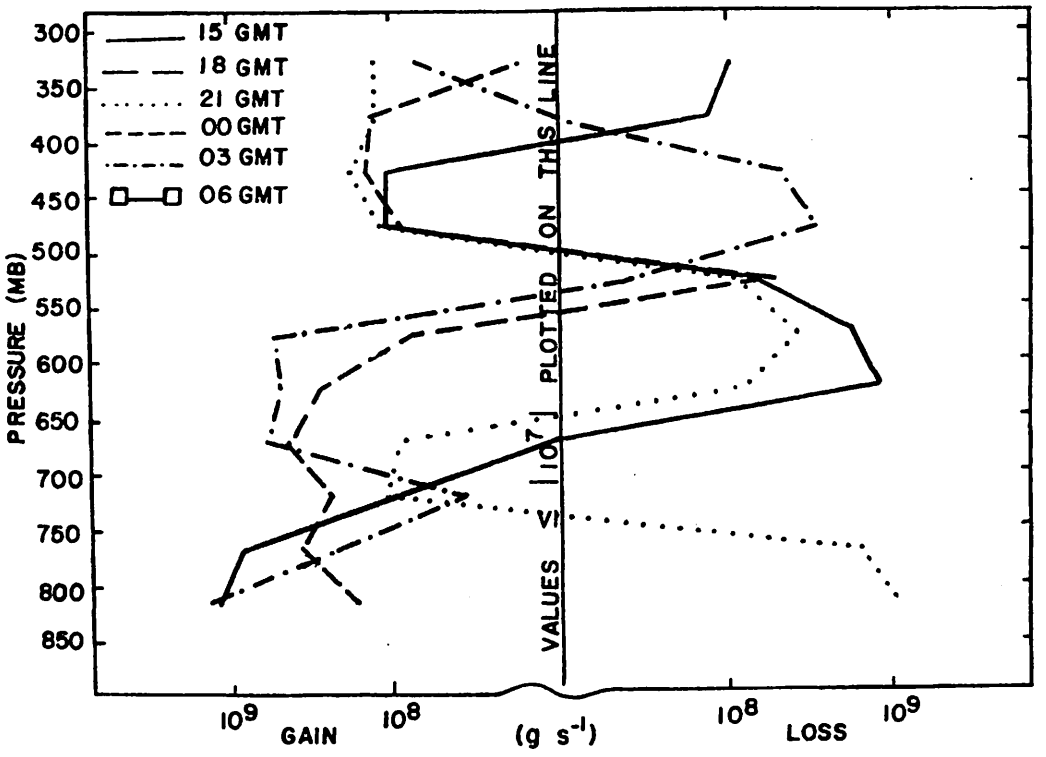

Fig. 5.8.5.1 Net horizontal transport of water vapor through boundaries of 50-mb layers (g s^{-1}) over the Texas HIPLEX area for 21 June 1977.

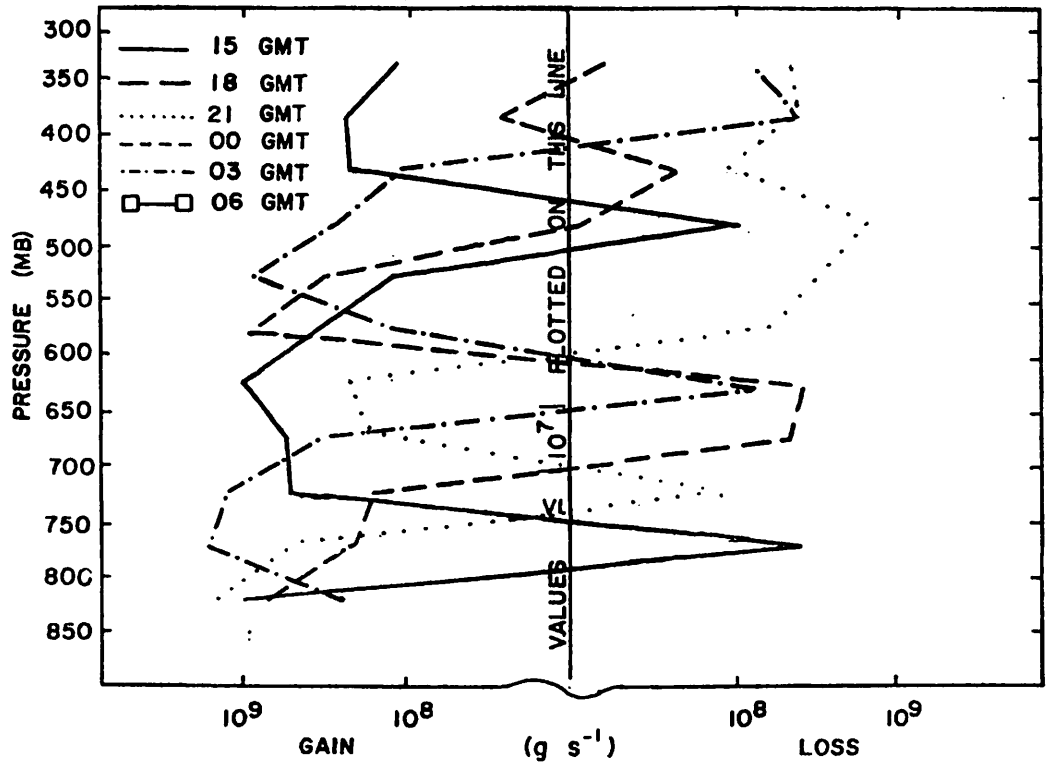

Fig. 5.8.5.2 Net vertical transport of water vapor through boundaries of 50-mb layers (g s^{-1}) over the Texas area for 21 June 1977.

into the network.

Figure 5.8.5.2 shows profiles of net vertical transport of water vapor. Although these profiles show large variations, a general net inflow occurred in most layers prior to convective activity. A large difference existed between profiles for 2100 and 0300 GMT. Prior to any convection, a maximum net outflow at 500 mb existed. During heavy convection a large net inflow occurred at 500 mb, indicating a "storage" of water vapor which is a characteristic during intense convection.

Figure 5.8.5.3 shows profiles of the vertical transport of water vapor through constant pressure surfaces. Strong upward transports occurred at 1500, 1800 and 0300 GMT for all layers below 500 mb. With no associated activity at 2100 GMT, downward transports occurred in all but the lower layer. These profiles show deviations with height, producing large variations in the profiles of net vertical transport (Fig. 5.8.5.2).

Figure 5.8.5.4 shows profiles of combined net horizontal and vertical transports of water vapor. These profiles generally show a strong net inflow in lower layers and a net outflow in upper layers. The strongest net inflow occurred at 0300 GMT in association with the line of heavy thunderstorms within the network. Prior to this activity, the large net outflow at 550 mb for 2100 GMT is also shown in Figs. 5.8.5.1 and 5.8.5.2.

Figure 5.8.5.5 shows profiles of the total mass of water vapor. Profiles for 1500 and 1800 GMT show a moisture inversion at 550 mb, which might have influenced the growth of the isolated cell at 1700 GMT. This moisture inversion dissipated by 2100 GMT, and the presence of convective activity at 0300 GMT was accompanied by a large increase in water vapor for all layers.

Figure 5.8.5.6 shows profiles of the local rate-of-change in the total mass of water vapor. Due to missing data at 0000 GMT, only two profiles were available. From 1500 to 1800 GMT, a large gain occurred in the lower layers. Due to upward transports shown in Fig. 5.8.5.3 for 1800 GMT, a gain in water vapor aloft occurred between 1800 and 2100 GMT.

5.9 22 June 1977

5.9.1 Radar

Charts of radar echoes for this day are shown in Fig. 5.9.1.1. Numerous echoes covering large portions of the area occurred throughout most of the period. Numerous cells with tops exceeding 9.1 km (30K ft) occurred during most of the 12-h period but were concentrated between 1700 and 2100 GMT. The echo areas and lines of cells associated with the

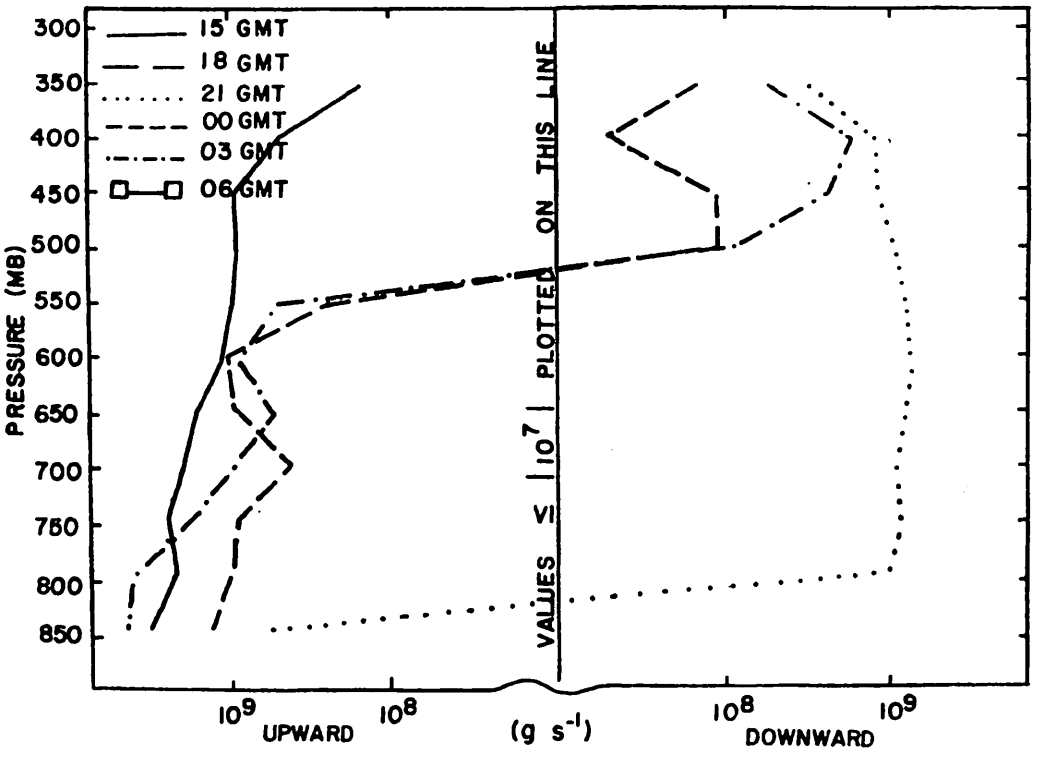

Fig. 5.8.5.3 Vertical transport of water vapor through constant pressure surfaces (g s^{-1}) over the Texas HIPLEX area for 21 June 1977.

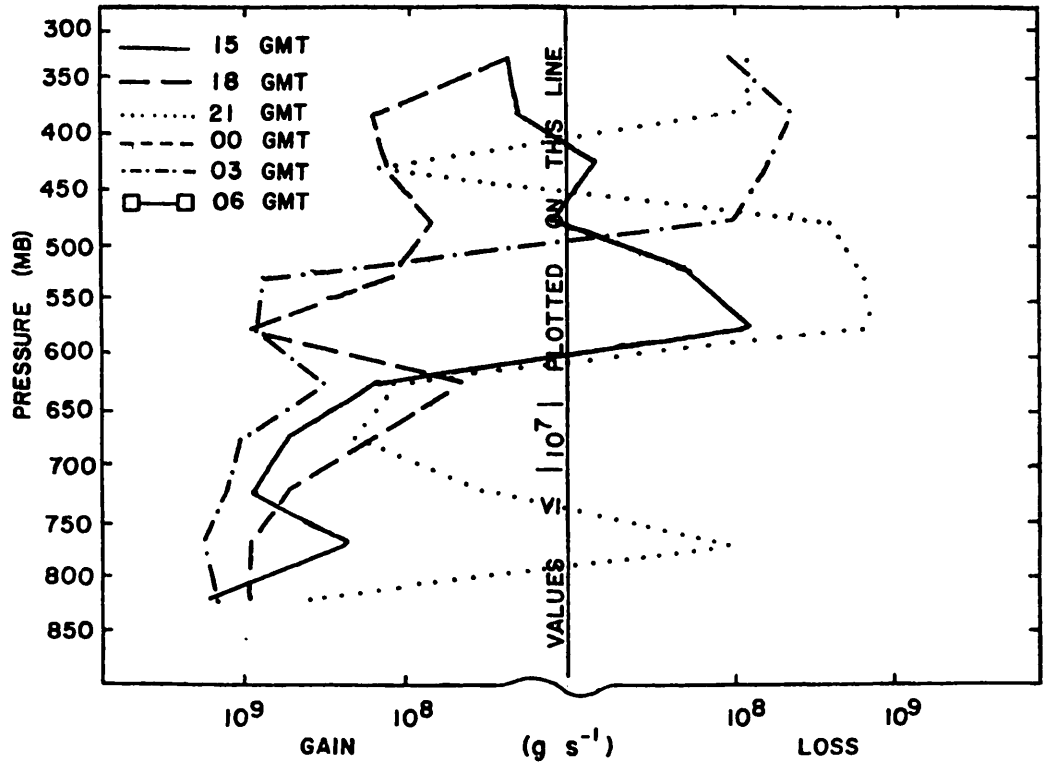

Fig. 5.8.5.4 Combined net horizontal and vertical transport of water vapor through boundaries of 50-mb layers (g s^{-1}) over the Texas HIPLEX area for 21 June 1977.

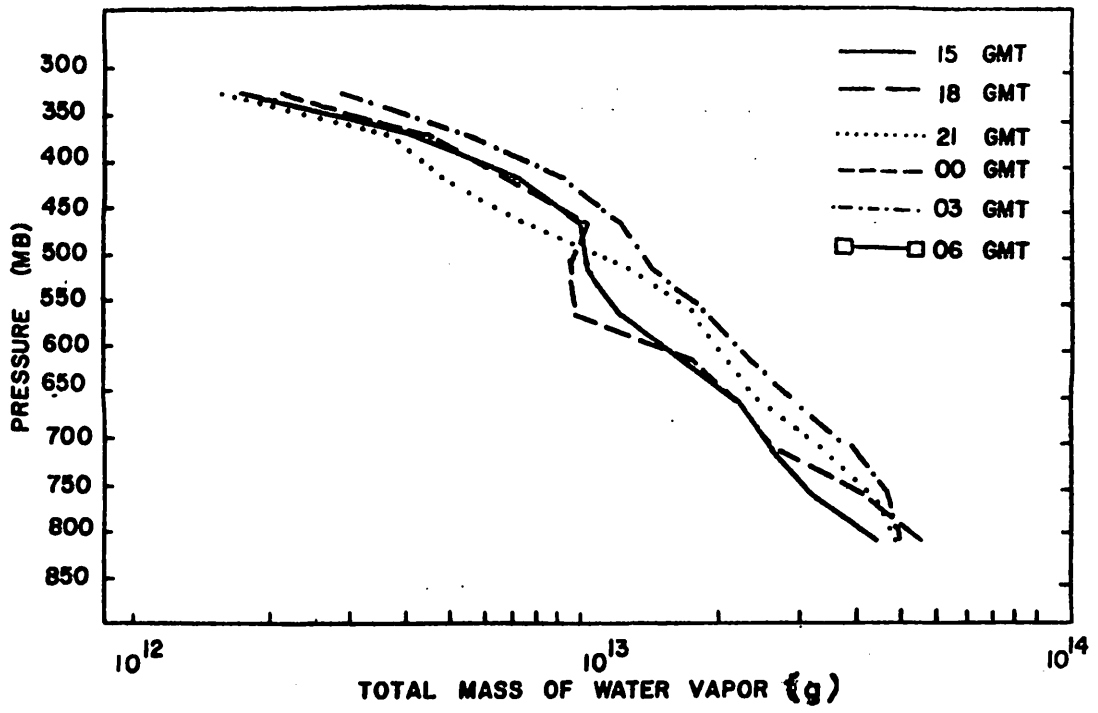

Fig. 5.8.5.5 Total mass of water vapor in layers 50 mb deep (g) over the Texas HIPLEX area for 21 June 1977.

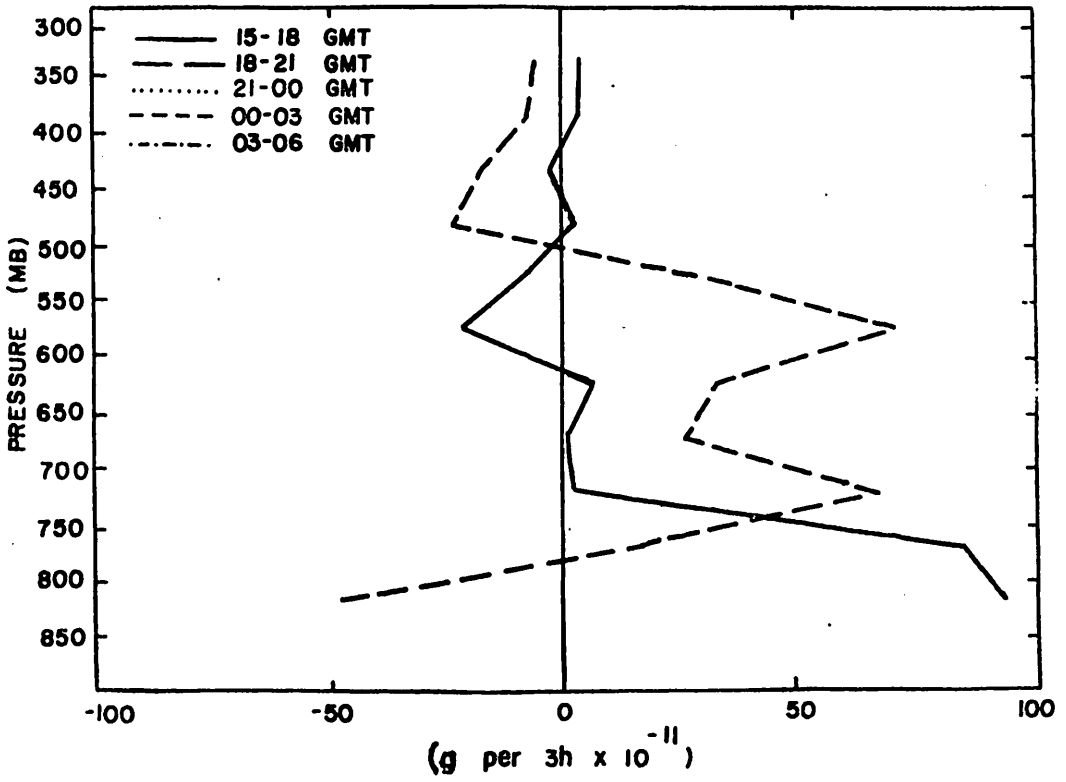

Fig. 5.8.5.6 Local rate-of-change in total mass of water vapor (g per 3h x 10^{-11}) over the Texas HIPLEX area for 21 June 1977.

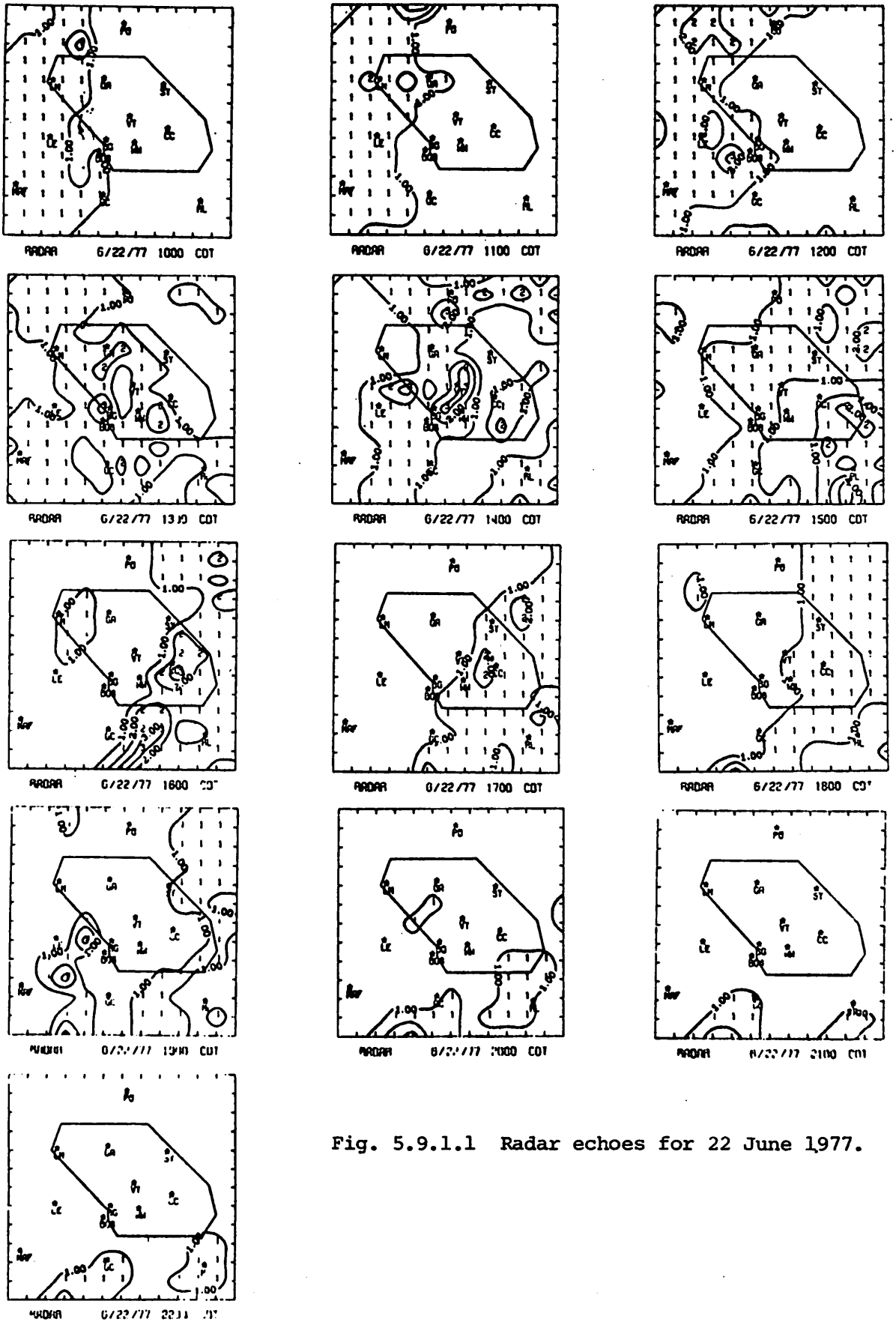

Fig. 5.9.1.1 Radar echoes for 22 June 1977.

areas moved from the northwest toward the southeast during the day.

5.9.2 Surface

Surface temperature fields (Fig. 5.9.2.1) show the passage of a squall line that bisects the area at 1900 GMT. A decrease in temperature accompanies the movement of the line. By 2300 GMT, a cool isolated region is observed over Snyder which slowly dissipates due to mixing and nocturnal cooling. Temperatures on this day are noticeably cool due to the effect of the line and the reduction of surface heating due to the cloudiness.

Fields of surface mixing ratio (Fig. 5.9.2.2) and surface equivalent potential temperature (Fig. 5.9.2.3) show well defined centers associated with the line. Although surface mixing ratios slowly increase with time, a reduction in surface equivalent potential temperature is reflected by the effect of the line passage on surface temperature.

Terrain-induced vertical motion fields (Fig. 5.9.2.4) show generally downward motion especially northeast of Snyder which decrease in time due to decreased wind speed. Charts of surface velocity divergence (Fig. 5.9.2.5) show areas of strong convergence and divergence. However, well defined centers of convergence are associated with the line passage followed by mostly divergence over the area by 0300 GMT. Vertical motion 50 mb above the surface (Fig. 5.9.2.6) remains small in magnitude prior to and following the line passage. A strong center of upward motion is observed over the center of the network at 2200 GMT associated with several cells trailing the line. Other small regions of upward motion correlate with intense echoes between 1900 and 2200 GMT.

Large values of surface moisture divergence (Fig. 5.9.2.7) and upward flux of moisture 50 mb above the surface (Fig. 5.9.2.8) also occurred in these areas. These well defined centers decrease in magnitude following the line, and were replaced by surface moisture divergence and a downward flux of moisture 50 mb above the surface. The surface vorticity (Fig. 5.9.2.9) does not show any strong centers of high or low values which persist for any significant time until the line moves over the area. From 2000 to 2300 GMT strong centers of cyclonic and anticyclonic vorticity occurred. Values of surface vorticity decrease following the line passage.

The effect of the line passage does not radically alter the sea level pressure field (Fig. 5.9.2.10). Lower pressures persist over the south-

Fig. 5.9.2.1 Surface temperature (C x 10^{-1}) for 22 June 1977.

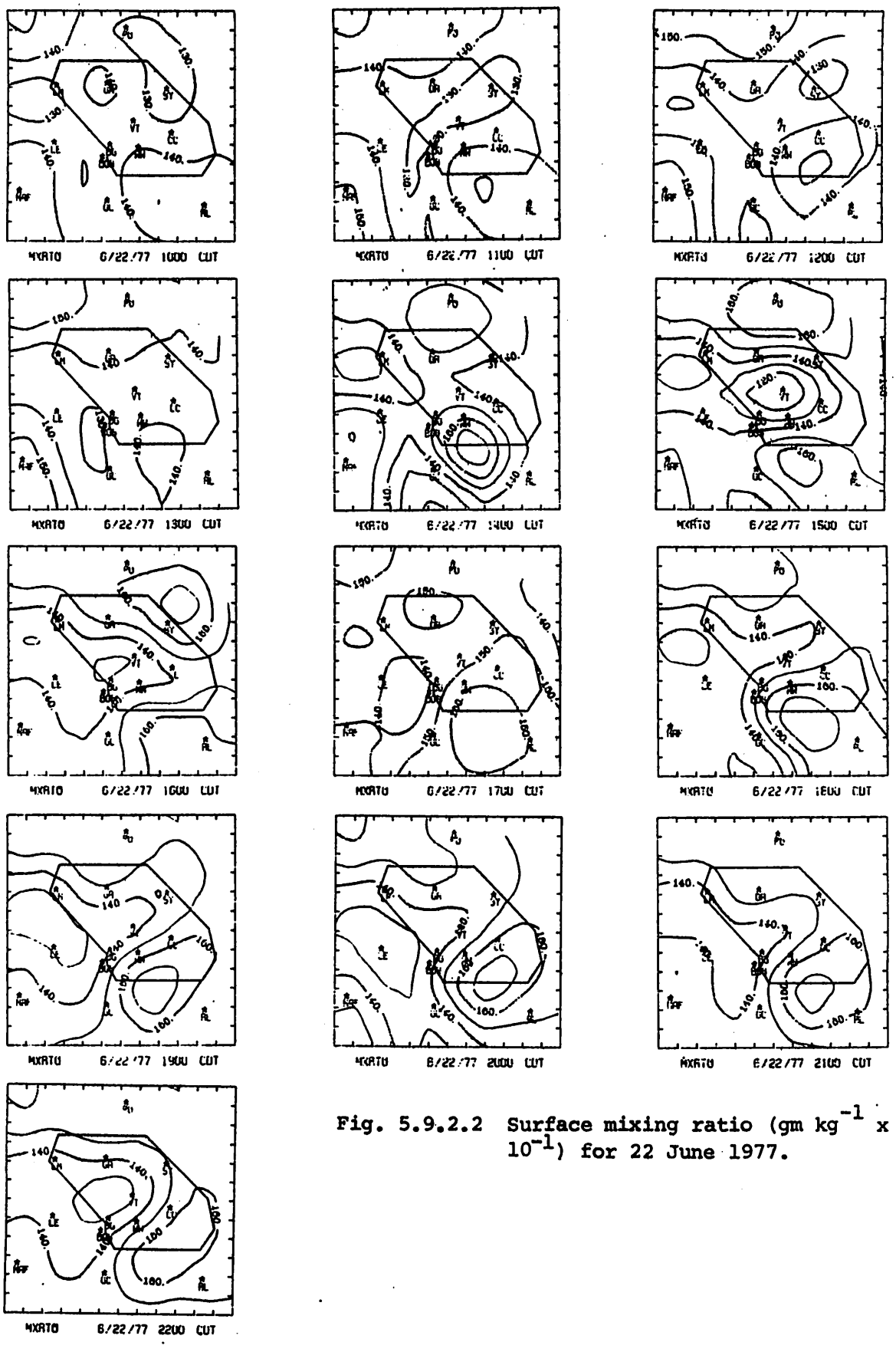

Fig. 5.9.2.2 Surface mixing ratio (gm kg^{-1} x 10^{-1}) for 22 June 1977.

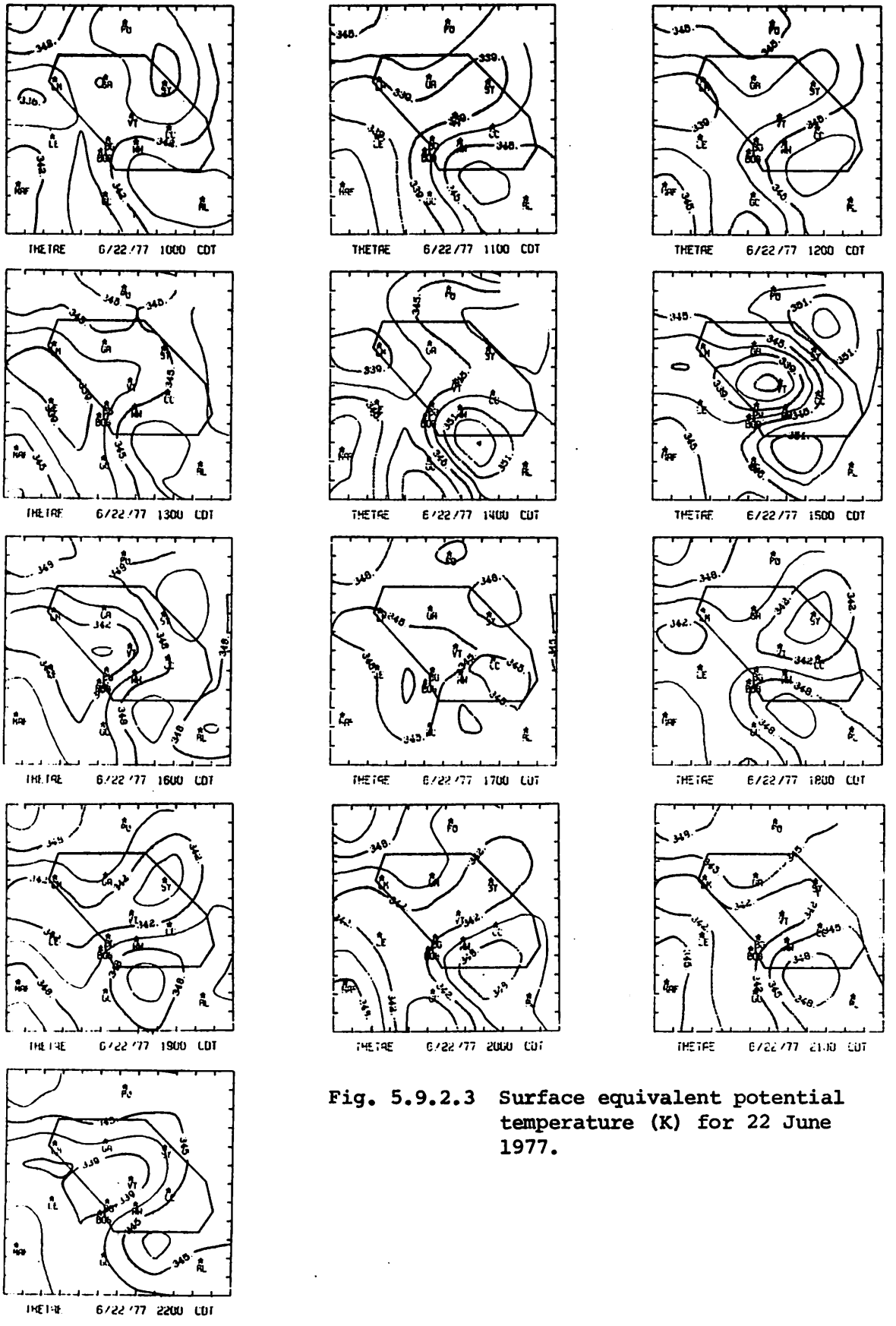

Fig. 5.9.2.3 Surface equivalent potential temperature (K) for 22 June 1977.

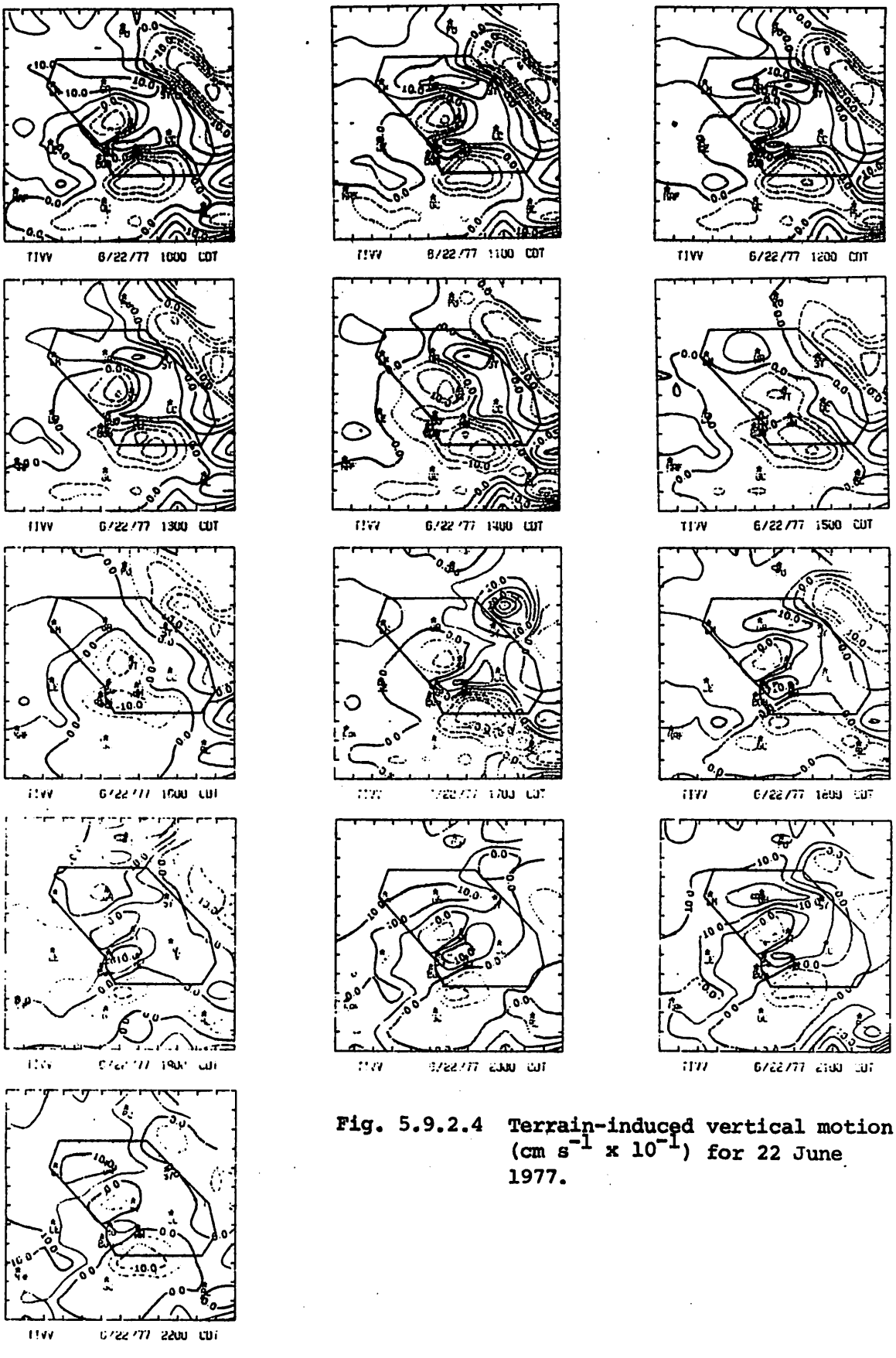

Fig. 5.9.2.4 Terrain-induced vertical motion (cm s^{-1} x 10^{-1}) for 22 June 1977.

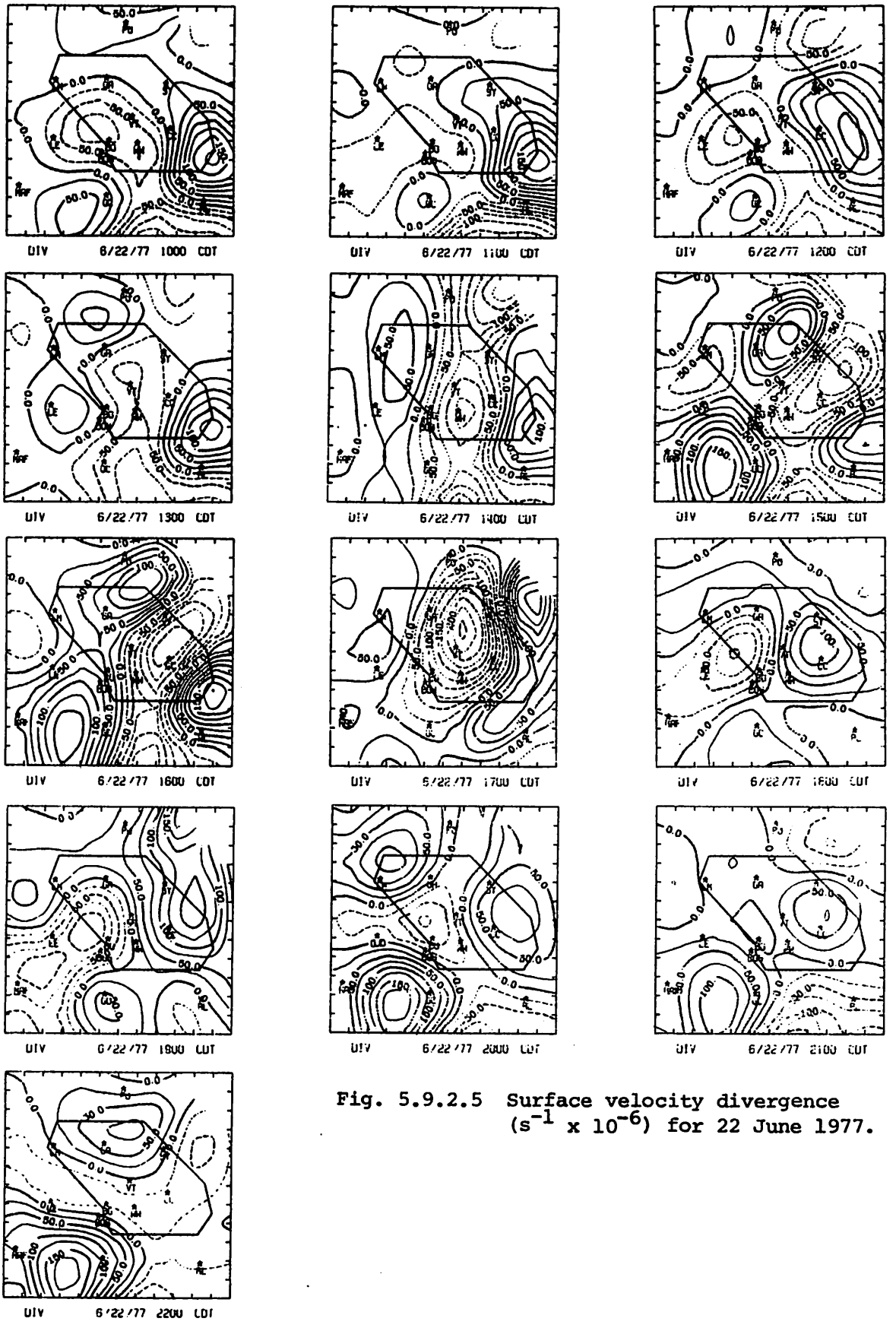

Fig. 5.9.2.5 Surface velocity divergence (s^{-1} x 10^{-6}) for 22 June 1977.

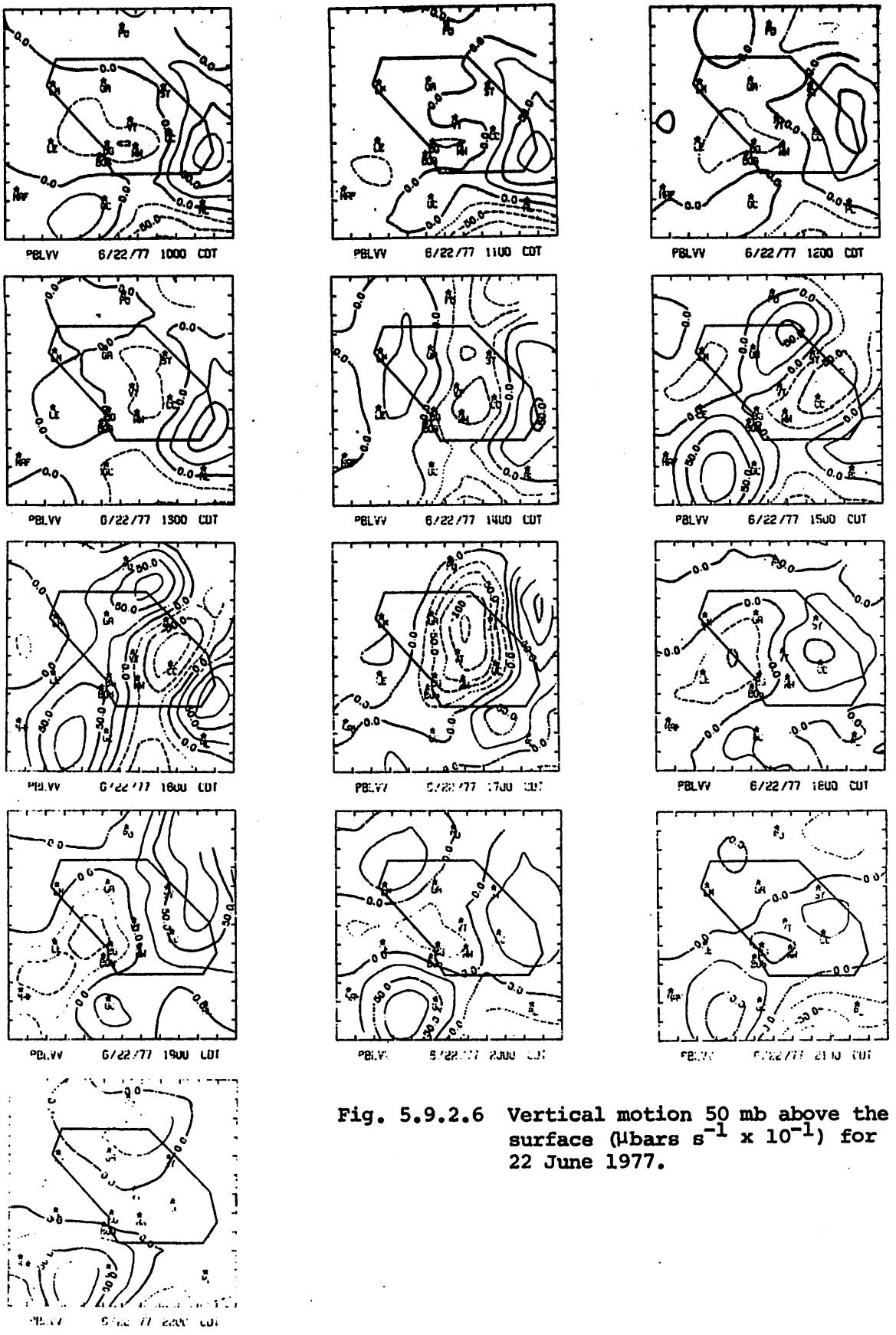

Fig. 5.9.2.6 Vertical motion 50 mb above the surface (μbars s^{-1} x 10^{-1}) for 22 June 1977.

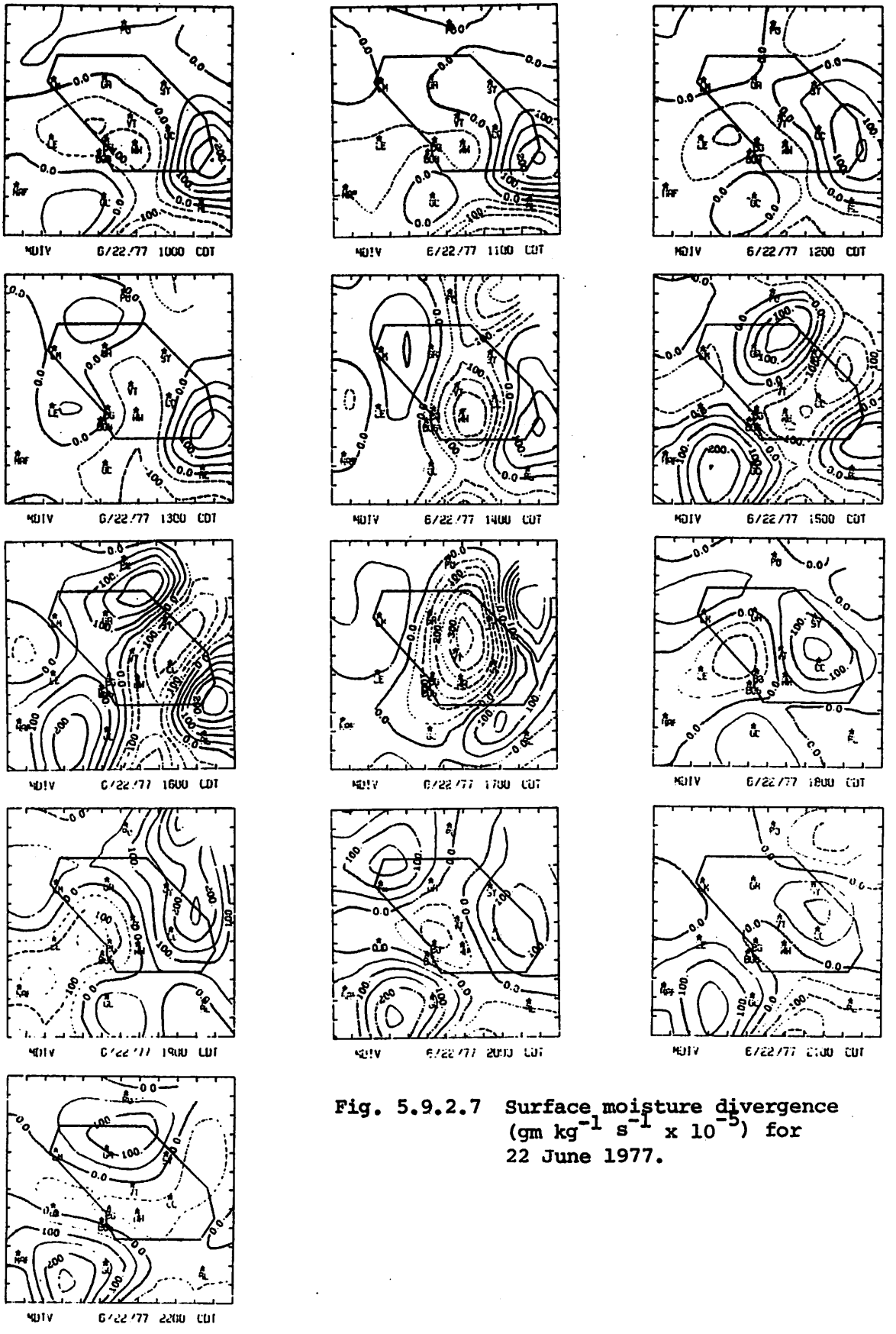

Fig. 5.9.2.7 Surface moisture divergence (gm kg^{-1} s^{-1} x 10^{-5}) for 22 June 1977.

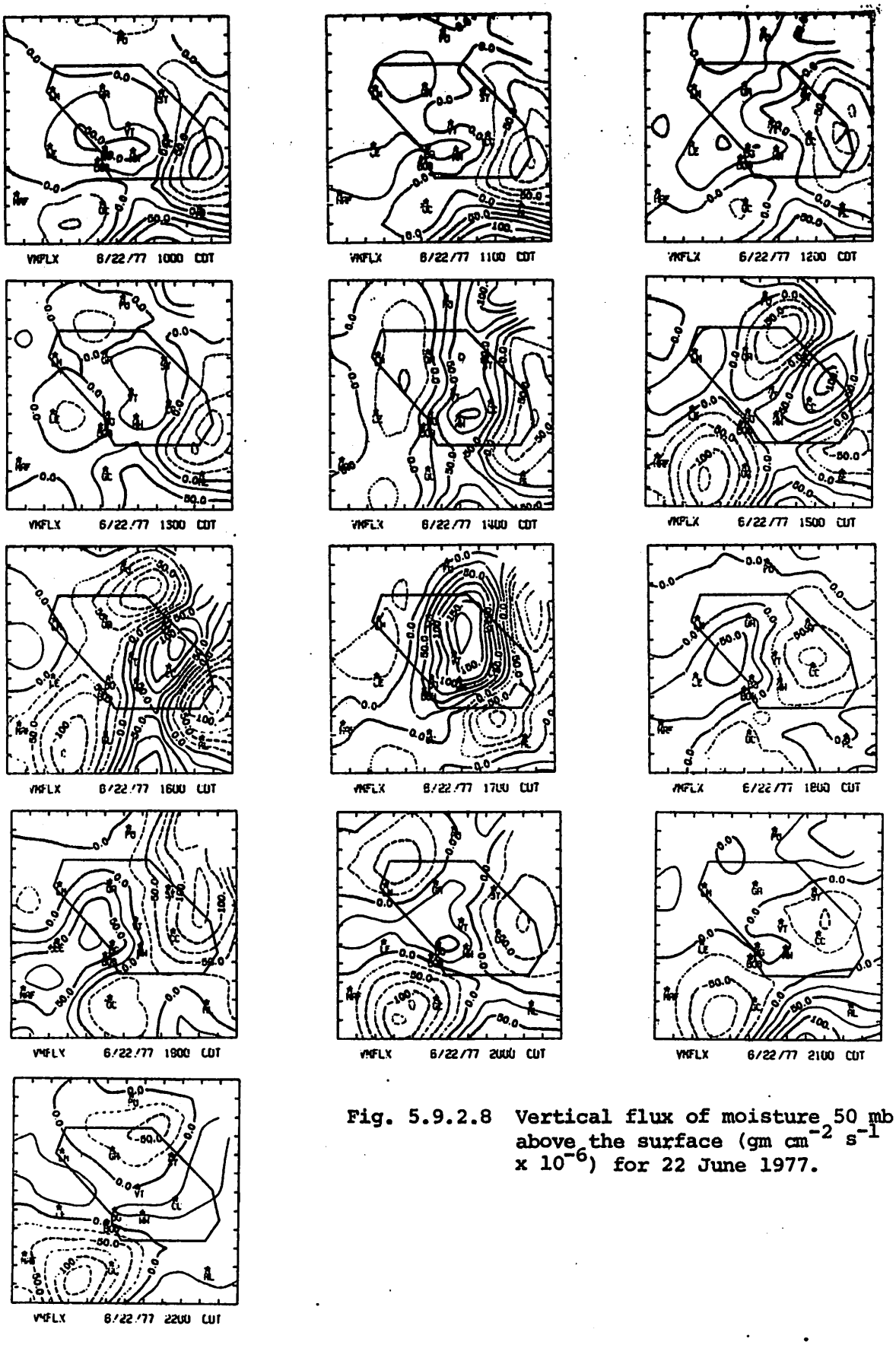

Fig. 5.9.2.8 Vertical flux of moisture 50 mb above the surface (gm cm^{-2} s^{-1} x 10^{-6}) for 22 June 1977.

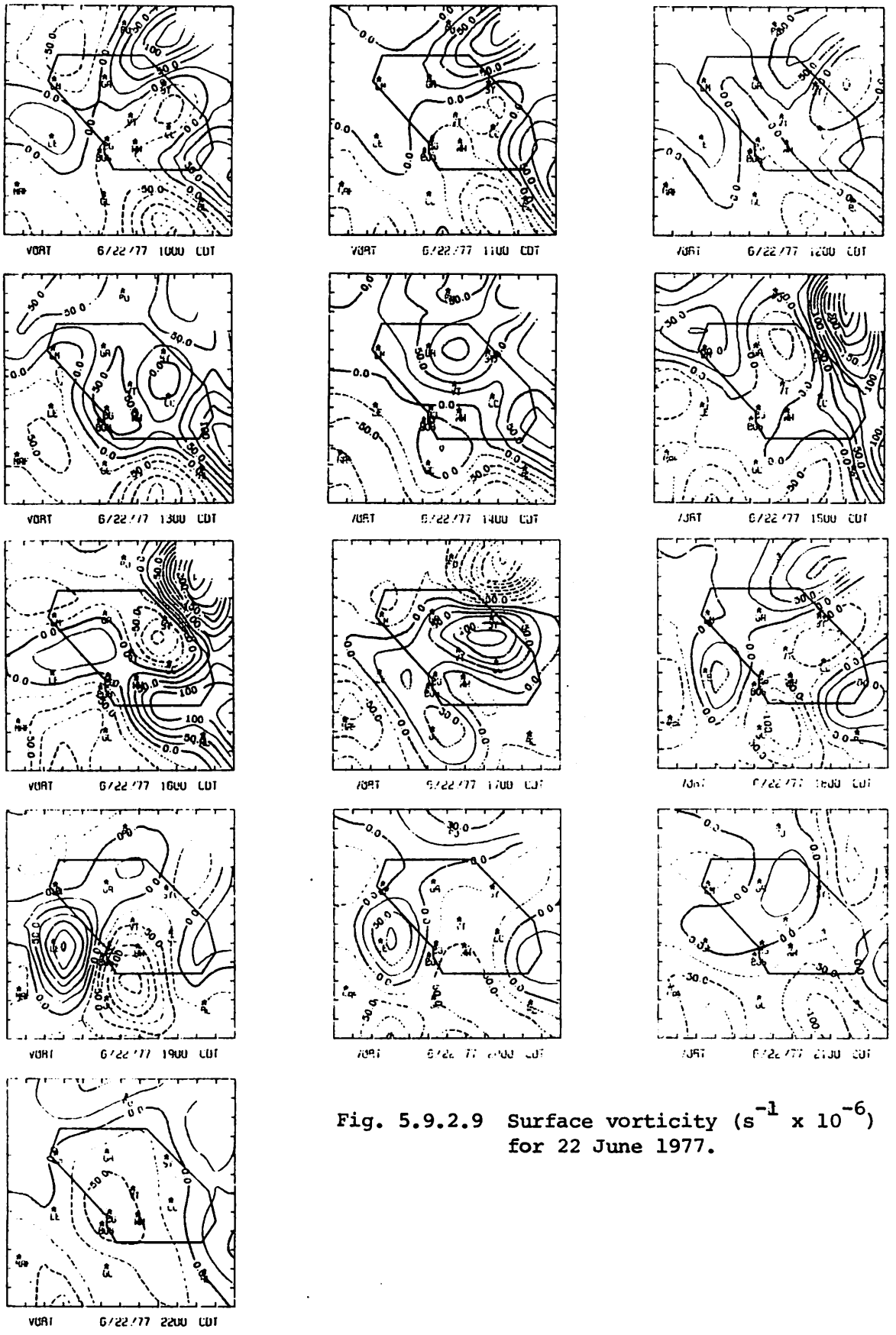

Fig. 5.9.2.9 Surface vorticity ($s^{-1} \times 10^{-6}$) for 22 June 1977.

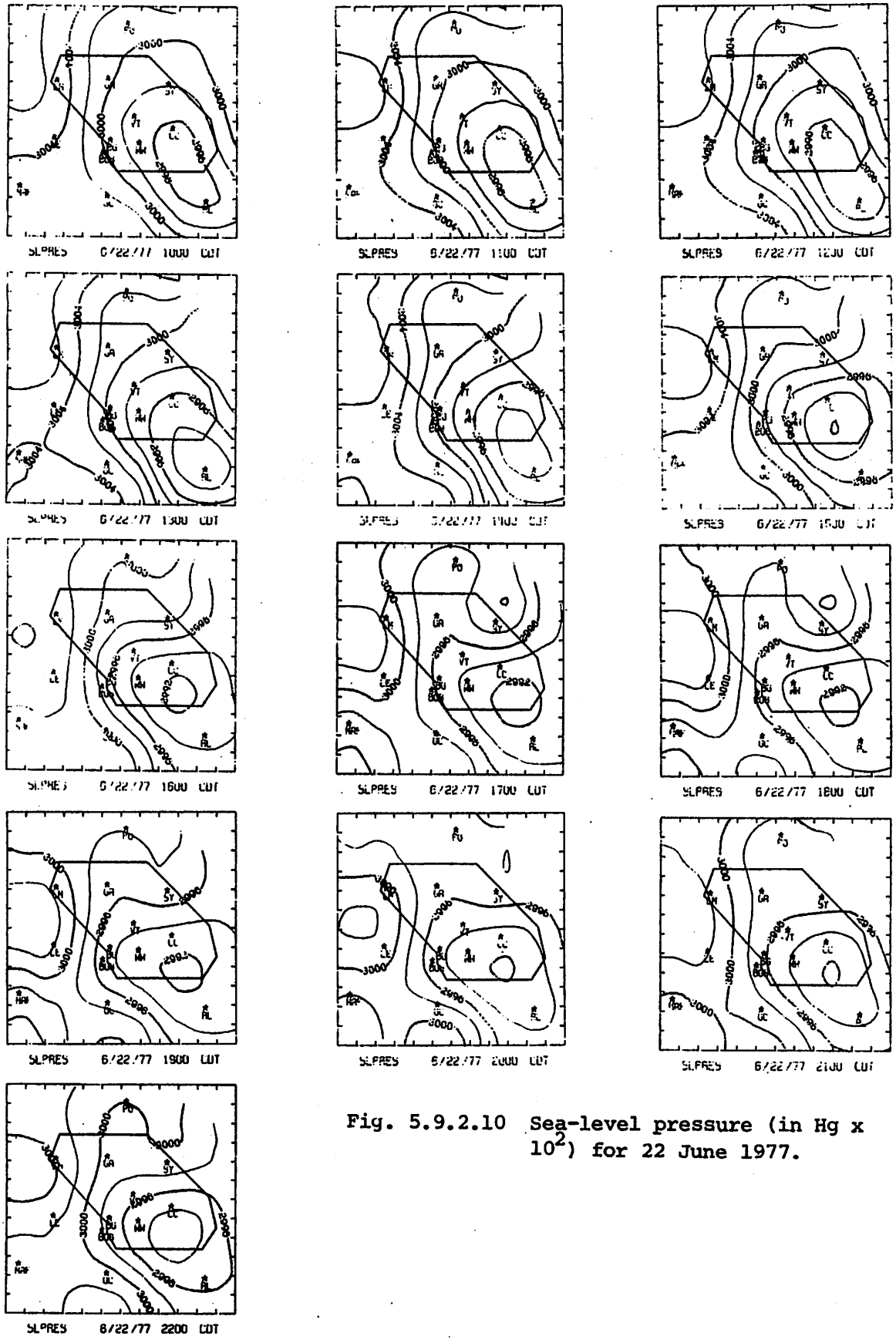

Fig. 5.9.2.10 Sea-level pressure (in Hg x 10^2) for 22 June 1977.

eastern region of the network which was observed on previous days. The change in pressure (Fig. 5.9.2.11) shows a slight decrease prior to the line passage which is followed by a pressure increase by 0200 GMT.

5.9.3 Upper-Level Kinematic Parameters

Moderate thunderstorm activity was present over the network at all times the limited sounding data were available on this day. Both horizontal mass and moisture convergence (Figs. 5.9.3.1 and 5.9.3.3) was present in low levels when data were available and vertical velocities were upward at all levels below 500 mb (Fig. 5.9.3.2).

5.9.4 Energetics

Net horizontal inflow of latent heat energy occurred in low- and mid-levels and outflow was calculated above 500 mb (Fig. 5.9.4.1). Vertical flux divergence of kinetic energy (Fig. 5.9.4.2) in low levels and convergence aloft is associated with the net upward transport of latent heat energy from lower levels to mid levels within an upward vertical velocity field. Local changes in latent heat energy were small when data were available (Fig. 5.9.4.3), and the residual term (-R) is positive at most levels indicating losses of latent heat energy during environmental condensation and heating (Fig. 5.9.4.4).

Diabatic heating is generally consistent with the -R profile in the latent heat budget showing heating in mid-levels from condensation (Fig. 5.9.4.5).

Horizontal flux divergence profiles of kinetic energy show net inflow in low levels, outflow in mid levels, and net inflow in upper levels (Fig. 5.9.4.6). Vertical flux divergence of kinetic energy dominates the atmosphere at most levels as kinetic energy is transported vertically by upward vertical velocities (Fig. 5.9.4.7).

5.9.5 Water Vapor Budget

Figure 5.9.5.1 shows profiles of net horizontal transport of water vapor. Profiles for 1500, 2100, and 0300 GMT terminate above 650 mb due to missing data. Following 1500 GMT and during times of strongest convection, a large net inflow occurred in lower layers. At 1800 GMT, a net outflow at 475 mb occurred, which is "characteristic" of times with intense echoes. Strong net inflows existed in all layers by 0000 GMT.

Figure 5.9.5.2 shows profiles of net vertical transport of water vapor. Only profiles for 1800 and 0000 GMT are available due to missing kinematic vertical velocities necessary for the computation. Both profiles are

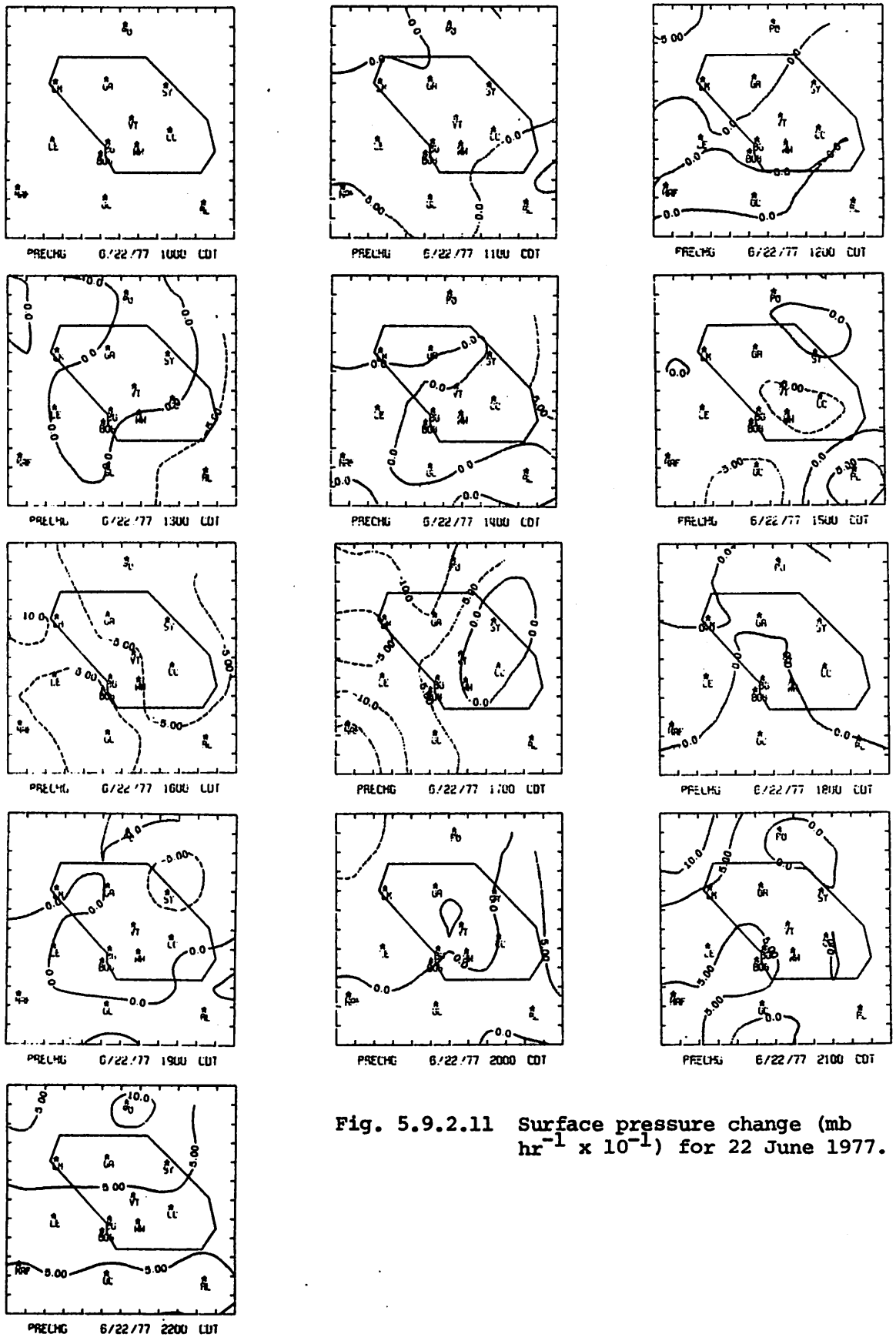

Fig. 5.9.2.11 Surface pressure change (mb hr^{-1} x 10^{-1}) for 22 June 1977.

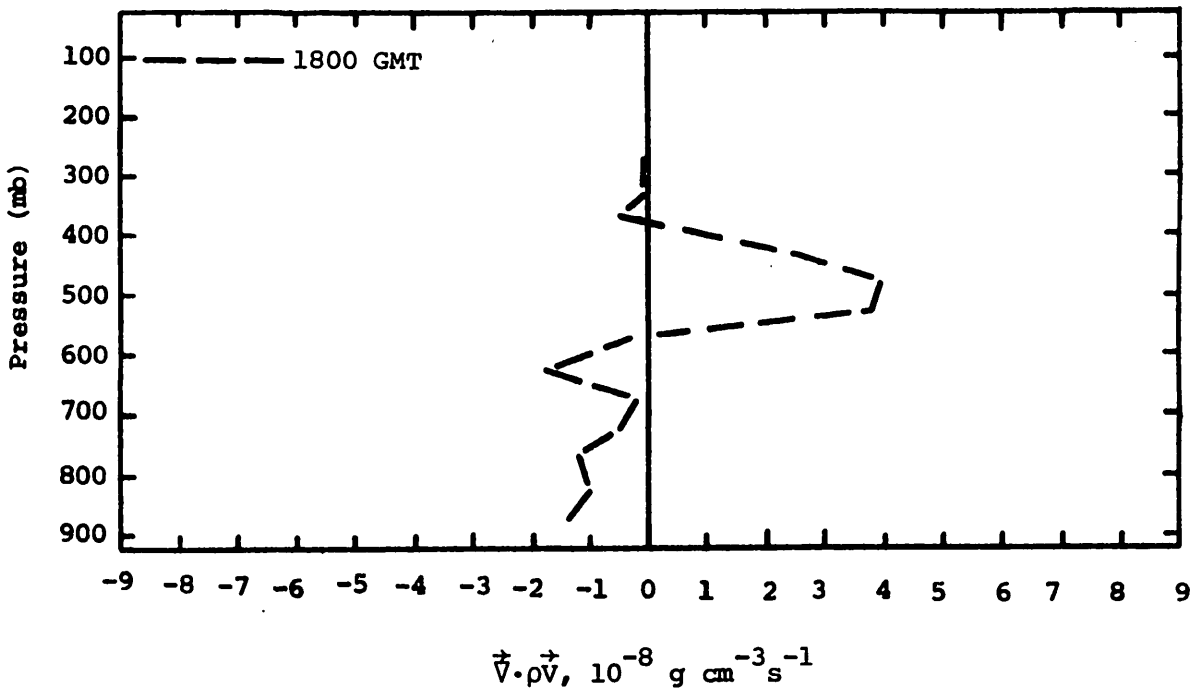

Fig. 5.9.3.1 Vertical profiles of mass divergence on 22 June 1977.

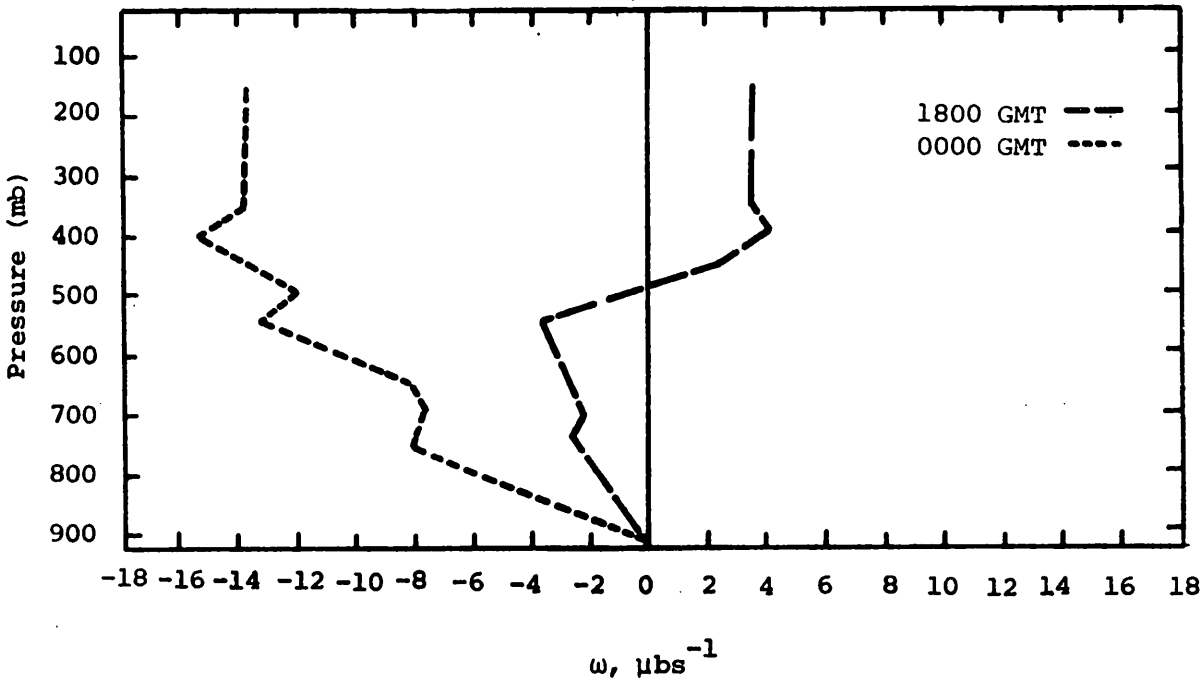

Fig. 5.9.3.2 Vertical profiles of vertical motion on 22 June 1977.

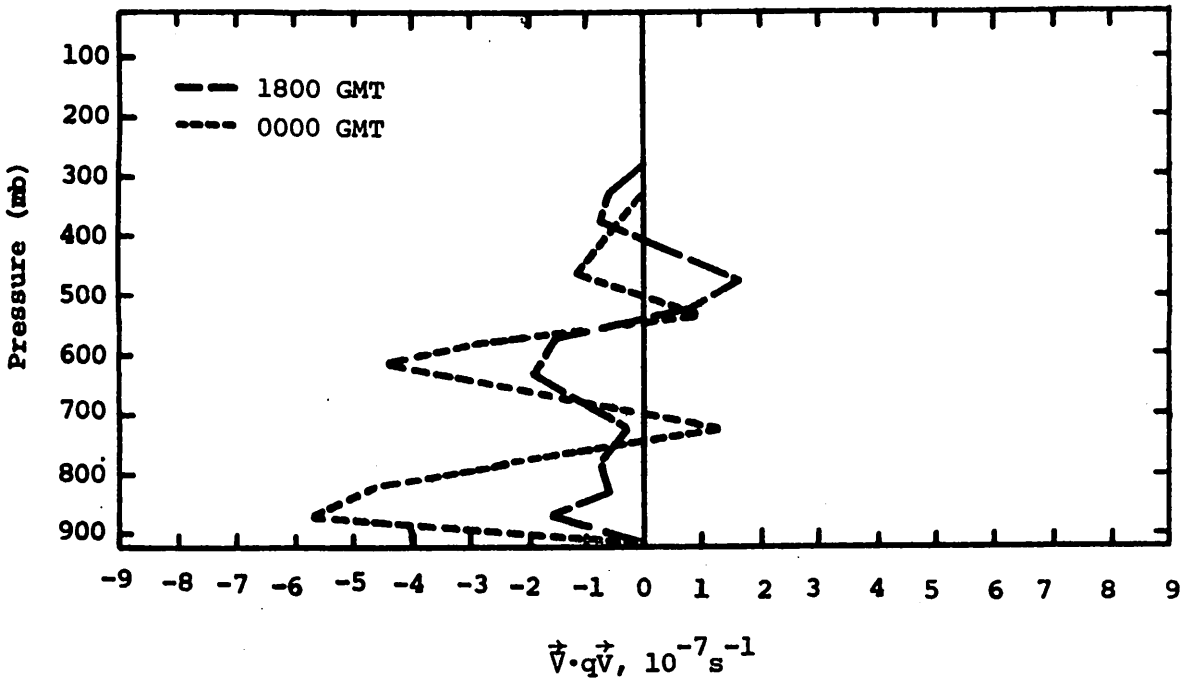

Fig. 5.9.3.3 Vertical profiles of moisture divergence on 22 June 1977.

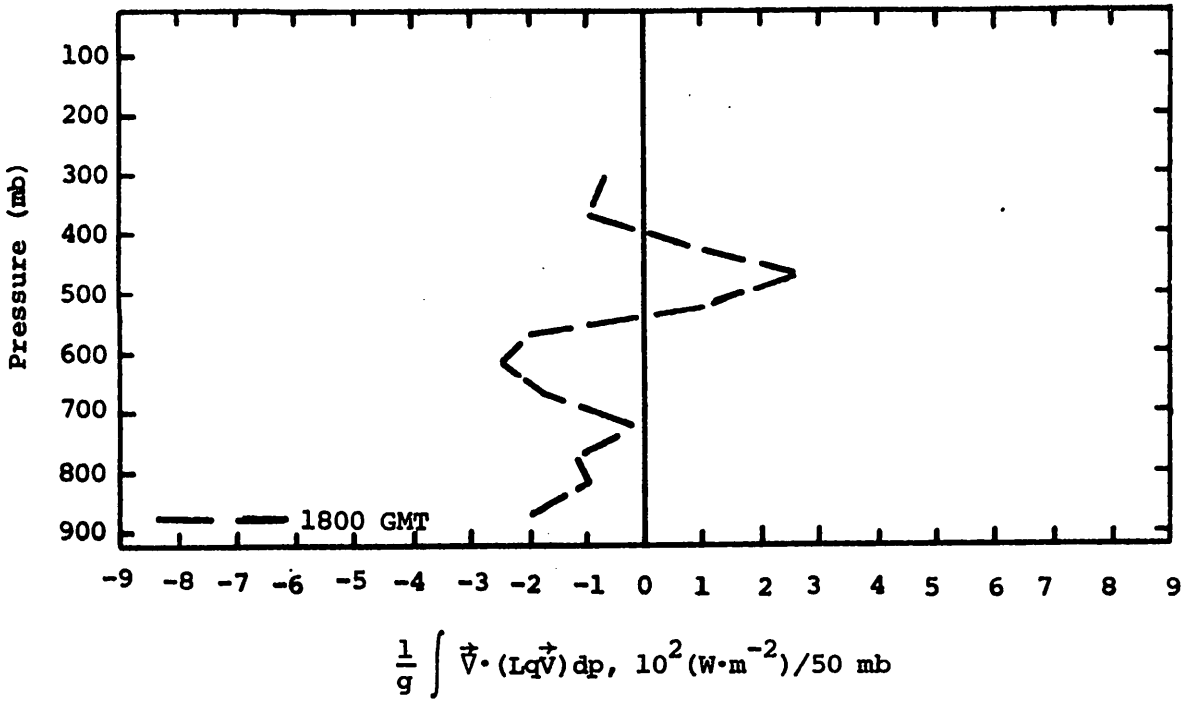

Fig. 5.9.4.1 Vertical profiles of the horizontal flux of latent heat energy on 22 June 1977.

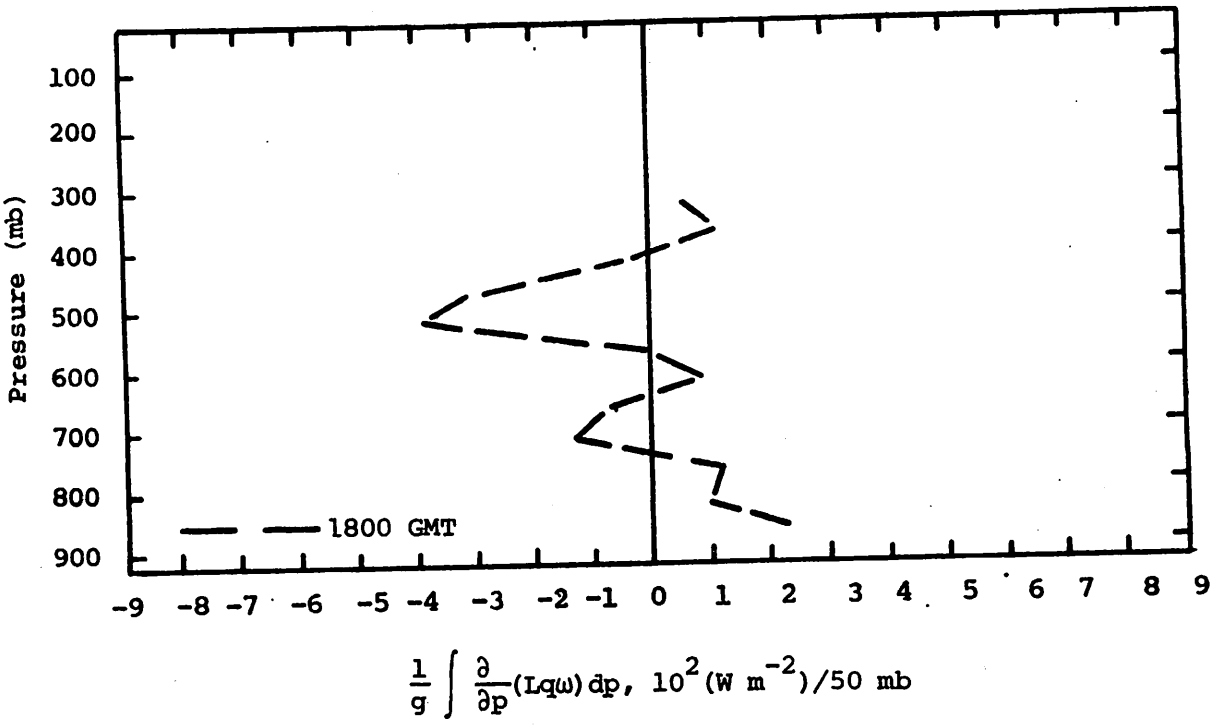

Fig. 5.9.4.2 Vertical profiles of the vertical flux of latent heat energy on 22 June 1977.

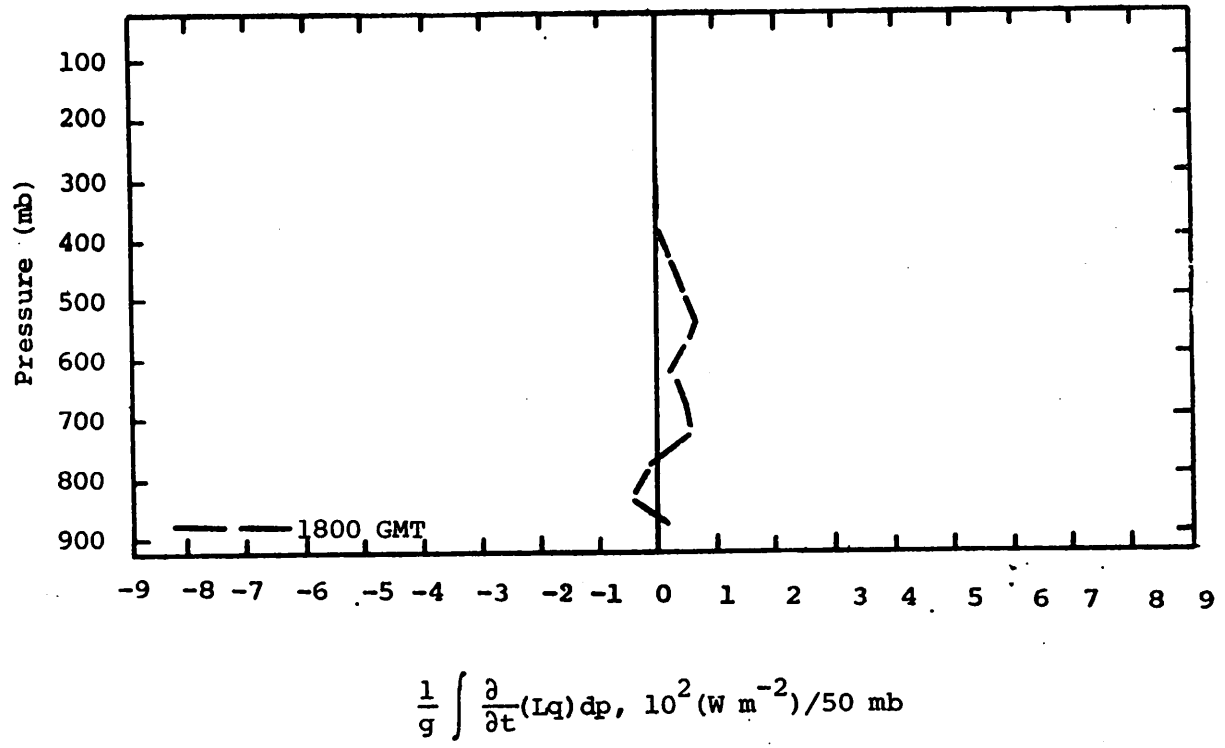

Fig. 5.9.4.3 Vertical profiles of the local change of latent heat energy on 22 June 1977.

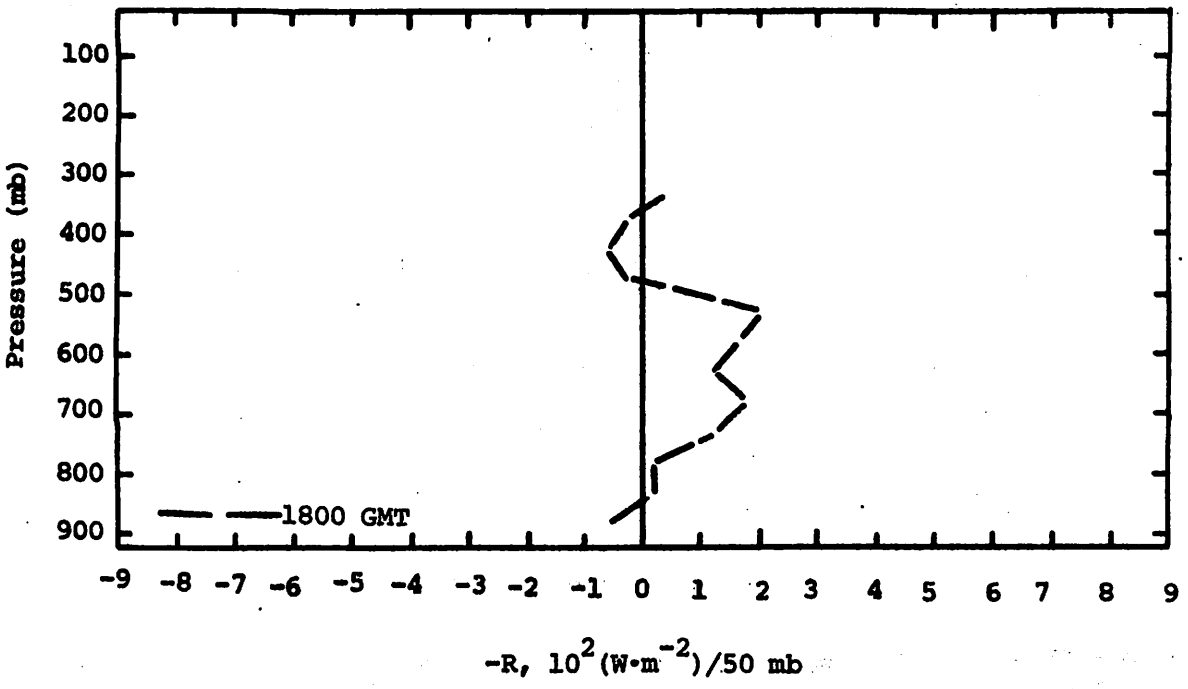

Fig. 5.9.4.4 Vertical profile of the residual of the latent heat energy equation on 22 June 1977.

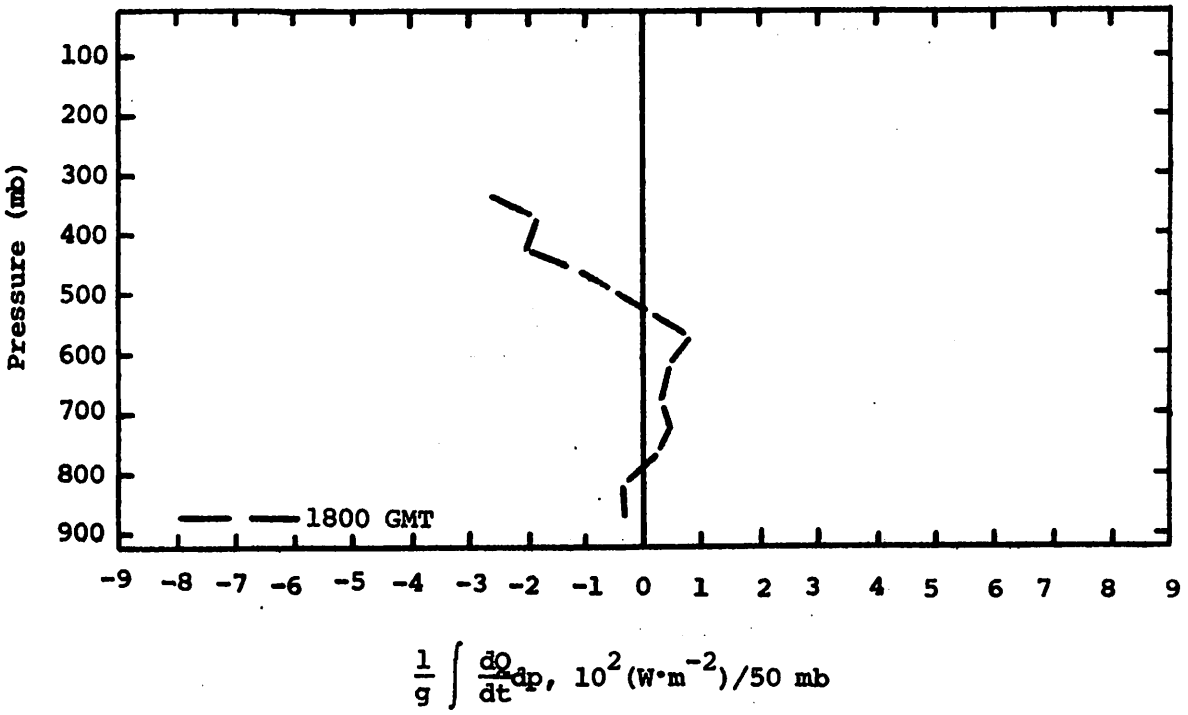

Fig. 5.9.4.5 Vertical profiles of diabatic heating computed from the first law of thermodynamics on 22 June 1977.

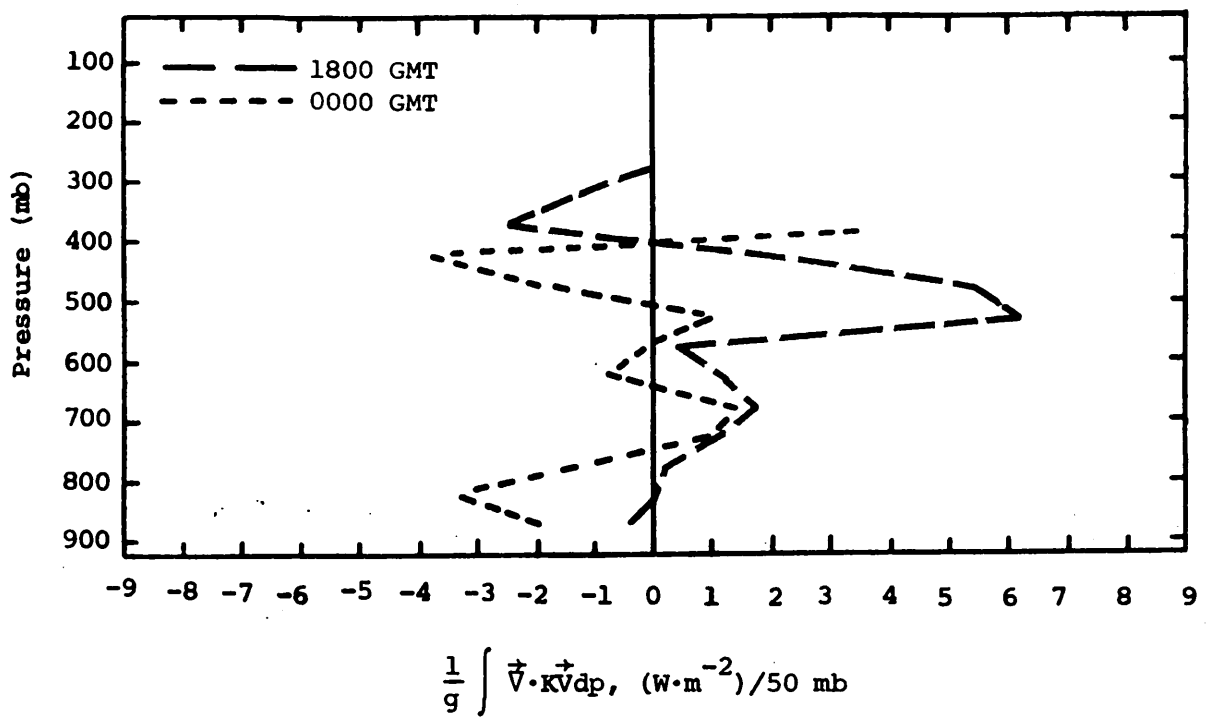

Fig. 5.9.4.6 Vertical profiles of the horizontal flux of kinetic energy on 22 June 1977.

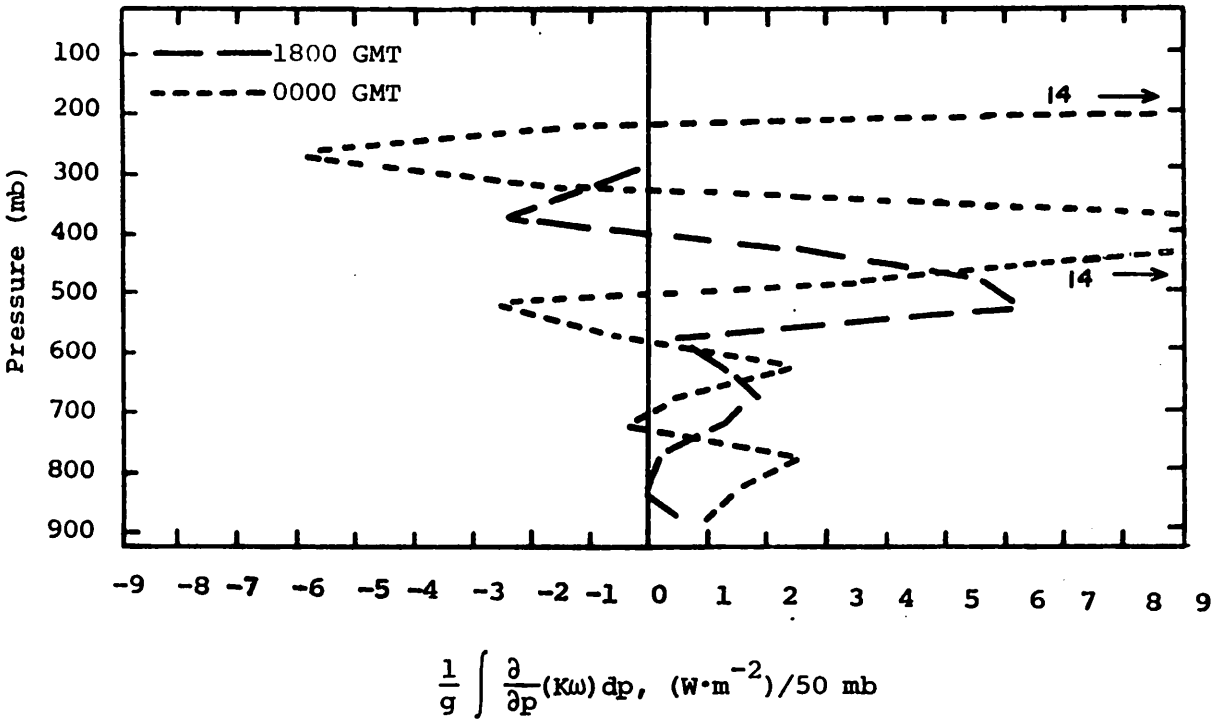

Fig. 5.9.4.7 Vertical profiles of the vertical flux of kinetic energy on 22 June 1977.

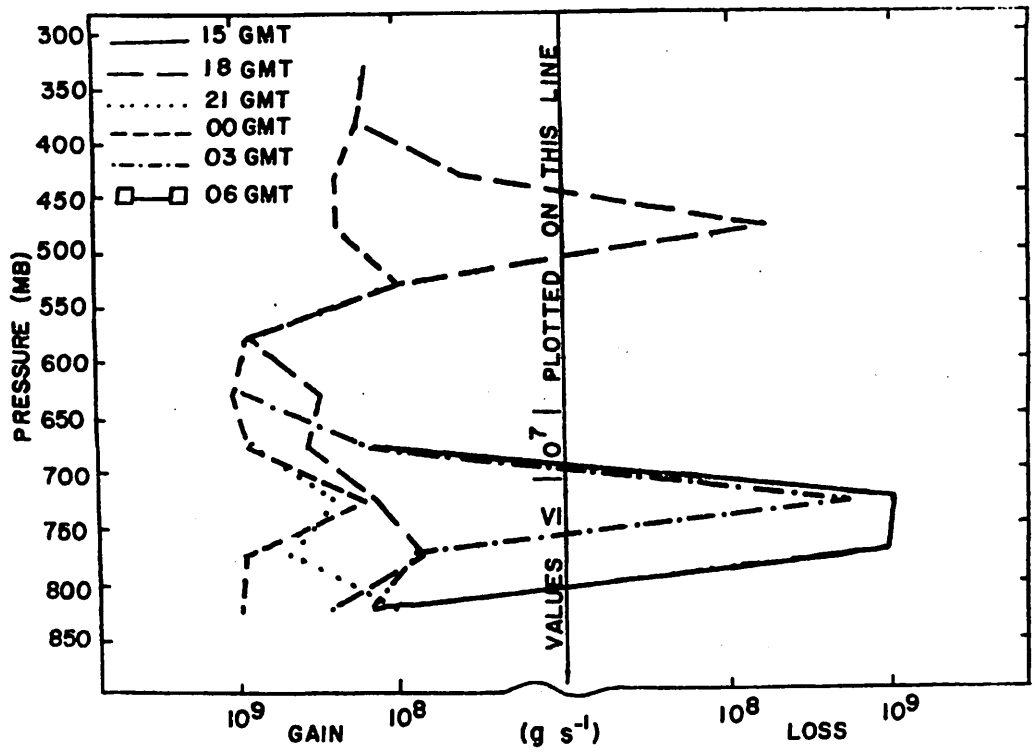

Fig. 5.9.5.1 Net horizontal transport of water vapor through boundaries of 50-mb layers (g s^{-1}) over the Texas HIPLEX area for 22 June 1977.

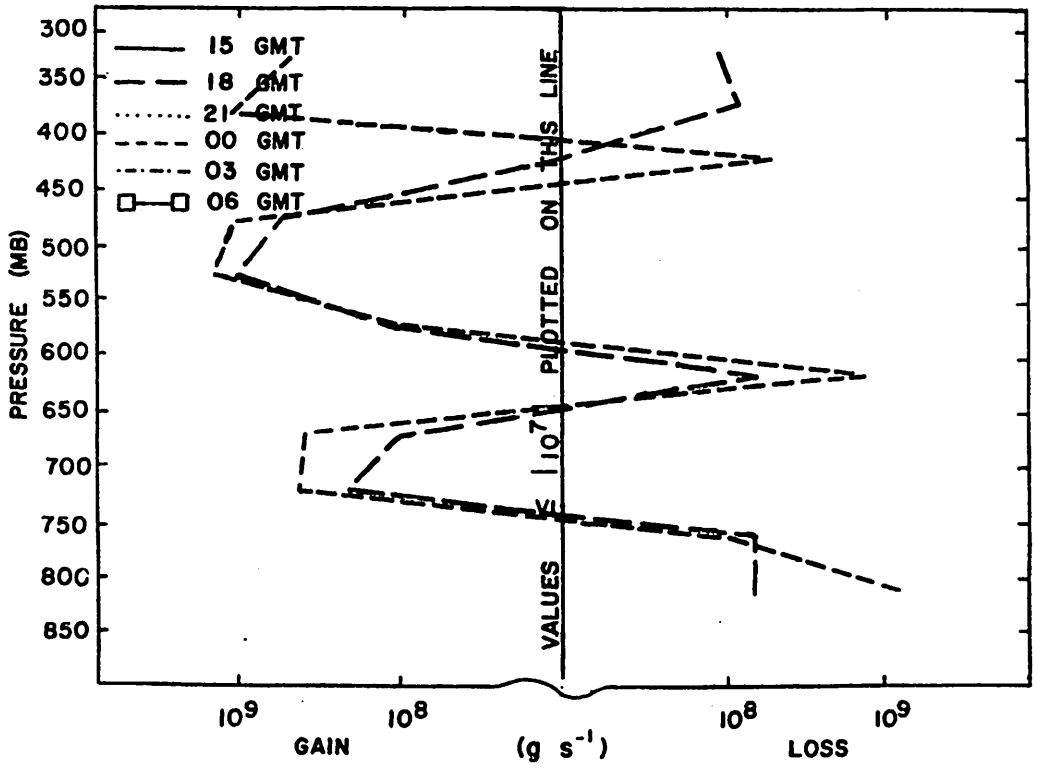

Fig. 5.9.5.2 Net vertical transport of water vapor through boundaries of 50-mb layers (g s^{-1}) over the Texas area for 22 June 1977.

similar and show several deep layers of net inflow near 700 and 500 mb.

Figure 5.9.5.3 shows profiles of vertical transport of water vapor through constant pressure surfaces. Again, due to missing data only profiles for 1800 and 0000 GMT are available. These profiles show strong upward vertical transports, especially at 0000 GMT.

Figure 5.9.5.4 shows profiles of combined net horizontal and vertical transport of water vapor. Profiles for 1500, 2100, and 0300 GMT are missing due to missing data and computational procedures. These profiles are similar and show a strong net inflow in layers above 750 mb. Transport of water vapor in layers above 400 mb remains high indicating a nearly uniform water vapor distribution with height.

Figure 5.9.5.5 shows profiles of the total mass of water vapor. Profiles for 1500, 2100, and 0300 GMT terminate above 650 mb due to missing data. Values of water vapor remain high in the lower layers throughout the day, indicating the presence of convective activity.

Figure 5.9.5.6 shows profiles of the local rate-of-change in the total mass of water vapor. Due to missing data, local changes in only the lower layers could be computed. Water vapor amounts increased with time throughout the day. Between 0000 and 0300 GMT, a large increase occurred which is attributed to decreased convective activity during this time.

5.10 23 June 1977

5.10.1 Radar

The charts of radar echoes for this day (Fig. 5.10.1.1) show that echoes occurred every hour throughout the period. A line of echoes moved from the southeast toward the northwest through the area between 1800 and 2200 GMT. This direction of movement is highly unusual since the echoes in this area usually move in the opposite direction. Not only is the line that moved over the area between 1900 and 2100 GMT with tops exceeding 9.1 km (30K ft) an interesting feature on this day, a large and isolated echo was located near the center of the area at 2200 GMT and moved westward to the edge of the area west of Lamesa by 0100 GMT. Very little convective activity was observed prior to 1800 GMT or after 0100 GMT.

5.10.2 Surface

The line of echoes passing through the area between 1900 and 0000 GMT is reflected in fields of surface temperature (Fig. 5.10.2.1). Several isolated centers of minimum surface temperature coincide with areas of convective activity. Lower temperatures occurred near Vincent and Snyder at 2000 GMT

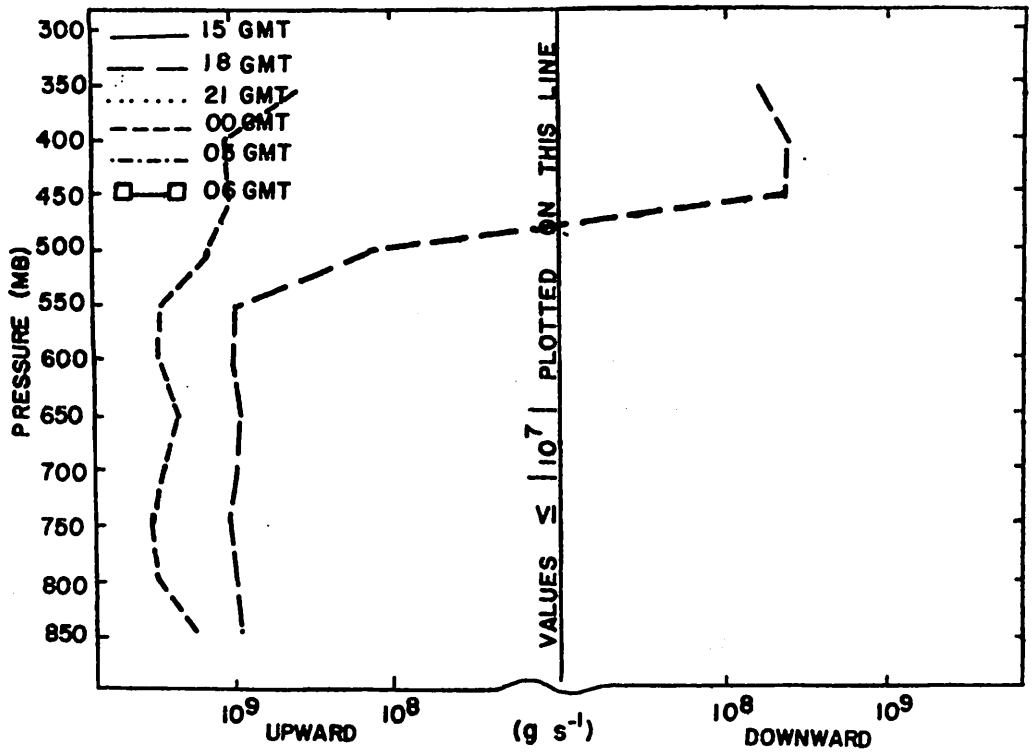

Fig. 5.9.5.3 Vertical transport of water vapor through constant pressure surfaces (g s^{-1}) over the Texas HIPLEX area for 22 June 1977.

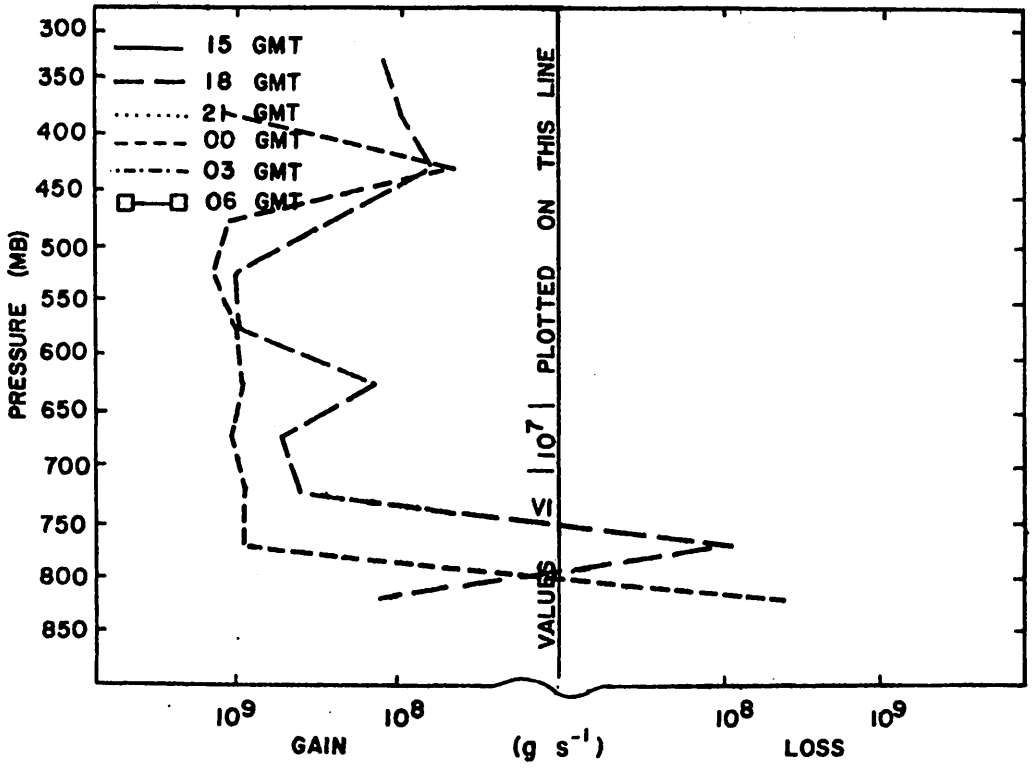

Fig. 5.9.5.4 Combined net horizontal and vertical transport of water vapor through boundaries of 50-mb layers (g s^{-1}) over the Texas HIPLEX area for 22 June 1977.

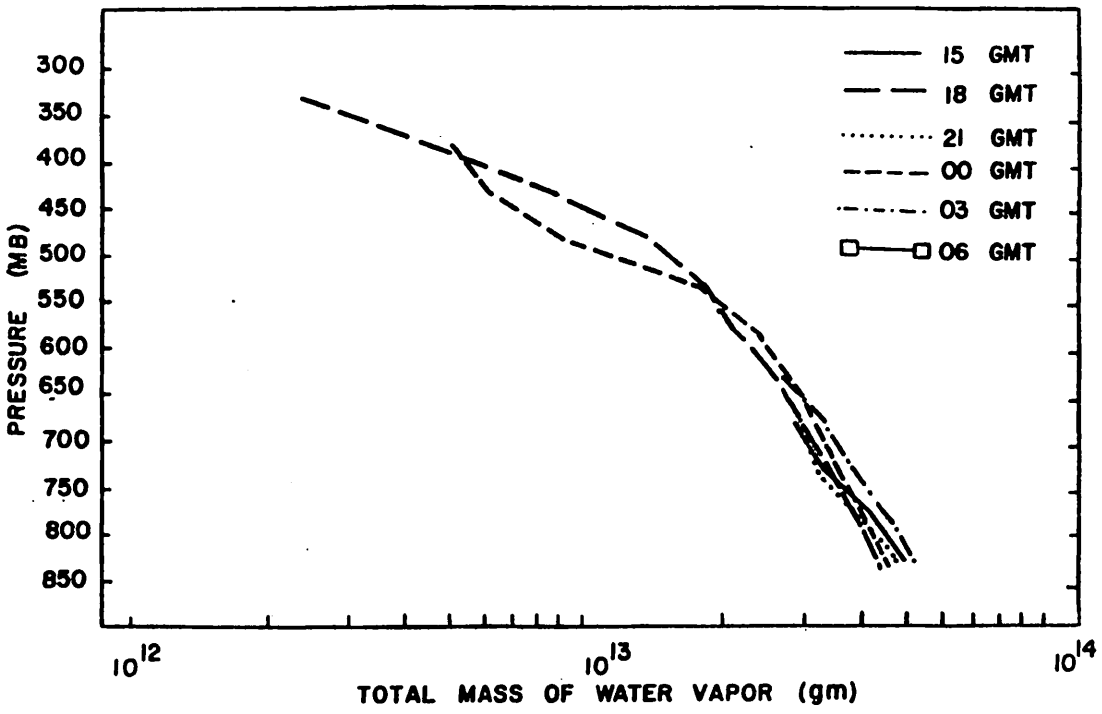

Fig. 5.9.5.5 Total mass of water vapor in layers 50 mb deep (g) over the Texas HIPLEX area for 22 June 1977.

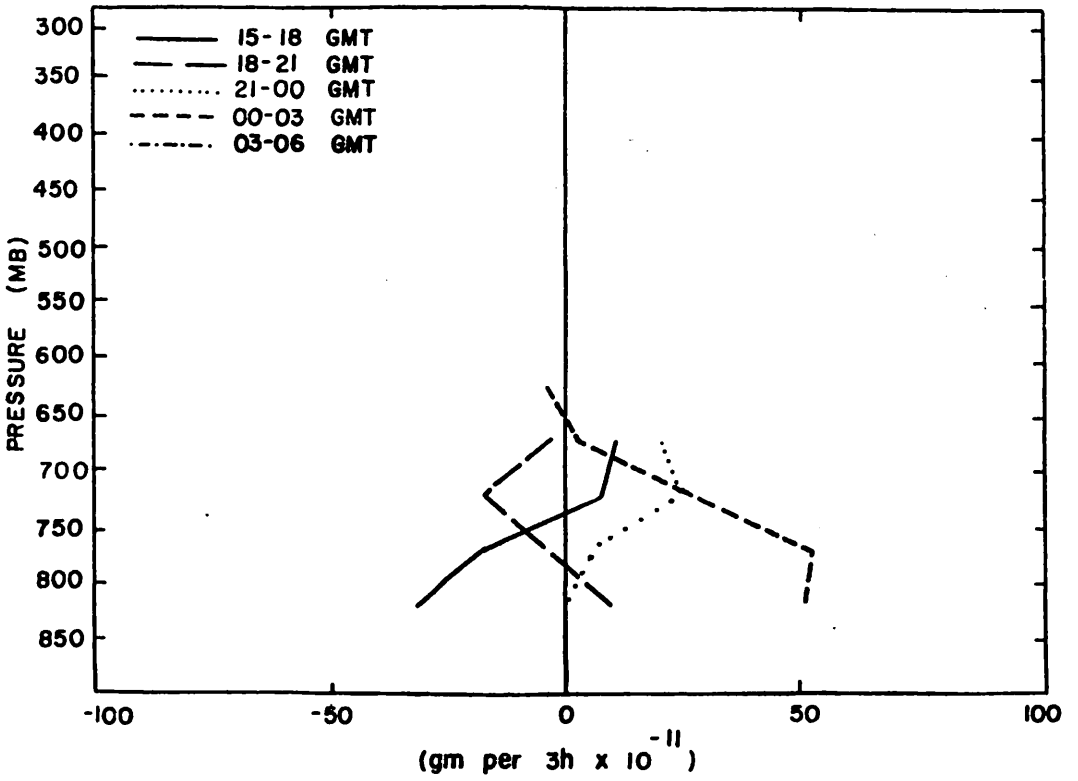

Fig. 5.9.5.6 Local rate-of-change in total mass of water vapor (g per 3h x 10^{-11}) over the Texas HIPLEX area for 22 June 1977.

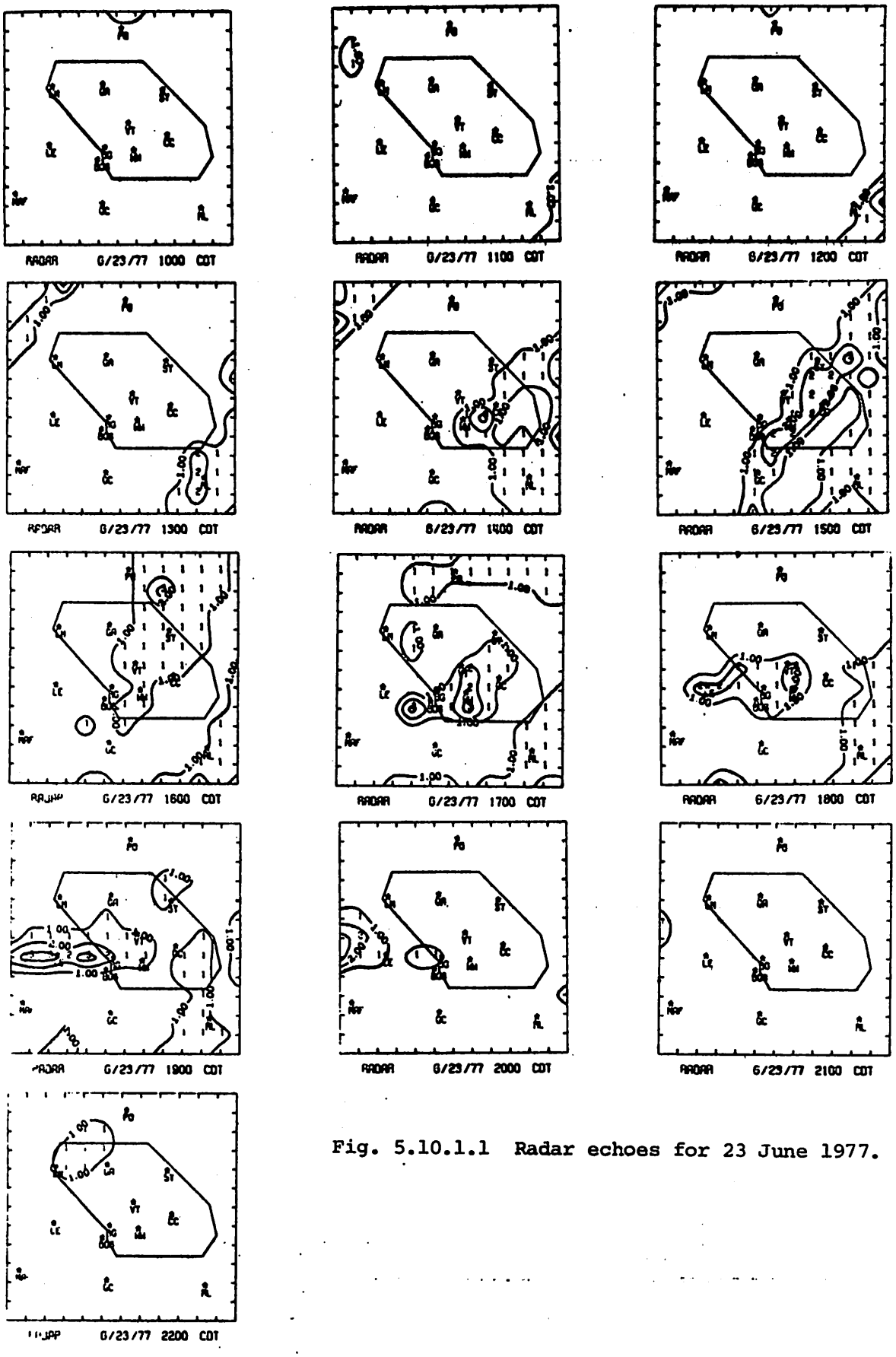

Fig. 5.10.1.1 Radar echoes for 23 June 1977.

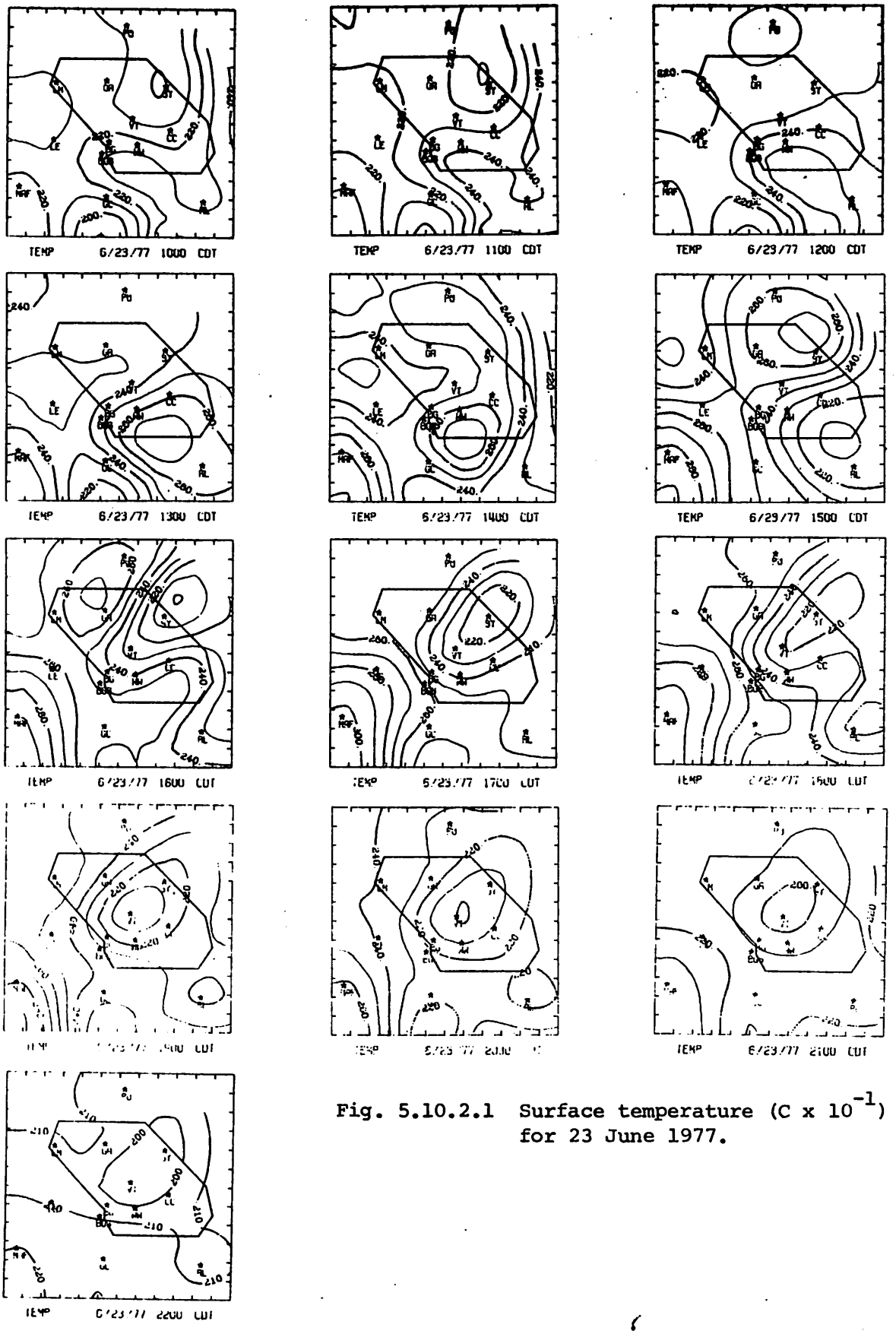

Fig. 5.10.2.1 Surface temperature (C x 10^{-1}) for 23 June 1977.

with the passage of the line. Fields of surface mixing ratio (Fig. 5.10.2.2) remained consistent with higher values in the southeast part of the area throughout the day. Mixing ratio reaches a maximum with the passage of the line at 2200 GMT near Robert Lee. A region of minimum mixing ratio was observed near Vincent throughout the day and was associated with regions of minimum surface temperature (Fig. 5.10.2.1). This might be due to the entrainment and subsequent downward transport of cool, dry air in this region. This pattern dominates fields of surface equivalent potential temperature (Fig. 5.10.2.3) which shows a large minimum center located over the center of the network.

Fields of terrain-induced vertical motion (Fig. 5.10.2.4) remain relatively unchanged throughout the day. However, upward motion of over 2 cm s^{-1} occurred near Gail in association with the passage of the line at 2100 GMT. A strong center of surface velocity divergence (Fig. 5.10.2.5) was observed at 2000 GMT in the vicinity of strong convection. Following passage and dissipation of the line, regions of strong divergence occurred around 0200 GMT. Vertical motion 50 mb above the surface (Fig. 5.10.2.6) remained small in magnitude with variable patterns.

Fields of surface moisture divergence (Fig. 5.10.2.7) show an area of strong convergence near Walsh-Watts in association with convective activity and surface velocity convergence at 2000 GMT. Following 0000 GMT surface moisture divergence dominated as convective activity dissipated. Vertical flux of moisture 50 mb above the surface (Fig. 5.10.2.8) showed organized centers associated with observed echoes. These centers decreased in magnitude following the passage of convective activity. A center of strong upward moisture flux 50 mb above the surface occurred at 2000 GMT which was associated with heavy activity over that region. Values of surface vorticity (Fig. 5.10.2.9) remained small, and show no persistent organized patterns or centers.

The lowest sea level pressures (Fig. 5.10.2.10) occurred over the southeastern part of the area with no appreciable change during the day (Fig. 5.10.2.11).

5.10.3 Upper-Level Kinematic Parameters

The vertical profiles of horizontal mass divergence show no noticeably important features until 2100 and 0000 GMT when moderately strong and deep convergence develops coincident with thunderstorm formation over the network (Fig. 5.10.3.1). By 0300 GMT the deep convergence changes to low-level divergence and weak mid-level convergence when all activity had diminished

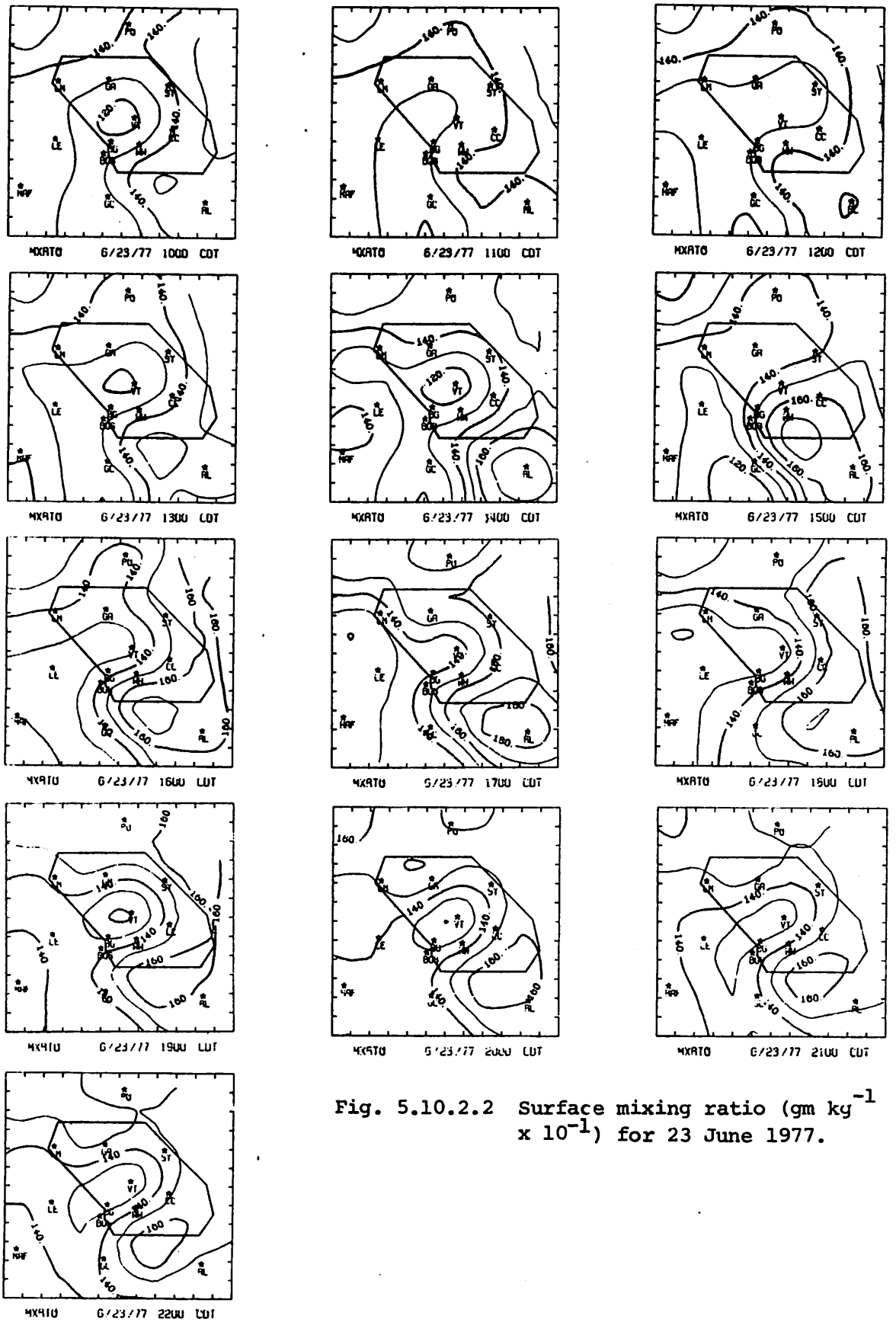

Fig. 5.10.2.2 Surface mixing ratio (gm kg^{-1} x 10^{-1}) for 23 June 1977.

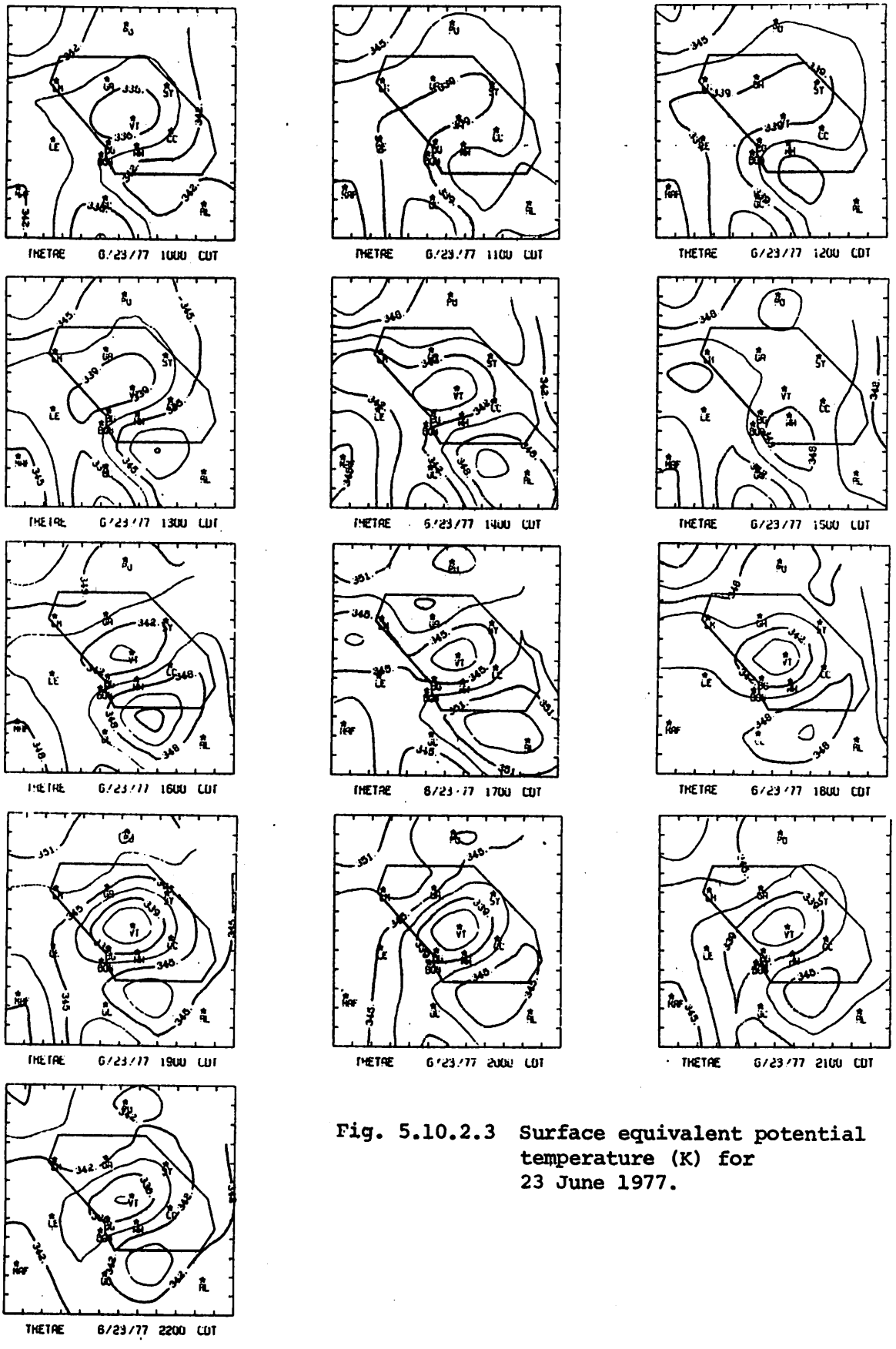

Fig. 5.10.2.3 Surface equivalent potential temperature (K) for 23 June 1977.

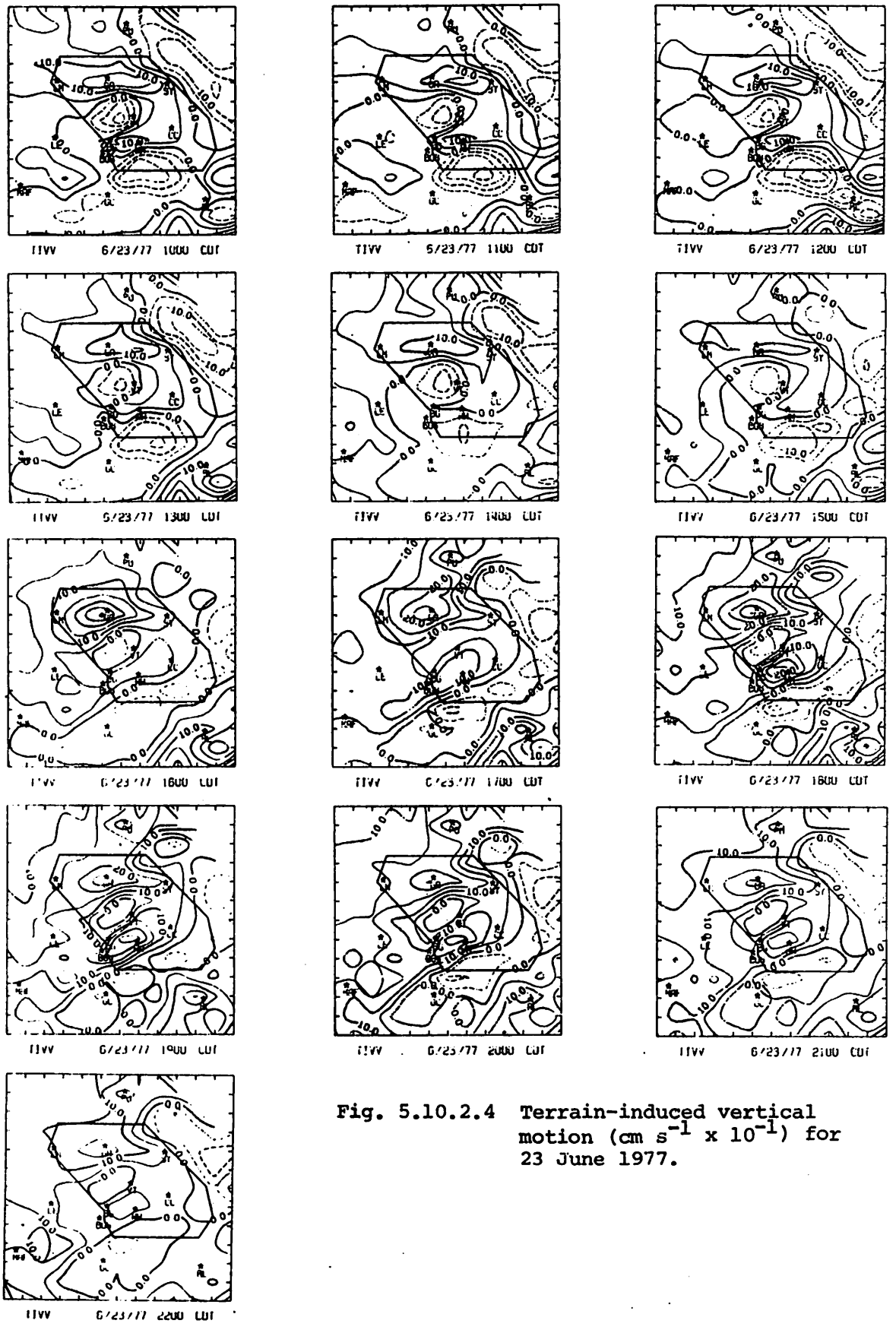

Fig. 5.10.2.4 Terrain-induced vertical motion (cm s^{-1} x 10^{-1}) for 23 June 1977.

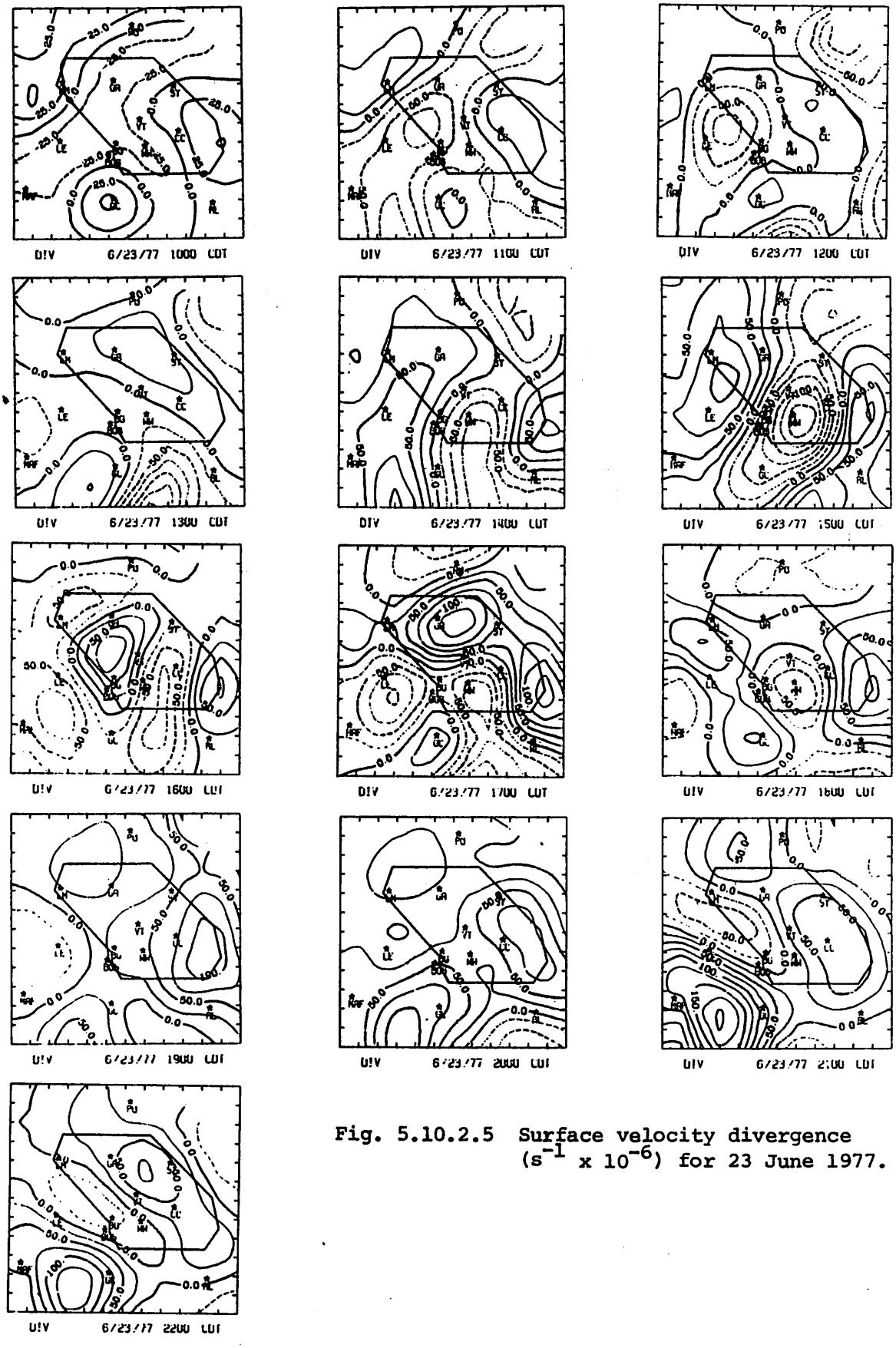

Fig. 5.10.2.5 Surface velocity divergence (s^{-1} x 10^{-6}) for 23 June 1977.

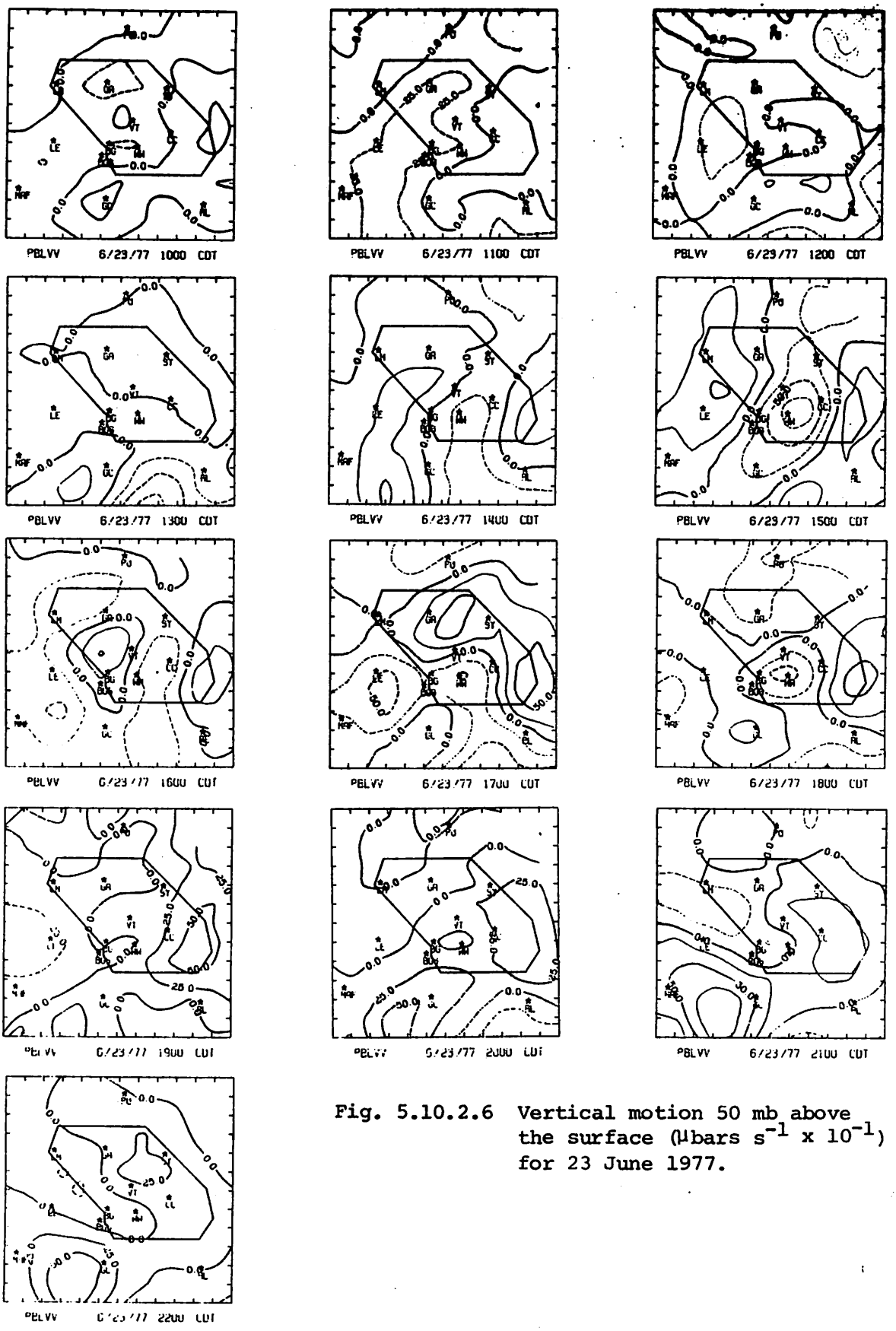

Fig. 5.10.2.6 Vertical motion 50 mb above the surface (μbars s^{-1} x 10^{-1}) for 23 June 1977.

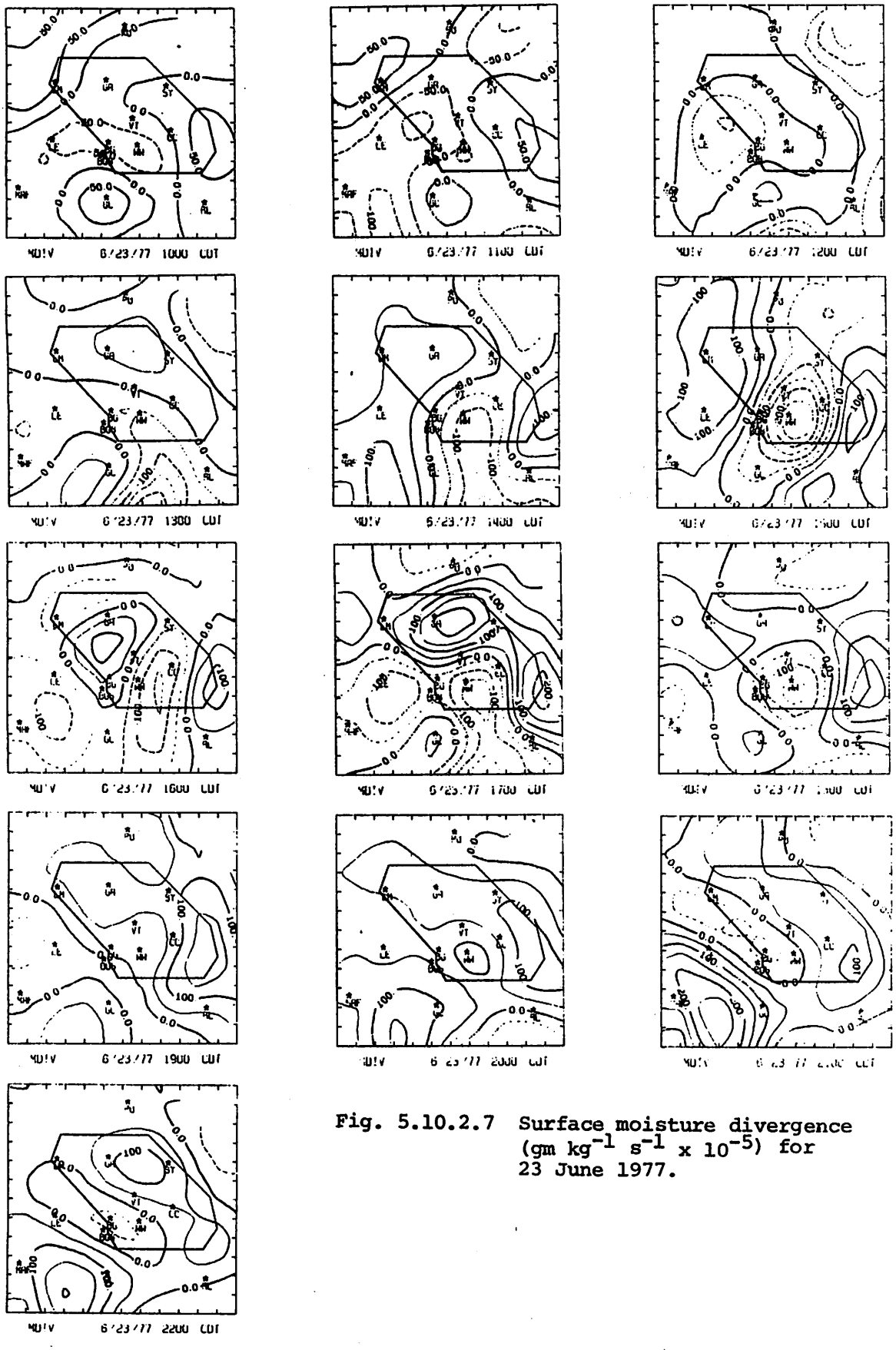

Fig. 5.10.2.7 Surface moisture divergence (gm kg^{-1} s^{-1} x 10^{-5}) for 23 June 1977.

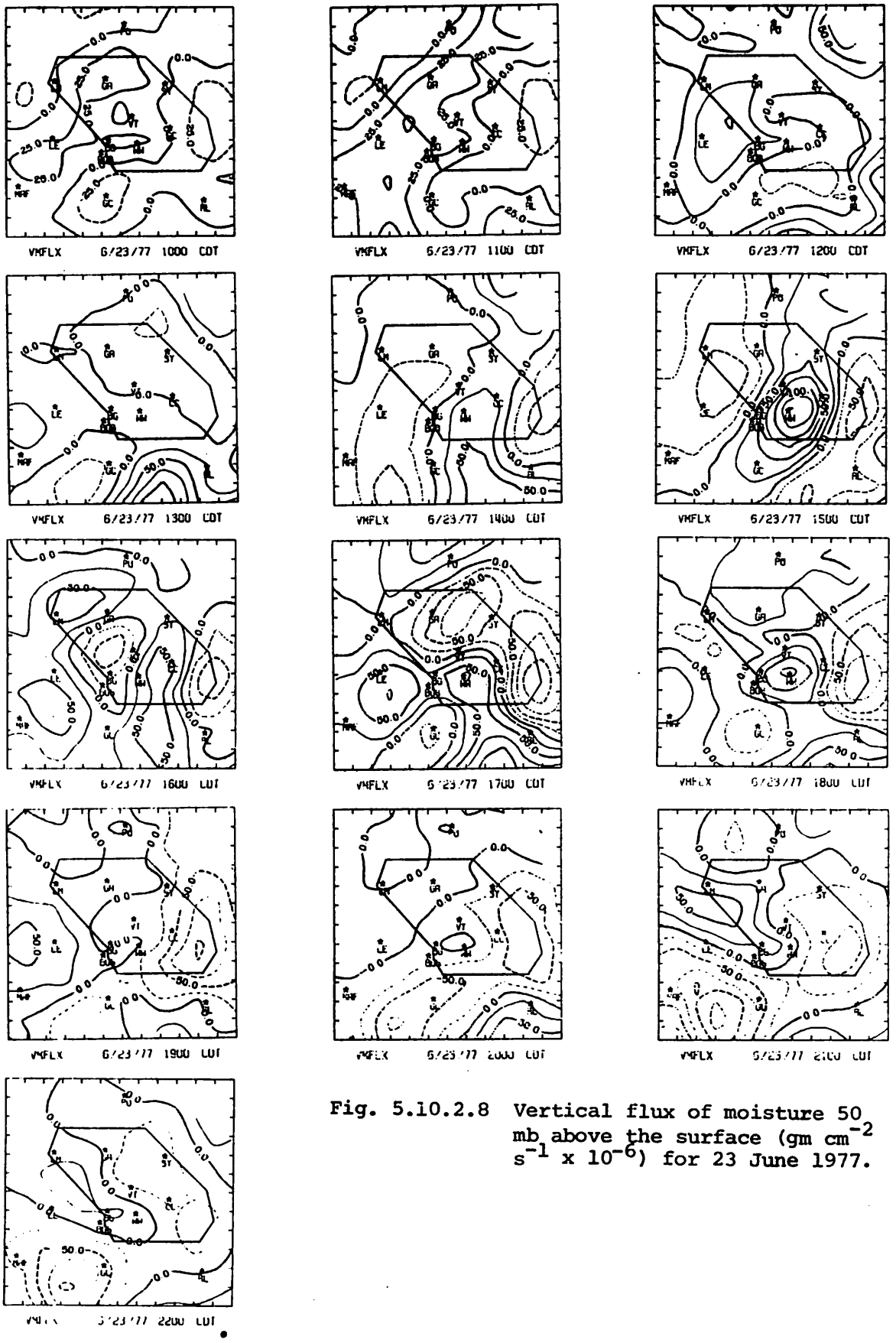

Fig. 5.10.2.8 Vertical flux of moisture 50 mb above the surface (gm cm^{-2} s^{-1} x 10^{-6}) for 23 June 1977.

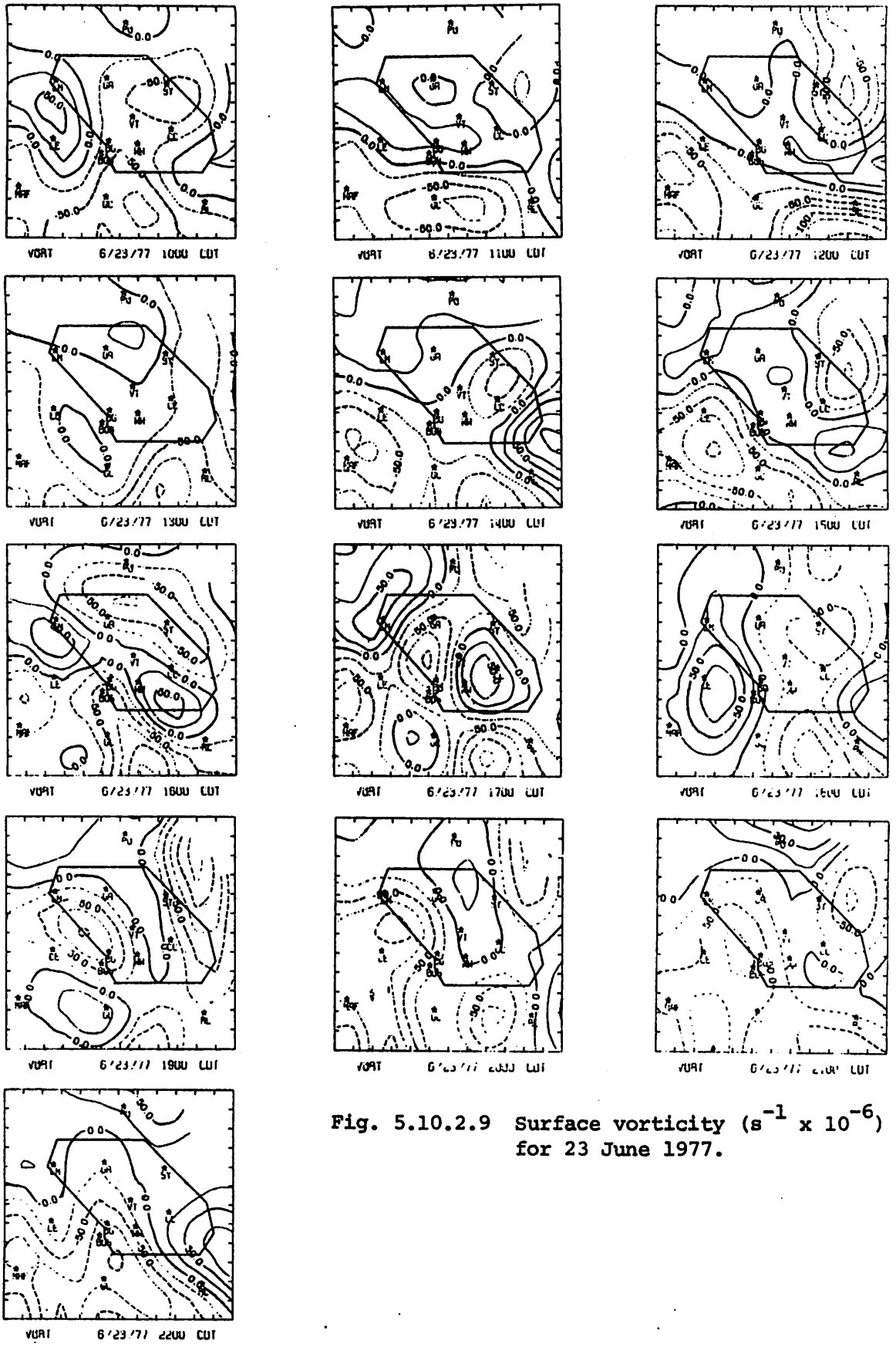

Fig. 5.10.2.9 Surface vorticity (s^{-1} x 10^{-6}) for 23 June 1977.

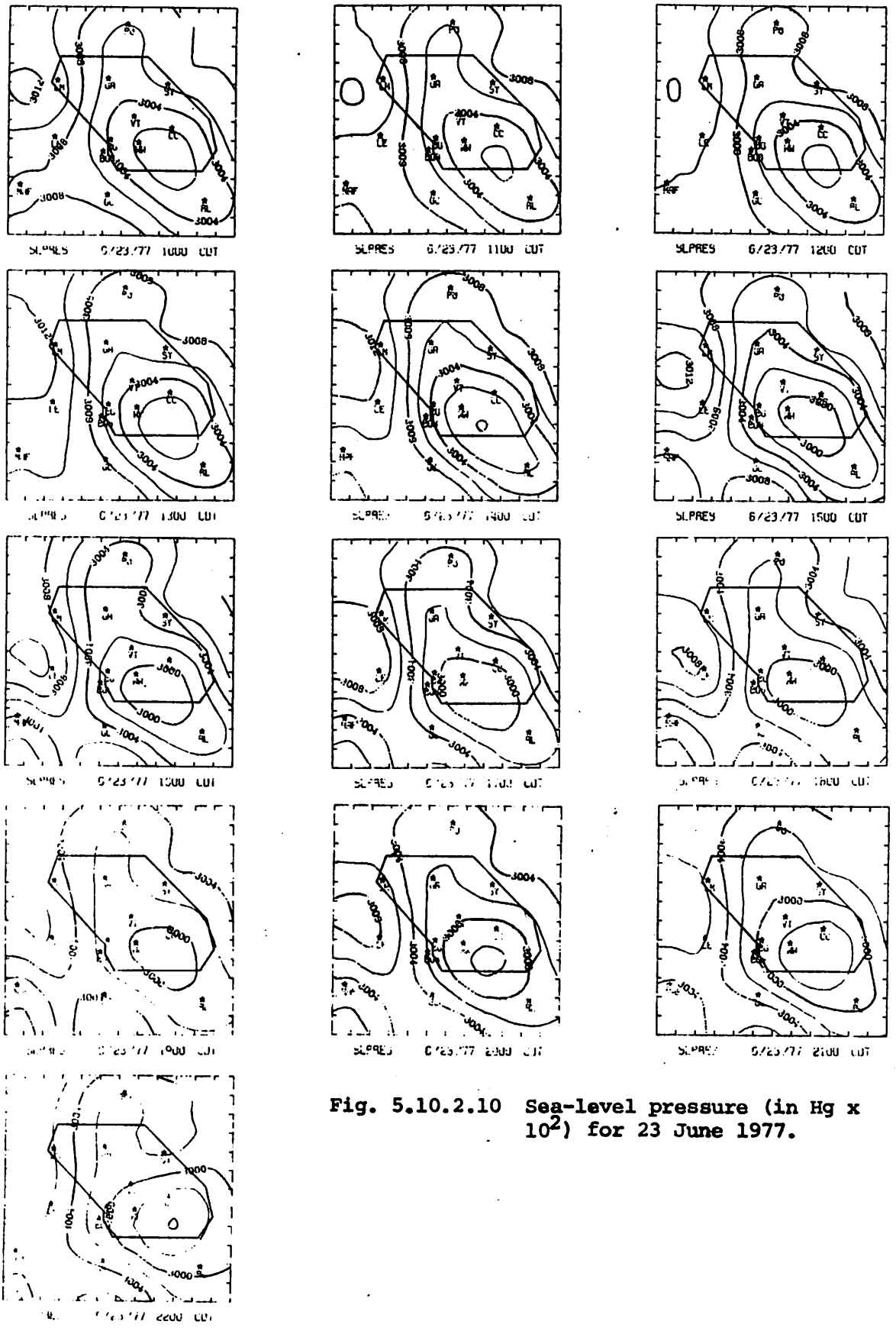

Fig. 5.10.2.10 Sea-level pressure (in Hg x 10^2) for 23 June 1977.

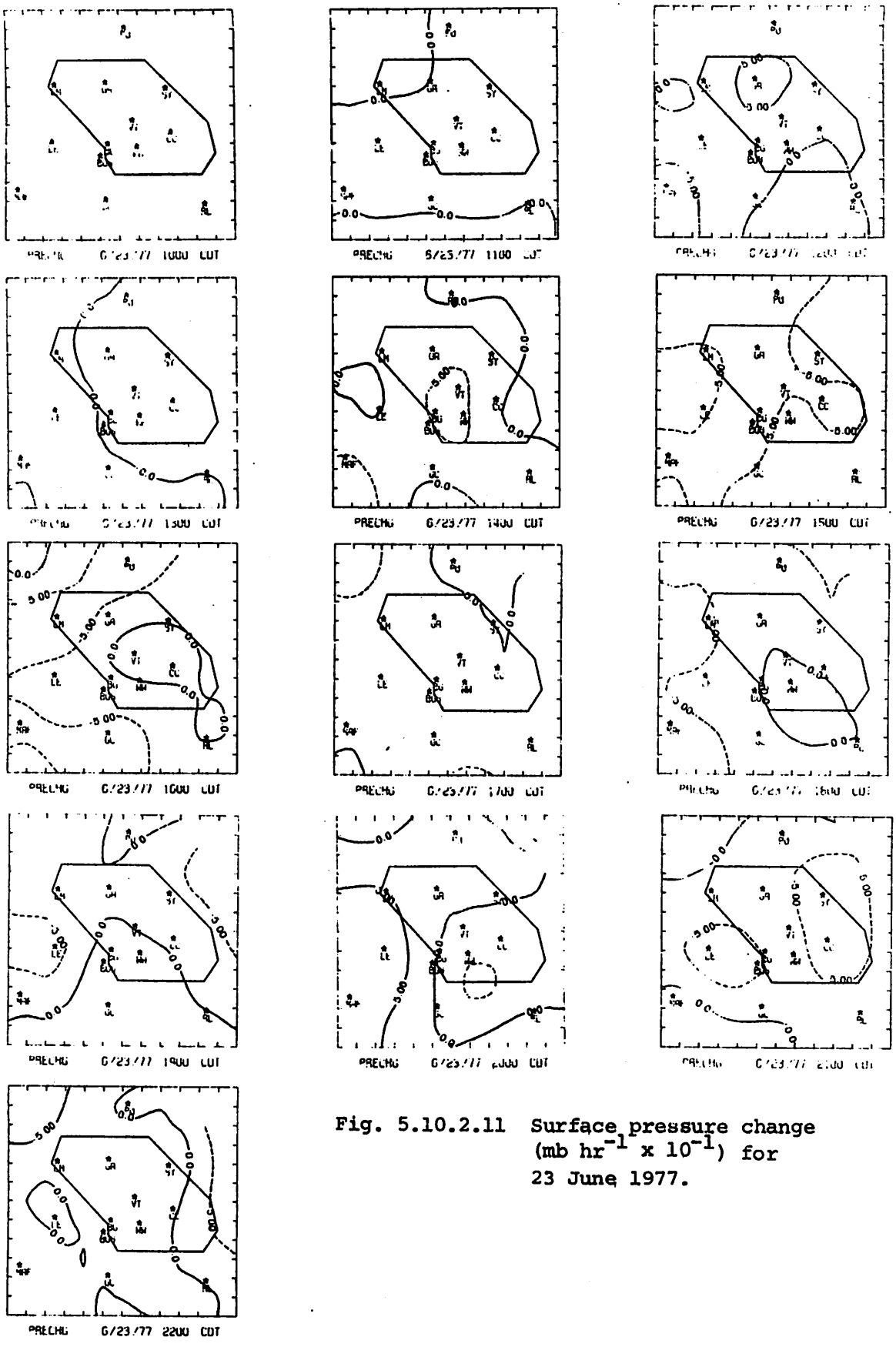

Fig. 5.10.2.11 Surface pressure change (mb hr^{-1} x 10^{-1}) for 23 June 1977.

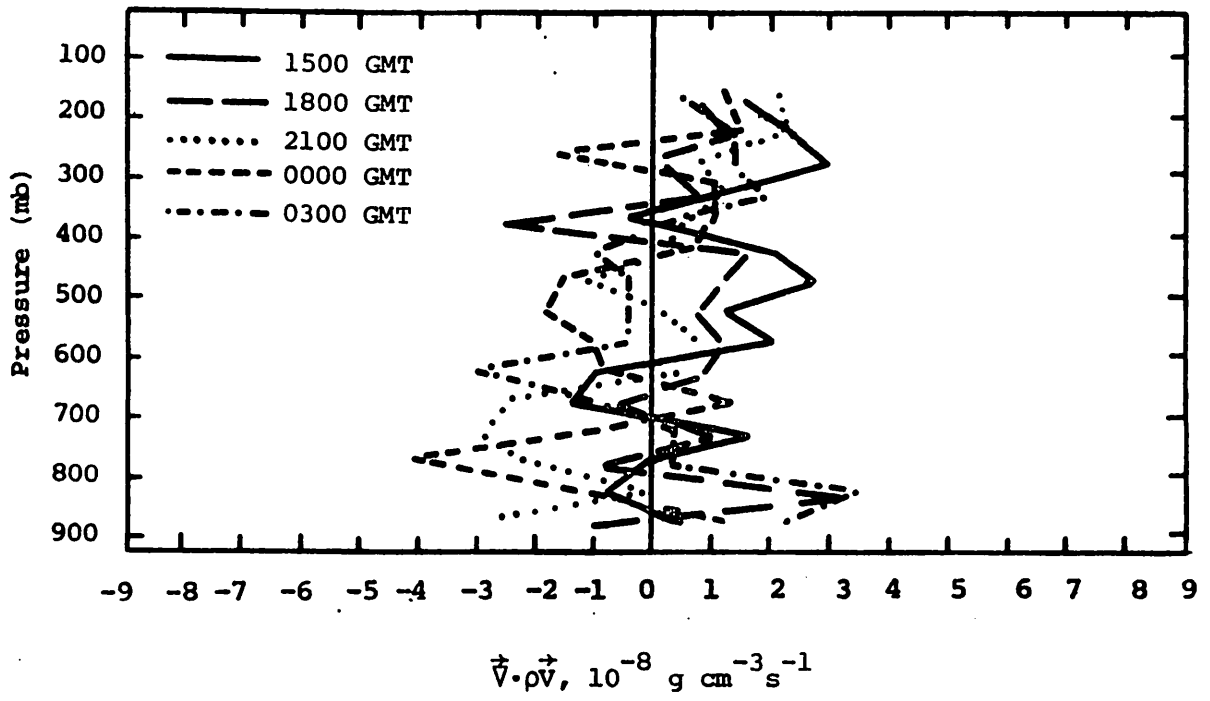

Fig. 5.10.3.1 Vertical profiles of mass divergence on 23 June 1977.

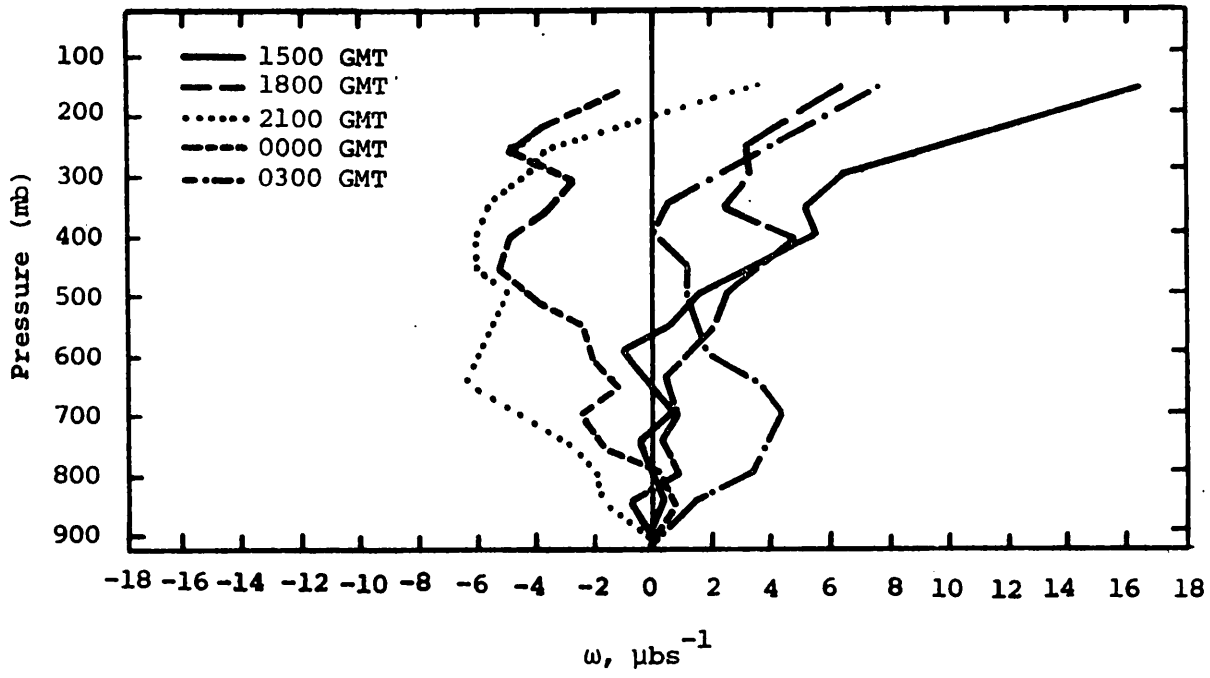

Fig. 5.10.3.2 Vertical profiles of vertical motion on 23 June 1977.

over the network.

Vertical velocities are near zero or downward at all levels both before and after storm development, and upwards at 2100 GMT and 0000 GMT when convection developed (Fig. 5.10.3.2).

Low-level horizontal moisture divergence was calculated both before and after the convective activity with convergence present at 2100 and 0000 GMT when storm development occurred (Fig. 5.10.3.3). Divergence values above 600 mb were relatively small at all times.

5.10.4 Energetics

Net horizontal outflow of latent heat energy occurred both before and after storm activity in low levels (Fig. 5.10.4.1). Net inflow was important only during times of activity. Vertical flux convergence of latent heat energy was computed in low levels before and after storm formation (1800 GMT and 0300 GMT) with weak flux divergence present at mid levels (Fig. 5.10.4.2). Vertical flux divergence and convergence were large in low- and mid-levels, respectively, during activity periods (2100 and 0000 GMT). Local changes of latent heat energy in low levels were relatively large before storm development, near zero at 2100 GMT, and negative afterwards (Fig. 5.10.4.3).

The residual term of the latent heat budget shows two important features (Fig. 5.10.4.4). At 1500 and 1800 GMT negative values below 600 mb are possibly associated with low-level cloud dissipation and evaporation, while positive values at most levels above 800 mb are probably caused by condensation that results in environmental heating when convective activity is present.

The diabatic heating profiles show no noticeably important features except above 300 mb when large cooling was calculated at all times except 2100 GMT (Fig.5.10.4.5).

Strong horizontal flux convergence in upper levels at 1800 GMT changes to divergence at 2100 GMT and returns to convergence at 0000 GMT (Fig. 5.10.4.6). The vertical flux divergence profiles show "near zero" values below 500 mb at all times and levels but become erratic and hard to interpret above 400 mb (Fig. 5.10.4.7).

5.10.5 Water Vapor Budget

Figure 5.10.5.1 shows vertical profiles of the net horizontal transport of water vapor. These profiles show a moisture stratification that is

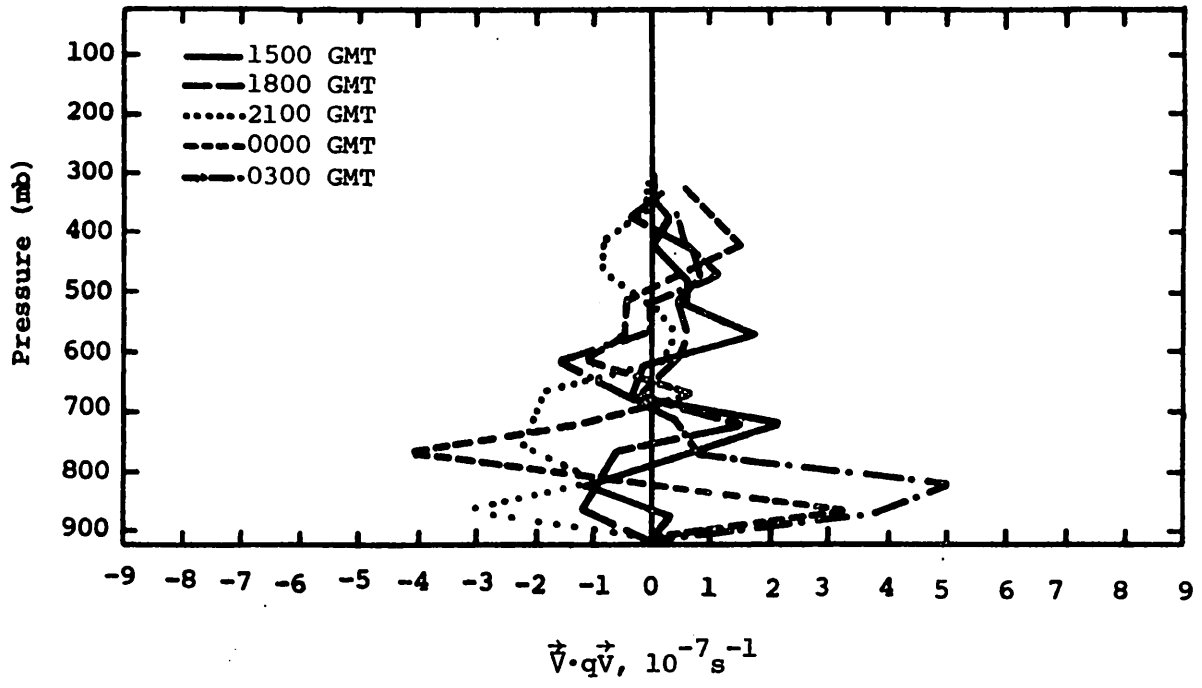

Fig. 5.10.3.3 Vertical profiles of moisture divergence on 23 June 1977.

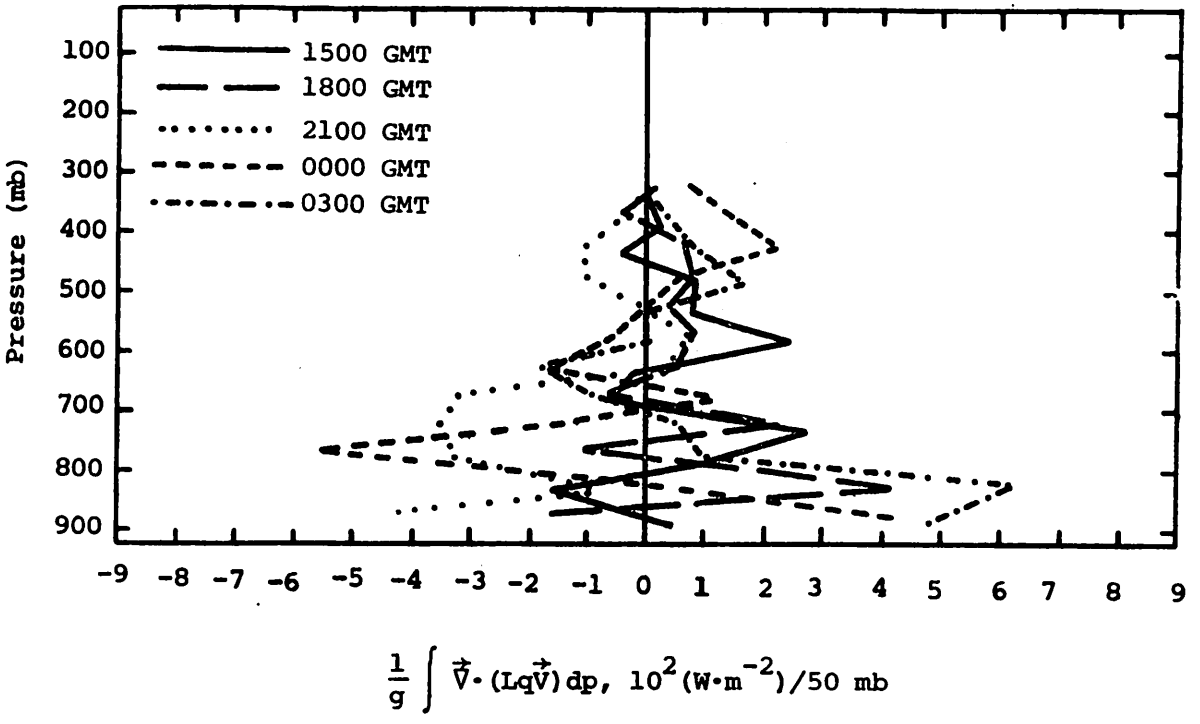

Fig. 5.10.4.1 Vertical profiles of the horizontal flux of latent heat energy on 23 June 1977.

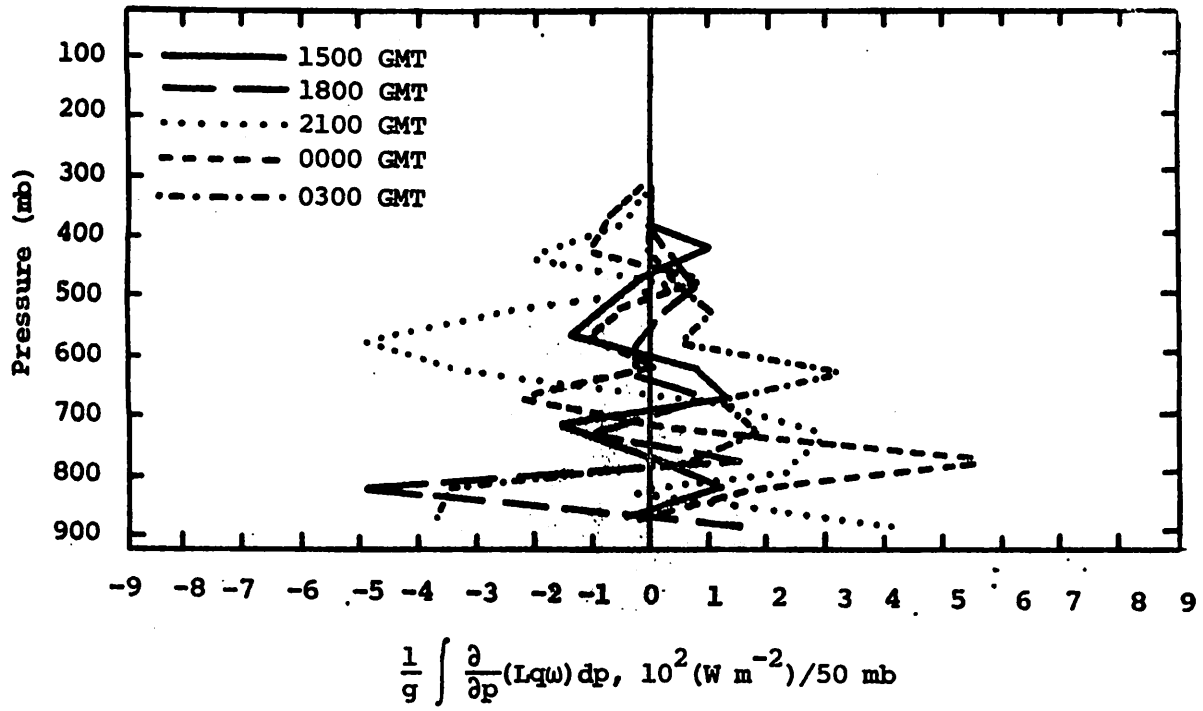

Fig. 5.10.4.2 Vertical profiles of the vertical flux of latent heat energy on 23 June 1977.

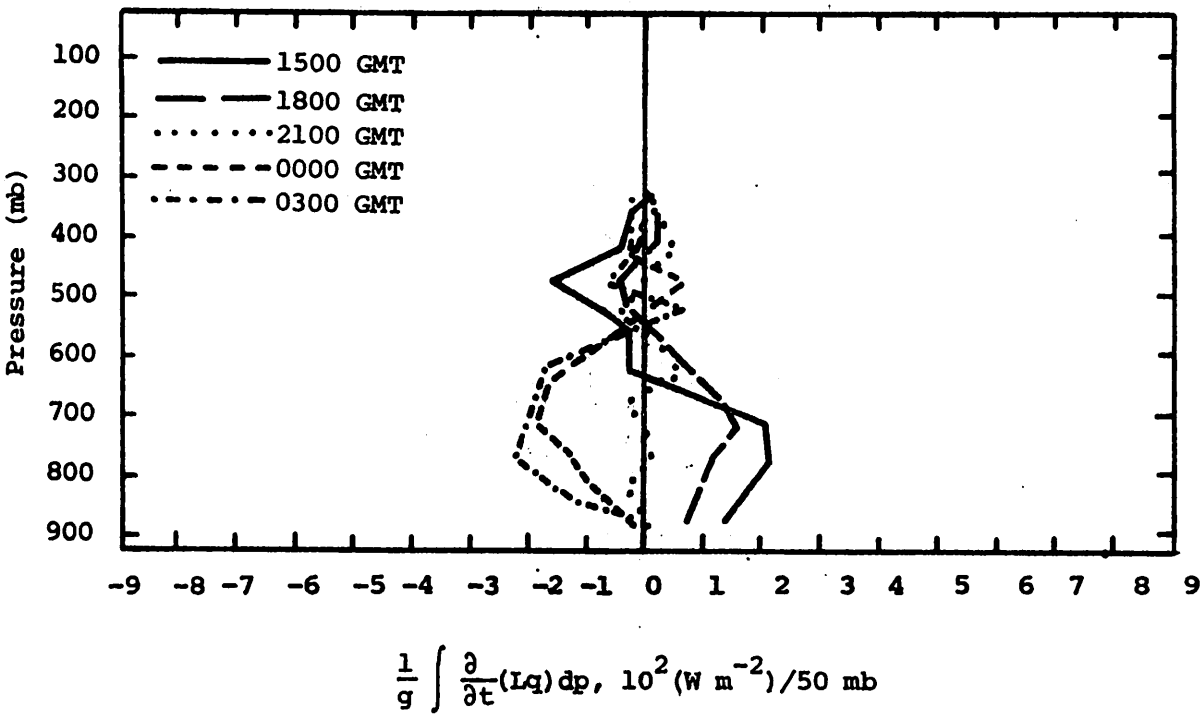

Fig. 5.10.4.3 Vertical profiles of the local change of latent heat energy on 23 June 1977.

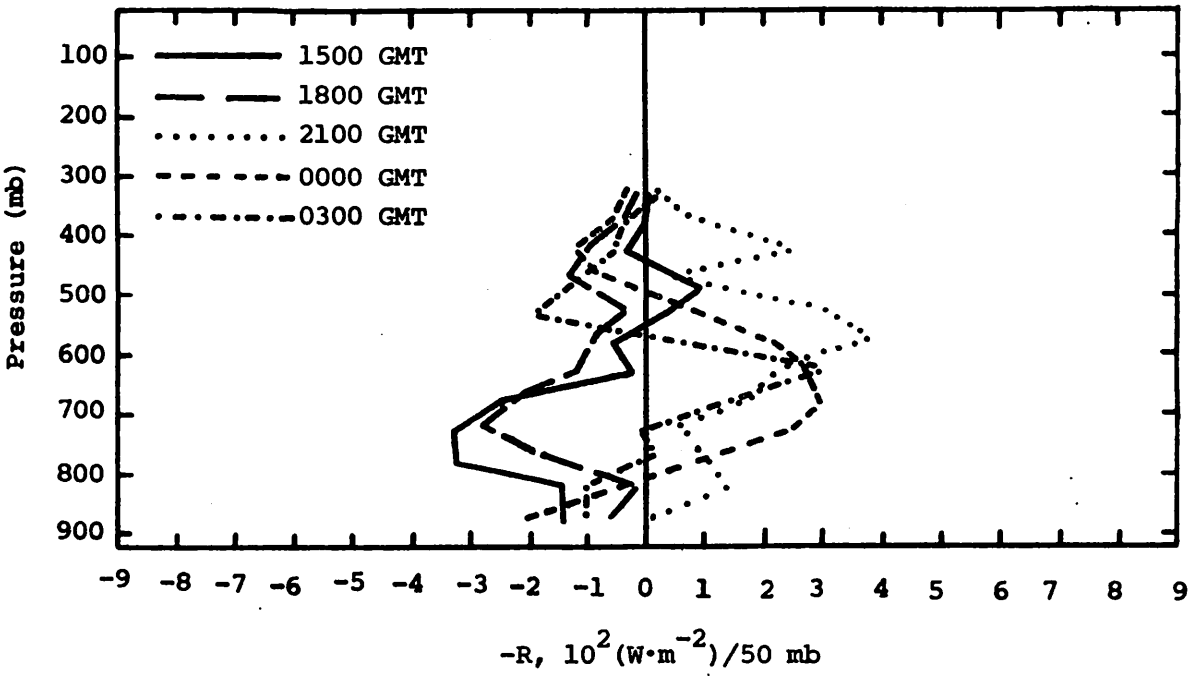

Fig. 5.10.4.4 Vertical profile of the residual of the latent heat energy equation on 23 June 1977.

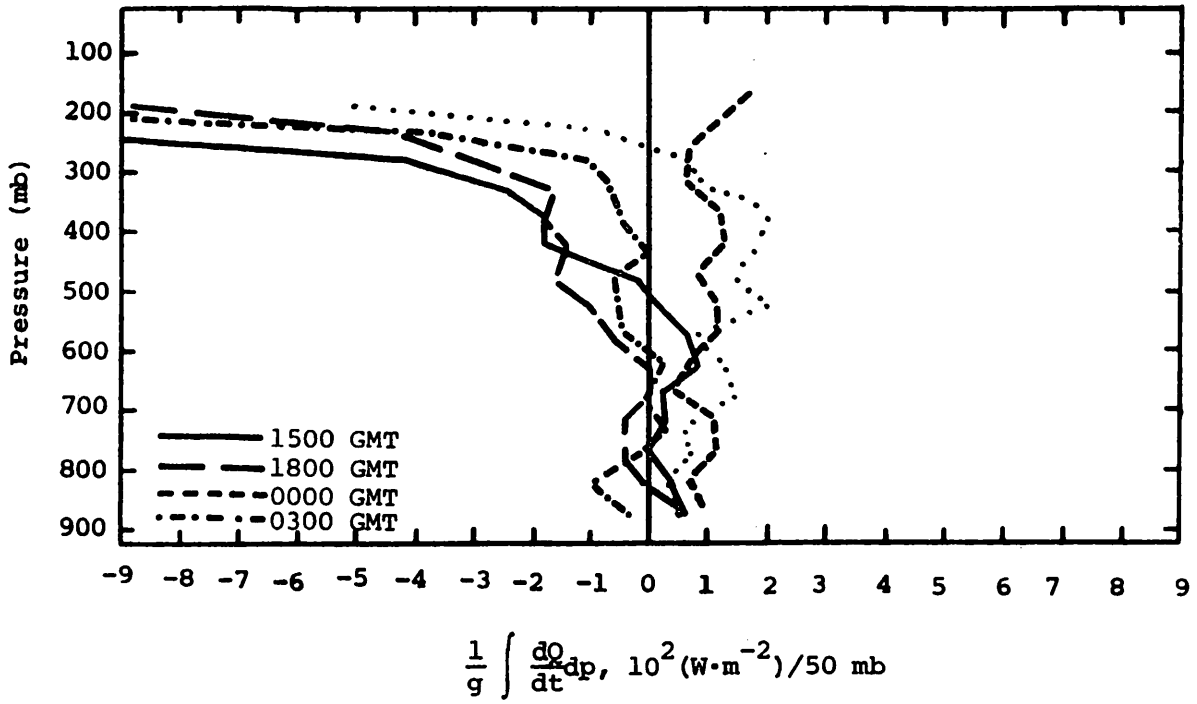

Fig. 5.10.4.5 Vertical profiles of diabatic heating computed from the first law of thermodynamics on 23 June 1977.

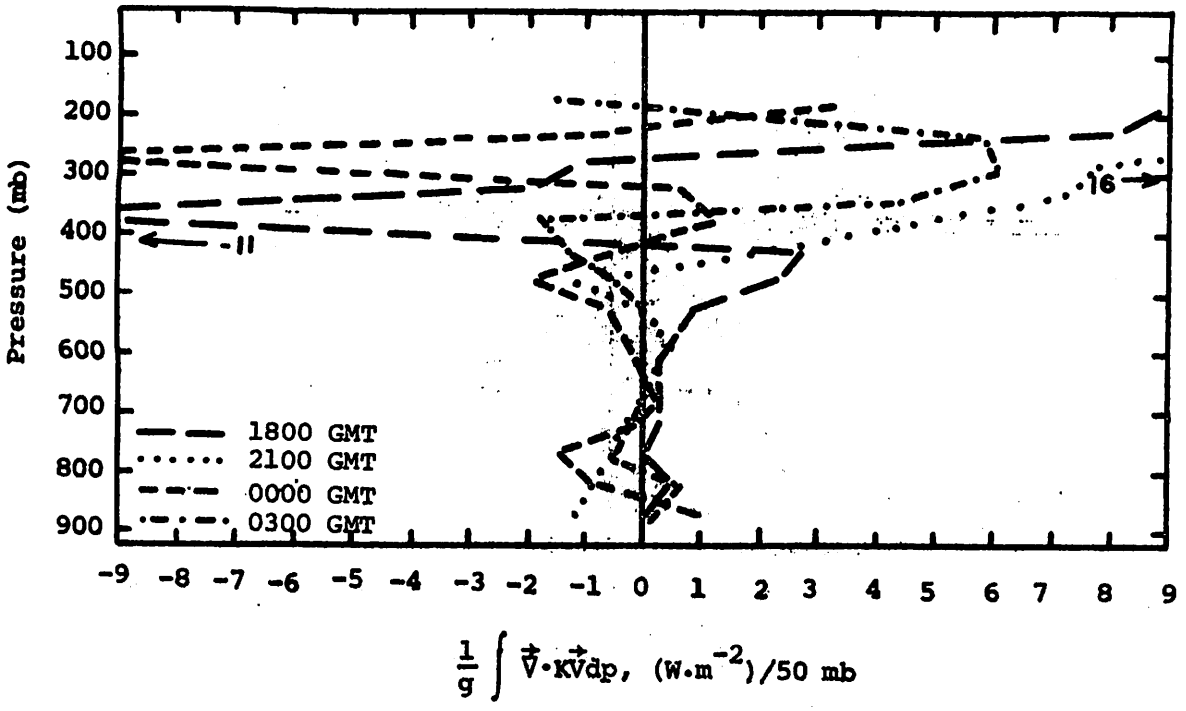

Fig. 5.10.4.6 Vertical profiles of the horizontal flux of kinetic energy on 23 June 1977.

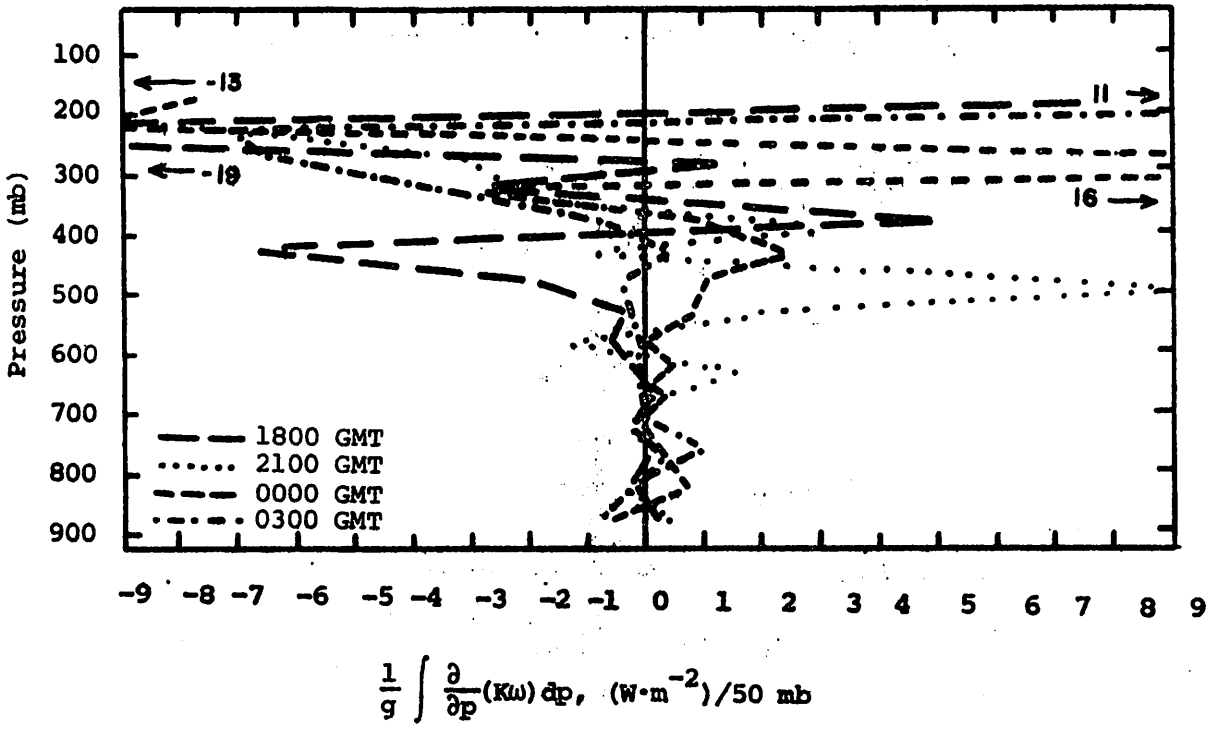

Fig. 5.10.4.7 Vertical profiles of the vertical flux of kinetic energy on 23 June 1977.

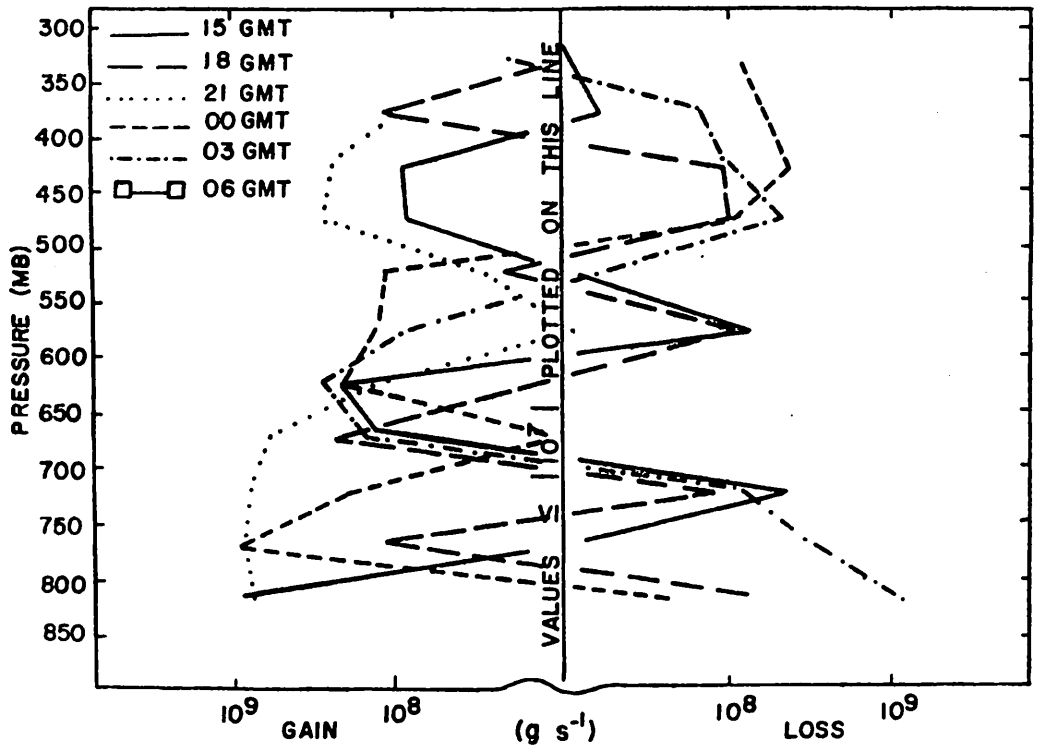

Fig. 5.10.5.1 Net horizontal transport of water vapor through boundaries of 50-mb layers (gm s^{-1}) over the Texas HIPLEX area for 23 June 1977.

present also in individual soundings. However, a general net inflow of water vapor occurred at 2100 GMT and 0000 GMT when maximum activity occurred.

Figure 5.10.5.2 shows profiles of the net vertical transport of water vapor. The moisture stratification in Figure 5.10.5.1 is also represented in these profiles. However, at 2100 GMT a large net inflow is observed in layers above 650 mb which is associated with an intensification of the line. Once heavy activity moves from the area at 0300 GMT, a large net outflow is observed in most layers.

Figure 5.10.5.3 shows profiles of vertical transport of water vapor through constant pressure surfaces. These profiles are shown to have spatial and temporal variations. During times of strong convection, large upward transports of water vapor are observed. At 0300 GMT, following movement of heavy activity from the area, a strong downward transport occurred.

Figure 5.10.5.4 shows profiles of combined net horizontal and vertical transport of water vapor. These profiles generally show a net inflow of water vapor prior to and during times of convection, and a net outflow once activity moves out. A large net inflow is observed at 2100 GMT, as the line intensifies over the area. At 0300 GMT a net outflow is observed in most

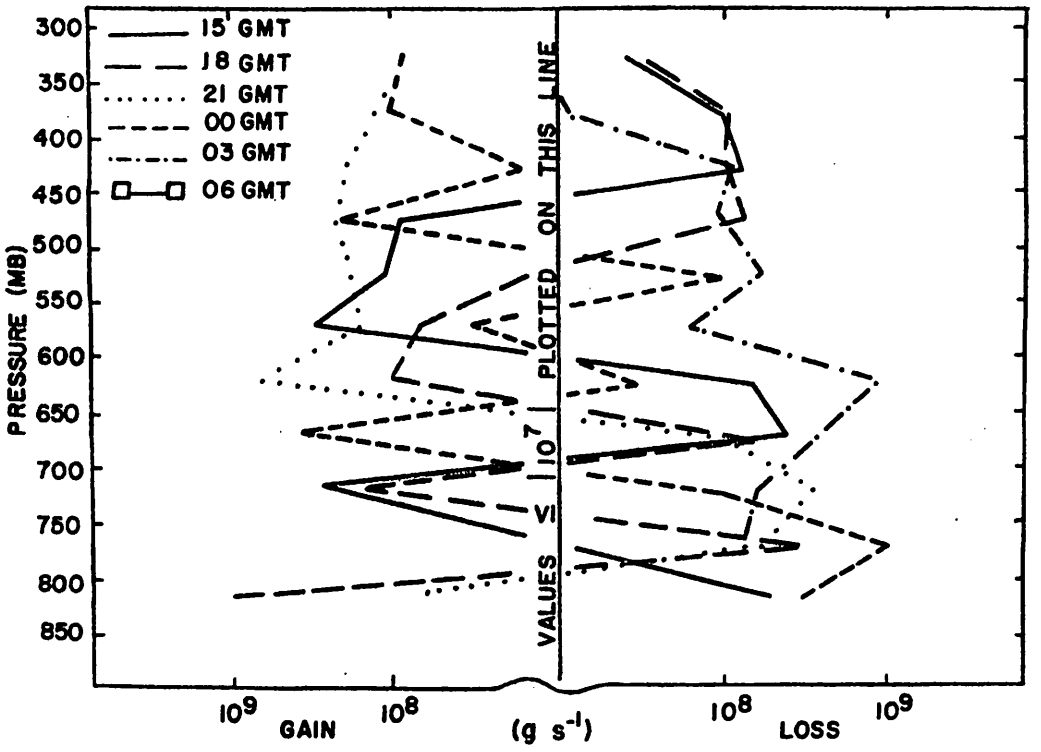

Fig. 5.10.5.2 Net vertical transport of water vapor through boundaries of 50-mb layers (gm s^{-1}) over the Texas area for 23 June 1977.

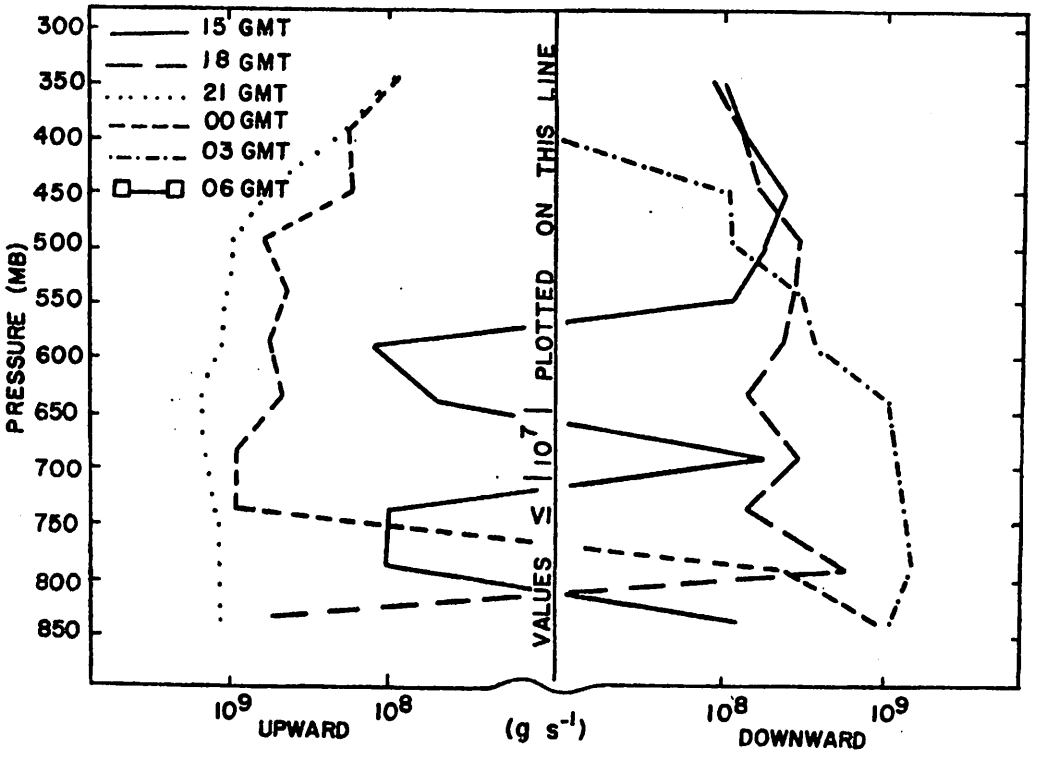

Fig. 5.10.5.3 Vertical transport of water vapor through constant pressure surfaces (gm s^{-1}) over the Texas HIPLEX area for 23 June 1977.

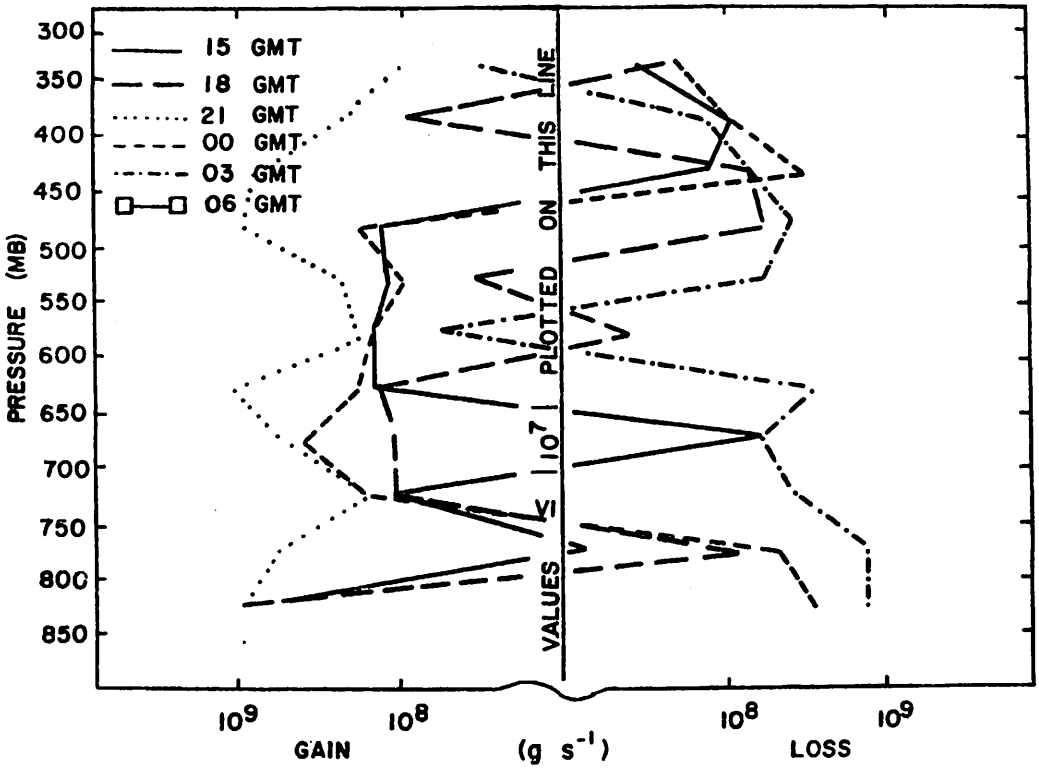

Fig. 5.10.5.4 Combined net horizontal and vertical transport of water vapor through boundaries of 50-mb layers (gm s^{-1}) over the Texas HIPLEX area for 23 June 1977.

layers with the decrease in activity.

Figure 5.10.5.5 shows vertical profiles of the total mass of water vapor. These profiles remain similar throughout the day with little temporal change. This was also seen in Figure 5.3.5.5 when moisture stratification was observed.

Figure 5.10.5.6 shows vertical profiles of the local rate-of-change of the total mass of water vapor. These profiles nearly balance each other in magnitude which indicates only a small variation in the total mass of water vapor. This can also be seen in Fig. 5.10.5.5 where the profiles remain similar throughout the day. Prior to the heaviest activity an increase in water vapor occurred in layers below 550 mb. Following the passage of the line of echoes, a similar decrease occurred in these same layers.

5.11 24 June 1977

5.11.1 Radar

Radar charts for this day are shown in Fig. 5.11.1.1. The period for which charts were prepared was extended to 0600 GMT on 25 June because of the echoes present over the area following the normal termination time. Also, rawinsonde runs were made at 0600 GMT in order to encompass the period of convective activity.

Scattered echoes with tops not exceeding 6.1 km (20K ft) occurred over the

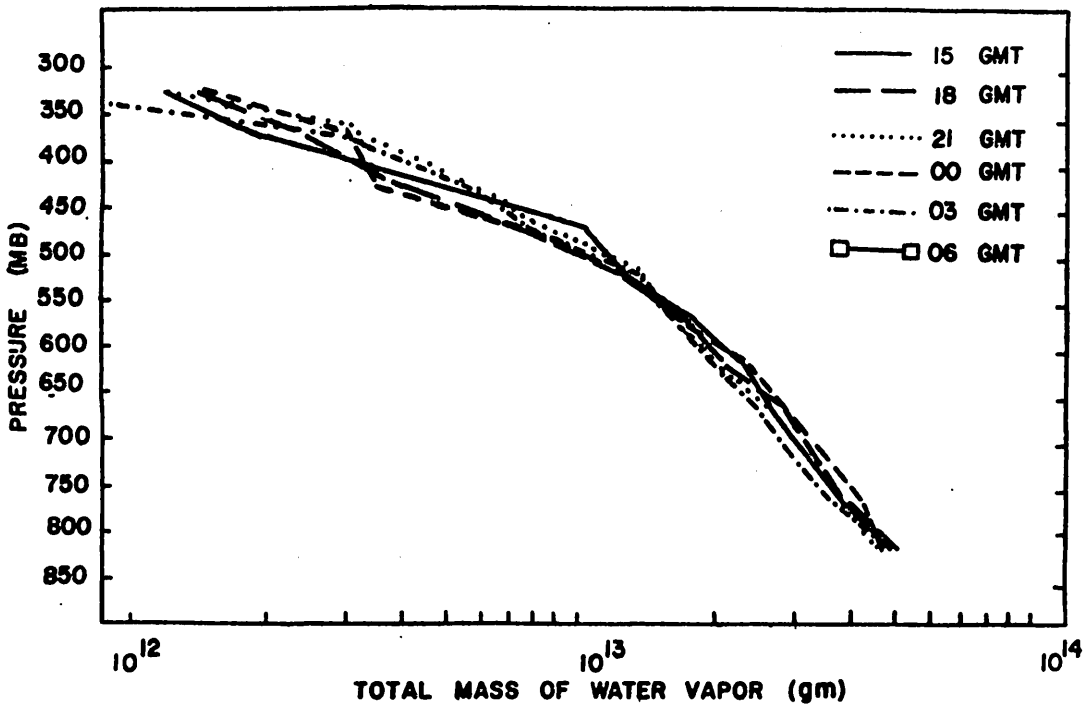

Fig. 5.10.5.5 Total mass of water vapor in layers 50 mb deep (gm) over the Texas HIPLEX area for 23 June 1977.

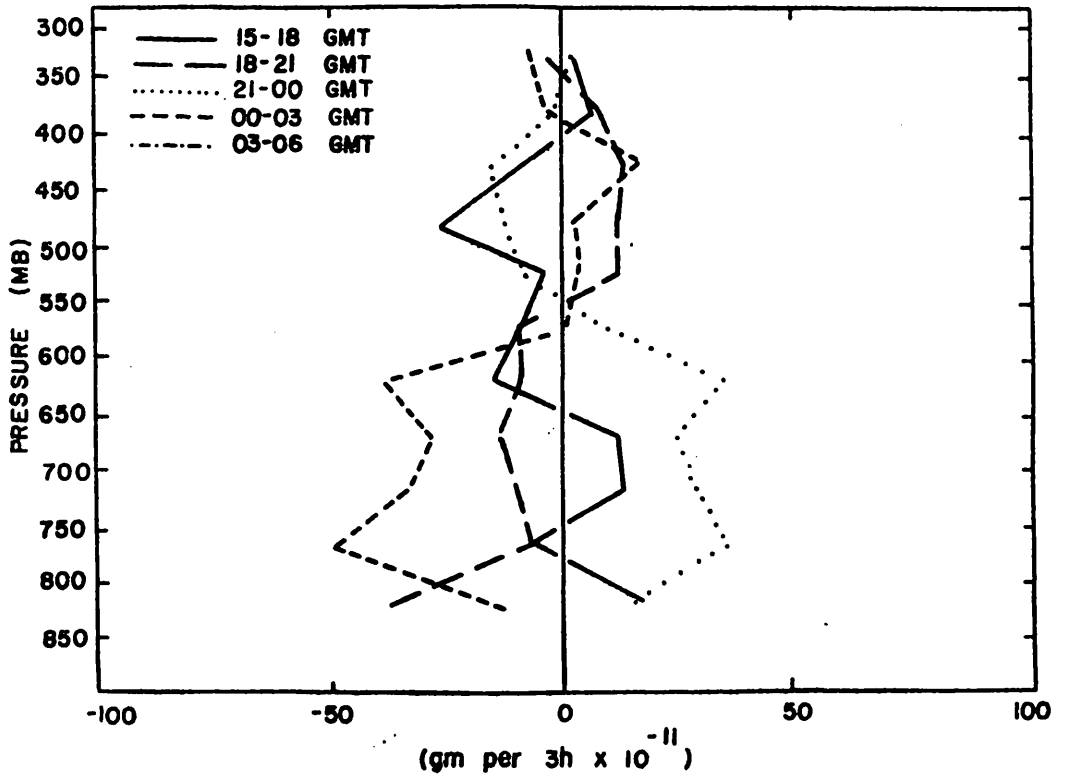

Fig. 5.10.5.6 Local rate-of-change in total mass of water vapor (gm per 3h x 10^{-11}) over the Texas HIPLEX area for 23 June 1977.

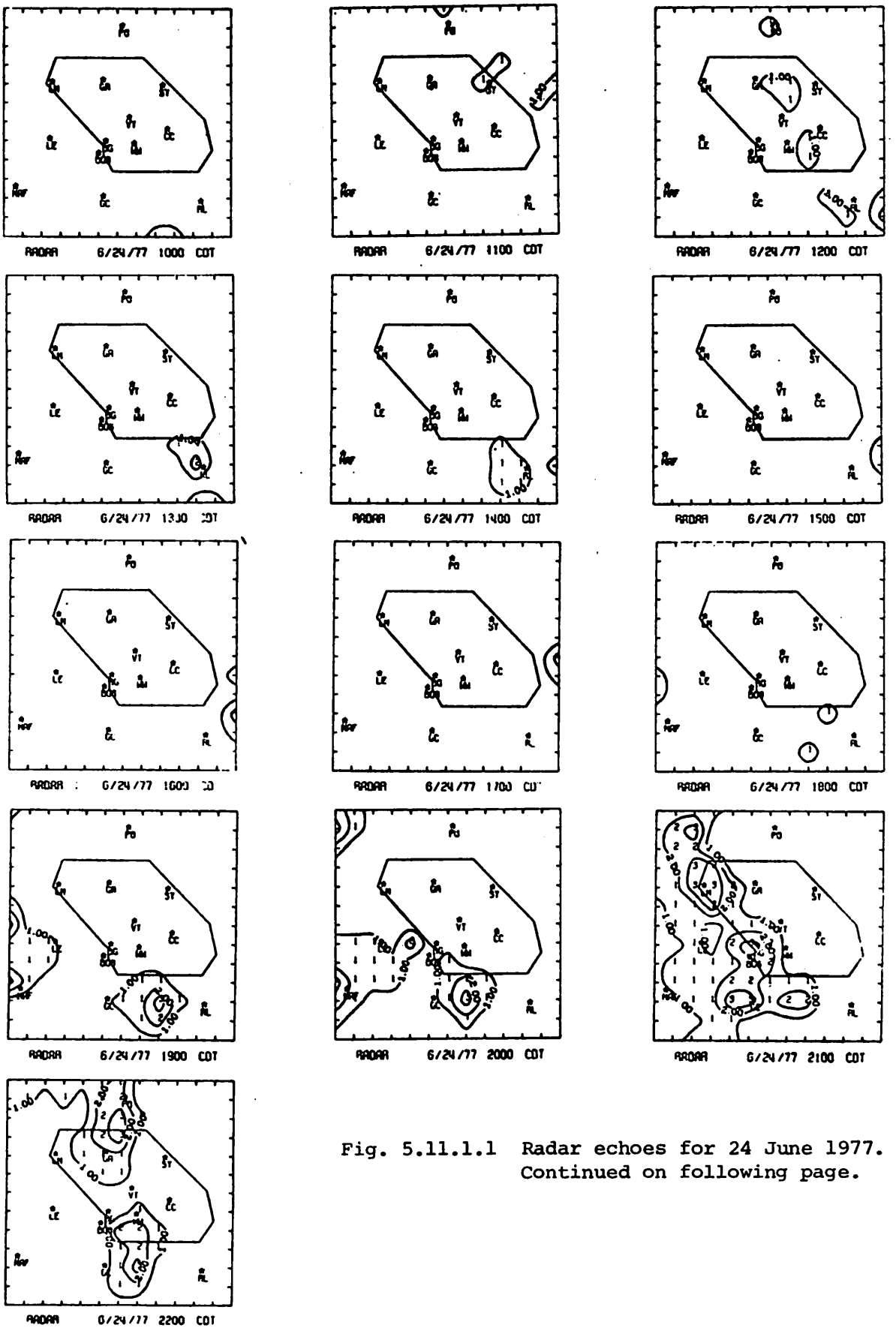

Fig. 5.11.1.1 Radar echoes for 24 June 1977.
Continued on following page.

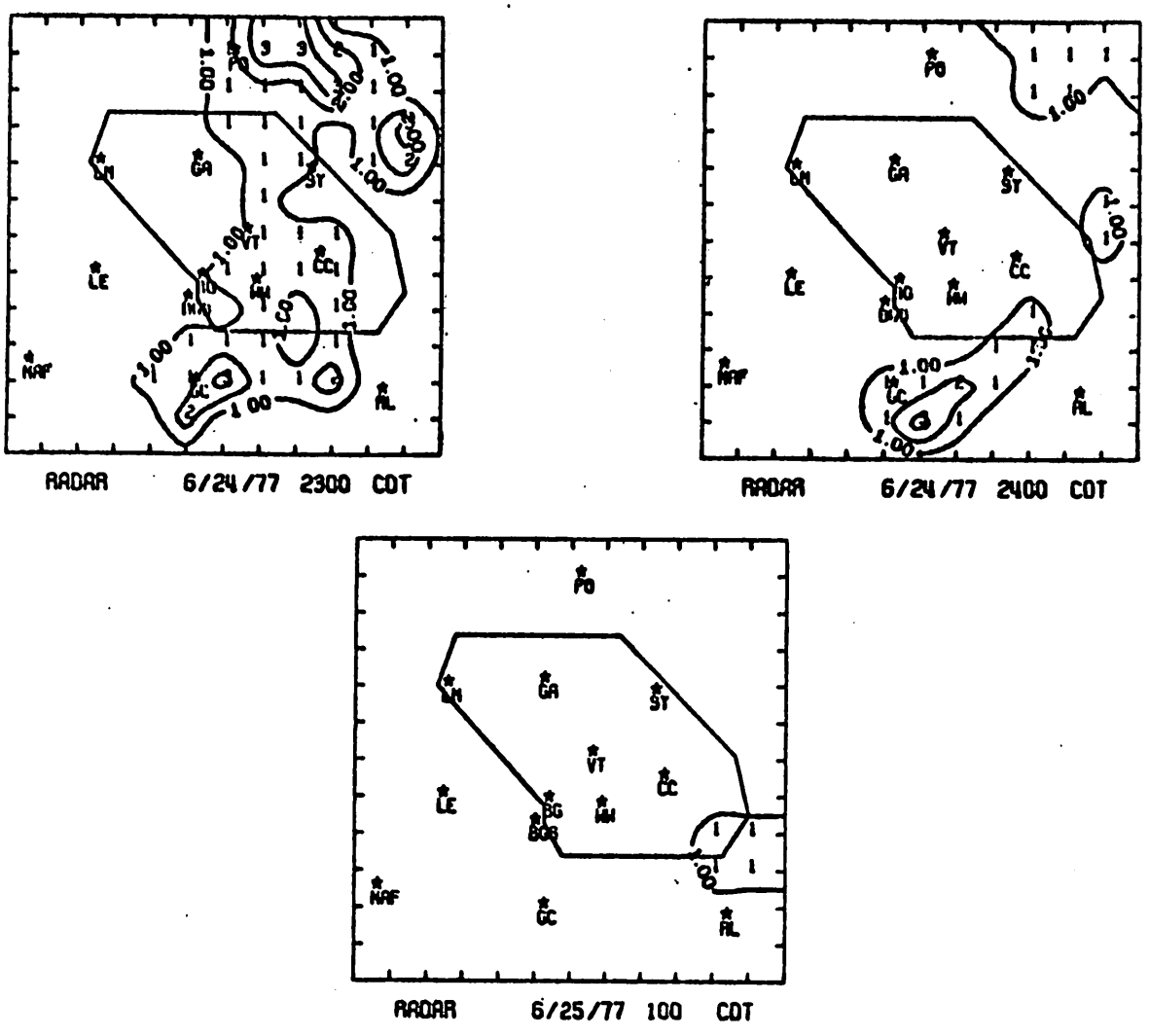

Fig. 5.11.1.1 (Continued)

Echo coverage extended to 0100 CDT on June 25 to cover period for which soundings were made.

area during the day prior to 0000 GMT at which time a thunderstorm with tops exceeding 9.1 km (30K ft) was observed west of Robert Lee while two other cells were beginning to penetrate the area west and north of Midland. By 0200 GMT a line of cells with tops exceeding 9.1 km (30K ft) was over the area and oriented along a line from northwest of Lamesa to south of Big Spring. This line moved slowly eastward with two principal cells, one passing near Post and the other near Garden City. By 0500 GMT only one major cell remained and it was located southeast of Garden City. At 0600 GMT only a small area of echoes north of Robert Lee with tops less than 6.1 km (20K ft) remained in the area.

5.11.2 Surface

The passage of the intense line of echoes is reflected in fields of surface temperature (Fig. 5.11.2.1) by a large decrease well behind the line. A temperature decrease of 10°C occurred at 0300 GMT. Surface mixing ratio patterns (Fig. 5.11.2.2) show little variation prior to convective activity, and generally show an increase of mixing ratio from west to east. A decrease in mixing ratio occurred behind the line associated with regions of minimum surface temperature and surface equivalent potential temperature (Fig. 5.11.2.3).

Terrain-induced vertical motion (Fig. 5.11.2.4) remained small in magnitude throughout the day with little contribution to the kinematic vertical motion. Small centers of surface velocity divergence (Fig. 5.11.2.5) were present prior to 0000 GMT when only light scattered echoes were observed. With the approach of the line at 0200 GMT, strong centers of convergence and divergence were observed in regions of strong convective activity. Fields of vertical motion 50 mb above the surface (Fig. 5.11.2.6), surface moisture divergence (Fig. 5.11.2.7), and vertical flux of moisture 50 mb above the surface (Fig. 5.11.2.8) all show the presence of this heavy convection. Prior to 0100 GMT, these fields showed no pronounced centers and varied in time. Fields of surface vorticity (Fig. 5.11.2.9) show the approach of the line at 0100 GMT by a region of strong cyclonic vorticity which moves eastward. By 0300 GMT two large centers of cyclonic vorticity were observed directly below the two strong isolated convective cells.

Sea level pressures (Fig. 5.11.2.10) generally decreased from west to east, with a low pressure center located over the southeastern portion of the area. This pattern remained similar until the line passed through the network at 0300 GMT. Figure 5.11.2.11 shows an increase in surface

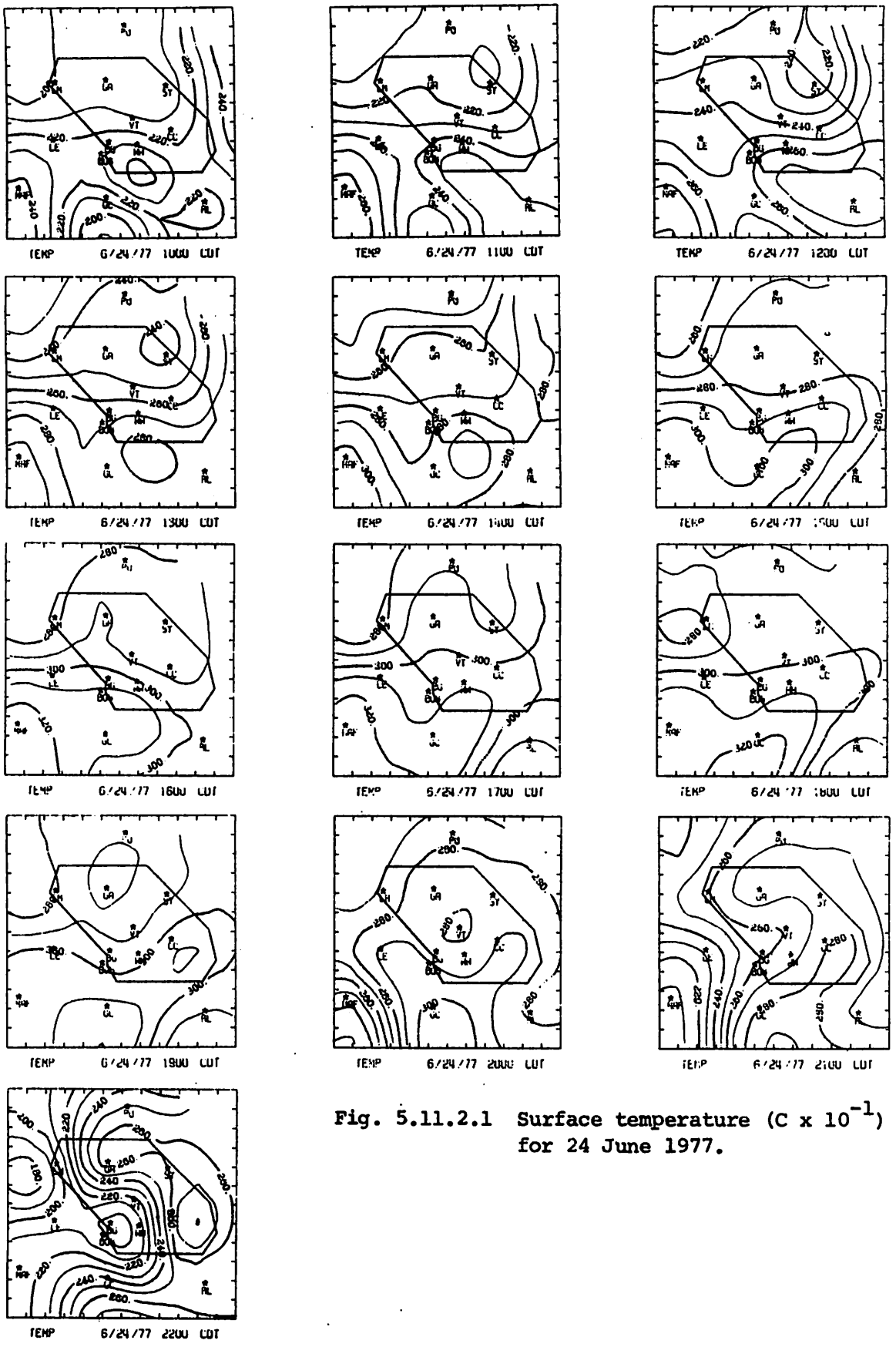

Fig. 5.11.2.1 Surface temperature (C x 10^{-1}) for 24 June 1977.

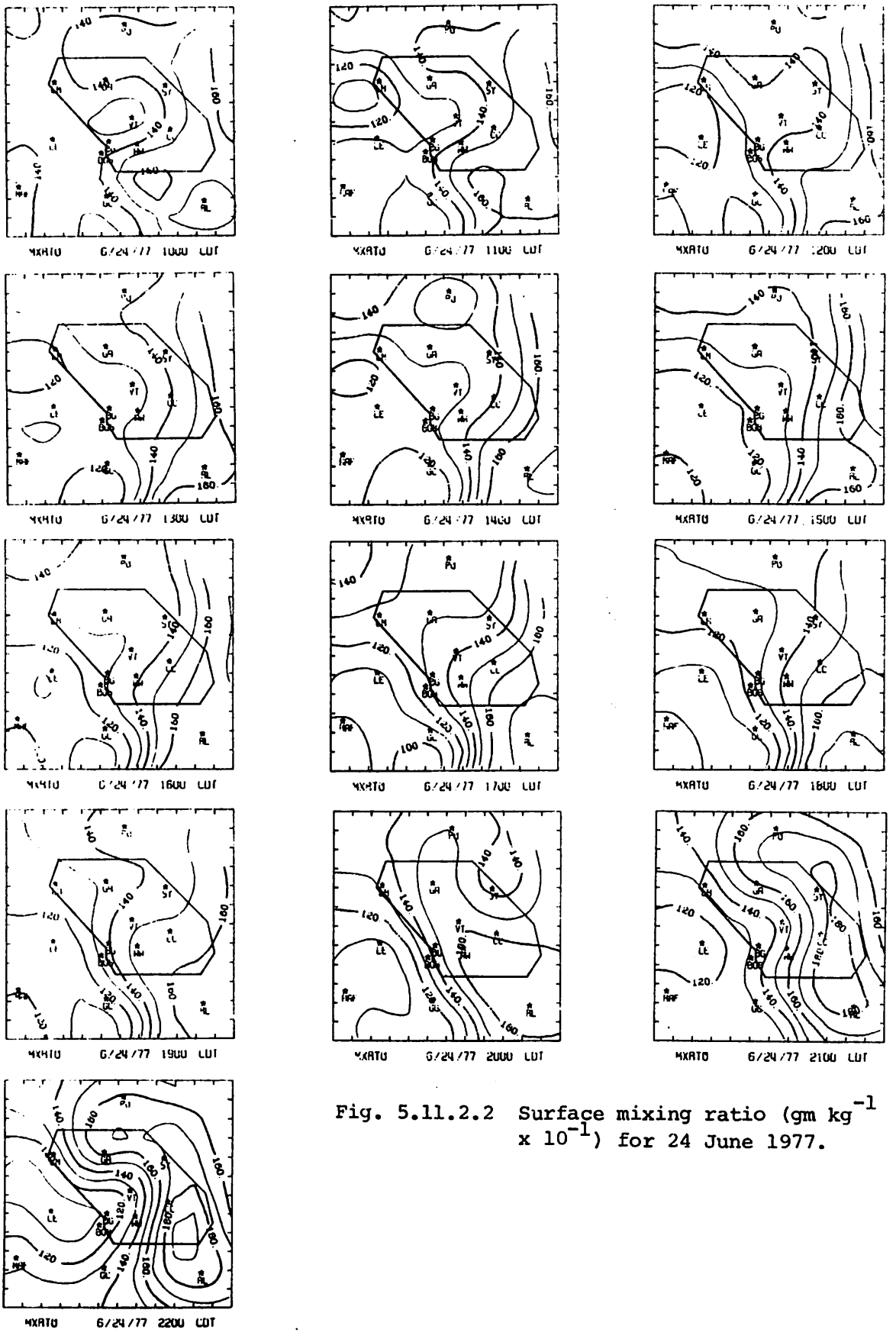

Fig. 5.11.2.2 Surface mixing ratio (gm kg^{-1} x 10^{-1}) for 24 June 1977.

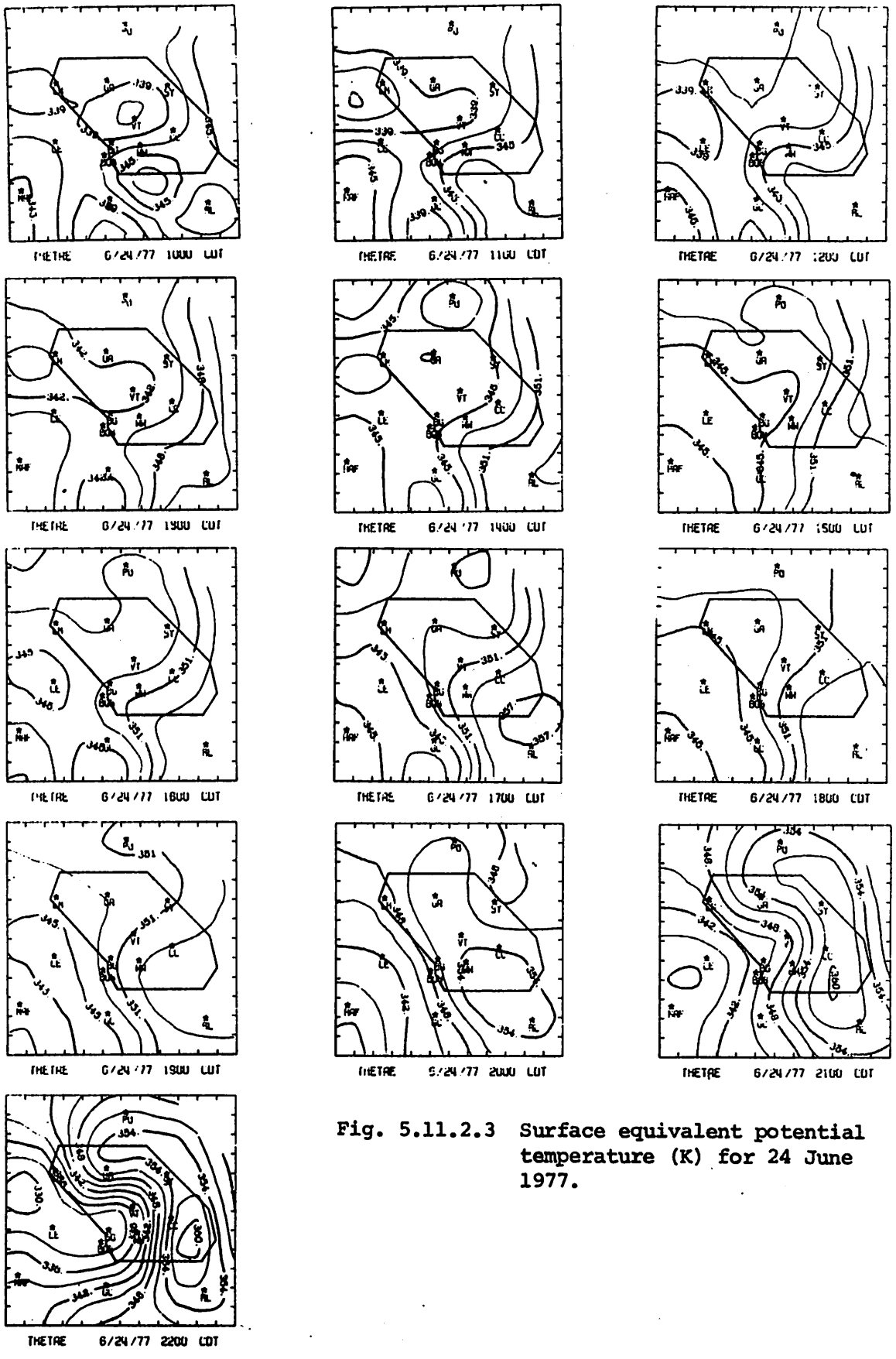

Fig. 5.11.2.3 Surface equivalent potential temperature (K) for 24 June 1977.

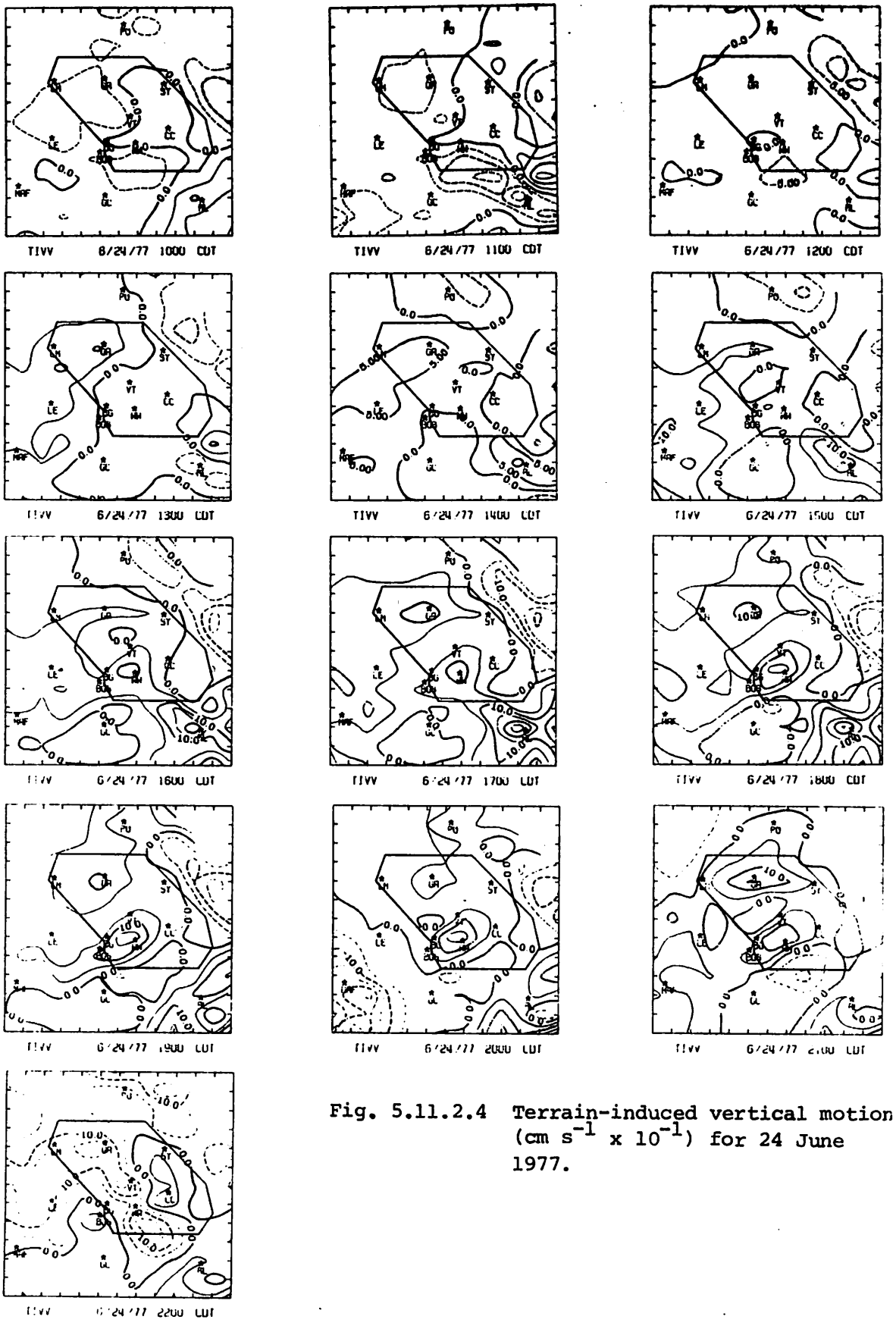

Fig. 5.11.2.4 Terrain-induced vertical motion (cm s^{-1} x 10^{-1}) for 24 June 1977.

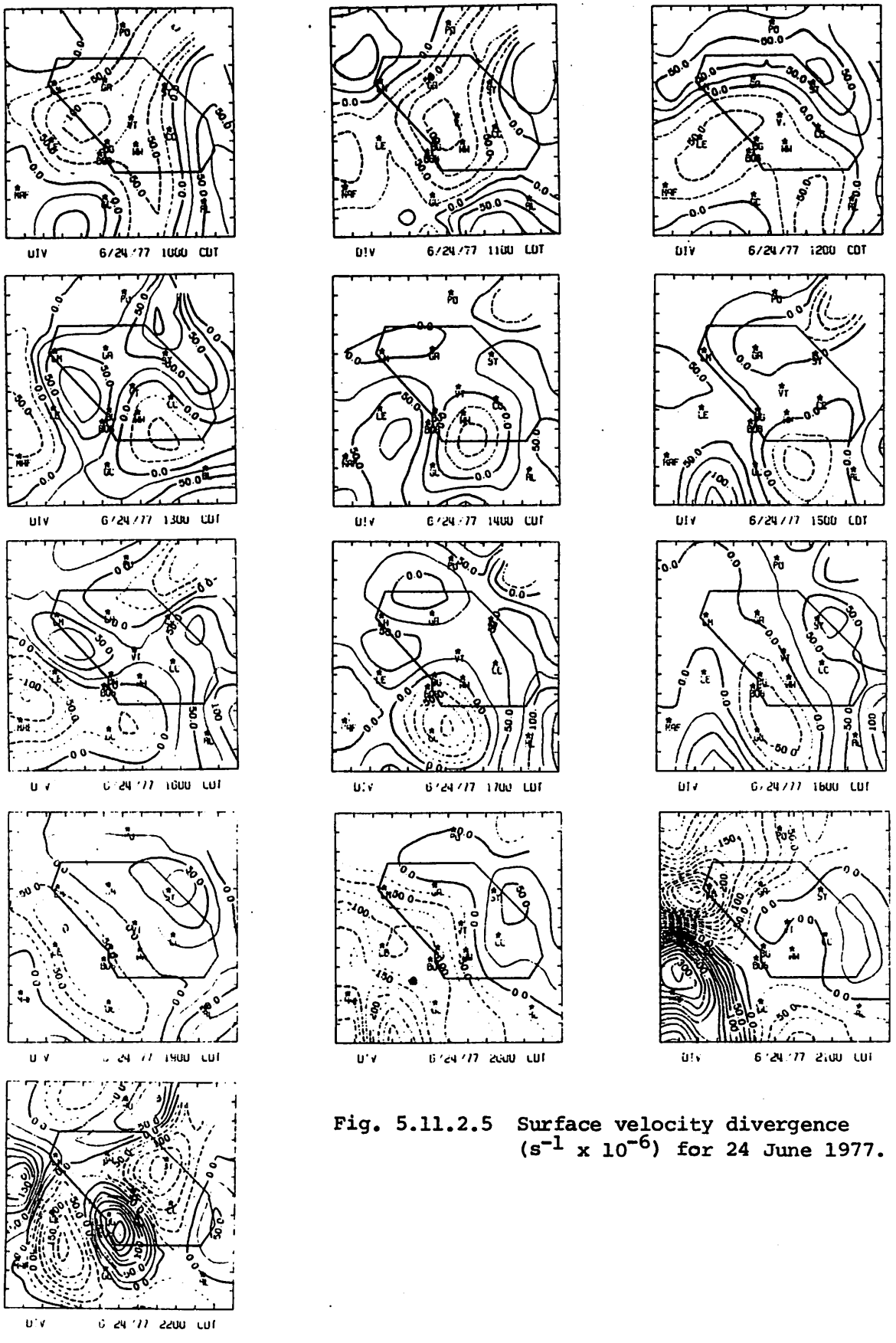

Fig. 5.11.2.5 Surface velocity divergence (s^{-1} x 10^{-6}) for 24 June 1977.

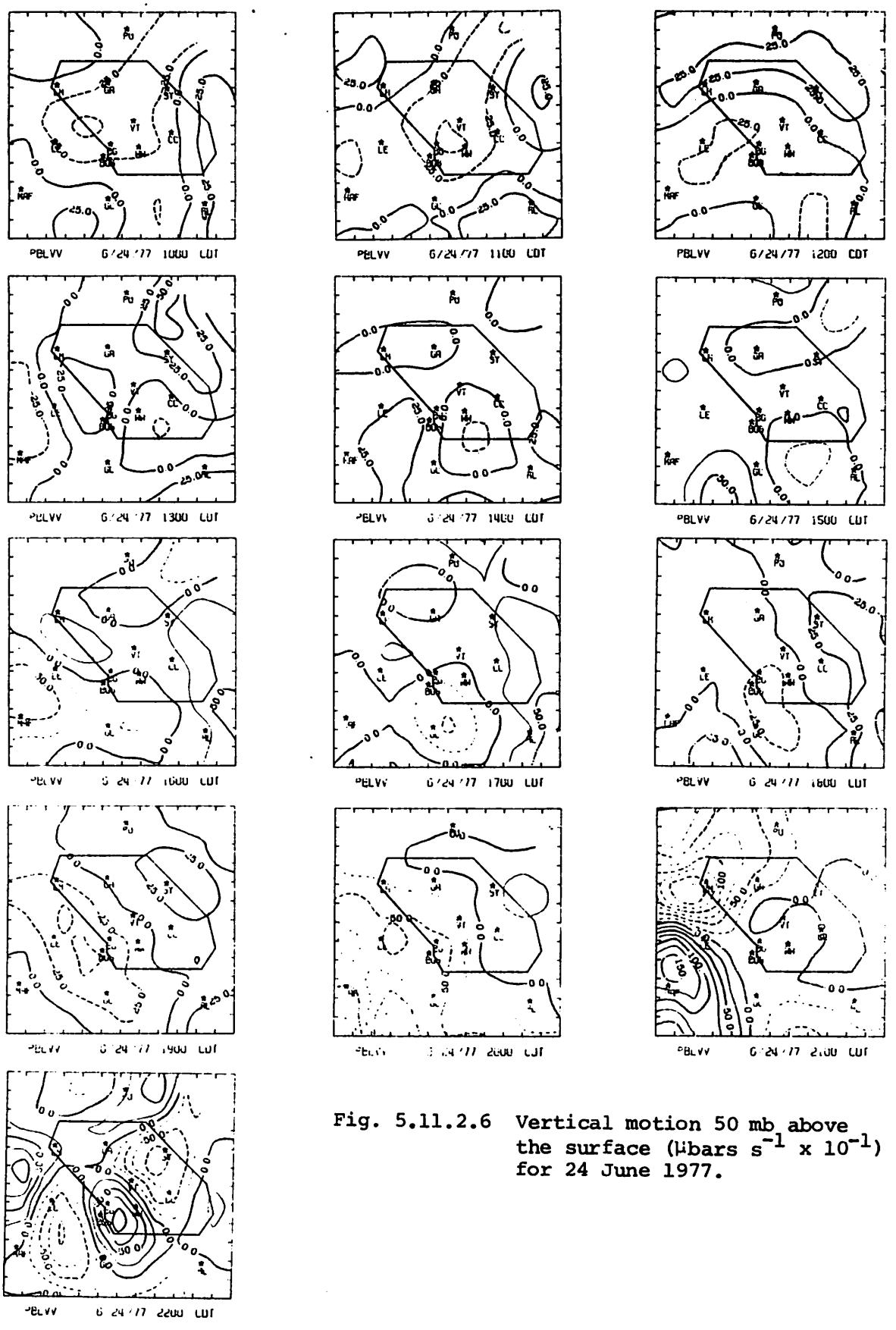

Fig. 5.11.2.6 Vertical motion 50 mb above the surface (μbars s^{-1} x 10^{-1}) for 24 June 1977.

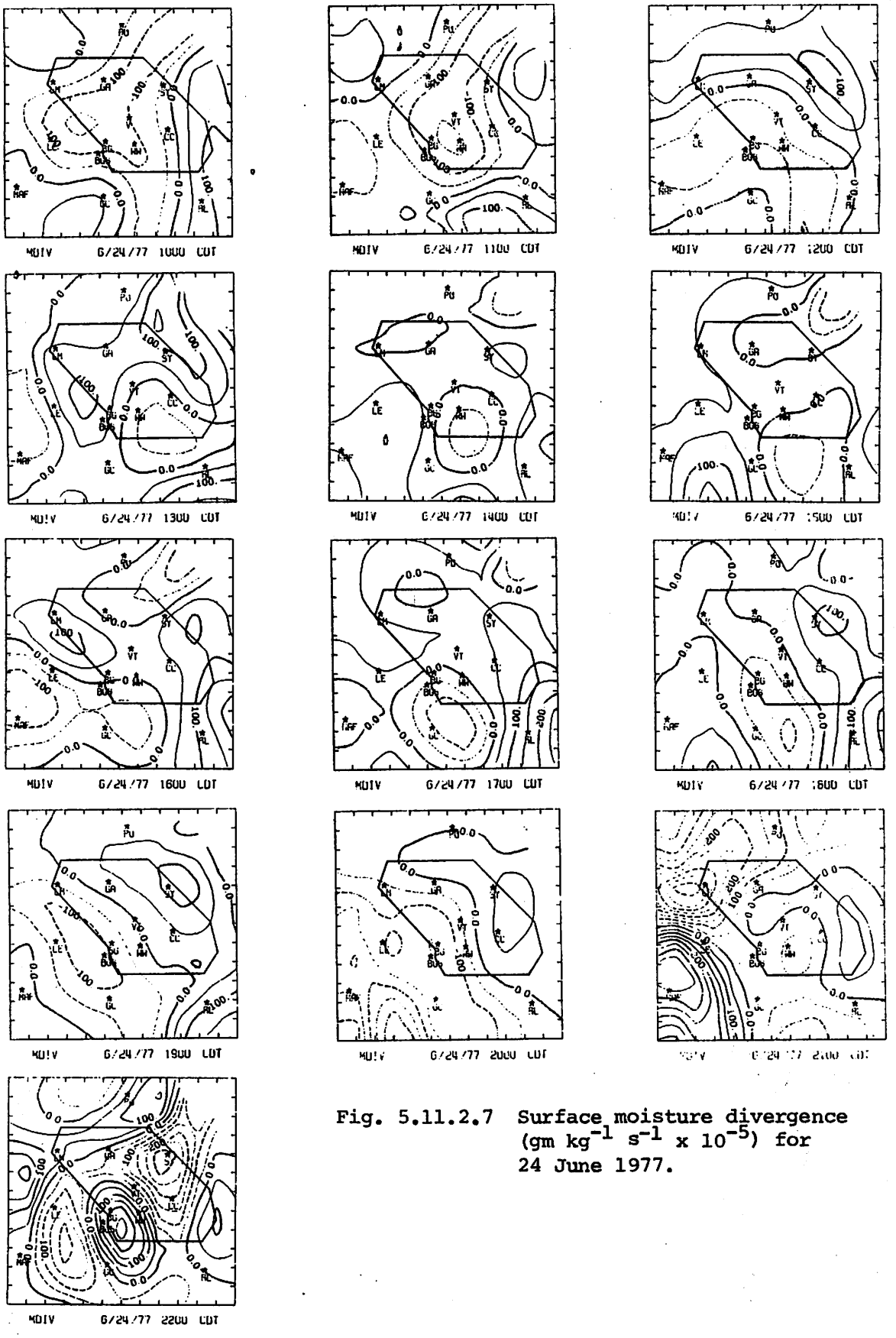

Fig. 5.11.2.7 Surface moisture divergence (gm kg^{-1} s^{-1} x 10^{-5}) for 24 June 1977.

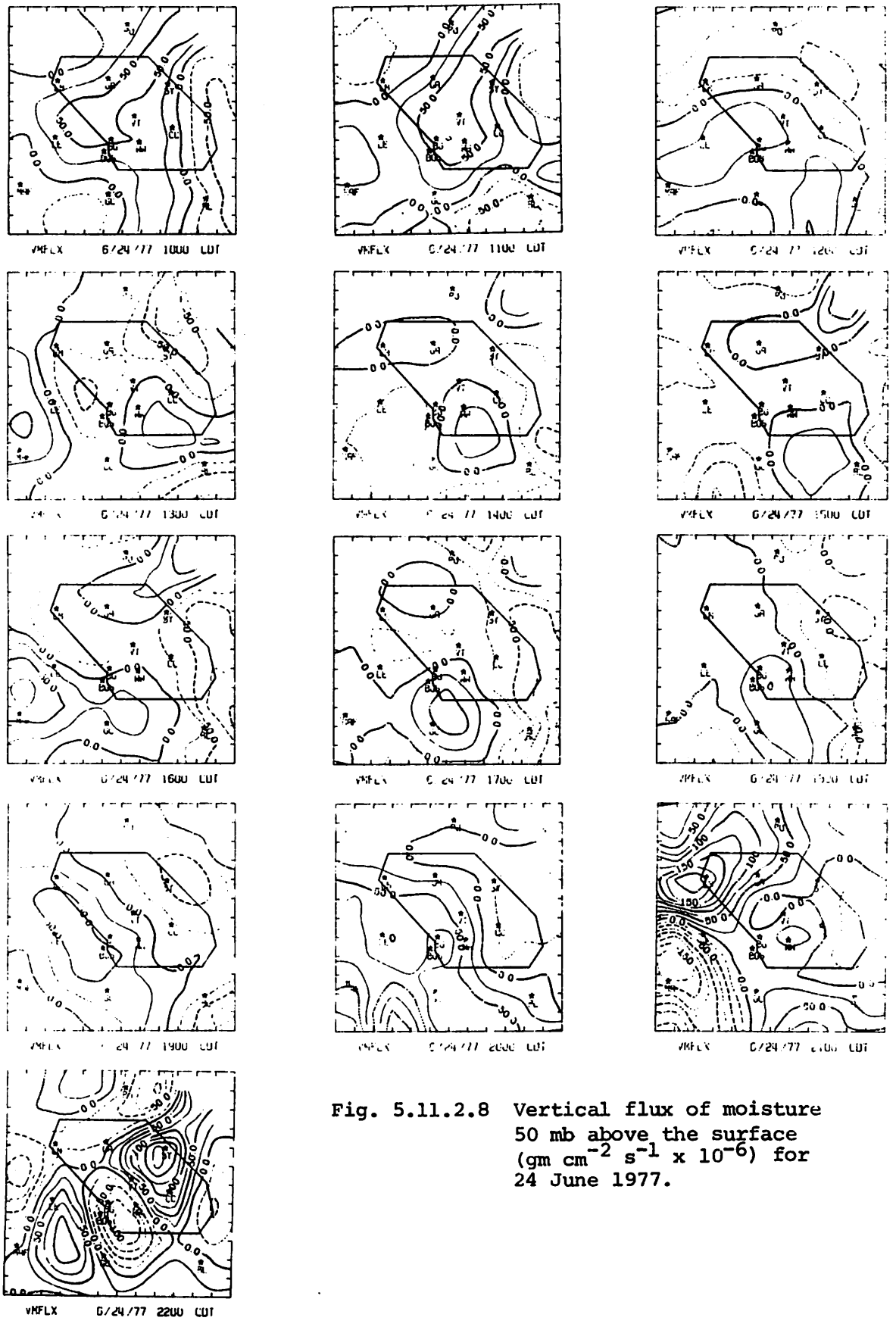

Fig. 5.11.2.8 Vertical flux of moisture 50 mb above the surface (gm cm^{-2} s^{-1} x 10^{-6}) for 24 June 1977.

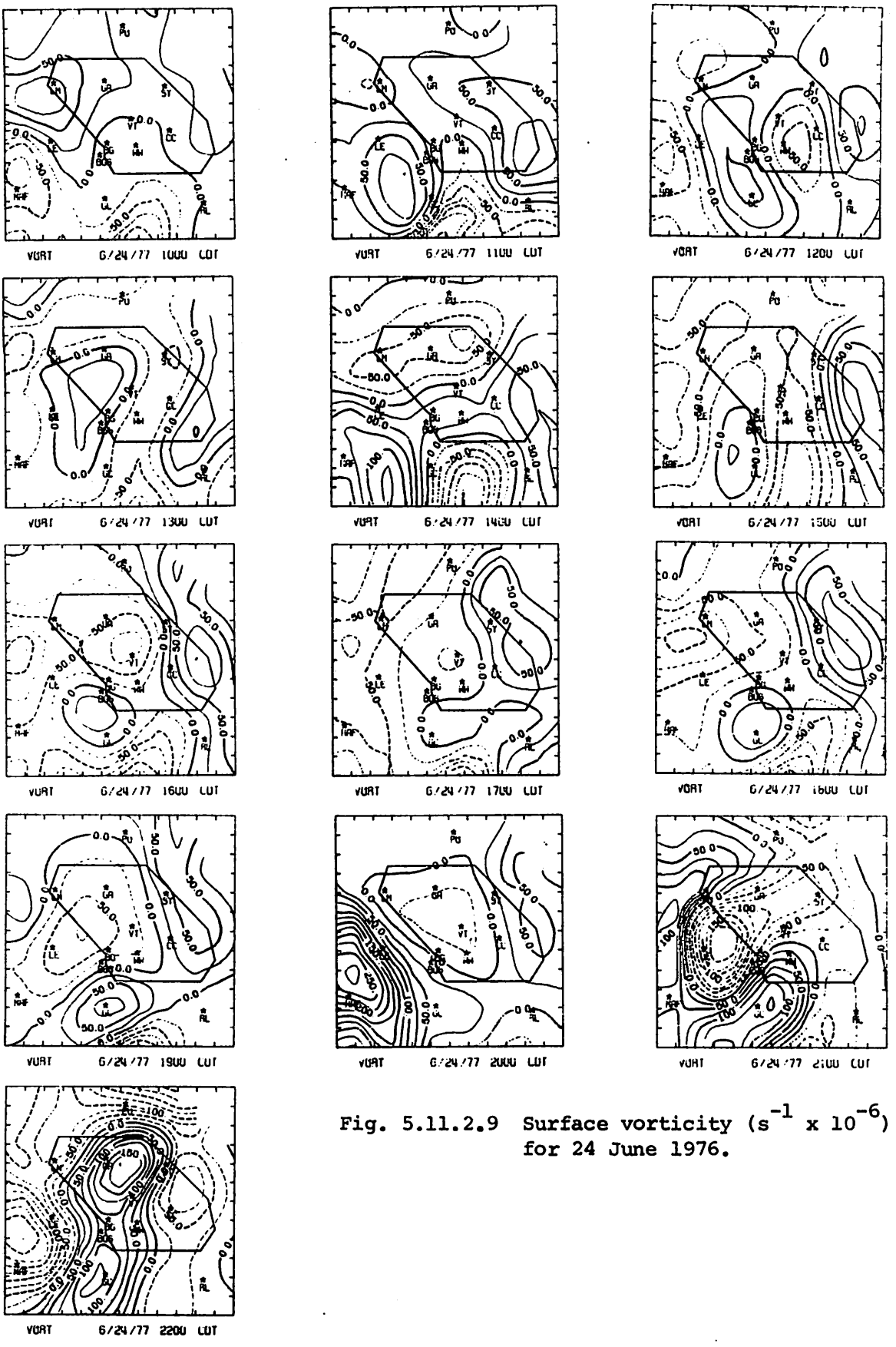

Fig. 5.11.2.9 Surface vorticity (s^{-1} x 10^{-6}) for 24 June 1976.

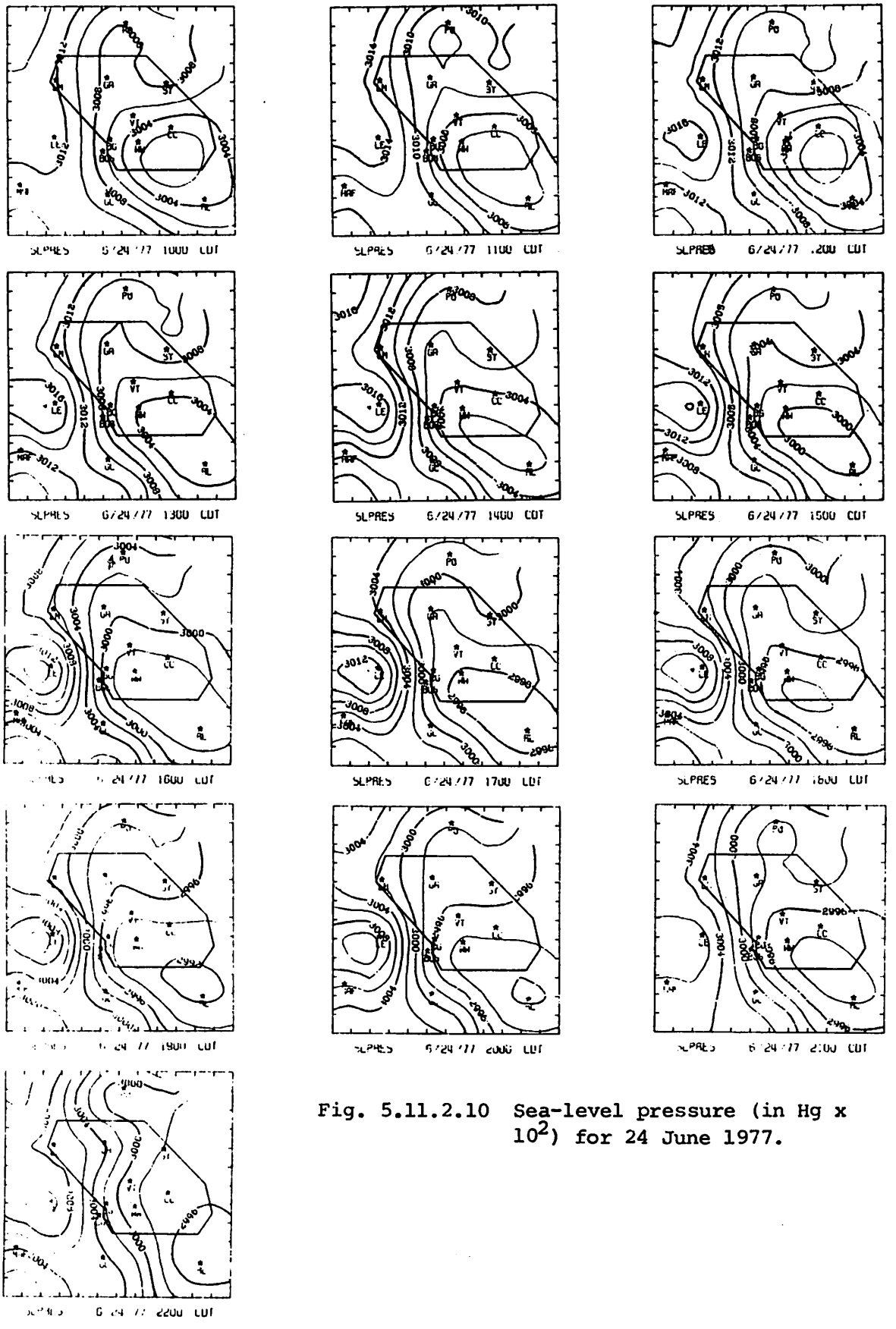

Fig. 5.11.2.10 Sea-level pressure (in Hg x 10^2) for 24 June 1977.

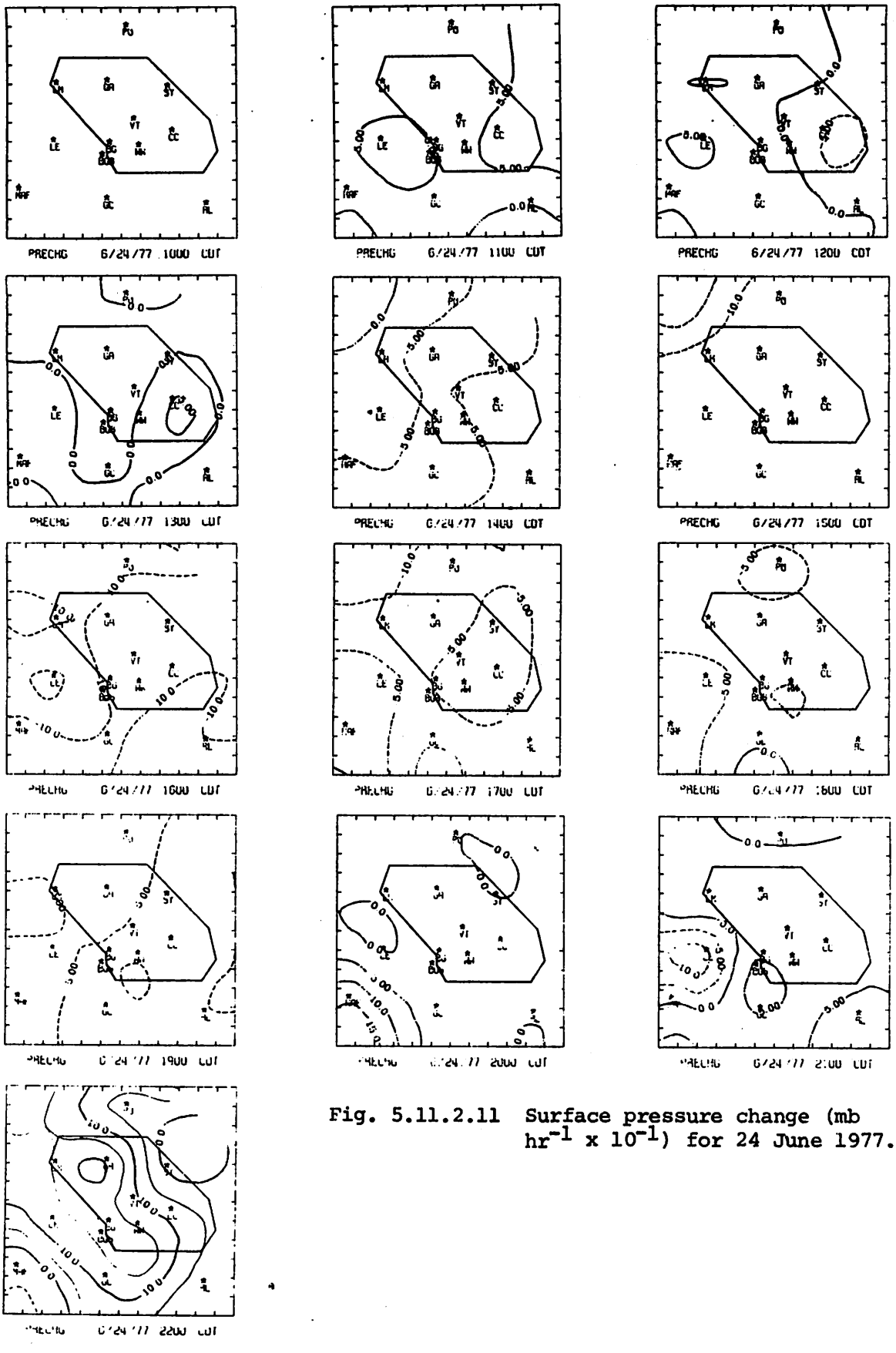

Fig. 5.11.2.11 Surface pressure change (mb hr^{-1} x 10^{-1}) for 24 June 1977.

pressure over the center of the network, due to large centers of surface velocity convergence shown in Figure 5.11.2.5.

Analysis of the surface data covered the usual period even though soundings were taken for one additional time.

5.11.3 Upper-Level Kinematic Parameters

Thunderstorm activity formed rapidly at 0000 GMT and continued through 0600 GMT when it diminished over the network. Low-level horizontal mass convergence was observed only at 0000 GMT and around 1500 GMT when very weak showers dissipated over the experiment area (Fig. 5.11.3.1). Before and after storm development at 0000 GMT, low-level mass divergence occurred below mass convergence between 700 and 400 mb. Vertical velocities were downward at low levels for all times except 1500 GMT and 0000 GMT when activity was present and forming over the network and strong downward with storm dissipation at 0600 GMT (Fig. 5.11.3.2).

Low-level horizontal moisture divergence and mid-level convergence occurred at all times except 1500 and 0000 GMT when activity was forming over the network (Fig. 5.11.3.3). When activity was forming, low-level horizontal convergence was present under mid-level divergence of water vapor.

5.11.4 Energetics

Net horizontal inflow of latent heat energy occurred in low levels during times of precipitation formation (1500 GMT and 0000 GMT) (Fig.5.11.4.1). Both before and after thunderstorm formation at 0000 GMT, net horizontal outflow of latent heat energy occurred in low levels, and inflow was present at mid levels, especially at 0600 GMT when dissipation occurred. Vertical flux convergence of latent heat energy was calculated in middle layers and convergence in lower layers during times without precipitation formation (Fig.5.11.4.2) as a net downward transport of latent energy occurred between mid- and low-levels within a sinking vertical velocity field.

Upward vertical velocities are associated with a net upward transport of latent heat energy created by vertical flux divergence and convergence in low- and mid-levels, respectively, at 1500 GMT and 0000 GMT. Local changes in latent heat energy were generally small except at 0000 GMT above 500 mb when values were positive and precipitation was developing, and at 0600 GMT above 600 mb when values were negative and thunderstorms were dissipating (Fig. 5.11.4.3).

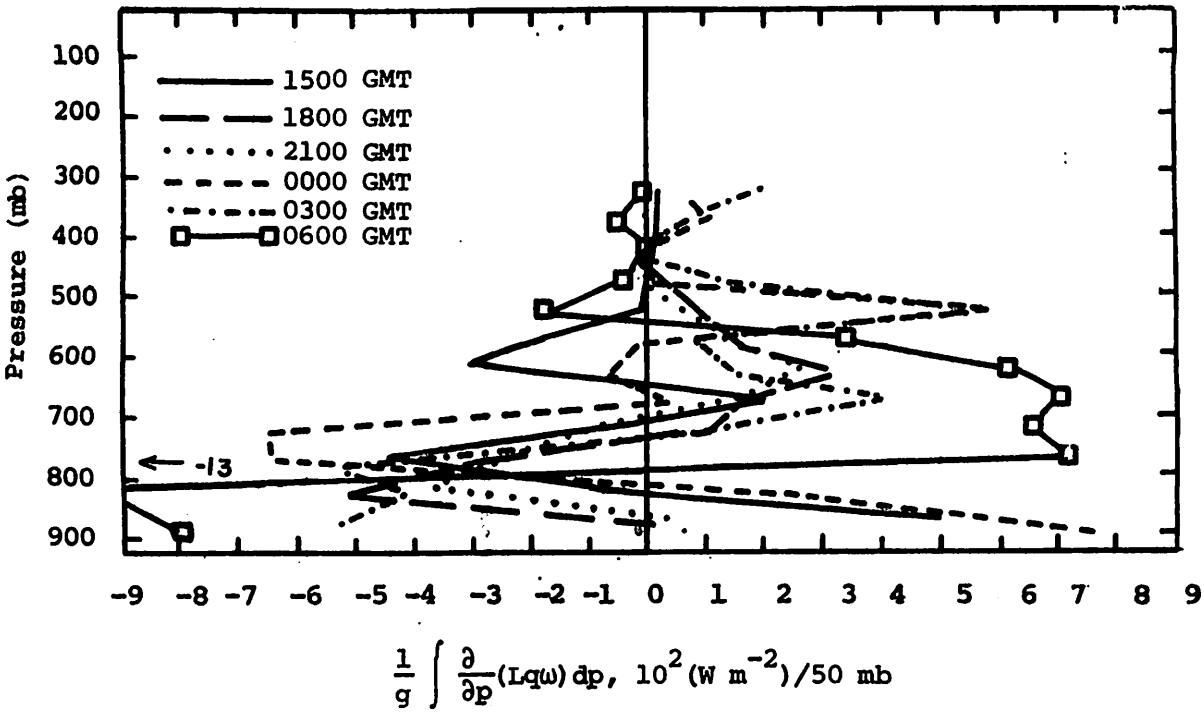

Fig. 5.11.4.2 Vertical profiles of the vertical flux of latent heat energy on 24 June 1977.

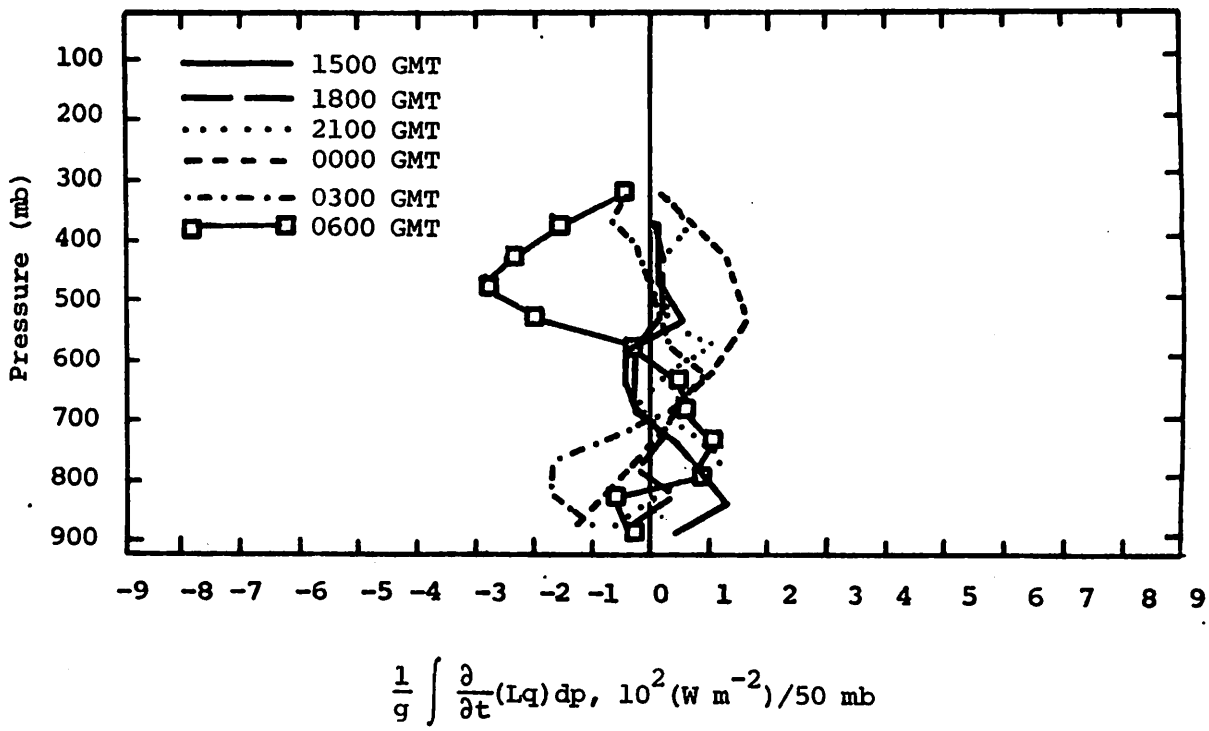

Fig. 5.11.4.3 Vertical profiles of the local change of latent heat energy on 24 June 1977.

Gains (negative -R values) dominated the vertical profiles of the latent heat residual term at most levels and times (Fig. 5.11.4.4). Between 1500 and 0000 GMT turbulent flux divergence of latent heat in low levels and convergence between 800 and 600 mb may have been associated with losses of latent heat in low levels and gains at mid levels since lapse rates became dry adiabatic up to 700 mb at 2100 GMT and thunderstorms formed at 0000 GMT. Negative values in low levels at 0600 GMT and positive values aloft are likely associated with evaporation (producing environmental cooling) and condensation (producing heating) during a period of diminishing convective activity.

The diabatic heating profiles (Fig. 5.11.4.5) support the interpretations given above for -R. The 0600 GMT profile is negative (cooling from evaporation) below 600 mb and positive above (warming from condensation), while the other profiles generally show the same sign at all levels and times except above 300 mb.

Horizontal flux divergence profiles of kinetic energy (Fig. 5.11.4.6) generally show net outflow of energy between 700 mb and the surface and around the 400-mb level. Net horizontal inflow was computed between 700 and 500 mb and above 300 mb. Vertical flux divergence profiles of kinetic energy (Fig. 5.11.4.7) generally showed flux convergence in low levels and divergence at mid levels at most times during the day. Erratic profiles above 300 mb are possibly related to strong winds above that level and larger errors in wind measurements that make these results hard to interpret.

5.11.5 Water Vapor Budget

Figure 5.11.5.1 shows vertical profiles of the net horizontal transport of water vapor. Profiles prior to 0300 GMT remained similar showing a net outflow up to 700 mb, and a net inflow in layers above 700 mb. Once strong convection occurred over the area, a stronger inflow of water vapor occurred between 700 and 500 mb with a general outflow in layers above. Such a large net outflow in layers above 500 mb seems to be a characteristic of intense convection with tops exceeding 9.1 km (30K ft). Such a characteristic also appears in Fig. 5.10.5.1 at 0000 GMT.

Figure 5.11.5.2 shows profiles of the net vertical transport of water vapor. These profiles generally show a net inflow in layers below 725 mb, and a net outflow in upper layers. However, once movement and dissipation of the line occurred at 0600 GMT, a large inflow of water vapor occurred in layers

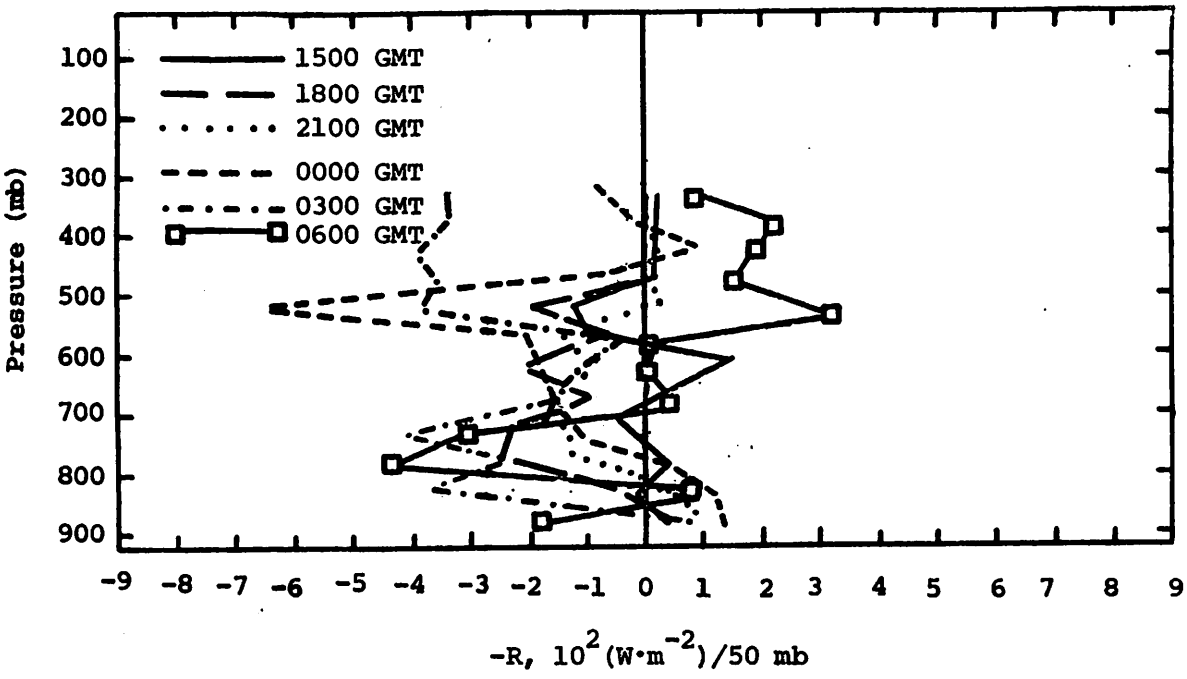

Fig. 5.11.4.4 Vertical profile of the residual of the latent heat energy equation on 24 June 1977.

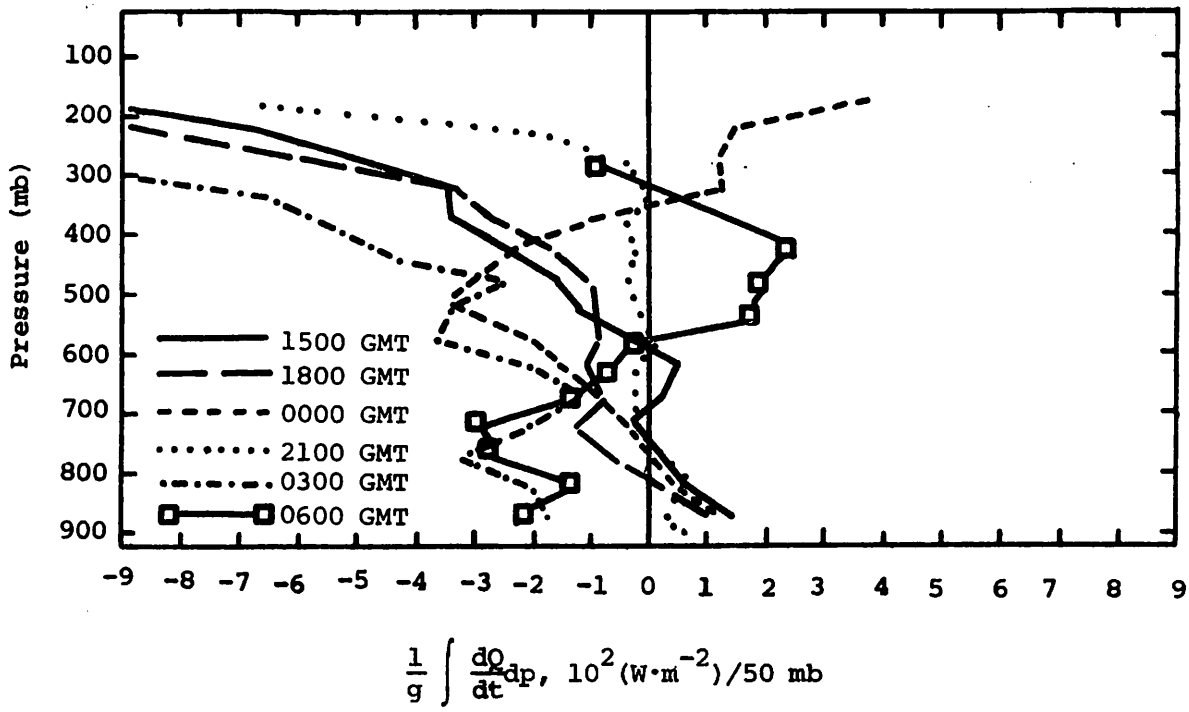

Fig. 5.11.4.5 Vertical profiles of diabatic heating computed from the first law of thermodynamics on 24 June 1977.

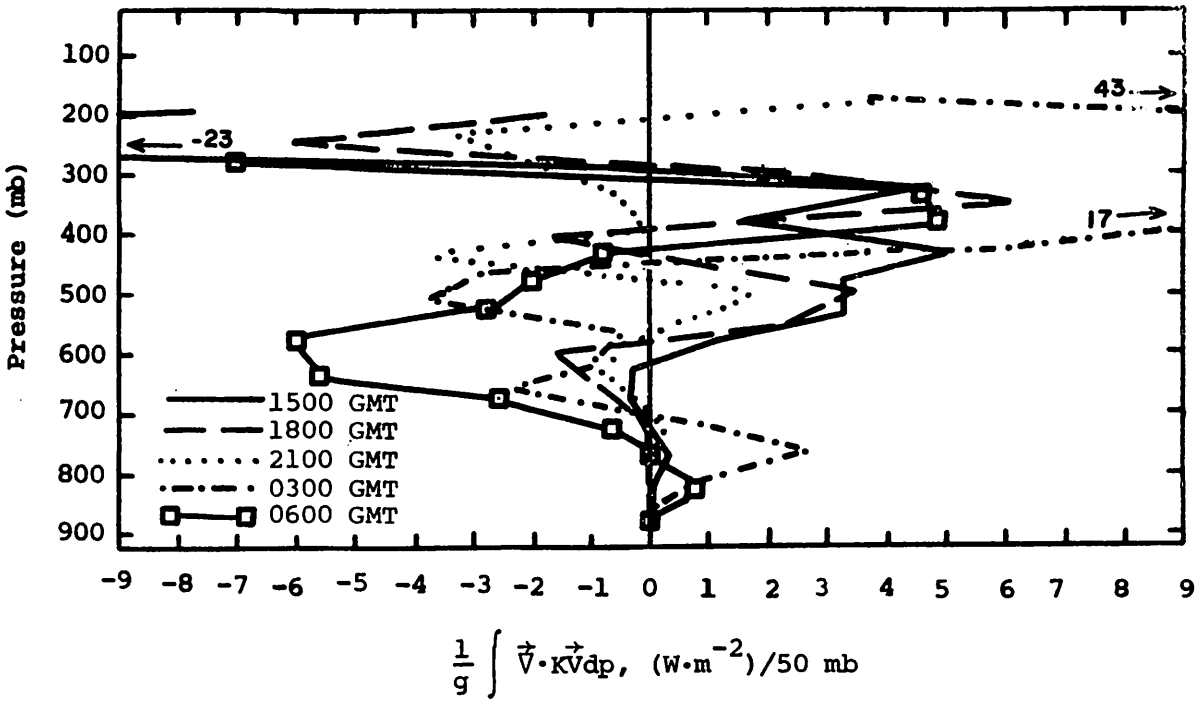

Fig. 5.11.4.6 Vertical profiles of the horizontal flux of kinetic energy on 24 June 1977.

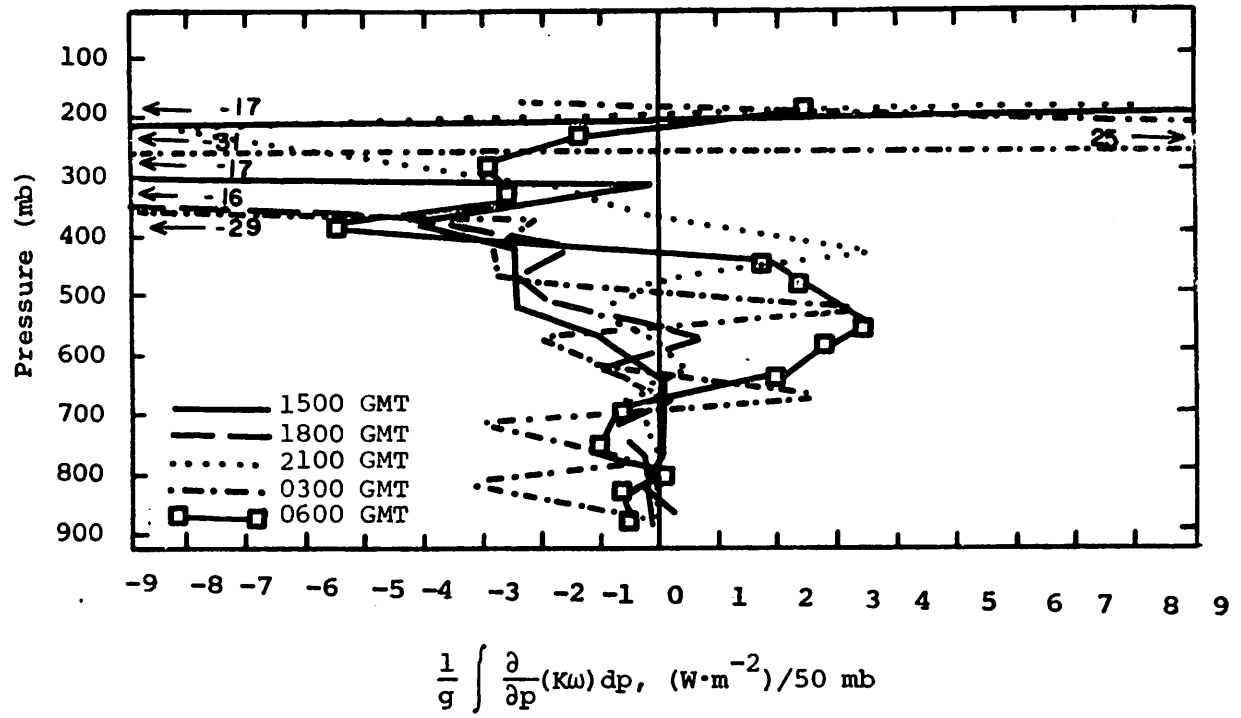

Fig. 5.11.4.7 Vertical profiles of the vertical flux of kinetic energy on 24 June 1977.

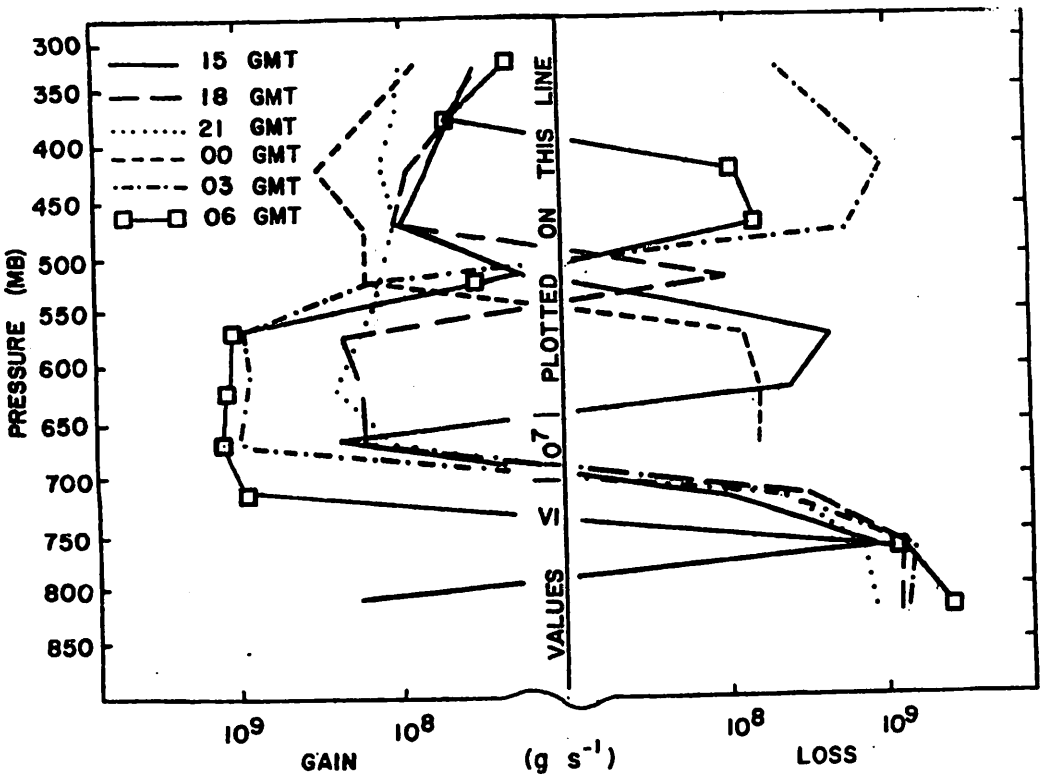

Fig. 5.11.5.1 Net horizontal transport of water vapor through boundaries of 50-mb layers (gm s^{-1}) over the Texas HIPLEX area for 24 June 1977.

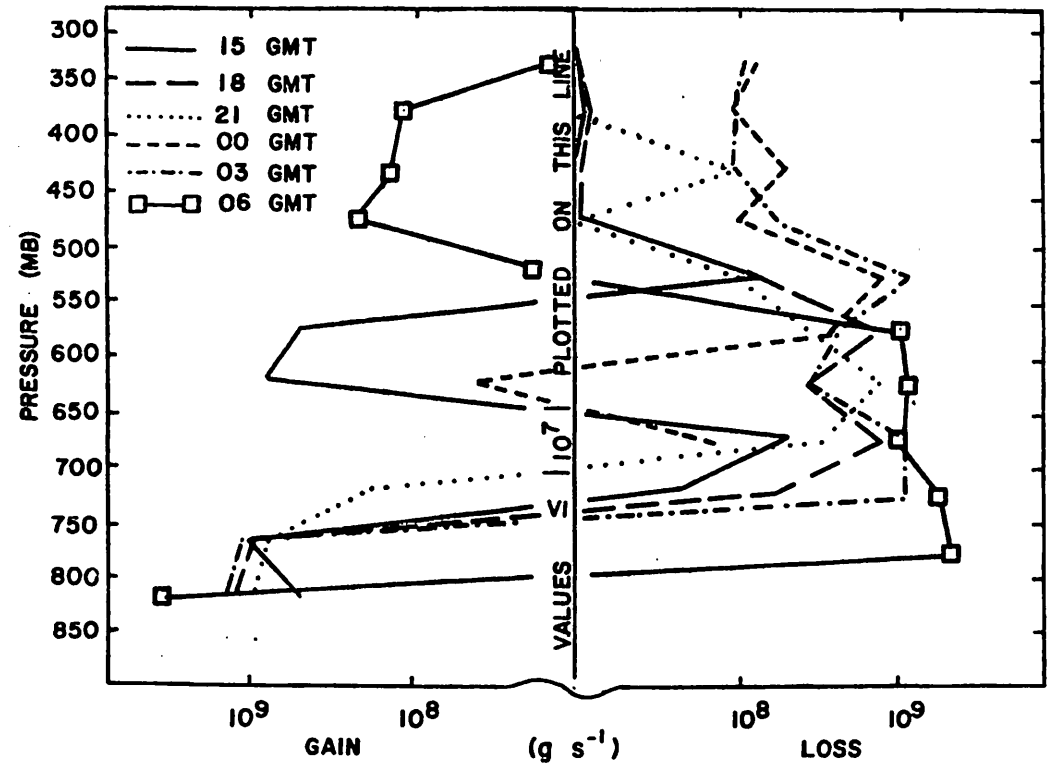

Fig. 5.11.5.2 Net vertical transport of water vapor through boundaries of 50-mb layers (gm s^{-1}) over the Texas HIPLEX area for 24 June 1977.

above 550 mb with a large net outflow in the lower layers.

Figure 5.11.5.3 shows profiles of vertical transport of water vapor through constant pressure surfaces. These profiles generally indicate strong downward transports for most times with the strongest coinciding with intense convective activity.

Figure 5.11.5.4 shows profiles of combined net horizontal and vertical transport of water vapor. These profiles generally show a net outflow in layers below 500 mb, and a net inflow in layers above this level. At 0300 GMT, with echo tops exceeding 9.1 km (30K ft) a large net outflow occurred above 500 mb. This strong net outflow also appears in Fig. 5.11.5.1.

Figure 5.11.5.5 shows vertical profiles of the total mass of water vapor. These profiles remain nearly similar prior to 0000 GMT, when light scattered echoes were observed over the area. Once strong convection occurred at 0000 GMT, an increase in the total mass of water vapor occurred in all layers and especially at 0300 GMT in layers above 500 mb. Once activity dissipated and moved from the area, a large decrease in water vapor occurred in most layers at 0600 GMT.

Figure 5.11.5.6 shows vertical profiles of the local rate-of-change in the total mass of water vapor. From 2100 to 0300 GMT, a general increase in water vapor occurred in all levels, especially between 650 and 500 mb. Such a storage of water vapor seems to be a characteristic prior to strong activity. This increase in water vapor can also be seen in Fig. 5.11.5.5. However, after movement and dissipation of the echo, a general loss of water vapor occurred at most levels between 0300 and 0600 GMT.

5.12 25 June 1977

5.12.1 Radar

The radar charts in Fig. 5.12.1.1 show numerous echoes of varying size, intensity, and areal coverage throughout the day. Cells with tops exceeding 9.1 km (30K ft) occurred each hour except from 1700 to 1900 GMT. The more intense and larger cells occurred between 2100 and 0300 GMT with as many as four distinct cells exceeding 9.1 km (30K ft) observed simultaneously.

5.12.2 Surface

The effects of the convective activity are reflected by large variations in the surface temperature fields (Fig. 5.12.2.1). Well-defined centers of minimum surface temperature are observed during times of heaviest activity, and correlate with the strongest echoes. Values of surface mixing ratio (Fig.

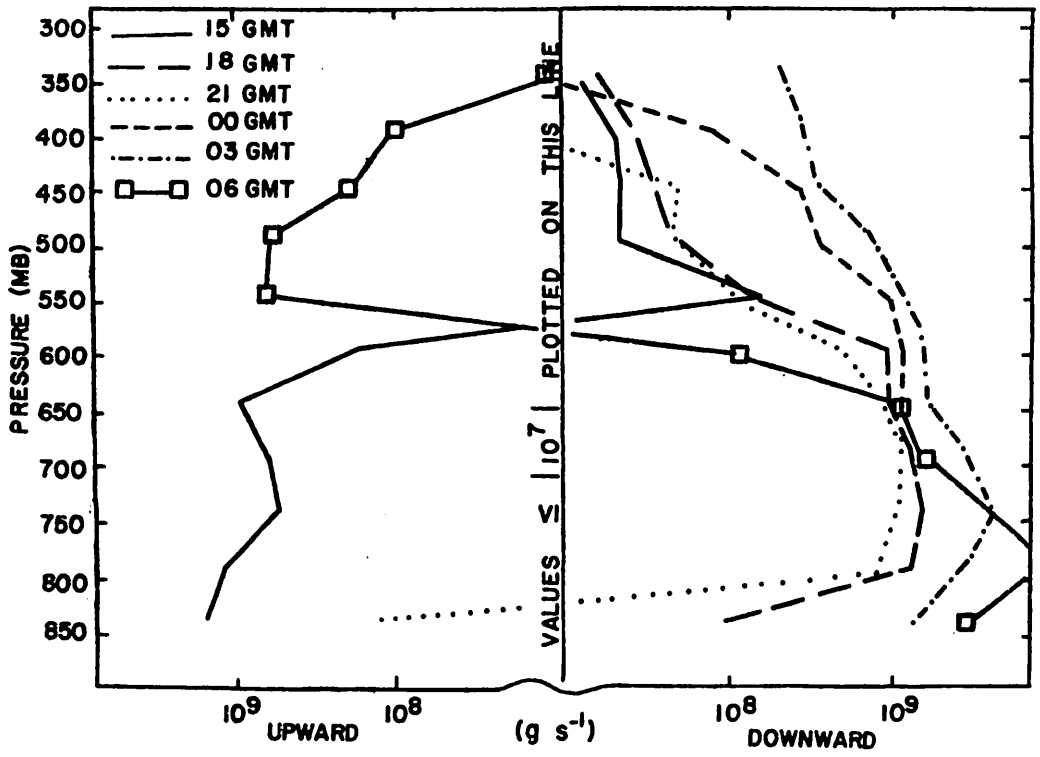

Fig. 5.11.5.3 Vertical transport of water vapor through constant pressure surfaces (gm s^{-1}) over the Texas HIPLEX area for 24 June 1977.

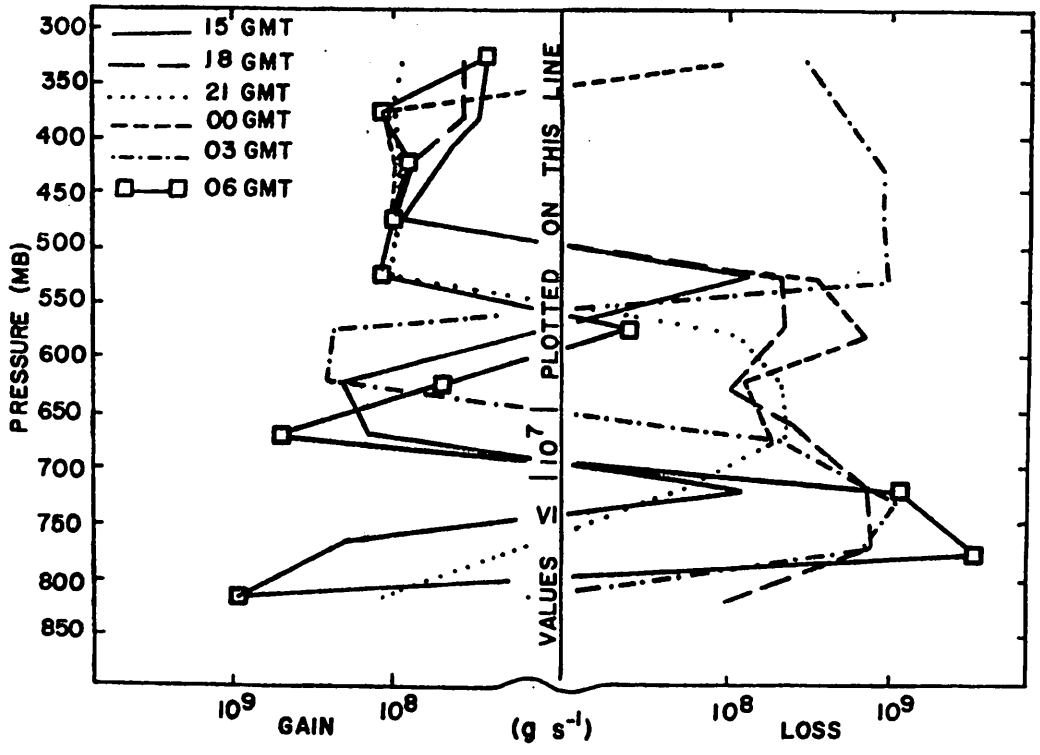

Fig. 5.11.5.4 Combined net horizontal and vertical transport of water vapor through boundaries of 50-mb layers (gm s^{-1}) over the Texas HIPLEX area for 24 June 1977.

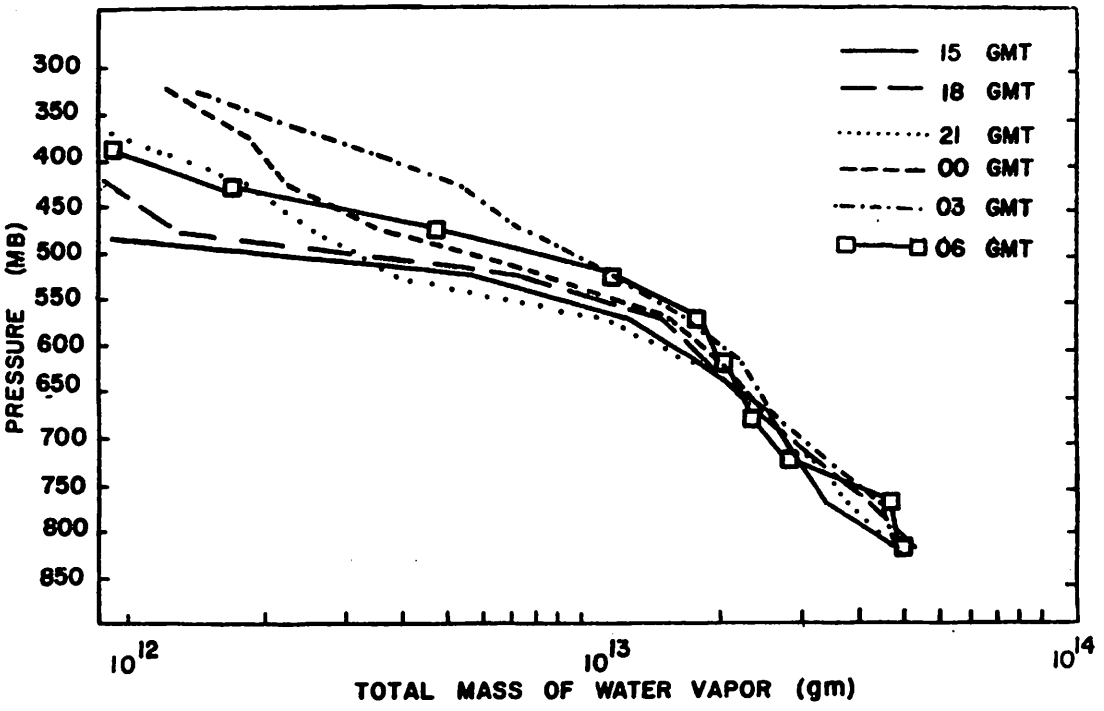

Fig. 5.11.5.5 Total mass of water vapor in layers 50 mb deep (gm) over the Texas HIPLEX area for 24 June 1977.

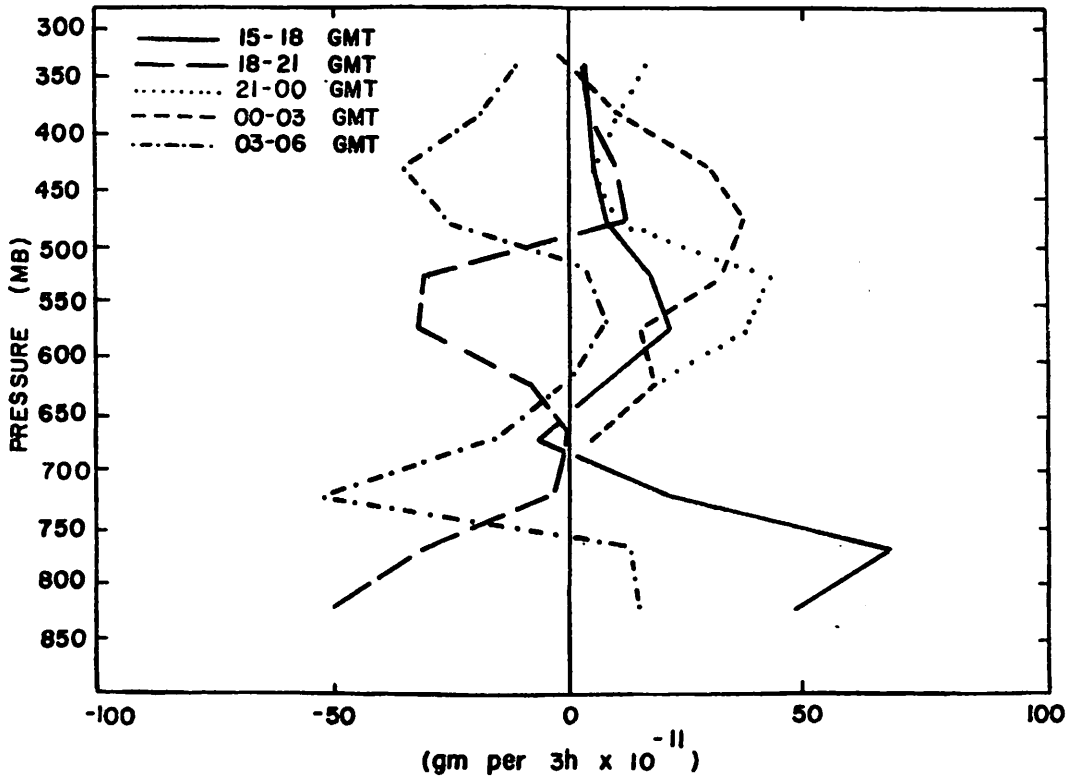

Fig. 5.11.5.6 Local rate-of-change in total mass of water vapor (gm per 3h x 10^{-11}) over the Texas HIPLEX area for 24 June 1977.

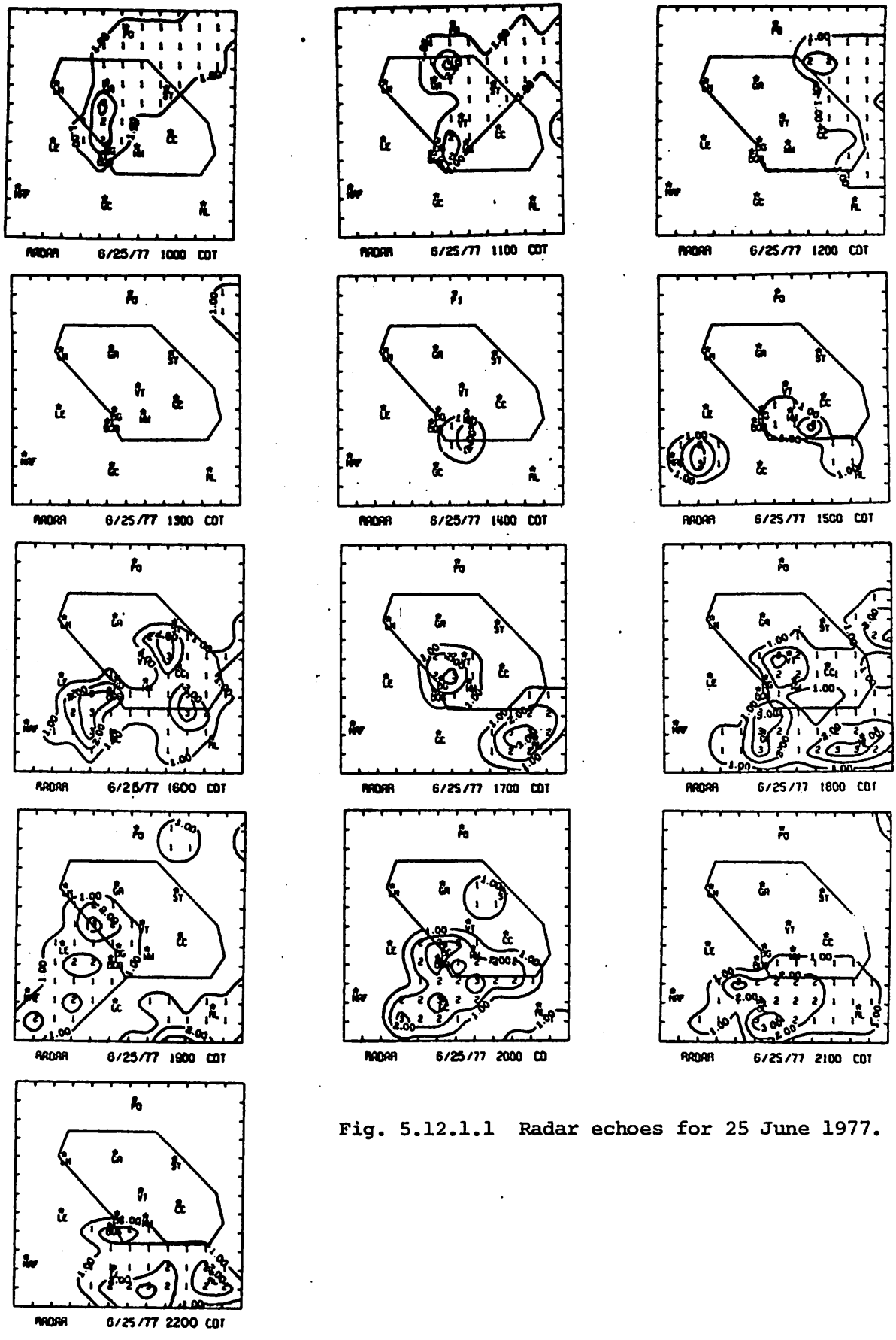

Fig. 5.12.1.1 Radar echoes for 25 June 1977.

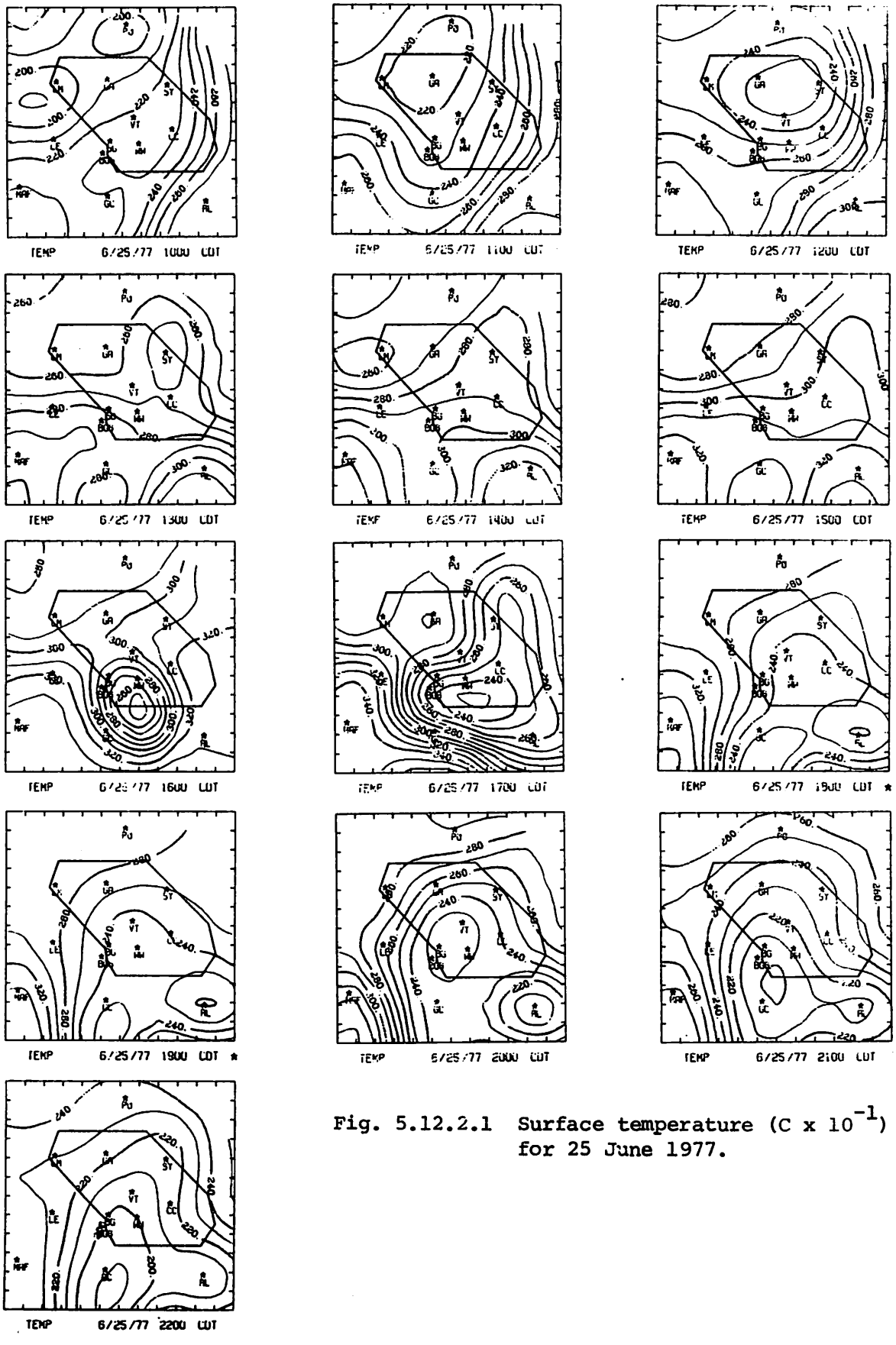

Fig. 5.12.2.1 Surface temperature (C x 10^{-1}) for 25 June 1977.

5.12.2.2) are greater to the east, but generally show centers of higher mixing ratio preceding the storm movement at 2200 and 2300 GMT. Fields of surface equivalent potential temperature (Fig. 5.12.2.3) show areas of strong minima in regions of convective activity.

The effect of terrain-induced vertical motion (Fig. 5.12.2.4) remains small with values not exceeding 2 cm s^{-1}. A center of downward motion is observed near Robert Lee throughout the day. Strong centers of surface velocity divergence (Fig. 5.12.2.5) occurred below radar echoes and correlate well with regions of minimum surface temperature. Downward vertical motion 50 mb above the surface (Fig. 5.12.2.6) occurred in these areas indicating a cold downdraft associated with heavy activity. Regions of upward vertical motion 50 mb above the surface preceded convective activity. Fields of surface moisture divergence (Fig. 5.12.2.7) and vertical flux of moisture 50 mb above the surface (Fig. 5.12.2.8) also show these results. Patterns of surface vorticity (Fig. 5.12.2.9) show centers of both cyclonic and anticyclonic vorticity associated with these echoes. Centers of cyclonic vorticity generally precede the echoes with anticyclonic centers behind.

Values of sea level pressure (Fig. 5.12.2.10) decreases from west to east with regions of high and low pressure near Lenorah and Robert Lee, respectively. This pattern shows relatively little change as reflected in Fig. 5.12.2.11.

5.12.3 Upper-Level Kinematic Parameters

Horizontal mass convergence in low levels was the most important feature in Fig. 5.12.3.1, especially at 2100 GMT and 0000 GMT when strong thunderstorm development occurred. At 2400 GMT mass divergence was computed above 600 mb, but by 0000 GMT strong mass convergence existed from the surface to 300 mb. Upward vertical velocities at mid-levels at 1500 GMT weaken at all levels to near zero values at 1800 GMT when storm dissipation occurred (Fig. 5.12.3.2). Before and during thunderstorm regeneration at 2100 and 0000 GMT, vertical velocities become strong upward at all levels.

Horizontal moisture convergence occurred at all levels and times between 800 and 700 mb, becoming strongest during times of activity (Fig. 5.12.3.3). Horizontal mass divergence was important at low-levels at 1500 GMT when storm dissipation was occurring, and at 2100 GMT in mid-levels when strong convective activity was developing.

5.12.4 Energetics

Horizontal flux convergence of latent heat energy dominates the vertical

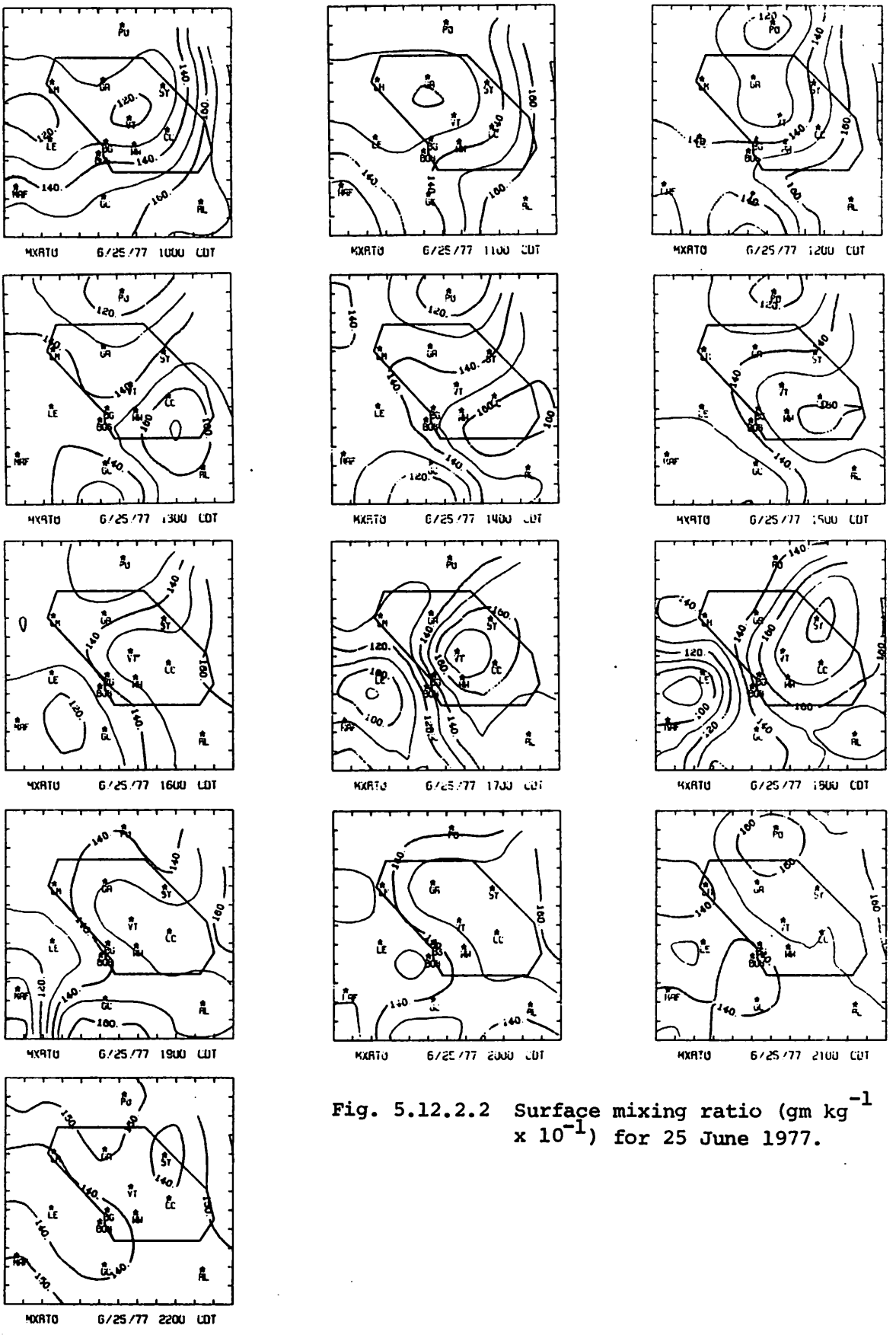

Fig. 5.12.2.2 Surface mixing ratio (gm kg^{-1} x 10^{-1}) for 25 June 1977.

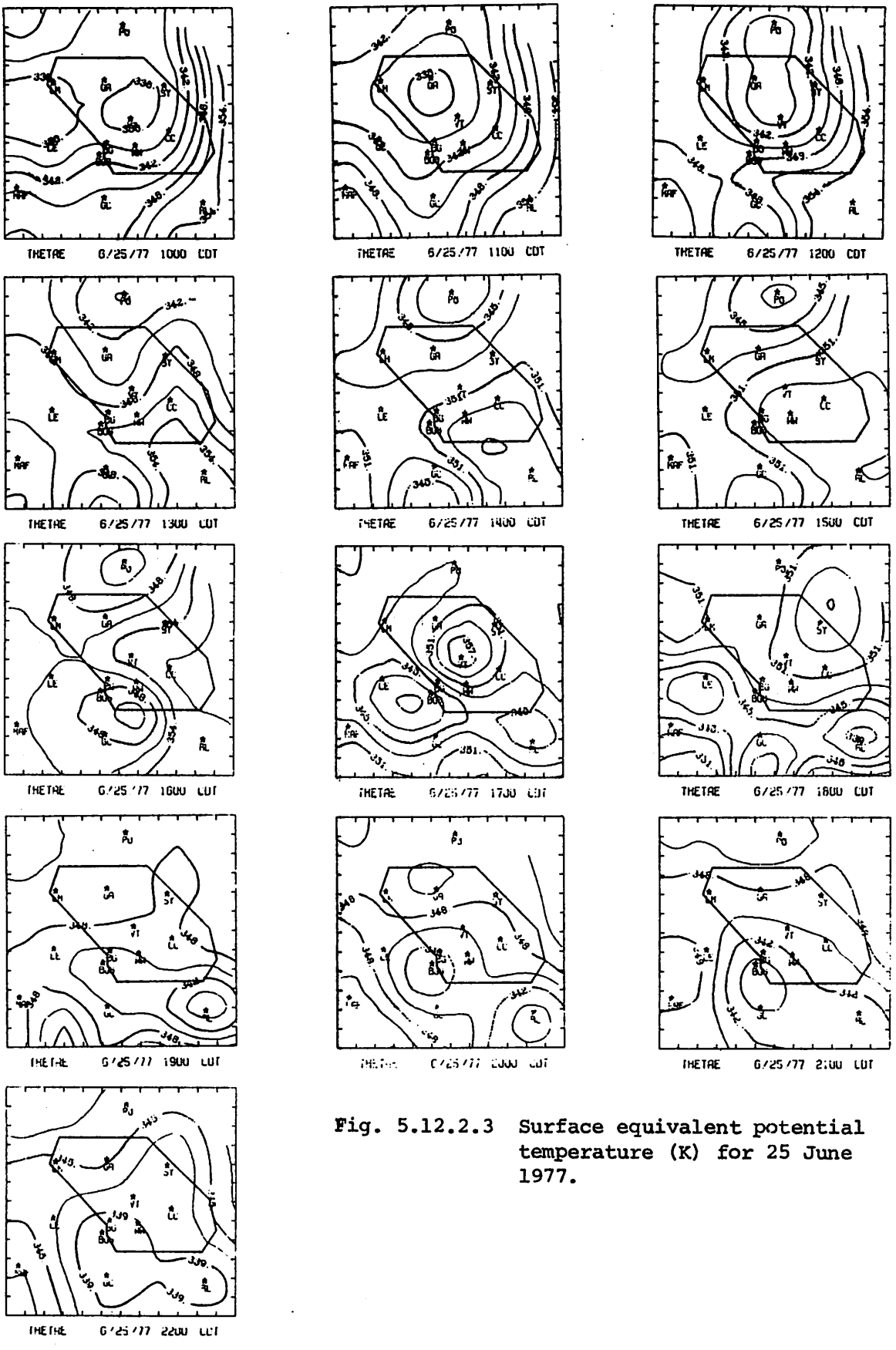

Fig. 5.12.2.3 Surface equivalent potential temperature (K) for 25 June 1977.

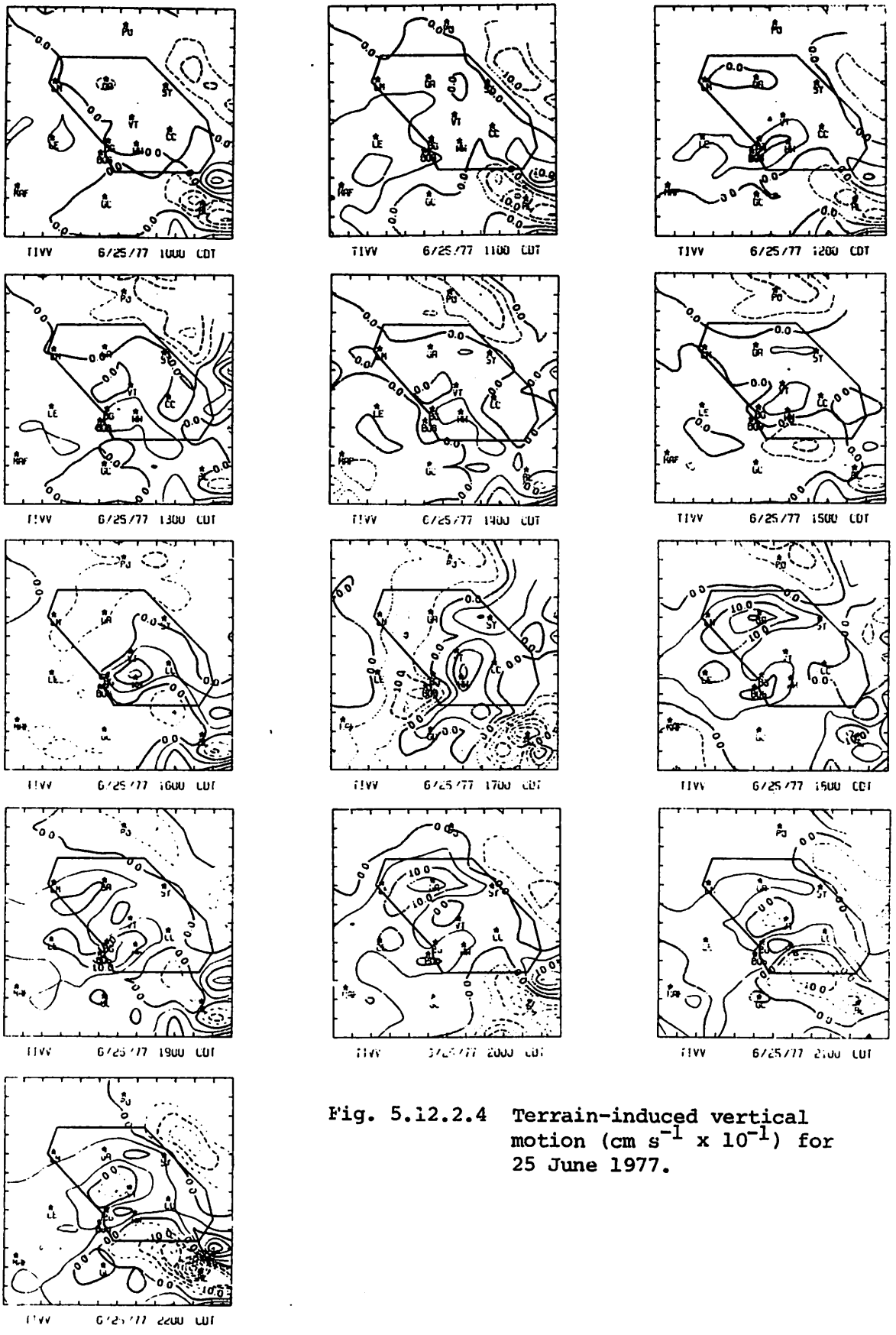

Fig. 5.12.2.4 Terrain-induced vertical motion (cm s^{-1} x 10^{-1}) for 25 June 1977.

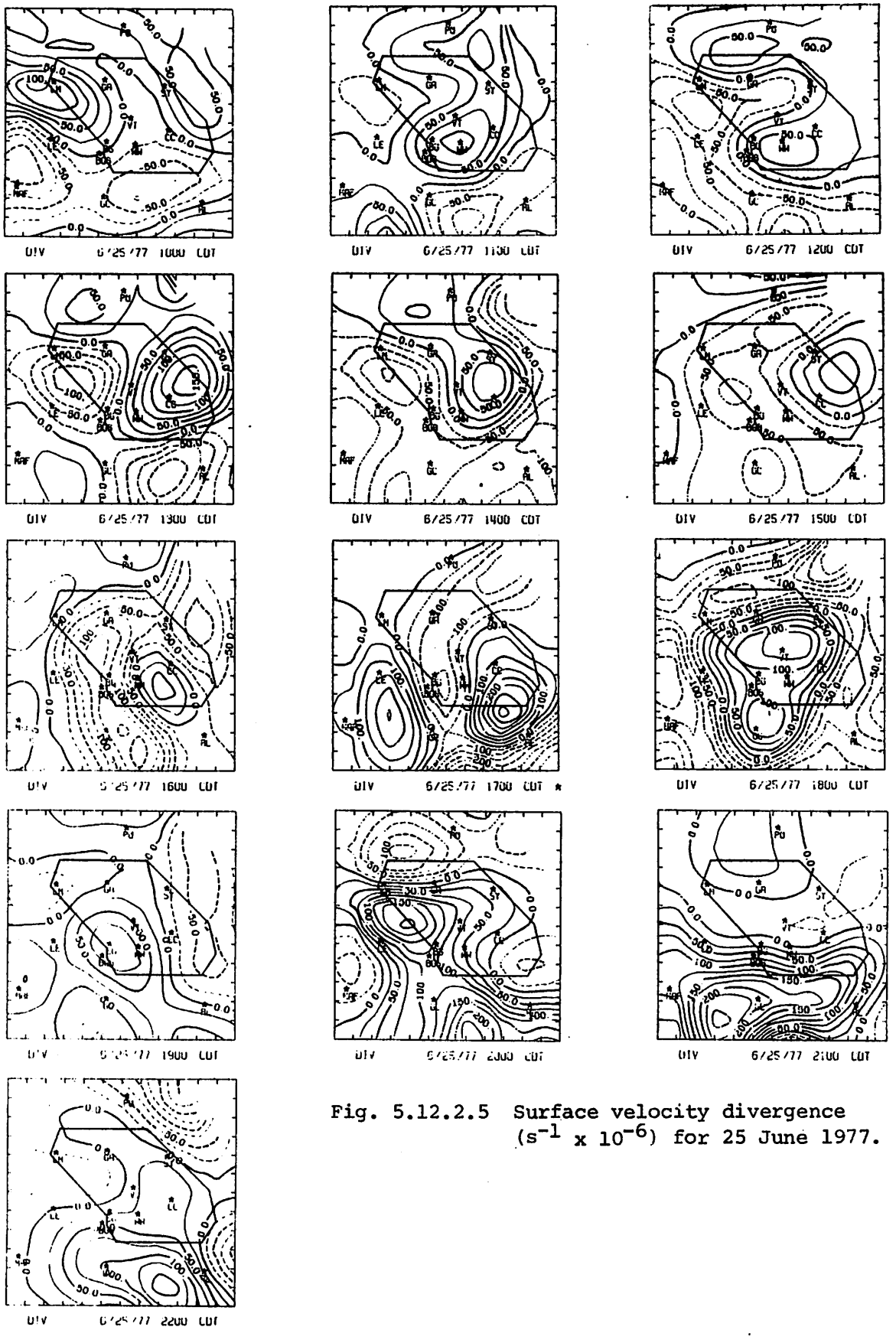

Fig. 5.12.2.5 Surface velocity divergence (s^{-1} x 10^{-6}) for 25 June 1977.

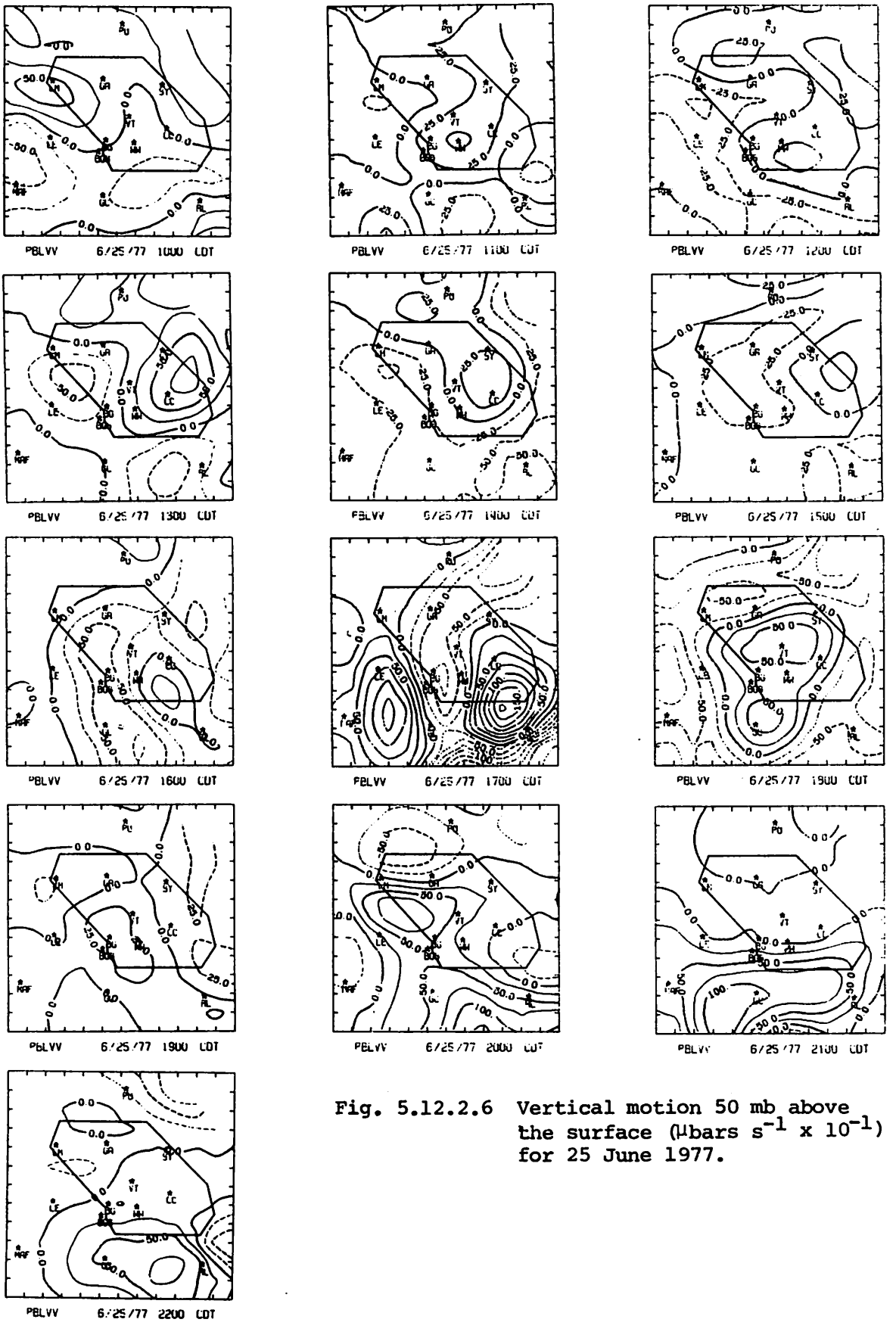

Fig. 5.12.2.6 Vertical motion 50 mb above the surface (μbars s^{-1} x 10^{-1}) for 25 June 1977.

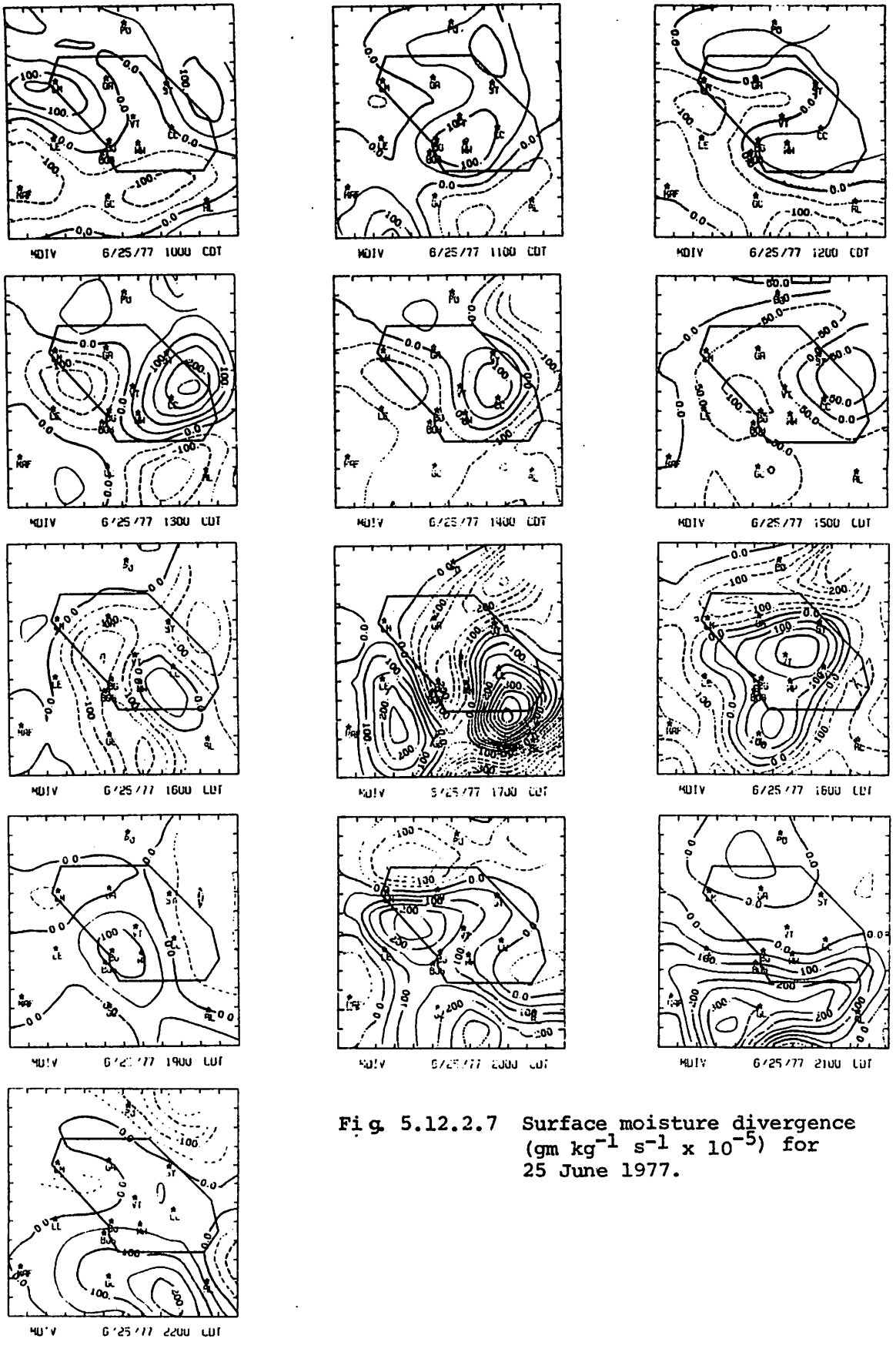

Fig. 5.12.2.7 Surface moisture divergence (gm kg^{-1} s^{-1} x 10^{-5}) for 25 June 1977.

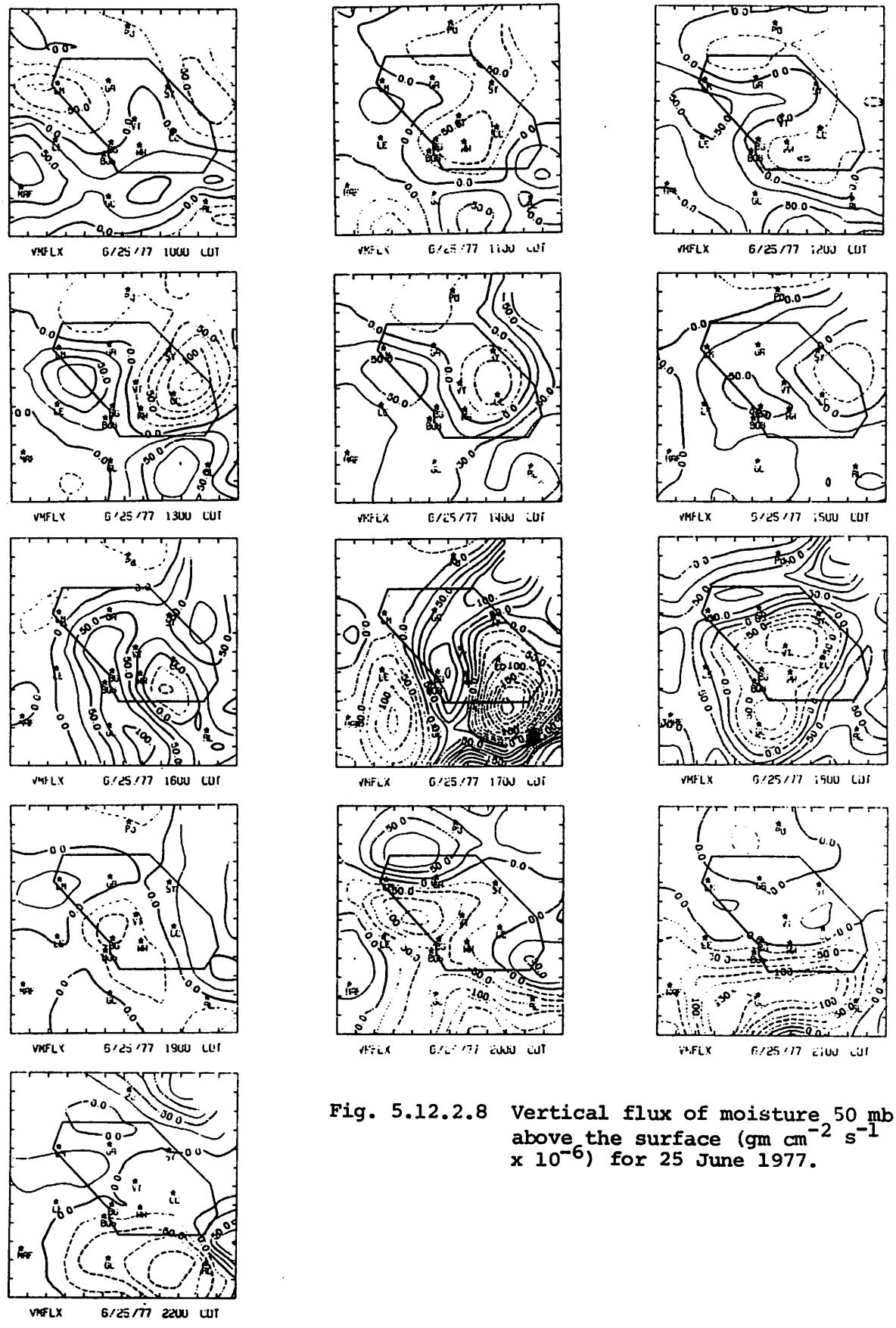

Fig. 5.12.2.8 Vertical flux of moisture 50 mb above the surface (gm cm^{-2} s^{-1} x 10^{-6}) for 25 June 1977.

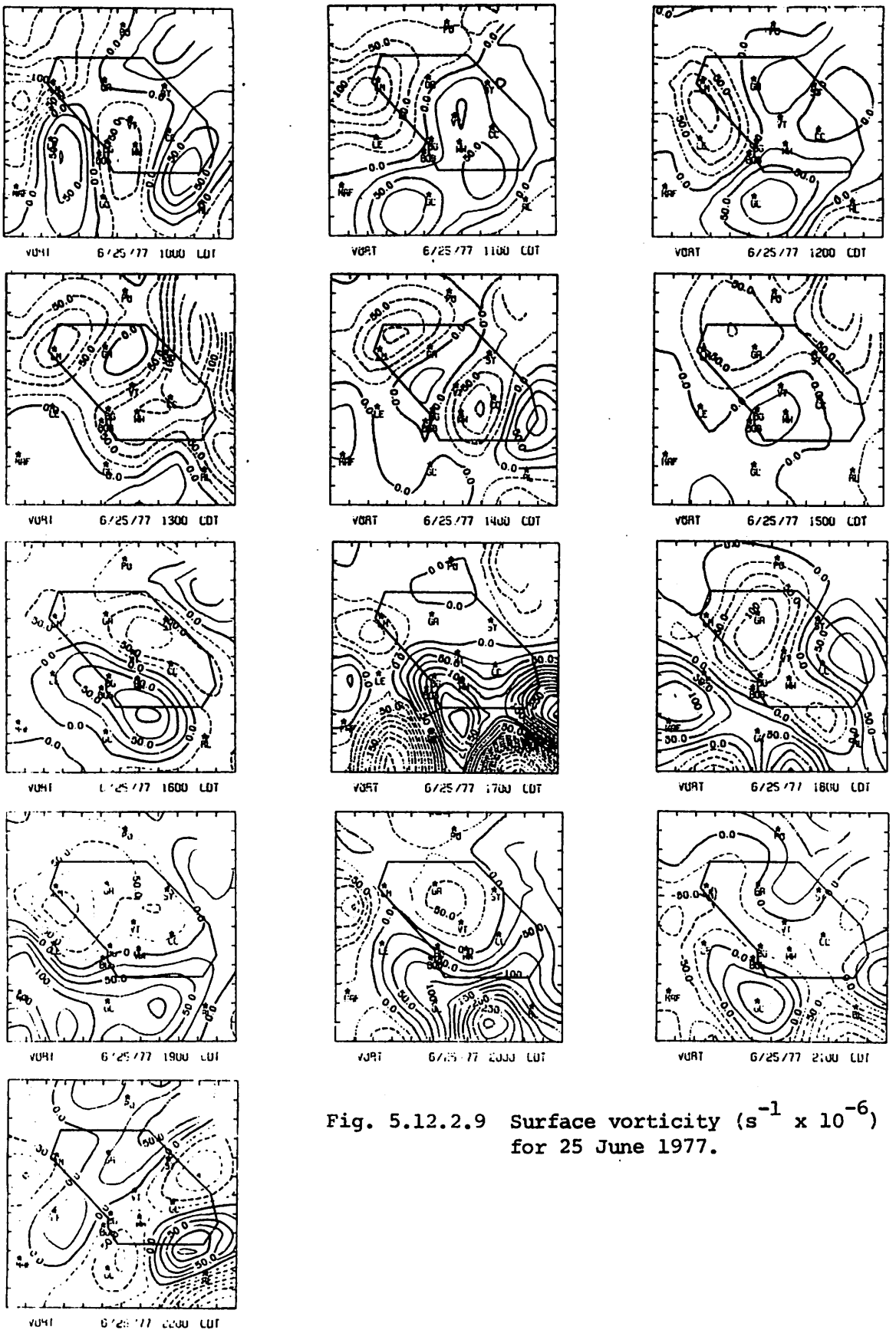

Fig. 5.12.2.9 Surface vorticity ($s^{-1} \times 10^{-6}$) for 25 June 1977.

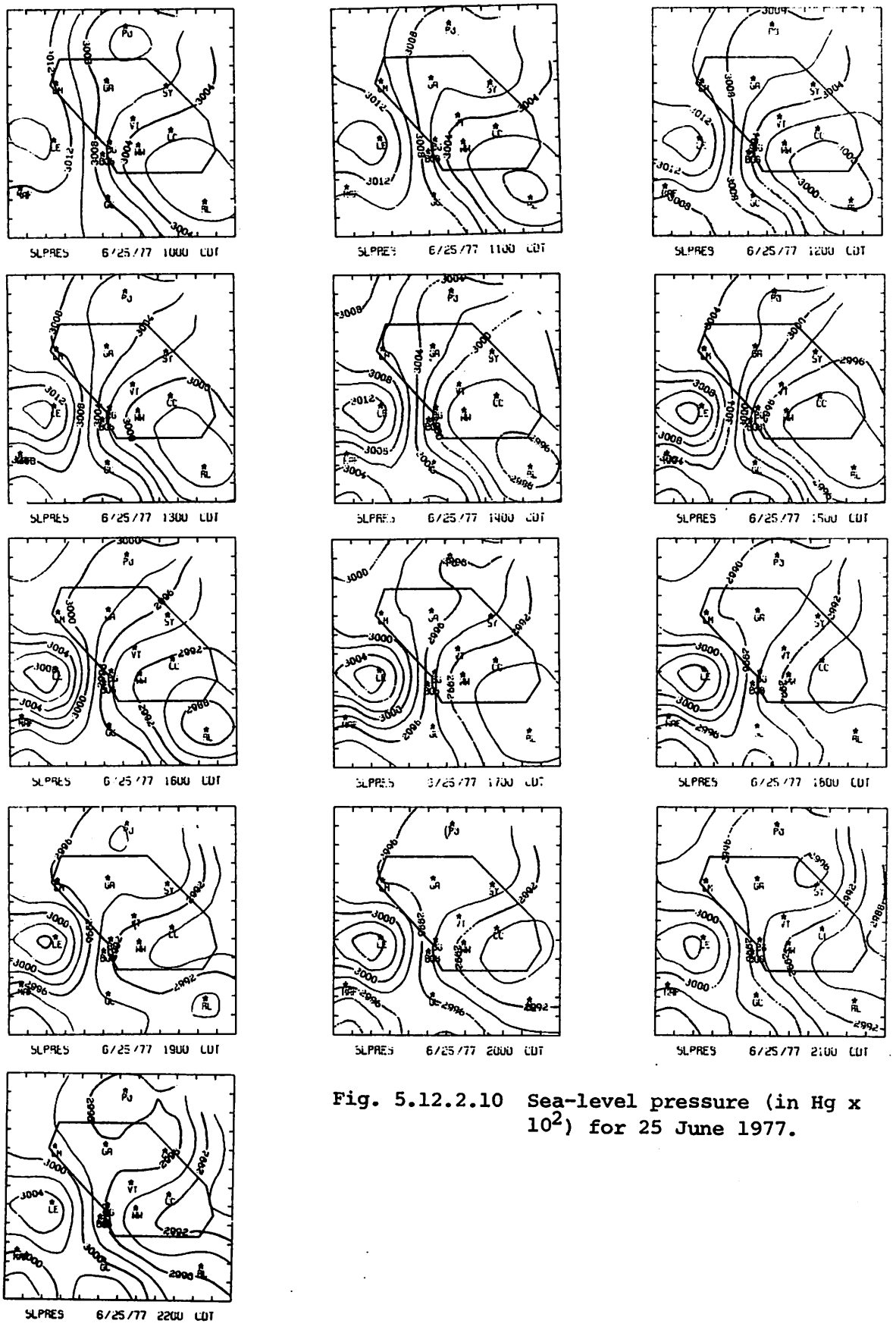

Fig. 5.12.2.10 Sea-level pressure (in Hg x 10^2) for 25 June 1977.

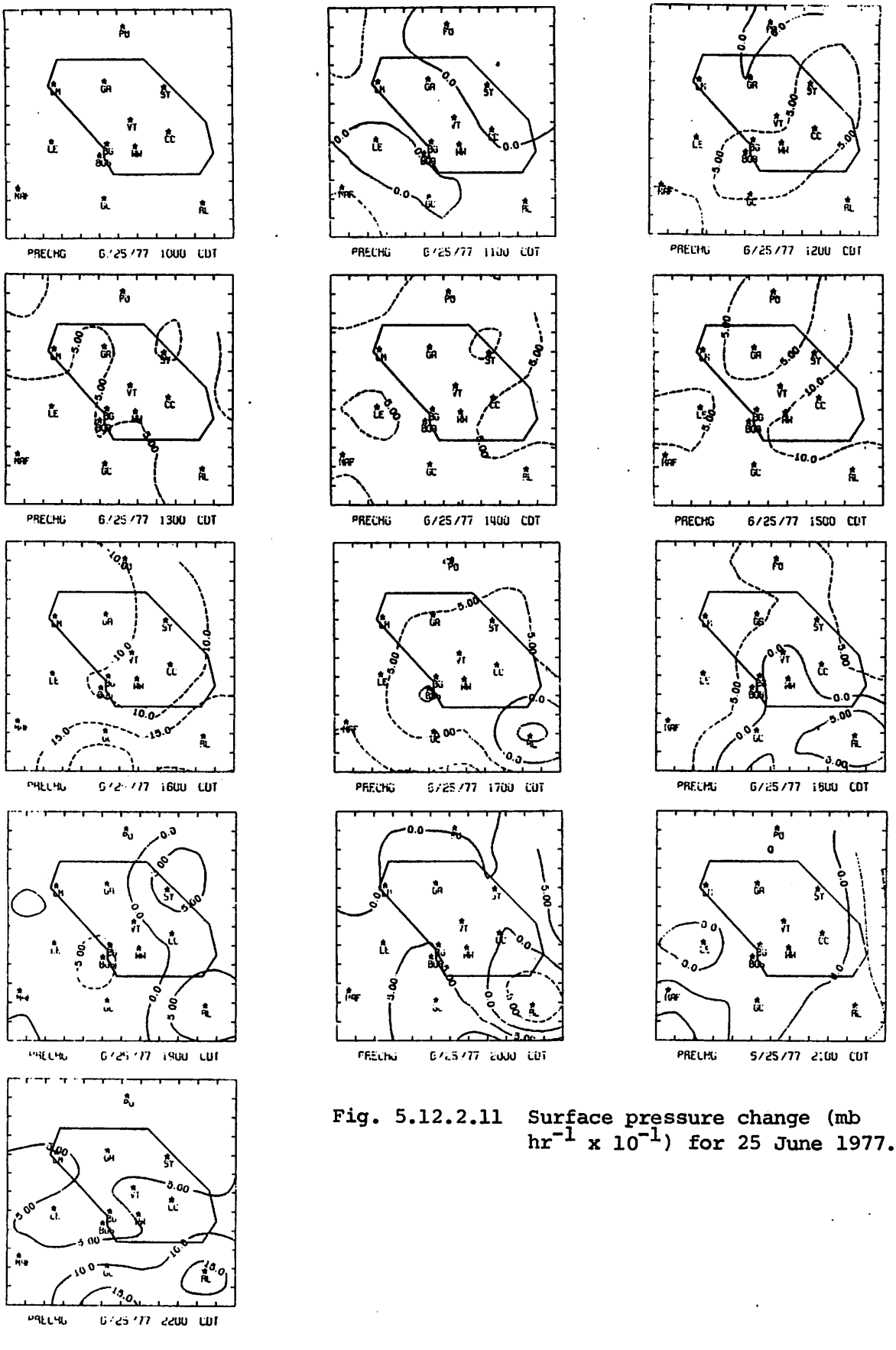

Fig. 5.12.2.11 Surface pressure change (mb hr^{-1} x 10^{-1}) for 25 June 1977.

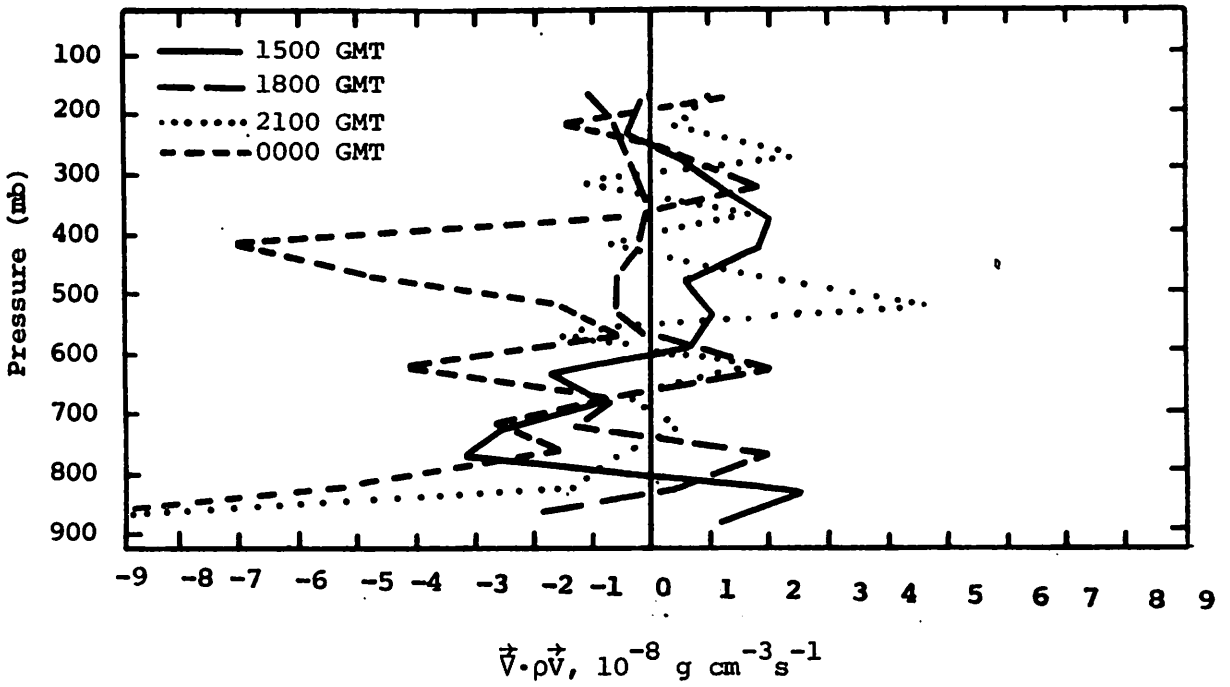

Fig. 5.12.3.1 Vertical profiles of mass divergence on 25 June 1977.

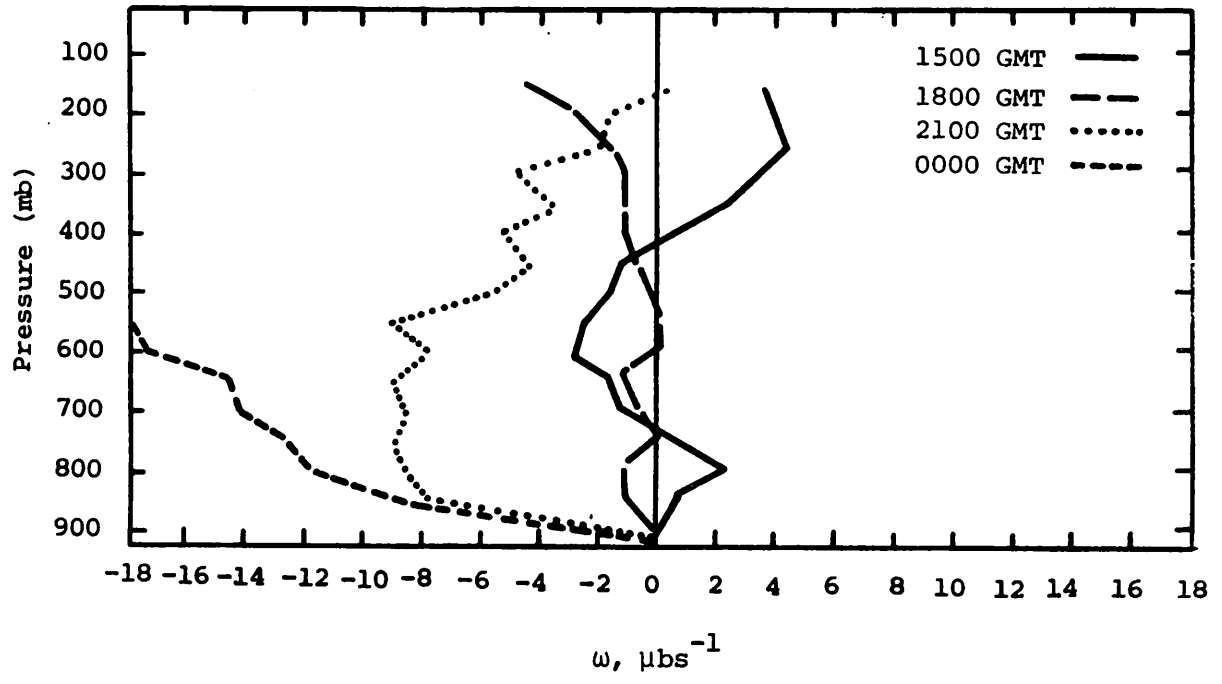

Fig. 5.12.3.2 Vertical profiles of vertical motion on 25 June 1977.

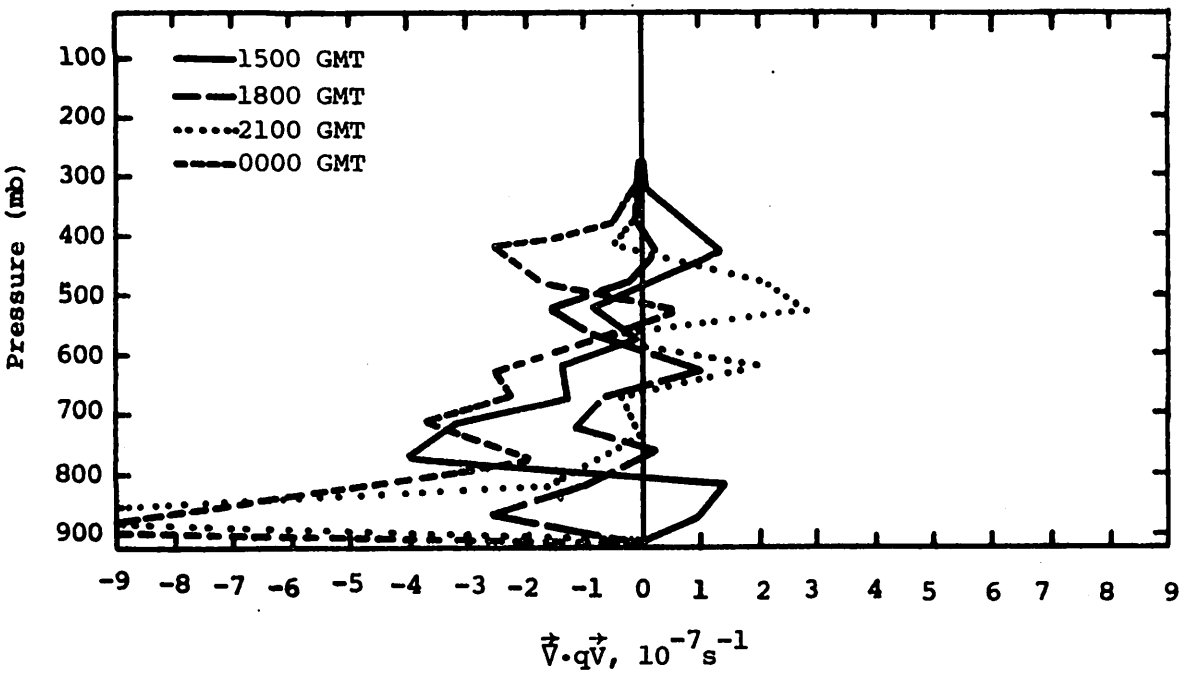

Fig. 5.12.3.3 Vertical profiles of moisture divergence on 25 June 1977.

profiles in Fig. 5.12.4.1 between 800 and 600 mb at all times. Flux divergence is large only at 1500 GMT below 800 mb, and at 2100 GMT between 600 and 400 mb when storm development occurred. Net inflow of latent heat energy was largest at 2100 GMT in low levels and correlated well with the strong thunderstorm formation. Vertical flux divergence of latent heat energy was computed in low levels and flux convergence aloft at 1500, 1800, and 2100 GMT (Fig. 5.12.4.2). Values were generally largest at 2100 GMT when upward vertical velocities were associated with a net transport of latent heat energy from low- to mid-levels. Local changes of latent heat energy were large and positive only in low levels prior to storm formation (Fig. 5.12.4.3).

The residual profiles from the latent heat budget equation (Fig. 5.12.4.4) show large losses of latent heat energy (positive -R values) only at 2100 GMT in low- and mid-levels. This distribution is consistent with environment heating created by precipitation development and is supported by the results shown in the diabatic heating profiles (Fig. 5.12.4.5). These profiles are consistent in sign at most levels and times with the latent heat budget residual except above the 300-mb level.

Horizontal flux divergence profiles of kinetic energy generally showed net inflow of energy in low levels and outflow aloft, except at 0000 GMT when net inflow occurred at all levels (Fig. 5.12.4.6). Vertical flux divergence of kinetic energy was small at most levels below

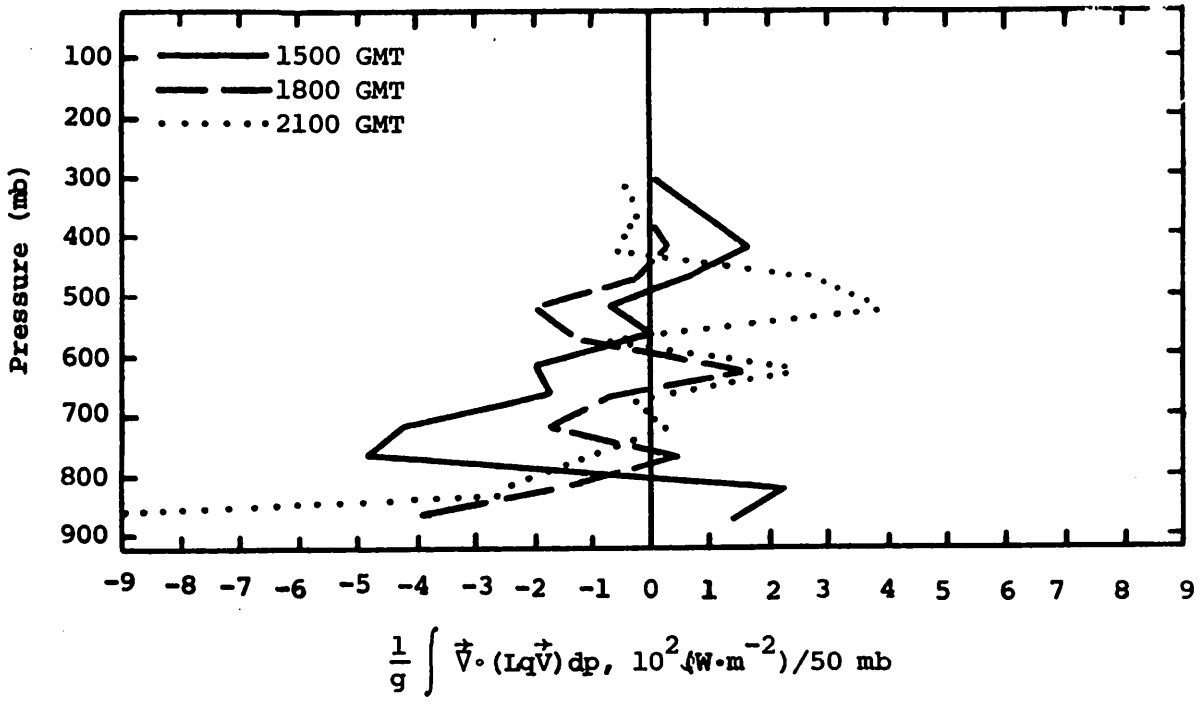

Fig. 5.12.4.1 Vertical profiles of the horizontal flux of latent heat energy on 25 June 1977.

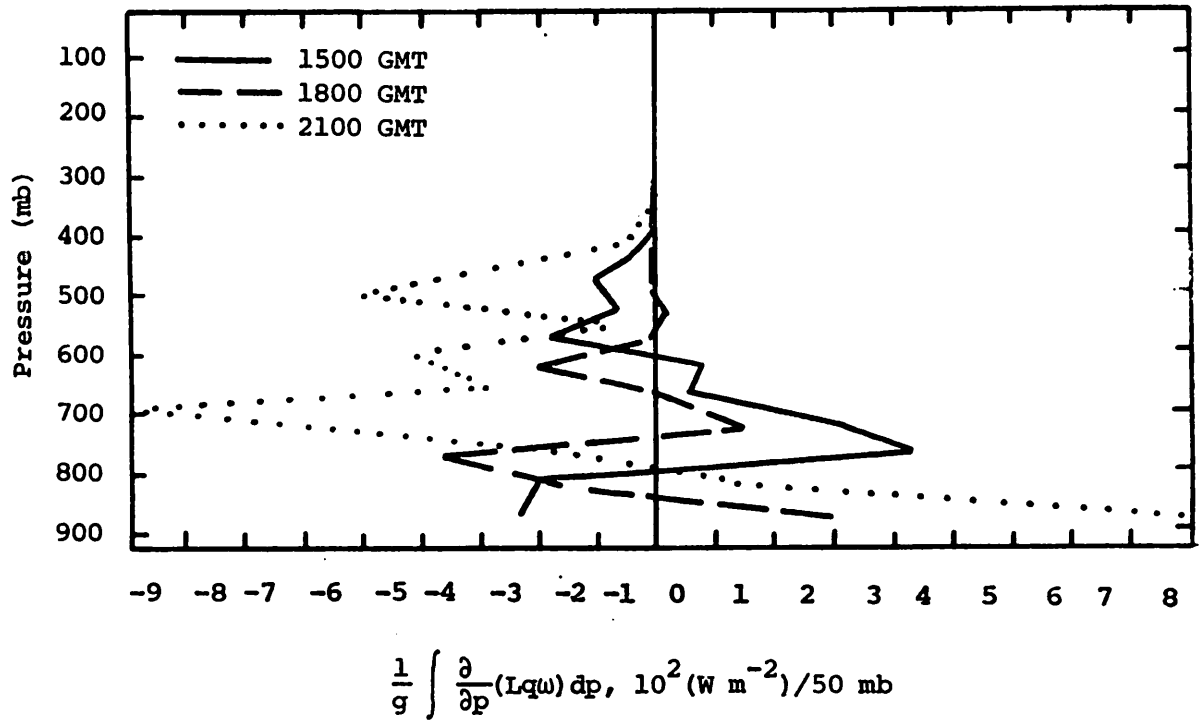

Fig. 5.12.4.2 Vertical profiles of the vertical flux of latent heat energy on 25 June 1977.

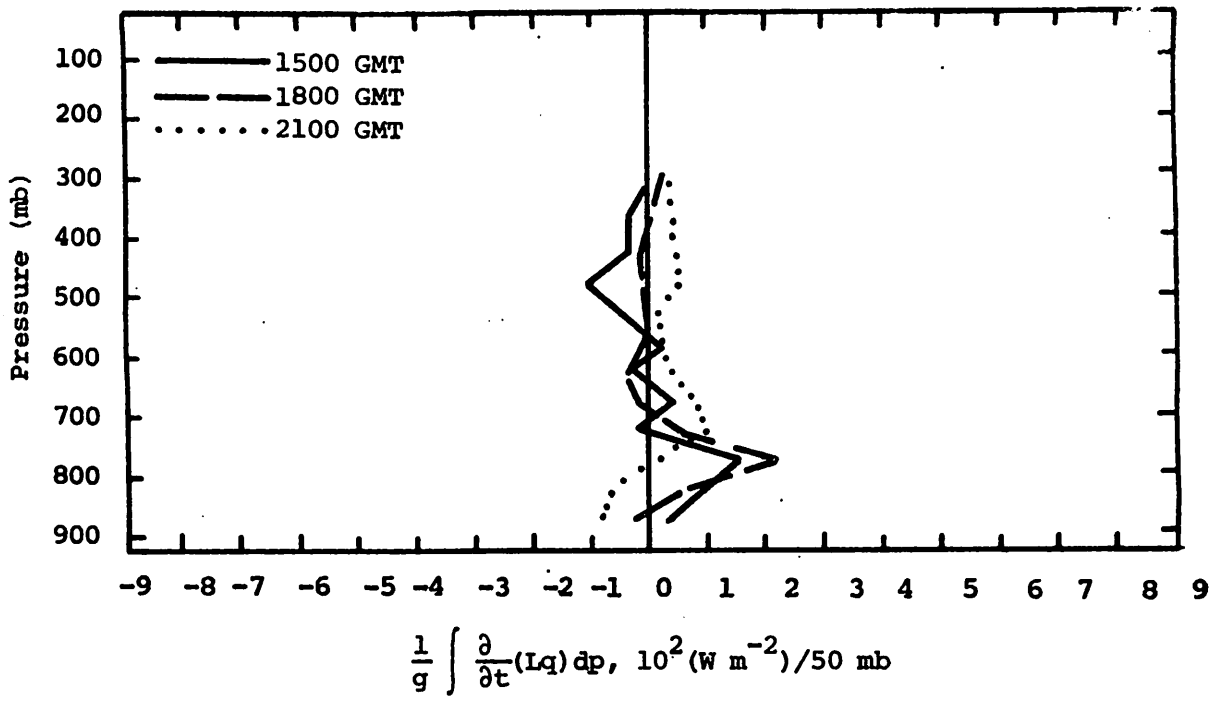

Fig. 5.12.4.3 Vertical profiles of the local change of latent heat energy on 25 June 1977.

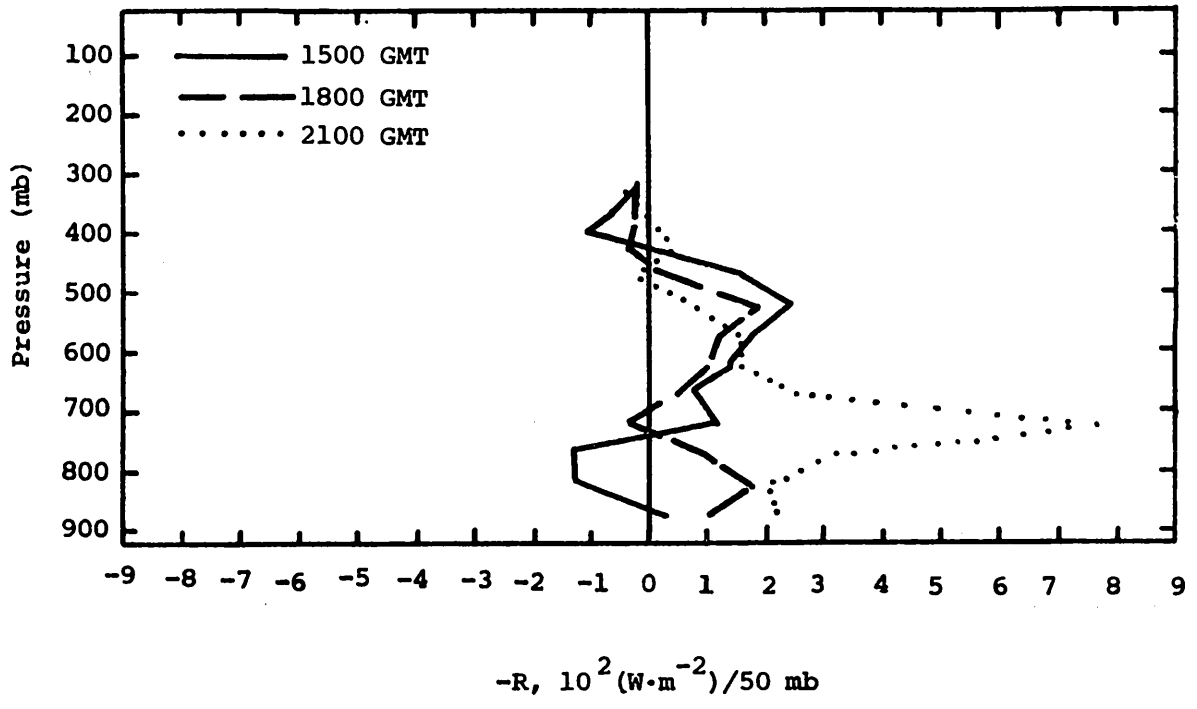

Fig. 5.12.4.4 Vertical profile of the residual of the latent heat energy equation on 25 June 1977.

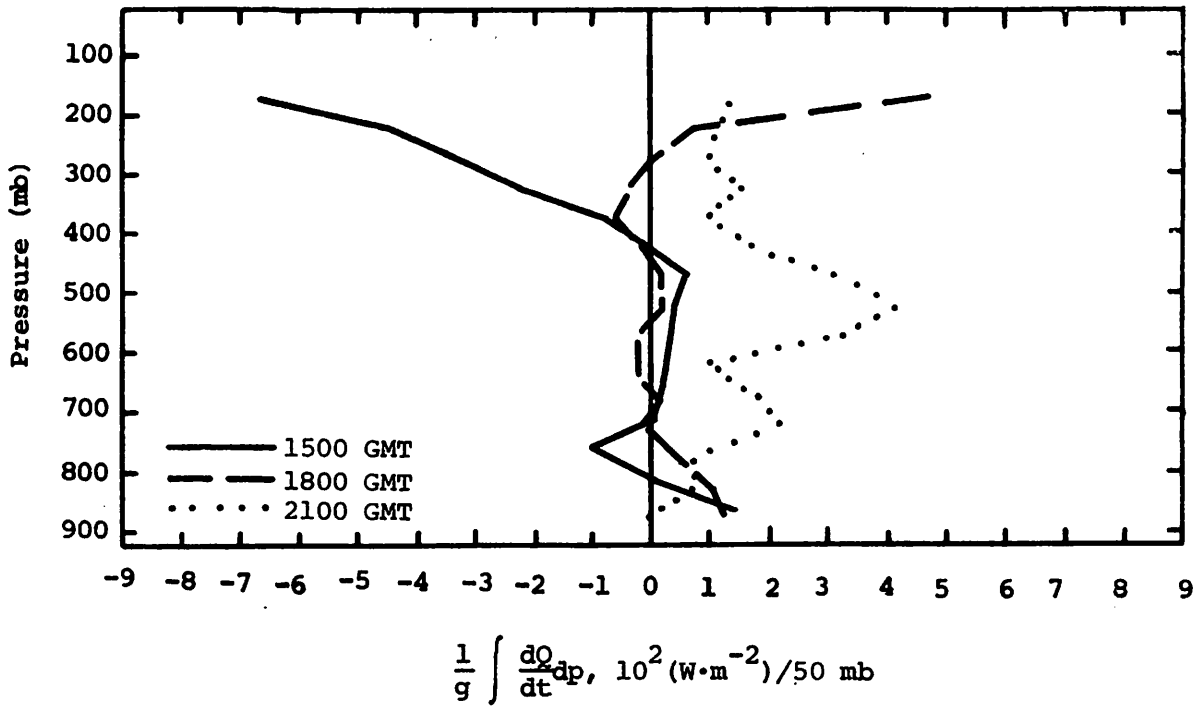

Fig. 5.12.4.5 Vertical profiles of diabatic heating computed from the first law of thermodynamics on 25 June 1977.

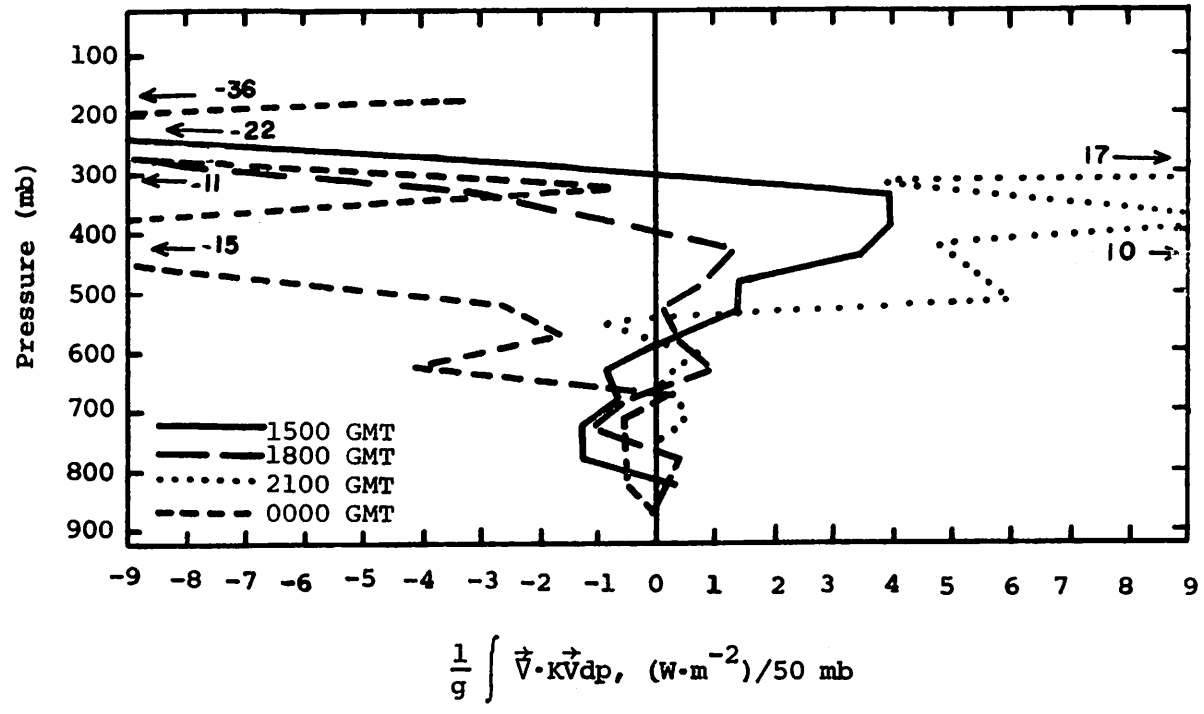

Fig. 5.12.4.6 Vertical profiles of the horizontal flux of kinetic energy on 25 June 1977.

700 mb (Fig. 5.12.4.7) with large flux convergence at mid levels followed by flux divergence of kinetic energy in upper levels at 1500 GMT. At 1800 and 2100 GMT, the pattern of convergence/divergence above 500 mb completely reverses.

5.12.5 Water Vapor Budget

Figure 5.12.5.1 shows vertical profiles of the net horizontal transport of water vapor. These profiles show a strong net inflow of water vapor in layers below 500 mb at all times, and during times of strong convection show a net outflow in layers above. This characteristic associated with strong convection has also been observed in Figs. 5.10.5.1 and 5.11.5.1 at 0000 and 0300 GMT, respectively.

Figure 5.12.5.2 shows profiles of the net vertical transport of water vapor. These profiles show a net outflow in lower layers and a net inflow in layers above. However, in cases of strong convection (i.e., 2100 and 0000 GMT) these profiles show a large net inflow in most layers. At these times, a large net inflow tends to "store" water vapor in upper layers between 575 and 450 mb.

Figure 5.12.5.3 shows profiles of vertical transport of water vapor through constant pressure surfaces and indicate strong upward transport of water vapor at most times. As would be expected, profiles for 2100 and 0000 GMT show maximum transports associated with increased net vertical transports (Fig. 5.12.5.2) during strong convection.

Figure 5.12.5.4 shows vertical profiles of combined net horizontal and vertical transport of water vapor. These profiles show a strong net inflow for most times and layers. A strong net inflow occurred in all layers during times of intense activity.

Figure 5.12.5.5 shows vertical profiles of the total mass of water vapor. These profiles remain similar, especially between 700 and 500 mb. This would be expected since heavy activity was observed over the network at all times except near 1800 GMT. This is also shown by decreased water vapor in the 1800 GMT profile for layers above 600 mb.

Figure 5.12.5.6 shows vertical profiles of the local rate-of-change in the total mass of water vapor. These profiles show large temporal variations in the lower and higher layers. Between 1500 and 1800 GMT, a loss of water vapor occurred as the activity moved from the area. At 2100 GMT, activity developed over the area, and is reflected by an increase in water vapor in most layers. From 2100 to 0000 GMT, a large loss of water vapor occurred in

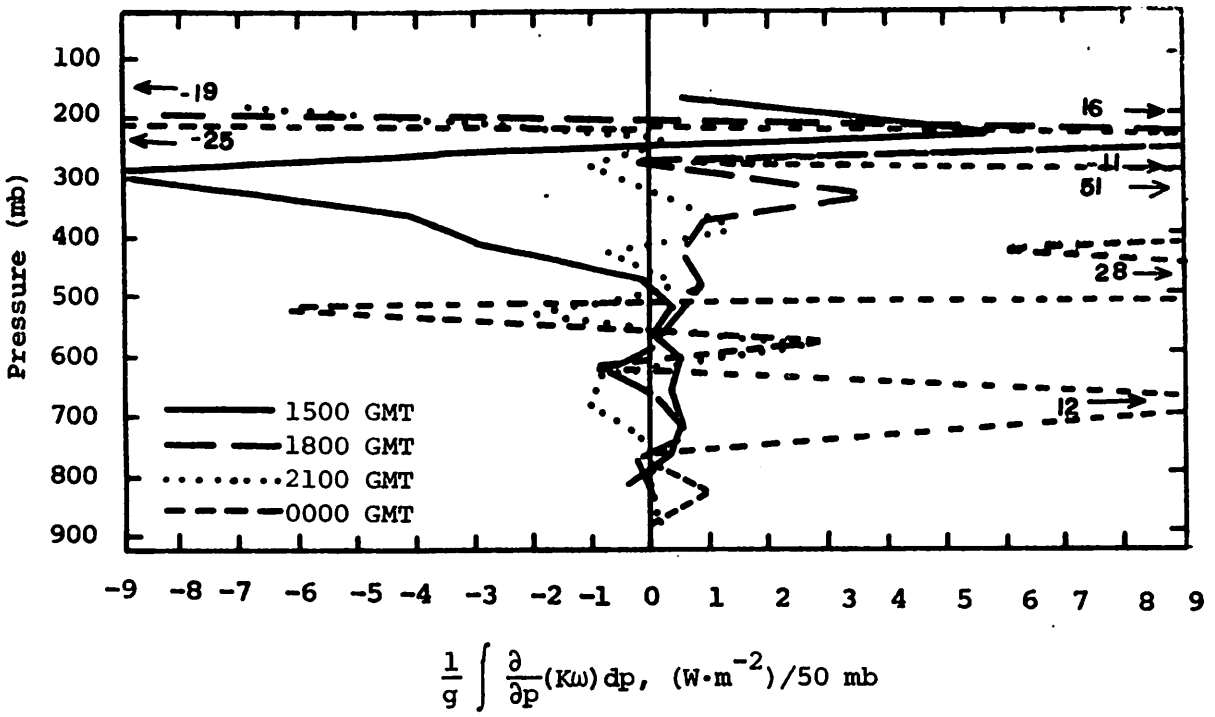

Fig. 5.12.4.7 Vertical profiles of the vertical flux of kinetic energy on 25 June 1977.

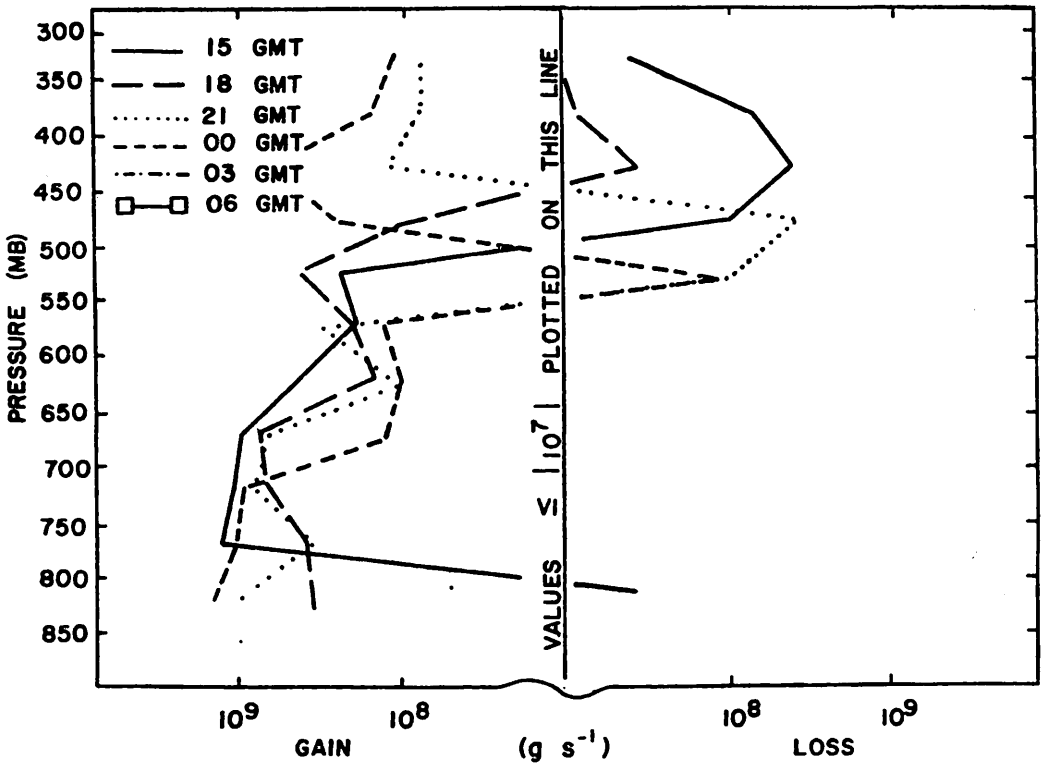

Fig. 5.12.5.1 Net horizontal transport of water vapor through boundaries of 50-mb layers (gm s^{-1}) over the Texas HIPLEX area for 25 June 1977.

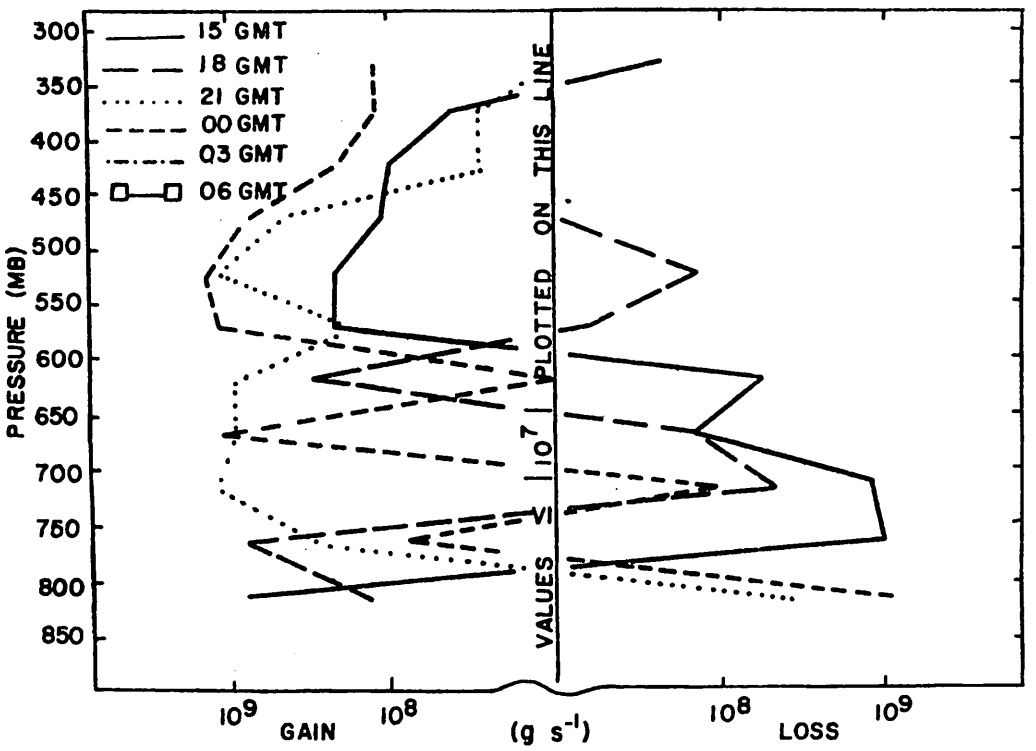

Fig. 5.12.5.2 Net vertical transport of water vapor through boundaries of 50-mb layers (gm s^{-1}) over the Texas HIPLEX area for 25 June 1977.

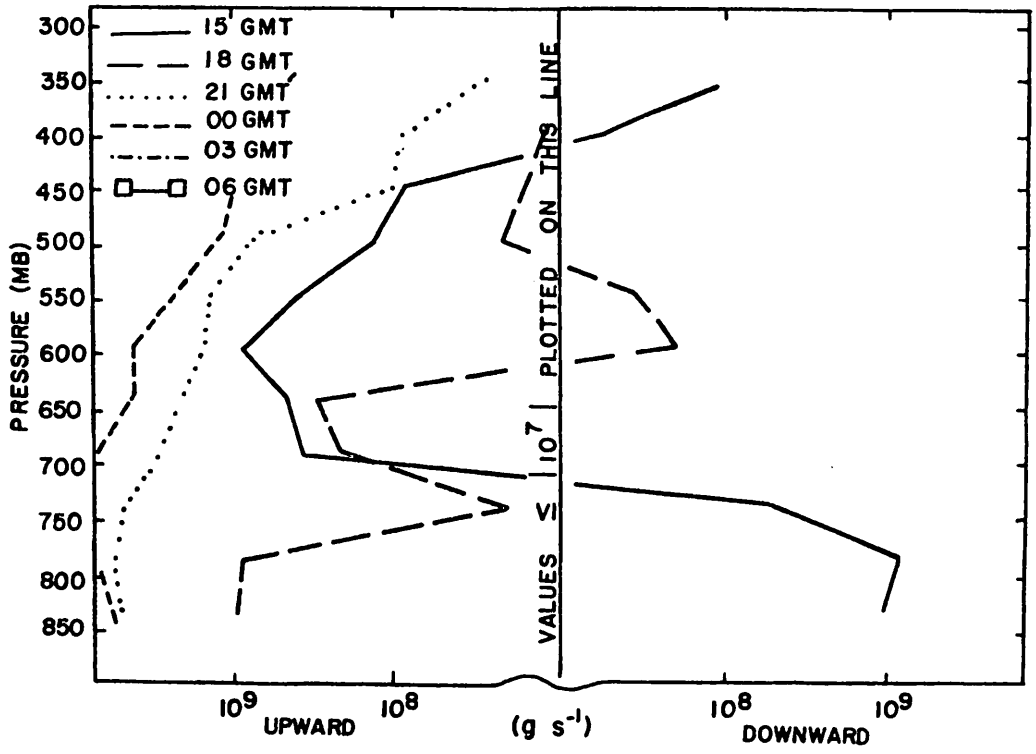

Fig. 5.12.5.3 Vertical transport of water vapor through constant pressure surfaces (gm s^{-1}) over the Texas HIPLEX area for 25 June 1977.

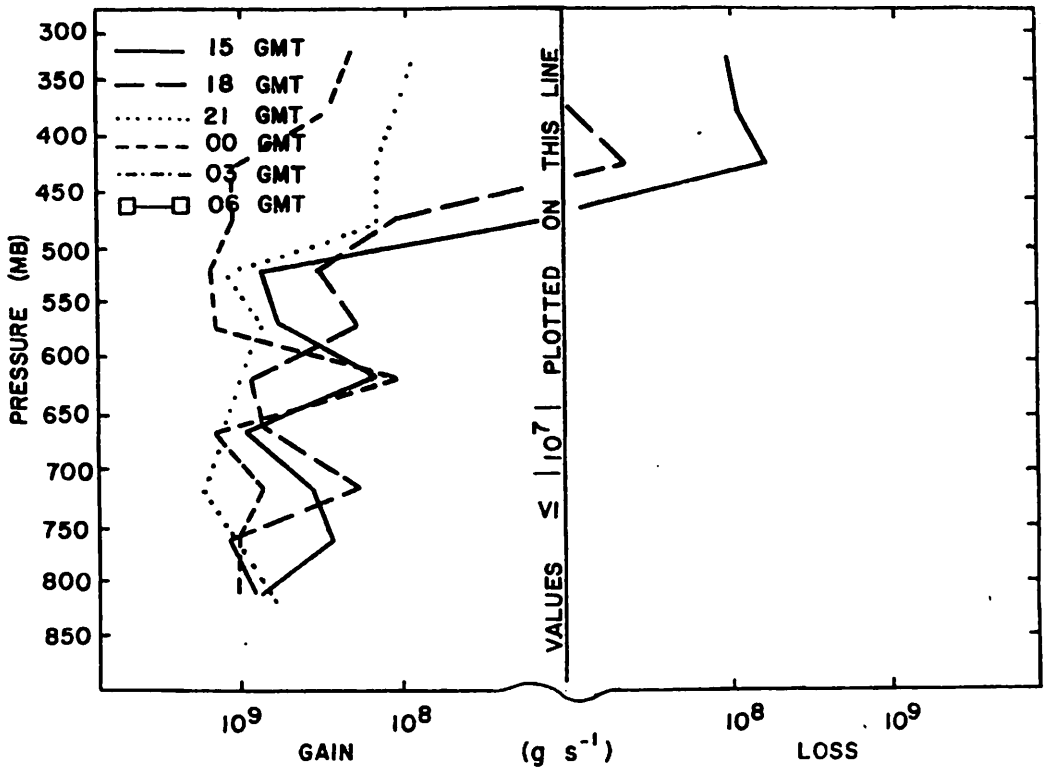

Fig. 5.12.5.4 Combined net horizontal and vertical transport of water vapor through boundaries of 50-mb layers (gm s^{-1}) over the Texas HIPLEX area for 25 June 1977.

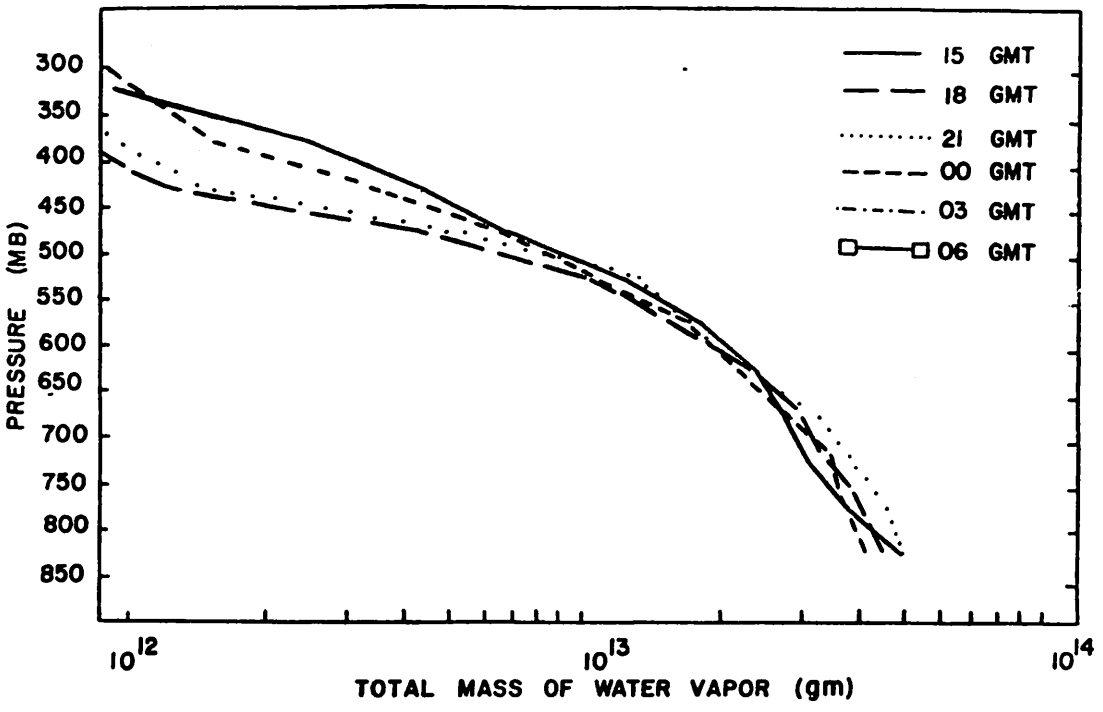

Fig. 5.12.5.5 Total mass of water vapor in layers 50 mb deep (gm) over the Texas HIPLEX area for 25 June 1977.

layers below 700 mb, and this might be attributed to condensation and precipitation occurring at this time.

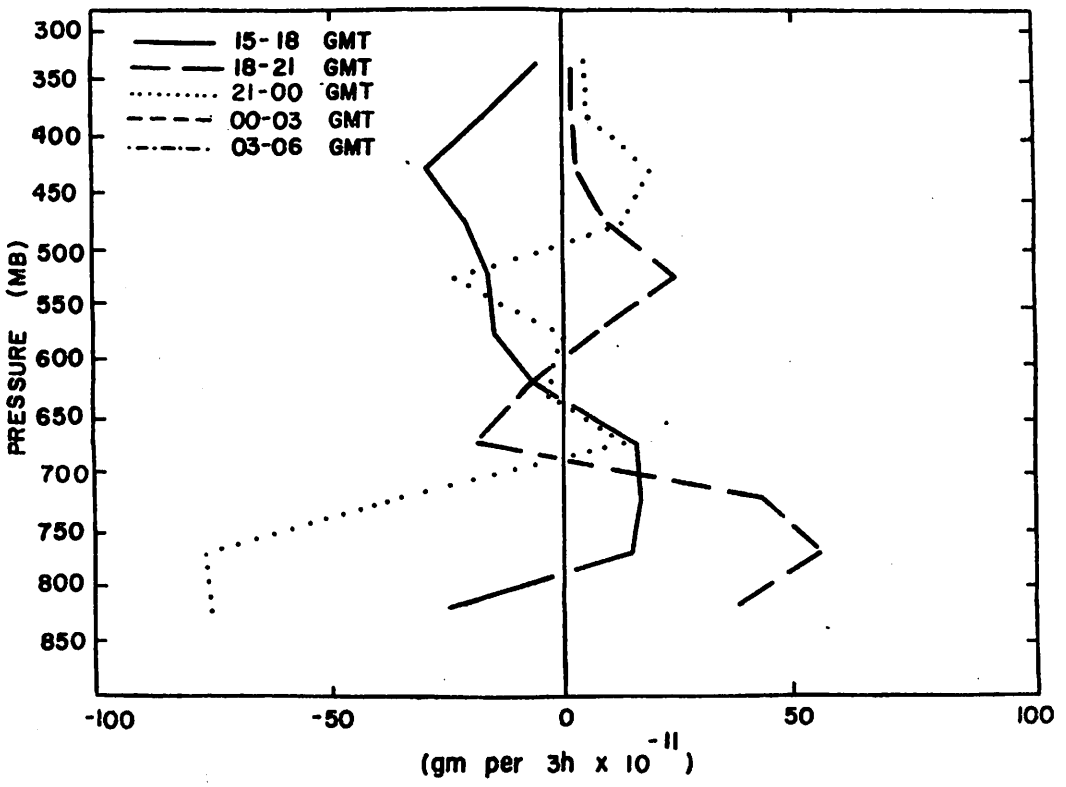

Fig. 5.12.5.6 Local rate-of-change in total mass of water vapor (gm per 3h x 10^{-11}) over the Texas HIPLEX area for 25 June 1977.

5.13 26 June 1977

5.13.1 Radar

Figure 5.13.1.1 shows echoes from 2000 through 0200 GMT in the southwest part of the area. A major cell formed or moved into the area at 2100 GMT, and divided into two distinct cells by 2200 GMT. The storm either moved westward or dissipated and was entirely out of the area by 0300 GMT. No echoes were observed prior to 2000 GMT or at 0300 GMT.

5.13.2 Surface

Fields of surface temperature (Fig. 5.13.2.1) do not show the effect of the storms that were over the southwest part of the area until 0000 GMT at which time the temperature began to drop about 10°C in two hours. The remainder of the network was dominated by surface heating, as the influence of the storm only affects the southwest region. Values of surface mixing ratio (Fig. 5.13.2.2) remain small except in regions of convection where a large increase occurred by 0000 GMT. Prior to this time, no distinct centers were

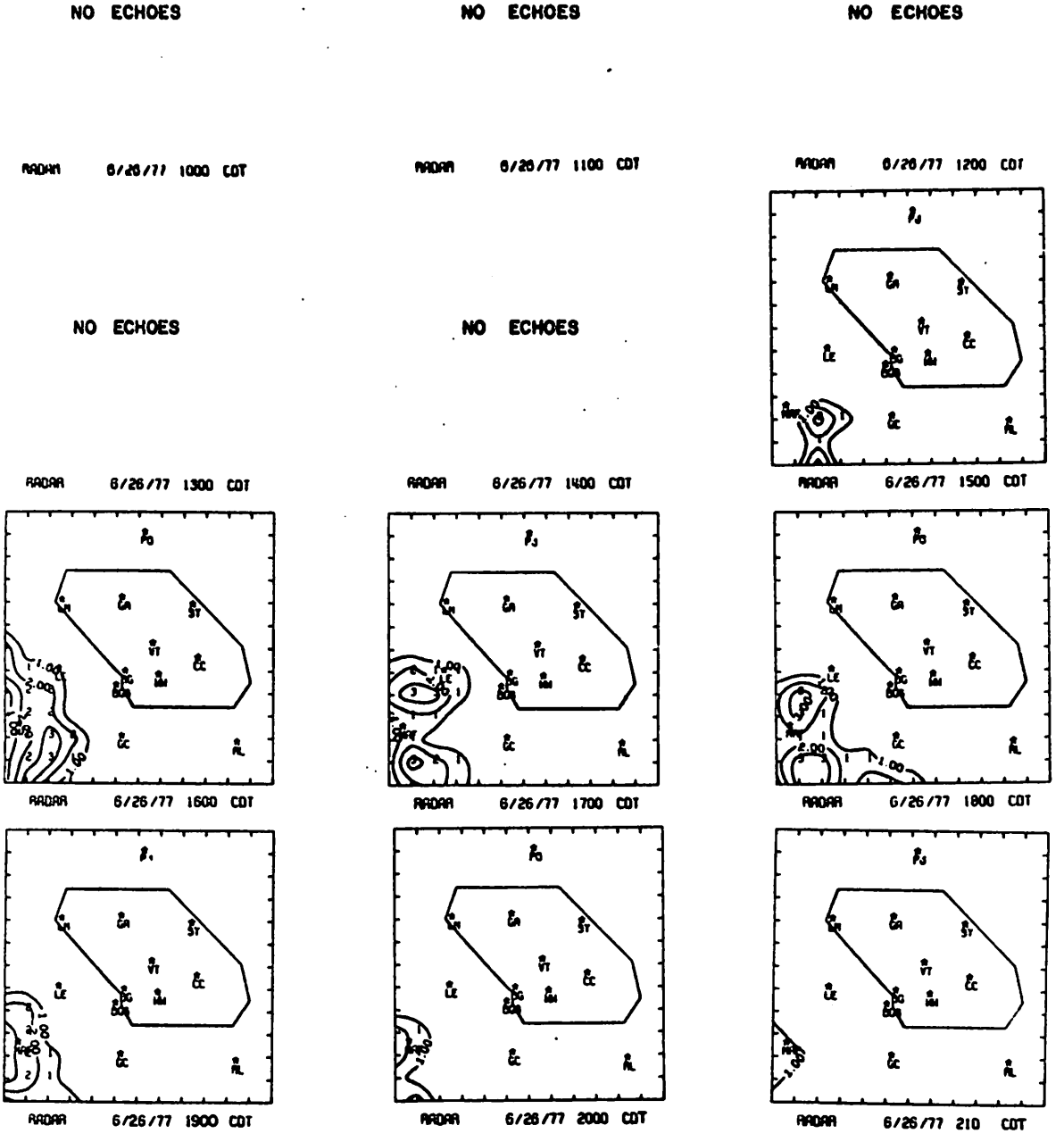

Fig. 5.13.1.1 Radar echoes for 26 June 1977.

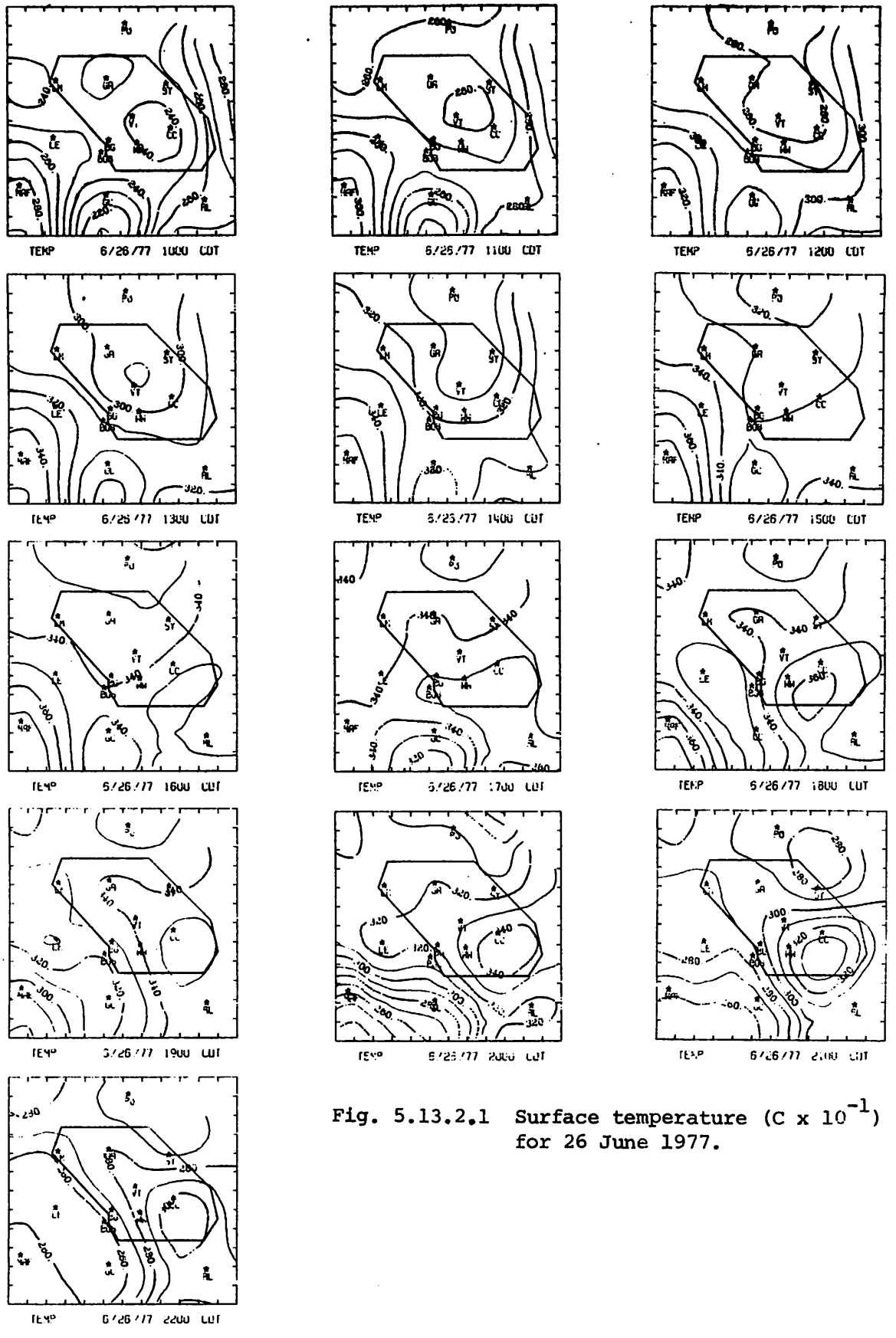

Fig. 5.13.2.1 Surface temperature (C x 10^{-1}) for 26 June 1977.

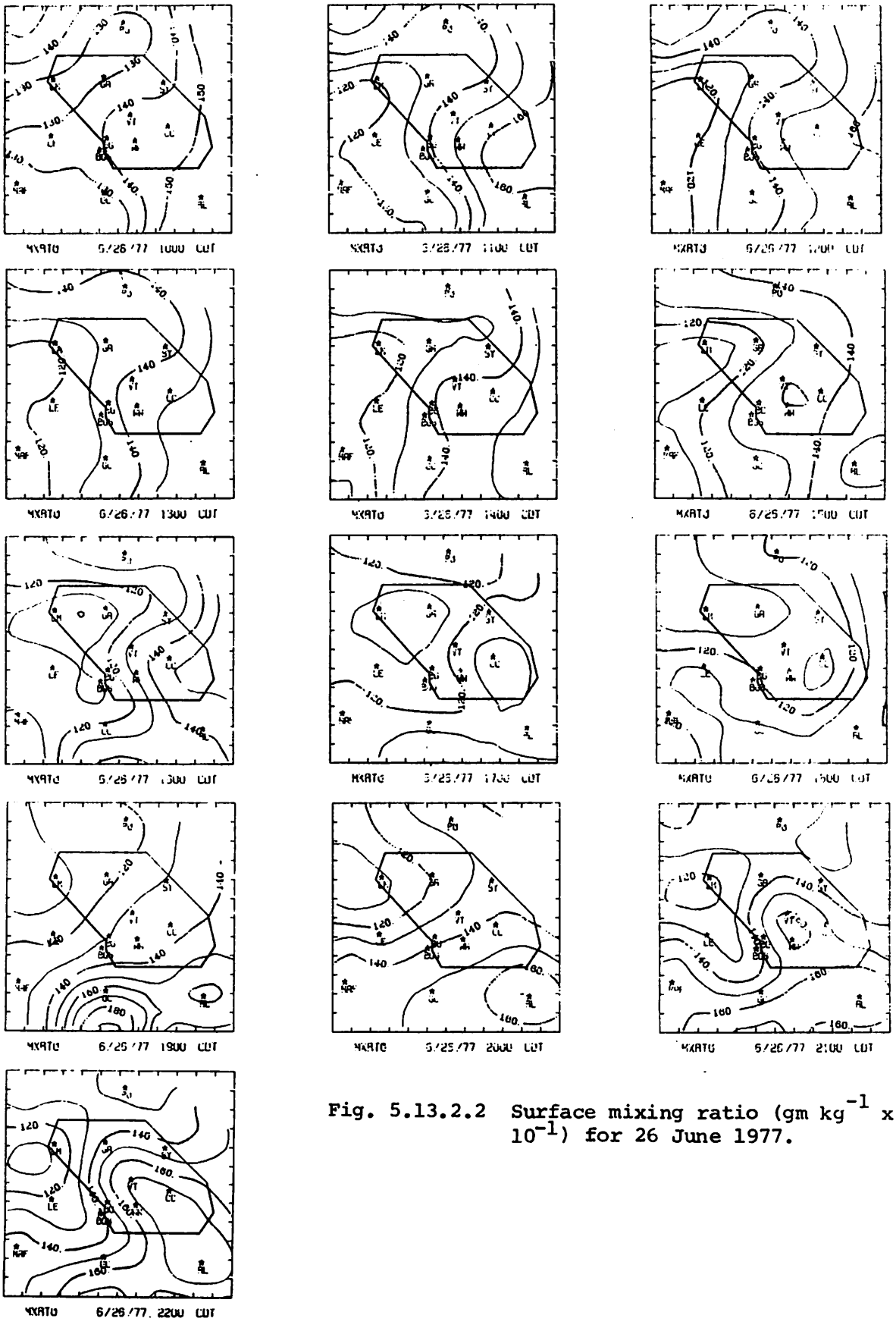

Fig. 5.13.2.2 Surface mixing ratio (gm kg^{-1} x 10^{-1}) for 26 June 1977.

observed. Although a center of lower surface equivalent potential temperature (Fig. 5.13.2.3) occurred near Lamesa, no distinct influence of the activity is reflected in the parameters analyzed.

The influence of terrain-induced vertical motion (Fig. 5.13.2.4) is minimal and reached a value near zero by 0300 GMT because of a decrease in wind speed. A prominent center of surface velocity divergence (Fig. 5.13.2.5) developed at 2100 GMT in the southwest corner of the area. However, a check of the data at Garden City shows the wind direction to be 180° out of phase which accounts for this large center. A region of convergence was located below the echo at 2100 and 0000 GMT. A center of strong downward vertical motion 50 mb above the surface (Fig. 5.13.2.6) appears as a result of surface velocity divergence beginning at 2100 GMT. Prior to convective activity, vertical motions were near zero.

Fields of surface moisture divergence (Fig. 5.13.2.7), vertical flux of moisture 50 mb above the surface (Fig. 5.13.2.8), and surface vorticity (Fig. 5.13.2.9) also show prominent centers near Garden City beginning at 2100 GMT. However, these centers result from surface velocity divergence, and are affected by the questionable wind at Garden City.

Fields of sea level pressure (Fig. 5.13.2.10) show a center of low pressure near Robert Lee throughout the day, with higher pressure to the west. Surface pressure changes (Fig. 5.13.2.11) remain small prior to 0200 GMT. A large decrease of pressure at 0200 GMT and subsequent increase near Midland at 0300 GMT is due to an error in Midland pressure data.

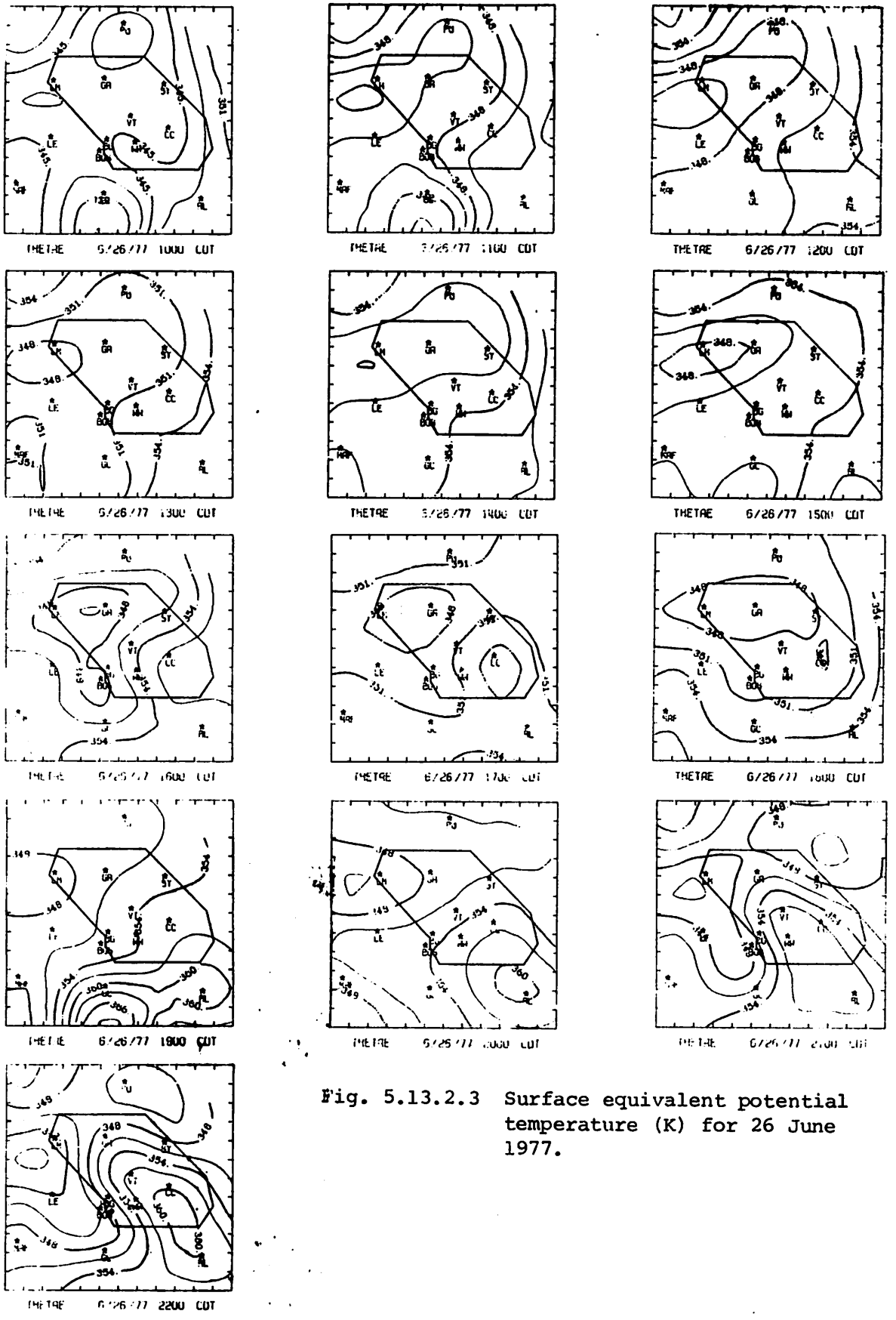

Fig. 5.13.2.3 Surface equivalent potential temperature (K) for 26 June 1977.

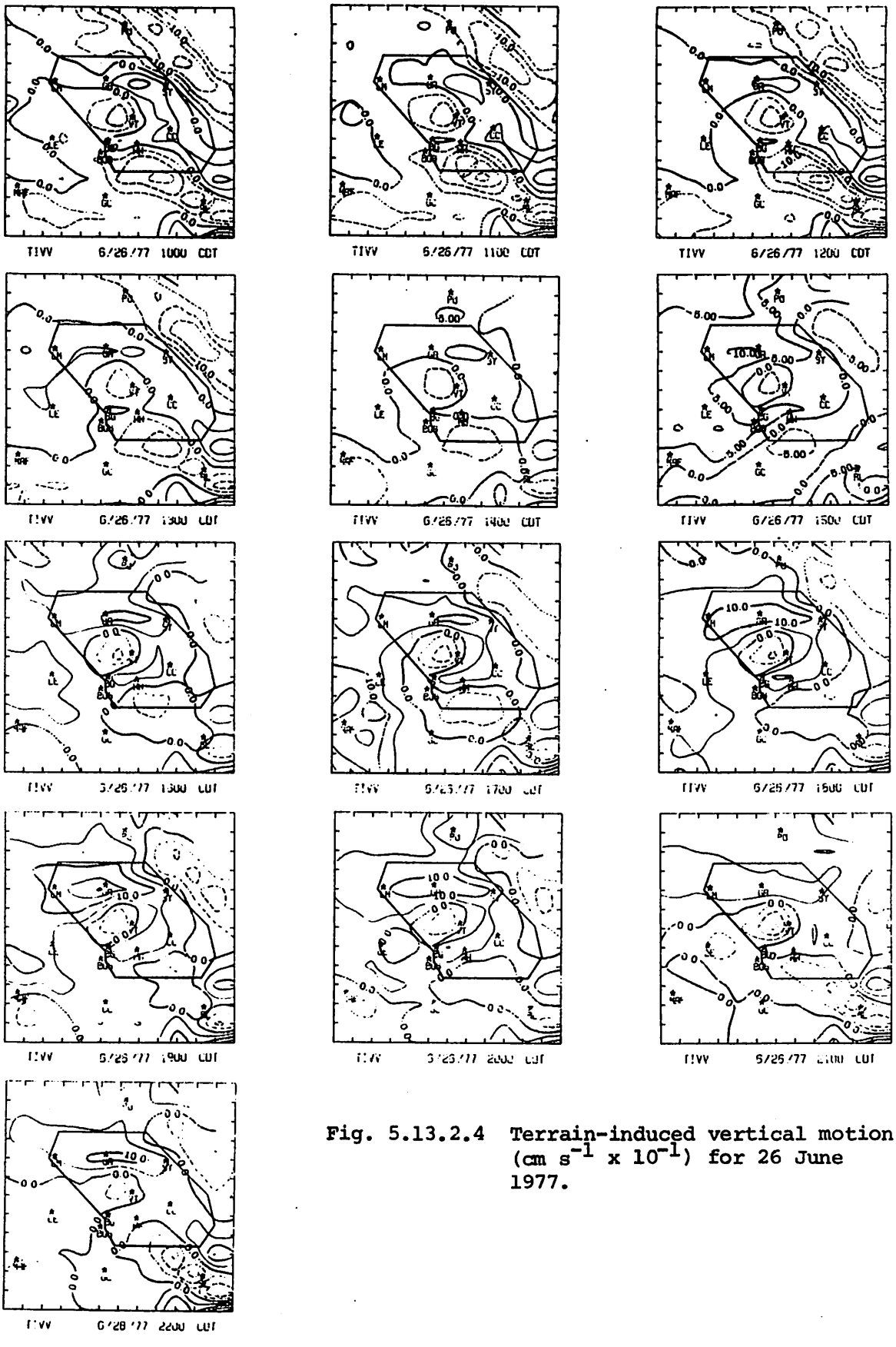

Fig. 5.13.2.4 Terrain-induced vertical motion (cm s^{-1} x 10^{-1}) for 26 June 1977.

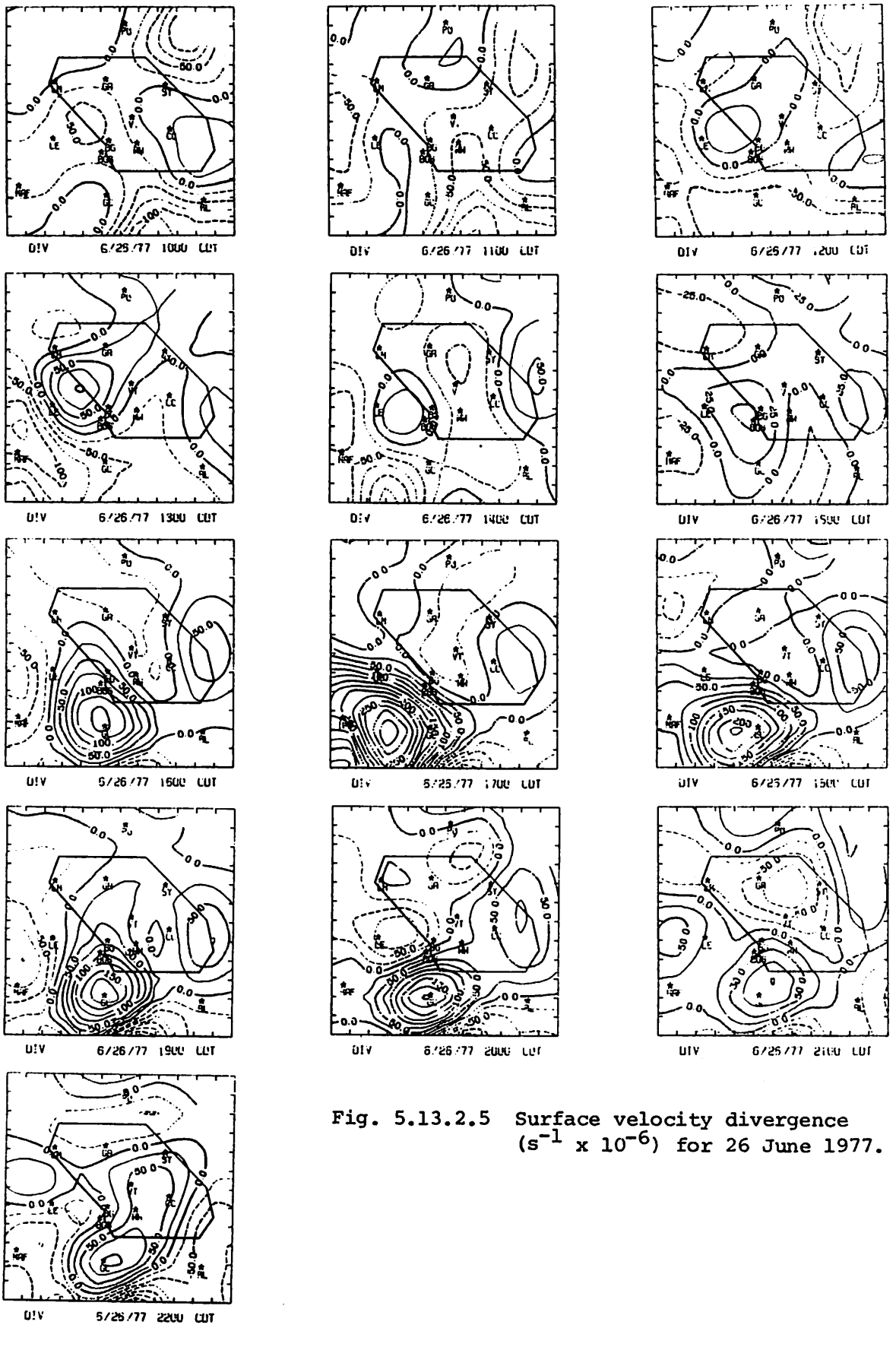

Fig. 5.13.2.5 Surface velocity divergence (s^{-1} x 10^{-6}) for 26 June 1977.

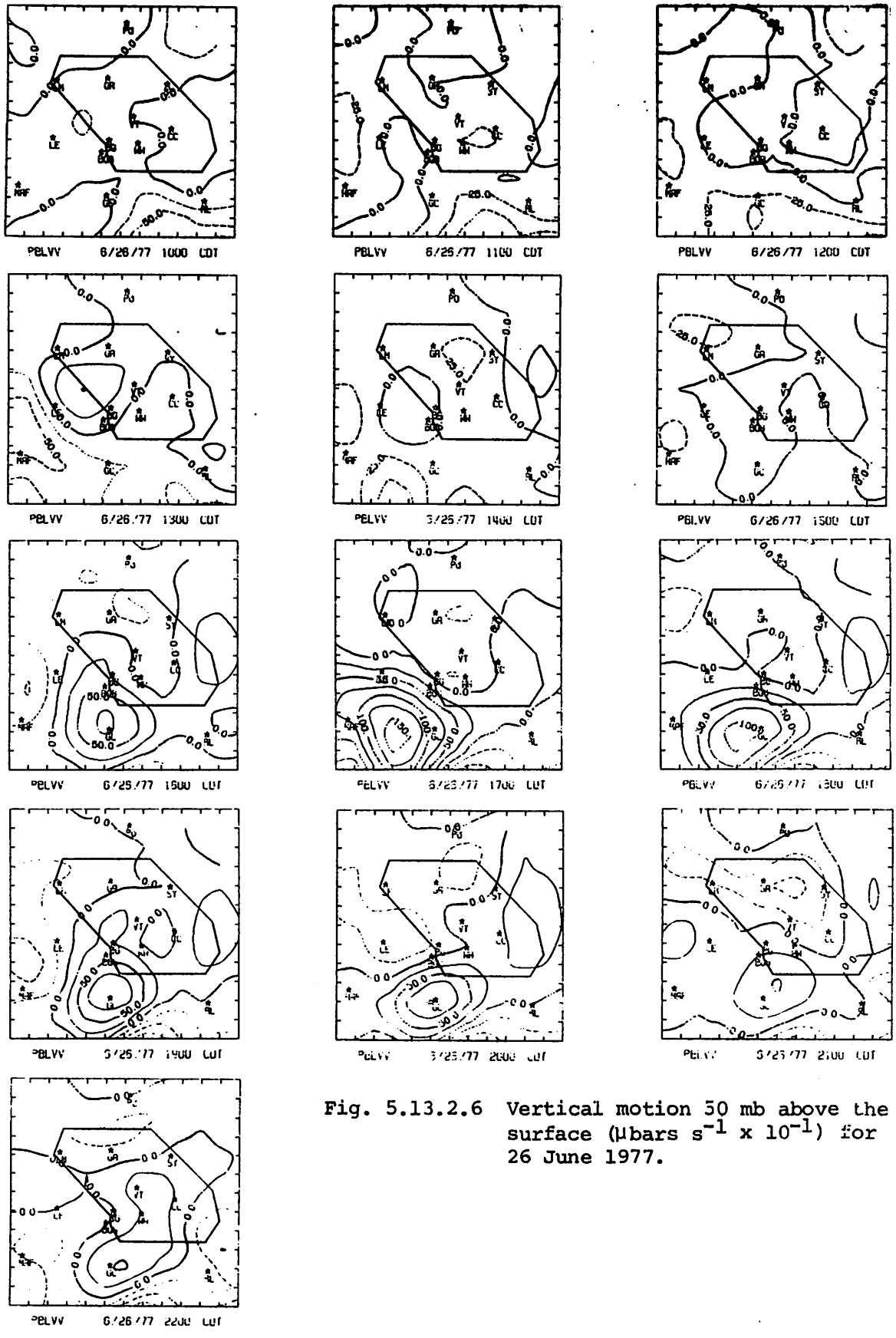

Fig. 5.13.2.6 Vertical motion 50 mb above the surface (μbars s^{-1} x 10^{-1}) for 26 June 1977.

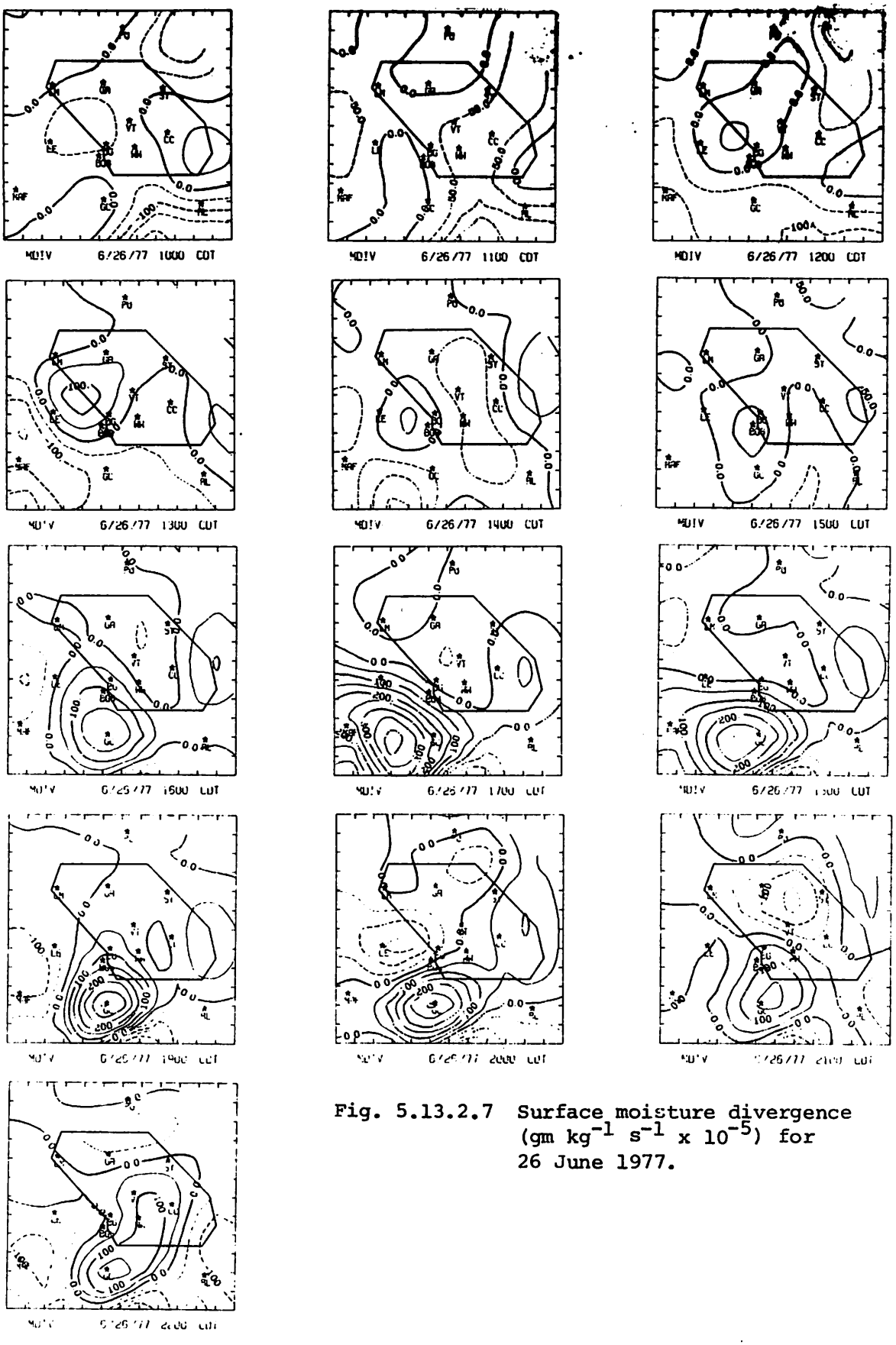

Fig. 5.13.2.7 Surface moisture divergence (gm kg^{-1} s^{-1} x 10^{-5}) for 26 June 1977.

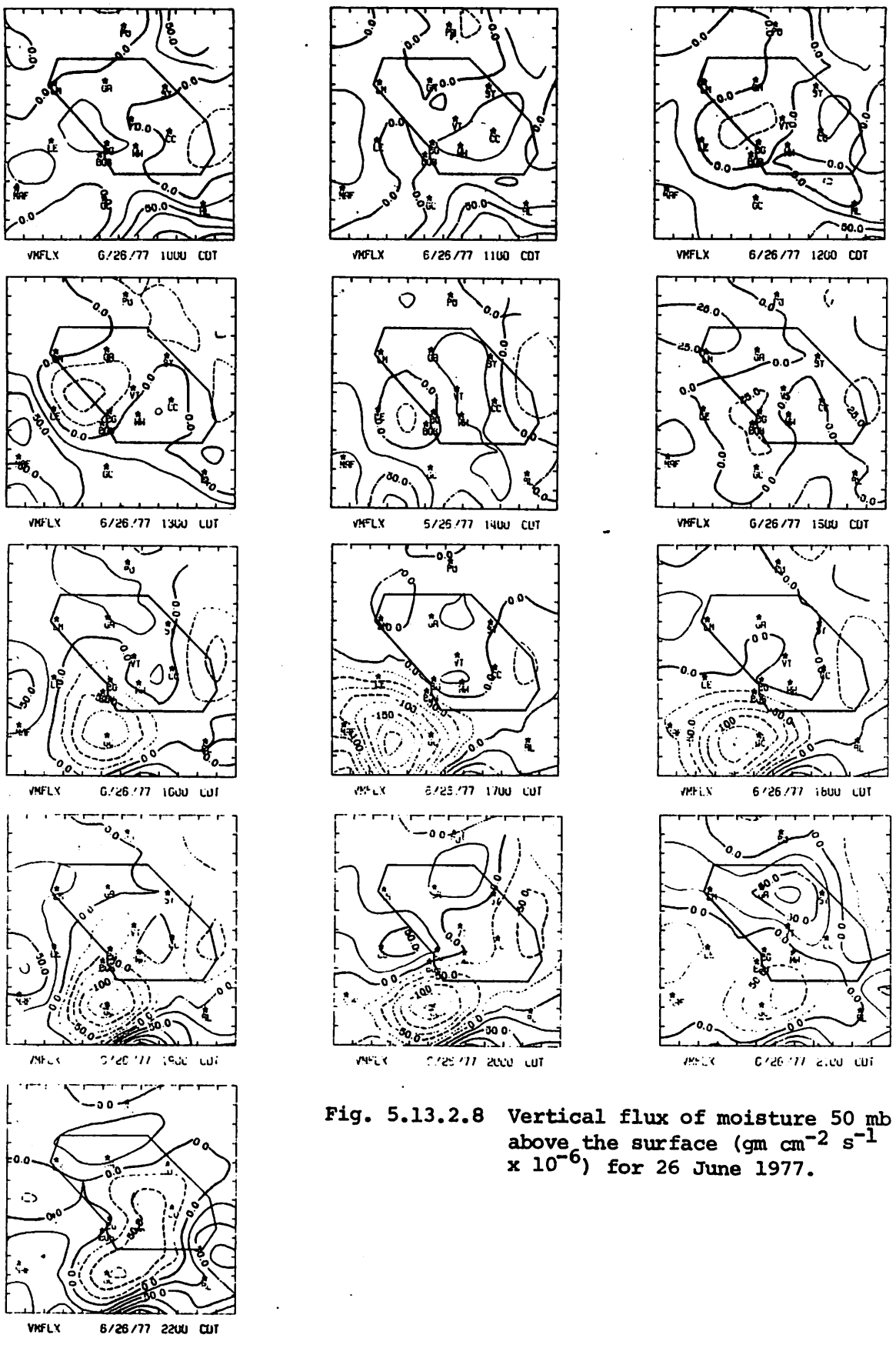

Fig. 5.13.2.8 Vertical flux of moisture 50 mb above the surface (gm cm^{-2} s^{-1} x 10^{-6}) for 26 June 1977.

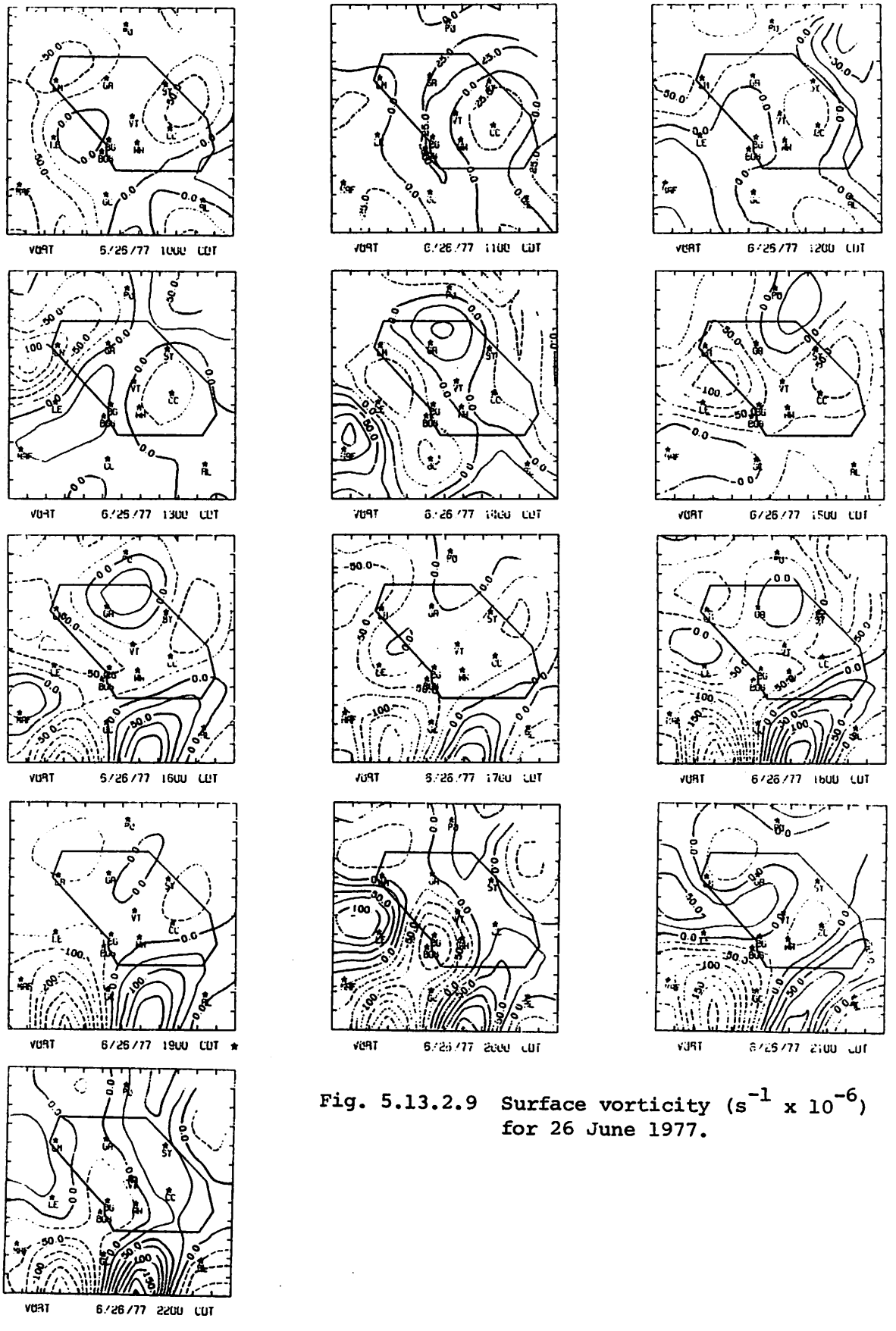

Fig. 5.13.2.9 Surface vorticity (s^{-1} x 10^{-6}) for 26 June 1977.

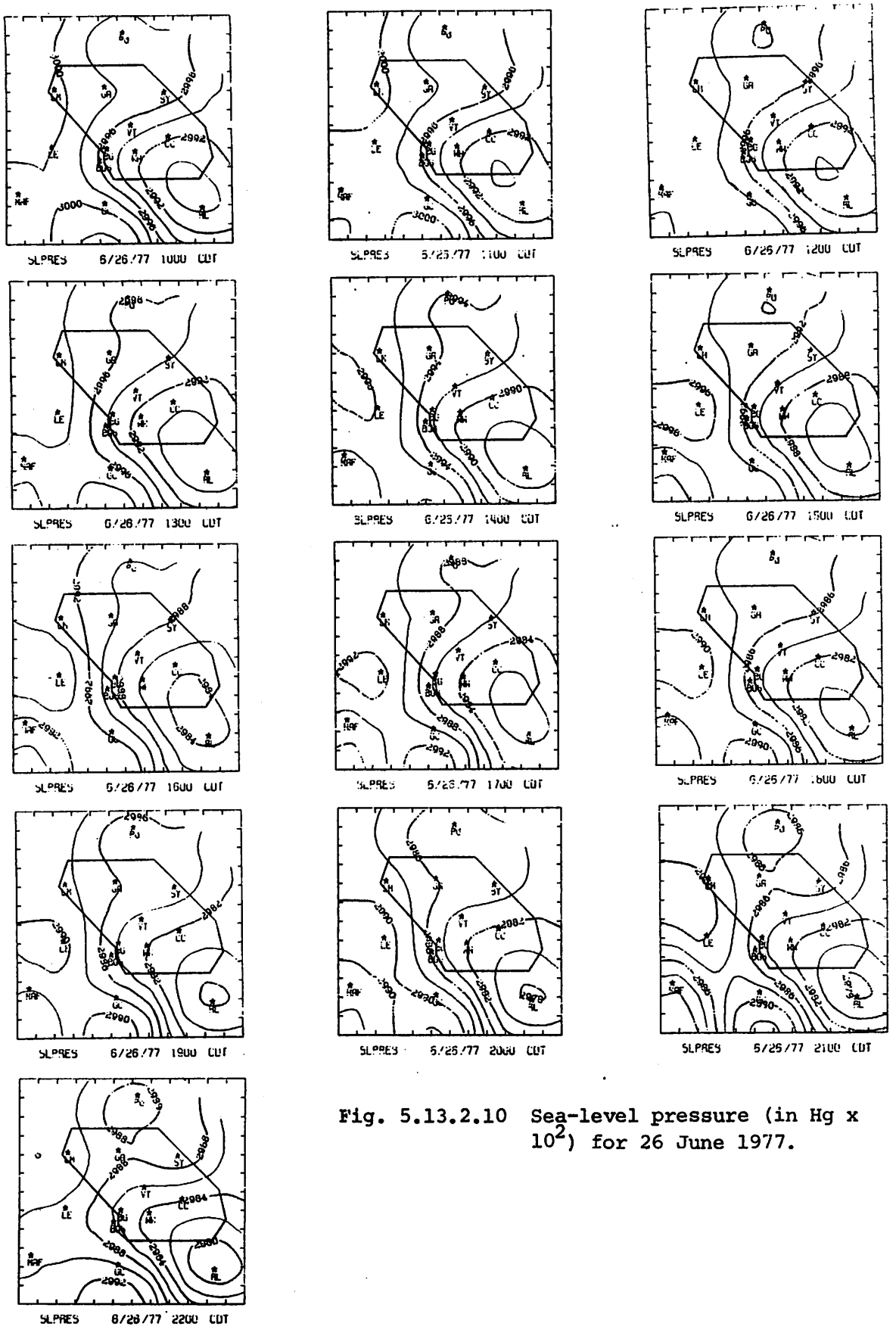

Fig. 5.13.2.10 Sea-level pressure (in Hg x 10^2) for 26 June 1977.

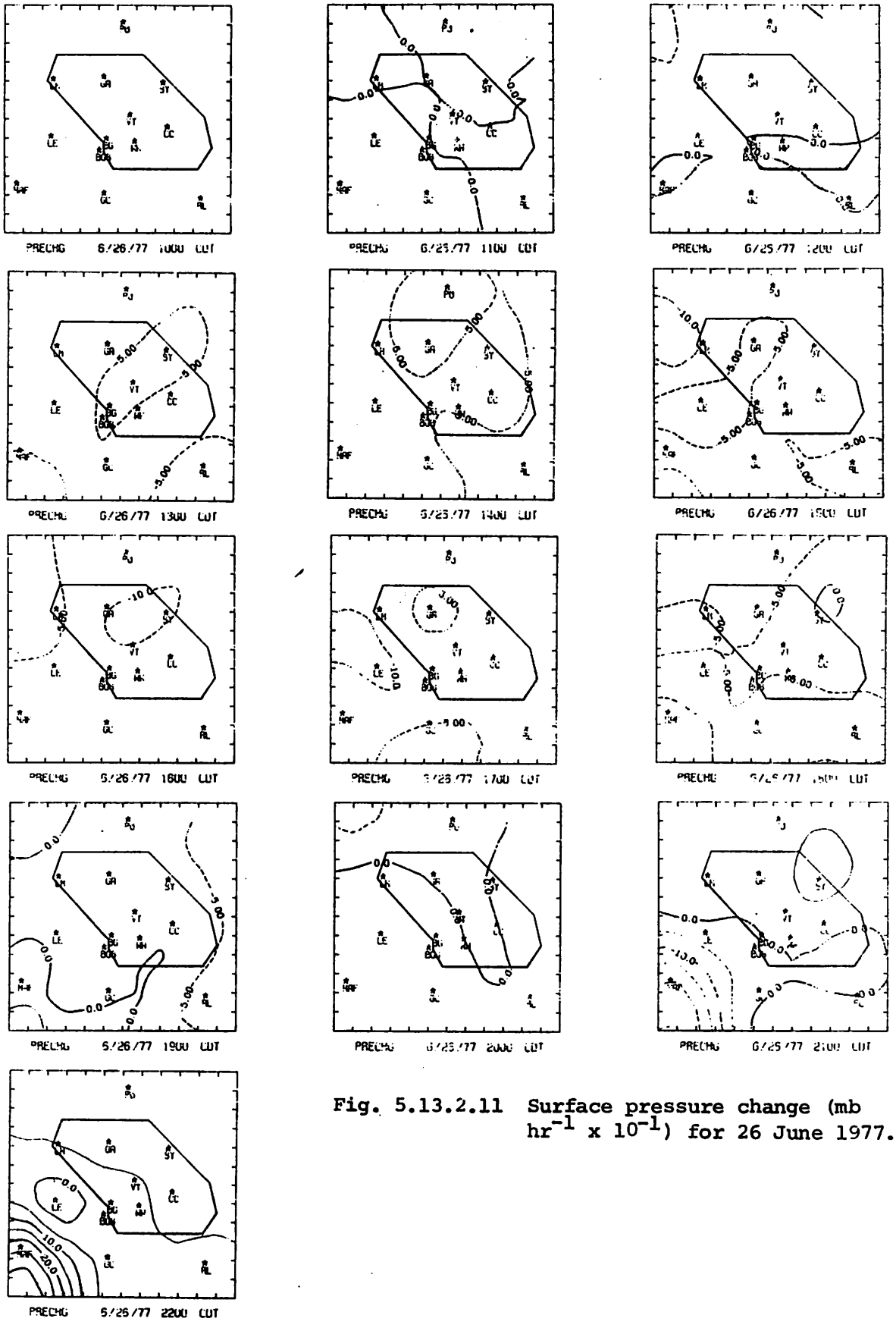

Fig. 5.13.2.11 Surface pressure change (mb hr^{-1} x 10^{-1}) for 26 June 1977.

5.14 27 June 1977

5.14.1 Radar

The radar charts for this day (Fig. 5.14.1.1) show a cell immediately west of Lamesa at 2200 GMT with tops exceeding 9.1 km (30K ft). This storm increased in areal coverage and remained to the west or northwest of Lamesa throughout the observational period. The storm was not completely over the HIPLEX area at any time during the day and little translational movement was indicated, although changes in echo patterns occurred apparently due to development and dissipation of the storm.

5.14.2 Surface

Surface temperature charts (Fig. 5.14.2.1) show the influence of the convective activity in the northwest part of the area with the development of a minimum temperature region at 2200 GMT. This region of minimum temperature is dry as reflected in fields of surface mixing ratio (Fig. 5.14.2.2). A center of higher mixing ratio developed over Vincent at 2400 GMT. This center also is reflected in fields of surface equivalent potential temperature (Fig. 5.14.2.3).

Fields of terrain-induced vertical motion (Fig. 5.14.2.4) show generally downward motion in regions of non convection. In regions of convective activity, terrain-induced vertical motion is near zero. Fields of surface velocity divergence (Fig. 5.14.2.5) show areas of slight convergence associated with the observed echoes. A large center of convergence existed at 0300 GMT southeastward of the echoes with divergence directly below. This resulted in downward vertical motion 50 mb above the surface (Fig. 5.14.2.6), which was accompanied by a decrease in temperature and mixing ratio. Only slight upward motion was associated with the observed echoes prior to 0300 GMT. Fields of surface moisture divergence (Fig. 5.14.2.7) and vertical flux of moisture 50 mb above the surface (Fig. 5.14.2.8) show these same features. Surface vorticity charts (Fig. 5.14.2.9) show an area of cyclonic vorticity north of Robert Lee throughout the day. Intense centers of both cyclonic and anticyclonic vorticity were associated with observed echoes at 0300 GMT.

Sea level pressure (Fig. 5.14.2.10) charts show lower pressure near Robert Lee than to the west. A pressure increase (Fig. 5.14.2.11) west of Lamesa at 0000 GMT is associated with the cold downdraft and corresponding surface velocity divergence patterns.

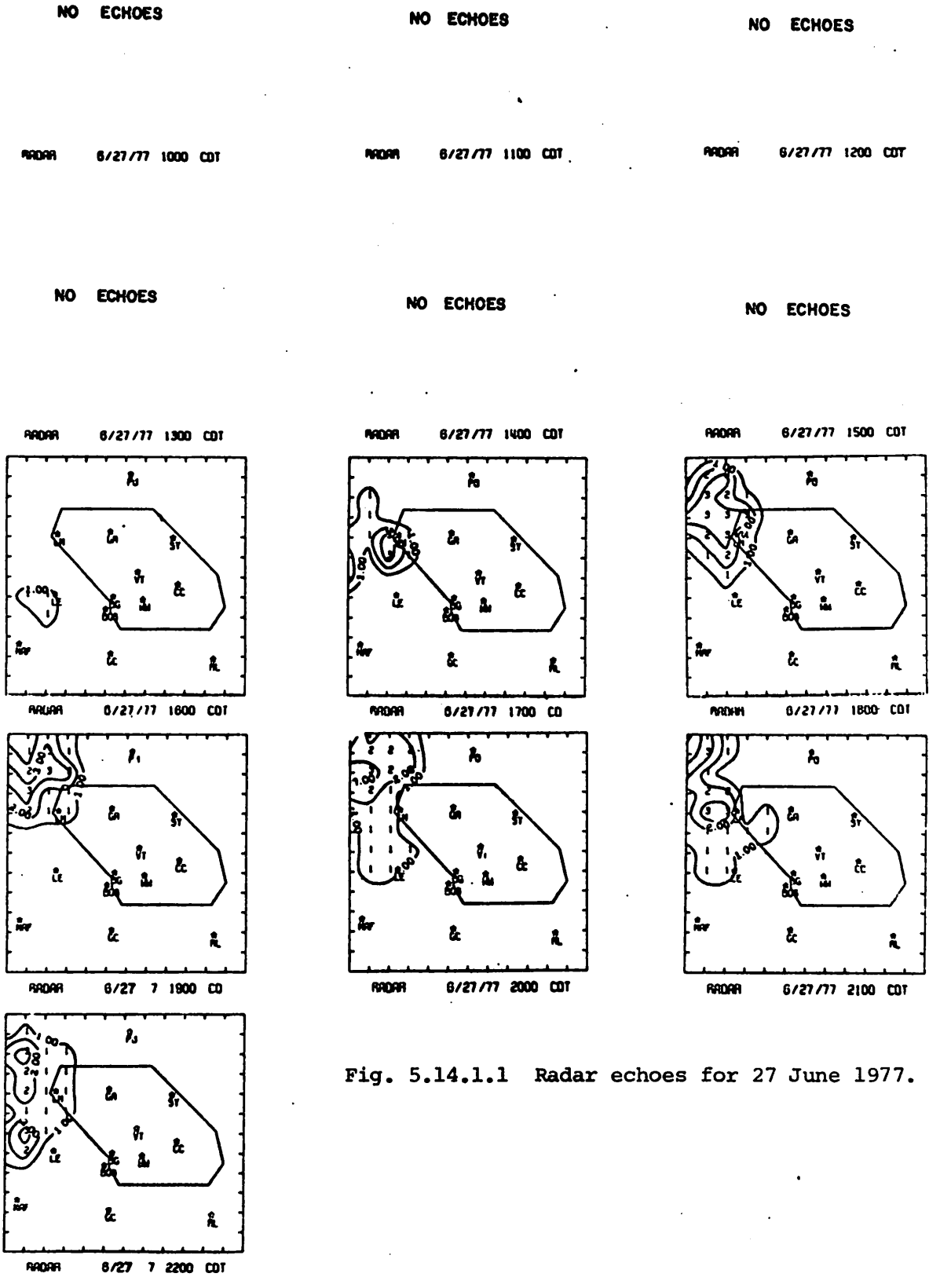

Fig. 5.14.1.1 Radar echoes for 27 June 1977.

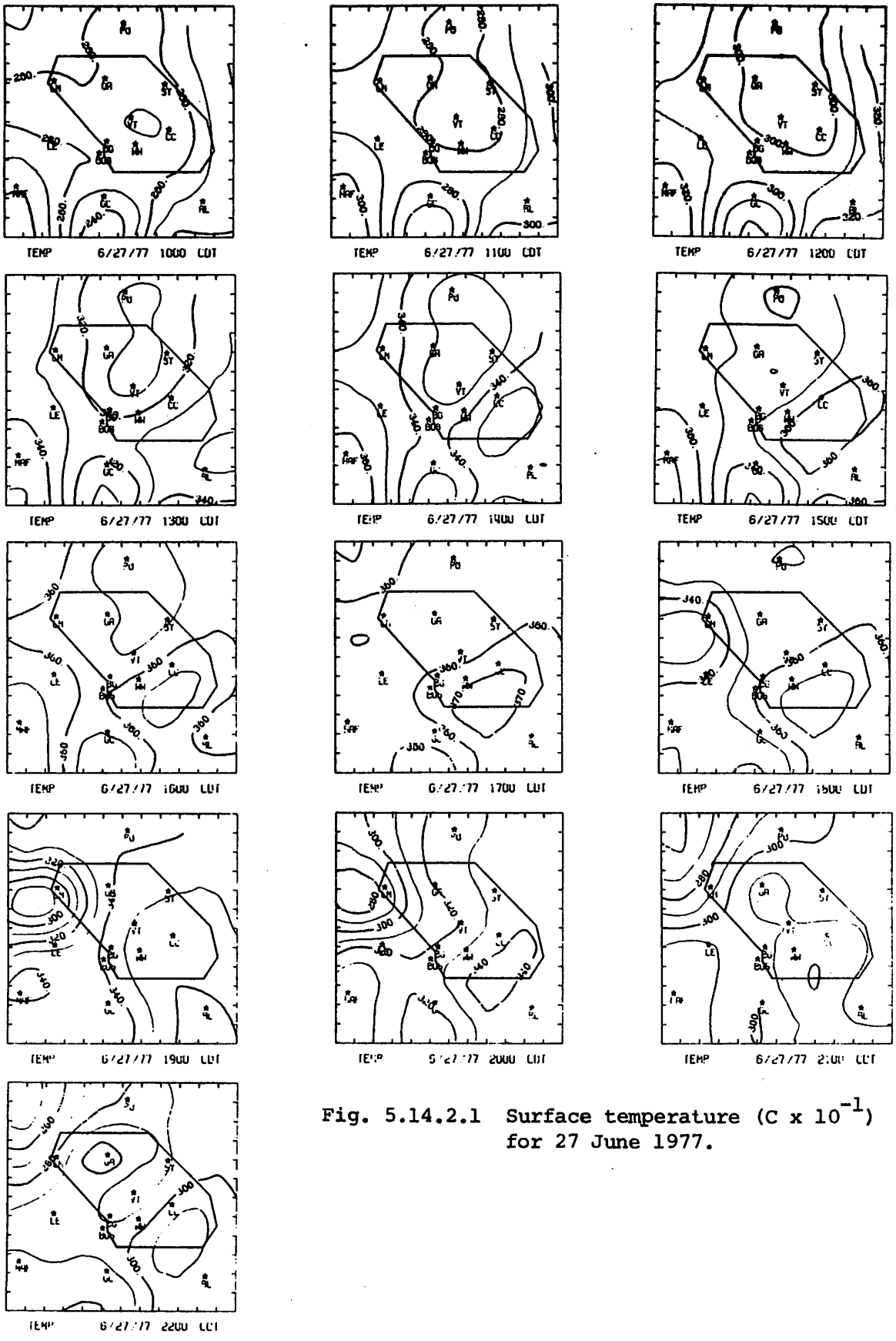

Fig. 5.14.2.1 Surface temperature (C x 10^{-1}) for 27 June 1977.

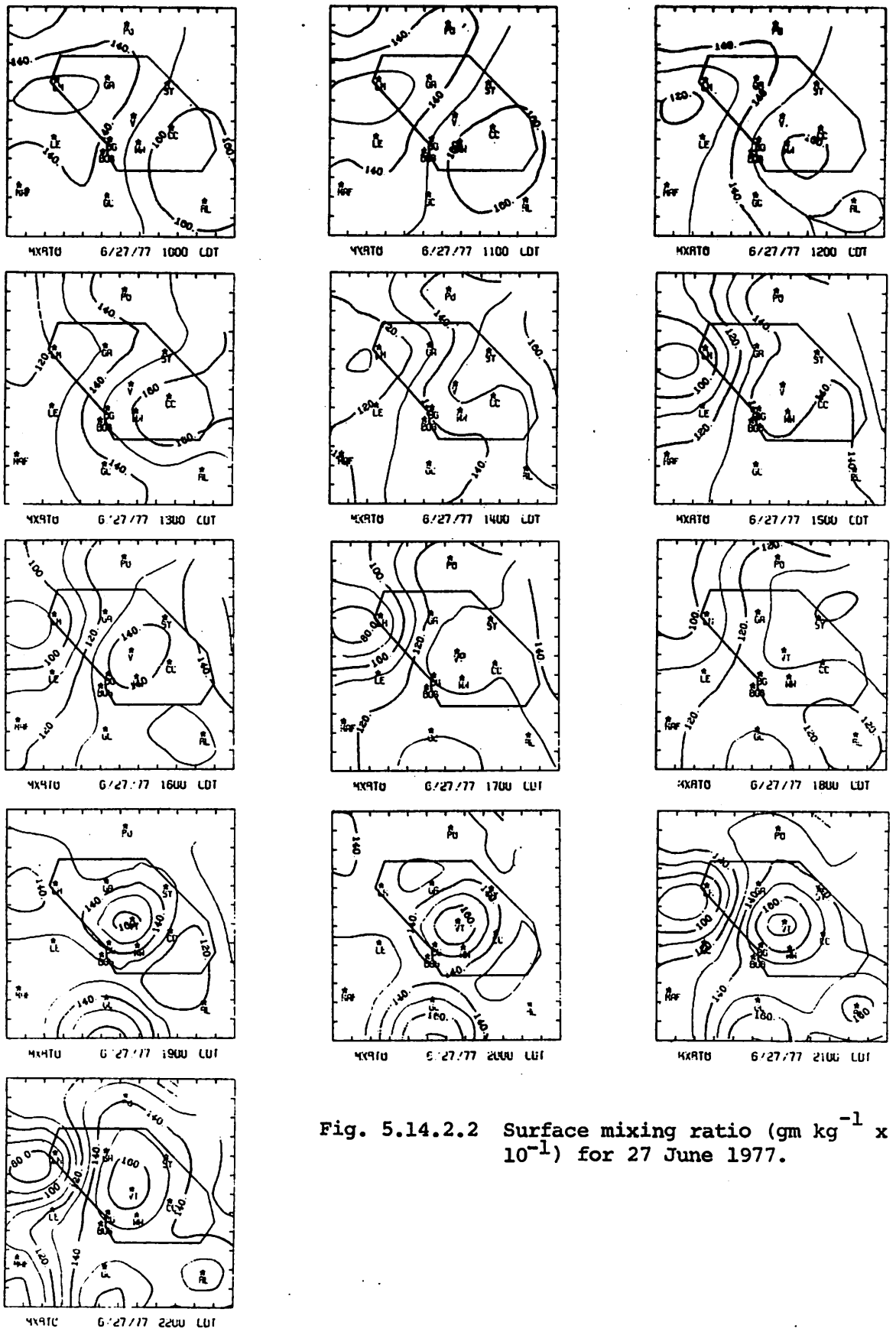

Fig. 5.14.2.2 Surface mixing ratio (gm kg^{-1} x 10^{-1}) for 27 June 1977.

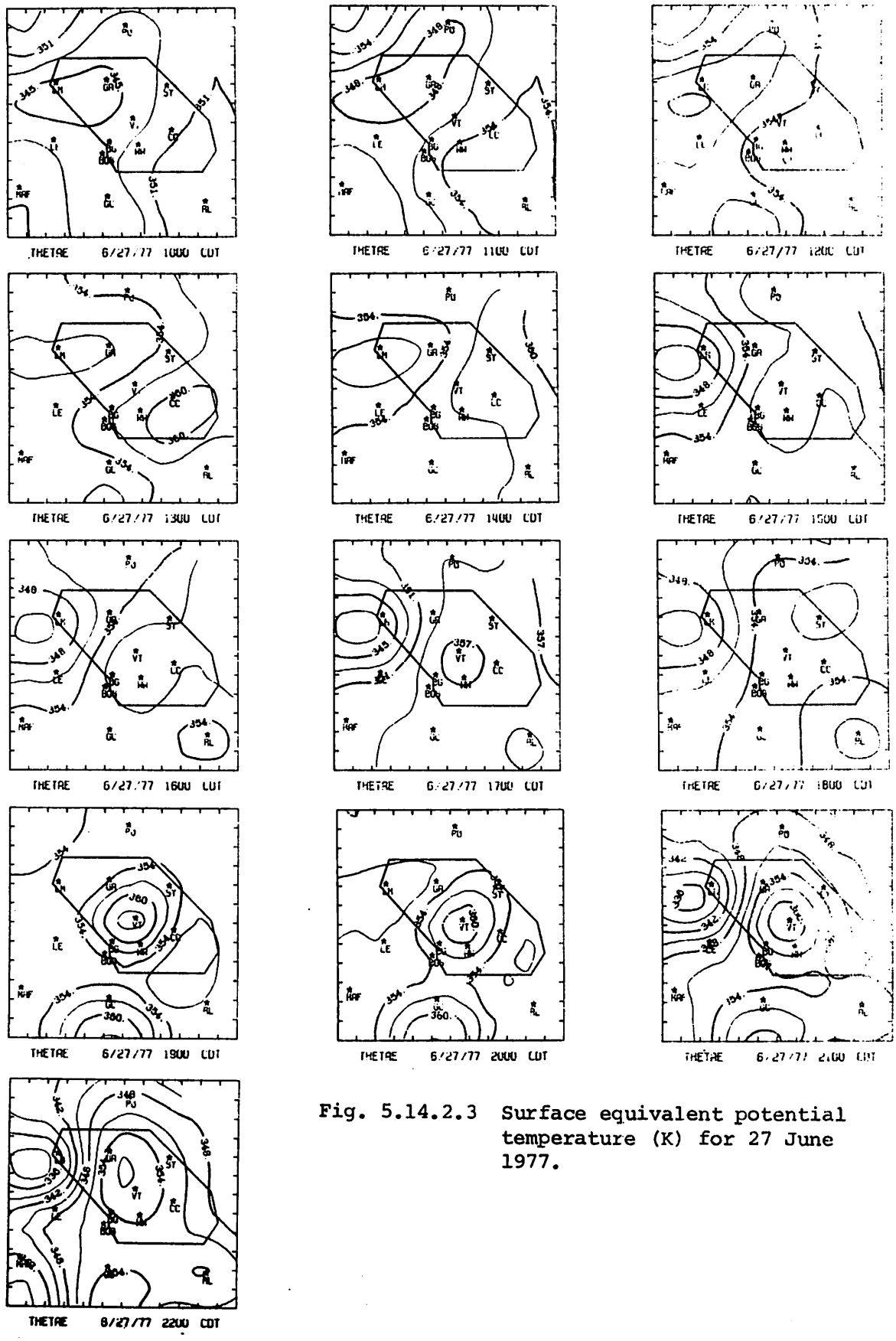

Fig. 5.14.2.3 Surface equivalent potential temperature (K) for 27 June 1977.

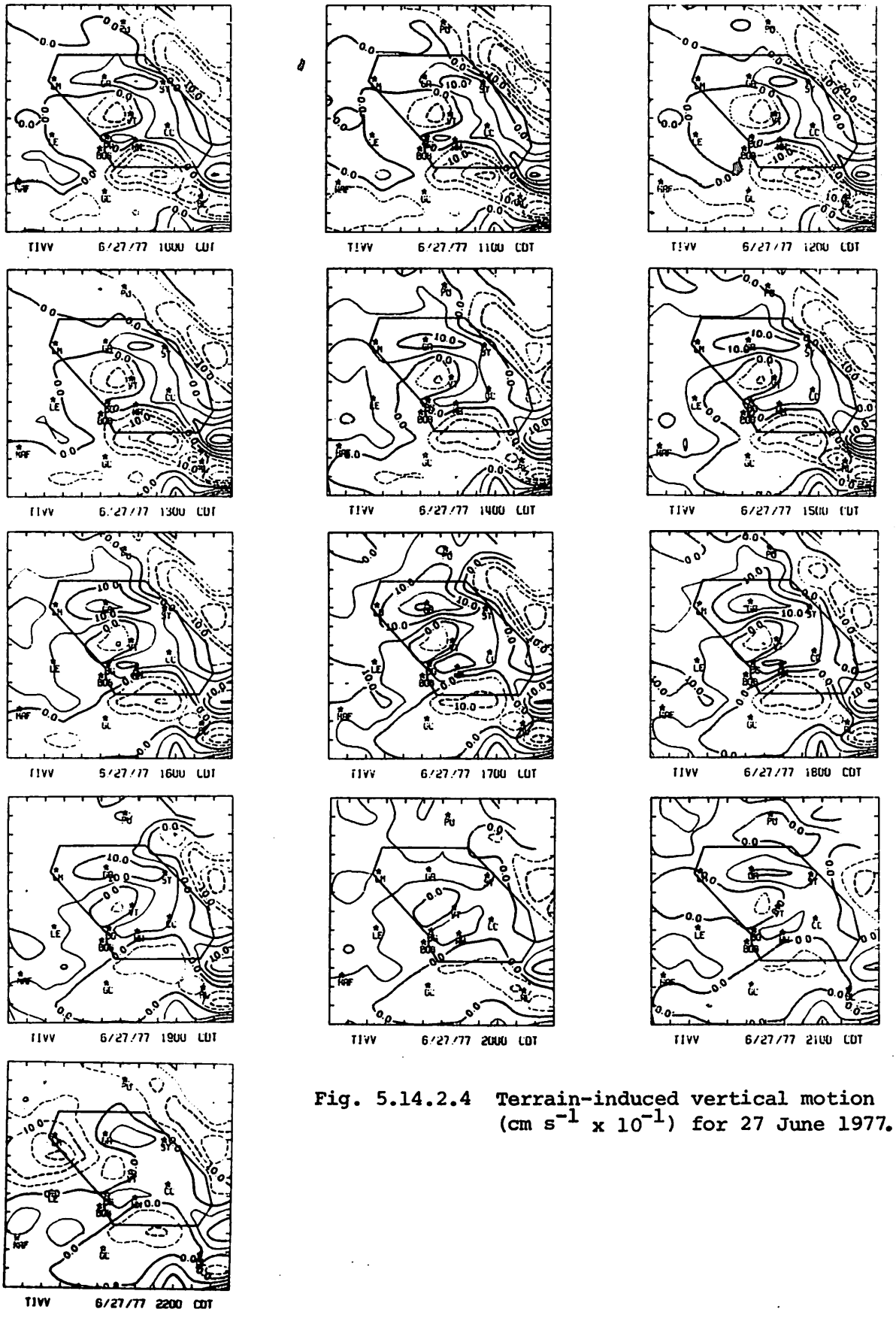

Fig. 5.14.2.4 Terrain-induced vertical motion (cm s^{-1} x 10^{-1}) for 27 June 1977.

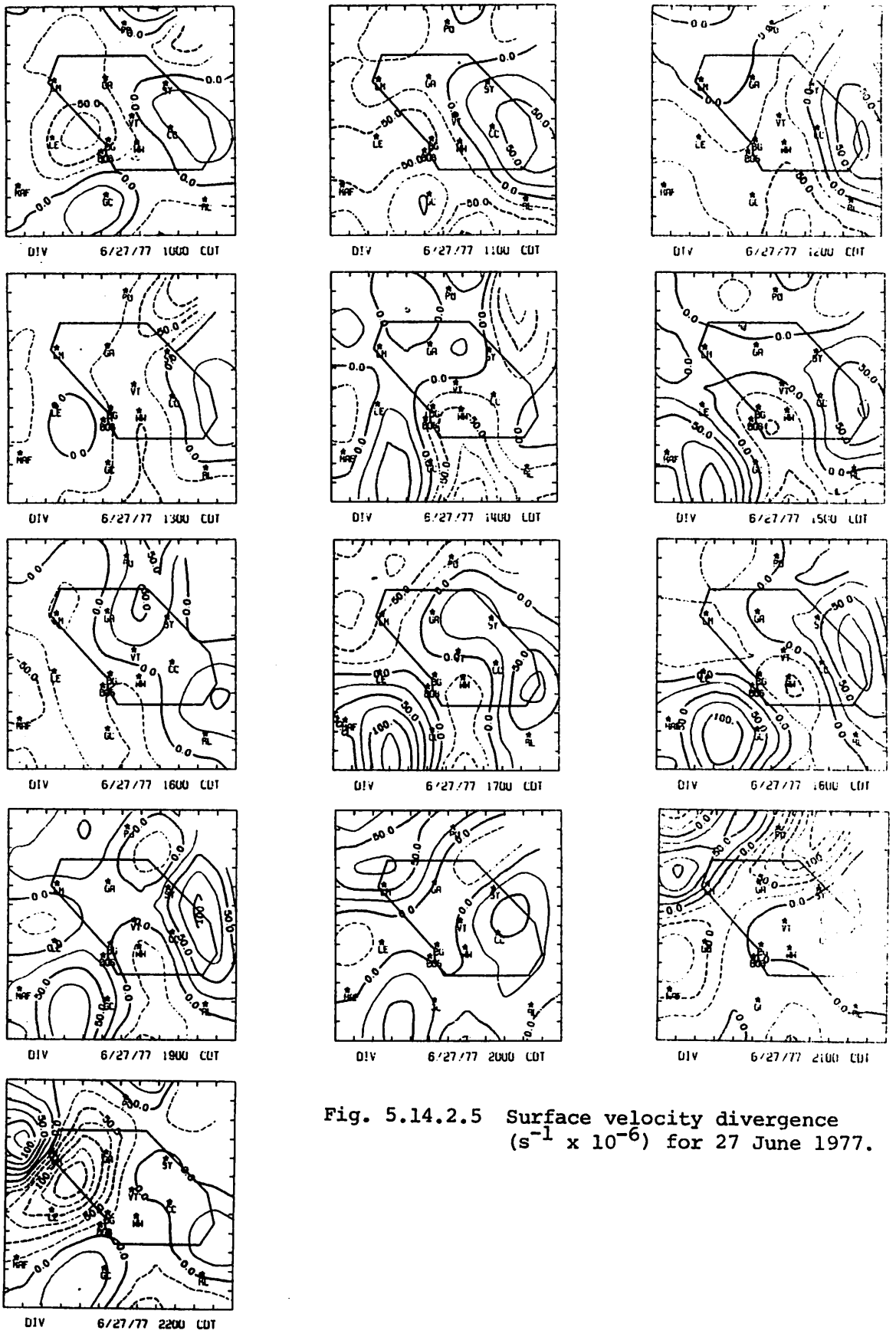

Fig. 5.14.2.5 Surface velocity divergence (s^{-1} x 10^{-6}) for 27 June 1977.

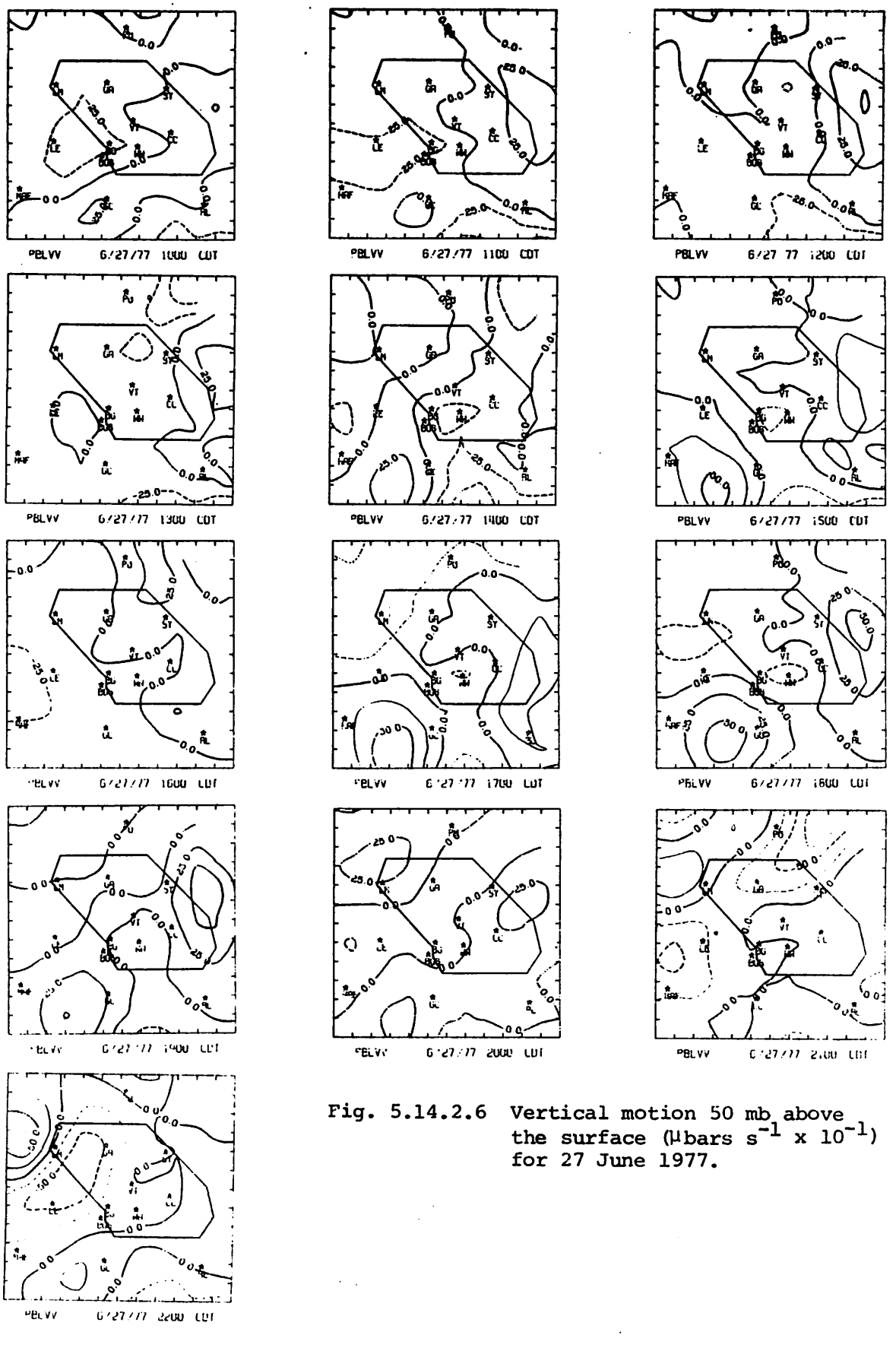

Fig. 5.14.2.6 Vertical motion 50 mb above the surface (μbars s^{-1} x 10^{-1}) for 27 June 1977.

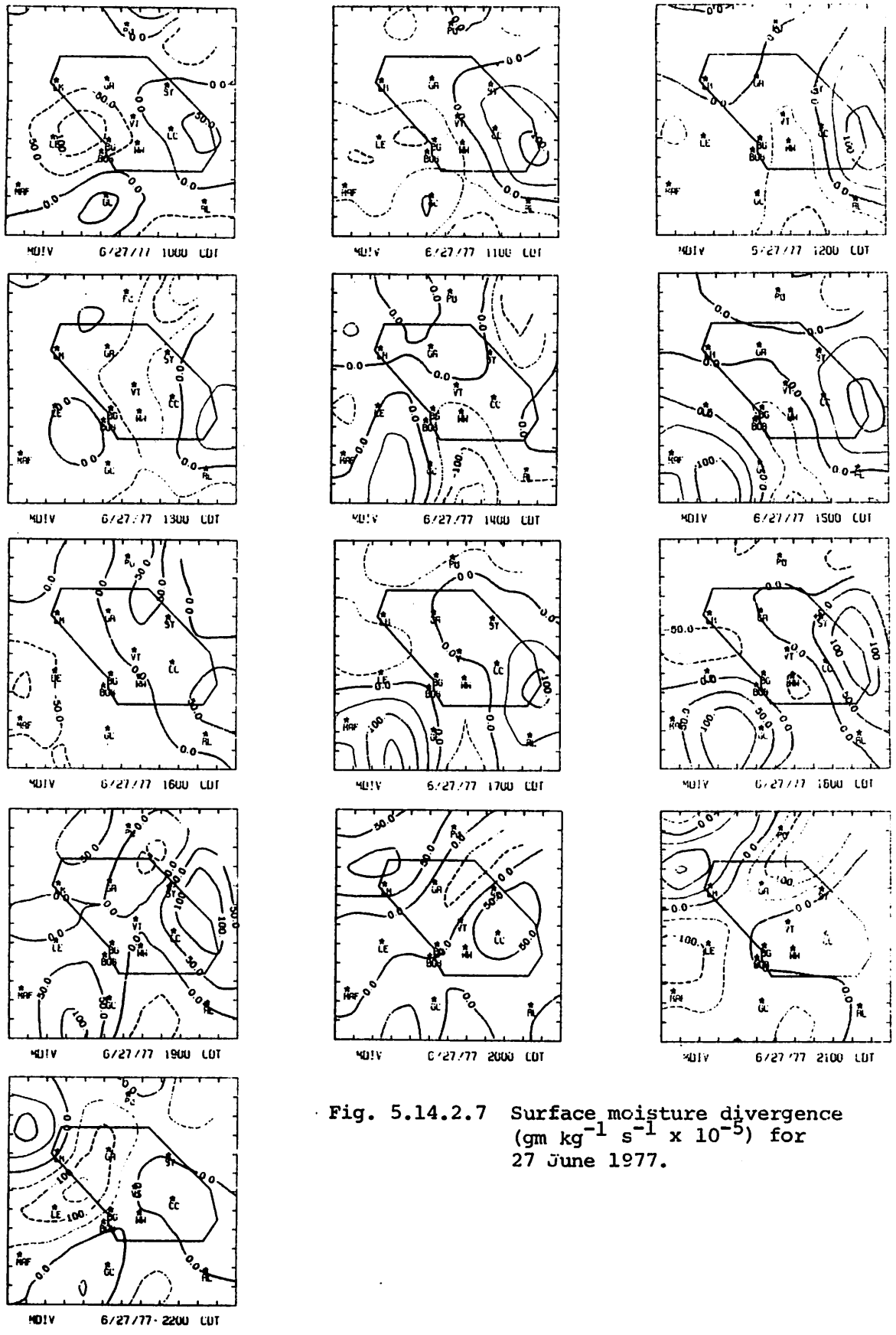

Fig. 5.14.2.7 Surface moisture divergence (gm kg^{-1} s^{-1} x 10^{-5}) for 27 June 1977.

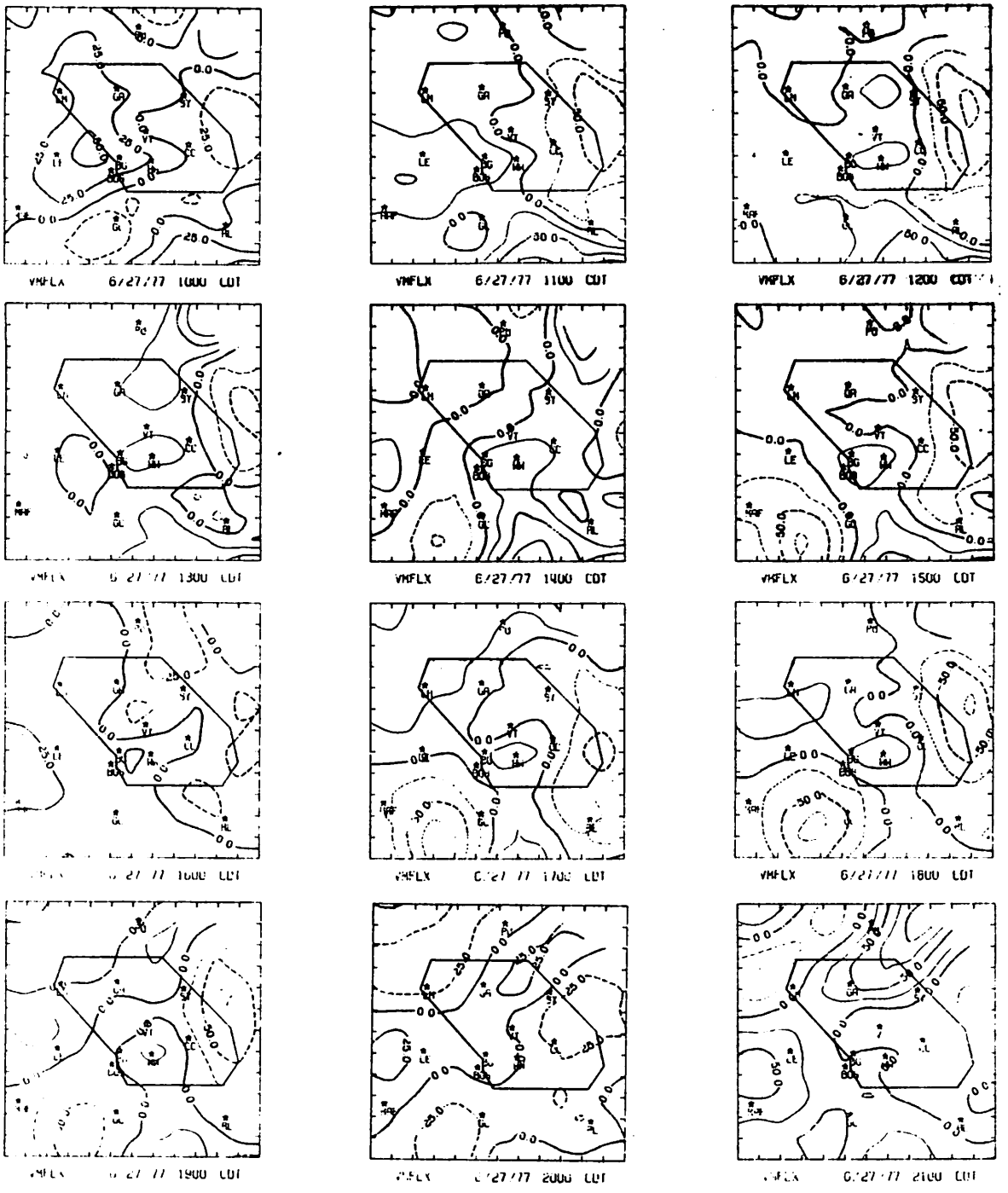

Fig. 5.14.2.8 Vertical flux of moisture 50 mb above the surface (gm cm^{-2} s^{-1} x 10^{-6}) for 27 June 1977.

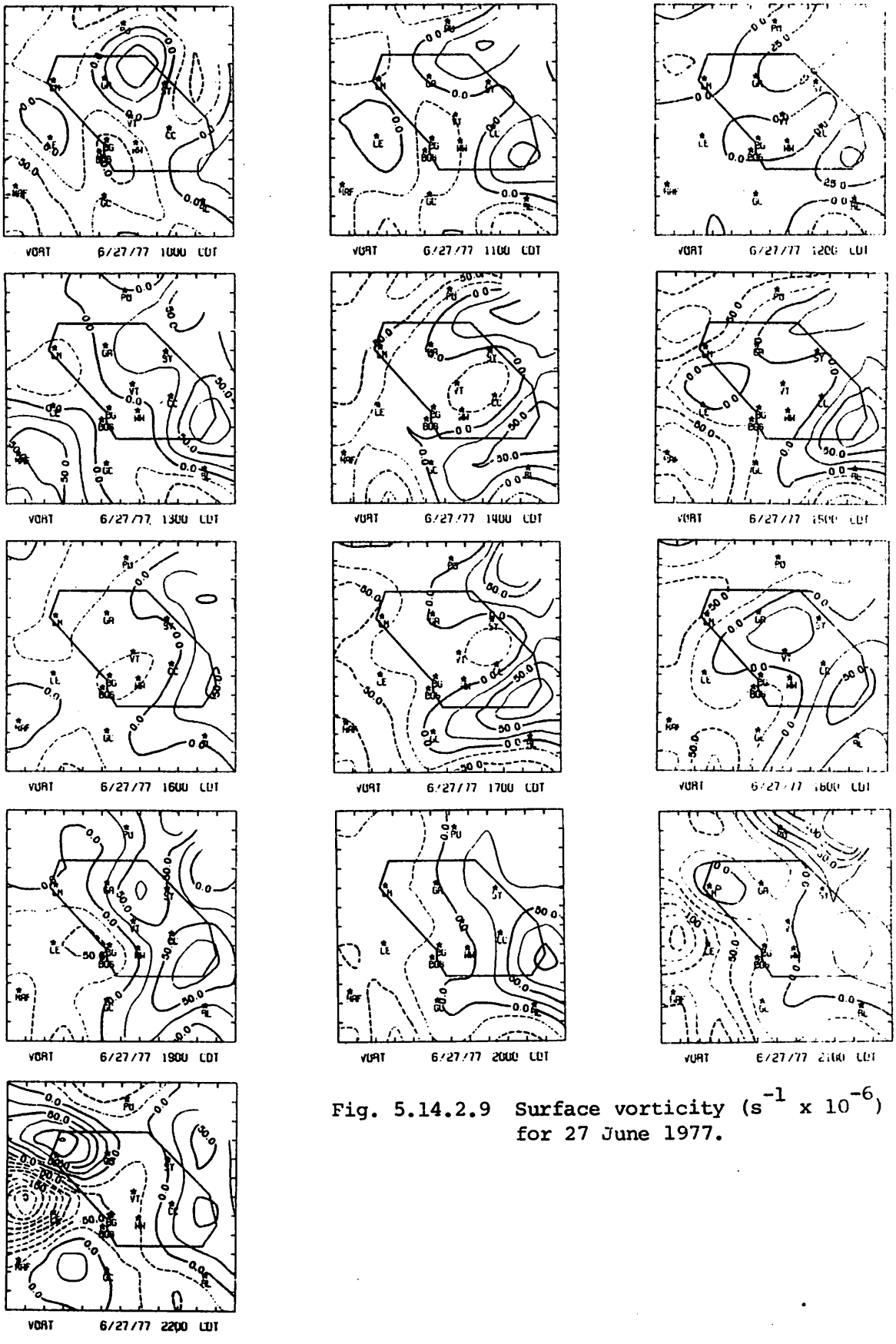

Fig. 5.14.2.9 Surface vorticity (s^{-1} x 10^{-6}) for 27 June 1977.

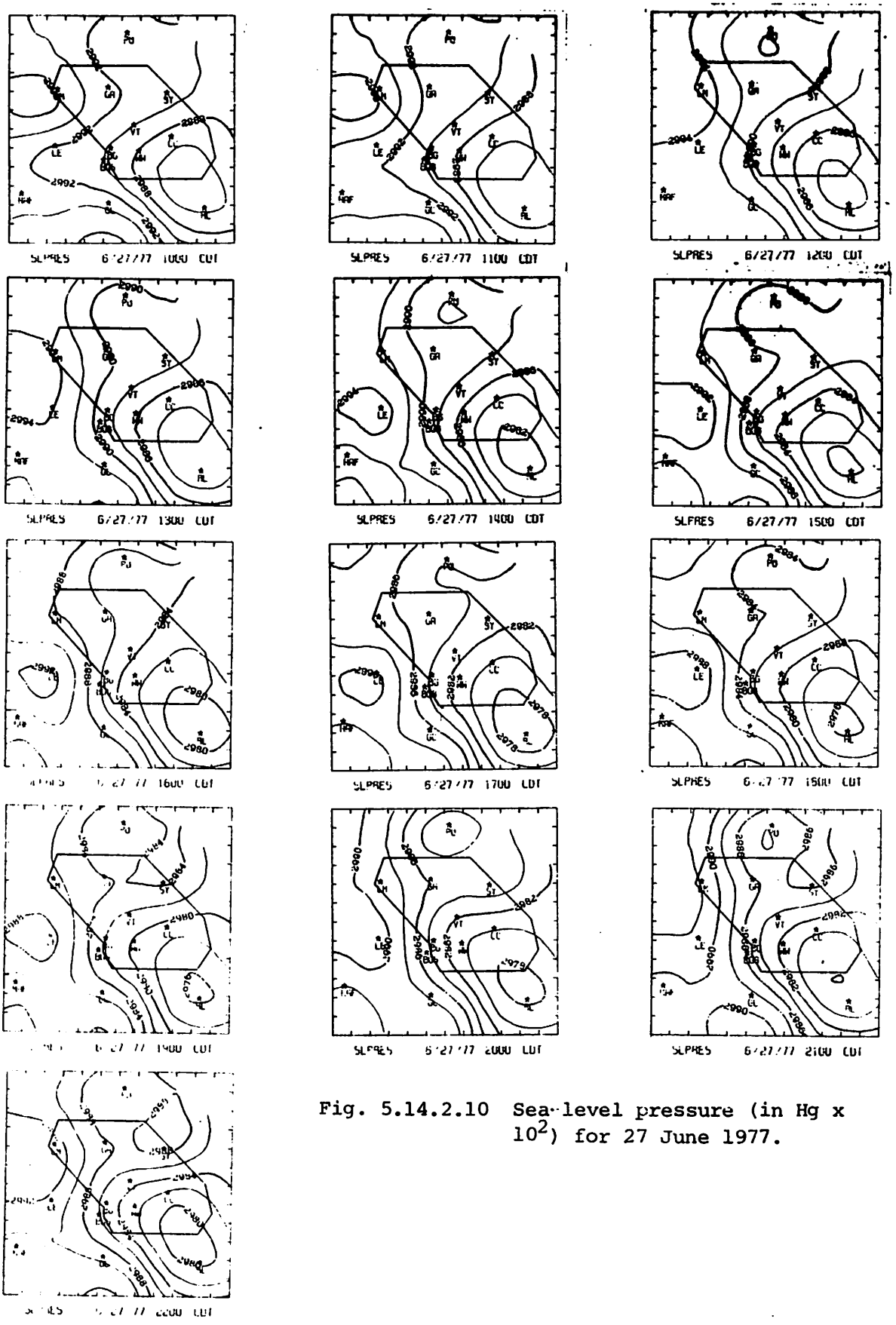

Fig. 5.14.2.10 Sea-level pressure (in Hg x 10^2) for 27 June 1977.

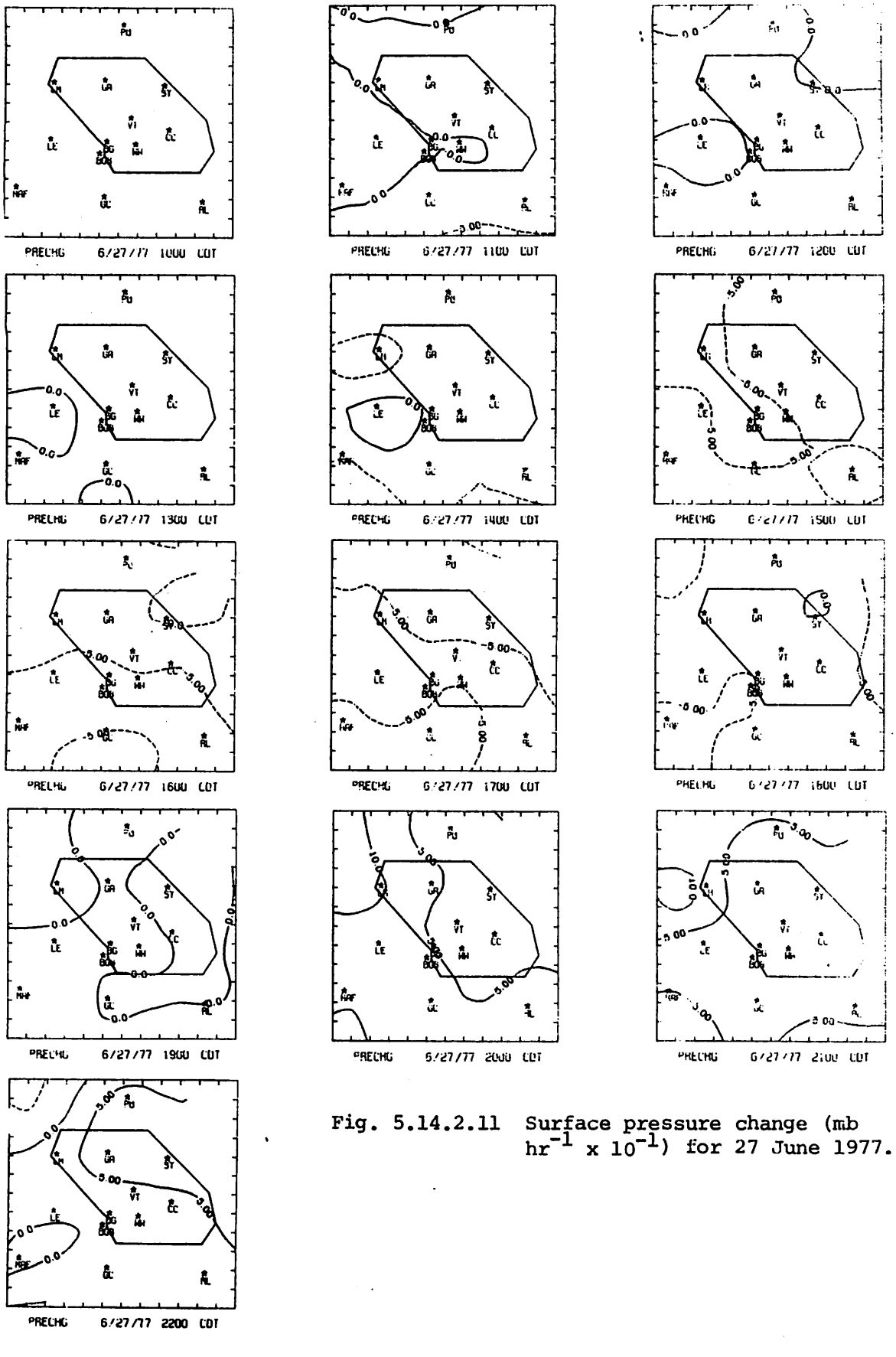

Fig. 5.14.2.11 Surface pressure change (mb hr^{-1} x 10^{-1}) for 27 June 1977.

5.14.3 Upper-Level Kinematic Parameters

Horizontal mass divergence profiles (Fig. 5.14.3.1) show mass divergence in low levels and mass convergence at mid levels at most times and levels. This pattern becomes very strong between 0000 GMT and 0300 GMT when activity was located just northwest of the network.

Vertical velocities were downward or near zero at all times for levels below 700 mb (Fig. 5.14.3.2). Upward velocities occurred only at 2230 GMT and 0000 GMT in mid- and upper-levels when storm development was present just northwest of the experiment area. Strong subsidence at 0300 GMT was possibly related to a downward circulation over the network created by the sinking in the environment outside the storm system immediately (~10 km) northwest of the PO-RL-MAF triangle.

Horizontal moisture divergence occurred at all times below 800 mb and became very large at 0300 GMT when subsidence was large over the network (Fig. 5.14.3.3). Moisture convergence was calculated at mid- or upper-levels at all times.

5.14.4 Energetics

Sufficient data were not available for computing the latent heat budget at any time during this day.

The horizontal and vertical flux divergence profiles of kinetic energy (Figs. 5.14.4.1 and 5.14.4.2) show small values at all times and levels between 700 and 300 mb. Strong horizontal flux divergence below 700 mb was present at 0300 GMT. Strong horizontal flux convergence and vertical flux divergence of kinetic energy at 0000 GMT completely reverses in pattern at 0300 GMT when activity was just outside the network.

5.14.5 Water Vapor Budget

Because of missing sounding data, it was not possible to compute the water vapor budget on this day.

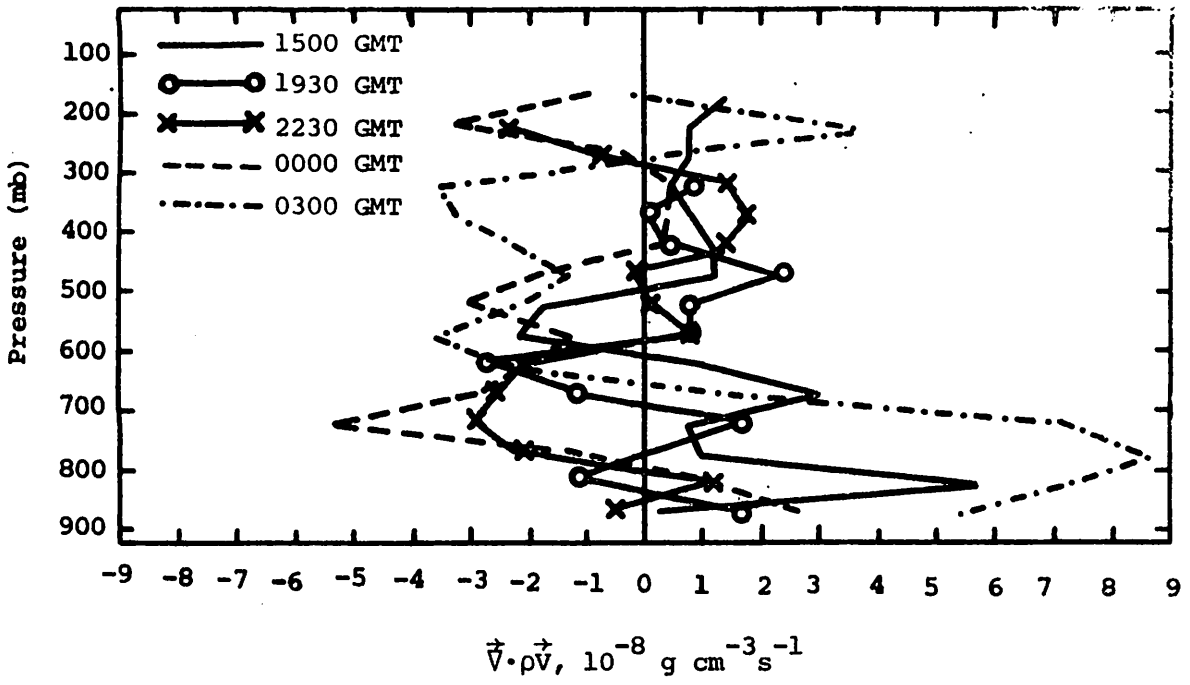

Fig. 5.14.3.1 Vertical profiles of mass divergence on 27 June 1977.

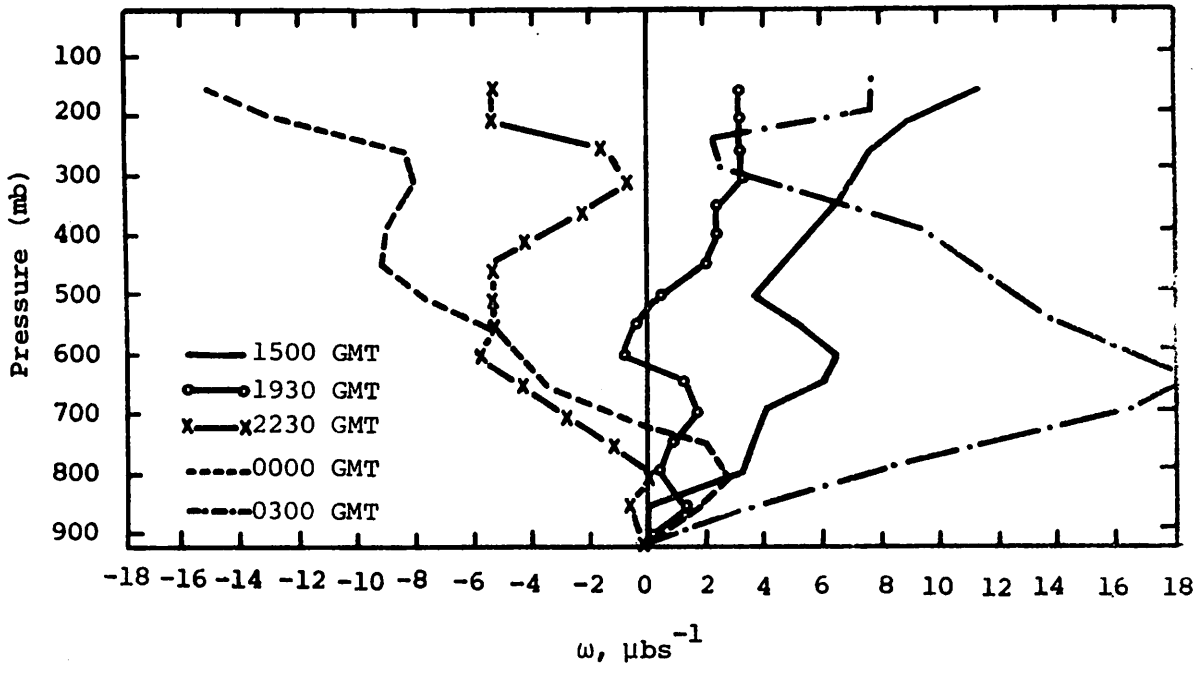

Fig. 5.14.3.2 Vertical profiles of vertical motion on 27 June 1977.

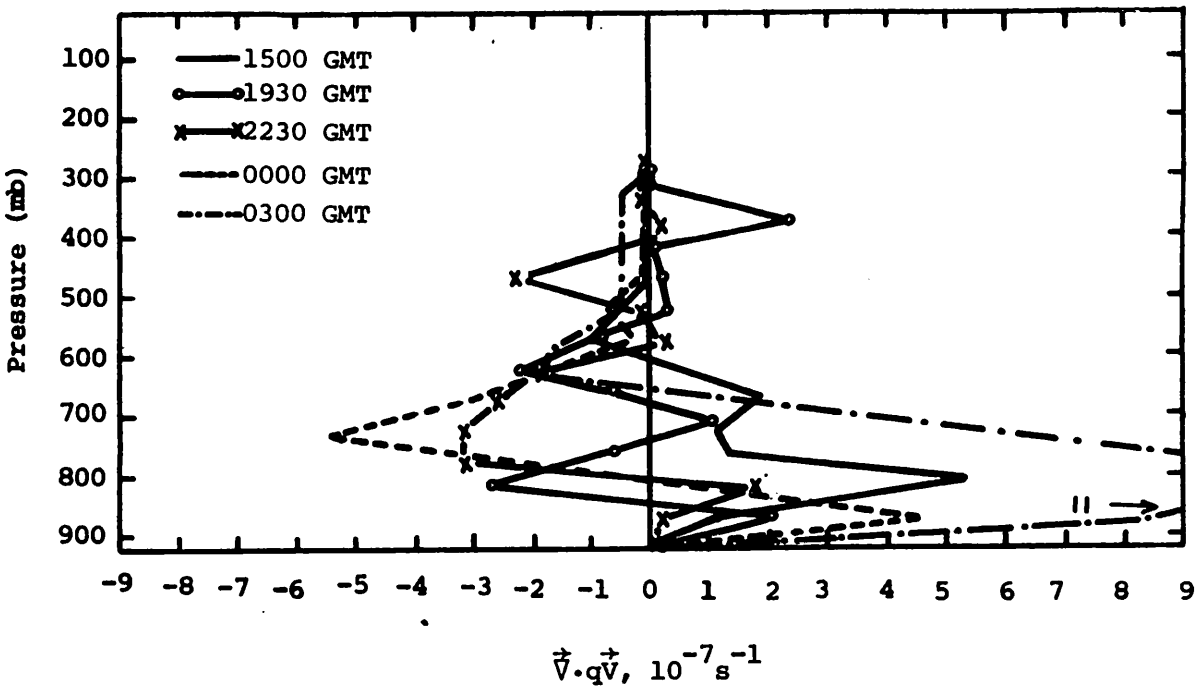

Fig. 5.14.3.3 Vertical profiles of moisture divergence on 27 June 1977.

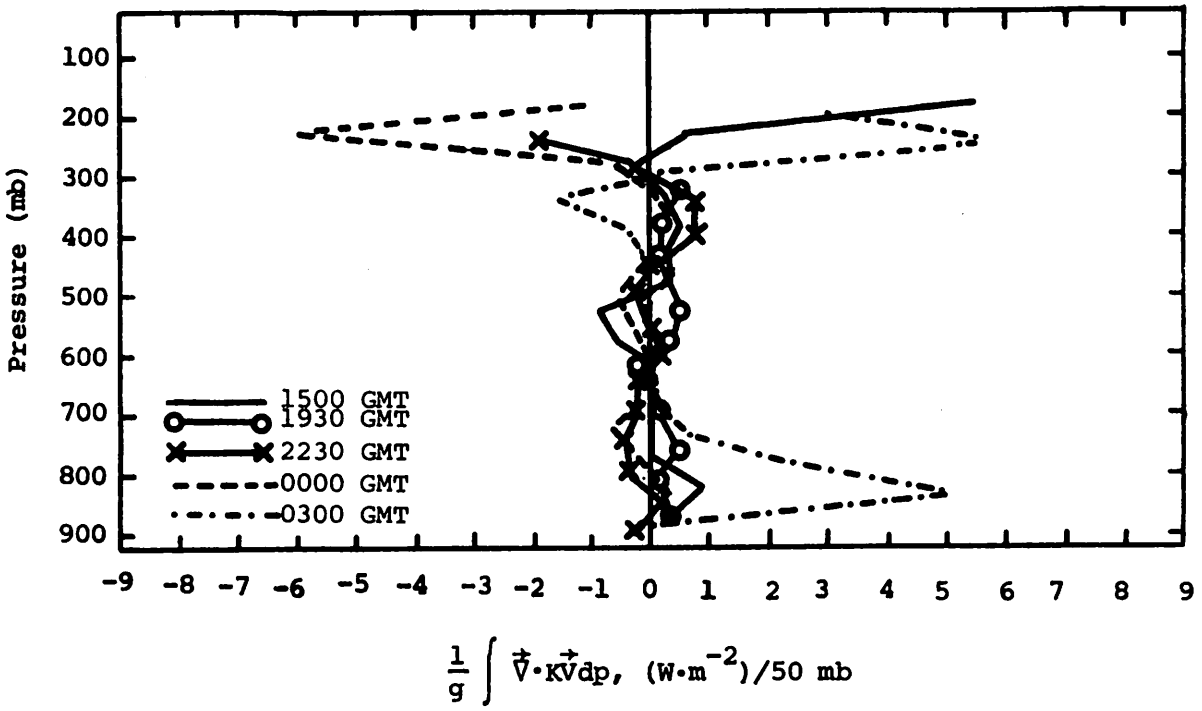

Fig. 5.14.4.1 Vertical profiles of the horizontal flux of kinetic energy on 27 June 1977.

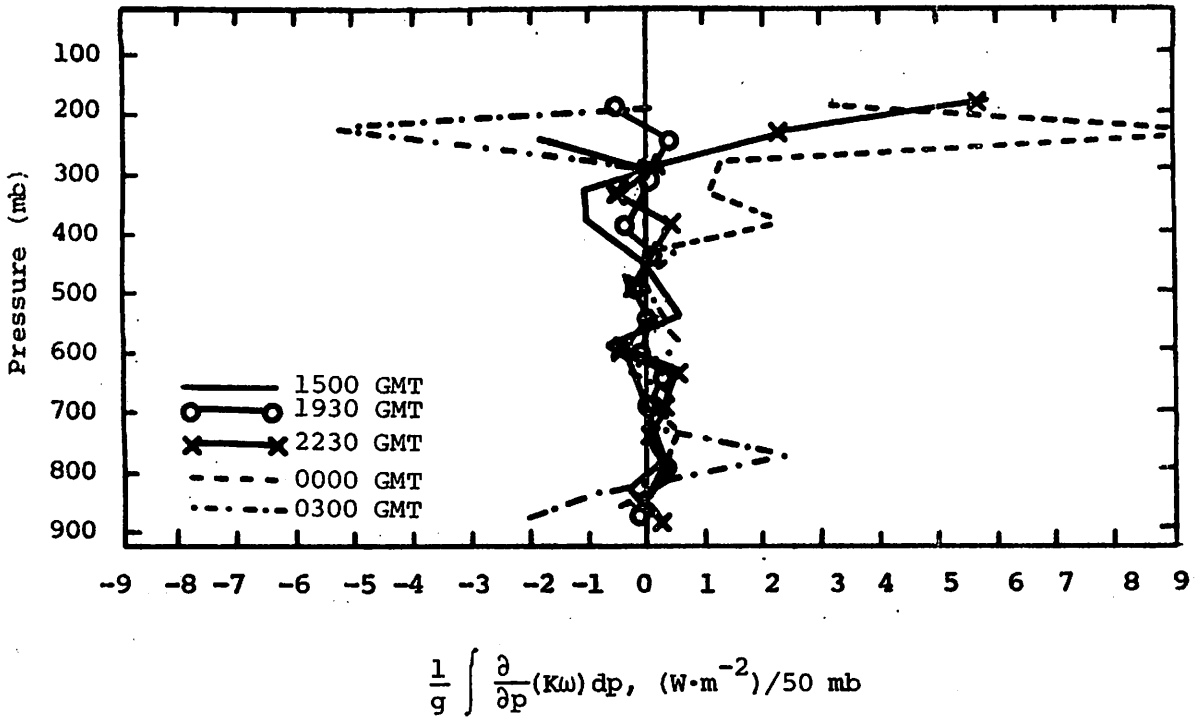

Fig. 5.14.4.2 Vertical profiles of the vertical flux of kinetic energy on 27 June 1977.

5.15 30 June 1977

5.15.1 Radar

The radar charts presented in Fig. 5.15.1.1 show no echoes prior to 2200 GMT at which time a cell with tops exceeding 9.1 km (30K ft) was located near Post and showers with tops below 6.1 km (20K ft) extended from near Gail westward to the border of the area. The cell moved westward and remained in the area until after 0000 GMT. Echoes remained at 0100 and 0200 GMT but it was evident that, at least over the HIPLEX area, dissipation was occurring. By 0300 GMT no echoes were present.

5.15.2 Surface

The echoes in the northern part of the area are accompanied by regions of minimum surface temperatures (Fig. 5.15.2.1). In other parts of the network, general diurnal temperature variations occurred. Values of surface mixing ratio (Fig. 5.15.2.2) remain high and nearly uniform with no well defined centers associated with the convective activity. These characteristics exist in surface equivalent potential temperature (Fig. 5.15.2.3), although a slight decrease occurred in regions of convective activity.

Fields of terrain-induced vertical motion (Fig. 5.15.2.4) show basically downward motion early in the day with a decrease in magnitude. The sign changed and upward and reversing motion occurred by 0200 GMT. This can be

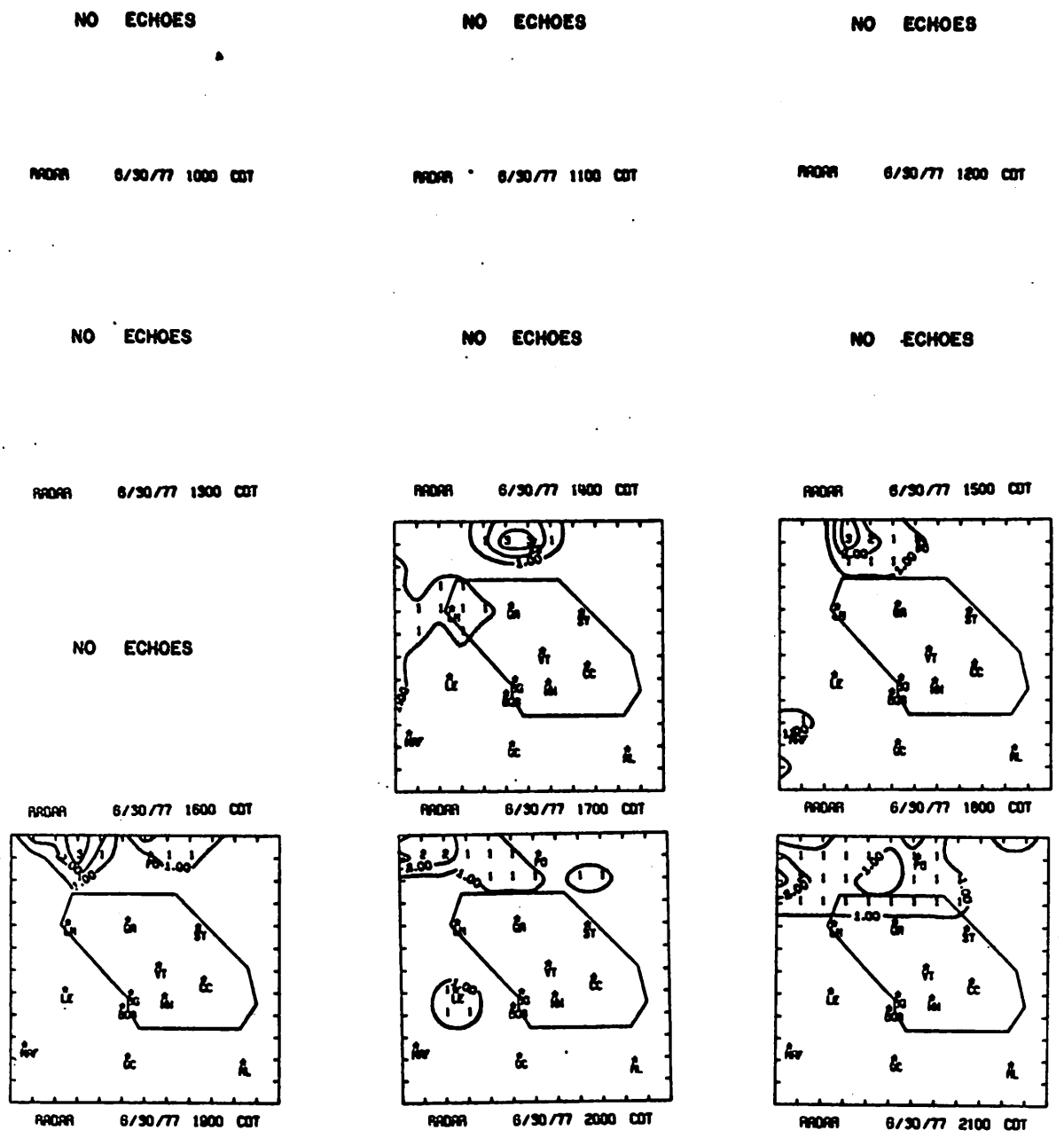

Fig. 5.15.1.1 Radar echoes for 30 June 1977.

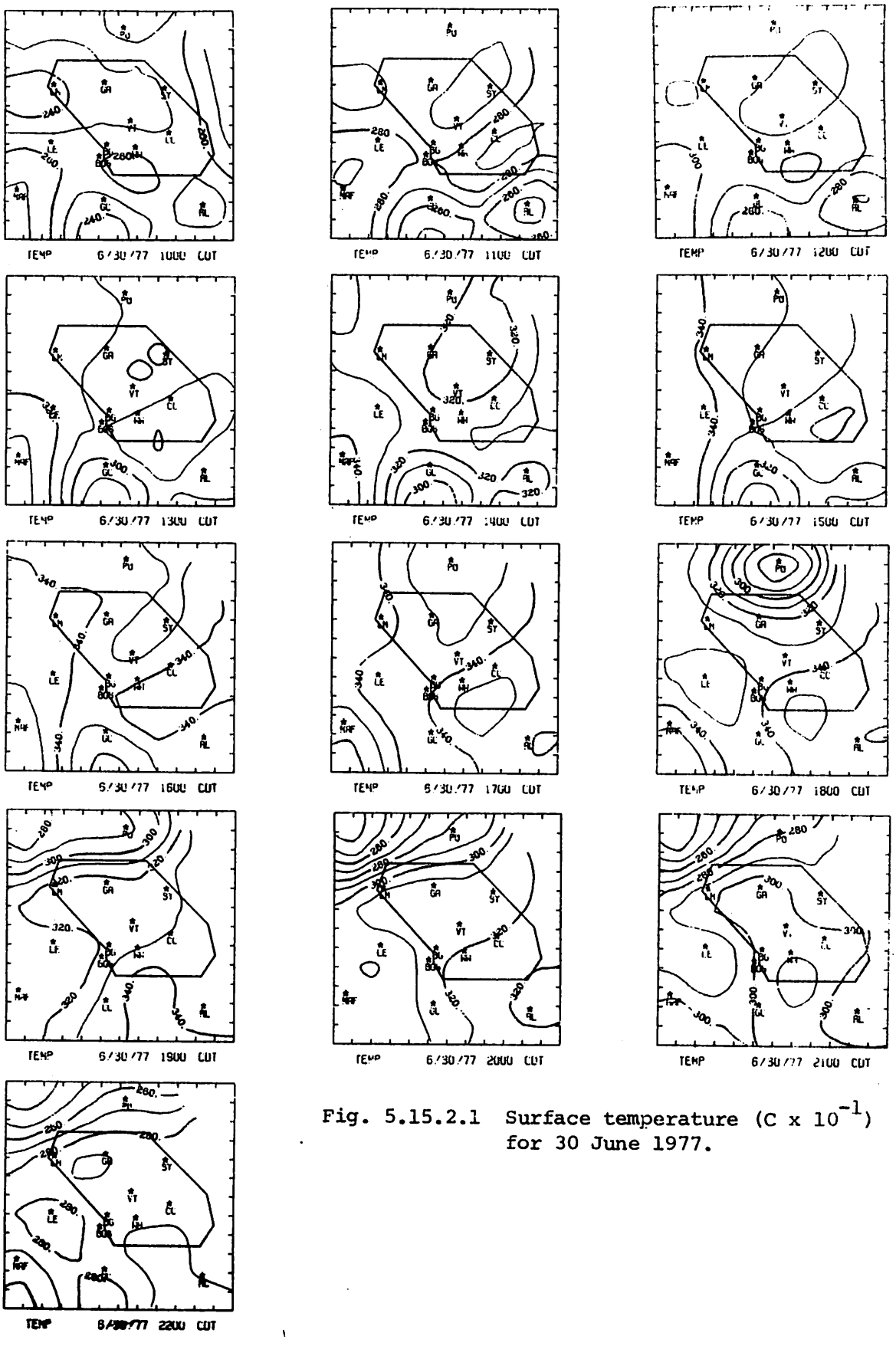

Fig. 5.15.2.1 Surface temperature (C x 10^{-1}) for 30 June 1977.

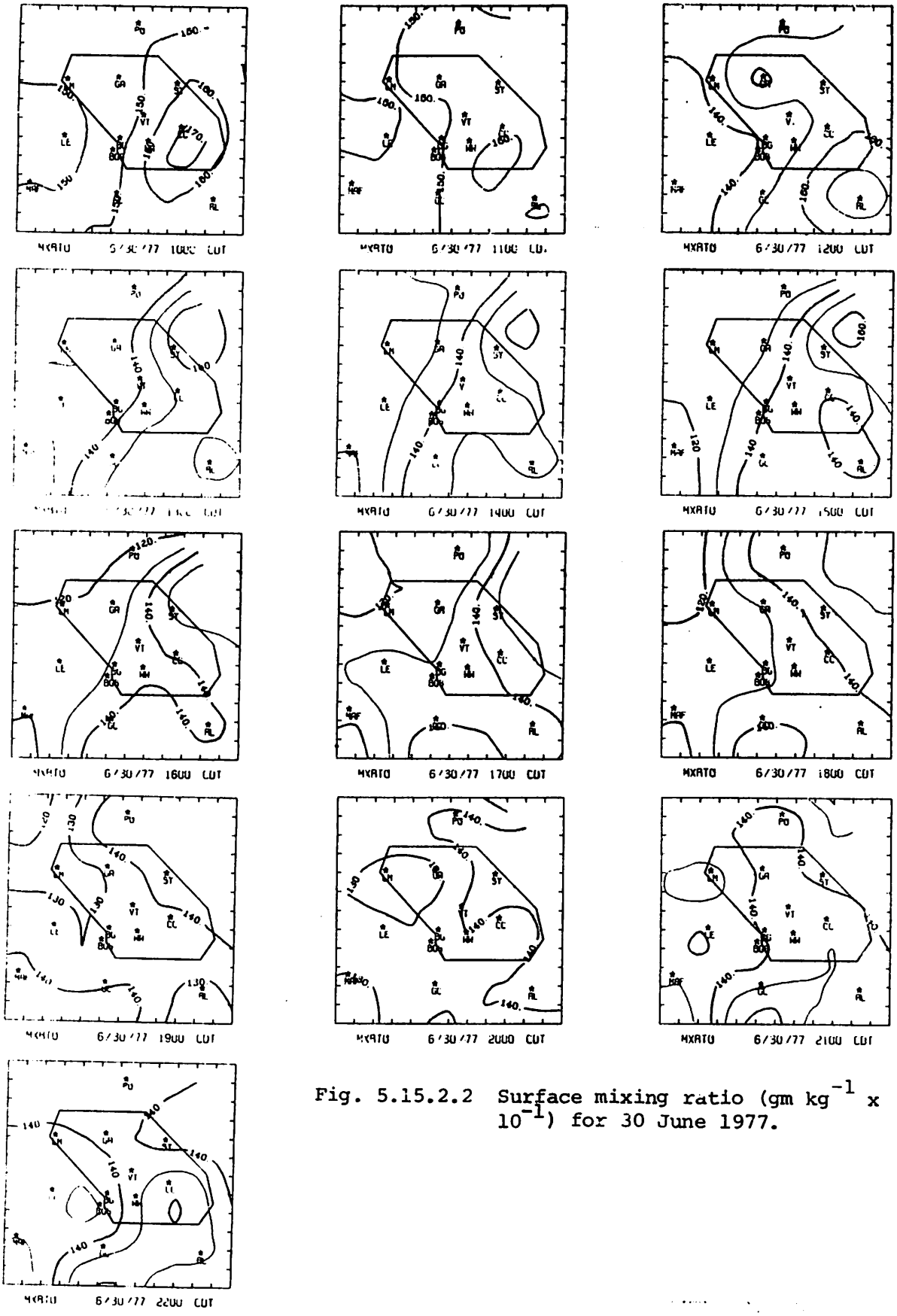

Fig. 5.15.2.2 Surface mixing ratio (gm kg^{-1} x 10^{-1}) for 30 June 1977.

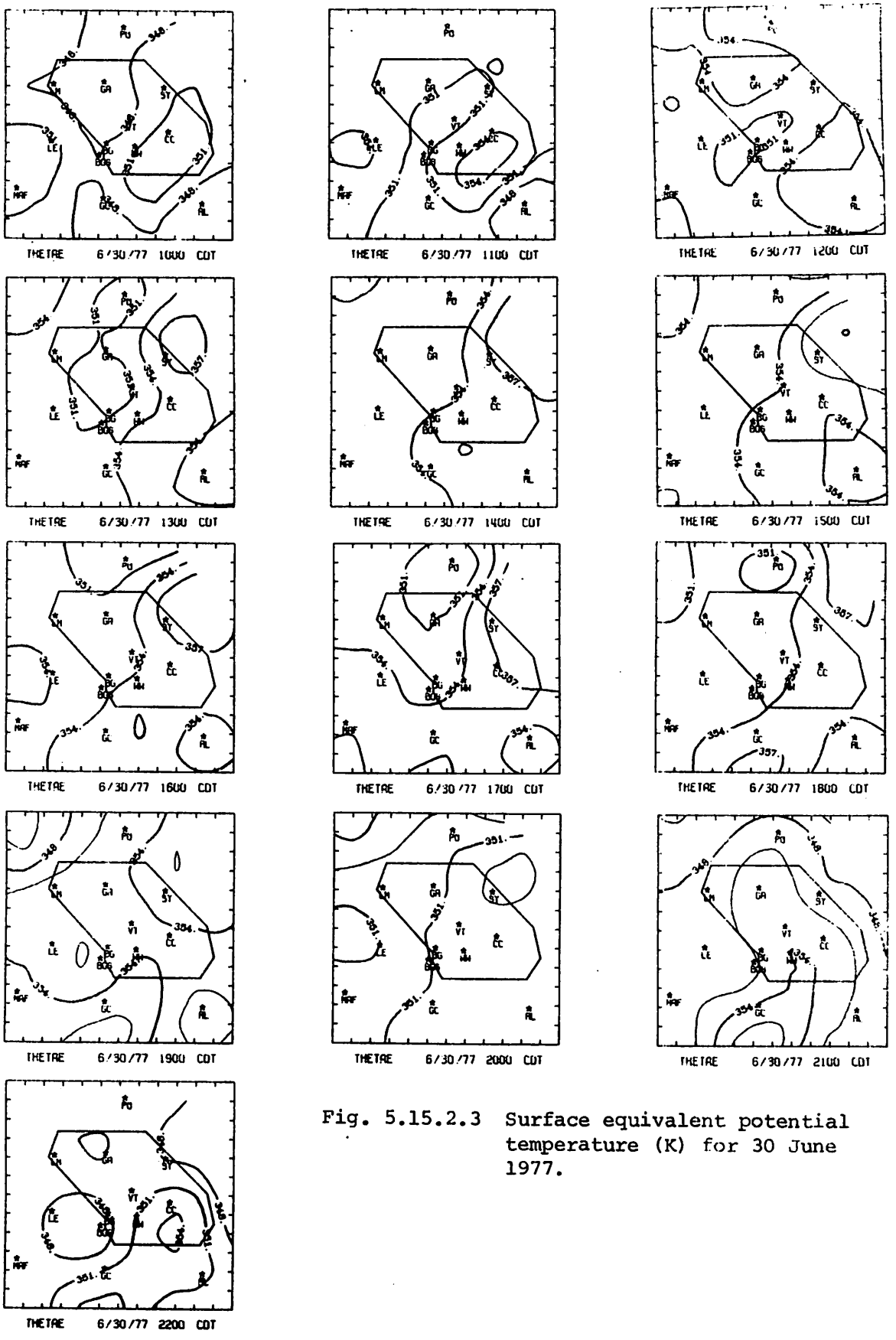

Fig. 5.15.2.3 Surface equivalent potential temperature (K) for 30 June 1977.

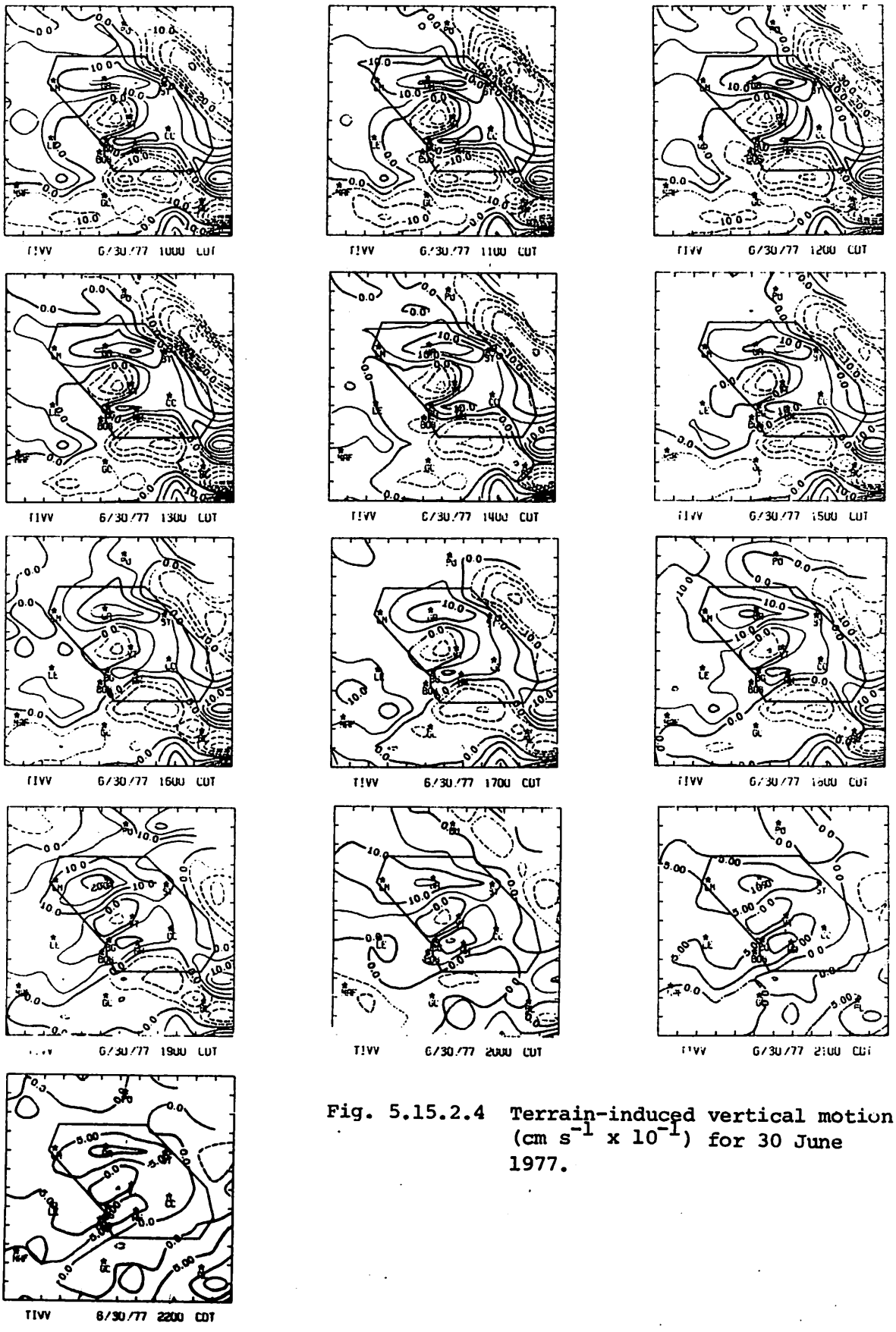

Fig. 5.15.2.4 Terrain-induced vertical motion (cm s^{-1} x 10^{-1}) for 30 June 1977.

attributed to a nocturnal decrease of horizontal wind speed coupled with backing of surface winds to the southeast. This results in slight upward motion in regions of convective activity.

Fields of surface velocity divergence (Fig. 5.15.2.5) show large variations in the well-defined centers of convergence and divergence. Prior to convective activity, centers of convergence existed and reached maximum values by 0000 GMT. At 0100 GMT, divergence and a cold downdraft occurred in association with dissipation of the echoes. These conditions are further accompanied by downward vertical motion 50 mb above the surface (Fig. 5.15.2.6). Centers of upward motion occurred prior to and during the heaviest activity.

Surface moisture convergence (Fig. 5.15.2.7) showed well-defined centers in areas of convection prior to 0100 GMT which resulted in an upward flux of moisture 50 mb above the surface (Fig. 5.15.2.8). Following dissipation of the convective activity the magnitude of the moisture flux decreased. Fields of surface vorticity (Fig. 5.15.2.9) show centers of cyclonic vorticity prior to convective activity. During dissipation, anticyclonic vorticity dominated which decreased to near zero by 0300 GMT.

The sea level pressure field (Fig. 5.15.2.10) shows a region of low pressure located between Robert Lee and Colorado City. This pattern remained rather constant with small pressure changes (Fig. 5.15.2.11). During the dissipation stage an increase of pressure occurred in regions of the cold downdraft.

5.15.3 Upper-Level Kinematic Parameters

The horizontal mass divergence profiles (Fig. 5.15.3.1) consistently showed low-level divergence and mid-level convergence at all times. Vertical velocities were downward or near zero at all times with levels below 500 mb corresponding nicely to the lack of precipitation formation during the day (Fig. 5.15.3.2). Horizontal moisture divergence profiles (Fig. 5.15.3.3) consistently showed moisture divergence in low-levels with weak convergence present in mid- and upper-layers for the entire day.

5.15.4 Energetics

Horizontal flux divergence of latent heat energy in low levels occurred throughout the day and was the only region where large values were computed (Fig. 5.15.4.1). Vertical flux divergence of latent heat energy at mid levels and flux convergence below was associated with a net downward transport of latent energy from mid- to lower-levels within a sinking environment (Fig.

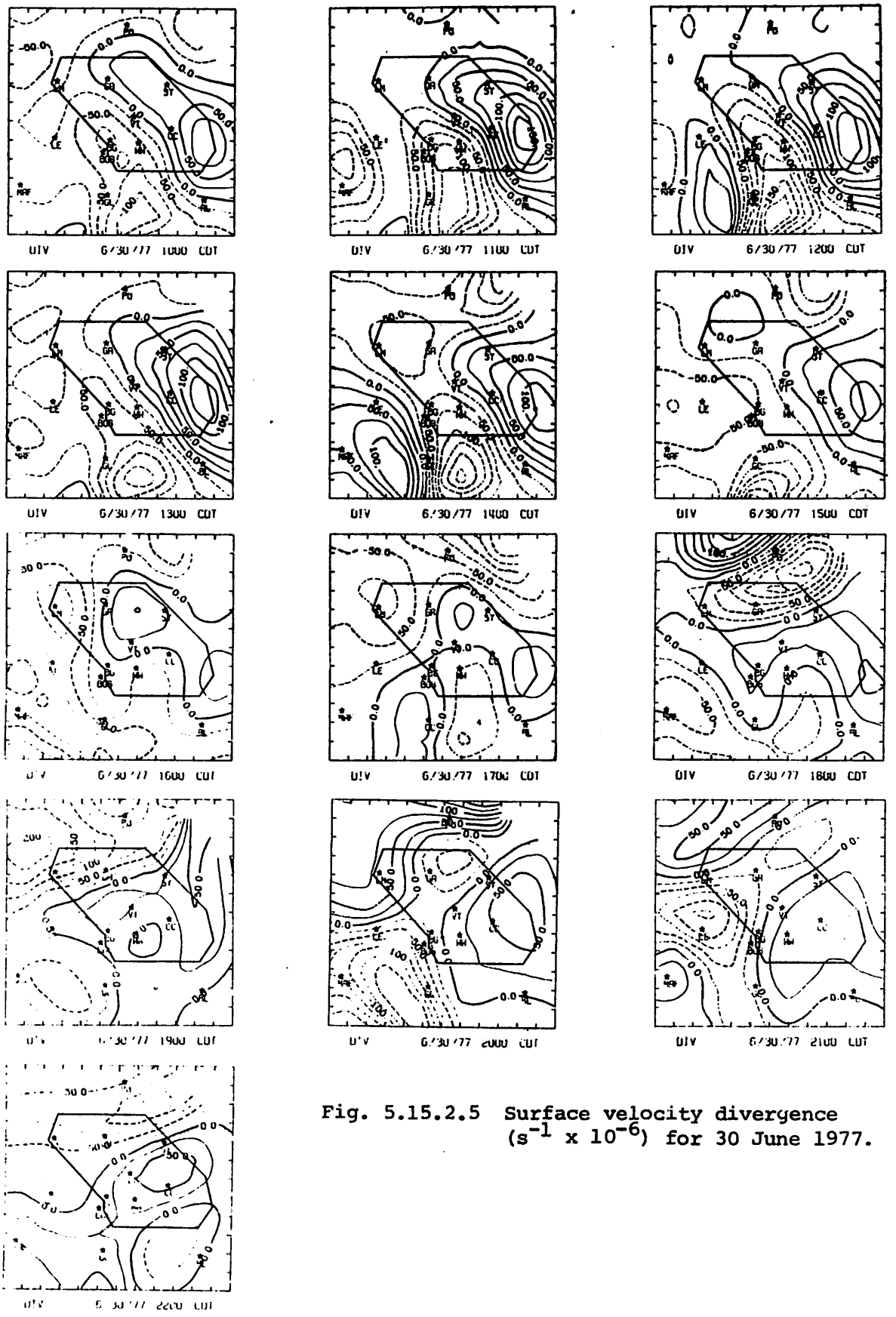

Fig. 5.15.2.5 Surface velocity divergence (s^{-1} x 10^{-6}) for 30 June 1977.

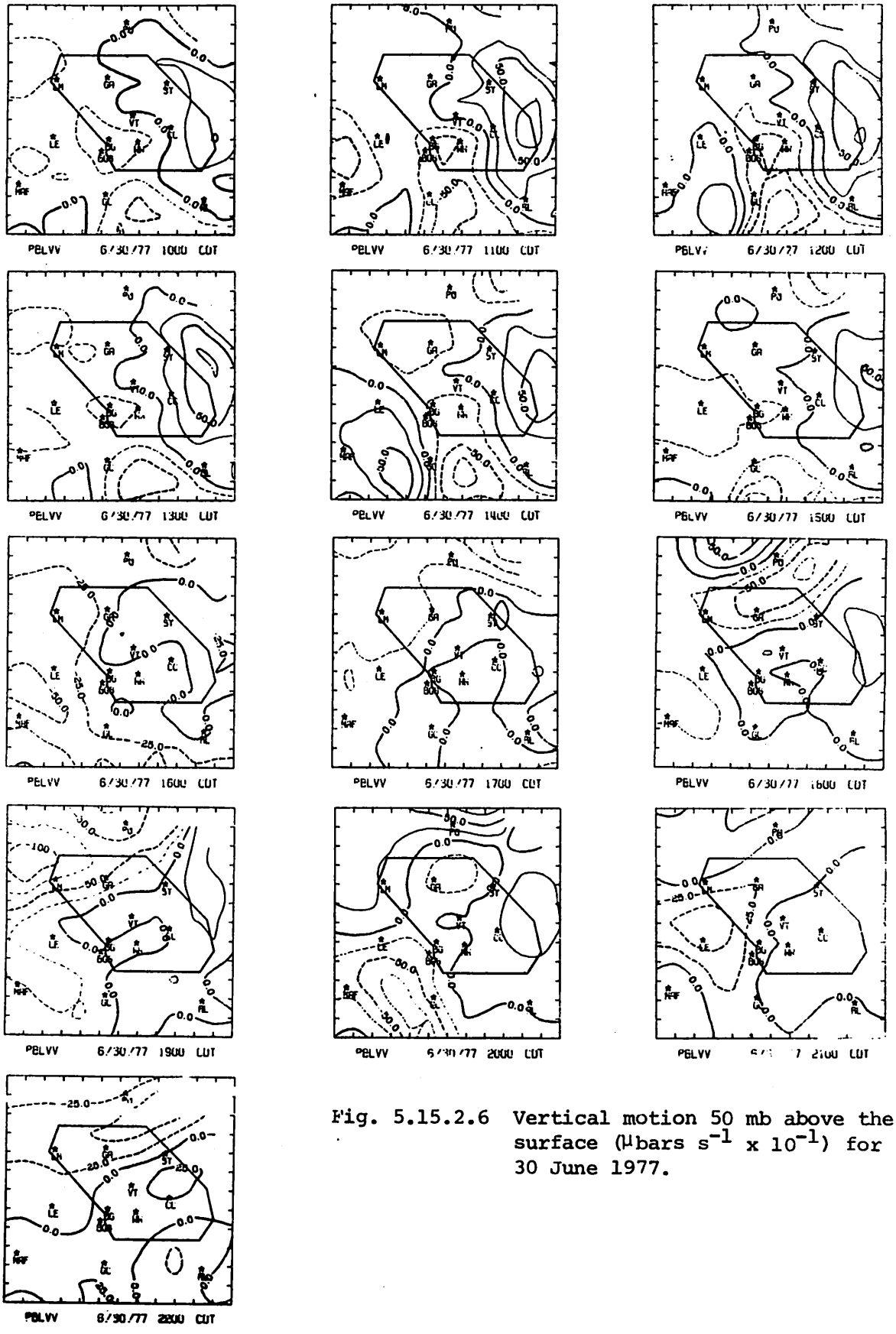

Fig. 5.15.2.6 Vertical motion 50 mb above the surface (μbars s^{-1} x 10^{-1}) for 30 June 1977.

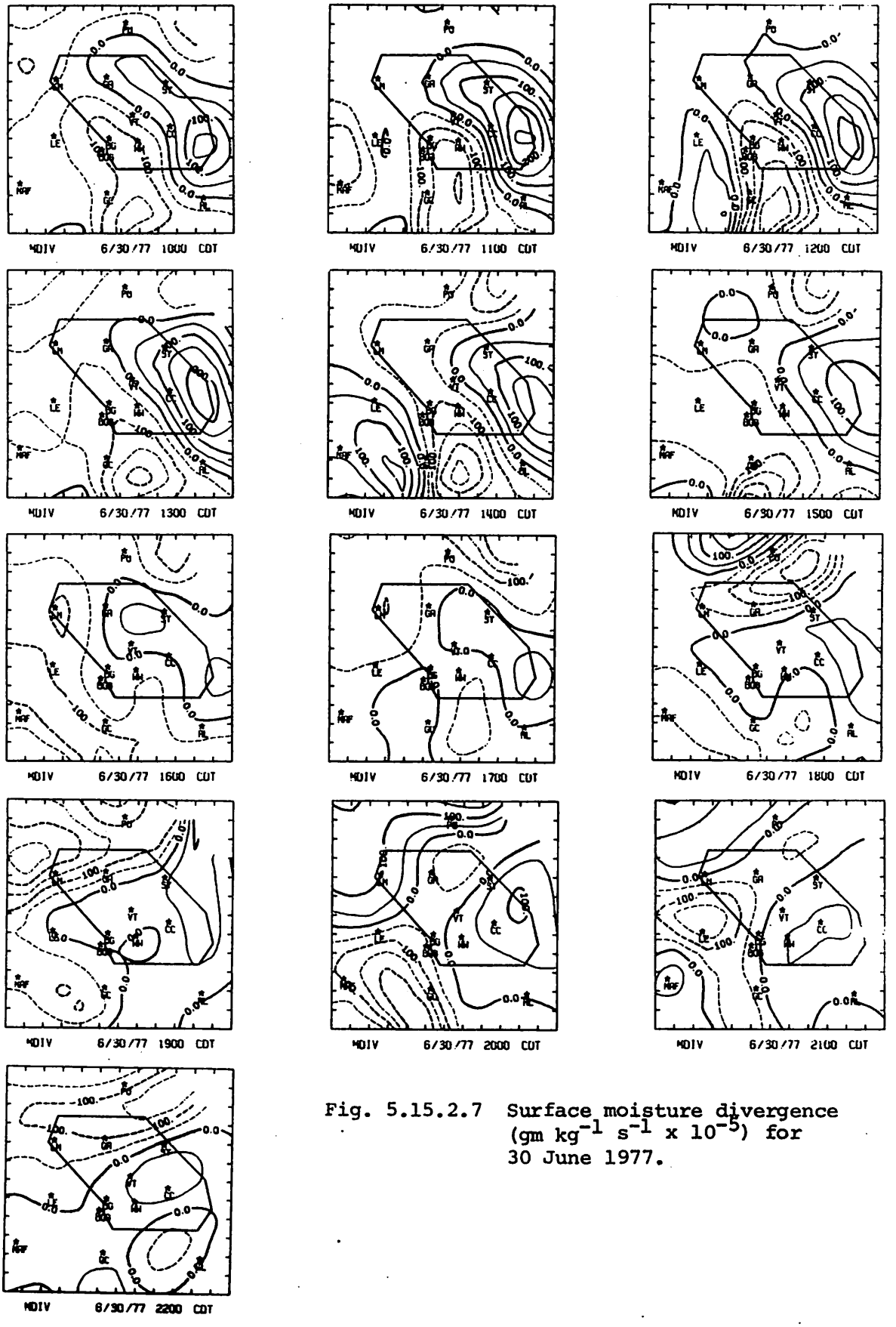

Fig. 5.15.2.7 Surface moisture divergence (gm kg^{-1} s^{-1} x 10^{-5}) for 30 June 1977.

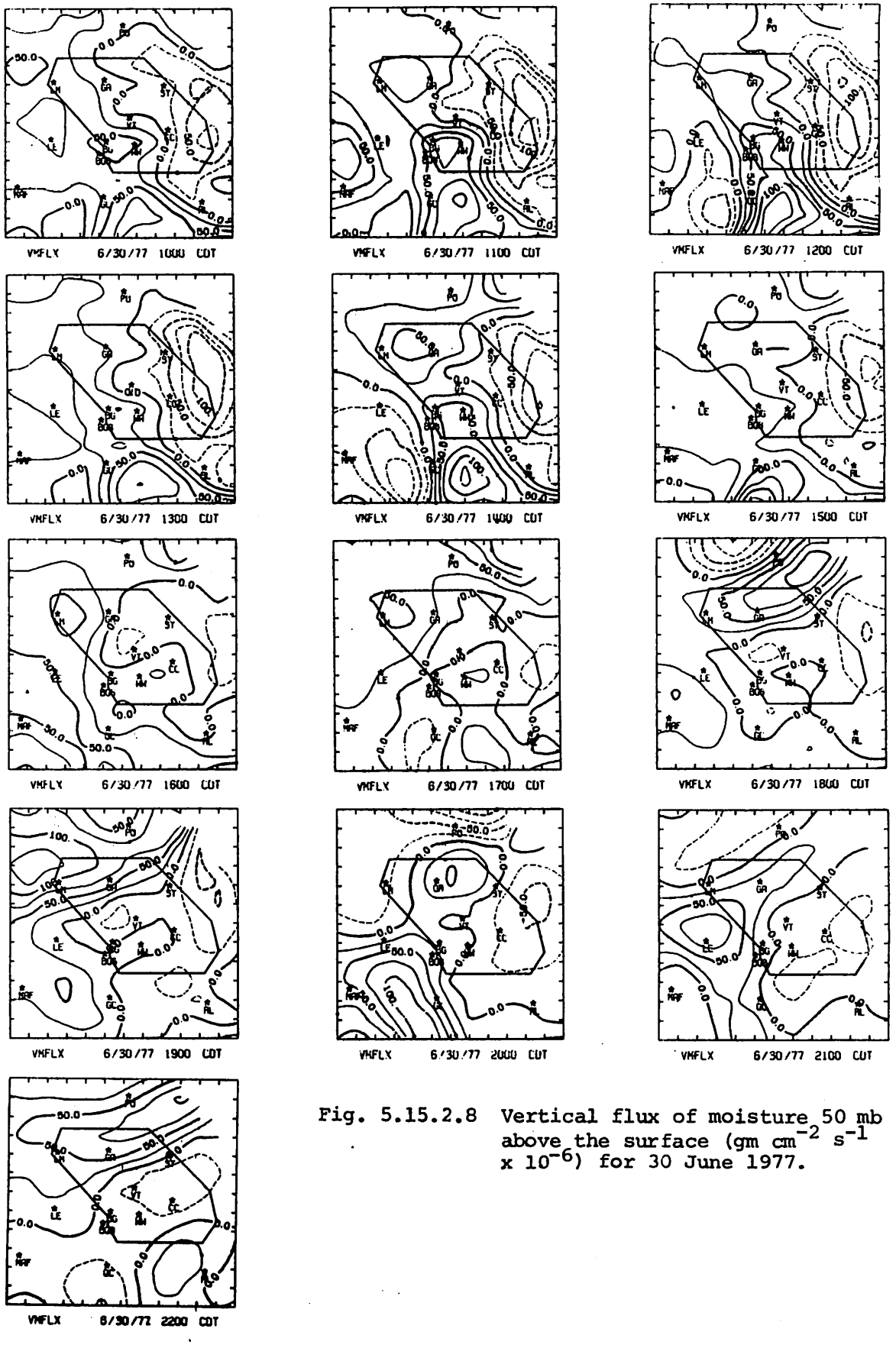

Fig. 5.15.2.8 Vertical flux of moisture 50 mb above the surface (gm cm^{-2} s^{-1} x 10^{-6}) for 30 June 1977.

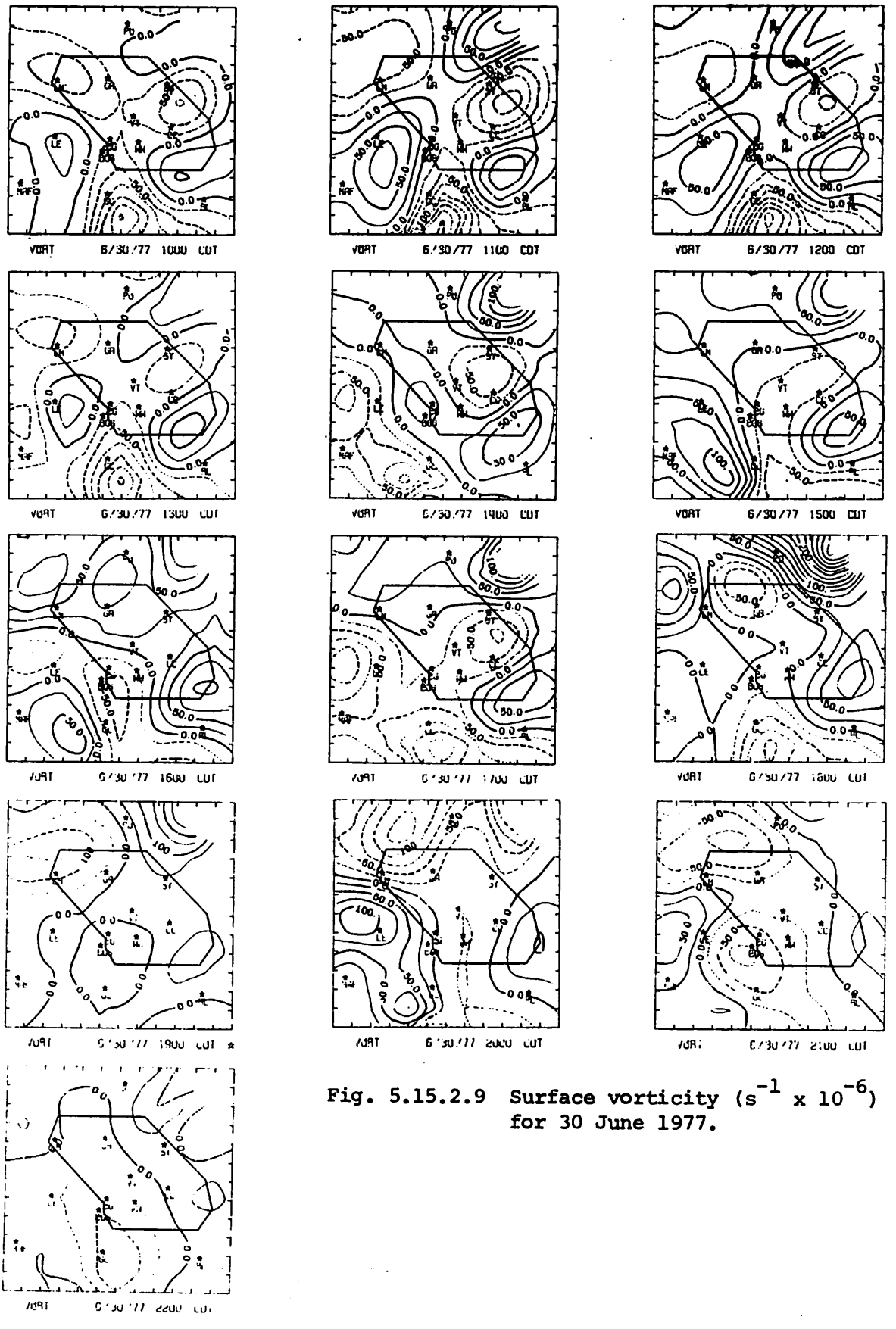

Fig. 5.15.2.9 Surface vorticity (s^{-1} x 10^{-6}) for 30 June 1977.

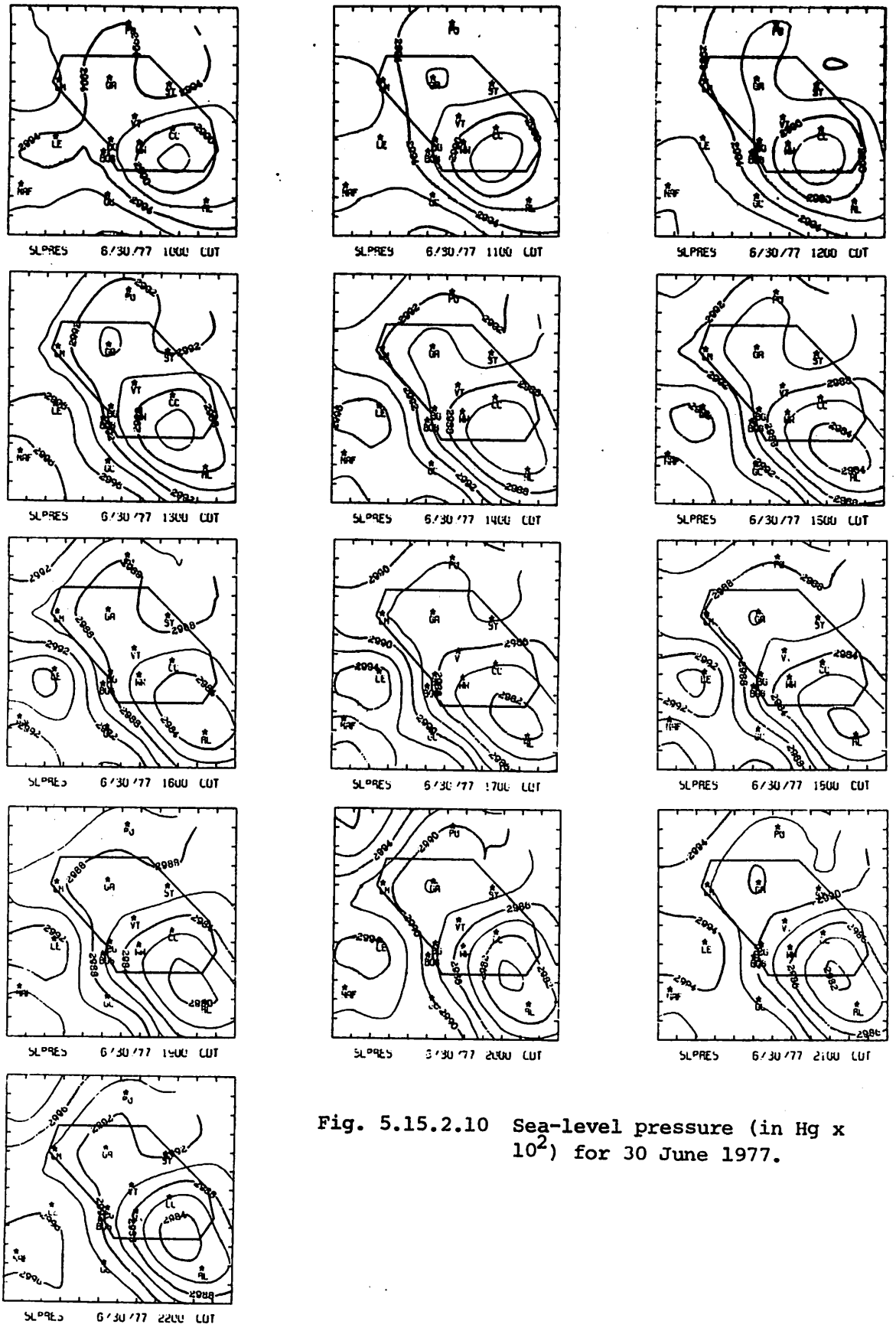

Fig. 5.15.2.10 Sea-level pressure (in Hg x 10^2) for 30 June 1977.

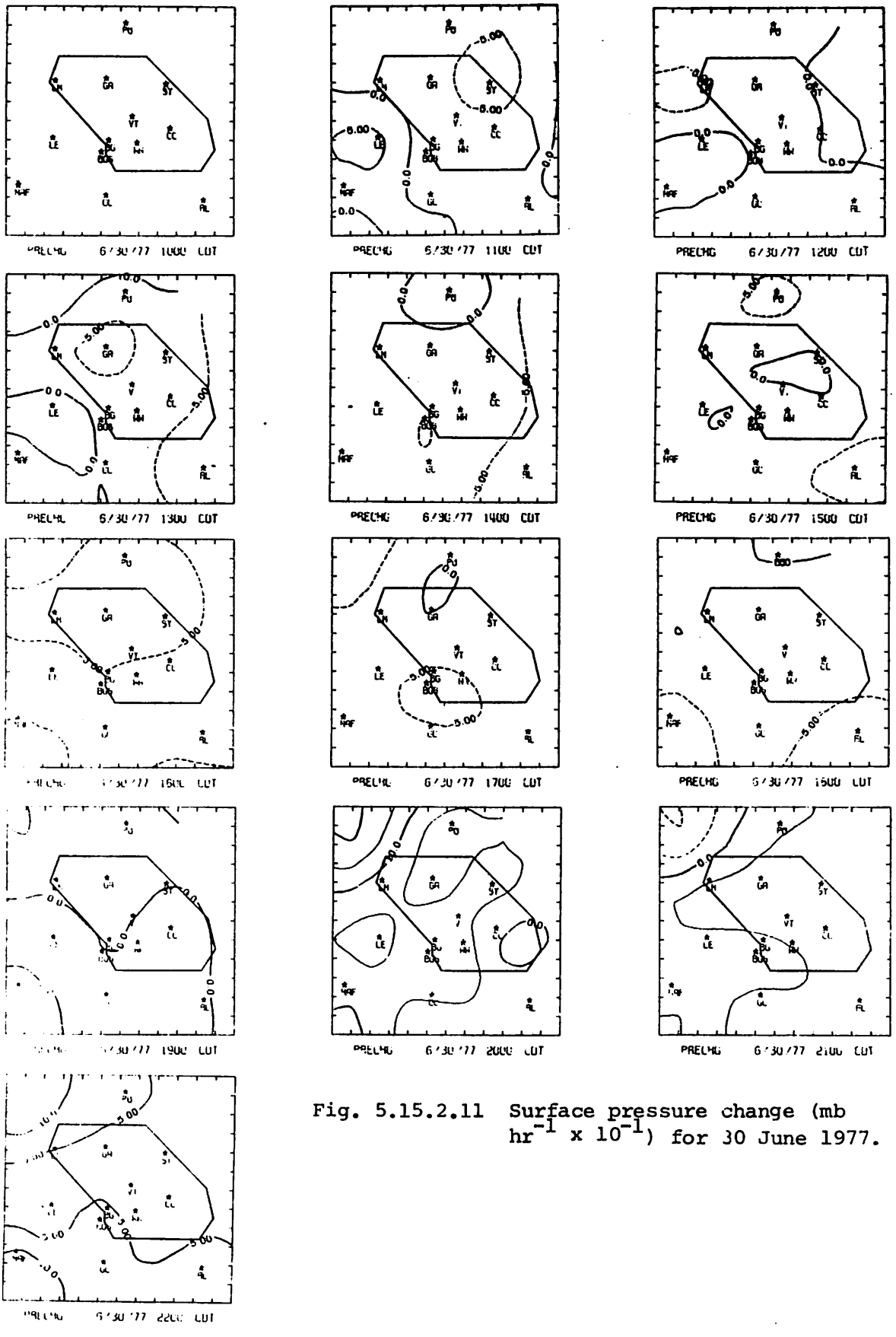

Fig. 5.15.2.11 Surface pressure change (mb hr^{-1} x 10^{-1}) for 30 June 1977.

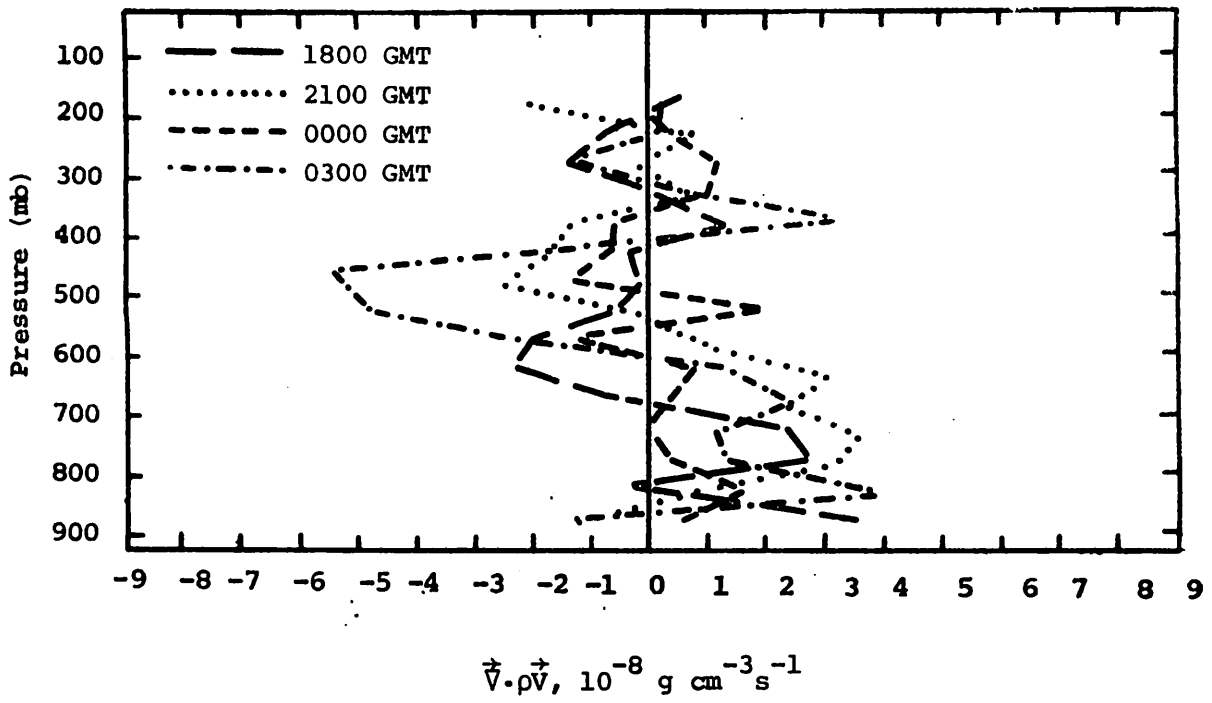

Fig. 5.15.3.1 Vertical profiles of mass divergence on 30 June 1977.

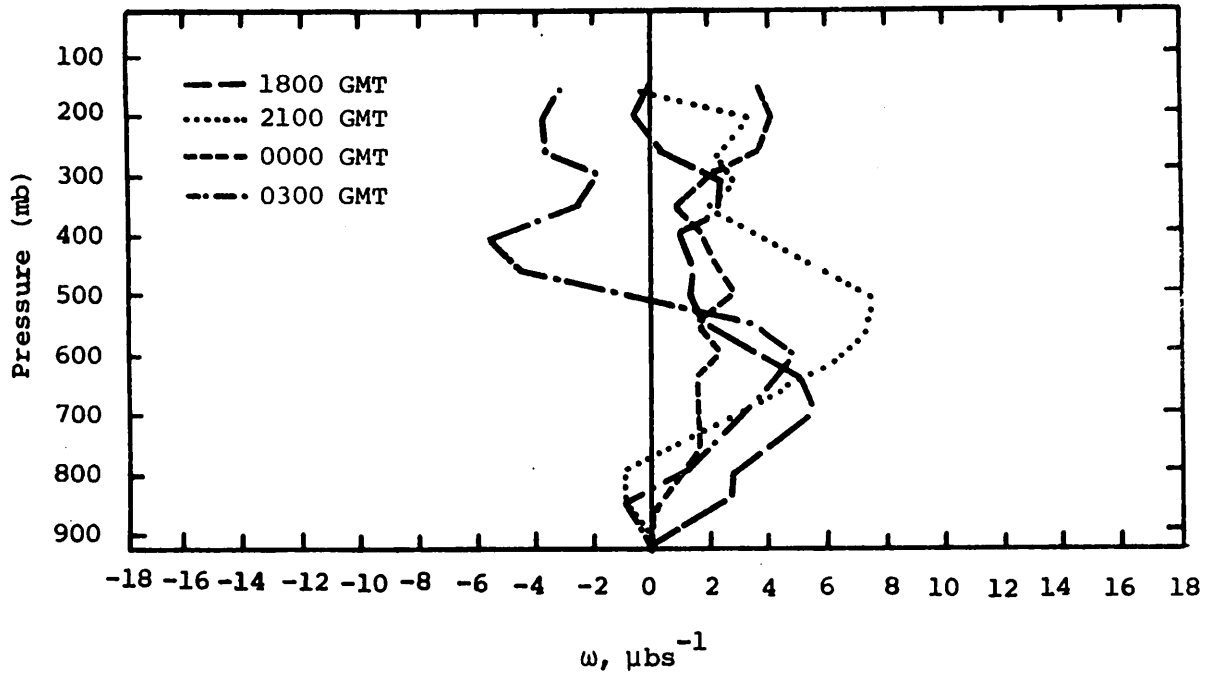

Fig. 5.15.3.2 Vertical profiles of vertical motion on 30 June 1977.

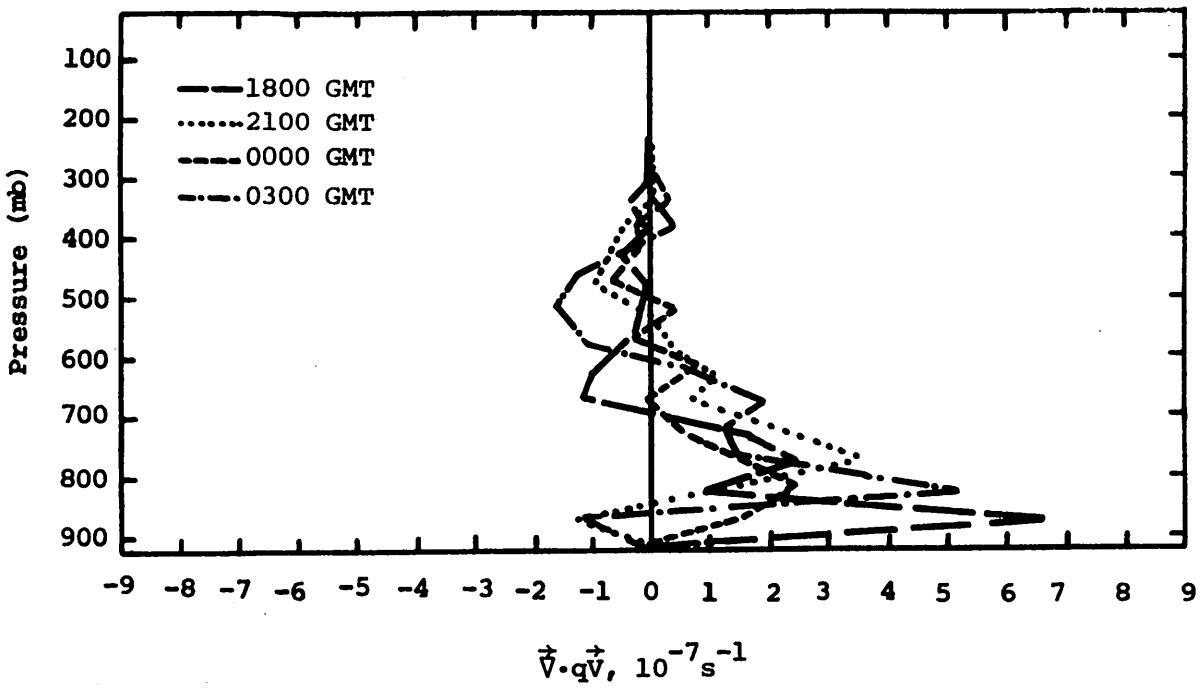

Fig. 5.15.3.3 Vertical profiles of moisture divergence on 30 June 1977.

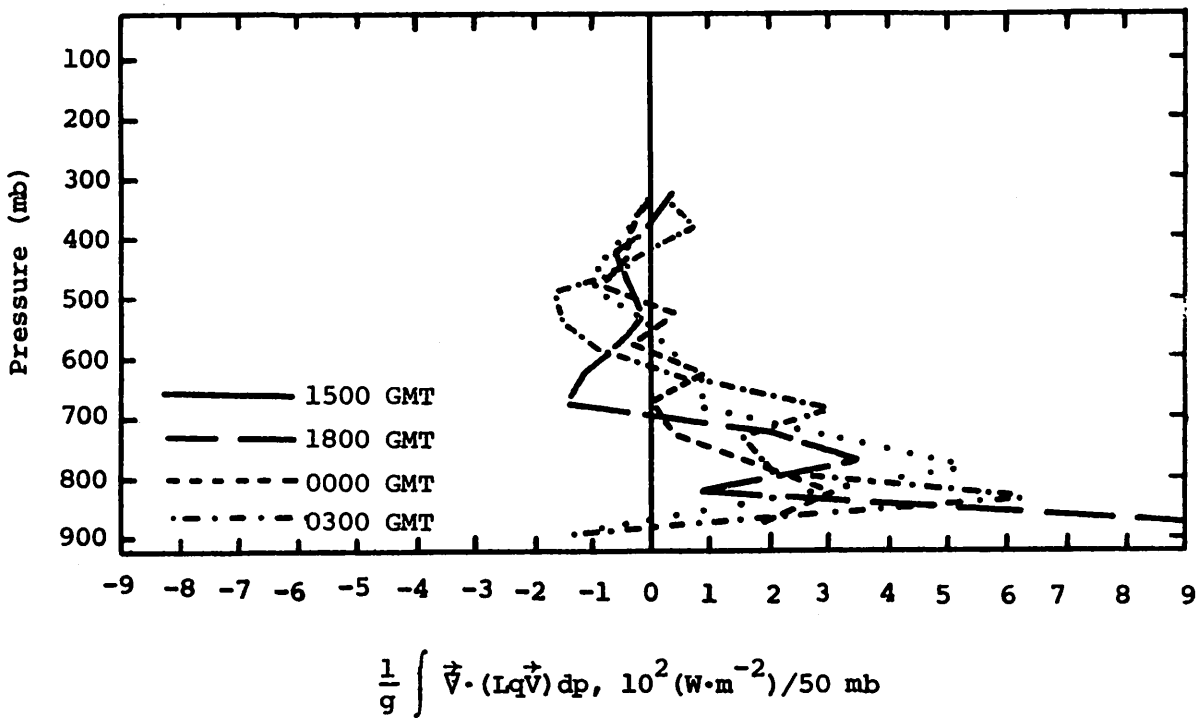

Fig. 5.15.4.1 Vertical profiles of the horizontal flux of latent heat energy on 30 June 1977.

5.15.4.2) during the entire day. Local changes of latent heat energy were generally positive between 800 and 600 mb between 1800 GMT and 0000 GMT and negative by 0300 GMT (Fig. 5.15.4.3).

Profiles of the residual term of the latent heat budget equation (-R) (Fig. 5.15.4.4) were negative at most levels between 850 and 600 mb except at 0300 GMT and above 600 mb at all times where values were small. These low-level increases of latent heat energy are apparently not related to evaporation since low-level cloud formation occurred over the network. Since lapse rates of temperature near the adiabatic value were present from the surface up to 700 mb between 1800 and 0000 GMT, turbulent flux convergence of water vapor (and latent heat energy) may have been responsible for positive local changes and negative -R values (increasing latent heat content) in low levels.

The diabatic heating profiles (Fig. 5.15.4.5) support this interpretation since values are generally small or slightly negative at most levels during a day when activity was absent and condensation/evaporation should have been at a minimum (or slightly negative if subsidence created some evaporation of observed clouds in mid levels).

Horizontal and vertical flux divergence profiles of kinetic energy (Figs. 5.15.4.6 and 5.15.4.7) are near zero at all times and levels except at 2100 and 0000 GMT when both horizontal and vertical flux convergence was computed in upper levels.

5.15.5 Water Vapor Budget

Figure 5.15.5.1 shows vertical profiles of the net horizontal transport of water vapor. These profiles remain similar and show a net outflow in lower layers and a net inflow in upper layers. Since the echoes occurred near the edge of the area, the magnitudes of these parameters are smaller than for cases of strong activity.

Figure 5.15.5.2 shows profiles of net vertical transport of water vapor. These profiles generally show a net inflow in layers below 700 mb, and a net outflow aloft.

Figure 5.15.5.3 shows profiles of the vertical transport of water vapor through constant pressure surfaces. These profiles show strong downward transports at most times. Once activity moves from the area at 0300 GMT, upward motion occurred above 500 mb.

Figure 5.15.5.4 shows profiles of combined net horizontal and vertical transport. These profiles show some spatial and temporal variations. A net

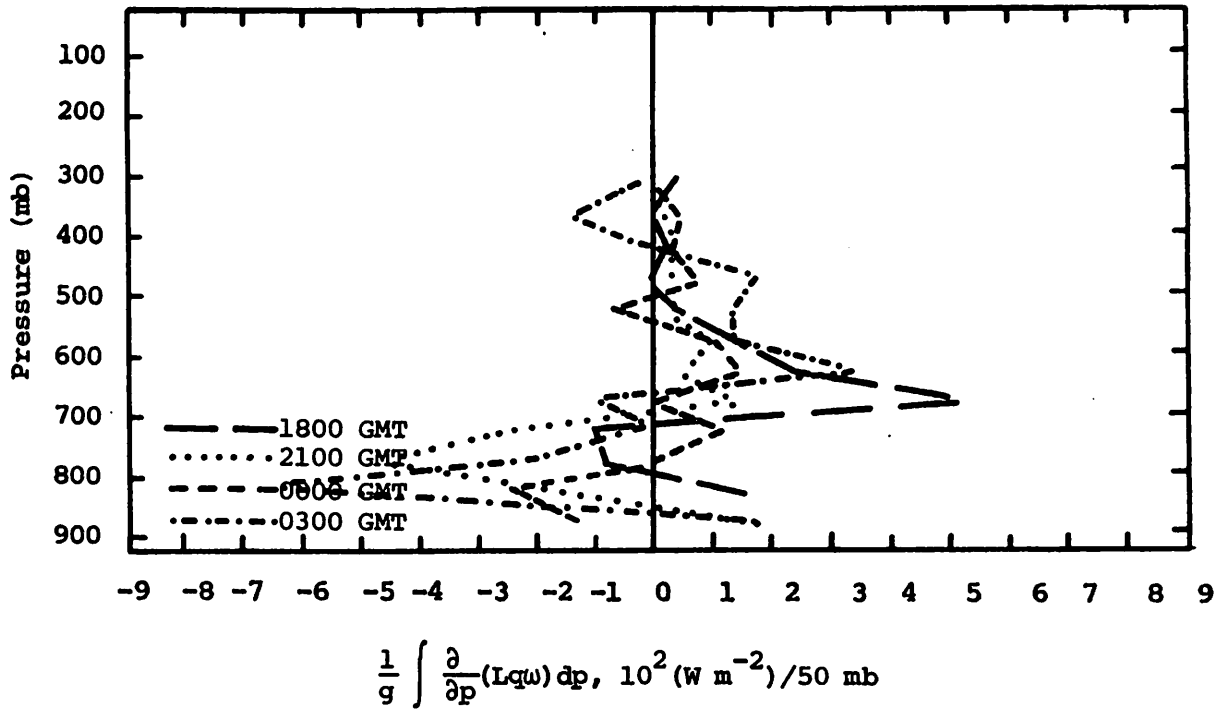

Fig. 5.15.4.2 Vertical profiles of the vertical flux of latent heat energy on 30 June 1977.

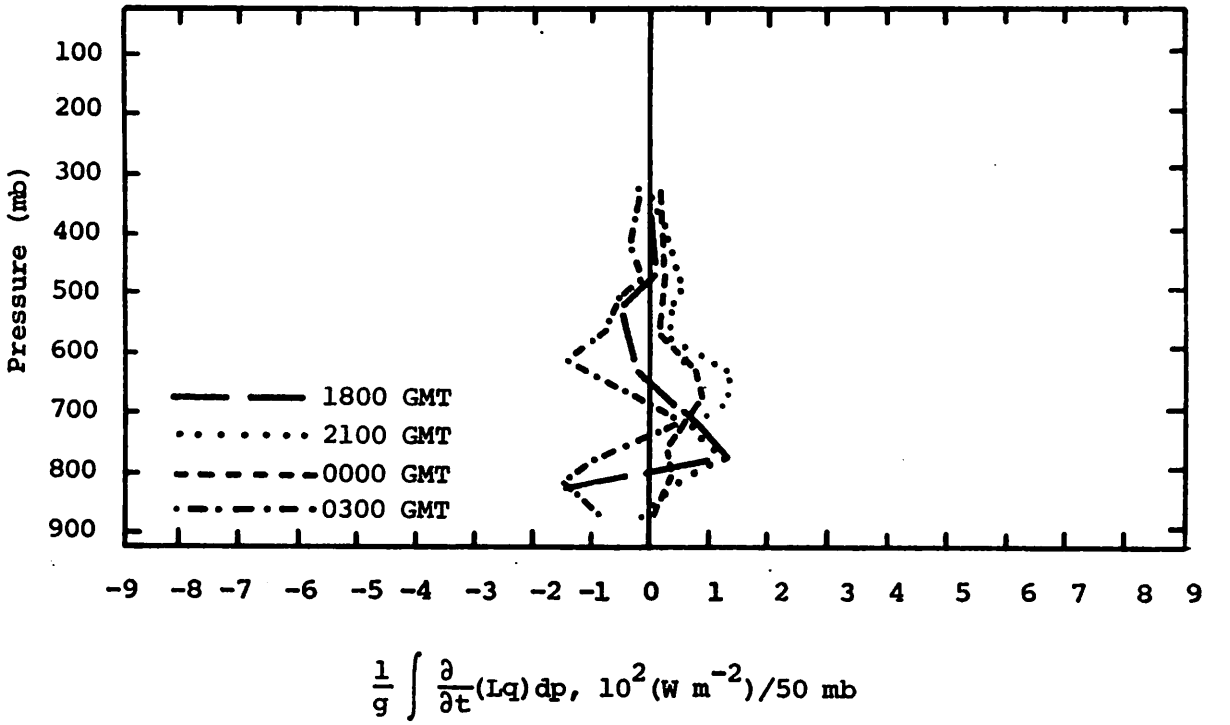

Fig. 5.15.4.3 Vertical profiles of the local change of latent heat energy on 30 June 1977.

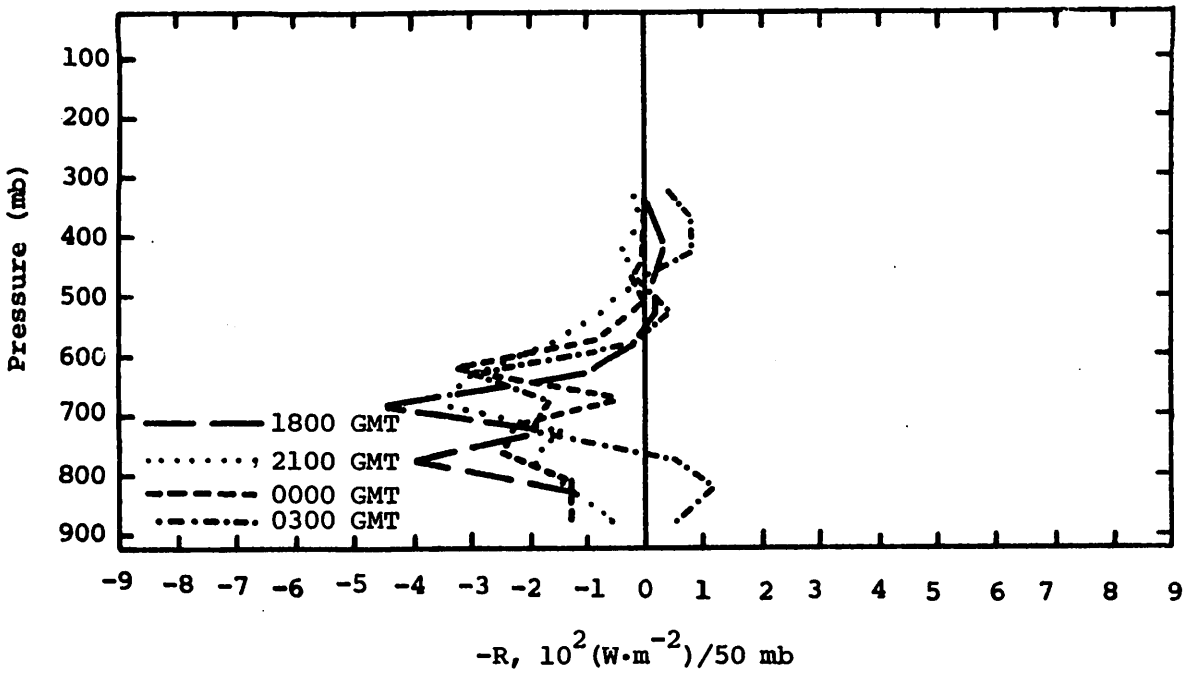

Fig. 5.15.4.4 Vertical profile of the residual of the latent heat energy equation on 30 June 1977.

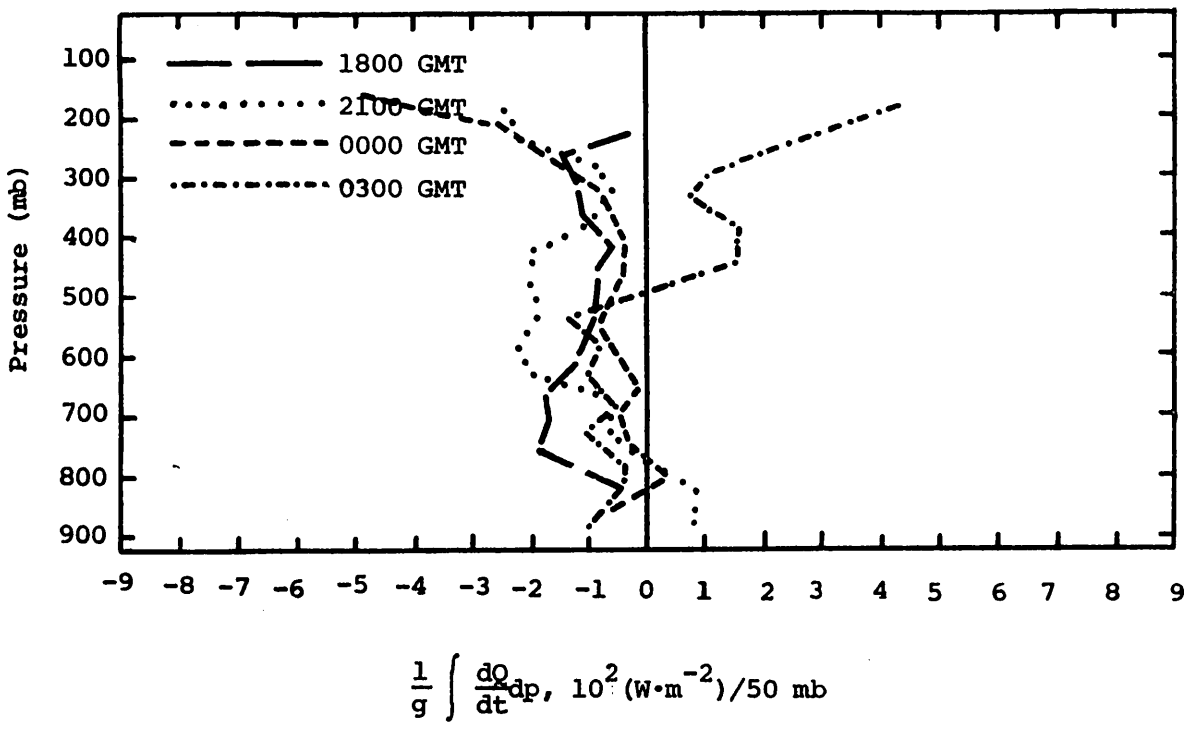

Fig. 5.15.4.5 Vertical profiles of diabatic heating computed from the first law of thermodynamics on 30 June 1977.

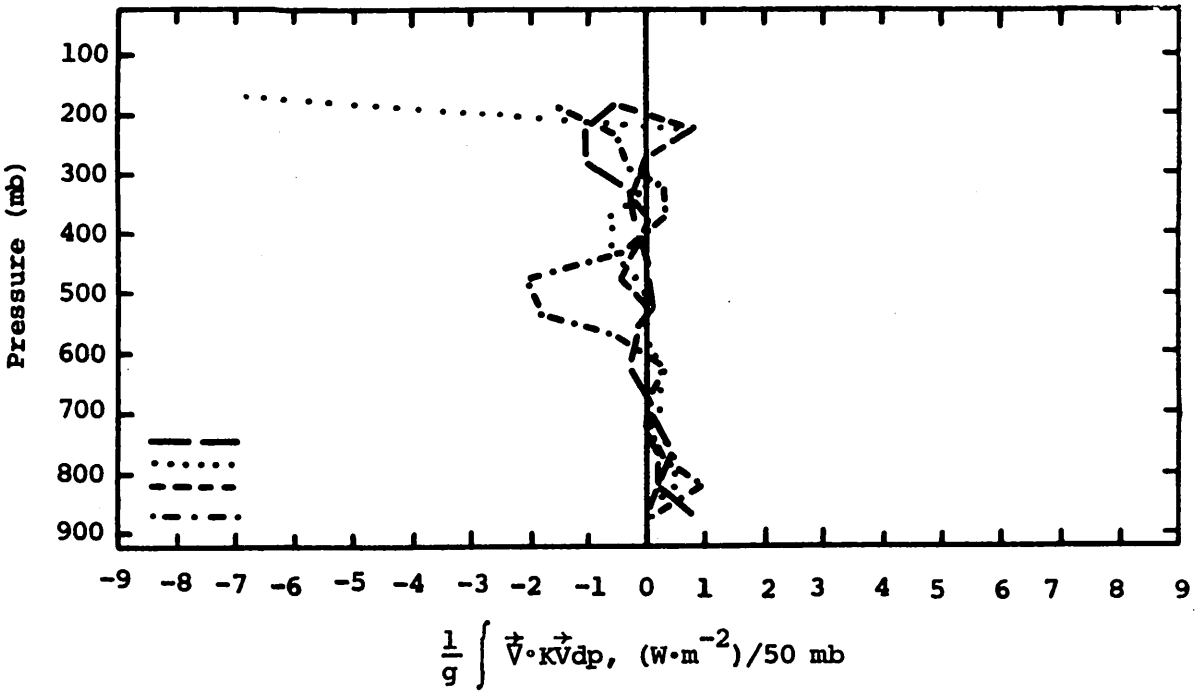

Fig. 5.15.4.6 Vertical profiles of the horizontal flux of kinetic energy on 30 June 1977.

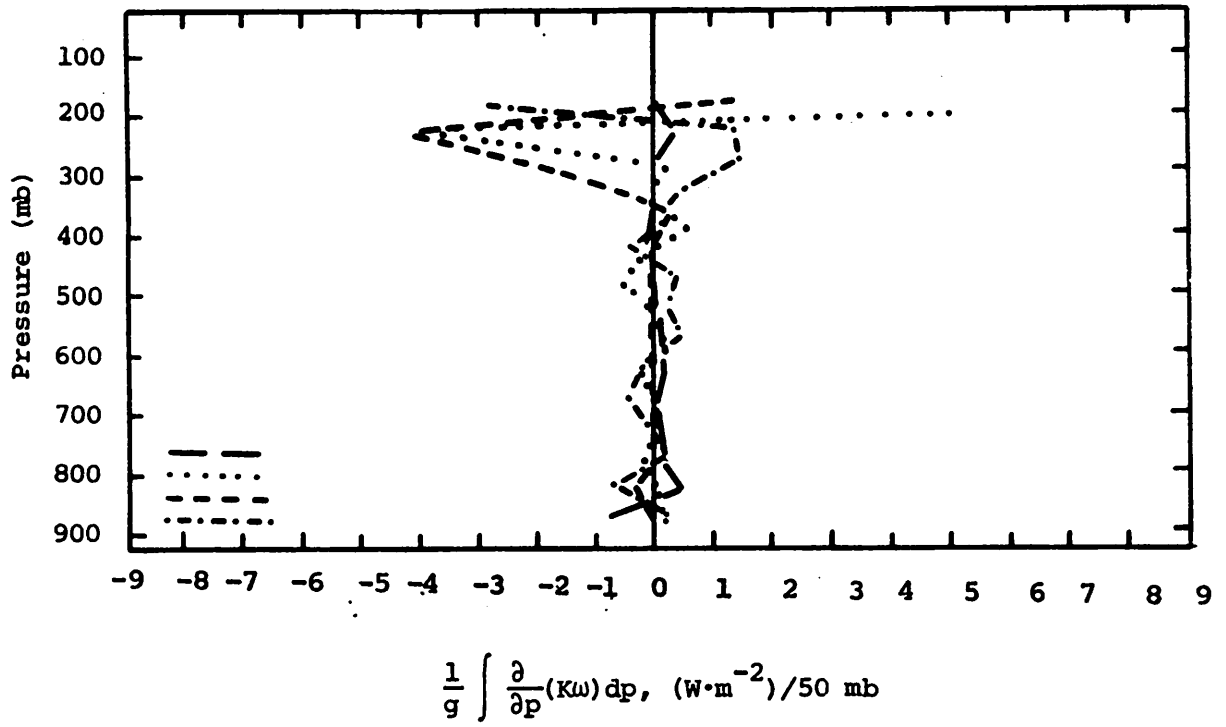

Fig. 5.15.4.7 Vertical profiles of the vertical flux of kinetic energy on 30 June 1977.

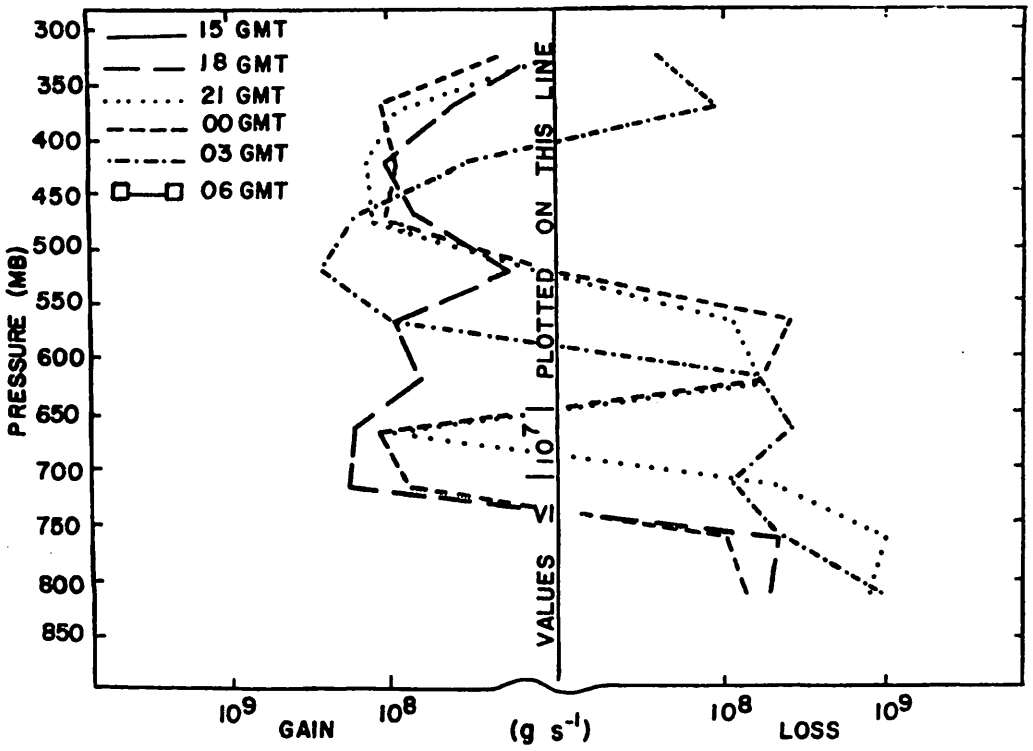

Fig. 5.15.5.1 Net horizontal transport of water vapor through boundaries of 50-mb layers (gm s^{-1}) over the Texas HIPLEX area for 30 June 1977.

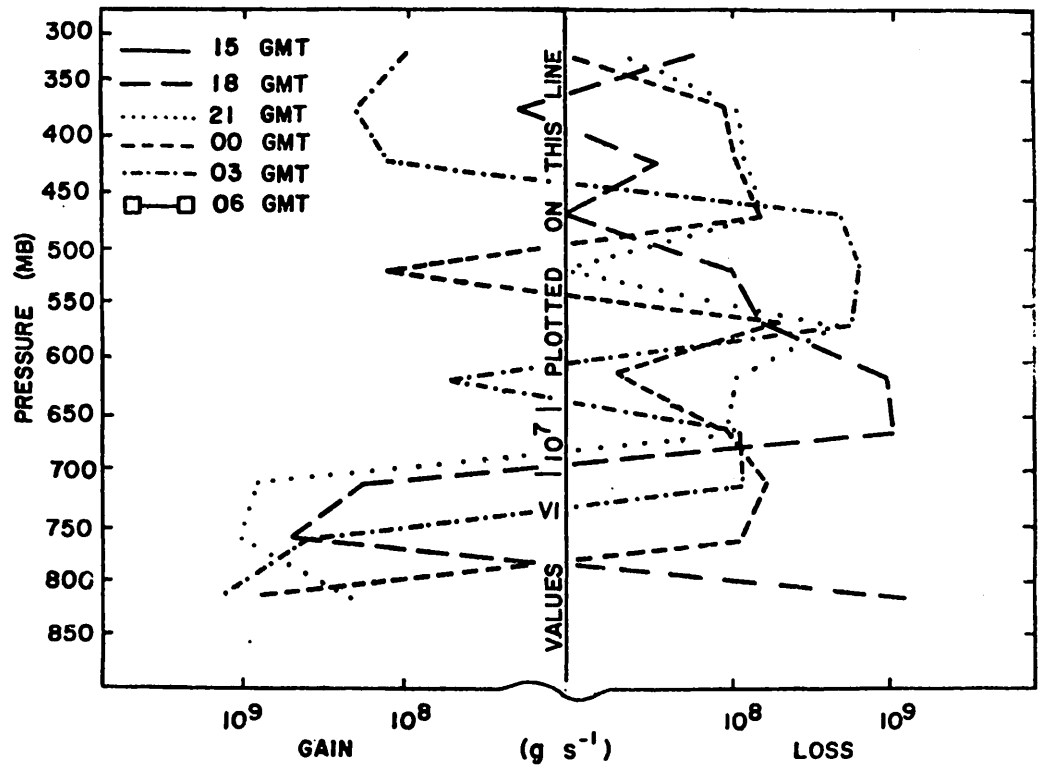

Fig. 5.15.5.2 Net vertical transport of water vapor through boundaries of 50-mb layers (gm s^{-1}) over the Texas HIPLEX area for 30 June 1977.

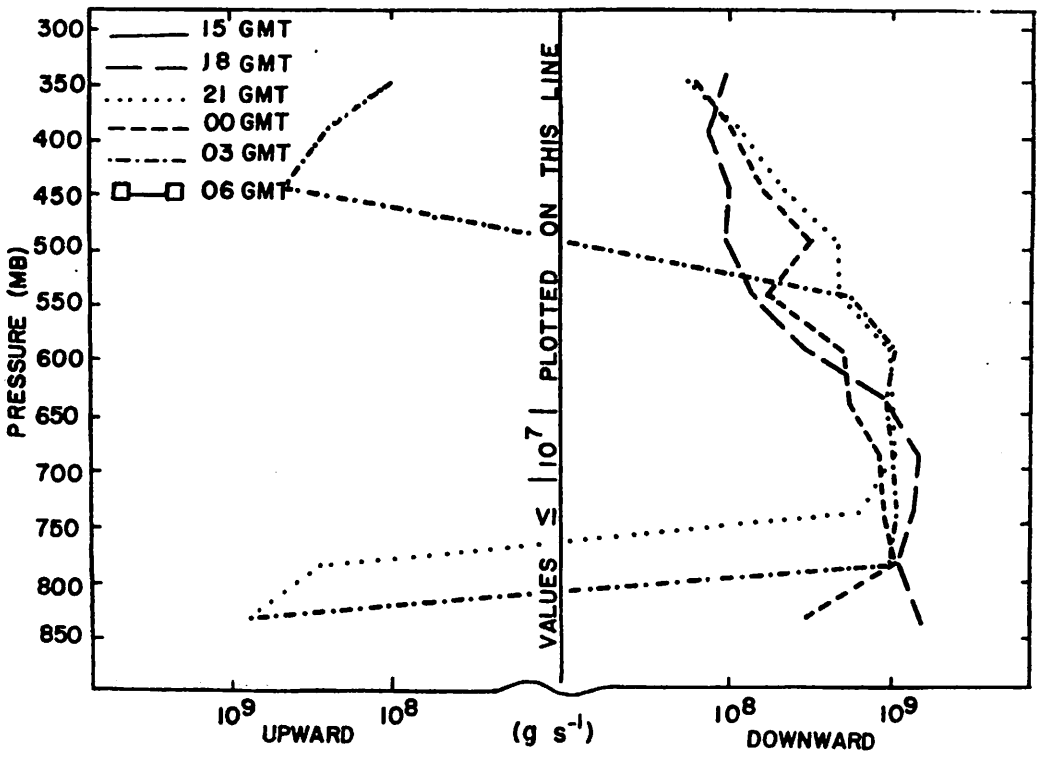

Fig. 5.15.5.3 Vertical transport of water vapor through constant pressure surfaces (gm s^{-1}) over the Texas HIPLEX area for 30 June 1977.

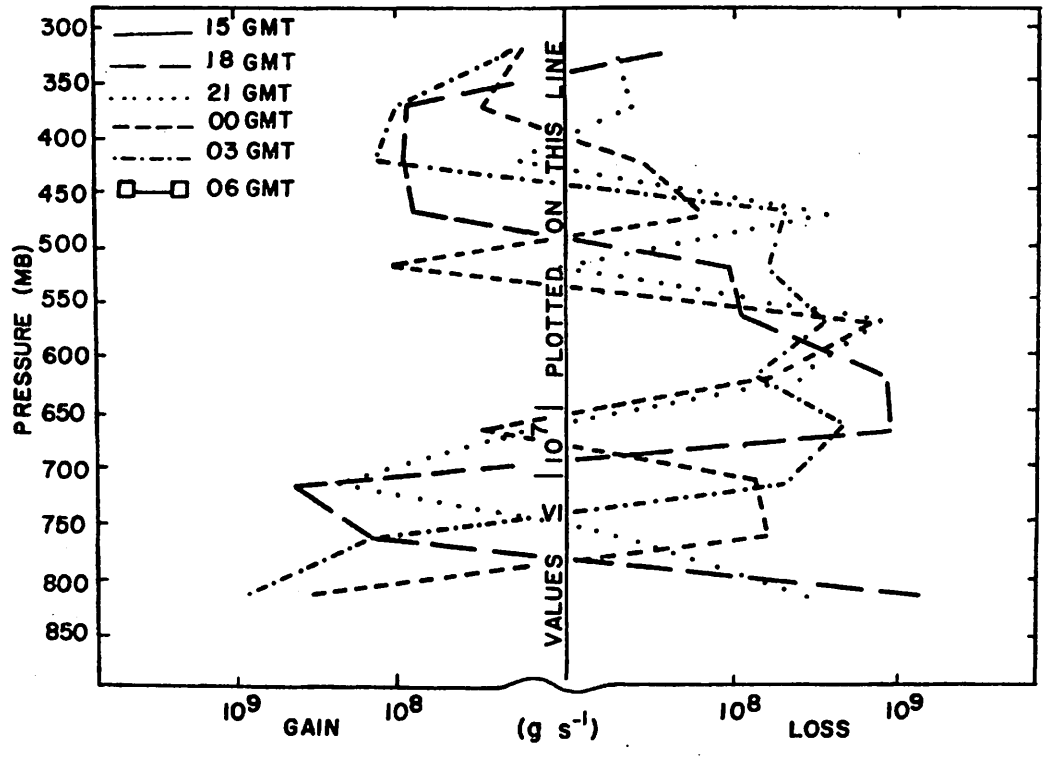

Fig. 5.15.5.4 Combined net horizontal and vertical transport of water vapor through boundaries of 50-mb layers (gm s^{-1}) over the Texas HIPLEX area for 30 June 1977.

outflow occurred between 700 and 500 mb, and a net inflow in other layers.

Figure 5.15.5.5 shows profiles of the total mass of water vapor. These profiles show an increase of water vapor with time until 0000 GMT.

Figure 5.15.5.6 shows vertical profiles of the local rate-of-change in the total mass of water vapor. These profiles show an increase of water vapor between 1800 and 0000 GMT, and a decrease in all layers by 0300 GMT which is also shown in Fig. 5.15.5.5. The decrease of water vapor observed between 0000 and 0300 GMT occurred as activity moved from the area or dissipated prior to 0300 GMT.

5.16 7 July 1977

5.16.1 Radar

Very little convective activity was observed by radar on this day (Fig. 5.16.1.1). Echoes were observed at 2100 GMT and from 0100 to 0300 GMT. Except at 2100 GMT when an isolated echo with tops less than 9.1 km (30K ft) was observed near Snyder, the echoes barely penetrated the northern boundary of the area.

5.16.2 Surface

Fields of surface temperature (Fig. 5.16.2.1) are mainly affected by surface heating. Surface mixing ratio (Fig. 5.16.2.2) was small in magnitude and showed no well-defined centers. Smaller values were observed in regions of minimum temperature. Surface equivalent potential temperatures (Fig. 5.16.2.3) do not exhibit any well-defined centers.

Terrain-induced vertical motion remains generally upward throughout the day. Surface velocity divergence (Fig. 5.16.2.5), vertical motion 50 mb above the surface (Fig. 5.16.2.6), surface moisture divergence (Fig. 5.16.2.7), and vertical flux of moisture 50 mb above the surface (Fig. 5.16.2.8) all remain variable and small in magnitude. Near the convective activity in the northern part of the area convergence and upward motion occurred. Fields of surface vorticity (Fig. 5.16.2.9) remain small in magnitude with several centers of anticyclonic vorticity near the center of the network. Charts of sea level pressure (Fig. 5.16.2.10) show a center of low pressure south of Colorado City. The surface pressure change (Fig. 5.16.2.11) shows a large increase of pressure near Robert Lee. However, this is due to the computational procedures and missing data at Robert Lee. Also, missing data at Vincent at 2000 GMT caused an incorrect pressure drop of 1 mb hr^{-1}.

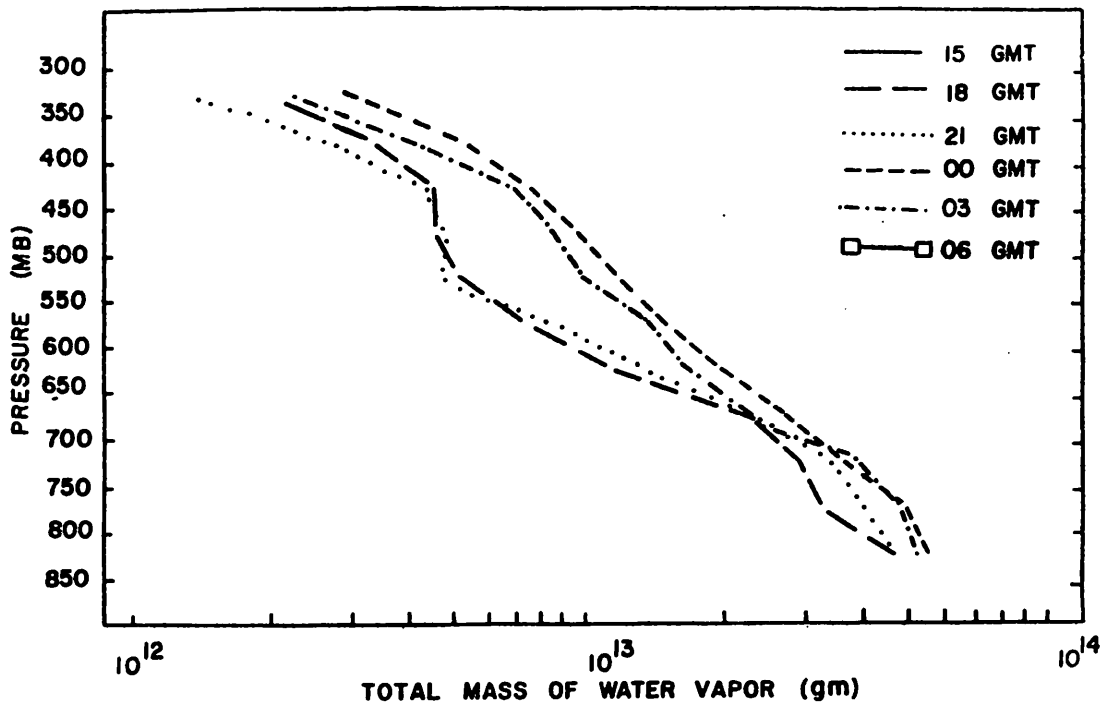

Fig. 5.15.5.5 Total mass of water vapor in layers 50 mb deep (gm) over the Texas HIPLEX area for 30 June 1977.

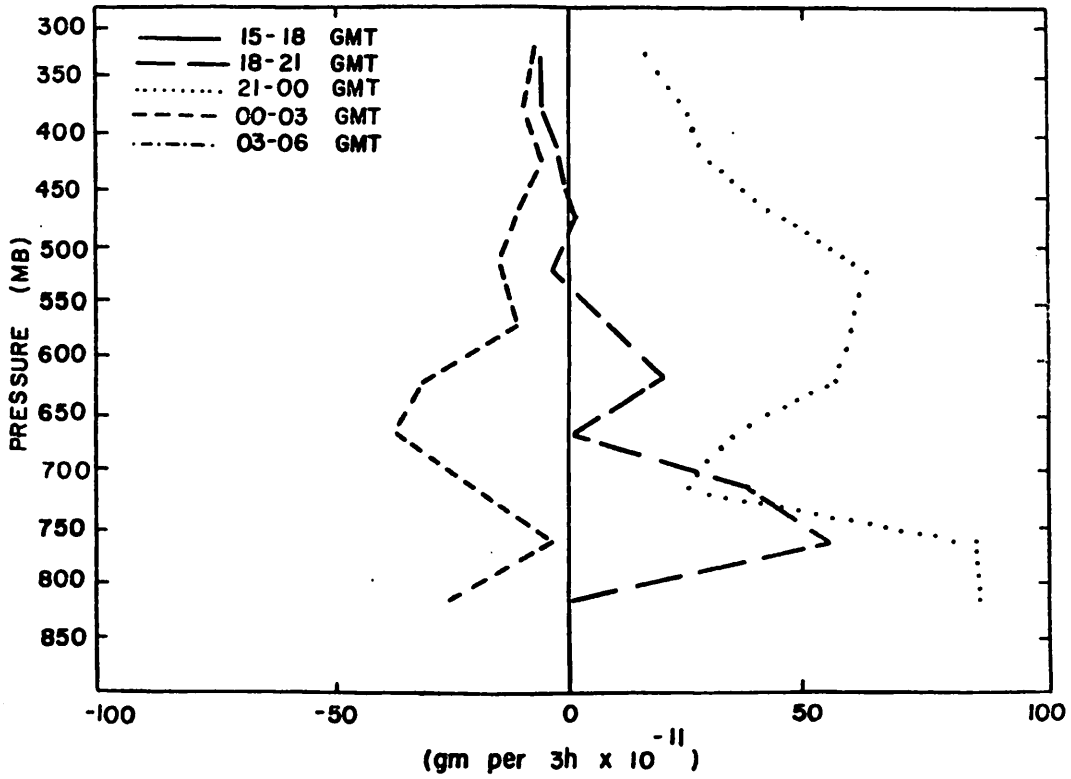

Fig. 5.15.5.6 Local rate-of-change in total mass of water vapor (gm per 3h x 10^{-11}) over the Texas HIPLEX area for 30 June 1977.

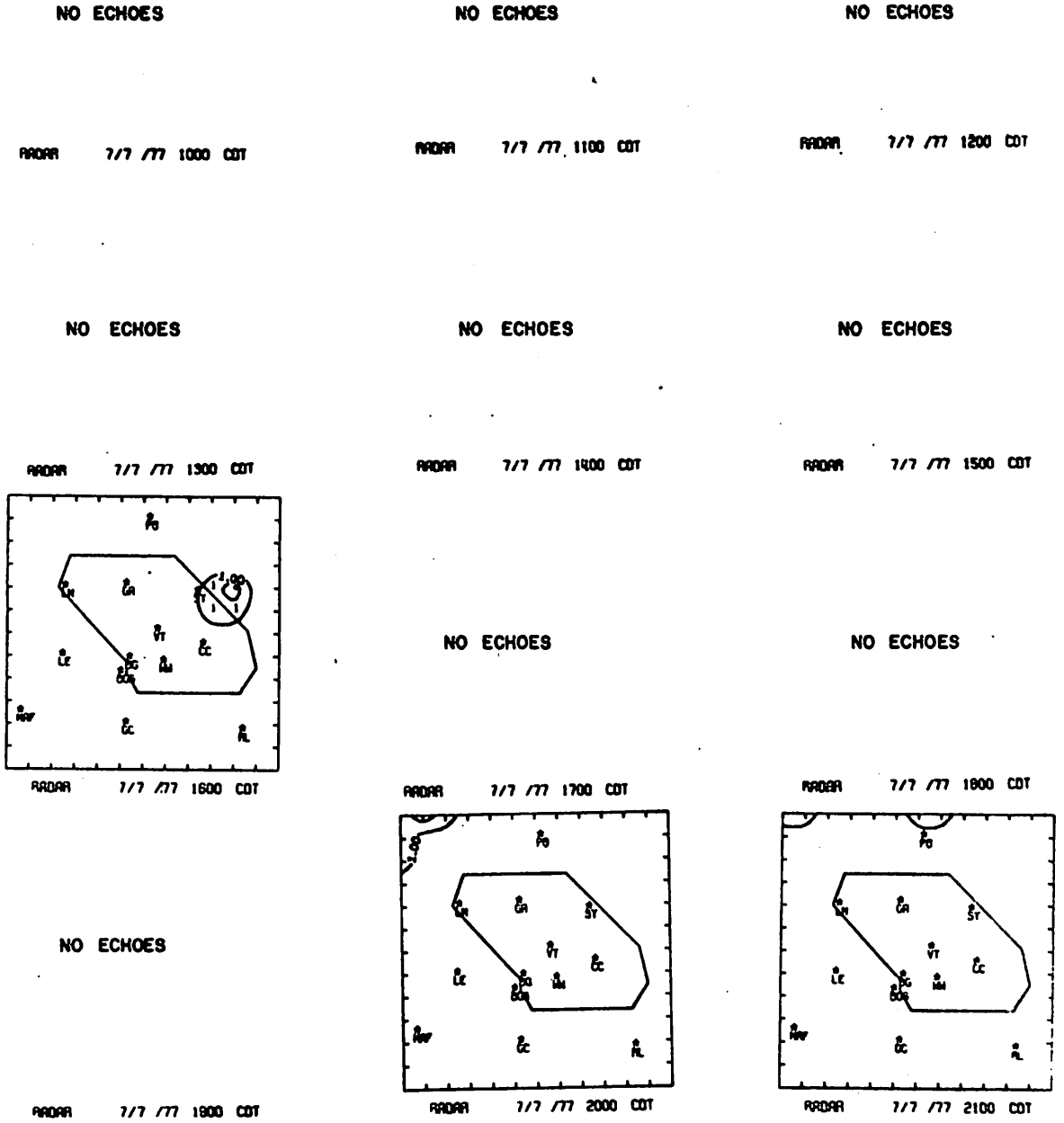

Fig. 5.16.1.1 Radar echoes for 7 July 1977.

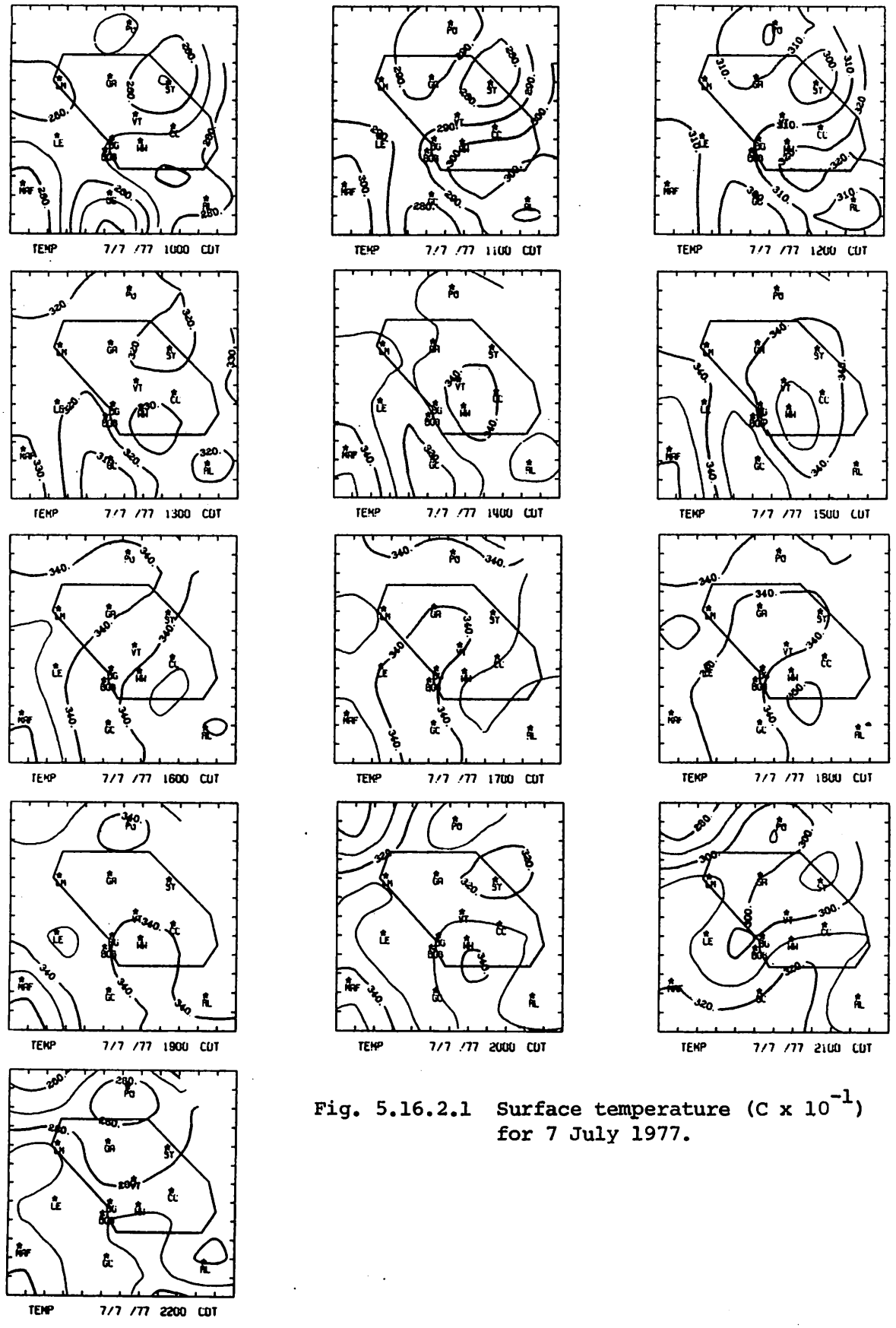

Fig. 5.16.2.1 Surface temperature (C x 10^{-1}) for 7 July 1977.

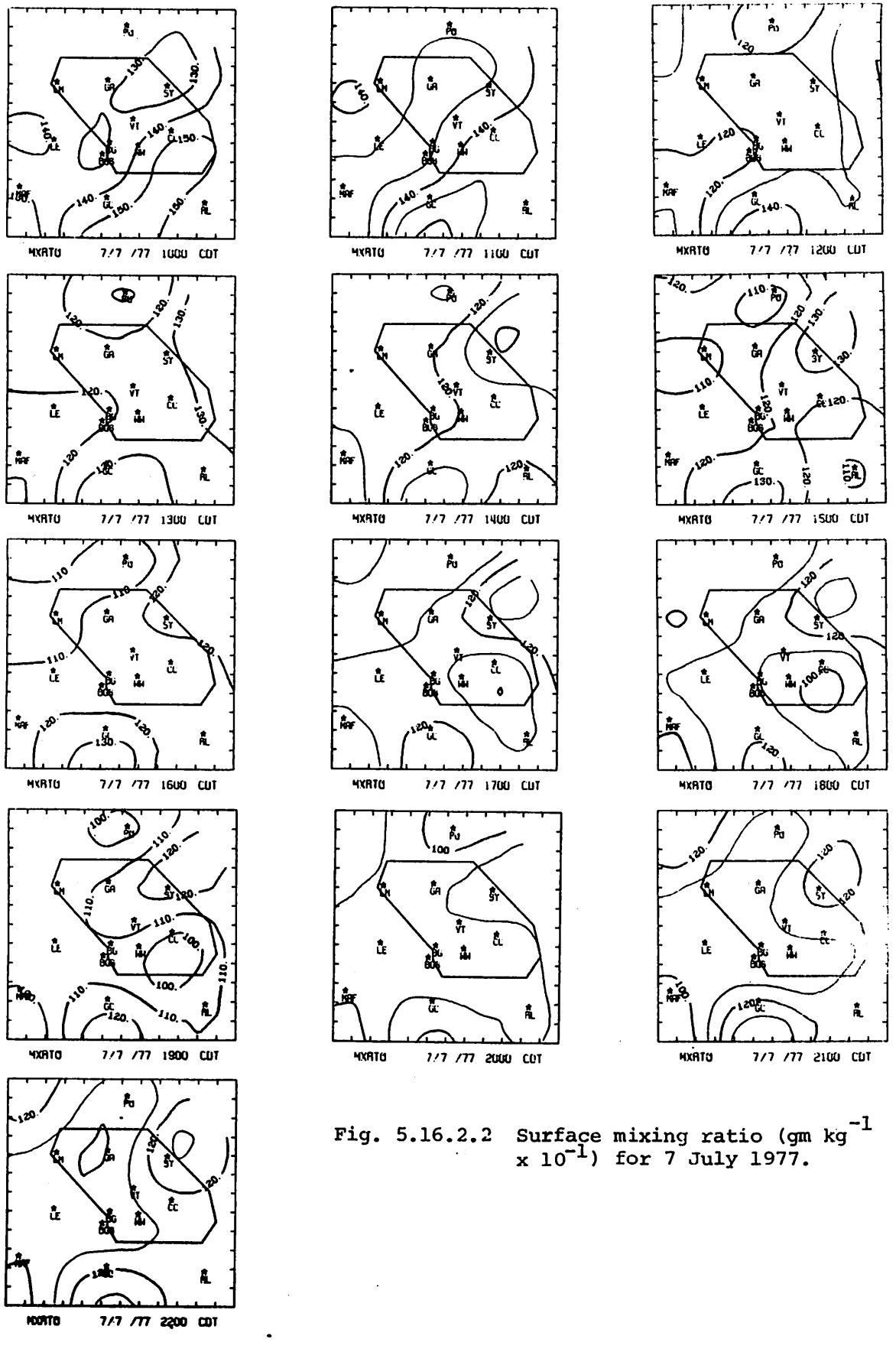

Fig. 5.16.2.2 Surface mixing ratio (gm kg^{-1} x 10^{-1}) for 7 July 1977.

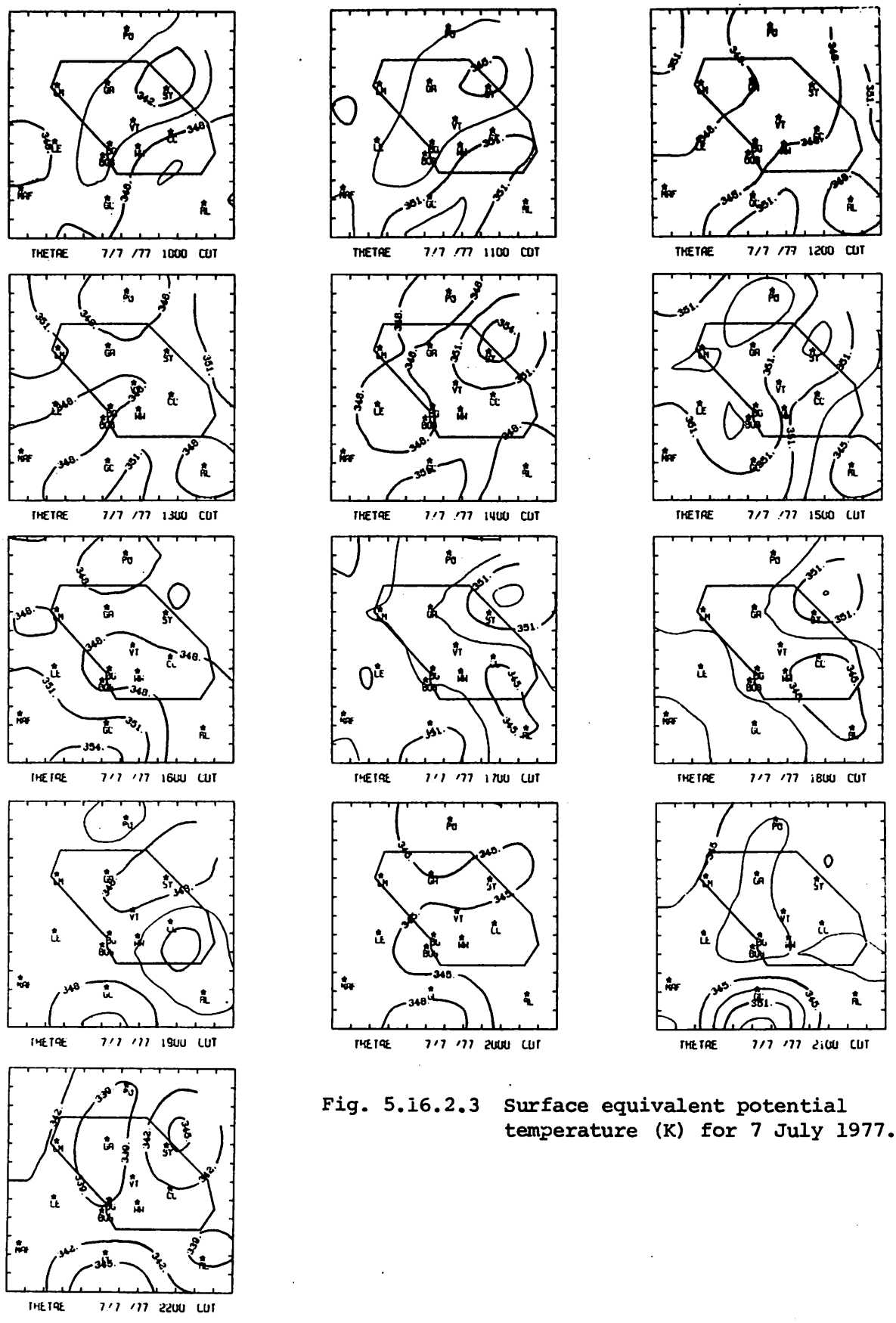

Fig. 5.16.2.3 Surface equivalent potential temperature (K) for 7 July 1977.

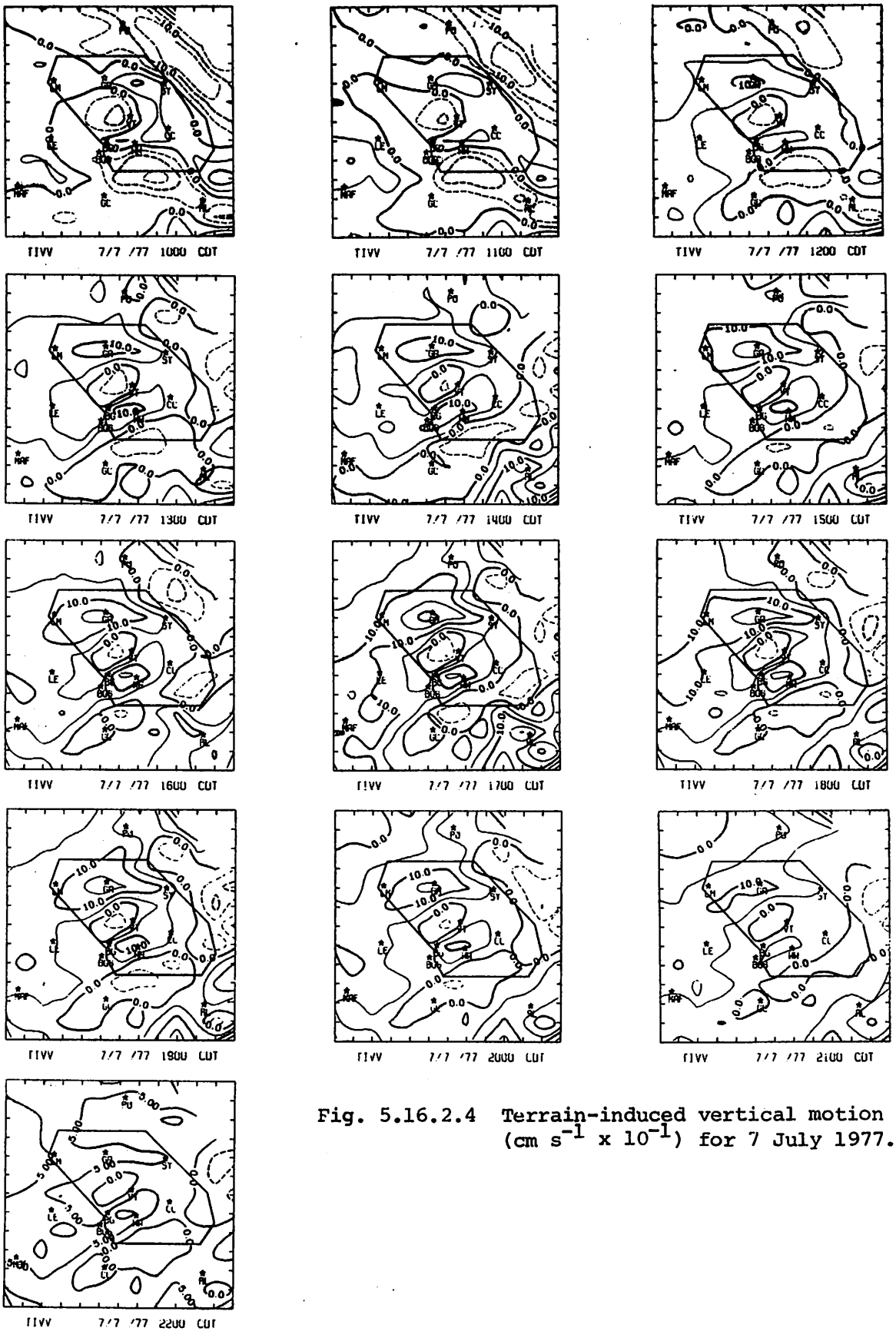

Fig. 5.16.2.4 Terrain-induced vertical motion (cm s^{-1} x 10^{-1}) for 7 July 1977.

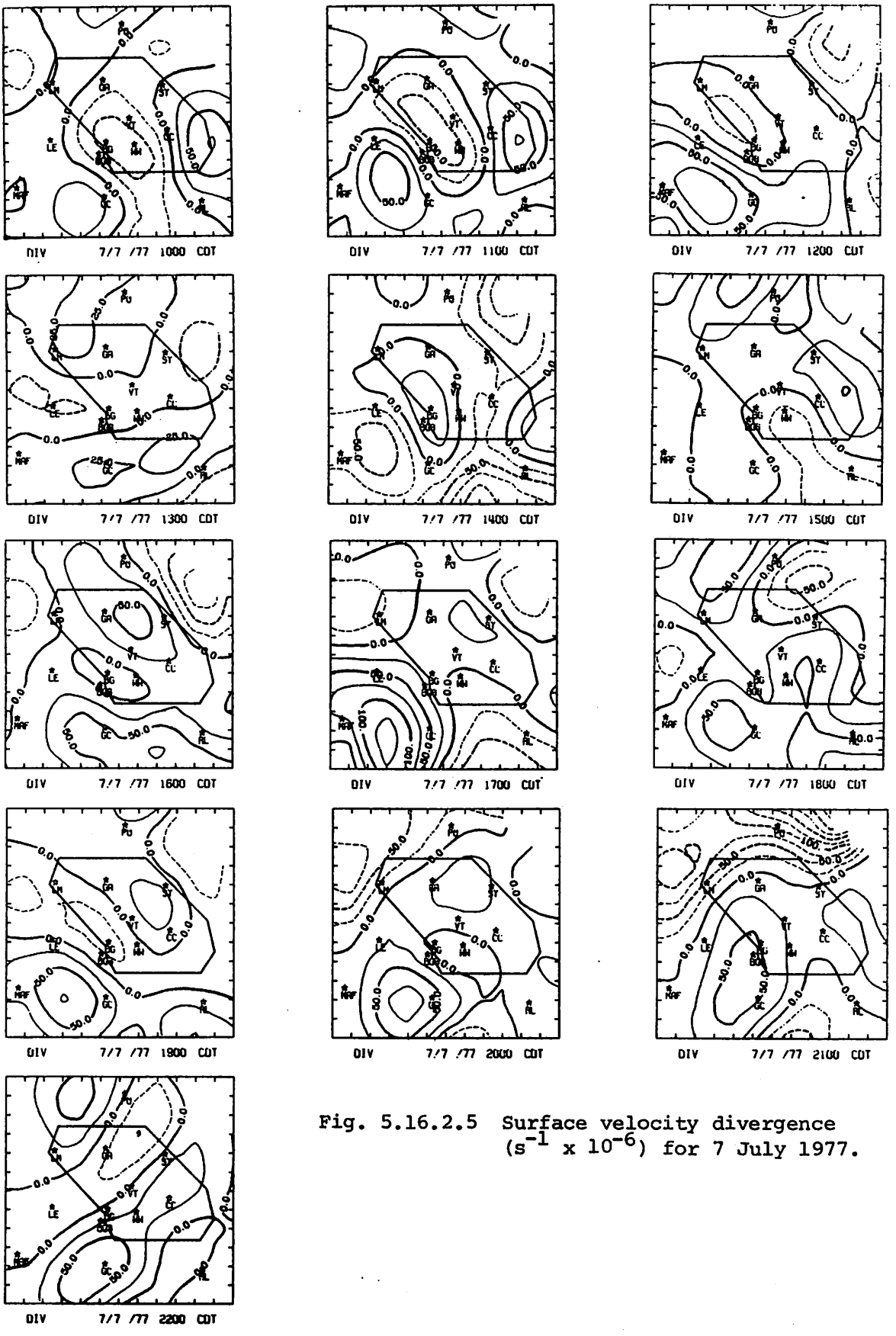

Fig. 5.16.2.5 Surface velocity divergence (s^{-1} x 10^{-6}) for 7 July 1977.

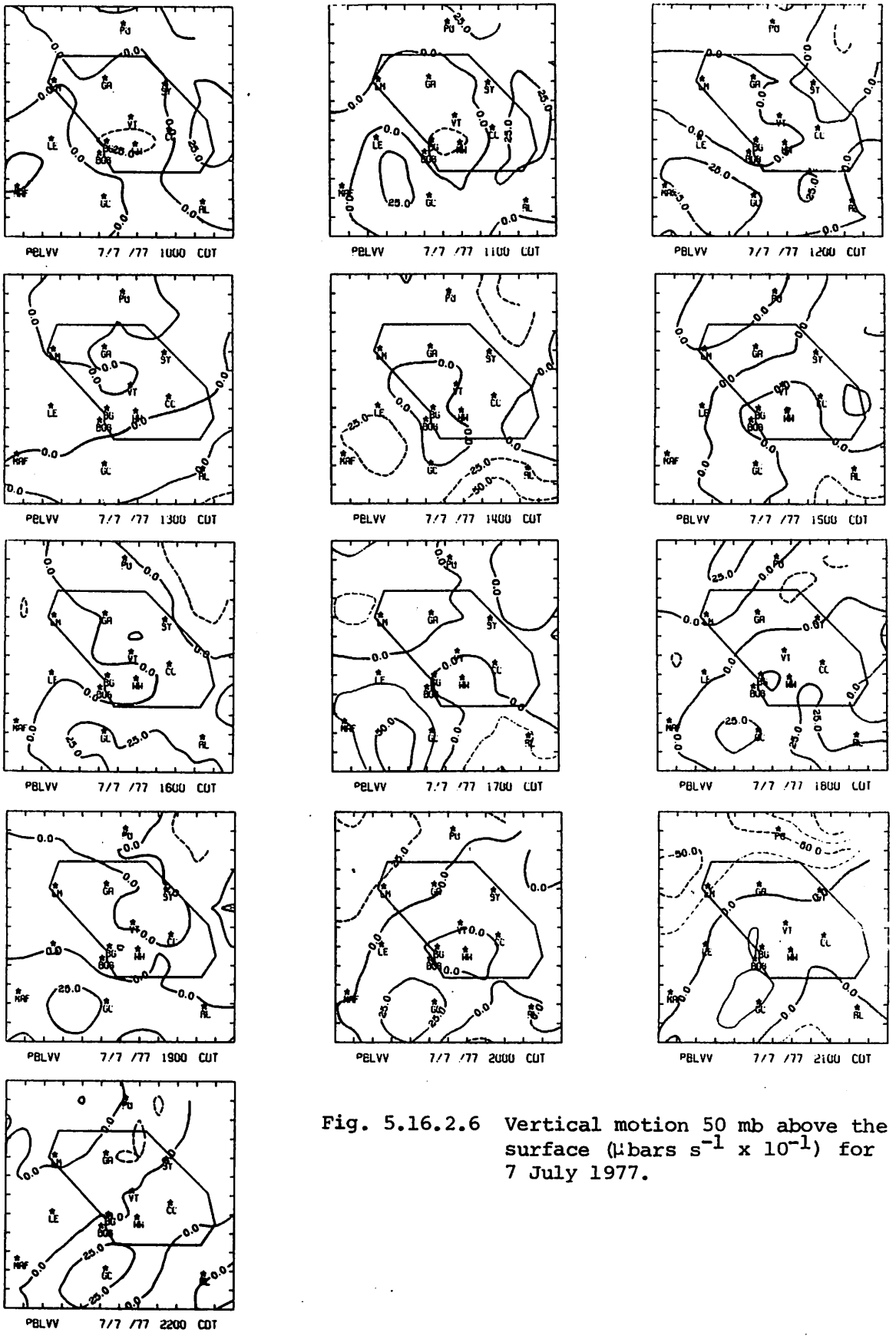

Fig. 5.16.2.6 Vertical motion 50 mb above the surface (μbars s^{-1} x 10^{-1}) for 7 July 1977.

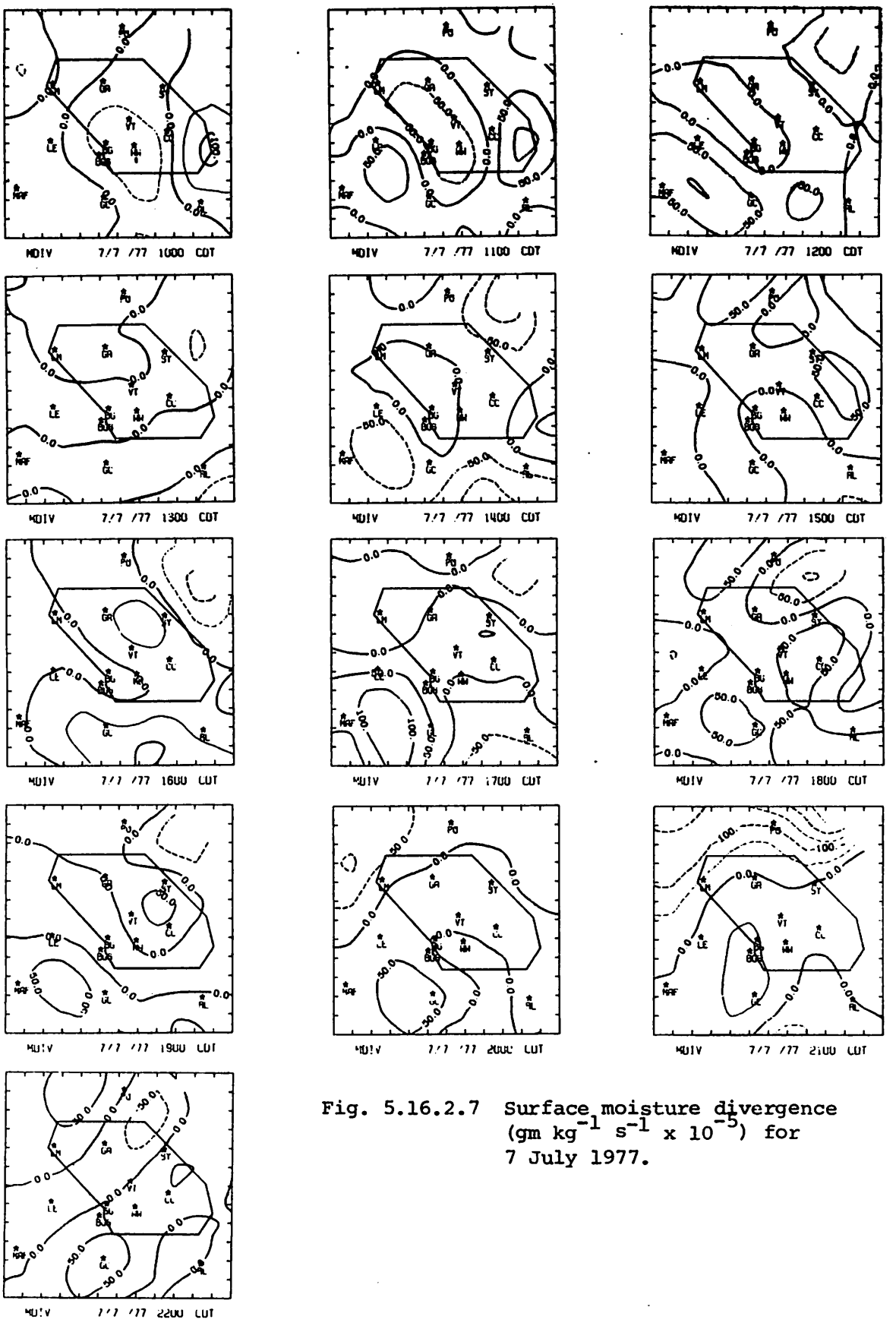

Fig. 5.16.2.7 Surface moisture divergence (gm kg^{-1} s^{-1} x 10^{-5}) for 7 July 1977.

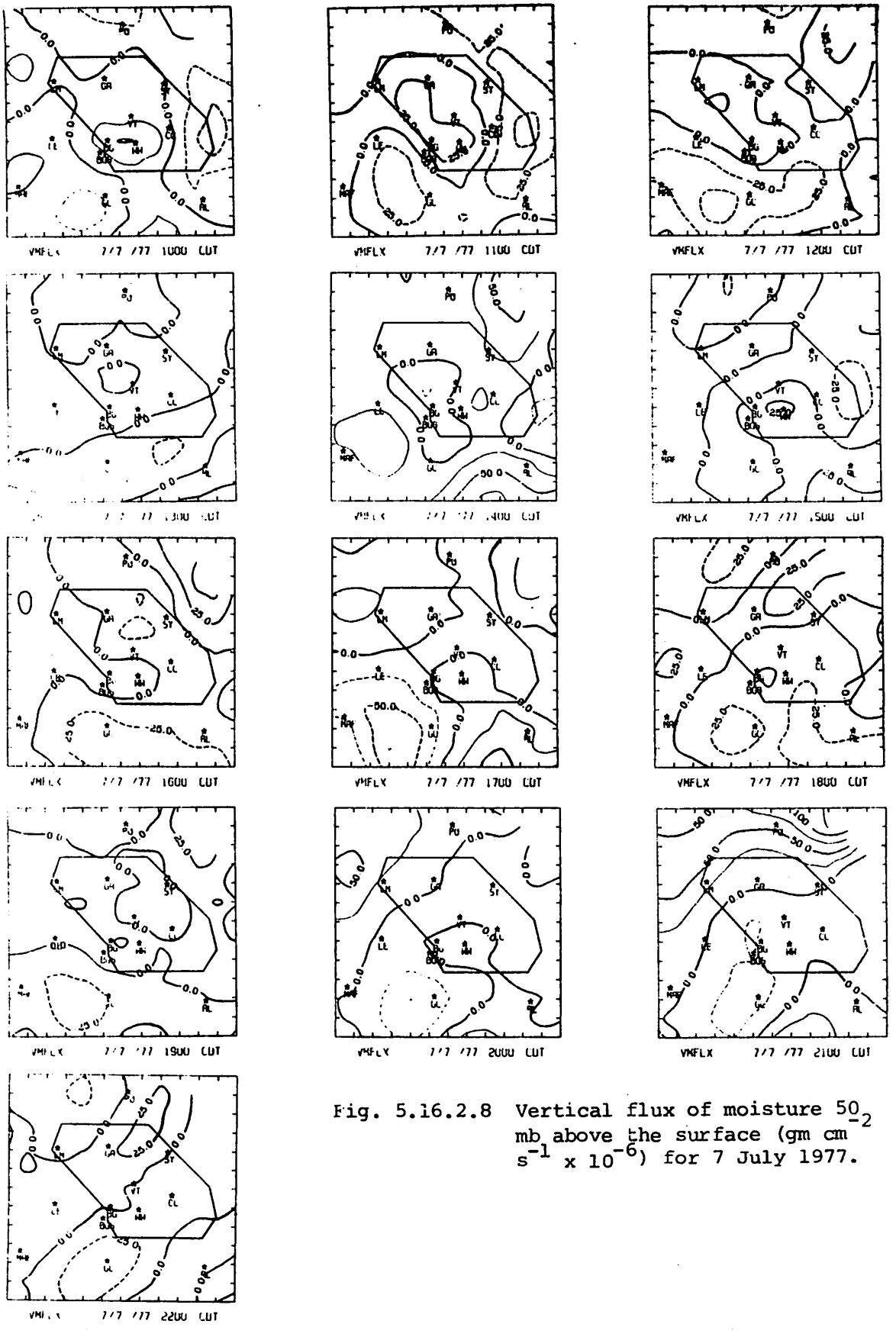

Fig. 5.16.2.8 Vertical flux of moisture 50 mb above the surface (gm cm s^{-1} x 10^{-6}) for 7 July 1977.

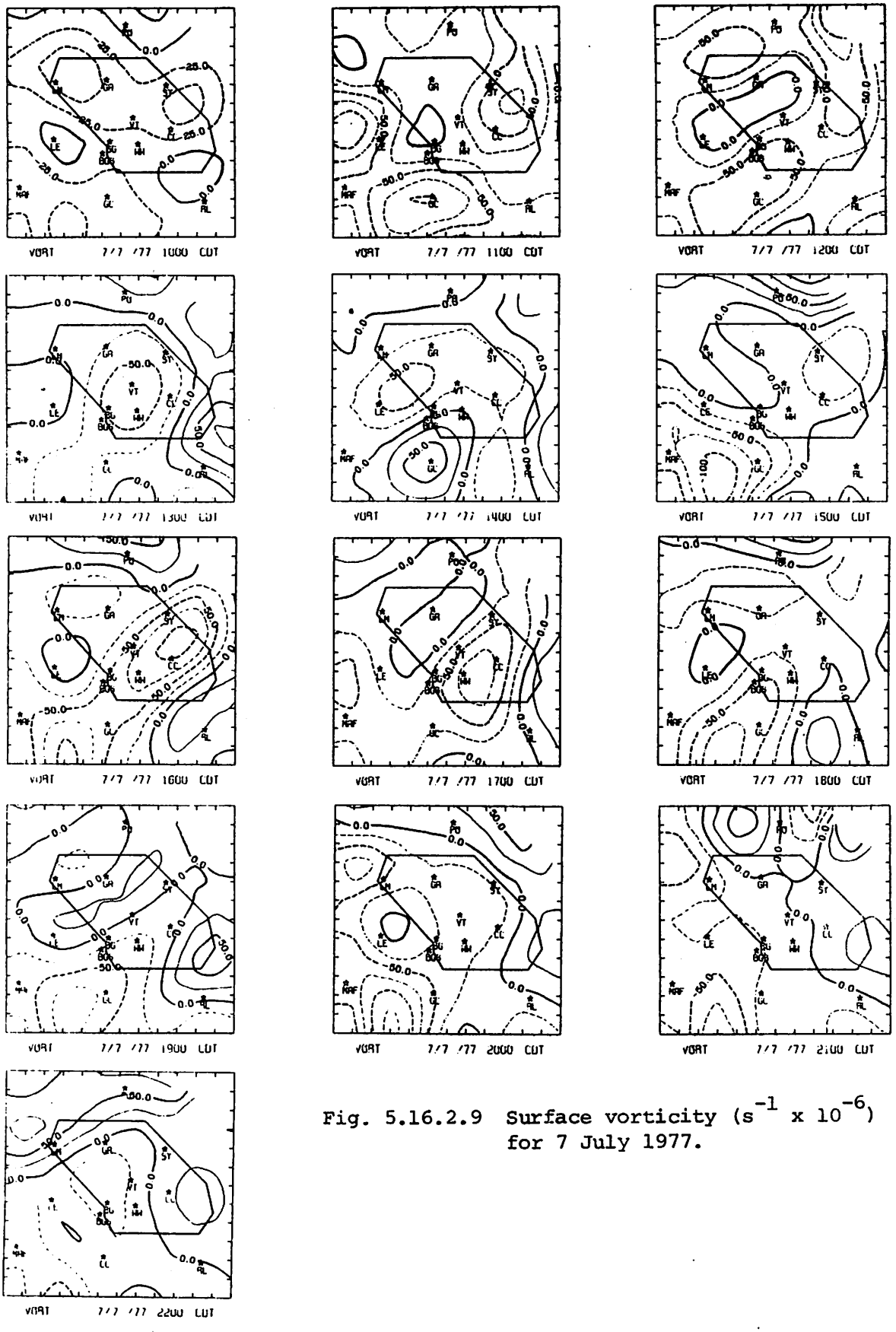

Fig. 5.16.2.9 Surface vorticity (s^{-1} x 10^{-6}) for 7 July 1977.

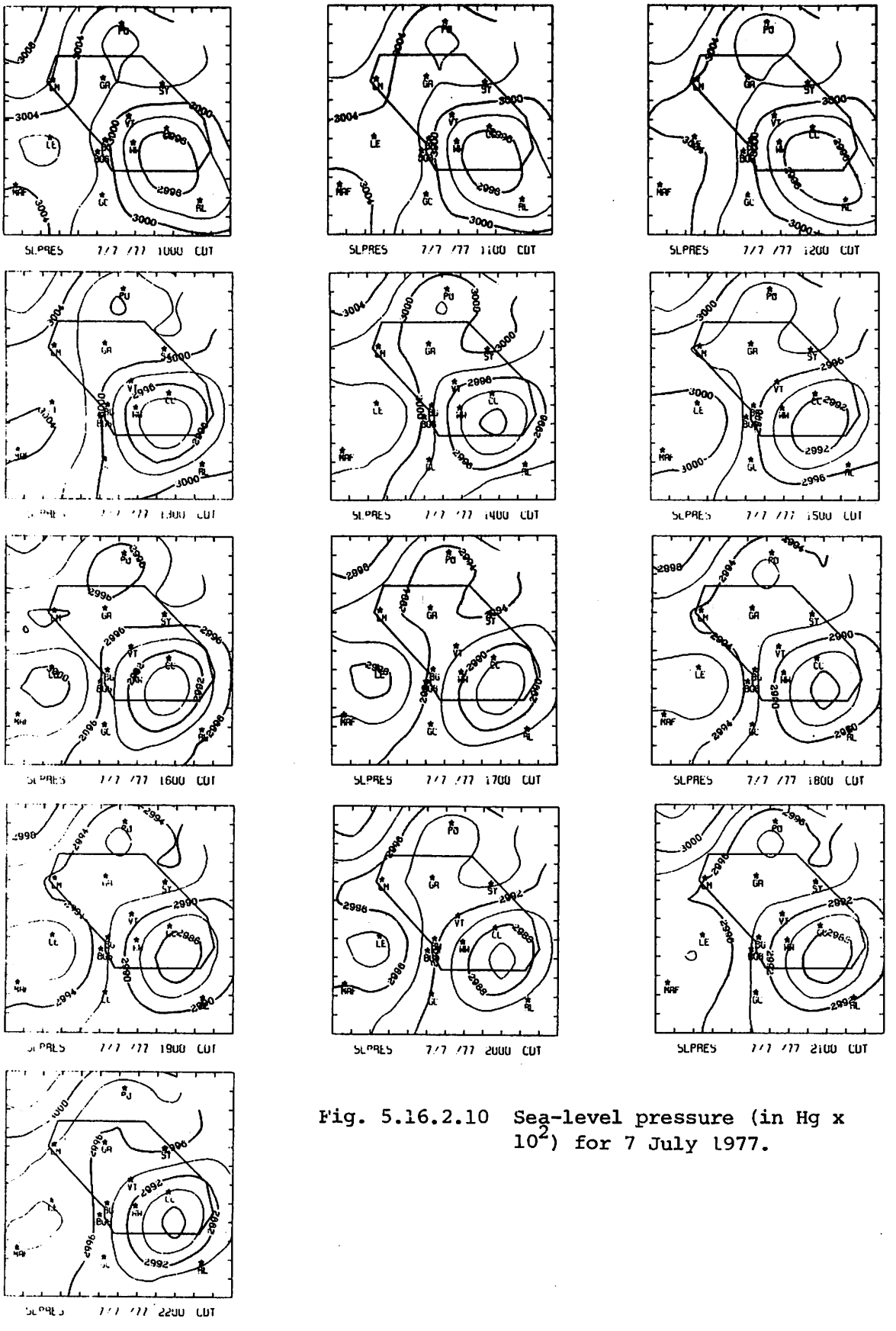

Fig. 5.16.2.10 Sea-level pressure (in Hg x 10^2) for 7 July 1977.

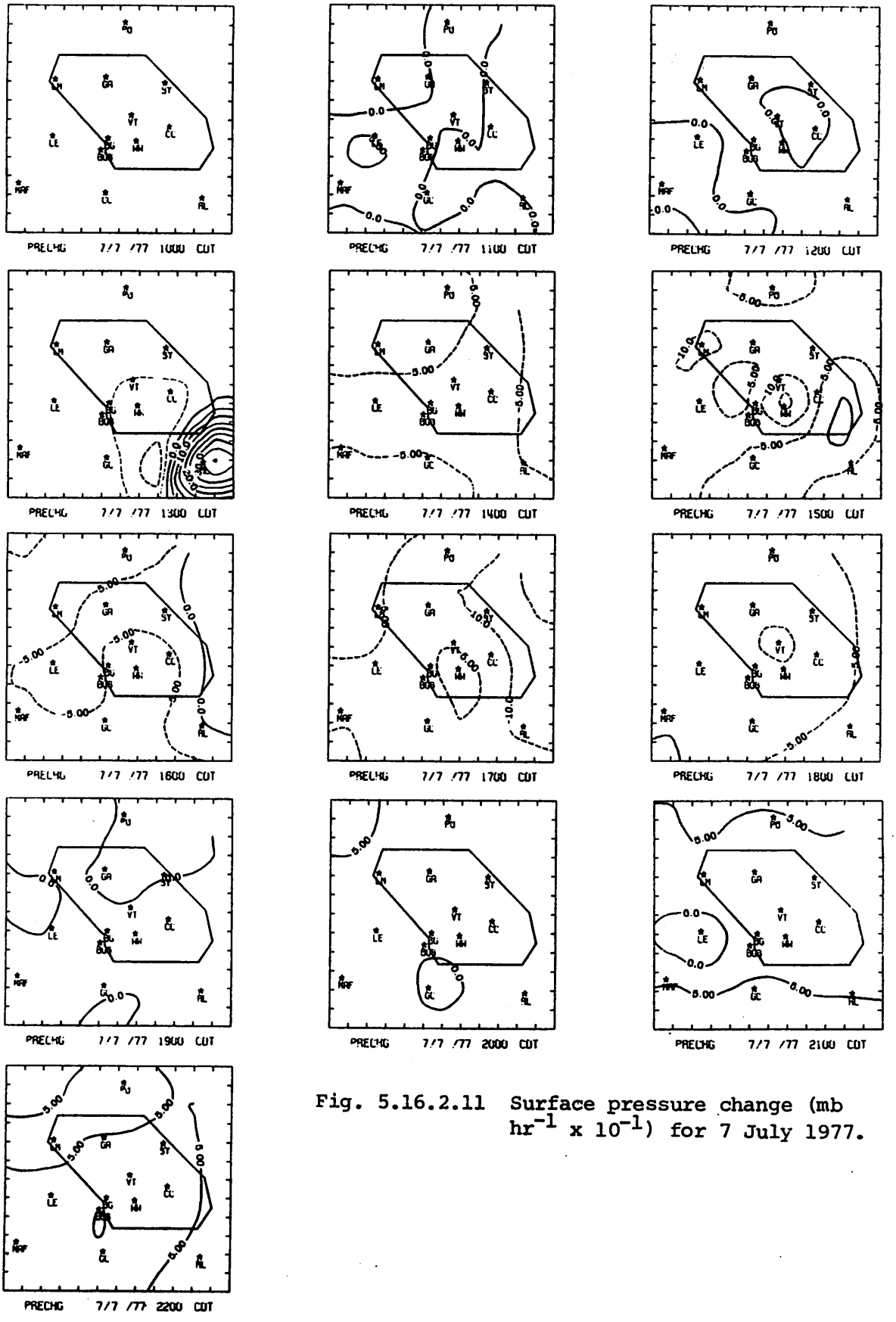

Fig. 5.16.2.11 Surface pressure change (mb hr^{-1} x 10^{-1}) for 7 July 1977.

5.16.3 Upper-Level Kinematic Parameters

The horizontal mass divergence profiles (Fig. 5.16.3.1) consistently showed low-level divergence and mid-level convergence at all times below 300 mb. Vertical velocities were downward or near zero at all times and levels (Fig. 5.16.3.2) corresponding well with the lack of precipitation during the day (over the network bounded by the MAF-PO-RL triangle). The horizontal moisture divergence profiles (Fig. 5.16.3.3) show low-level moisture divergence and weak mid-level convergence at most levels and for all time periods.

5.16.4 Energetics

Horizontal flux divergence of latent heat energy in low levels occurred throughout the day and weak convergence at mid levels (Fig. 5.16.4.1). Vertical flux divergence of latent heat energy at mid levels and flux convergence in low levels (Fig. 5.16.4.2) was associated with a net downward transport of latent heat energy from mid- to lower-levels within a field of downward vertical velocities. Local changes of latent heat energy were generally positive between 800 and 600 mb between 1500 and 2100 GMT and negative after 0000 GMT (Fig. 5.16.4.3).

Profiles of the residual term (-R) from the latent heat budget equation (Fig. 5.16.4.4) were negative at most levels between 800 and 600 mb except at 0300 GMT when large negative values extended up to 500 mb. These low- and mid-level increases of latent heat energy are apparently not related to evaporation since low-level cumulus cloud formation occurred over the network during the day. Since lapse rates of temperature near the dry adiabatic value were observed from the surface up to 700 mb between 1500 and 0000 GMT, turbulent flux convergence of water vapor (and latent heat energy) may have been responsible for positive local changes and negative -R values (increasing latent heat content) in low levels.

The diabatic heating profiles (Fig. 5.16.4.5) support this interpretation since values are generally small or slightly negative at most levels during the day when activity was absent and condensation/evaporation should have been at a minimum (or slightly negative if subsidence produced some evaporation of cloud water). Low-level heating before 0000 GMT and cooling at 0300 GMT is probably associated with radiational heating and cooling at the ground and turbulent mixing in the boundary layer.

The horizontal and vertical flux divergence profiles of kinetic energy (Figs. 5.16.4.6 and 5.16.4.7) are near zero at all times and levels and show

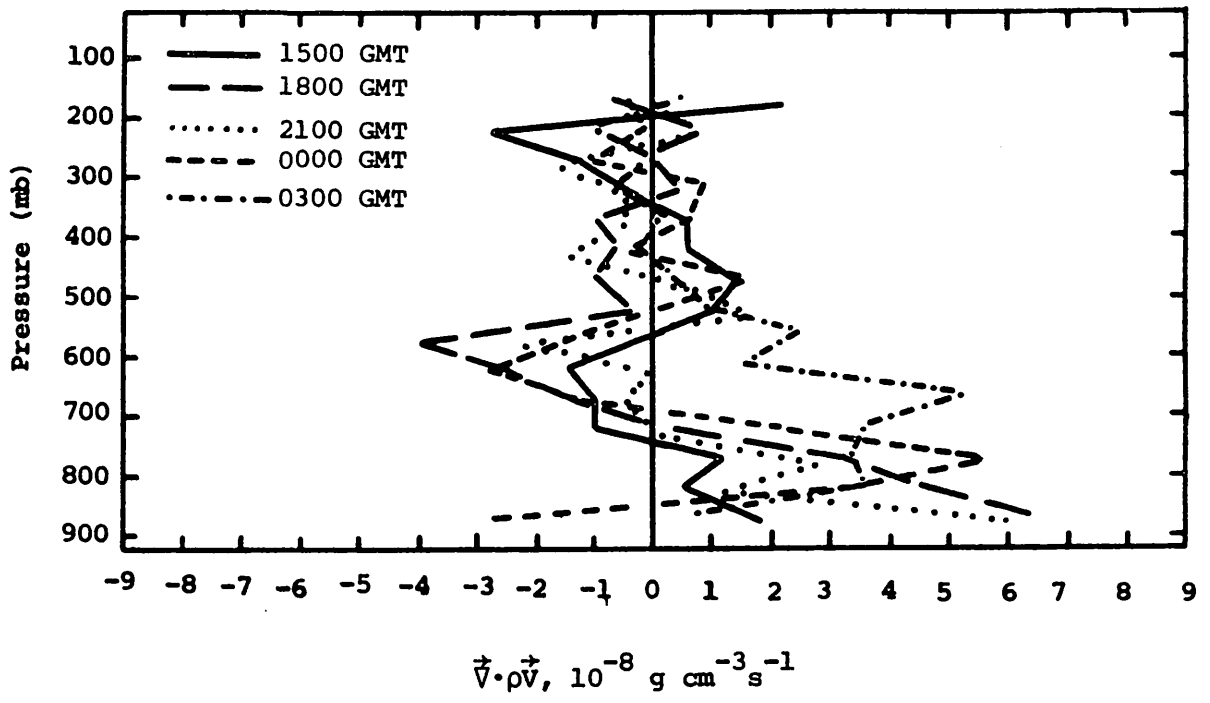

Fig. 5.16.3.1 Vertical profiles of mass divergence on 7 July 1977.

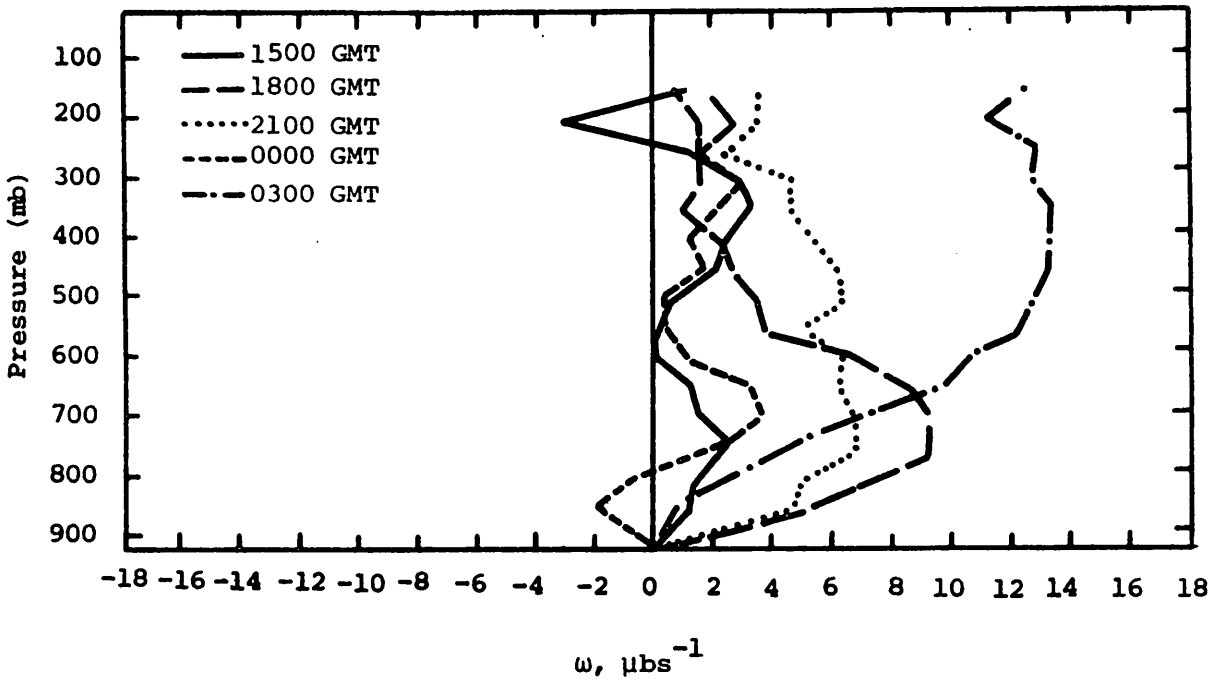

Fig. 5.16.3.2 Vertical profiles of vertical motion on 7 July 1977.

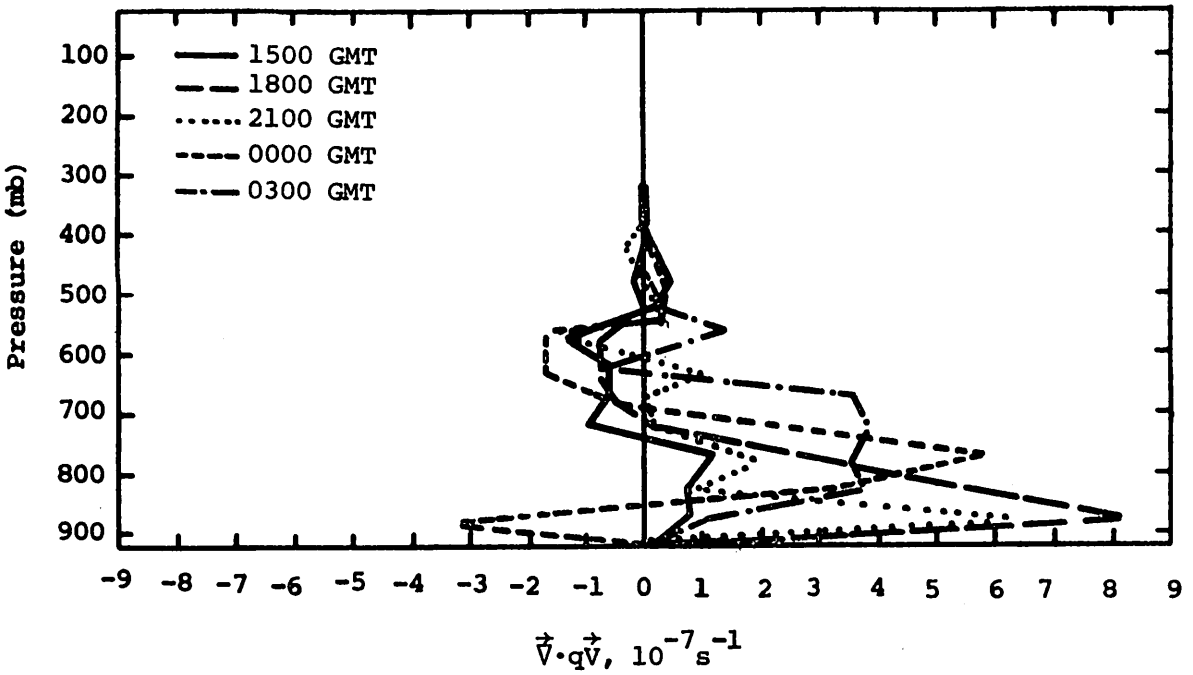

Fig. 5.16.3.3 Vertical profiles of moisture divergence on 7 July 1977.

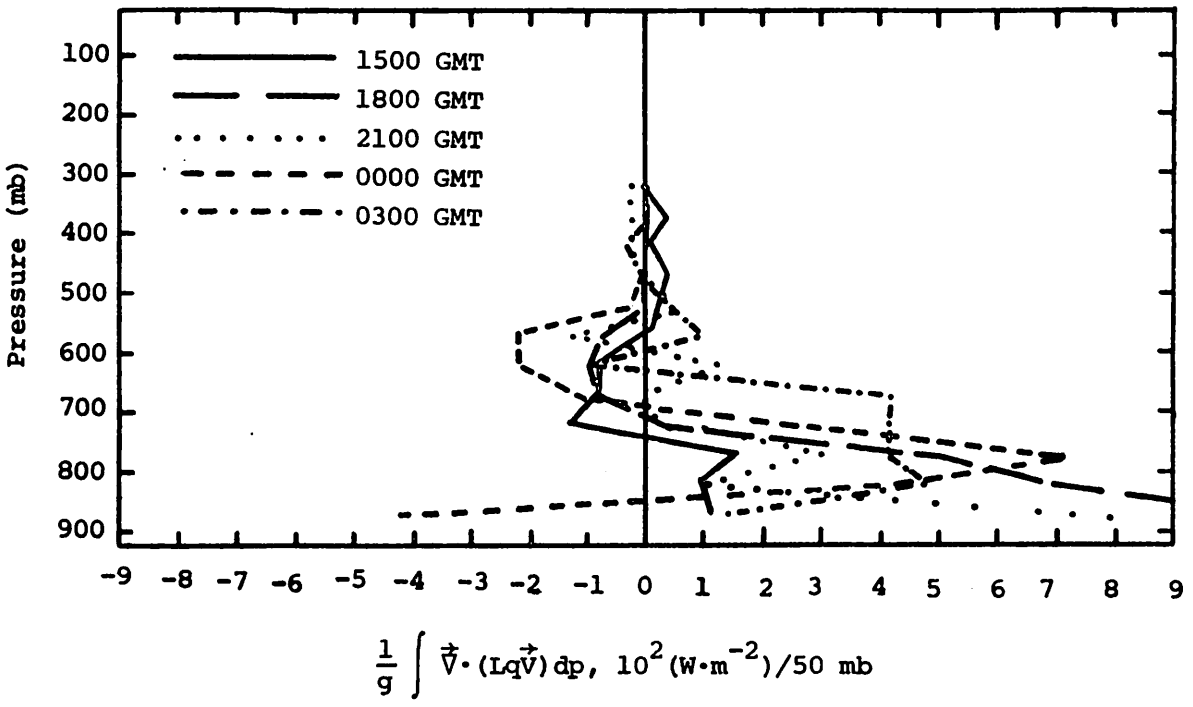

Fig. 5.16.4.1 Vertical profiles of the horizontal flux of latent heat energy on 7 July 1977.

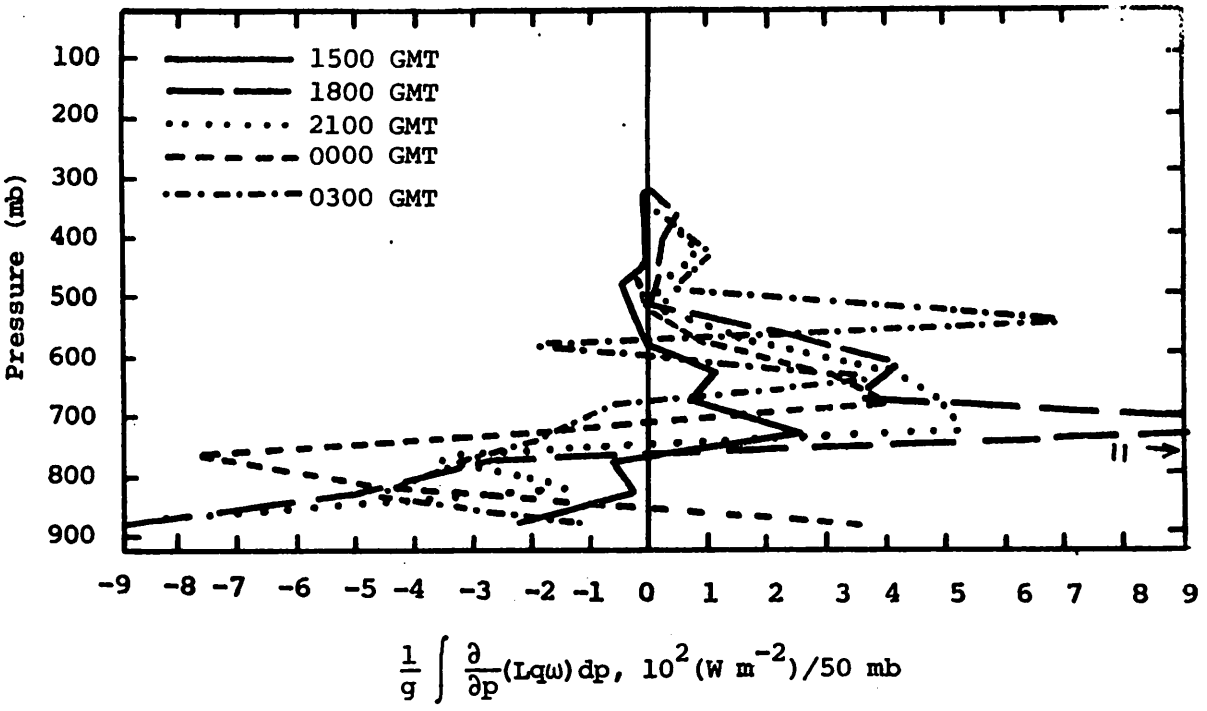

Fig. 5.16.4.2 Vertical profiles of the vertical flux of latent heat energy on 7 July 1977.

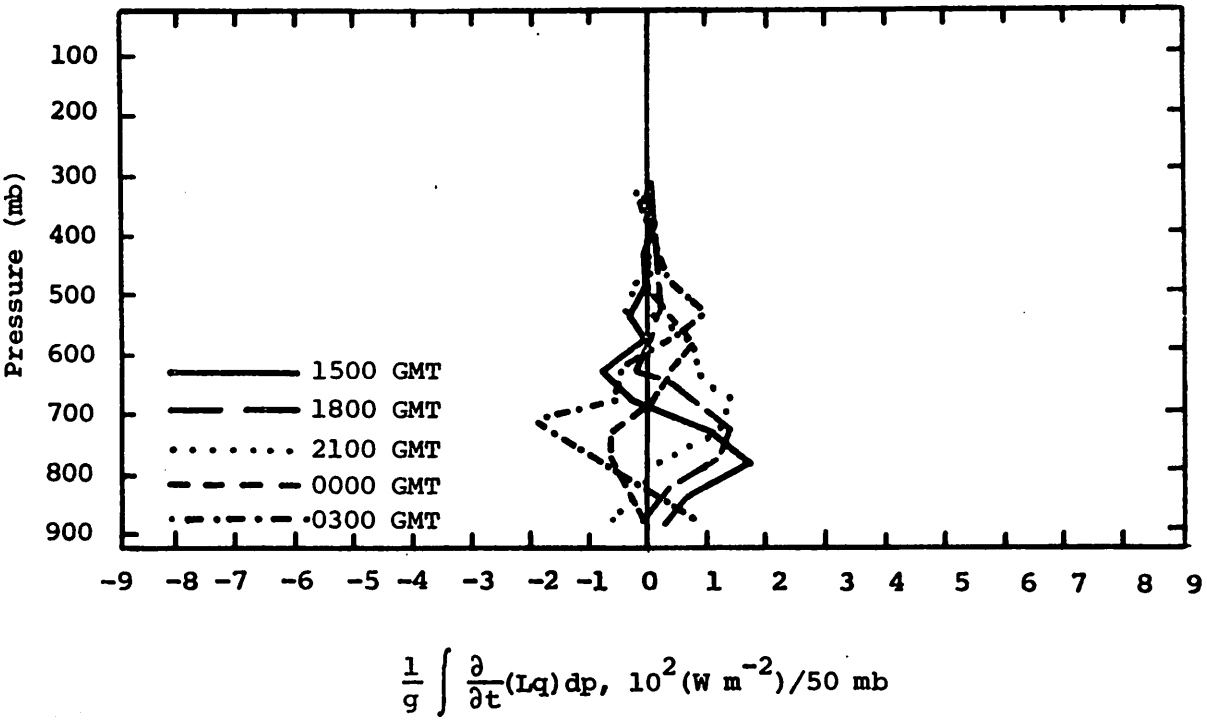

Fig. 5.16.4.3 Vertical profiles of the local change of latent heat energy on 7 July 1977.

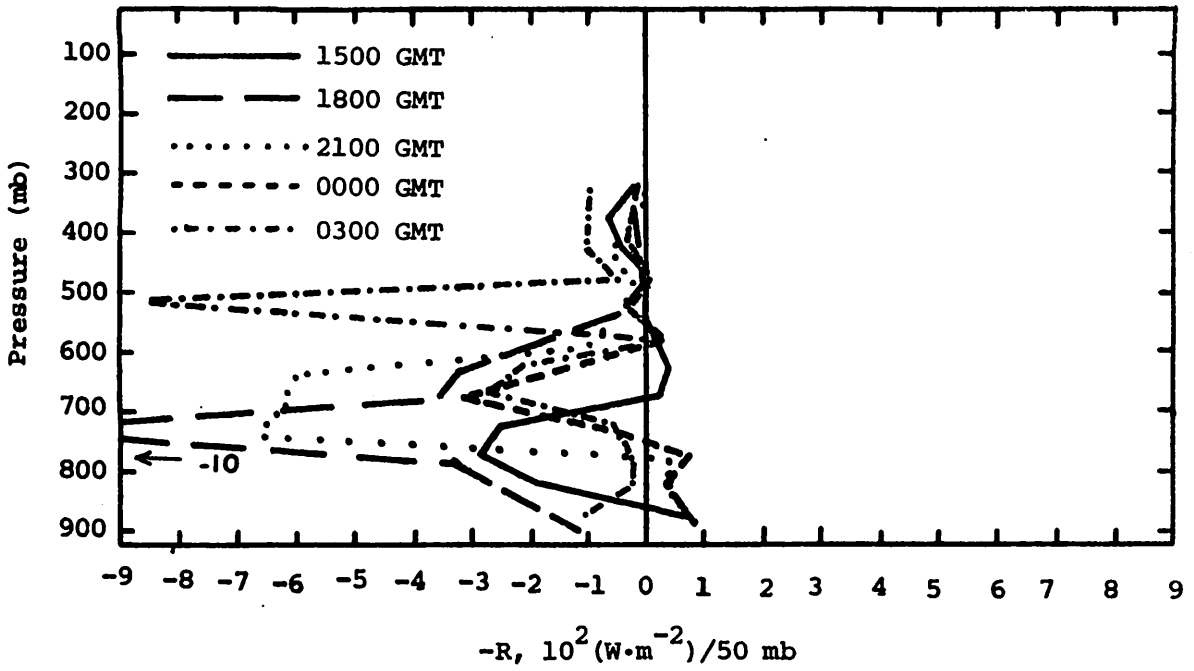

Fig. 5.16.4.4 Vertical profile of the residual of the latent heat energy equation on 7 July 1977.

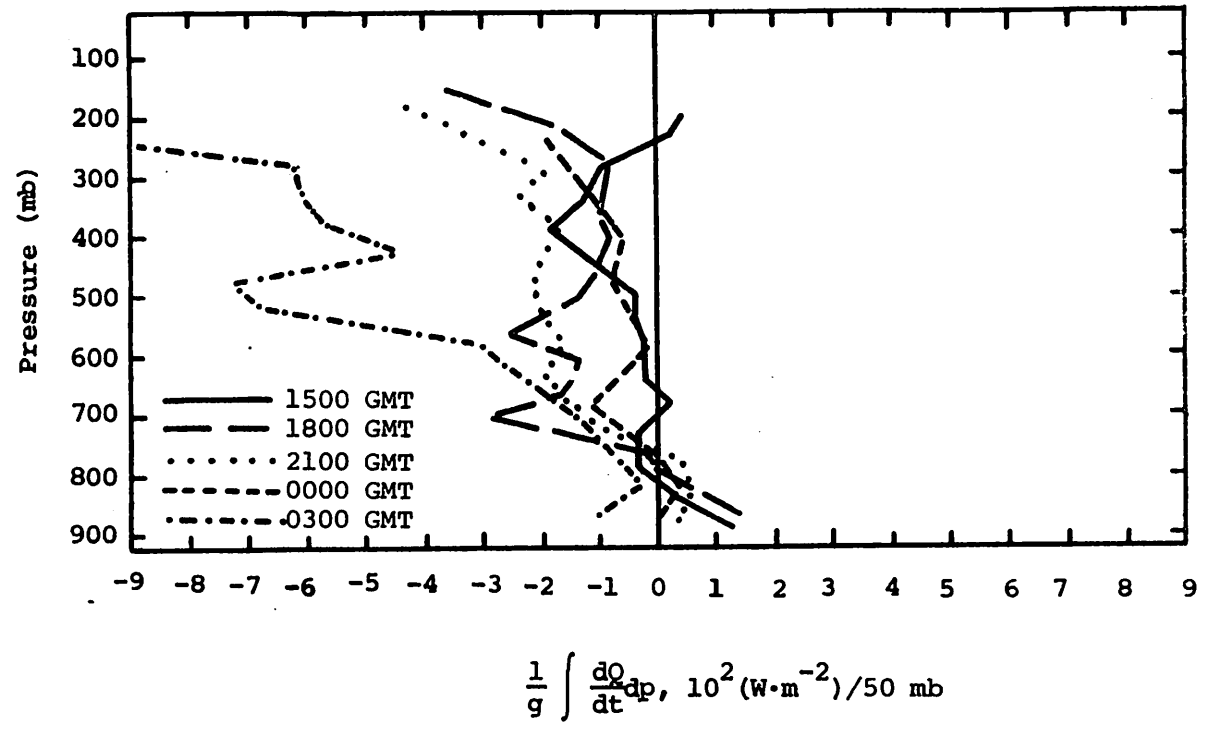

Fig. 5.16.4.5 Vertical profiles of diabatic heating computed from the first law of thermodynamics on 7 July 1977.

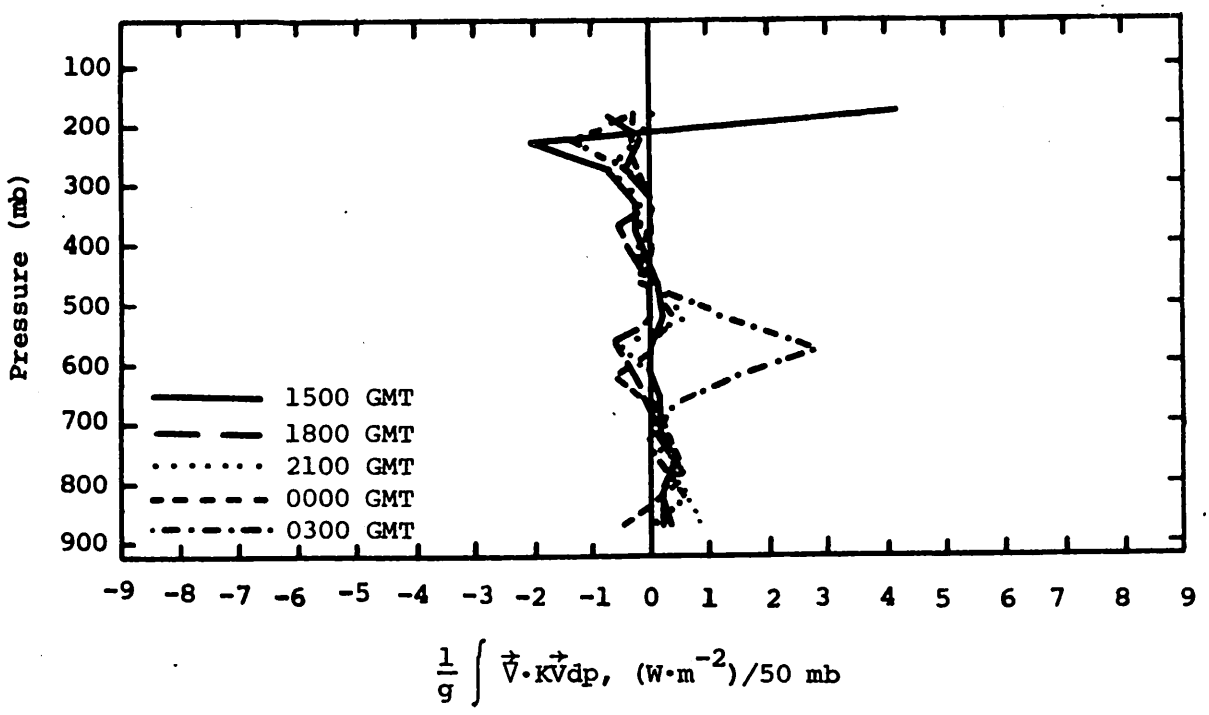

Fig. 5.16.4.6 Vertical profiles of the horizontal flux of kinetic energy on 7 July 1977.

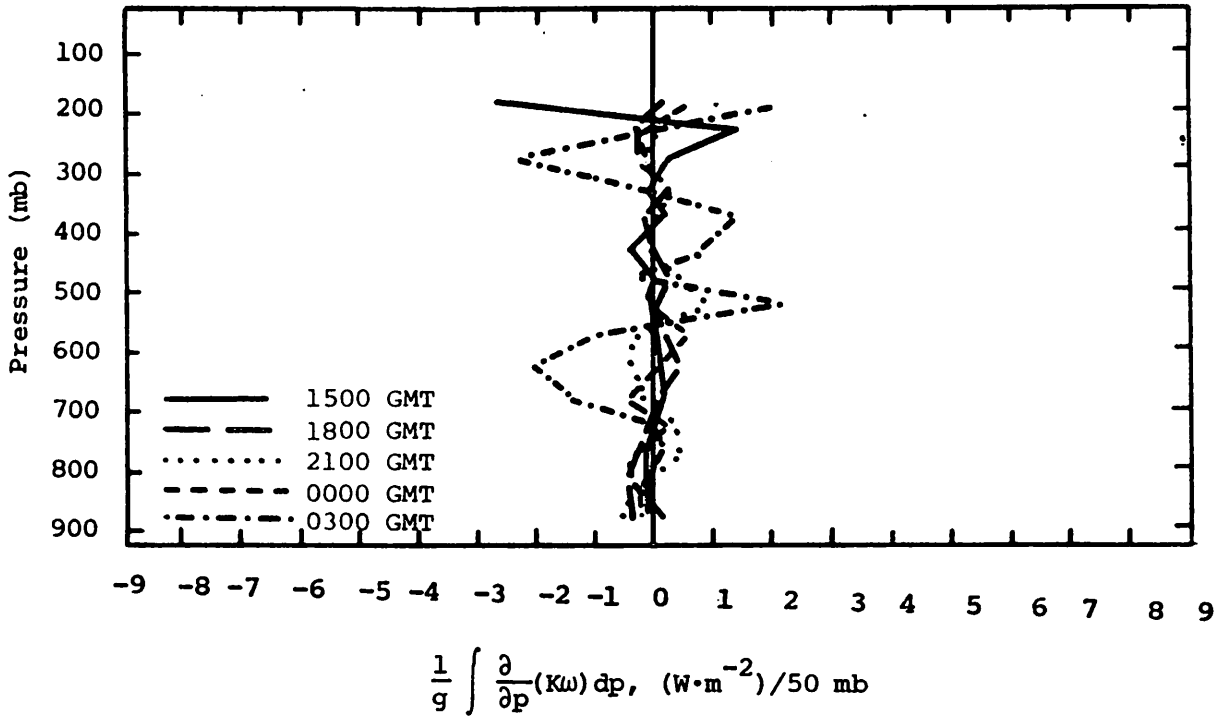

Fig. 5.16.4.7 Vertical profiles of the vertical flux of kinetic energy on 7 July 1977.

no noticeably important features related to the observed weather pattern.

5.16.5 Water Vapor Budget

Figure 5.16.5.1 shows vertical profiles of the net horizontal transport of water vapor. These profiles show generally a net inflow in layers between 700 and 500 mb, and a net outflow in other layers. Since no organized activity occurred over the area, these profiles follow the same pattern throughout the day.

Figure 5.16.5.2 shows profiles of the net vertical transport of water vapor. Again, these profiles follow a similar pattern throughout the day and show a net inflow in lower layers and a net outflow above.

Figure 5.16.5.3 shows profiles of vertical transport of water vapor through constant pressure surfaces. These profiles show strong downward transport at all times that reaches a maximum value around 750 mb.

Figure 5.16.5.4 shows profiles of the combined net horizontal and vertical transport of water vapor. These profiles generally show a net inflow in lower layers and a net outflow aloft.

Figure 5.16.5.5 shows profiles of the total mass of water vapor. These profiles do not vary much in time, but show a general increase of water vapor up to 500 mb. These profiles also show a smaller mass of water vapor over the network than on days containing convective activity.

Figure 5.16.5.6 shows profiles of the local rate-of-change in the total mass of water vapor. These profiles show a general increase of water vapor with time especially in lower layers. A large increase of water vapor occurred between 750 and 650 mb from 1800 to 2100 GMT prior to the appearance of the first echo at 2100 GMT.

5.17 8 July 1977

5.17.1 Radar

Charts of radar echoes (Fig. 5.17.1.1) show the presence of convective activity for all time periods except 0200 and 0300 GMT. At 1500 GMT a cell with tops exceeding 9.1 km (30K ft) was located north of Lamesa and west of Post. This cell appeared to decrease in altitude and by 1700 GMT most of the northern half of the area was covered with rain showers with tops less than 6.1 km (20K ft). Several cells moved southward through the area between 1700 and 2100 GMT. The echoes suggest that this may be a line although, except possibly at 1900 GMT, the cells appear to occur in a more or less random order. However, the echoes moved toward the south during the day and exited the area by 0200 GMT.

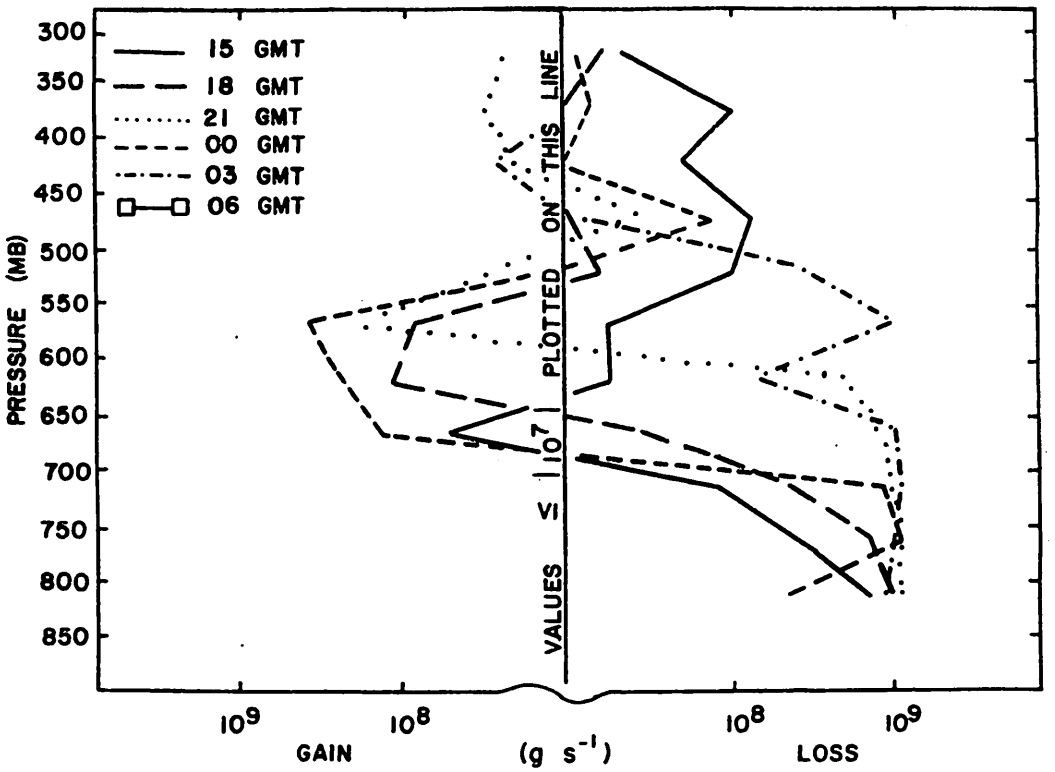

Fig. 5.16.5.1 Net horizontal transport of water vapor through boundaries of 50-mb layers (gm s^{-1}) over the Texas HIPLEX area for 7 July 1977.

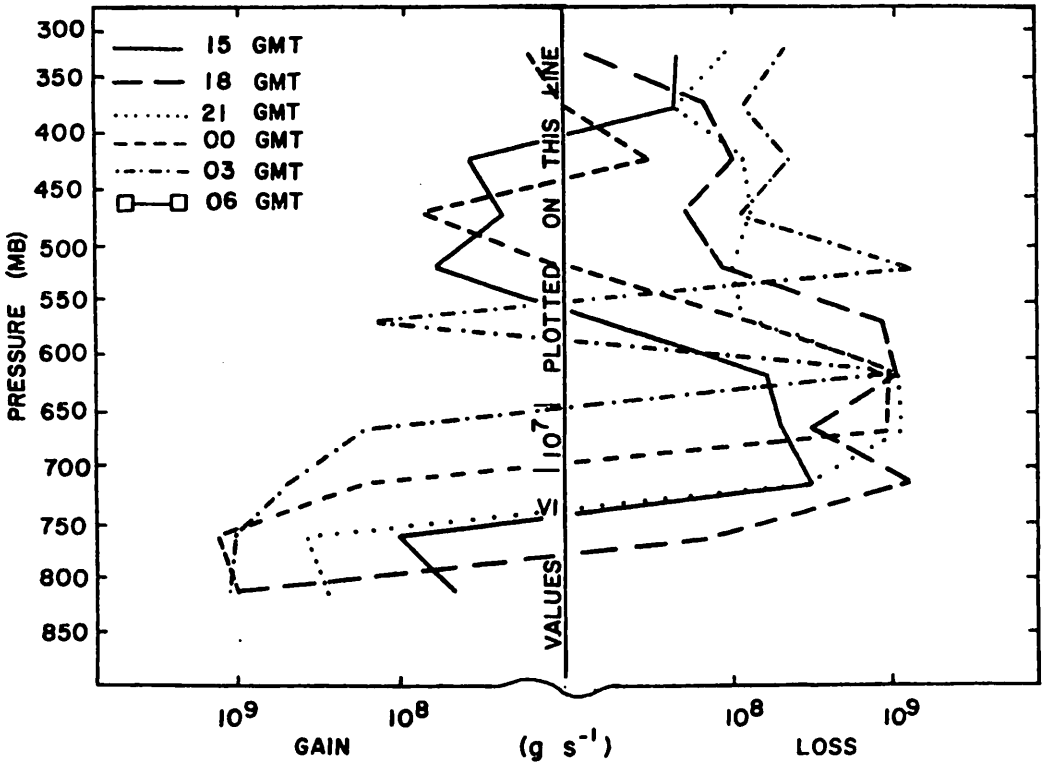

Fig. 5.16.5.2 Net vertical transport of water vapor through boundaries of 50-mb layers (gm s^{-1}) over the Texas HIPLEX area for 7 July 1977.

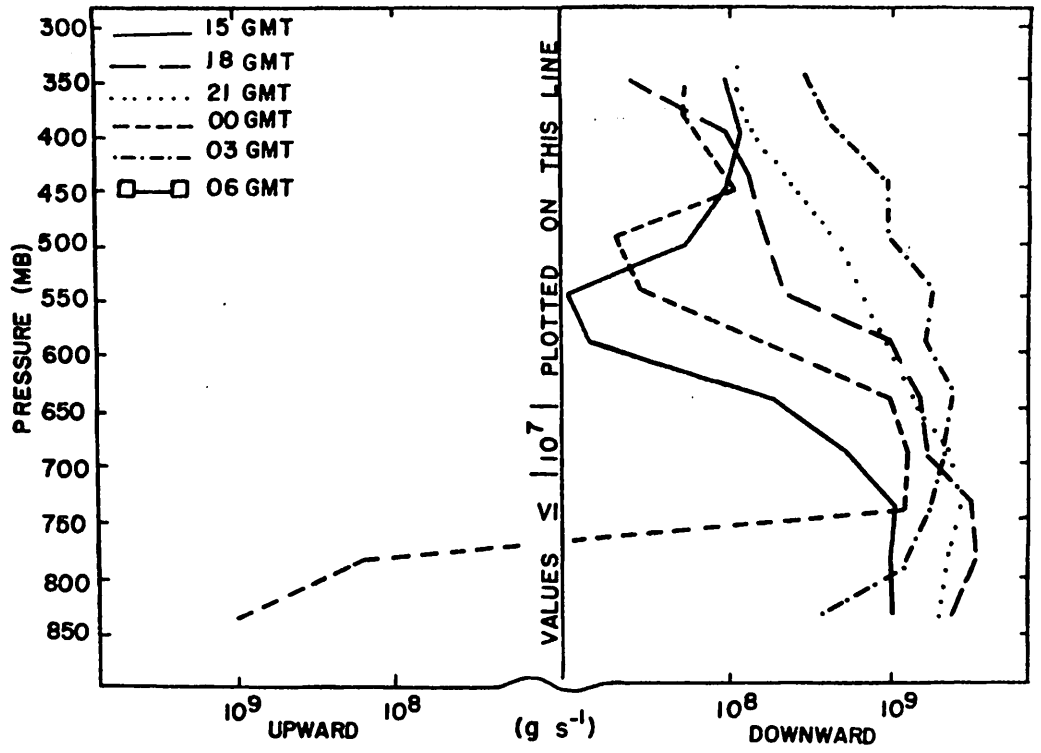

Fig. 5.16.5.3 Vertical transport of water vapor through constant pressure surfaces (gm s^{-1}) over the Texas HIPLEX area for 7 July 1977.

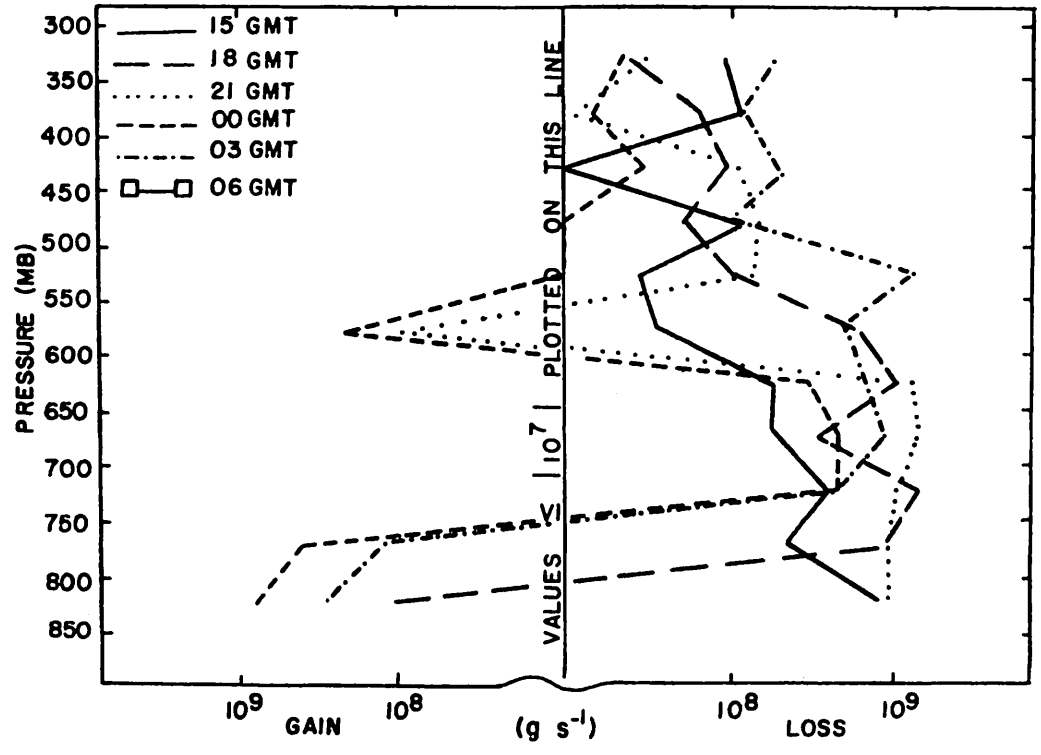

Fig. 5.16.5.4 Combined net horizontal and vertical transport of water vapor through boundaries of 50-mb layers (gm s^{-1}) over the Texas HIPLEX area for 7 July 1977.

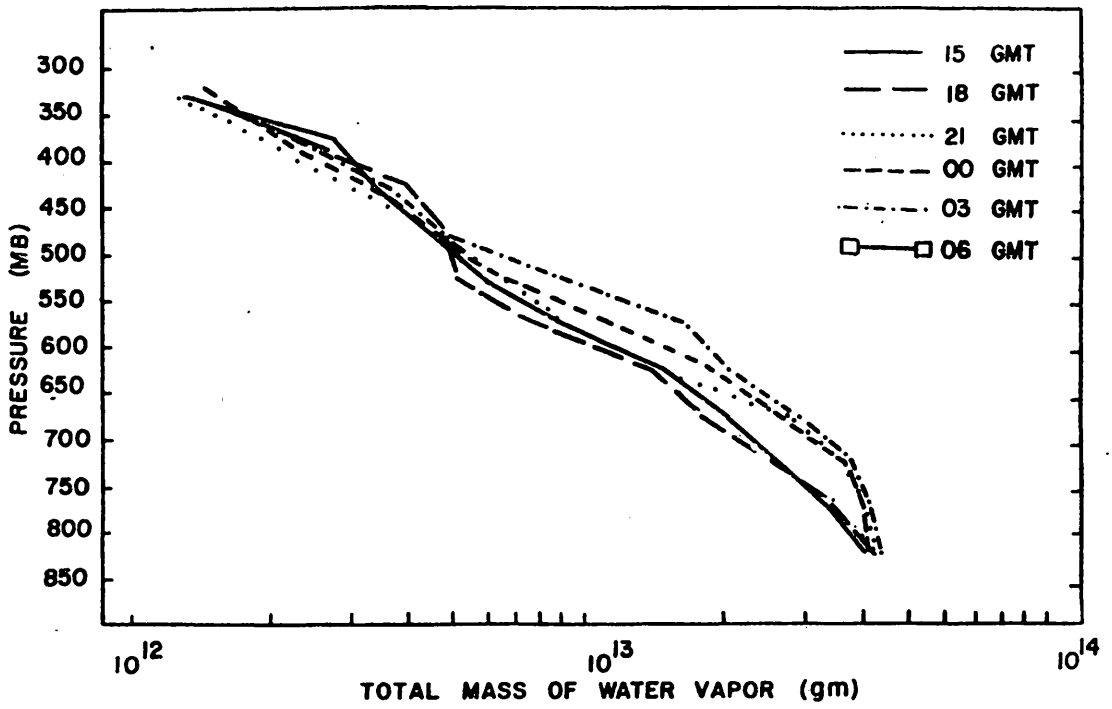

Fig. 5.16.5.5 Total mass of water vapor in layers 50 mb deep (gm) over the Texas HIPLEX area for 7 July 1977.

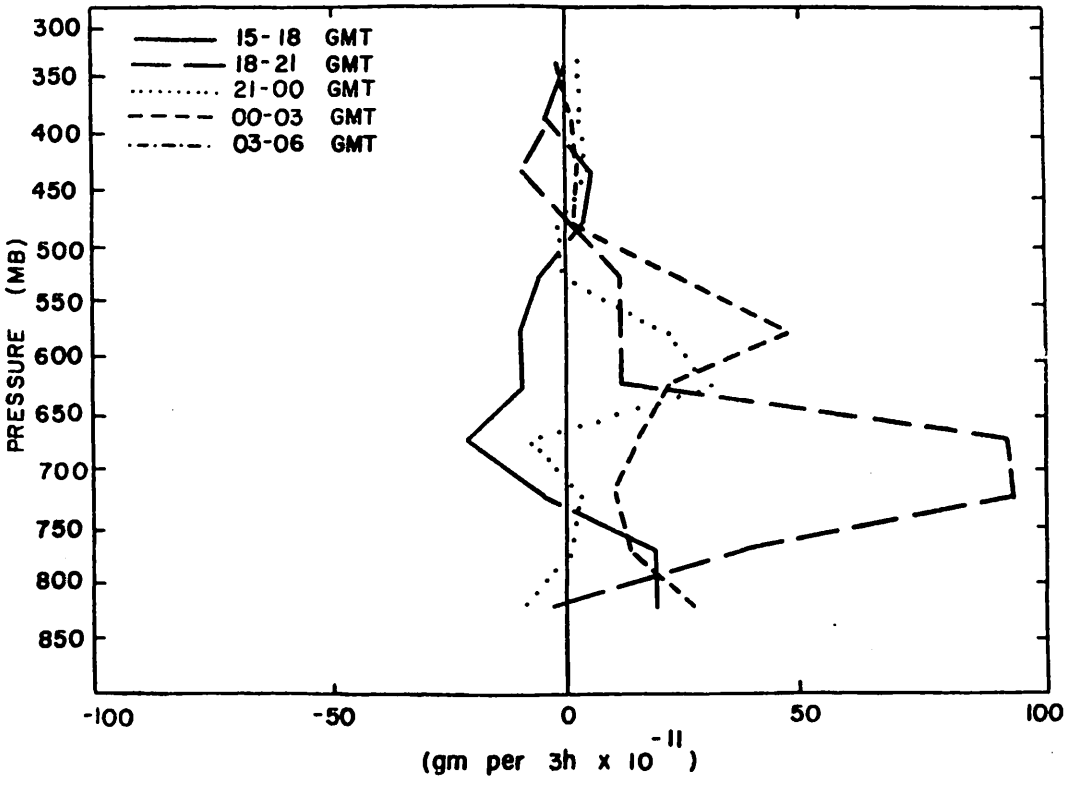

Fig. 5.16.5.6 Local rate-of-change in total mass of water vapor (gm per 3h x 10^{-11}) over the Texas HIPLEX area for 7 July 1977.

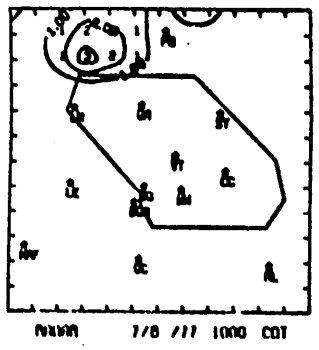

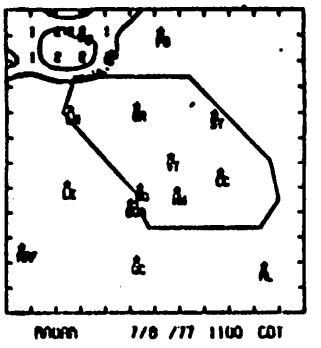

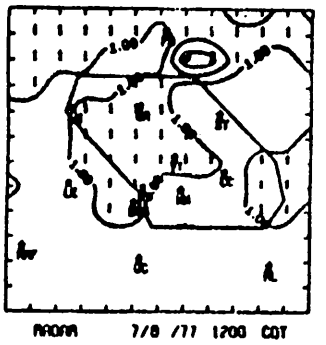

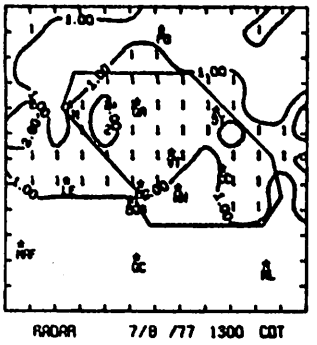

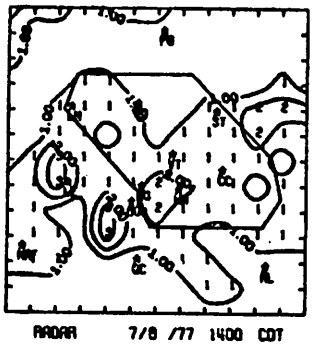

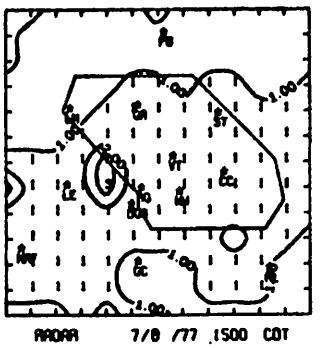

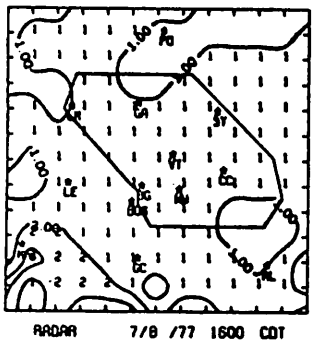

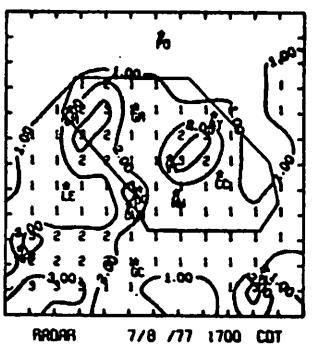

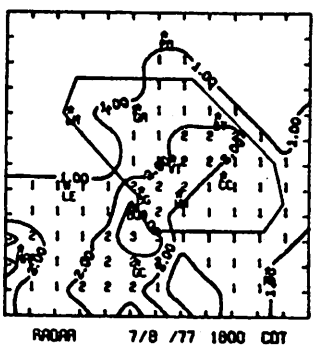

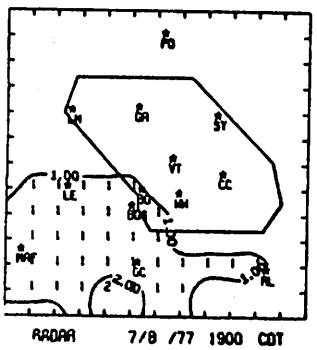

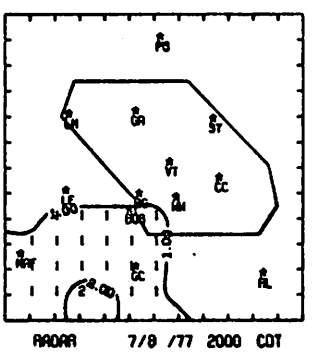

NO ECHOES

RADAR 7/8 /77 2100 CDT

NO ECHOES

RADAR 7/8 /77 2200 CDT

Fig. 5.17.1.1 Radar echoes for 8 July 1977.

5.17.2 Surface

Large variations in patterns of surface temperature (Fig. 5.17.2.1) are associated with the convective activity. Centers of minimum temperature correlate with strong echoes. Fields of surface mixing ratio (Fig. 5.17.2.2) also vary, but values remain high throughout the day. Centers of low surface mixing ratio are correlated with centers of minimum surface temperature. This correlation is also evident by well defined centers of minimum surface equivalent potential temperature (Fig. 5.17.2.3) over the center of the network. These large differences in equivalent potential temperature decrease with the dissipation of convective activity by 0200 GMT.

Terrain-induced vertical motion (Fig. 5.17.2.4) shows large variations due to the effect of convection on surface wind fields. These vertical motions decrease to near zero at 0200 GMT in association with dissipation of the convective activity. Large centers of surface velocity convergence (Fig. 5.17.2.5) occurred prior to 2100 GMT followed by strong divergence and eventual dissipation. These fields result in strong upward vertical motion 50 mb above the surface (Fig. 5.17.2.6) prior to 2100 GMT and downward motion thereafter. Centers of minimum surface temperature also correlate with centers of downward motion which further indicated the presence of cold downdrafts. Fields of surface moisture convergence (Fig. 5.17.2.7) prior to 2100 GMT show large centers in regions of strong convection. Centers of surface moisture divergence occur in regions of minimum surface mixing ratio (Fig. 5.17.2.2). Upward and downward vertical flux of moisture 50 mb above the surface (Fig. 5.17.2.8) also correlates well with surface moisture convergence and divergence fields, respectively. Following dissipation, the moisture flux decreases to near zero. Prominent centers of surface vorticity (Fig. 5.17.2.9) occur with the strong echoes, but change rapidly.

Fields of sea level pressure (Fig. 5.17.2.10) show a center of low pressure south of Colorado City, and a center of high pressure near Lenorah. However, this pattern changes as reflected in the surface pressure change (Fig. 5.17.2.11). Large pressure changes associated with the convective activity occurred in regions of downdrafts. Once dissipation occurred, pressure changes become negligible.

5.17.3 Upper-Level Kinematic Parameters

Horizontal mass convergence in low levels increases between 1500 and 1800 GMT as thunderstorm development occurs over the network (Fig. 5.17.3.1). By 0000 GMT horizontal mass divergence was calculated in low layers during a

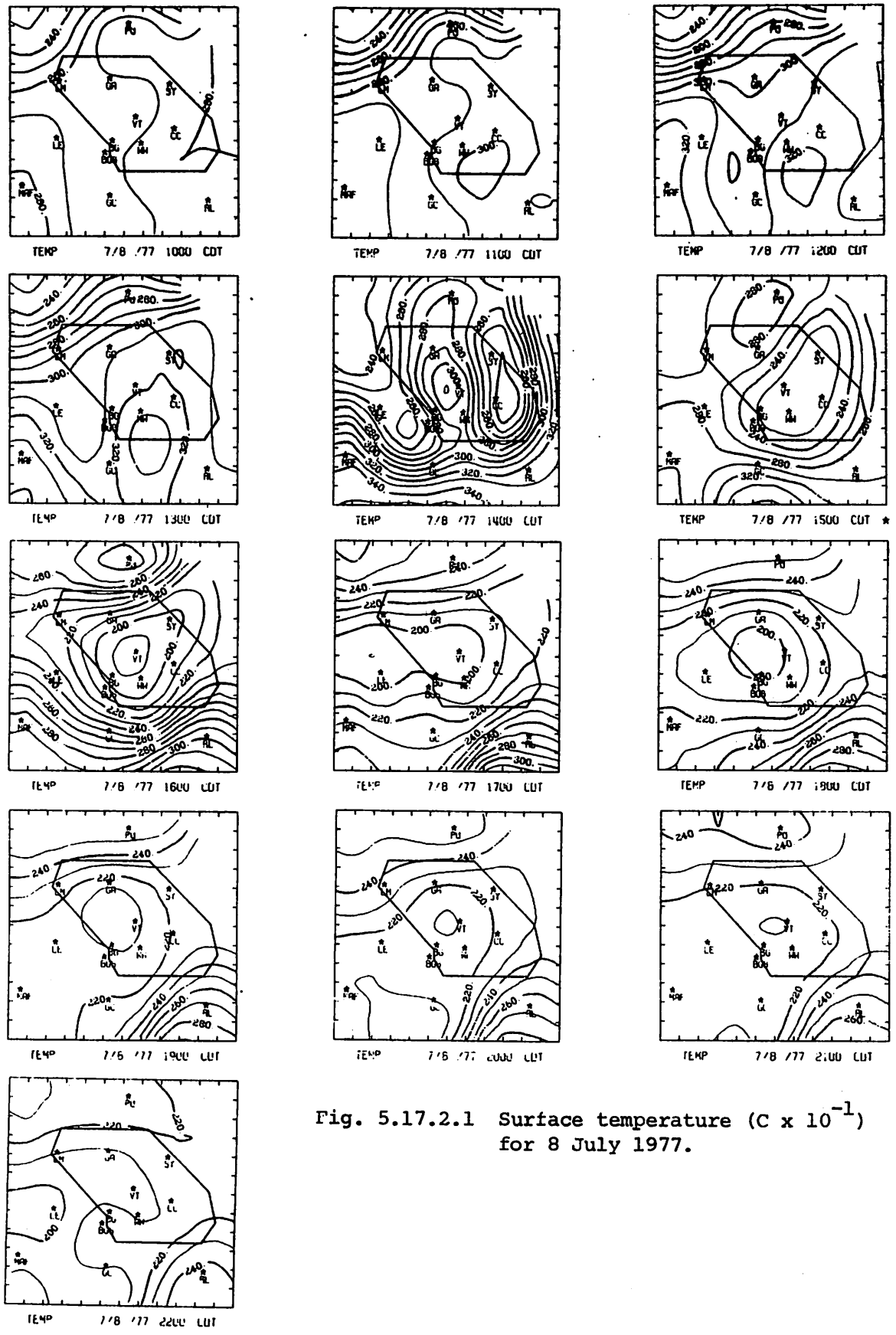

Fig. 5.17.2.1 Surface temperature (C x 10^{-1}) for 8 July 1977.

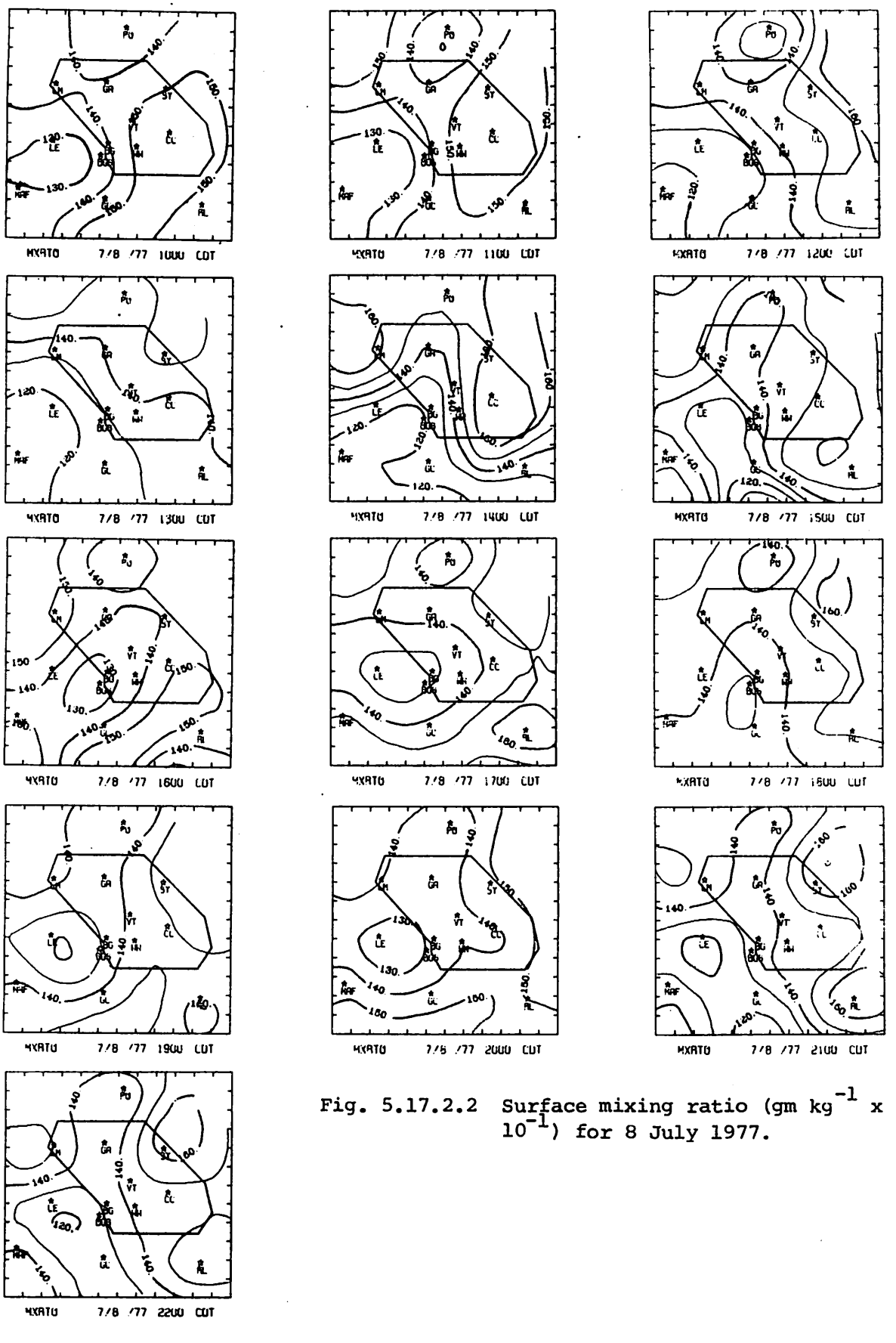

Fig. 5.17.2.2 Surface mixing ratio (gm kg^{-1} x 10^{-1}) for 8 July 1977.

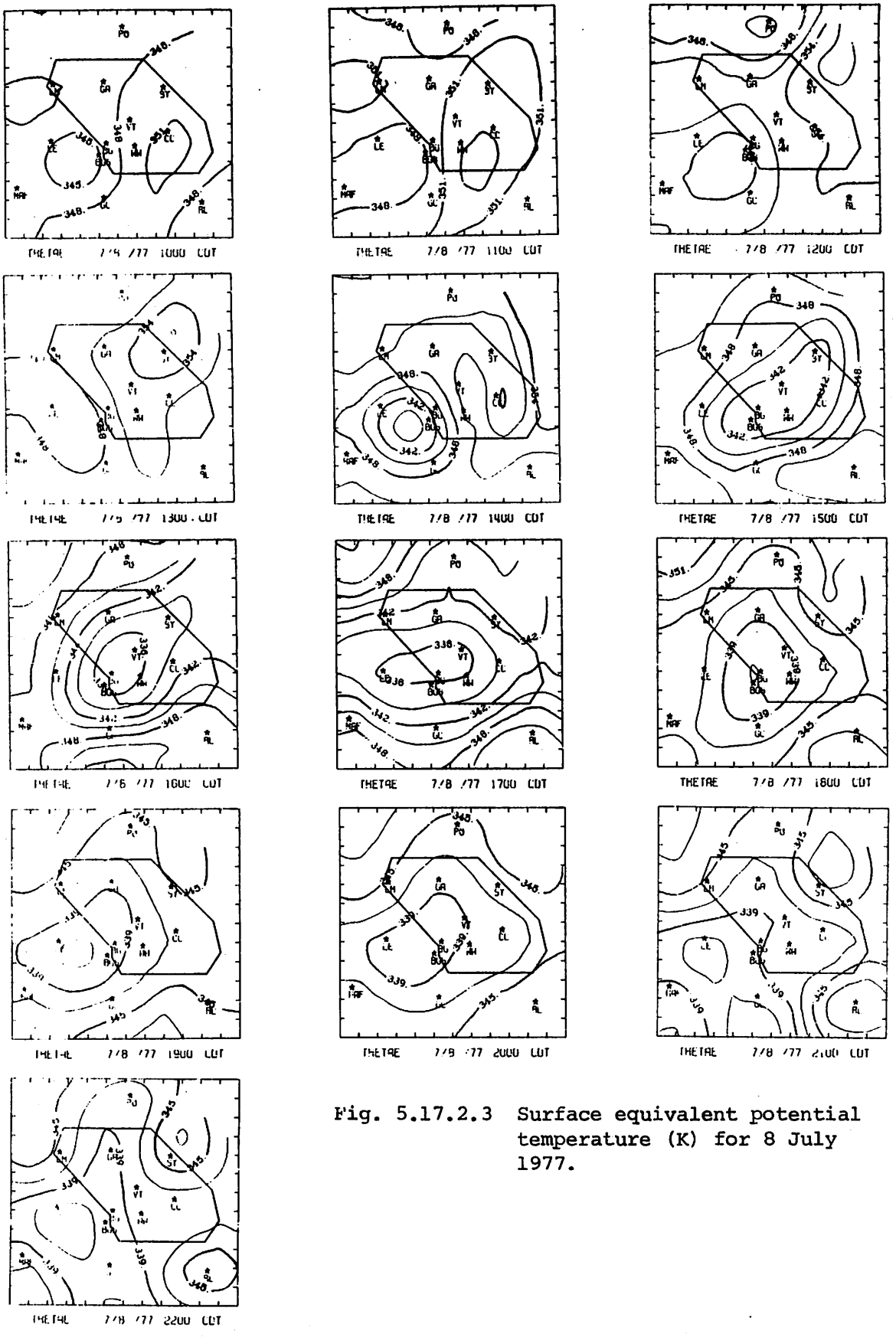

Fig. 5.17.2.3 Surface equivalent potential temperature (K) for 8 July 1977.

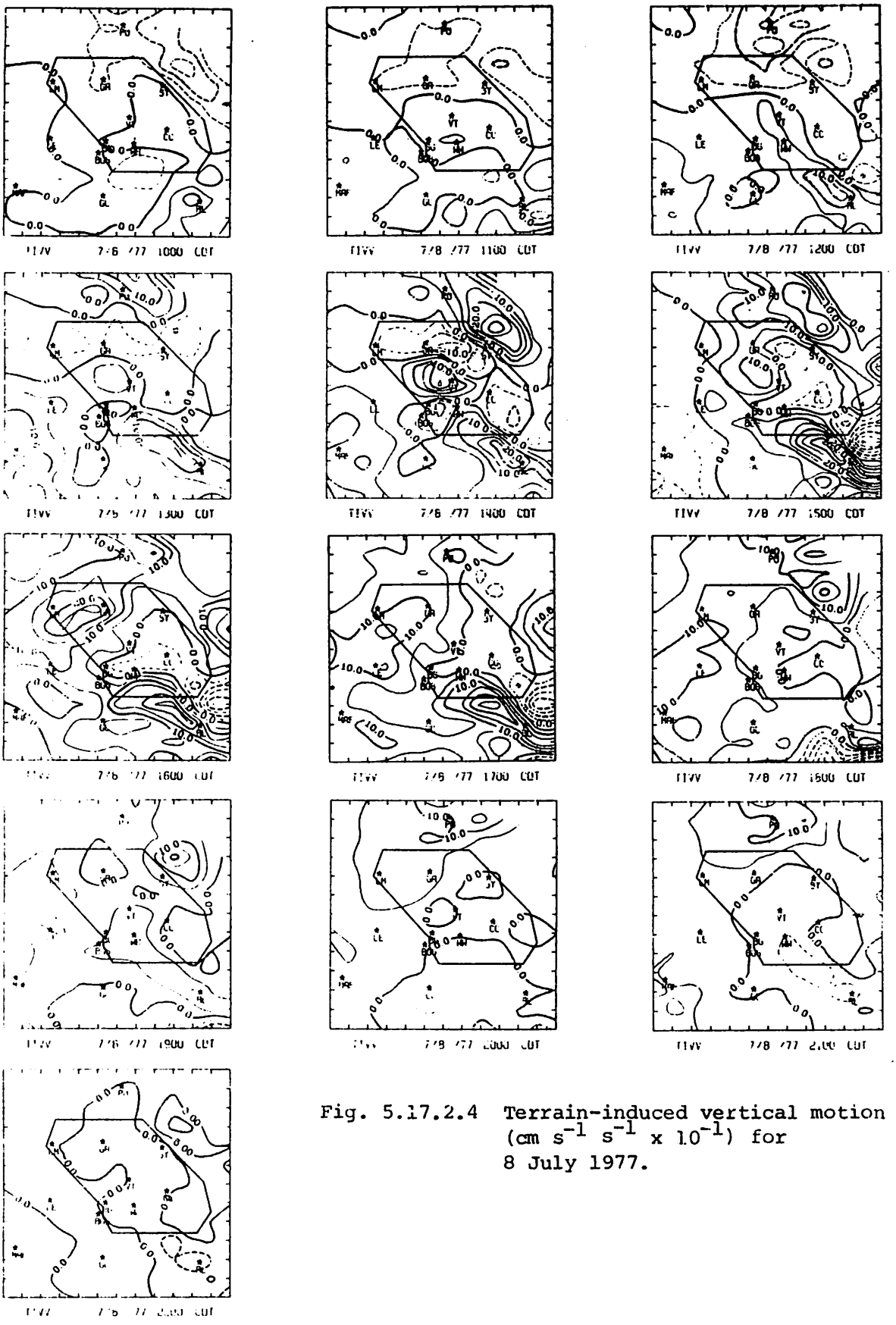

Fig. 5.17.2.4 Terrain-induced vertical motion (cm s^{-1} s^{-1} x 10^{-1}) for 8 July 1977.

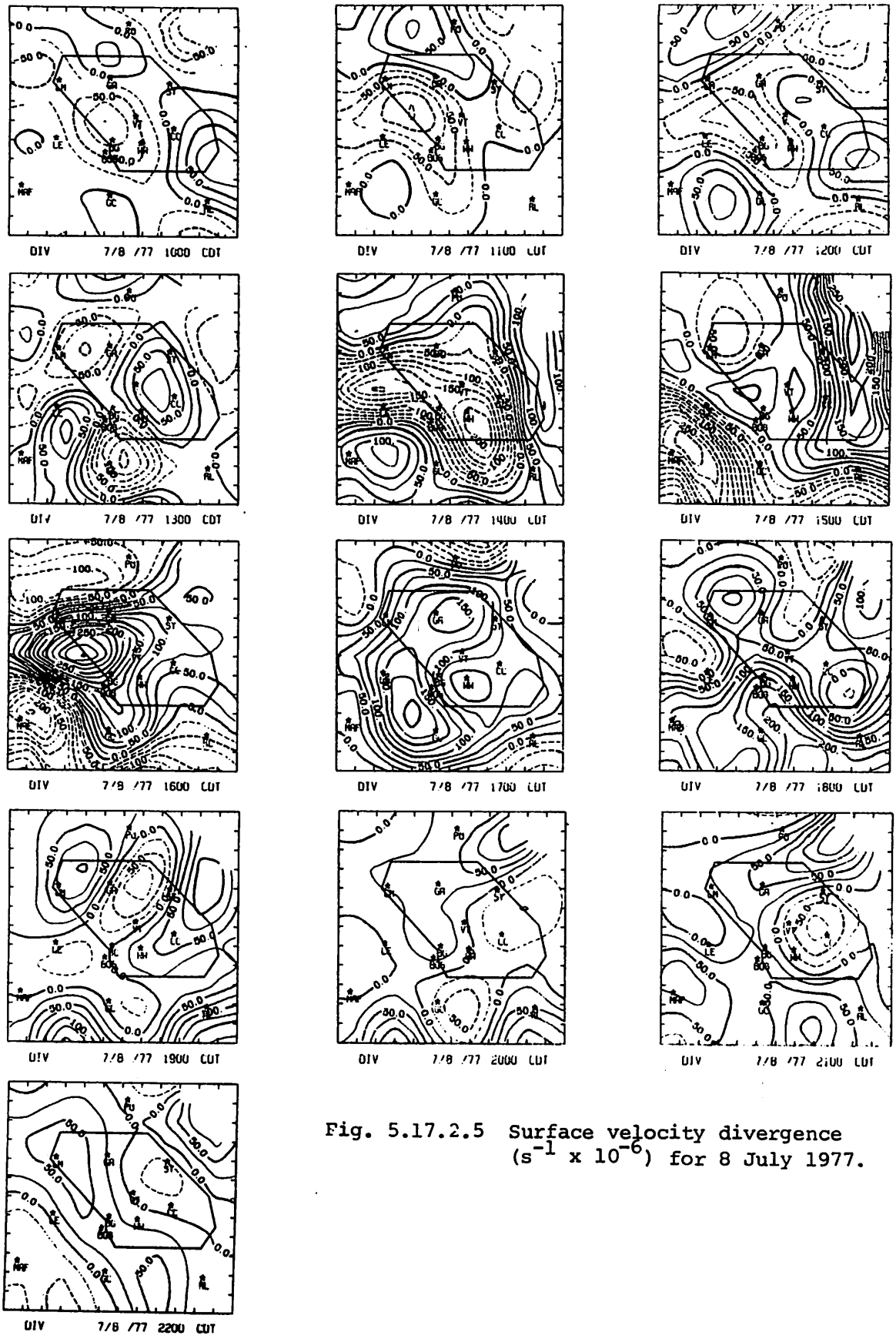

Fig. 5.17.2.5 Surface velocity divergence ($s^{-1} \times 10^{-6}$) for 8 July 1977.

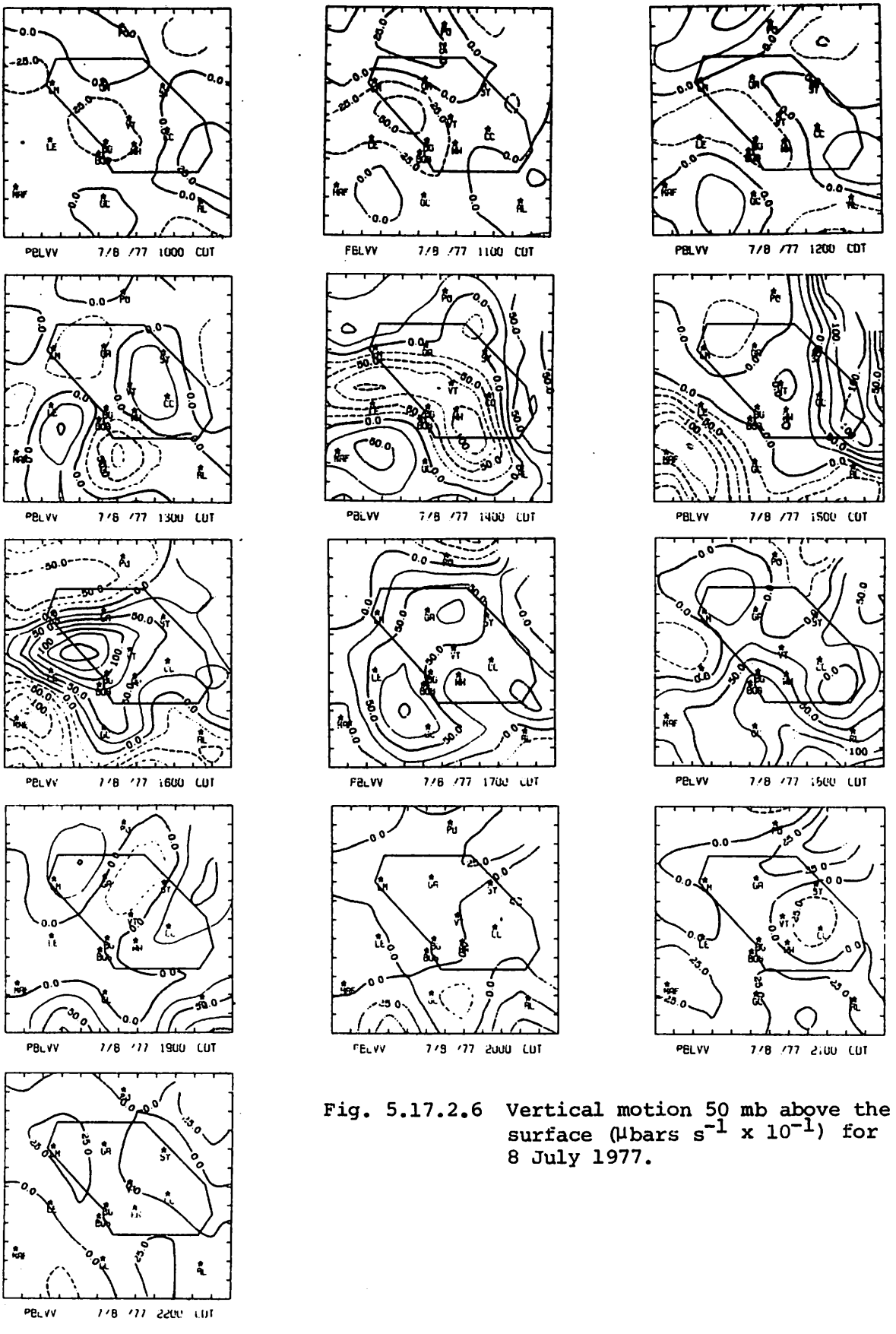

Fig. 5.17.2.6 Vertical motion 50 mb above the surface (μbars s^{-1} x 10^{-1}) for 8 July 1977.

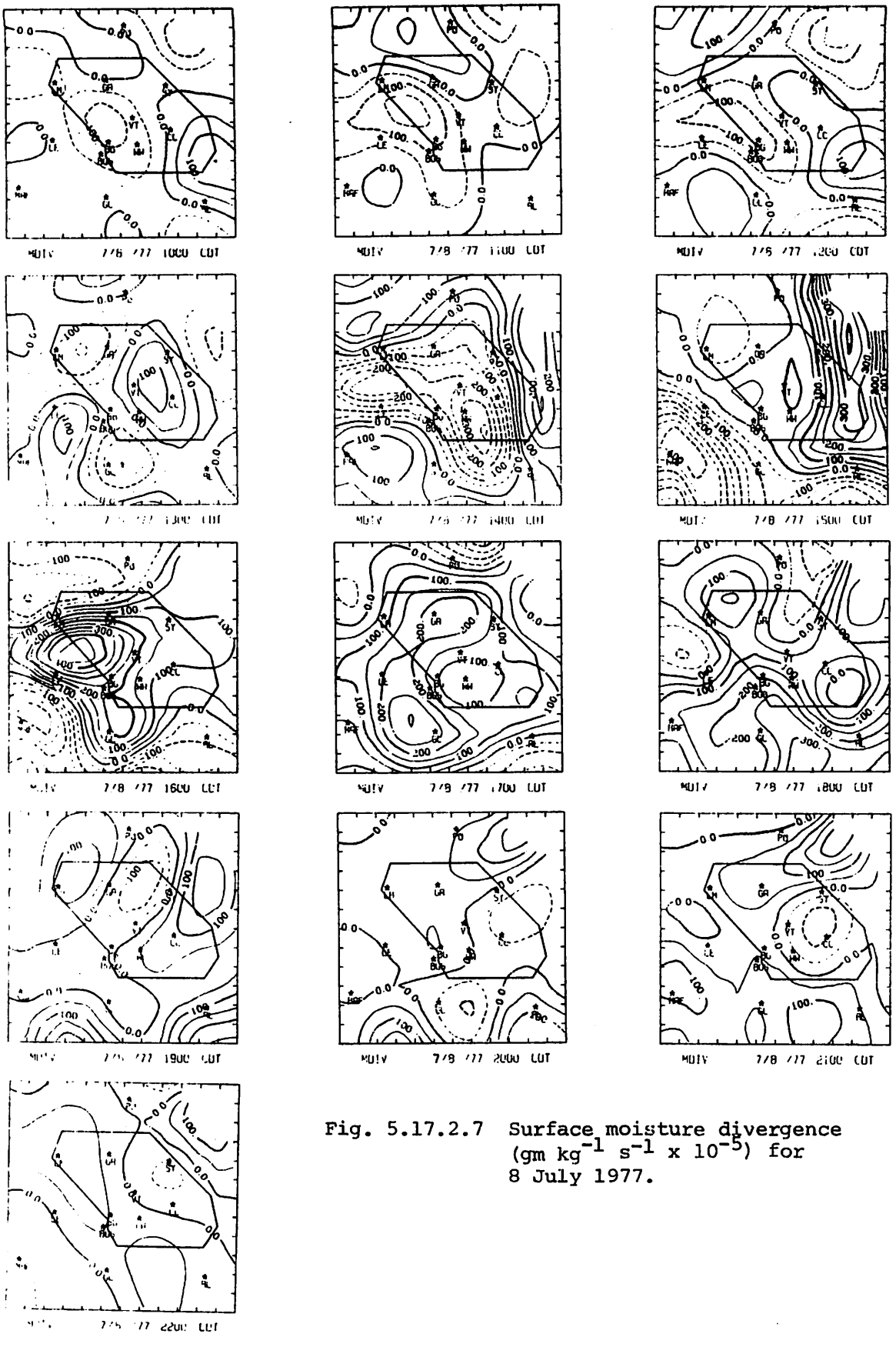

Fig. 5.17.2.7 Surface moisture divergence (gm kg^{-1} s^{-1} x 10^{-5}) for 8 July 1977.

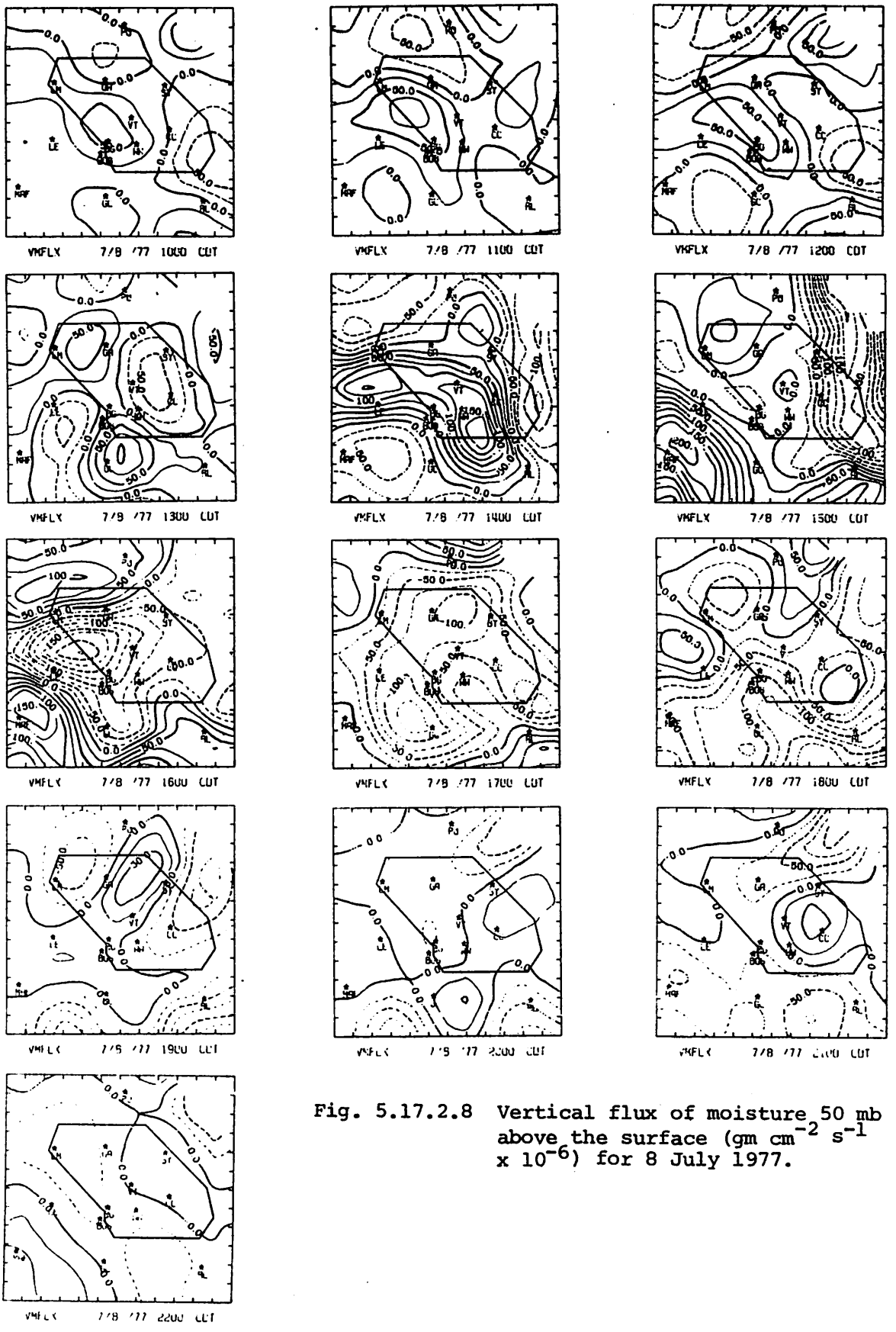

Fig. 5.17.2.8 Vertical flux of moisture 50 mb above the surface (gm cm^{-2} s^{-1} x 10^{-6}) for 8 July 1977.

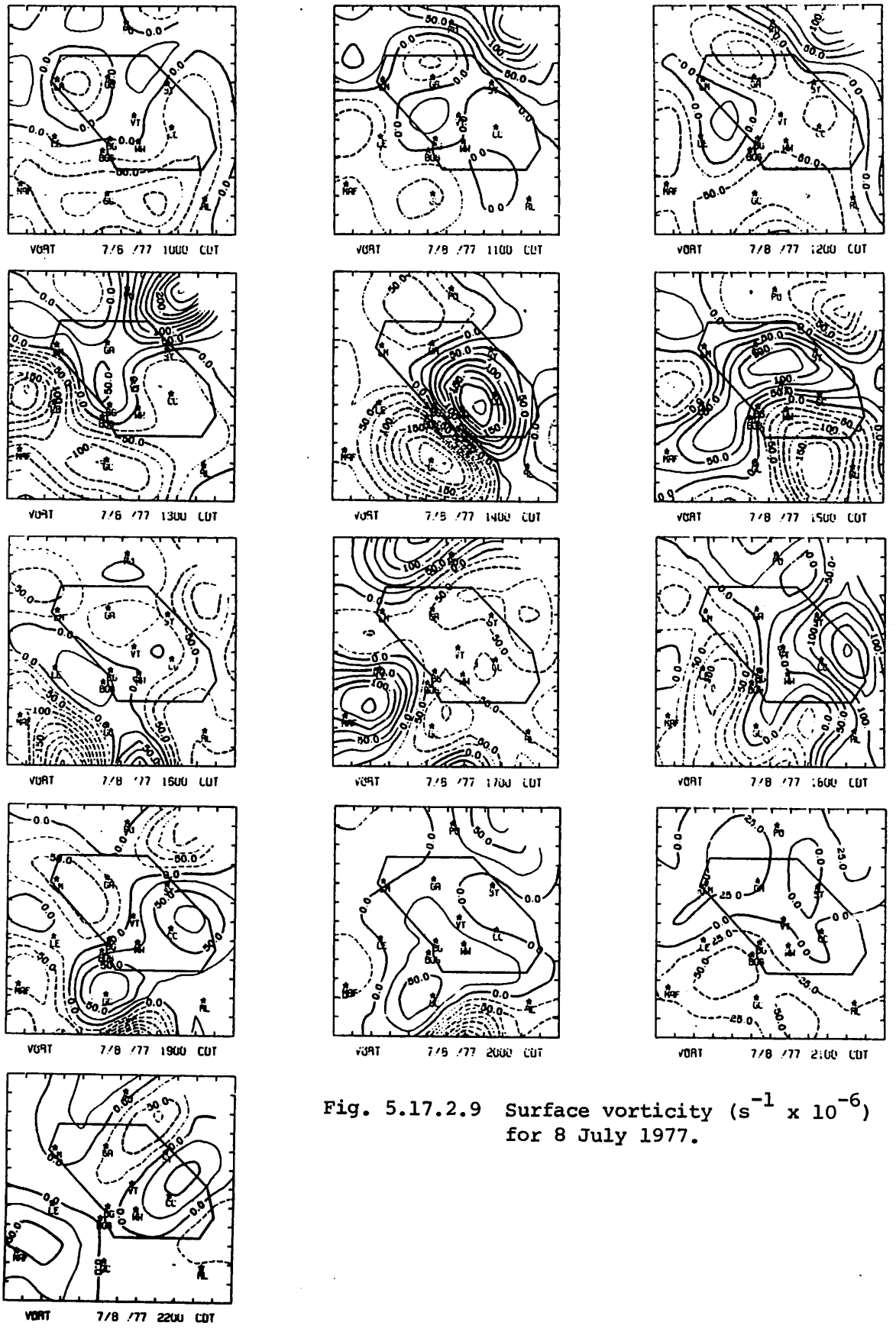

Fig. 5.17.2.9 Surface vorticity ($s^{-1} \times 10^{-6}$) for 8 July 1977.

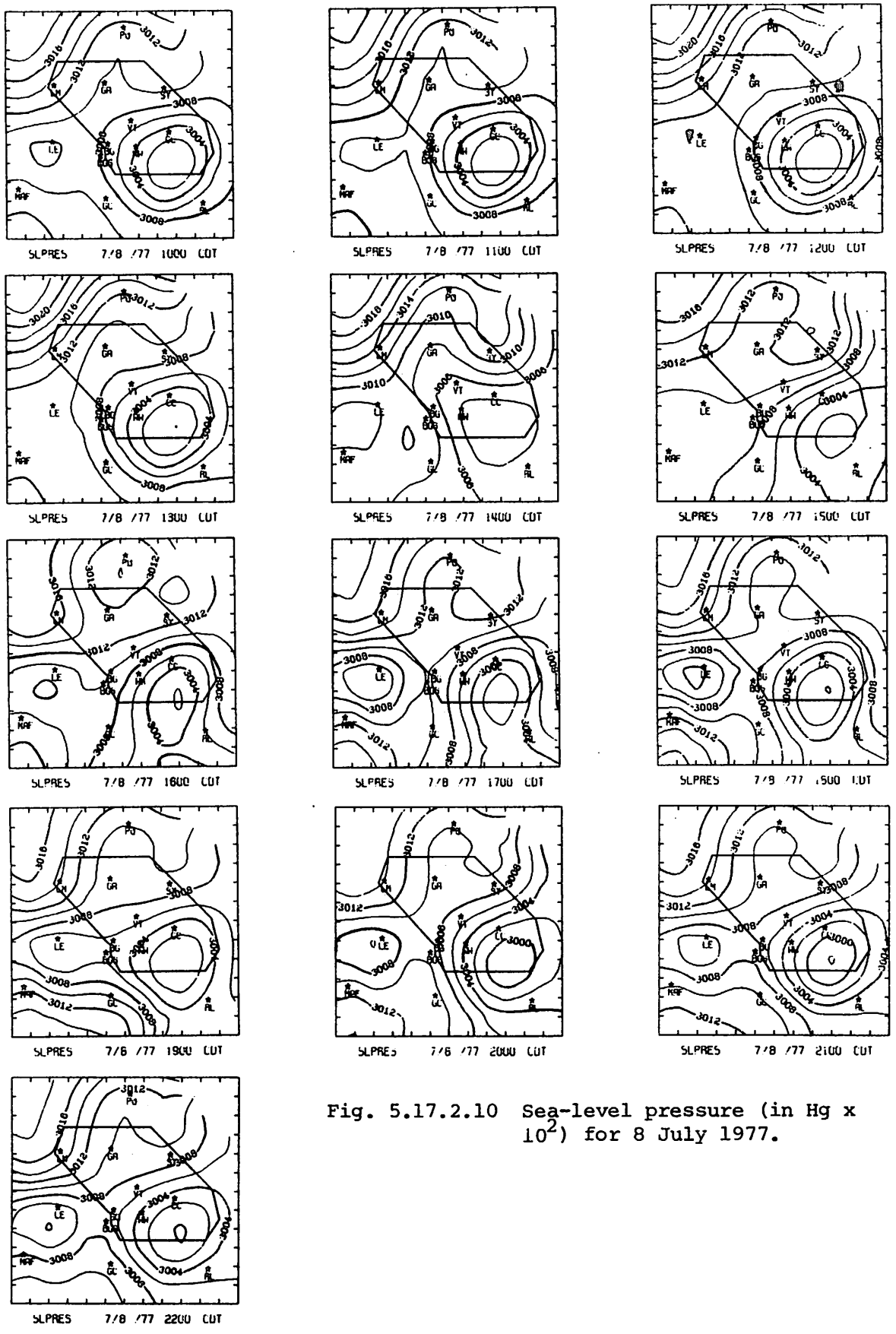

Fig. 5.17.2.10 Sea-level pressure (in Hg x 10^2) for 8 July 1977.

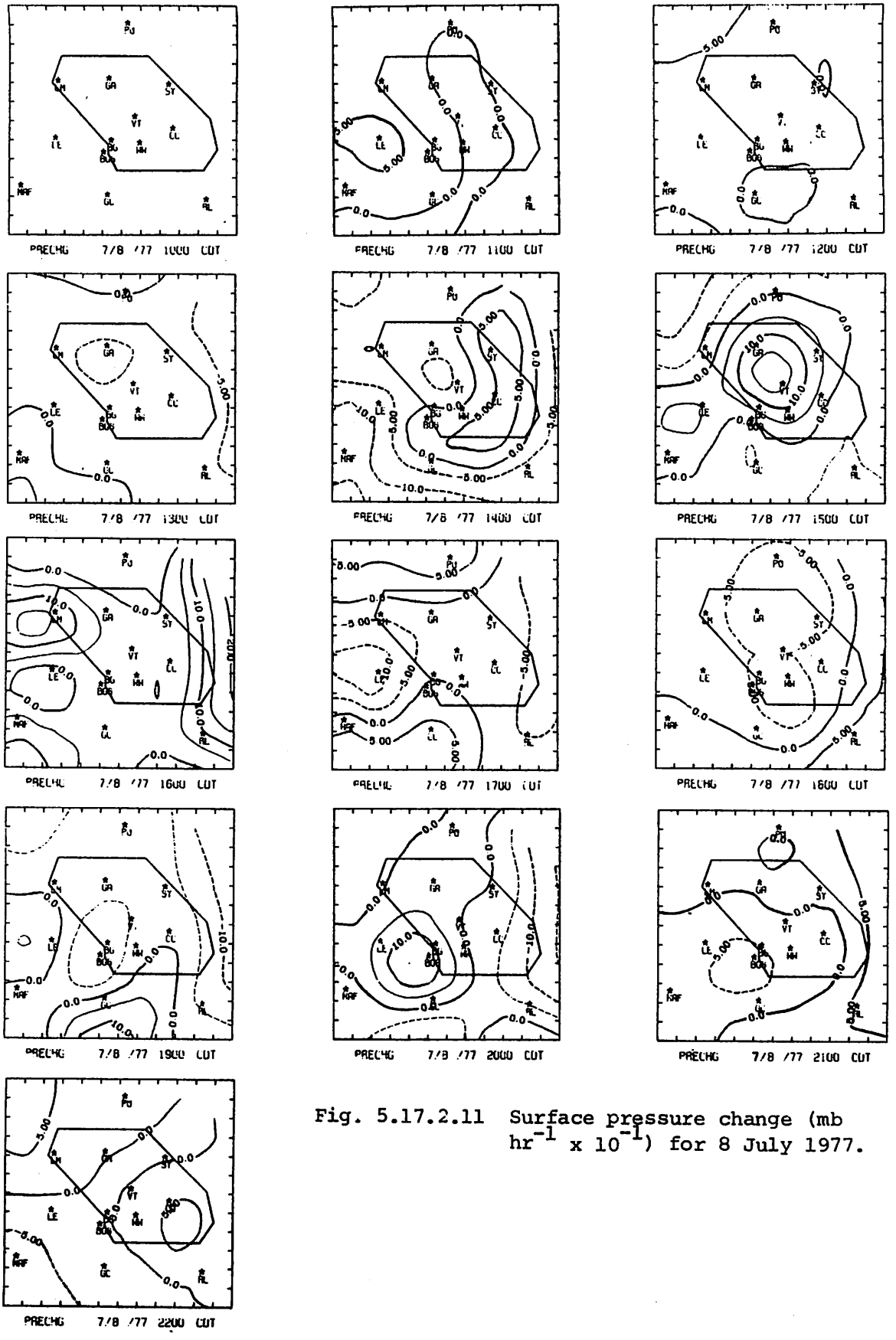

Fig. 5.17.2.11 Surface pressure change (mb hr^{-1} x 10^{-1}) for 8 July 1977.

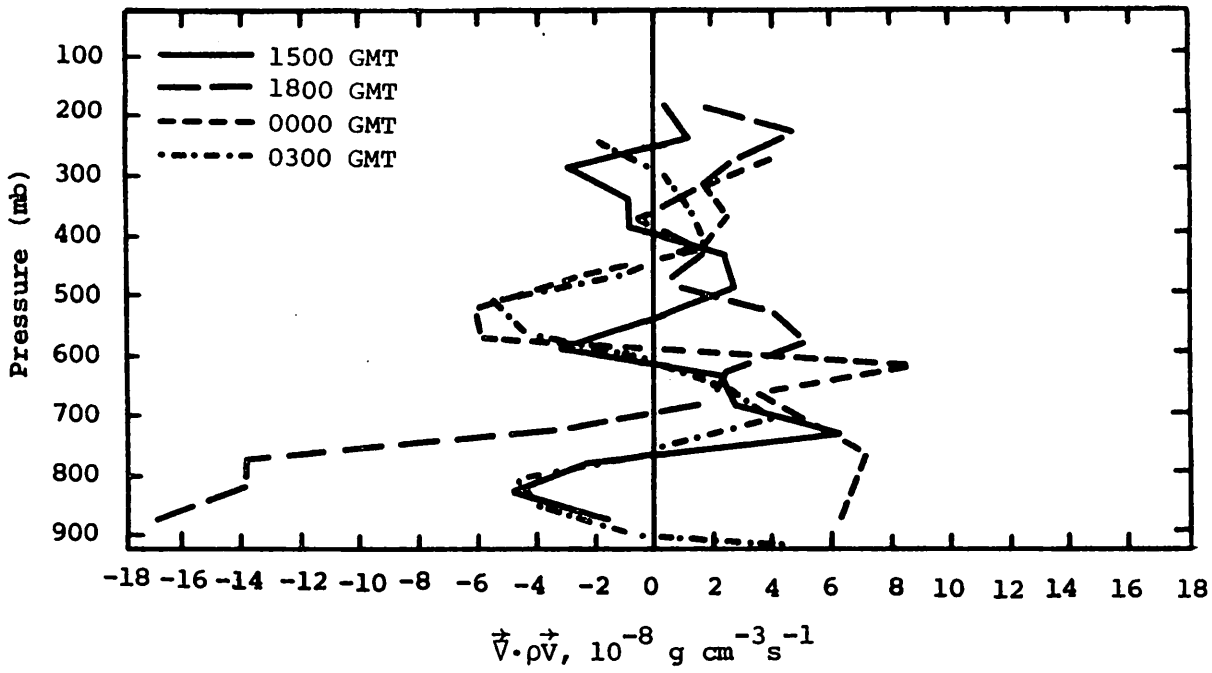

Fig. 5.17.3.1 Vertical profiles of mass divergence on 8 July 1977.

time of diminishing activity. Vertical velocities at all levels changed from near zero at 1500 GMT to strong upward at 1800 GMT, and switched to downward after 2100 GMT (Fig. 5.17.3.2) corresponding well with precipitation development and dissipation during the day.

Strong low-level horizontal moisture convergence was calculated before and during storm formation at 1500 and 1800 GMT and low-level moisture divergence occurred during storm dissipation at 0000 and 0300 GMT (Fig. 5.17.3.3). Small values generally appear above 500 mb.

5.17.4 Energetics

Net horizontal inflow of latent heat energy in low levels is shown in Figure 5.17.4.1 before and during storm formation at 1500 and 1800 GMT. This pattern reverses to net outflow during times of diminishing activity at 0000 GMT and 0300 GMT. Vertical flux divergence of latent heat energy in low levels and flux convergence at mid- and high-levels occurs during storm formation as a net upward transport of latent heat energy was computed from low- to mid-levels (Fig. 5.17.4.2). The vertical distribution of convergence/divergence of latent heat energy reverses at 0000 and 0300 GMT so that subsidence at these times points to a net downward transport of energy from mid- to low-levels. Local changes of latent heat energy were positive at most levels at 1500 and 1800 GMT before and during storm development, and near zero or slightly negative at 0000 and 0300 GMT when activity diminished and moved out

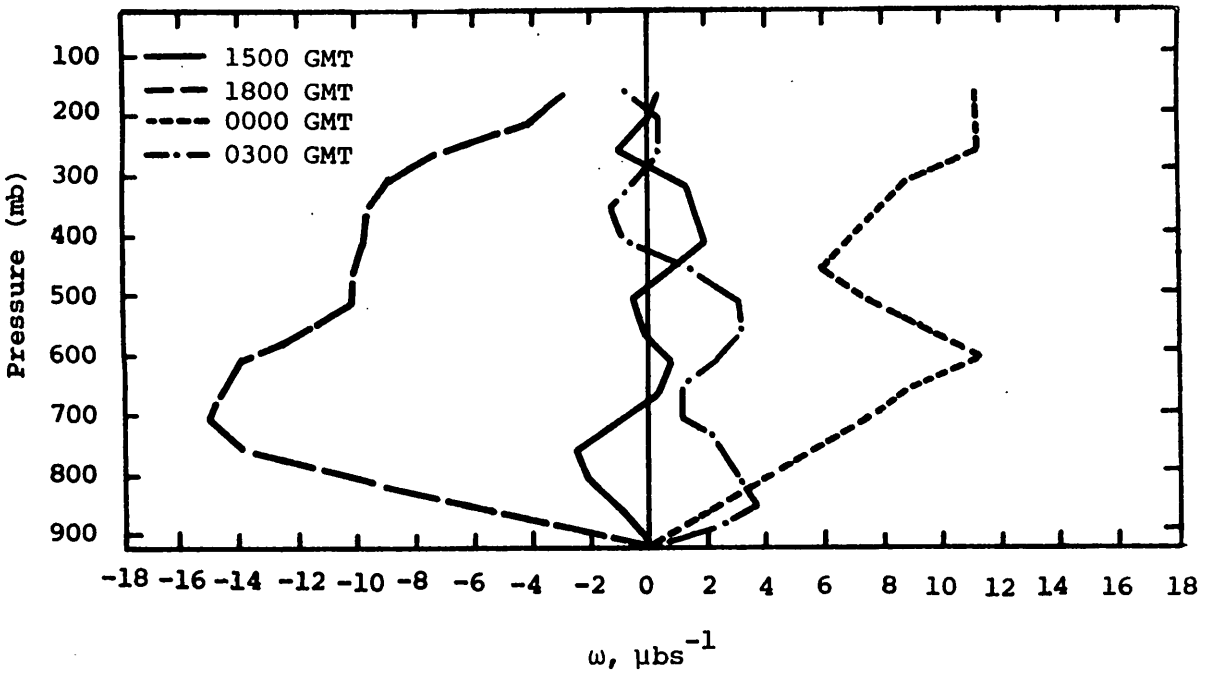

Fig. 5.17.3.2 Vertical profiles of vertical motion on 8 July 1977.

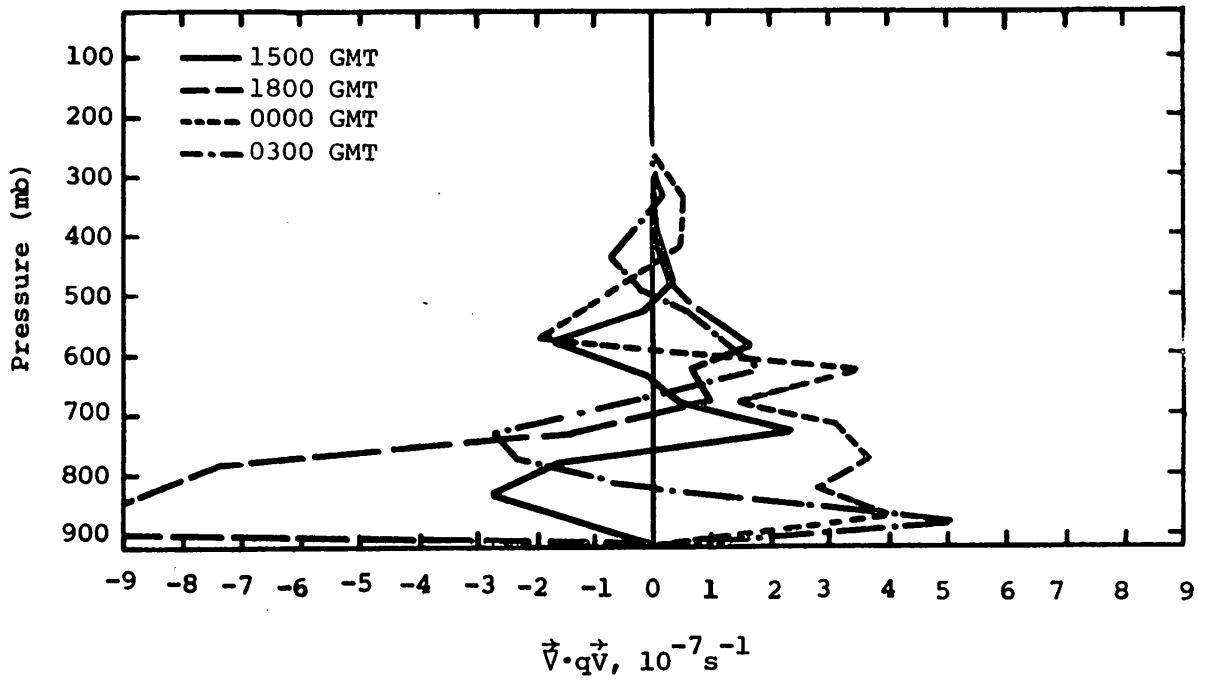

Fig. 5.17.3.3 Vertical profiles of moisture divergence on 8 July 1977.

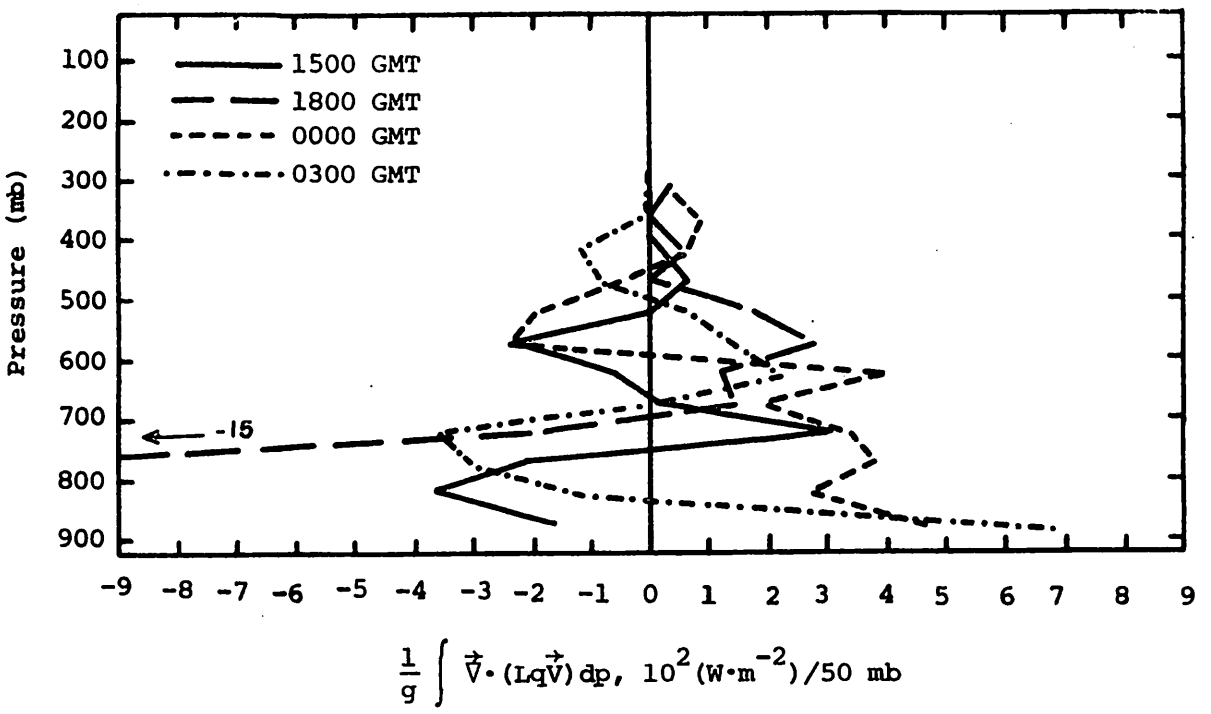

Fig. 5.17.4.1 Vertical profiles of the horizontal flux of latent heat energy on 8 July 1977.

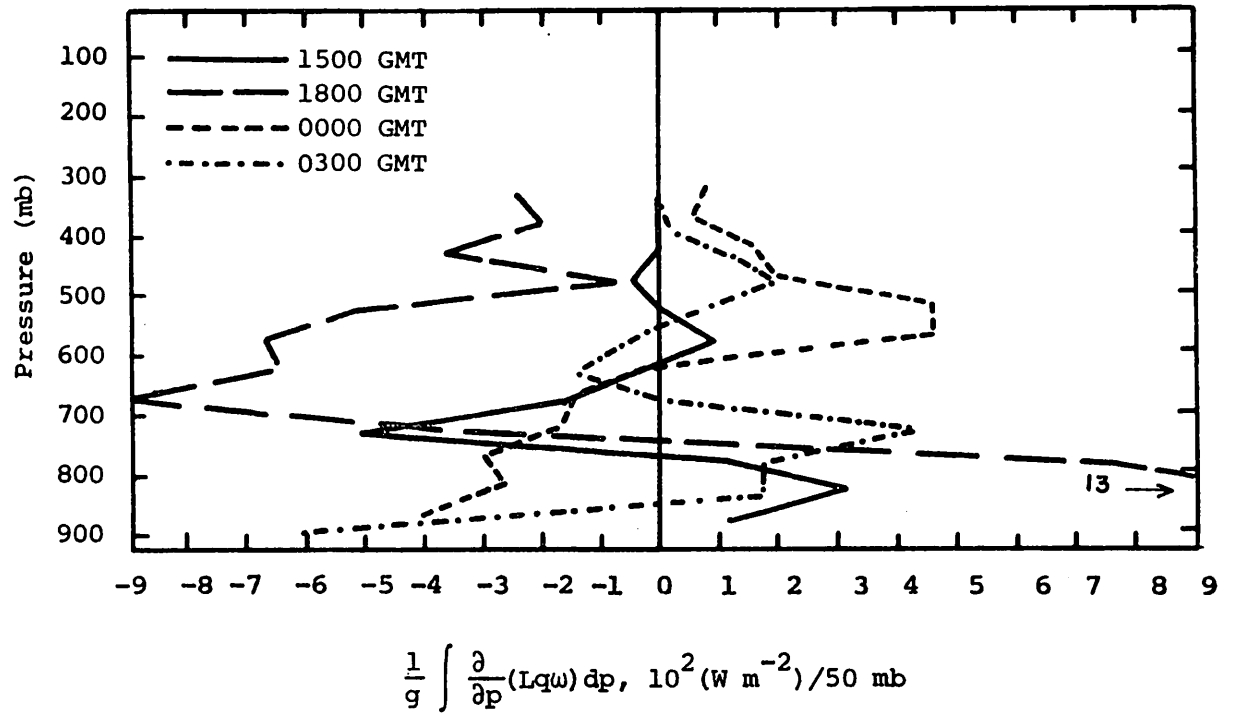

Fig. 5.17.4.2 Vertical profiles of the vertical flux of latent heat energy on 8 July 1977.

of the network (Fig. 5.17.4.3).

The vertical profiles of the residual from the latent heat budget equation (Fig. 5.17.4.4) show strong positive values of -R at 1800 GMT when storm formation occurred and losses of latent heat content from condensation (producing environmental warming) would be expected. By 0000 and 0300 GMT values were generally negative at all levels consistent with evaporation of cloud water and precipitation that occurred with storm dissipation.

The diabatic heating profiles (Fig. 5.17.4.5) generally agree in sign and magnitude with the -R profiles just presented and support the tentative conclusions given. Diabatic heating from condensation at 1800 GMT is followed by cooling from evaporation at 0000 GMT as storm development and dissipation occurred over the area.

The horizontal and vertical flux divergence profiles for kinetic energy (Figs. 5.17.4.6 and 5.17.4.7) reveal only small values of each term at most times and levels, and show no noticeably important features related to the observed weather.

5.17.5 Water Vapor Budget

Figure 5.17.5.1 shows profiles of the net horizontal transport of water vapor. These profiles generally show a net inflow in layers below 650 mb, and a net outflow aloft.

Figure 5.17.5.2 shows profiles of the net vertical transport of water vapor. These profiles show large temporal variations of strong net inflow and net outflow. Figure 5.17.5.3 shows profiles of the vertical transport of water vapor through constant pressure surfaces. Again, these transports vary in time showing both strong upward and downward motion throughout the day. Such variation of water vapor transport can also be seen in Fig. 5.17.5.2.

Figure 5.17.5.4 shows profiles of the combined net horizontal and vertical transport of water vapor. Although these profiles show a temporal variation, a general net outflow occurred especially as the activity moved out around 0300 GMT. A strong net inflow occurred in layers above 750 mb at 1800 GMT prior to heavy activity entering the area.

Figure 5.17.5.5 shows profiles of the total mass of water vapor. These profiles show little variation in layers below 600 mb. However, in layers aloft a large increase in water vapor occurred at 0000 and 0300 GMT during dissipation and movement of the activity from the network.

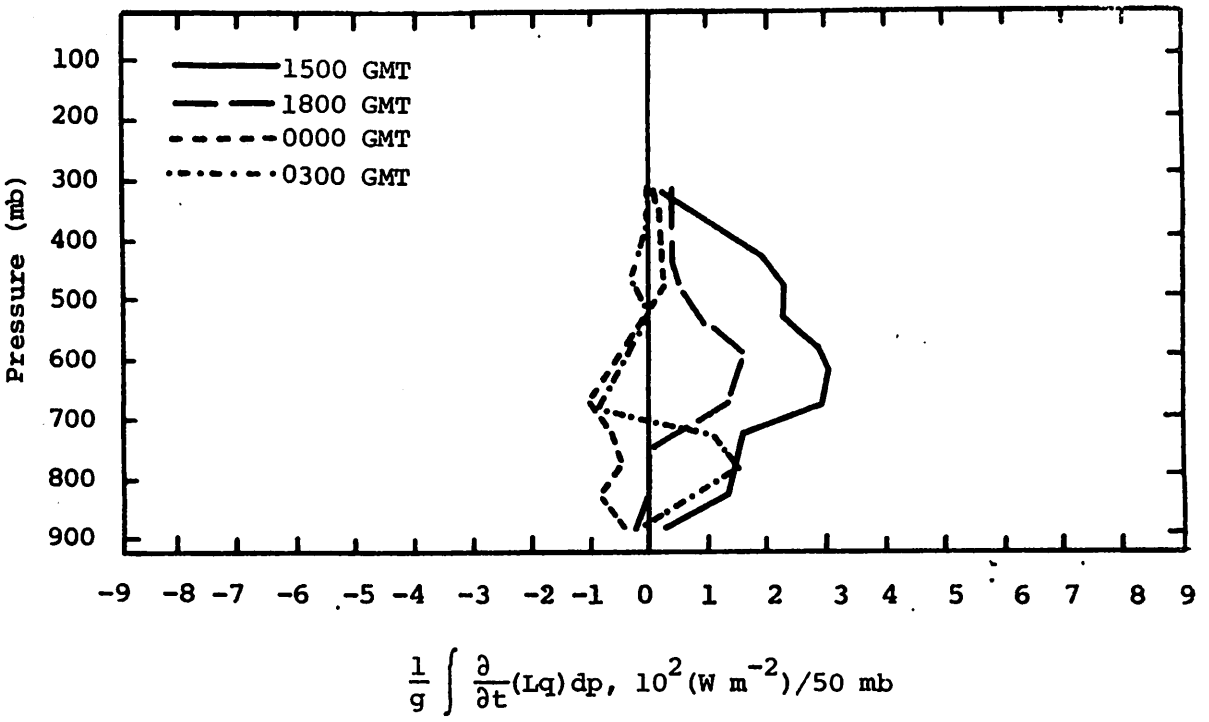

Fig. 5.17.4.3 Vertical profiles of the local change of latent heat energy on 8 July 1977.

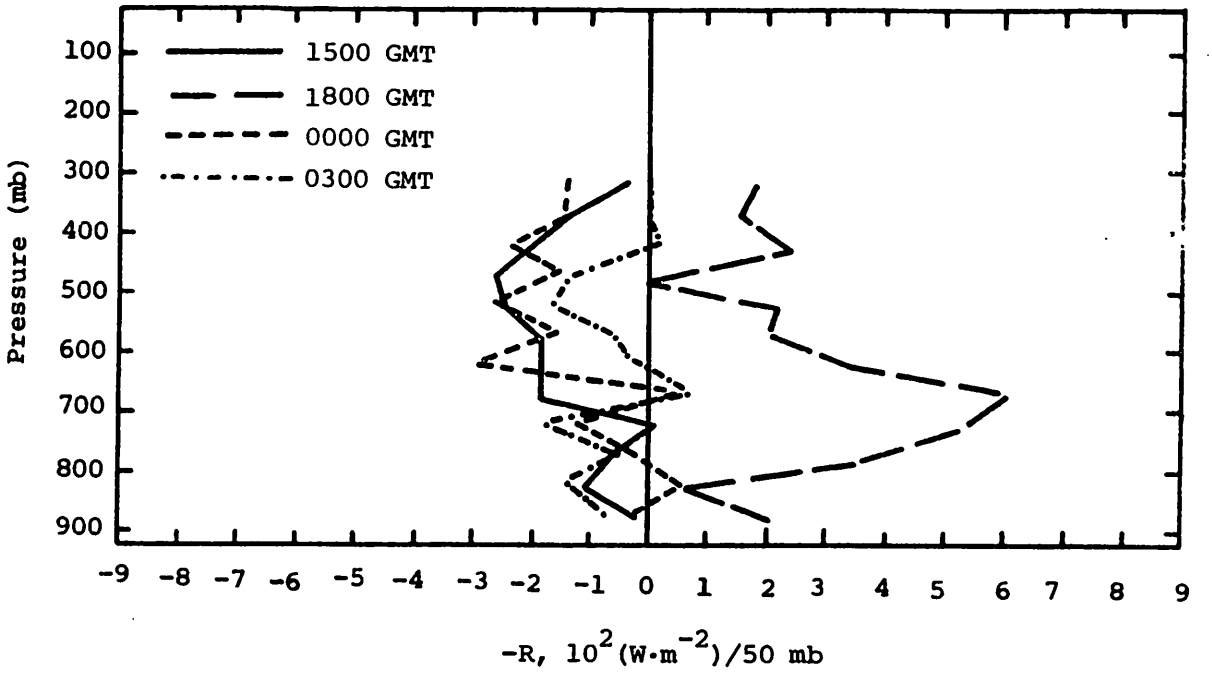

Fig. 5.17.4.4 Vertical profile of the residual of the latent heat energy equation on 8 July 1977.

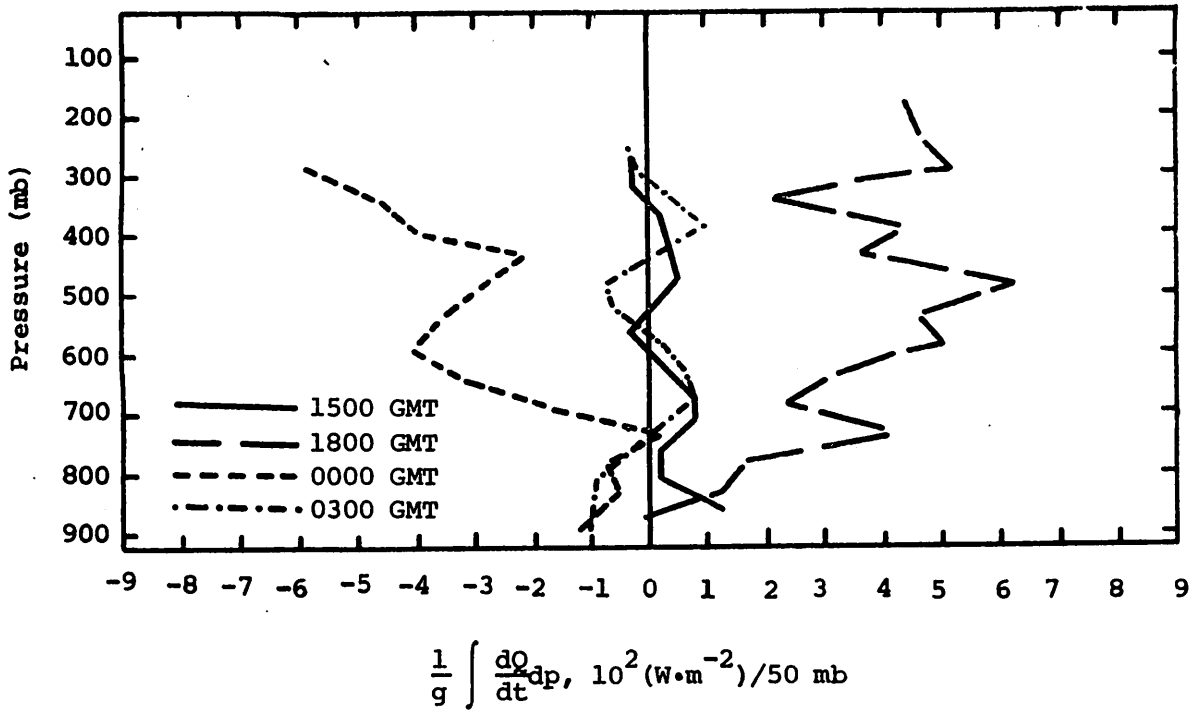

Fig. 5.17.4.5 Vertical profiles of diabatic heating computed from the first law of thermodynamics on 8 July 1977.

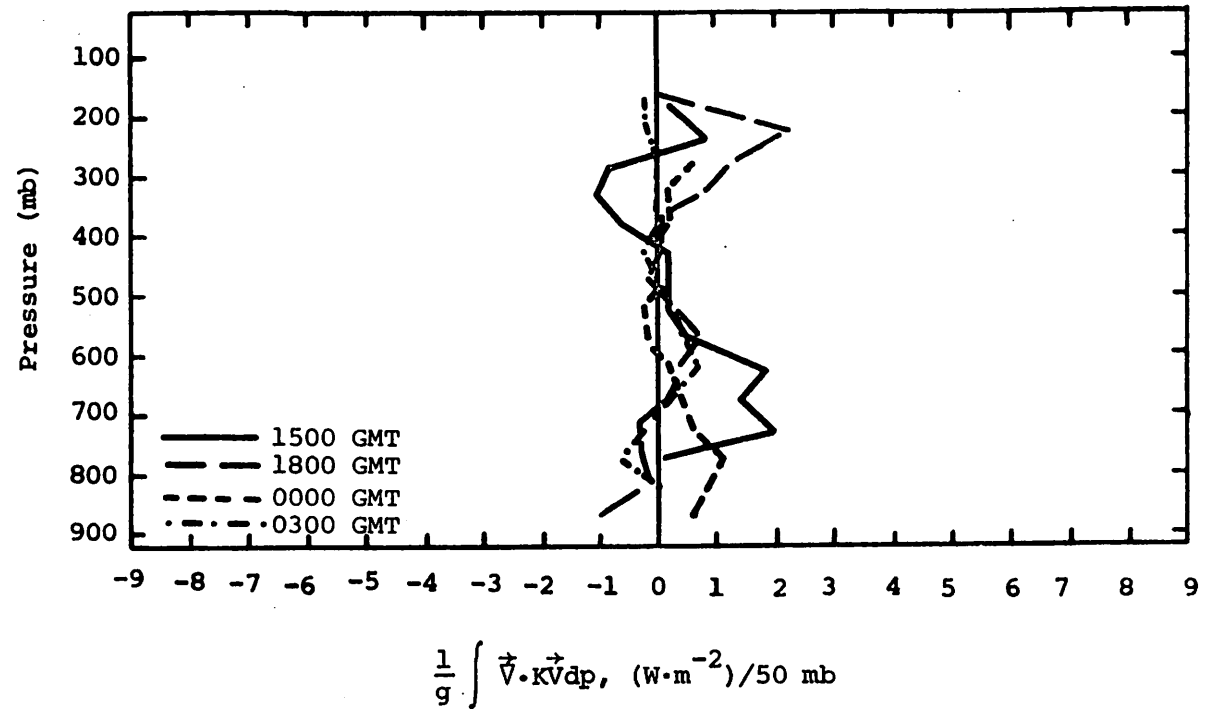

Fig. 5.17.4.6 Vertical profiles of the horizontal flux of kinetic energy on 8 July 1977.

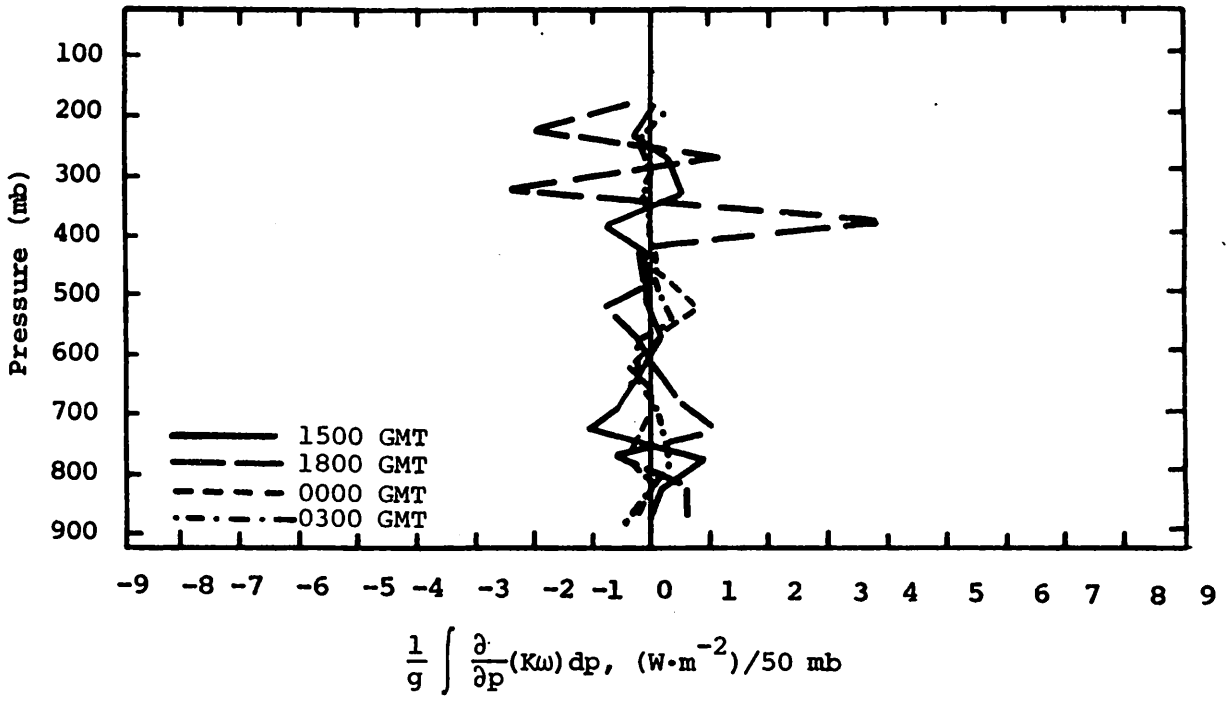

Fig. 5.17.4.7 Vertical profiles of the vertical flux of kinetic energy on 8 July 1977.

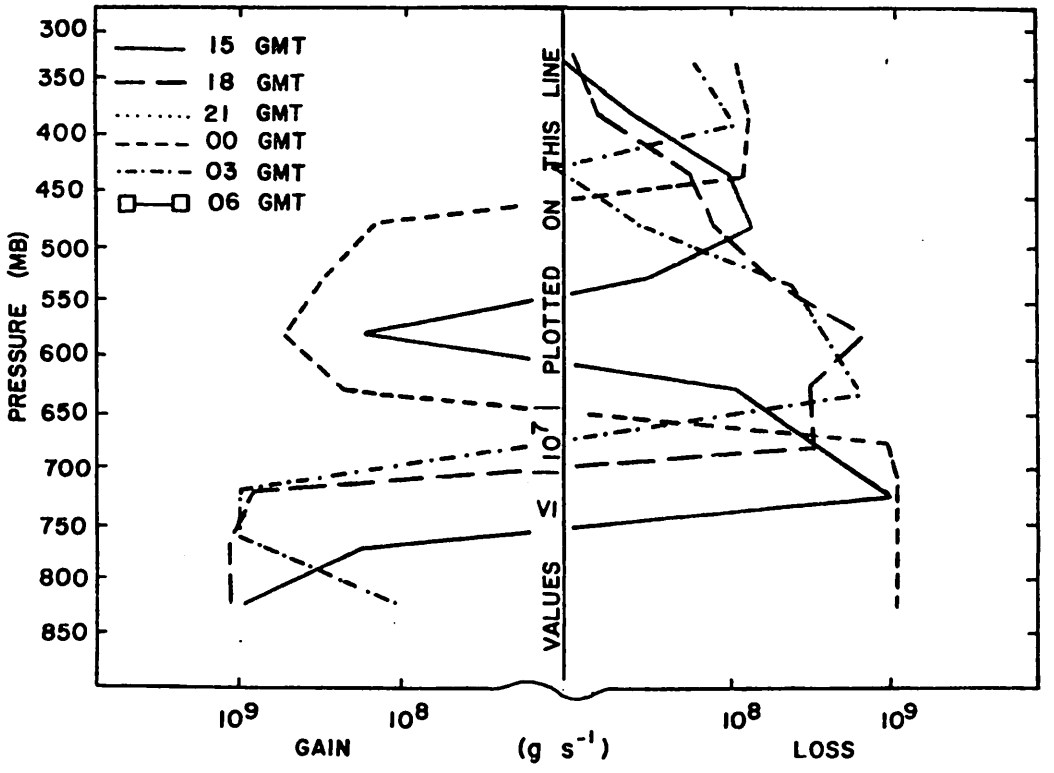

Fig. 5.17.5.1 Net horizontal transport of water vapor through boundaries of 50-mb layers (gm s^{-1}) over the Texas HIPLEX area for 8 July 1977.

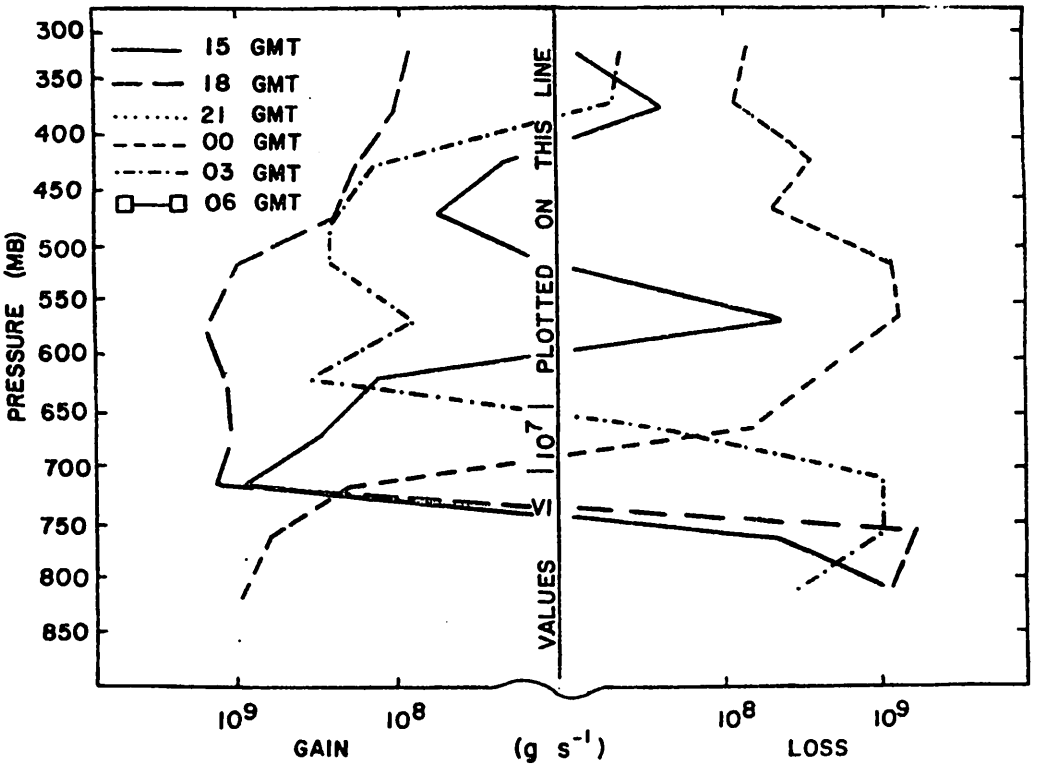

Fig. 5.17.5.2 Net vertical transport of water vapor through boundaries of 50-mb layers (gm s^{-1}) over the Texas HIPLEX area for 8 July 1977.

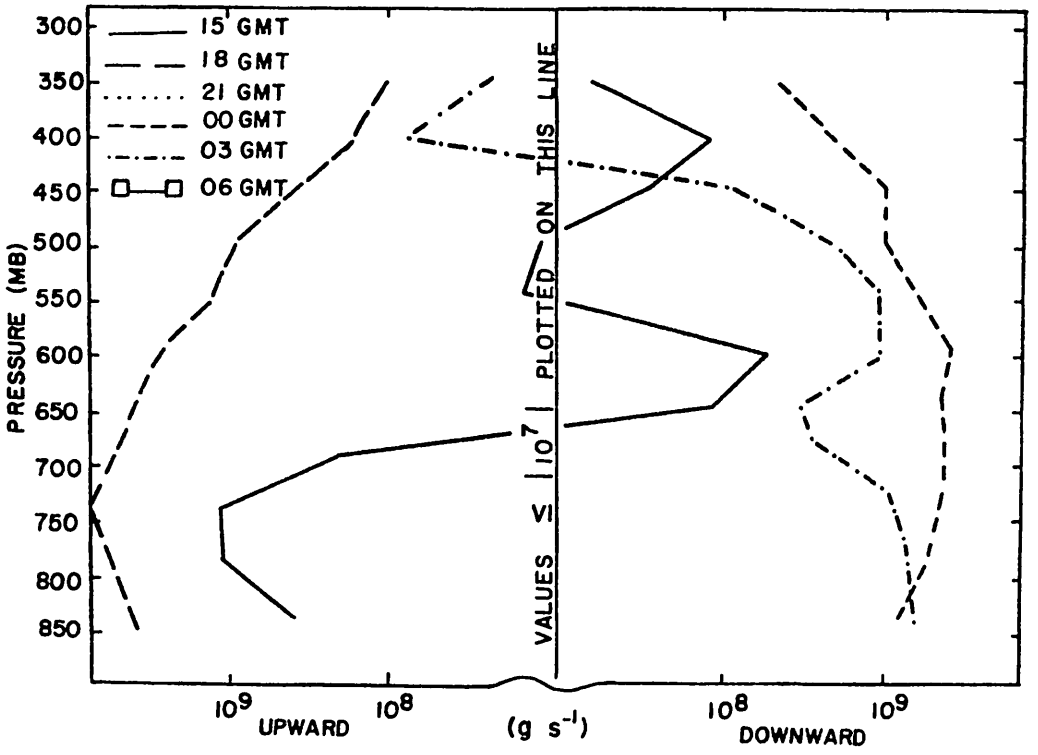

Fig. 5.17.5.3 Vertical transport of water vapor through constant pressure surfaces (gm s^{-1}) over the Texas HIPLEX area for 8 July 1977.

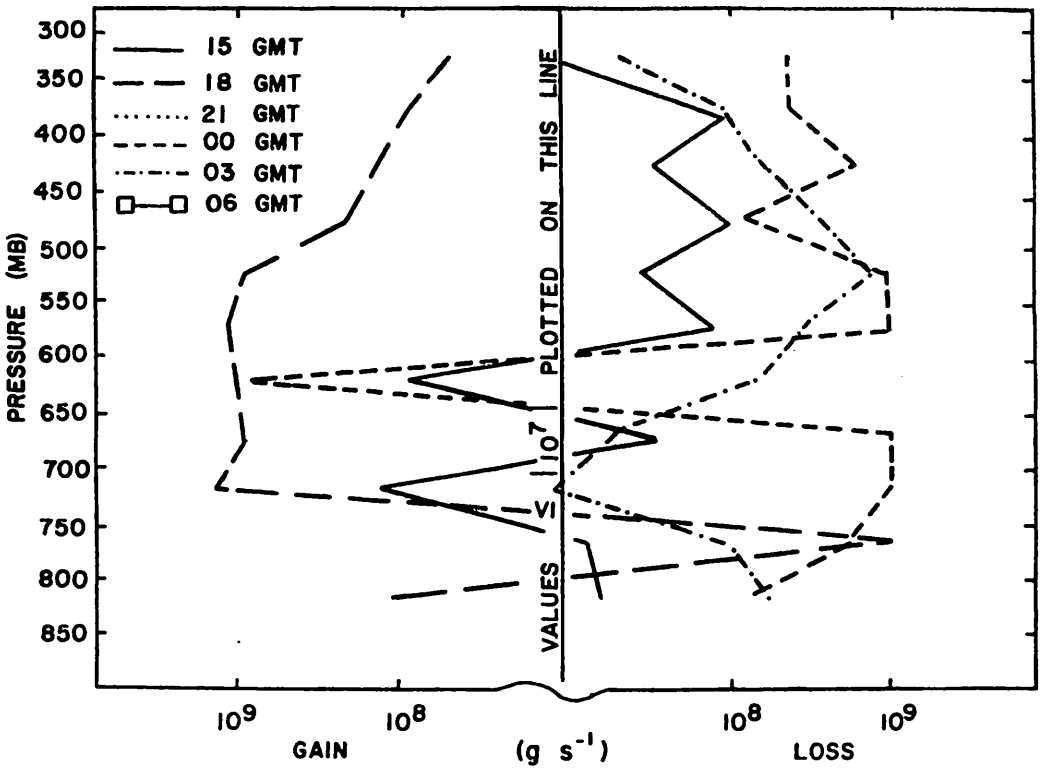

Fig. 5.17.5.4 Combined net horizontal and vertical transport of water vapor through boundaries of 50-mb layers (gm s^{-1}) over the Texas HIPLEX area for 8 July 1977.

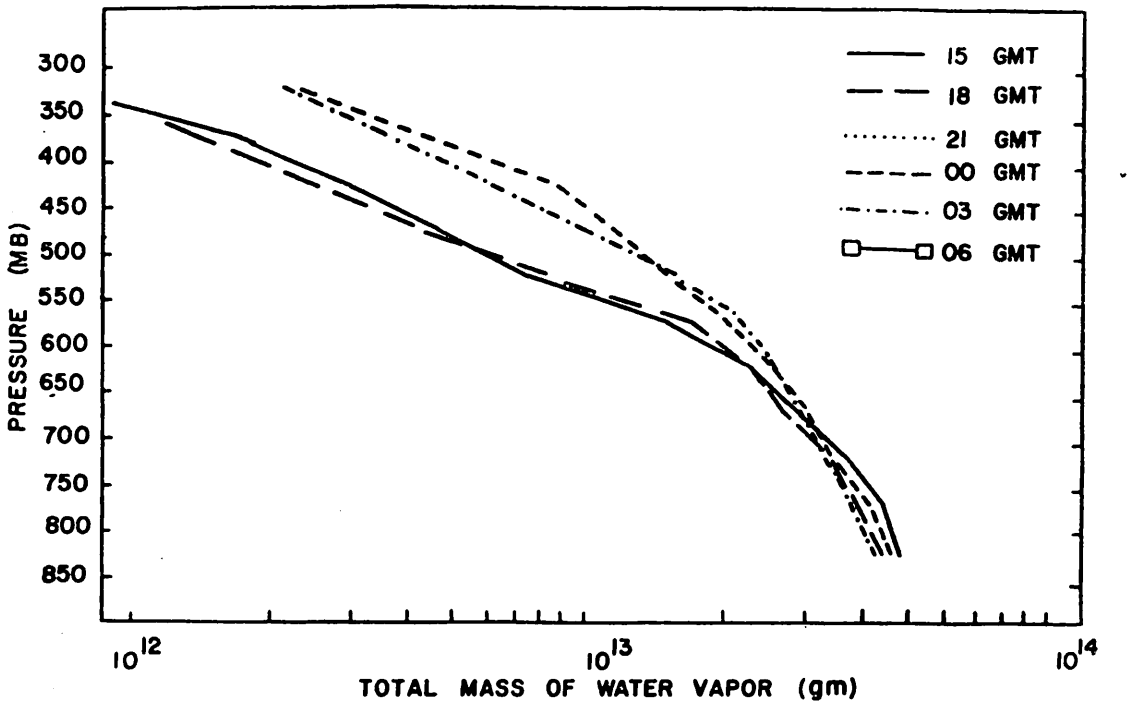

Fig. 5.17.5.5 Total mass of water vapor in layers 50 mb deep (gm) over the Texas HIPLEX area for 8 July 1977.

Figure 5.17.5.6 shows profiles of the local rate-of-change in the total mass of water vapor. These profiles generally show an increase in water vapor between 600 and 500 mb, and a decrease in other layers. Unfortunately, due to missing data at 2100 GMT for layers above 725 mb several profiles could not be presented.

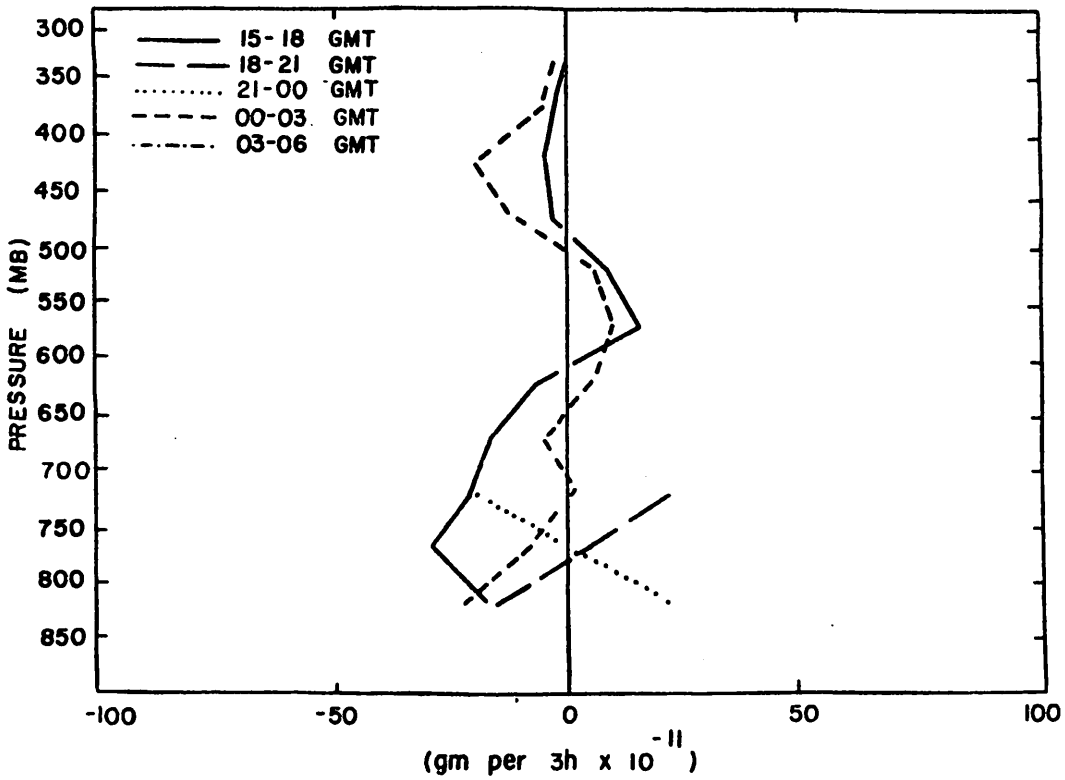

Fig. 5.17.5.6 Local rate-of-change in total mass of water vapor (gm per 3h x 10^{-11}) over the Texas HIPLEX area for 8 July 1977.

5.18 9 July 1977

5.18.1 Radar

Numerous echoes indicating the presence of cells with tops exceeding 9.1 km (30K ft) and extensive areas with tops below 6.1 km (20K ft) were observed on this day between 1700 and 0100 GMT (Fig. 5.18.1.1). The most intense cells occurred between 1900 and 2200 GMT and without any apparent organization.

5.18.2 Surface

The influence of the convective activity is reflected in fields of surface temperature (Fig. 5.18.2.1). Few well-defined centers were present and they were associated with the strongest echoes. Surface temperatures were

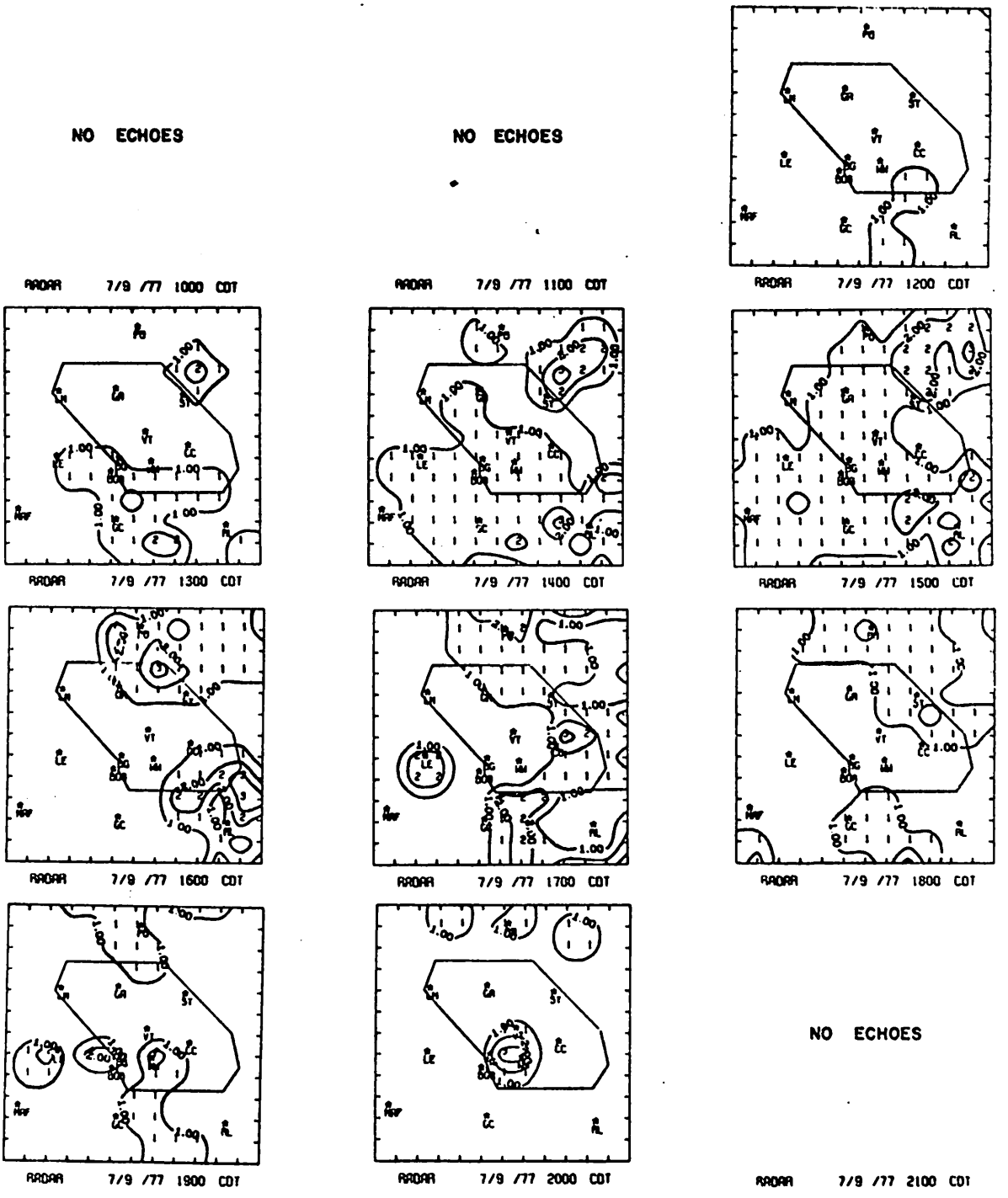

Fig. 5.18.1.1 Radar echoes for 9 July 1977.

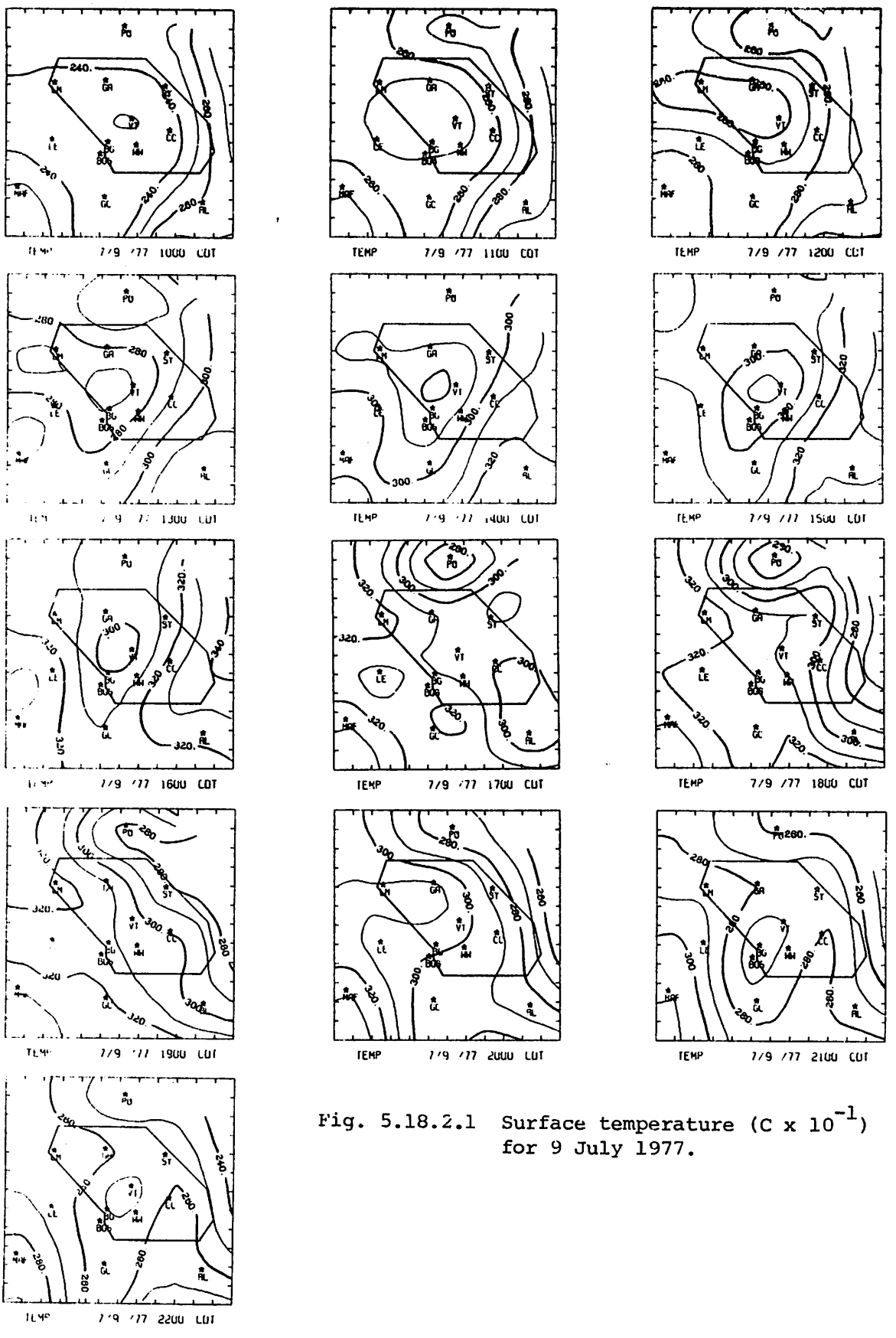

Fig. 5.18.2.1 Surface temperature (C x 10^{-1}) for 9 July 1977.

slightly higher than on 8 July 1977 possibly due to a decreased cloud cover. Values of surface mixing ratio (Fig. 5.18.2.2) were slightly smaller than on 8 July 1977, especially in western portions of the area. Patterns show little variation and generally show increasing magnitudes from west to east. This is reflected in the surface equivalent potential temperature (Fig. 5.18.2.3). A center of minimum surface equivalent potential temperature was observed near Lenorah throughout the day.

Horizontal wind speed remained light which resulted in small values of terrain-induced vertical motion (Fig. 5.18.2.4). Upward terrain-induced vertical motions occurred late in the day due to backing of horizontal winds to the southeast. Although values of surface velocity divergence (Fig. 5.18.2.5) were smaller than on 8 July 1977, prominent centers of convergence and divergence existed. Centers of surface velocity convergence preceded the intense echoes which was followed by centers of surface velocity divergence. This resulted in upward and downward centers of vertical motion 50 mb above the surface (Fig. 5.18.2.6). Values of surface moisture divergence (Fig. 5.18.2.7) and vertical flux of moisture 50 mb above the surface (Fig. 5.18.2.8) were also small due to low surface mixing ratios (Fig. 5.18.2.2) and small surface velocity divergence values (Fig. 5.18.2.5). Several centers of cyclonic vorticity (Fig. 5.18.2.9) developed at 2000 GMT that were associated with the strong echoes. Centers of anticyclonic vorticity developed prior to dissipation.

The sea level pressure pattern (Fig. 5.18.2.10) shows a usual center of low pressure south of Colorado City with higher pressure to the northwest. The surface pressure change (Fig. 5.18.2.11) remained small with a slight decrease indicated throughout the day. The large center of pressure decrease located over Robert Lee at 1700 GMT is erroneous due to missing data at Robert Lee at 1600 GMT.

5.18.3 Upper-Level Kinematic Parameters

The vertical profiles of horizontal mass divergence (Fig. 5.18.3.1) generally show convergence between 800 and 600 mb and mass divergence between 600 and 400 mb at most times of the day. Vertical velocities were near zero and slightly upward between 1500 and 2230 GMT when moderate thunderstorm activity developed over the area (Fig. 5.18.3.2). Vertical velocities were clearly downward after 0000 GMT when storm development diminished.

Horizontal moisture divergence in low levels and in the 600- to 300-mb layer occurred at most times, but relatively strong moisture convergence was

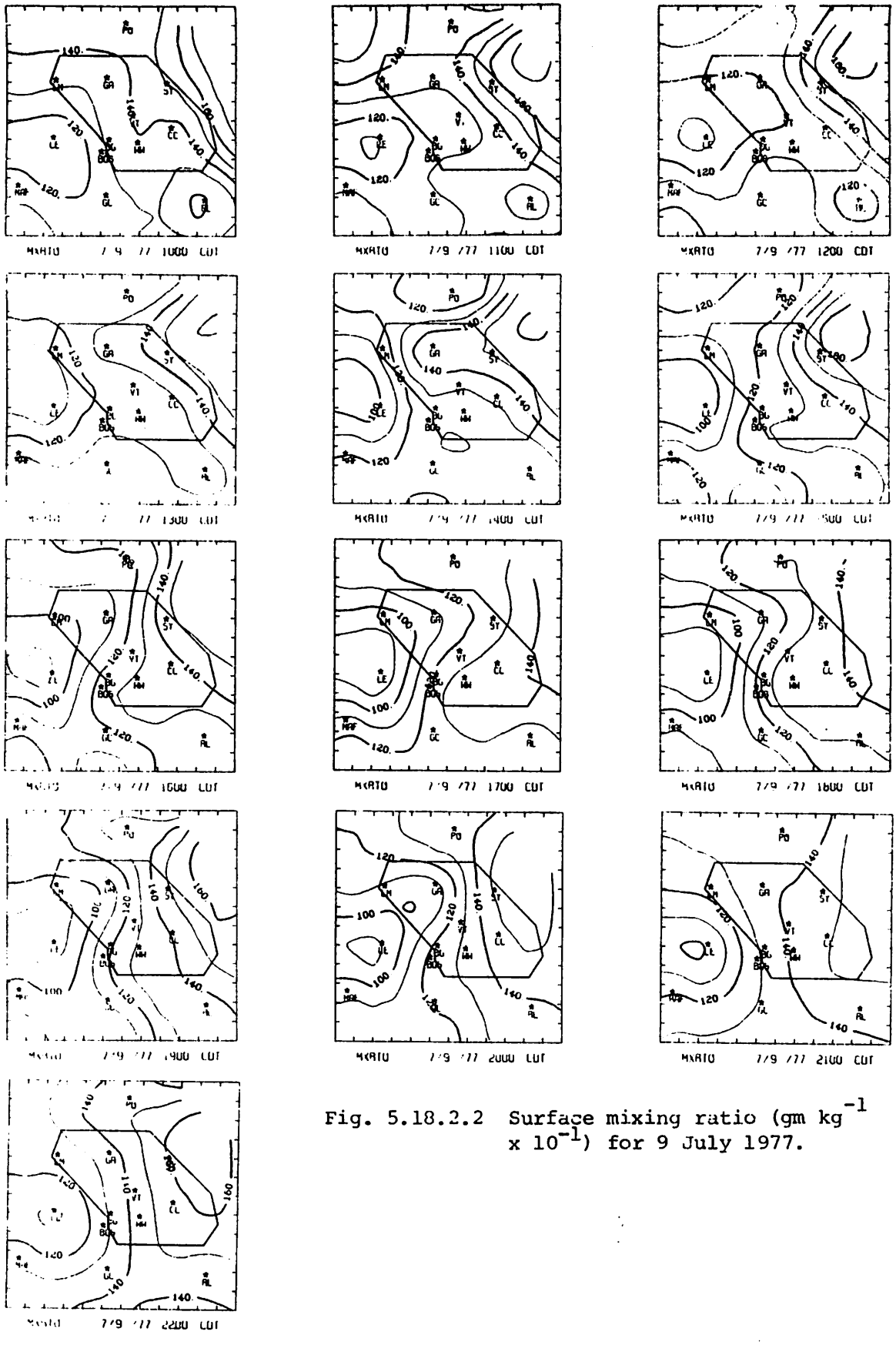

Fig. 5.18.2.2 Surface mixing ratio (gm kg^{-1} x 10^{-1}) for 9 July 1977.

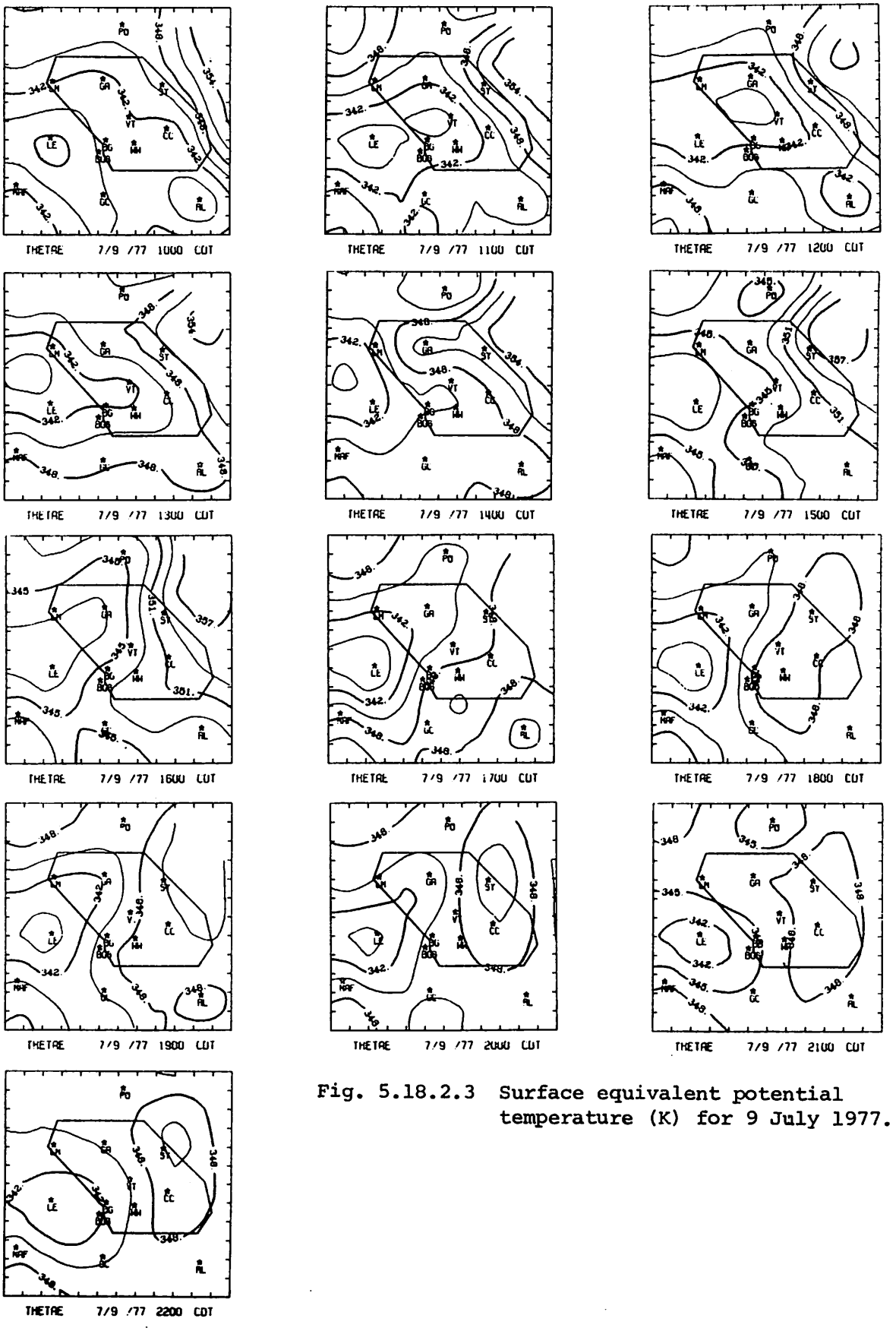

Fig. 5.18.2.3 Surface equivalent potential temperature (K) for 9 July 1977.

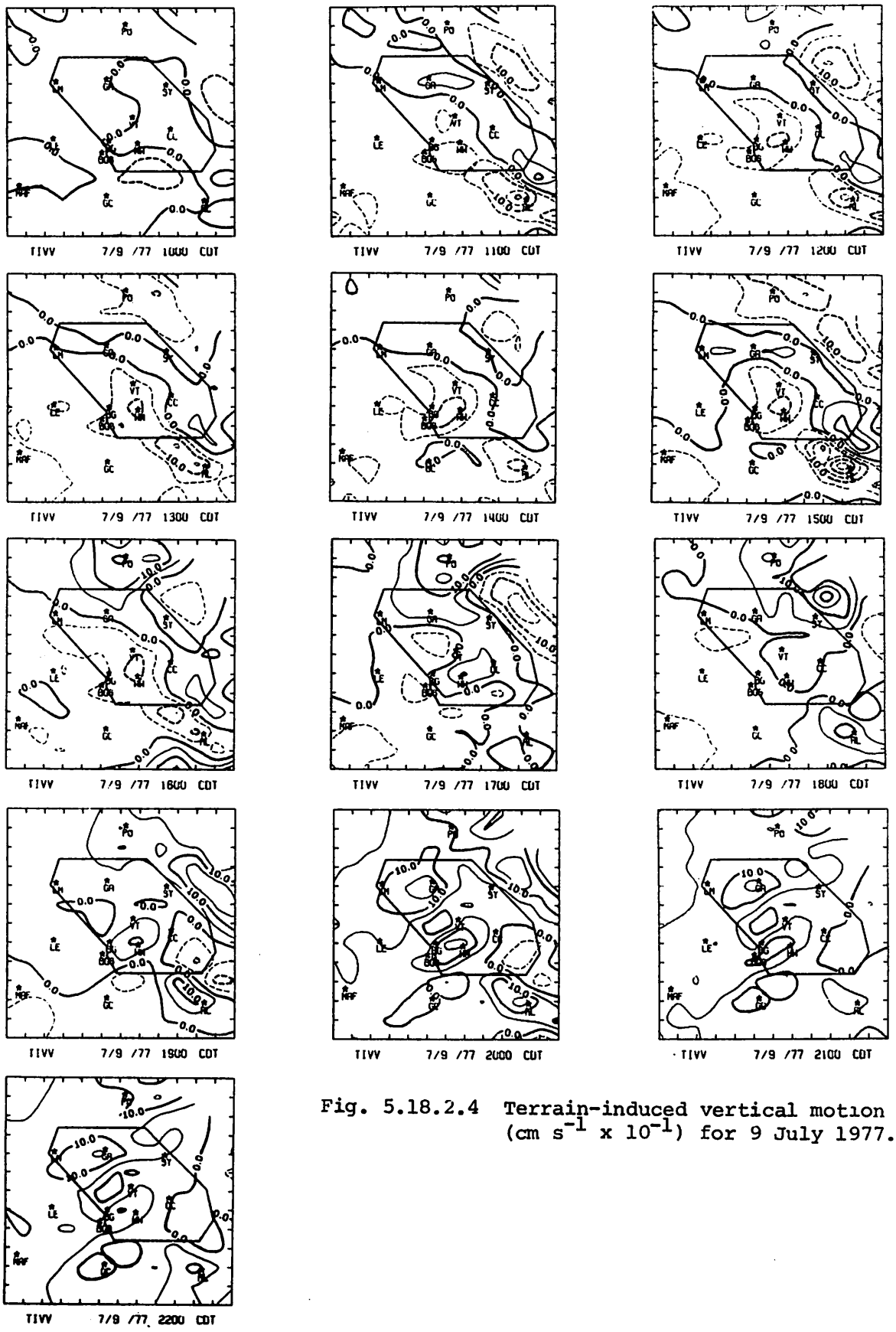

Fig. 5.18.2.4 Terrain-induced vertical motion (cm s^{-1} x 10^{-1}) for 9 July 1977.

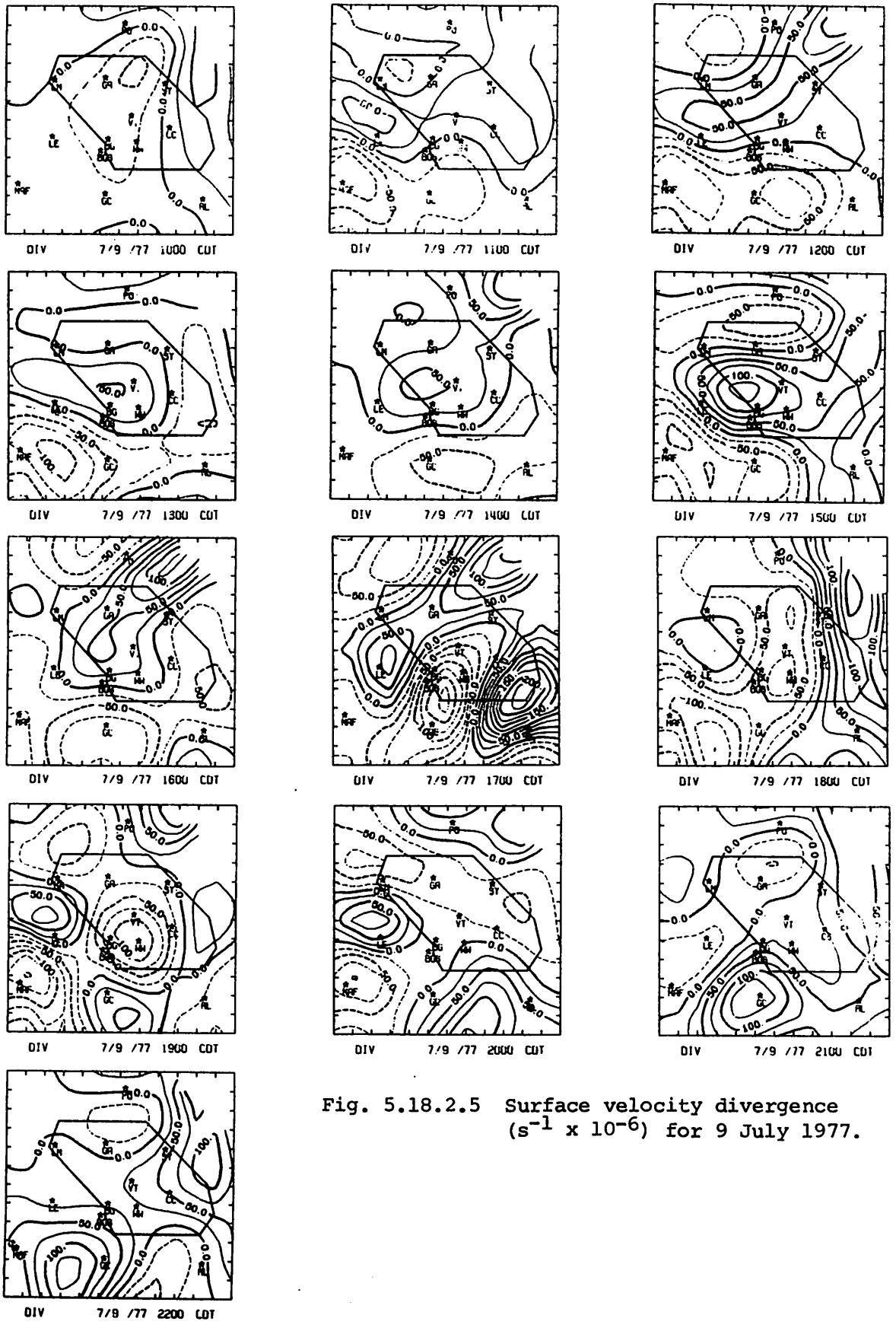

Fig. 5.18.2.5 Surface velocity divergence (s^{-1} x 10^{-6}) for 9 July 1977.

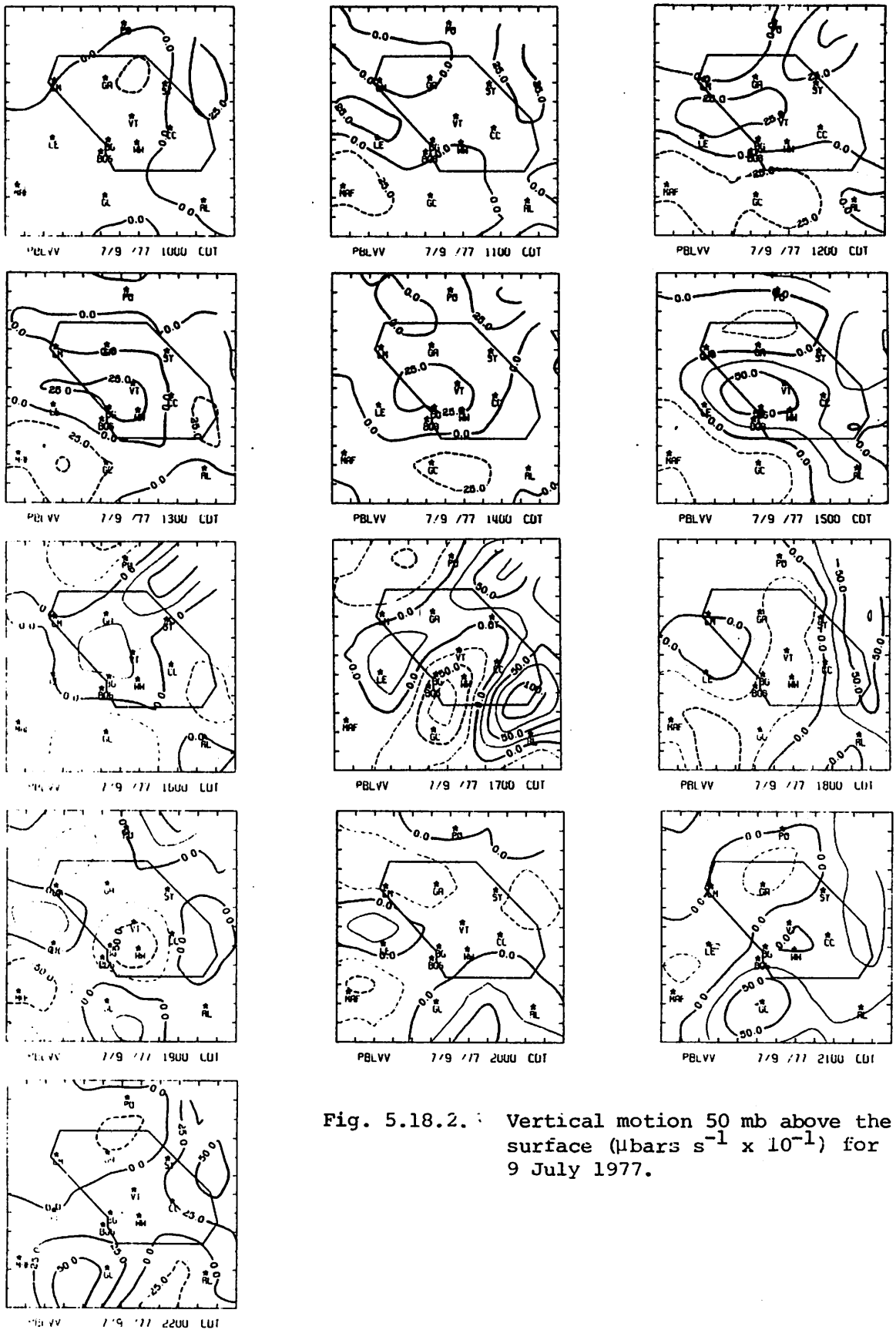

Fig. 5.18.2. Vertical motion 50 mb above the surface (μbars s^{-1} x 10^{-1}) for 9 July 1977.

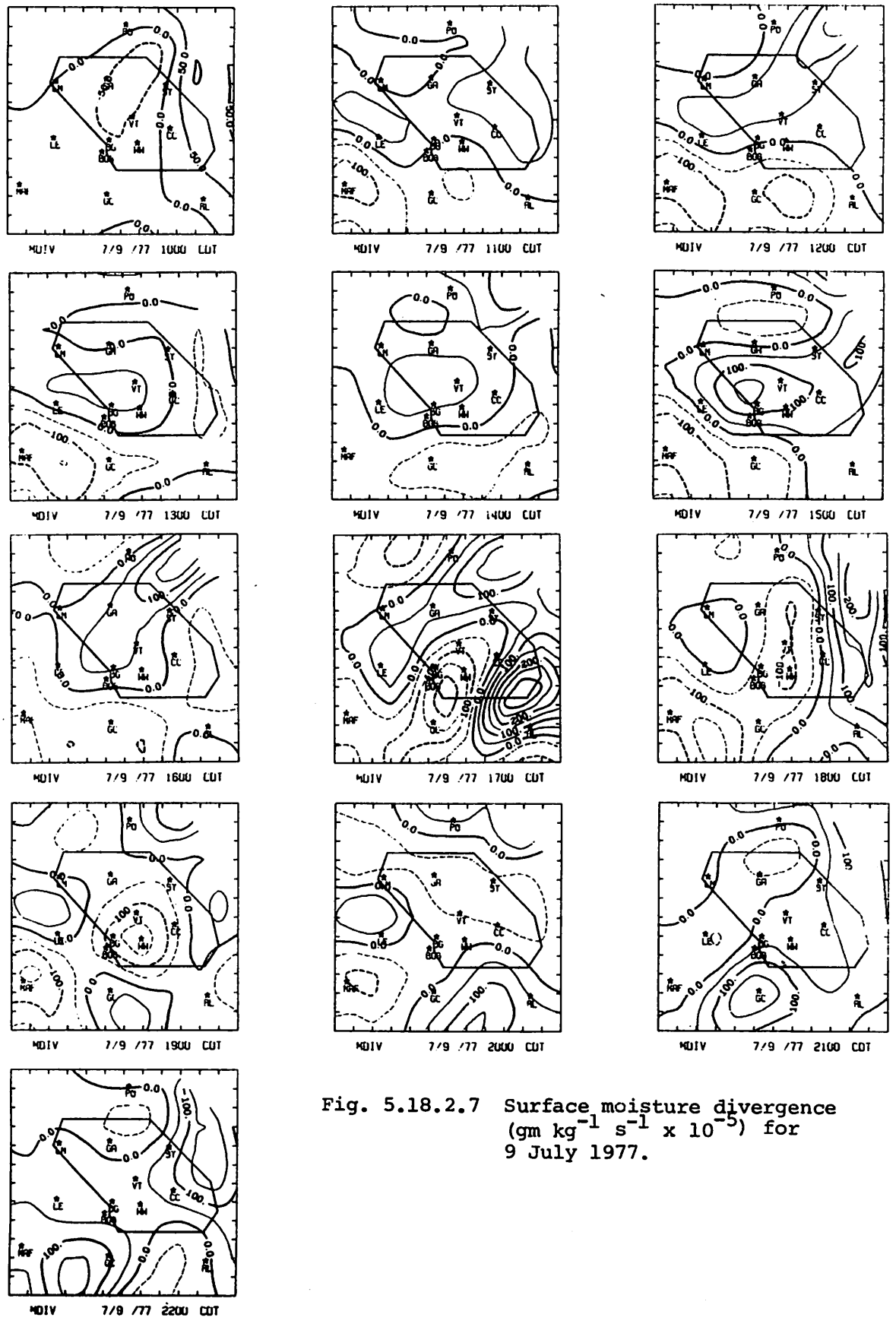

Fig. 5.18.2.7 Surface moisture divergence (gm kg^{-1} s^{-1} x 10^{-5}) for 9 July 1977.

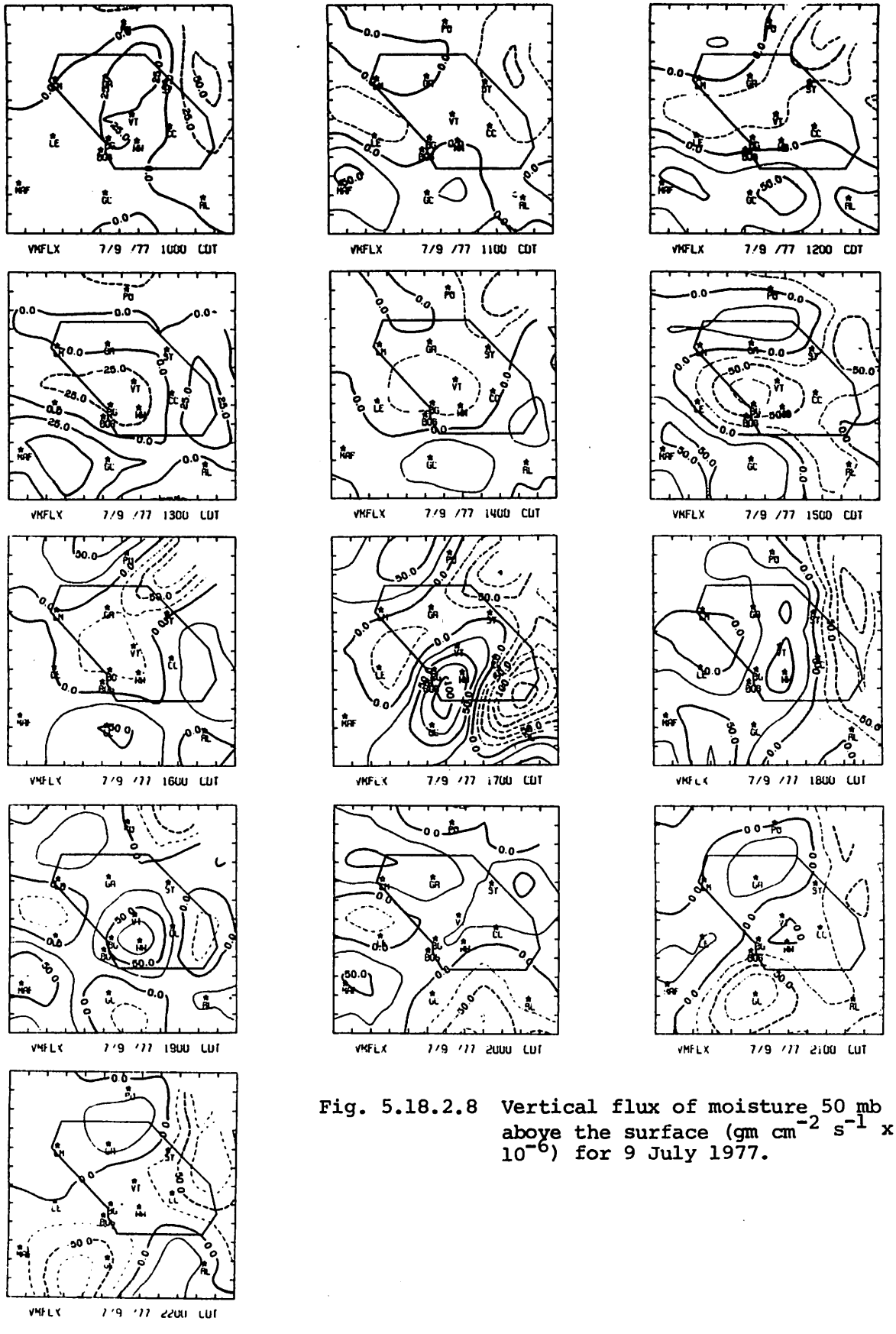

Fig. 5.18.2.8 Vertical flux of moisture 50 mb above the surface (gm cm^{-2} s^{-1} x 10^{-6}) for 9 July 1977.

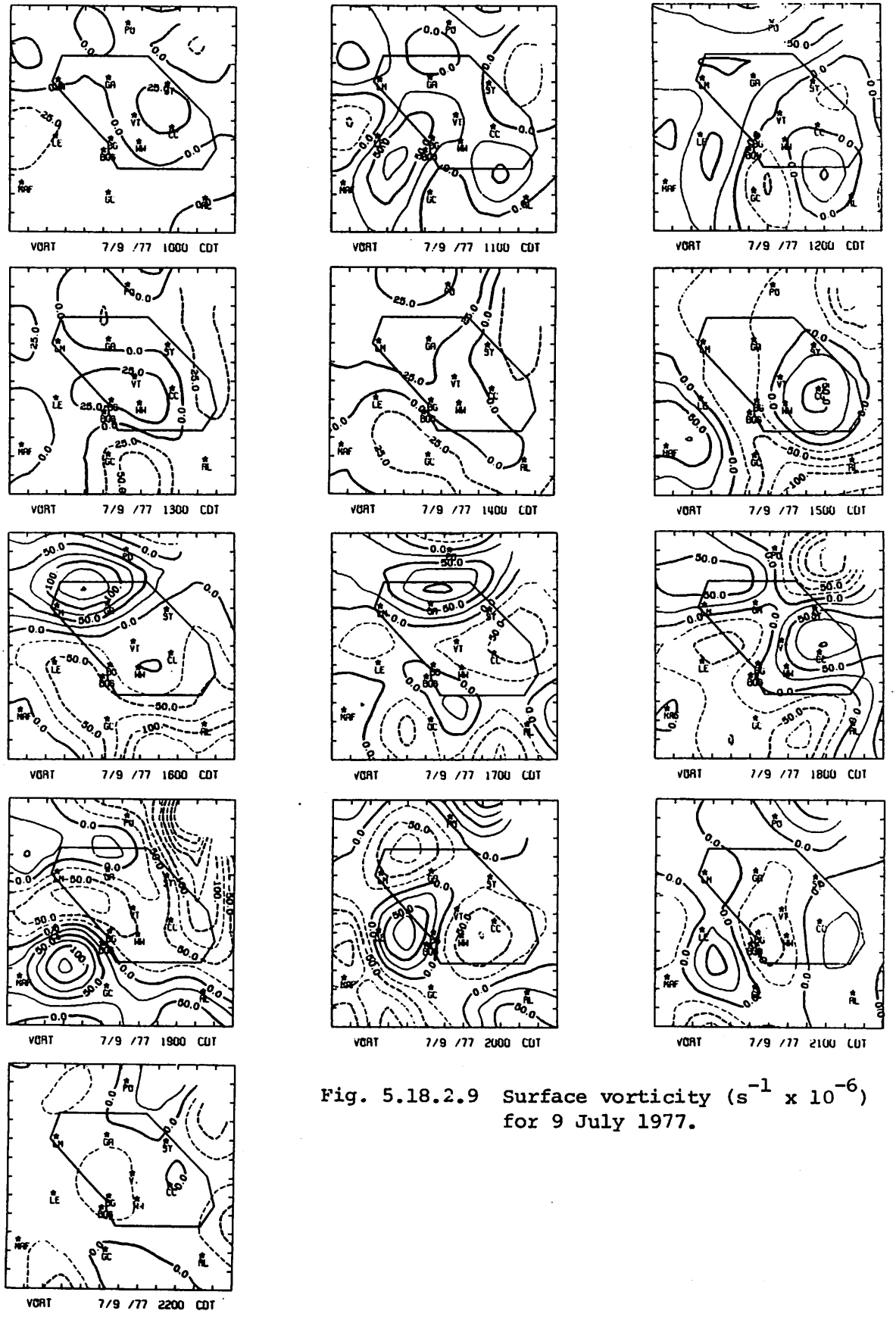

Fig. 5.18.2.9 Surface vorticity (s^{-1} x 10^{-6}) for 9 July 1977.

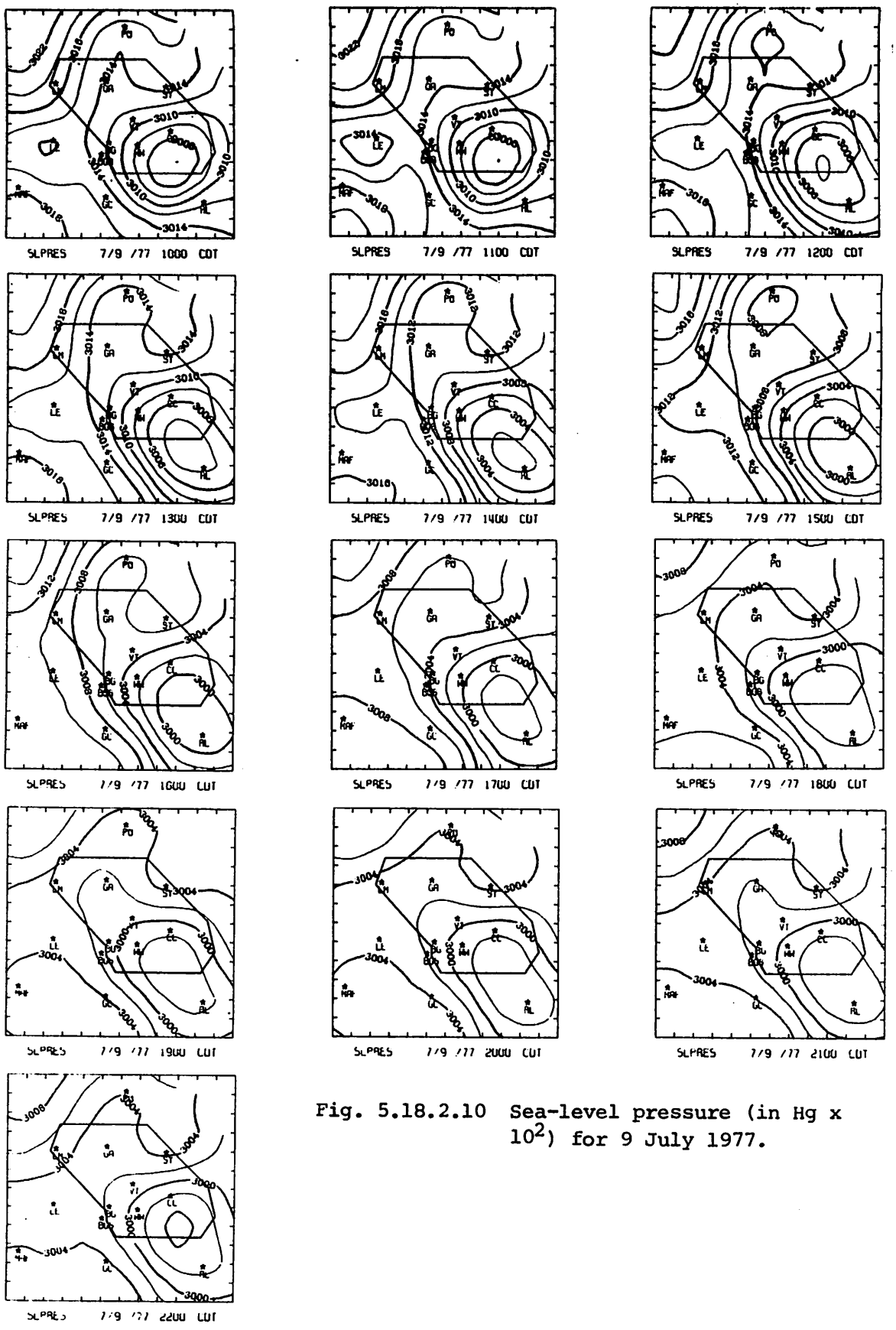

Fig. 5.18.2.10 Sea-level pressure (in Hg x 10^2) for 9 July 1977.

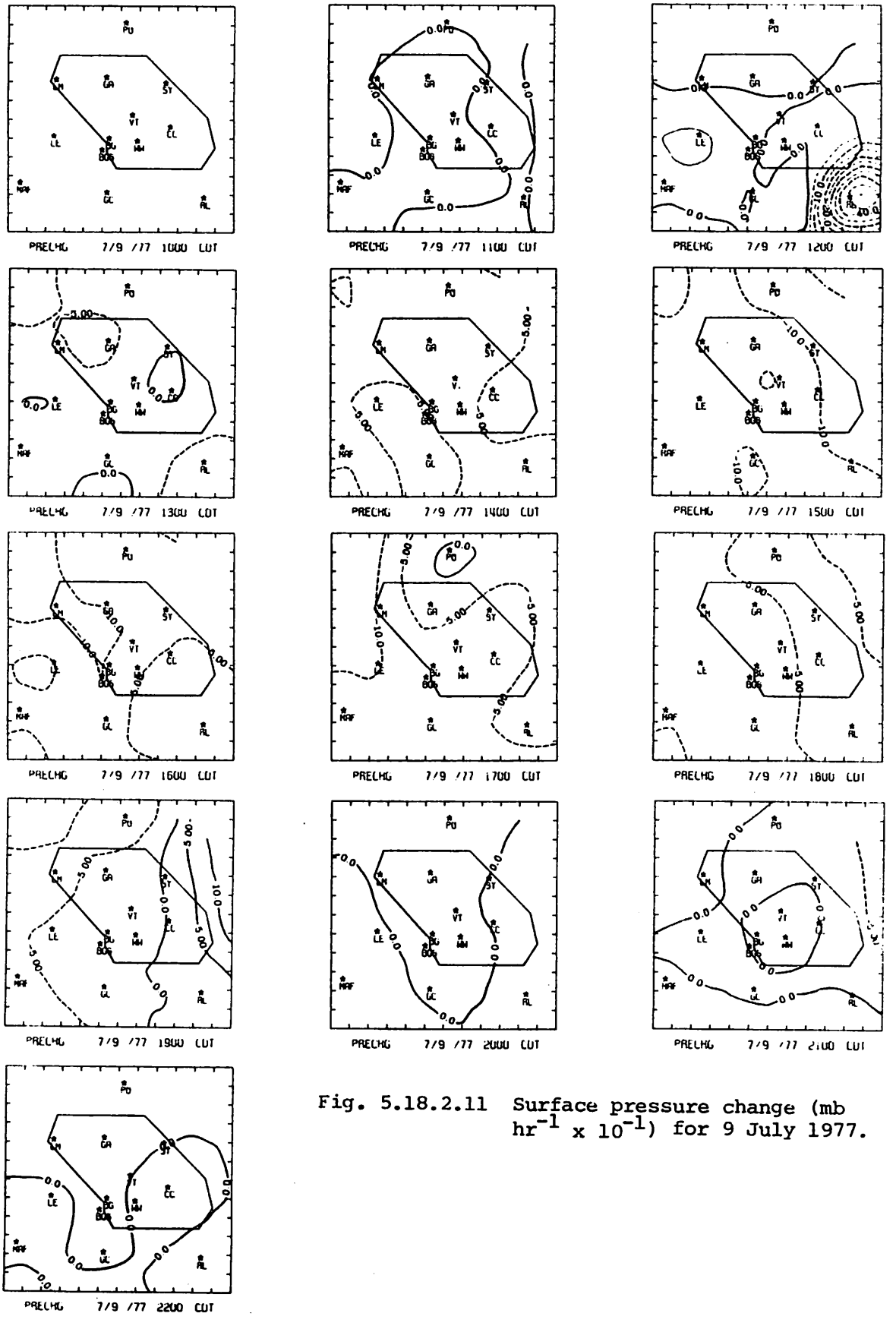

Fig. 5.18.2.11 Surface pressure change (mb hr^{-1} x 10^{-1}) for 9 July 1977.

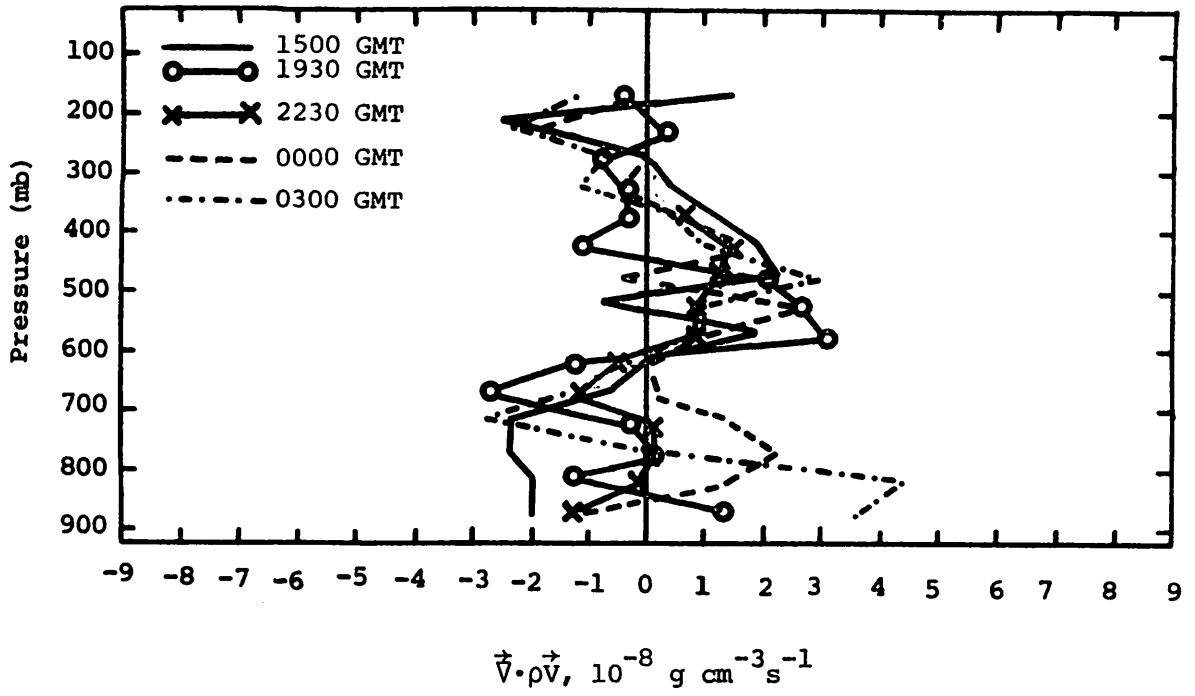

Fig. 5.18.3.1 Vertical profiles of mass divergence on 9 July 1977.

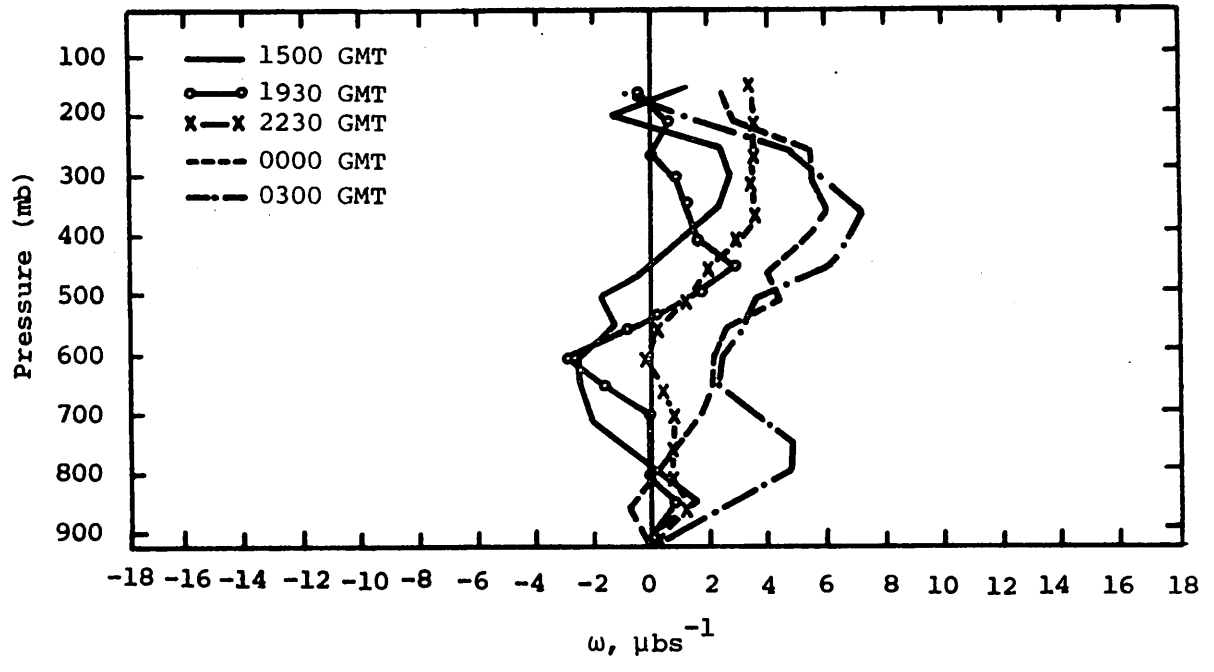

Fig. 5.18.3.2 Vertical profiles of vertical motion on 9 July 1977.

computed between 800 and 600 mb before and during storm development (Fig. 5.18.3.3).

5.18.4 Energetics

Net horizontal flux divergence of latent heat energy below 850 mb and above 600 mb with flux convergence between 850 and 600 mb, for all time periods, is shown in Figure 5.18.4.1. Vertical flux convergence of latent heat energy was calculated in low levels and above 600 mb with vertical flux divergence of latent heat energy present between 800 and 600 mb at all times (Fig. 5.18.4.2). Local changes of latent heat energy (Fig. 5.18.4.3) were near zero at 1500 and 1930 GMT but were large positive at 2230 GMT at mid levels when precipitation was ongoing and diminishing.

Profiles of the residual of the latent heat budget (Fig. 5.18.4.4) were small at all levels at 1500 and 1930 GMT but showed large negative value (evaporation and gains of latent heat content) at most levels at 2230 GMT. This profile was likely associated with evaporation of cloud water and precipitation as activity was generally decreasing over the network at this time.

The diabatic heating profiles (Fig. 5.18.4.5) were generally similar to the -R profiles from the latent heat budget equation. Diabatic effects were small at most levels and times but the large cooling that should have been associated with evaporation at 2230 GMT in mid levels was not clearly shown. Since a dry adiabatic lapse rate was present between about the surface and 650 mb at 2230 GMT, turbulent fluxes of both heat and moisture may have been important in creating differences in these profiles at this time.

The horizontal and vertical flux divergence profiles of kinetic energy (Figs. 5.18.4.6 and 5.18.4.7) were very near zero at all times and levels, and were not noticeably related to the observed echo patterns.

5.18.5 Water Vapor Budget

Because of missing or incomplete sounding data the water vapor budget could not be computed on this day.

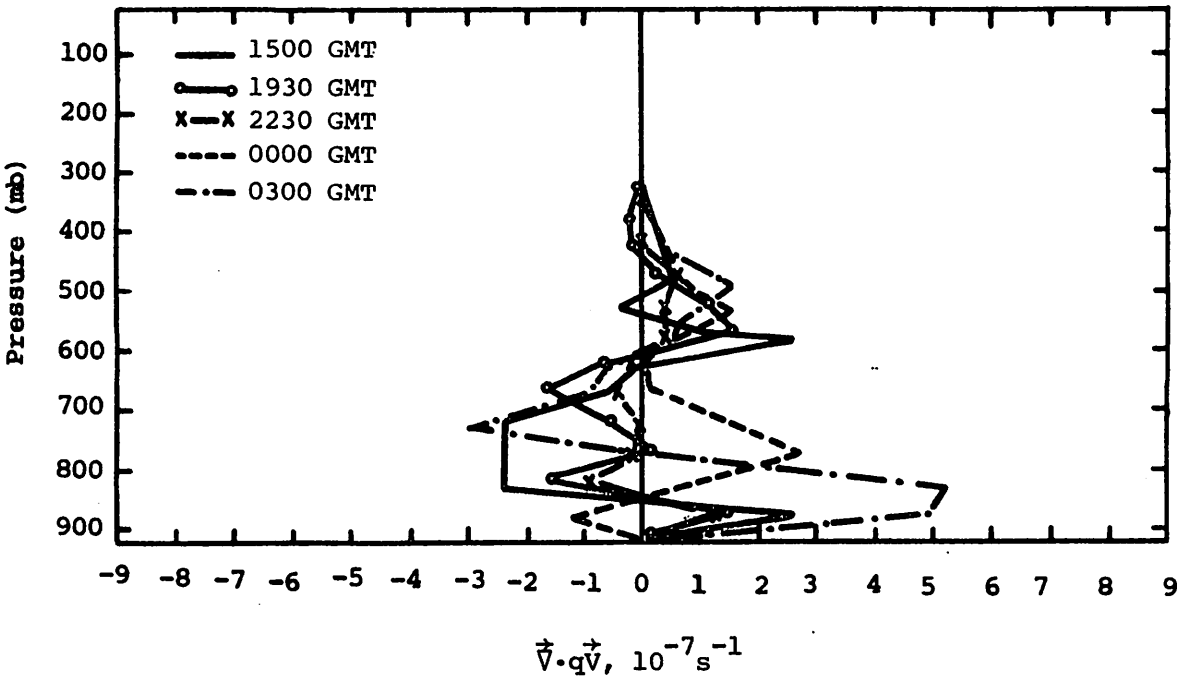

Fig. 5.18.3.3 Vertical profiles of moisture divergence on 9 July 1977.

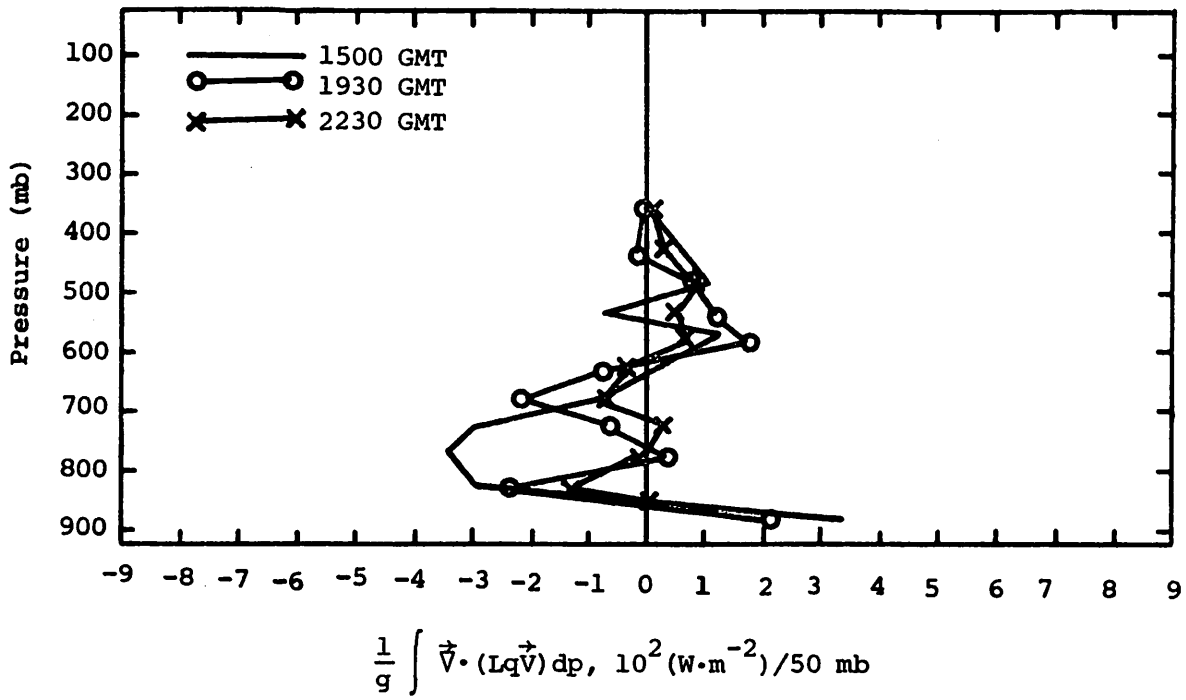

Fig. 5.18.4.1 Vertical profiles of the horizontal flux of latent heat energy on 9 July 1977.

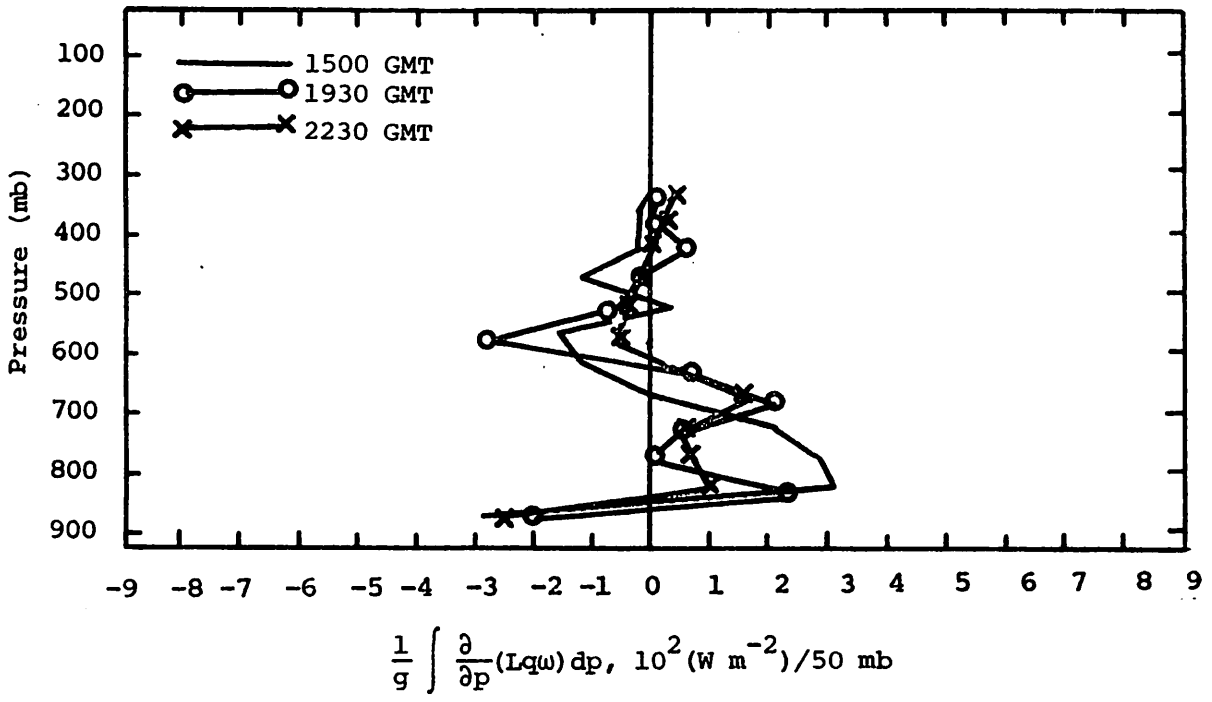

Fig. 5.18.4.2 Vertical profiles of the vertical flux of latent heat energy on 9 July 1977.

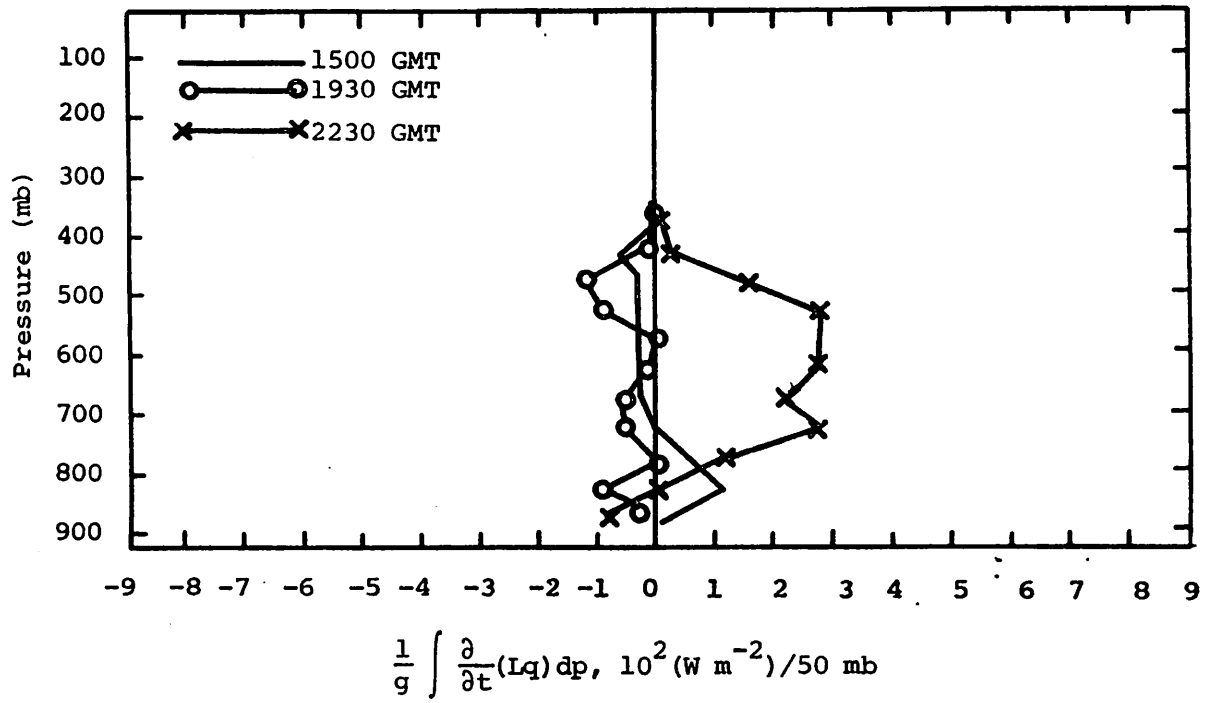

Fig. 5.18.4.3 Vertical profiles of the local change of latent heat energy on 9 July 1977.

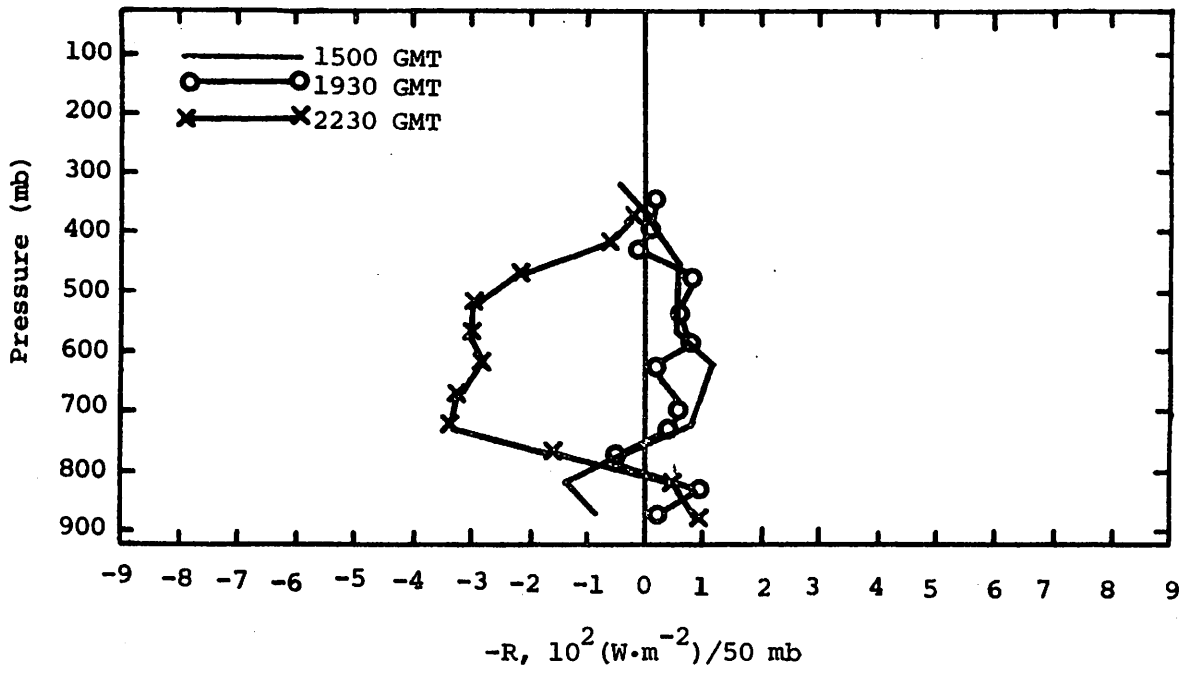

Fig. 5.18.4.4 Vertical profile of the residual of the latent heat energy equation on 9 July 1977.

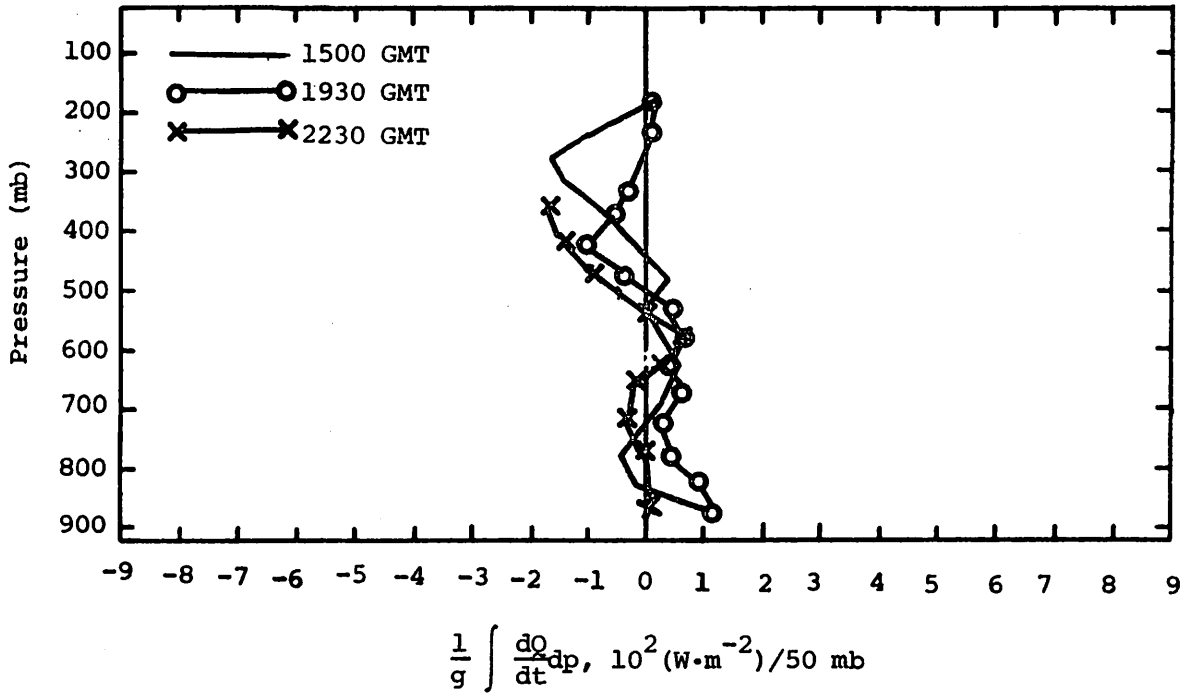

Fig. 5.18.4.5 Vertical profiles of diabatic heating computed from the first law of thermodynamics on 9 July 1977.

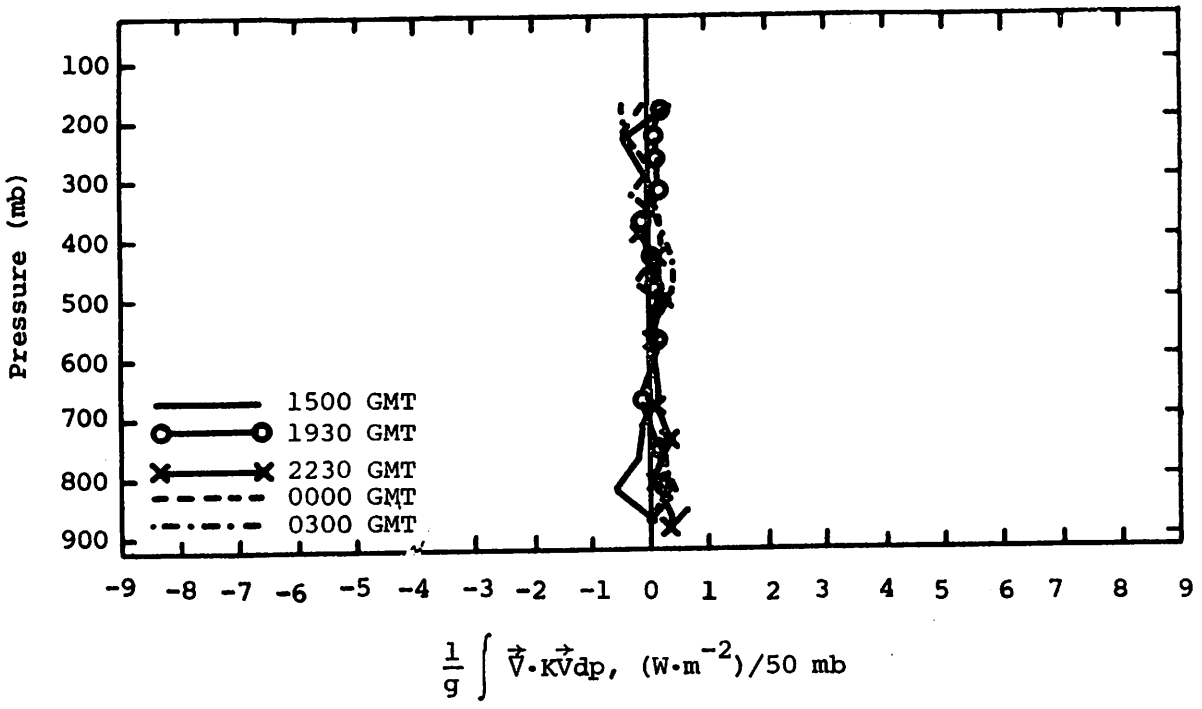

Fig. 5.18.4.6 Vertical profiles of the horizontal flux of kinetic energy on 9 July 1977.

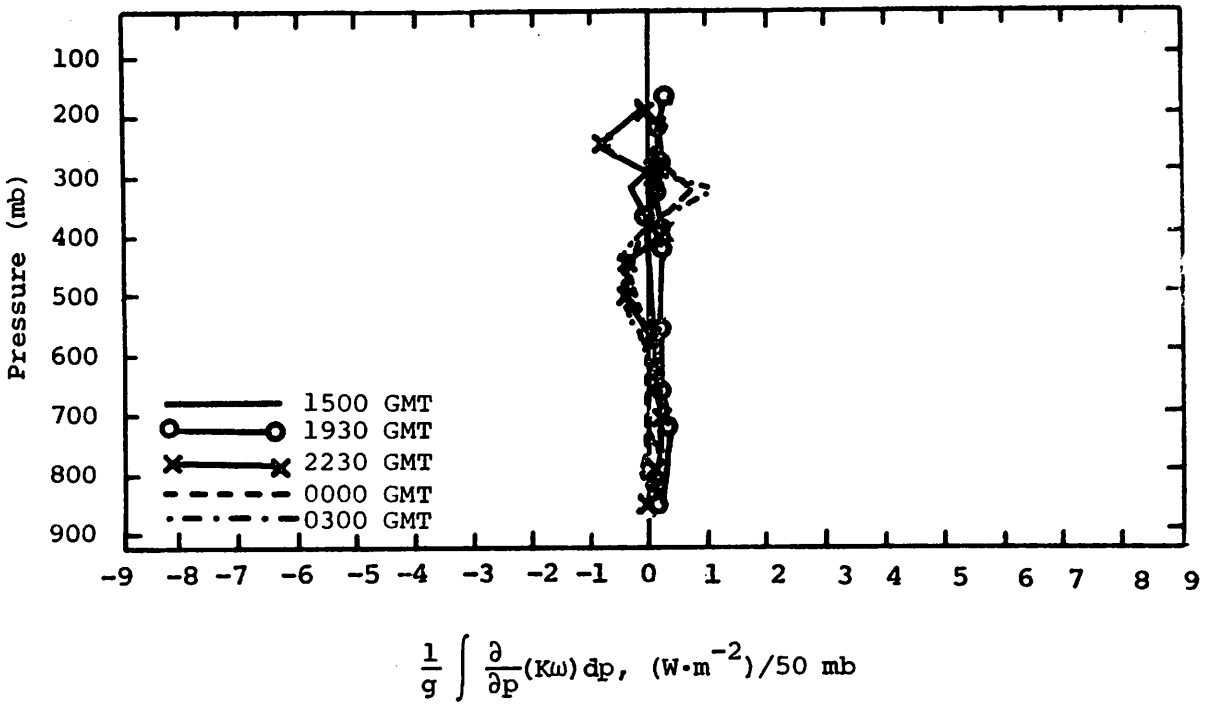

Fig. 5.18.4.7 Vertical profiles of the vertical flux of kinetic energy on 9 July 1977.

5.19 10 July 1977

5.19.1 Radar

There were no radar echoes observed on this day.

5.19.2 Surface

Surface temperatures (Fig. 5.19.2.1) show the effects of diurnal surface heating with maximum temperatures exceeding 36°C. Surface mixing ratios (Fig. 5.19.2.2) show low values throughout the day with a moist center located over Vincent, and a dry center over Lenorah. These moist and dry areas are also reflected in charts of surface equivalent potential temperature (Fig. 5.19.2.3).

Terrain-induced vertical motion (Fig. 5.19.2.4) remained small in magnitude throughout the day and made no significant contribution to kinematic vertical velocity. Surface velocity devergence (Fig. 5.19.2.5) and vertical motion 50 mb above the surface (Fig. 5.19.2.6) show small centers throughout the day. These patterns also are reflected by surface moisture divergence (Fig. 5.19.2.7) and vertical flux of moisture 50 mb above the surface (Fig. 5.19.2.8) and remain small in magnitude due to the low values of surface mixing ratio. Surface vorticity fields (Fig. 5.19.2.9) show no large organized centers, and remain variable throughout the day. Surface vorticity decreased with time during the day due to nocturnal reduction in surface wind speed.

Sea level pressure patterns (Fig. 5.19.2.10) remained similar to previous days, showing a center of low pressure near Robert Lee. Surface pressure changes (Fig. 5.19.2.11) were small. The decrease in pressure observed at 2000 GMT was due to missing data at Vincent.

5.19.3 Upper-Level Kinematic Parameters

Horizontal mass divergence in low levels and mass convergence at mid- and upper-levels are the dominant features of the profiles in Fig. 5.19.3.1. Vertical velocities are downward at most levels and times except 0300 GMT when weak upward motion was computed (Fig. 5.19.3.2). The pattern is generally consistent with no development of thunderstorm activity during the day. The moisture divergence profiles showed divergence in low levels and mostly weak convergence above 700 mb at all times except 0300 GMT when the reverse vertical pattern was computed (Fig. 5.19.3.3).

5.19.4 Energetics

Net horizontal outflow of latent heat energy in low levels and weak inflow in mid levels was computed at most times during the day (Fig. 5.19.4.1)

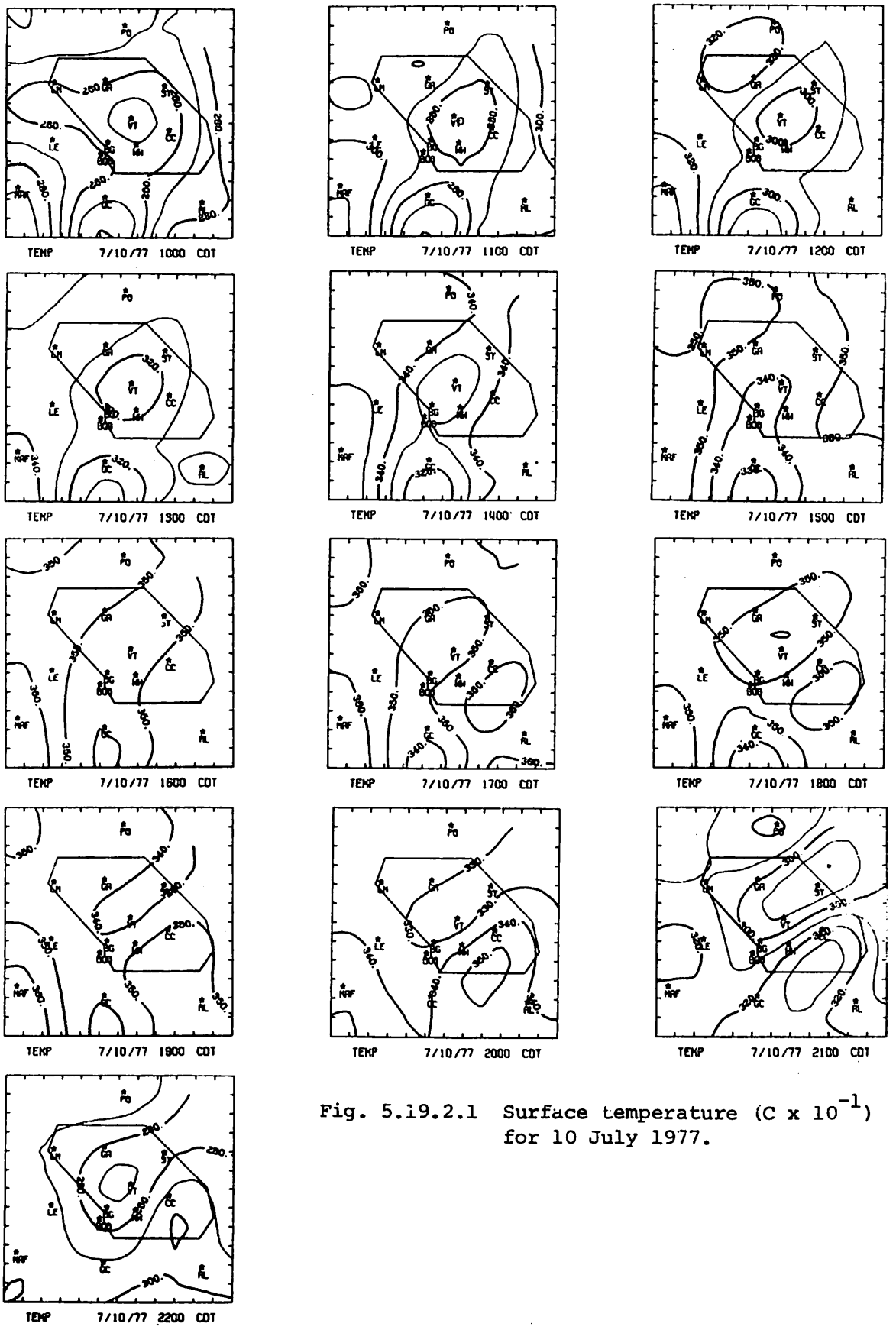

Fig. 5.19.2.1 Surface temperature (C x 10^{-1}) for 10 July 1977.

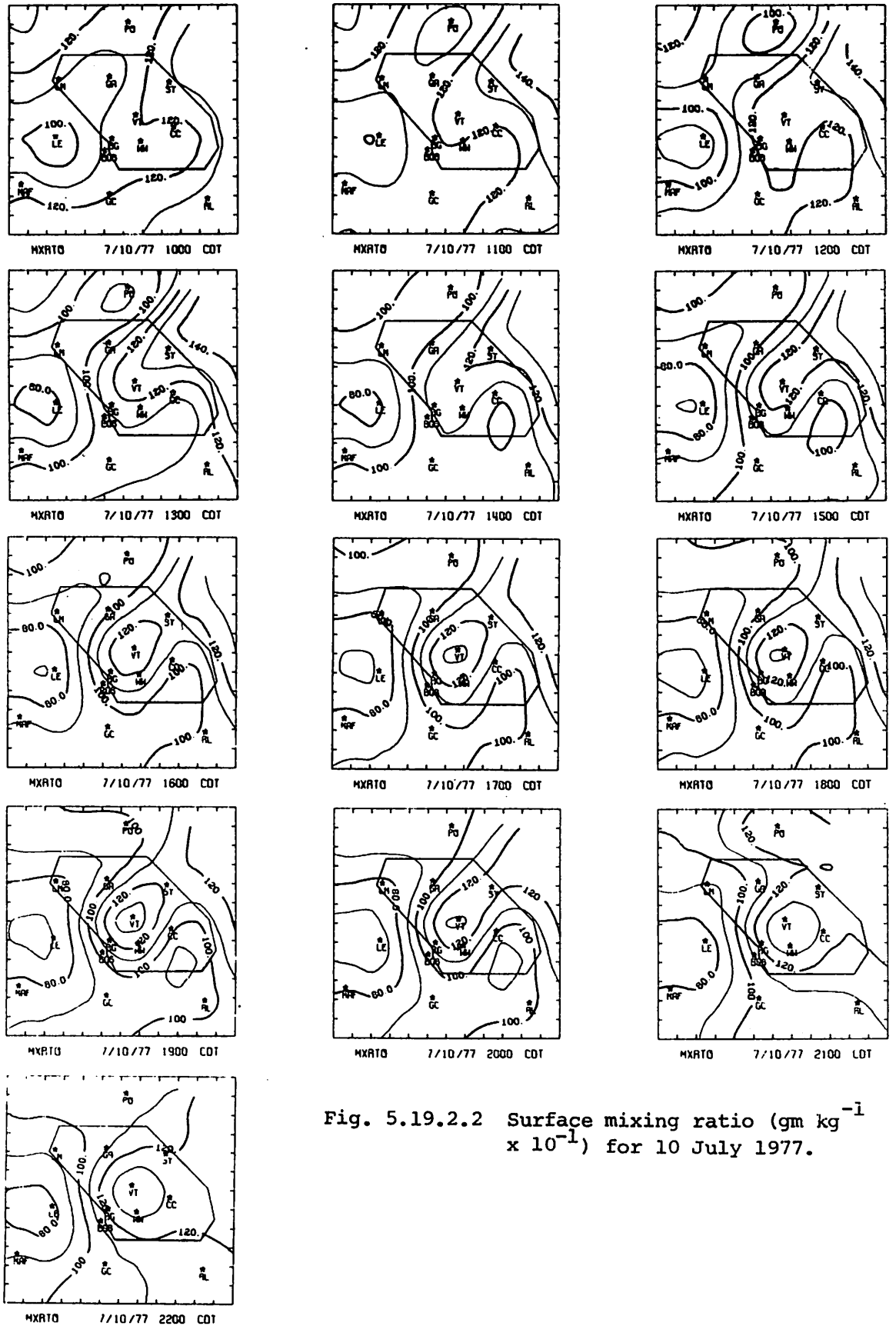

Fig. 5.19.2.2 Surface mixing ratio (gm kg^{-1} x 10^{-1}) for 10 July 1977.

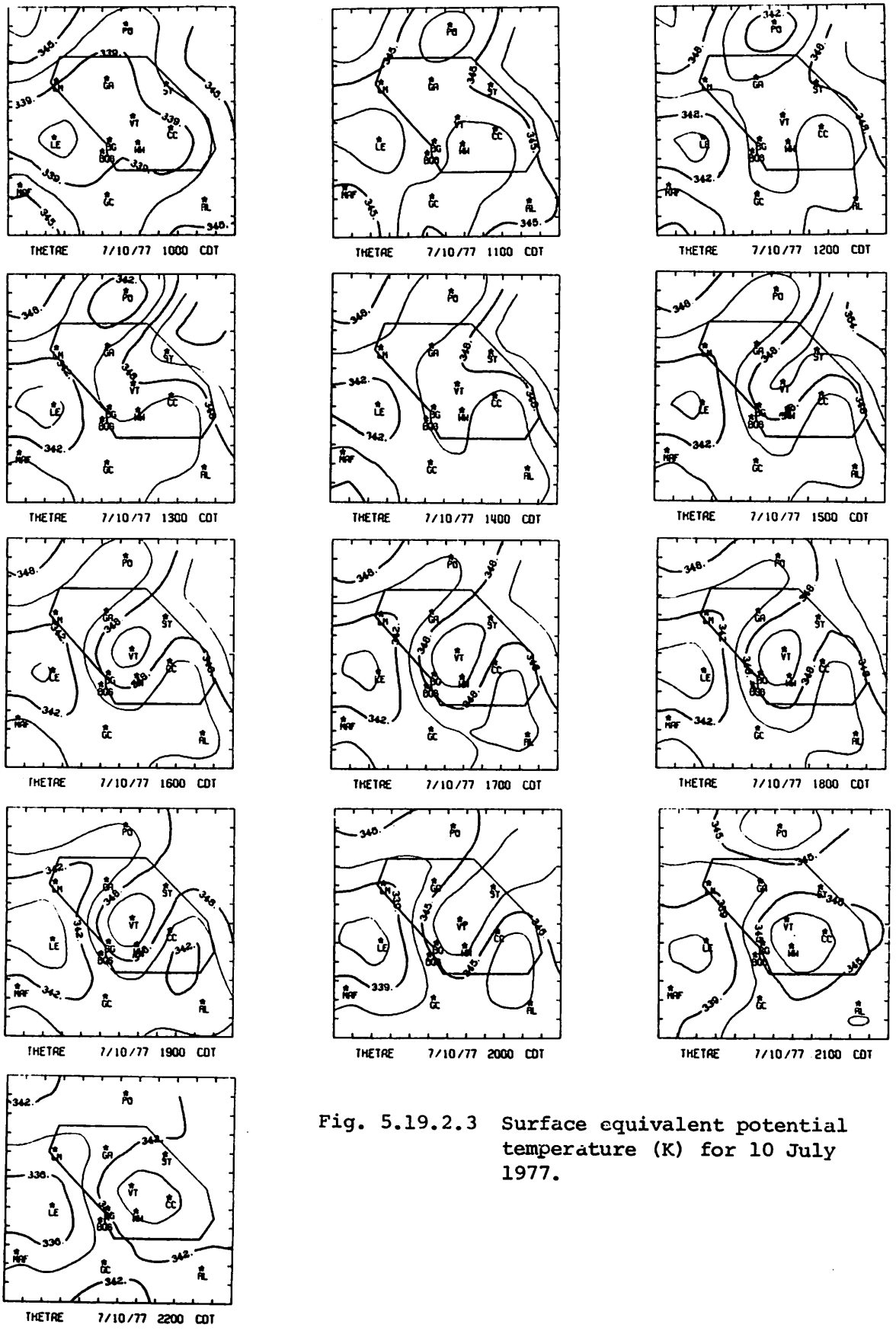

Fig. 5.19.2.3 Surface equivalent potential temperature (K) for 10 July 1977.

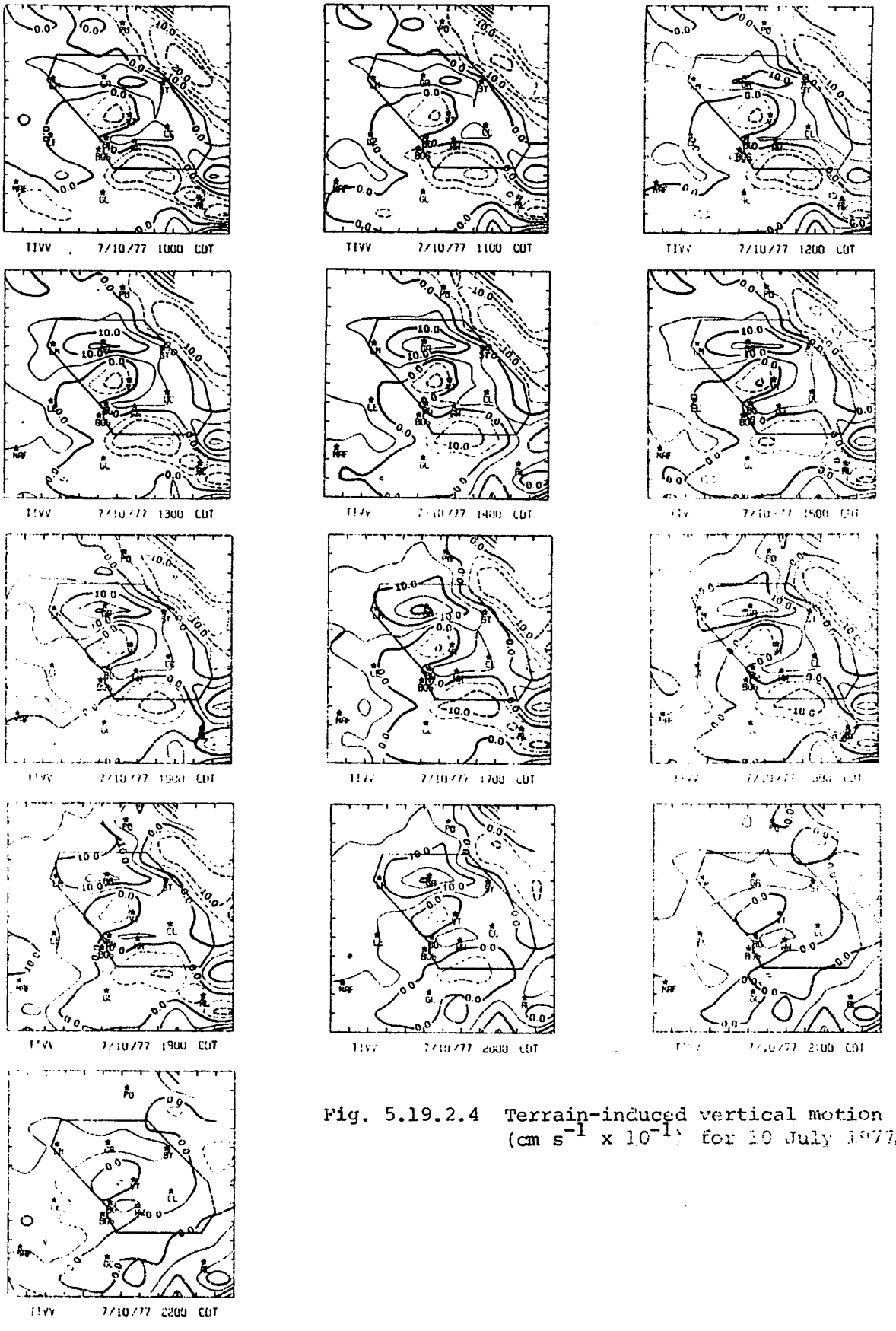

Fig. 5.19.2.4 Terrain-induced vertical motion (cm s^{-1} x 10^{-1}) for 10 July 1977.

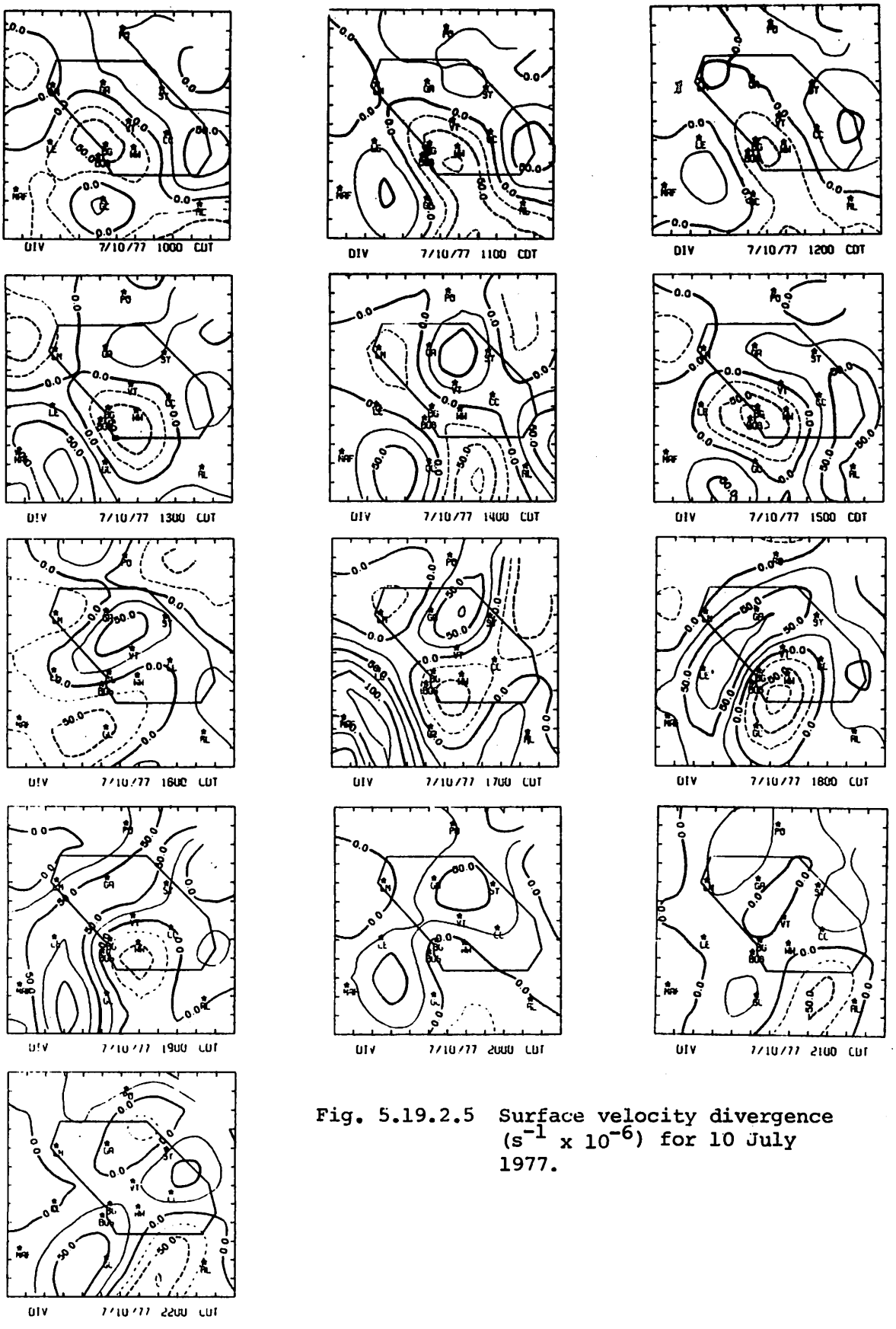

Fig. 5.19.2.5 Surface velocity divergence (s^{-1} x 10^{-6}) for 10 July 1977.

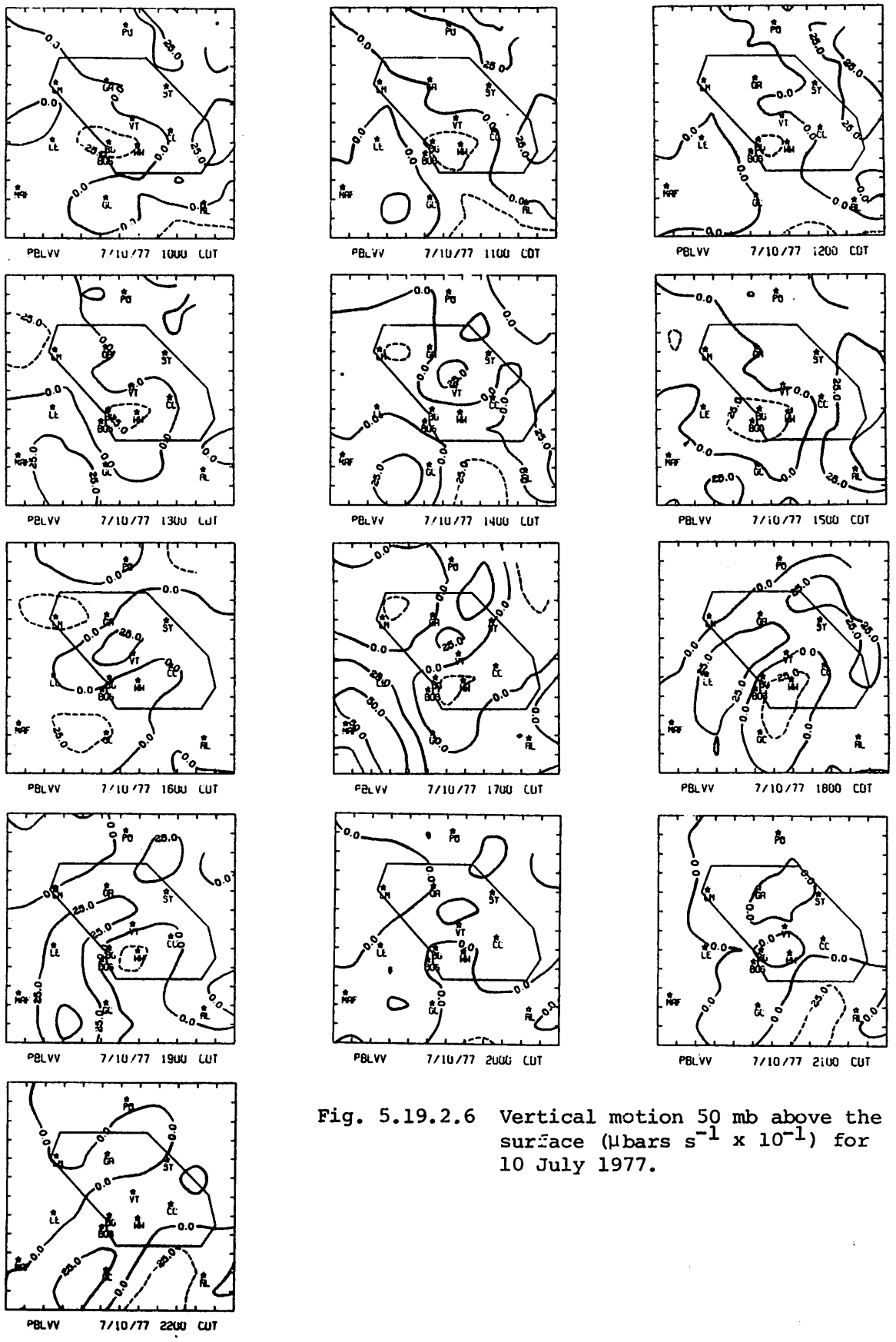

Fig. 5.19.2.6 Vertical motion 50 mb above the surface (μbars s^{-1} x 10^{-1}) for 10 July 1977.

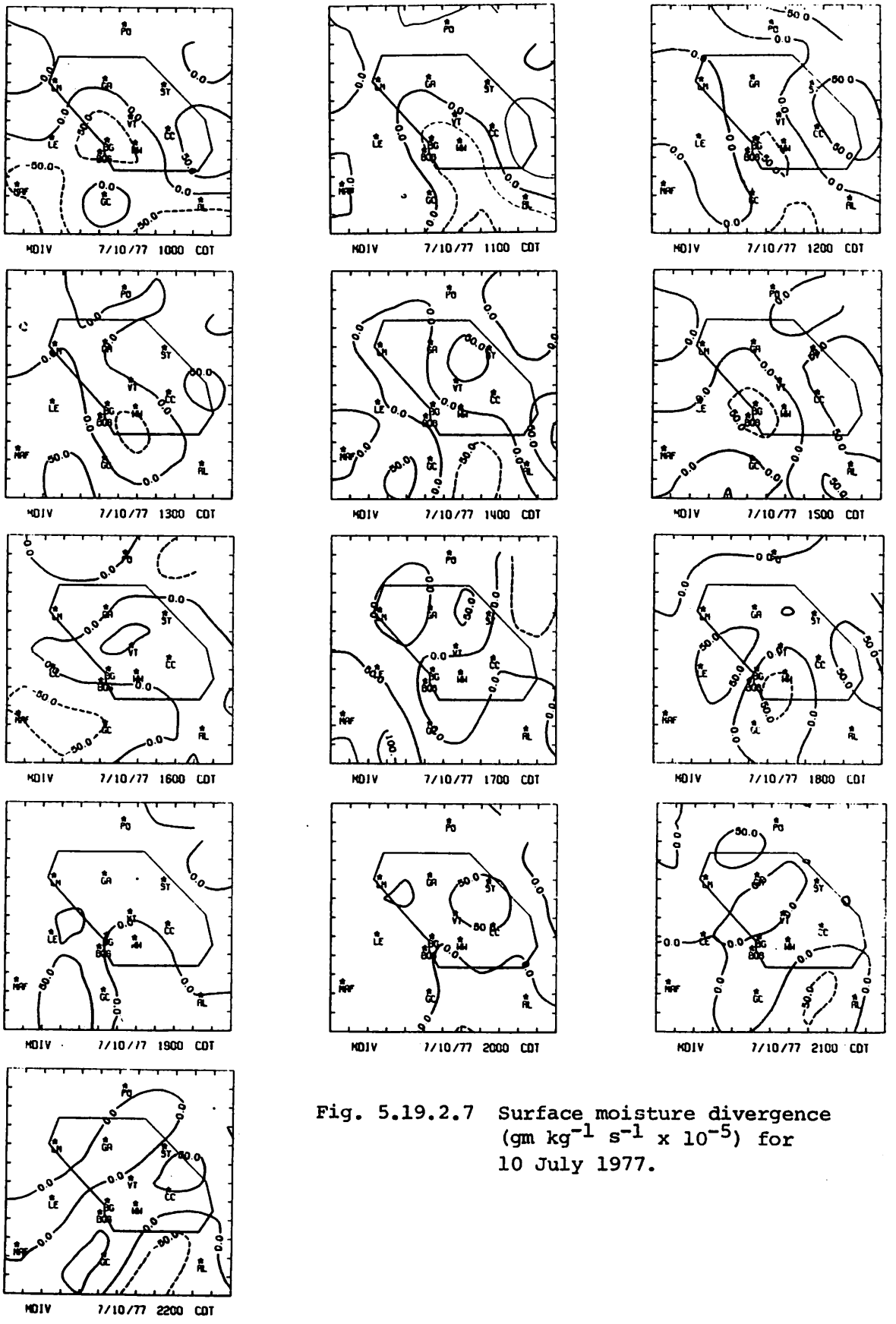

Fig. 5.19.2.7 Surface moisture divergence (gm kg^{-1} s^{-1} x 10^{-5}) for 10 July 1977.

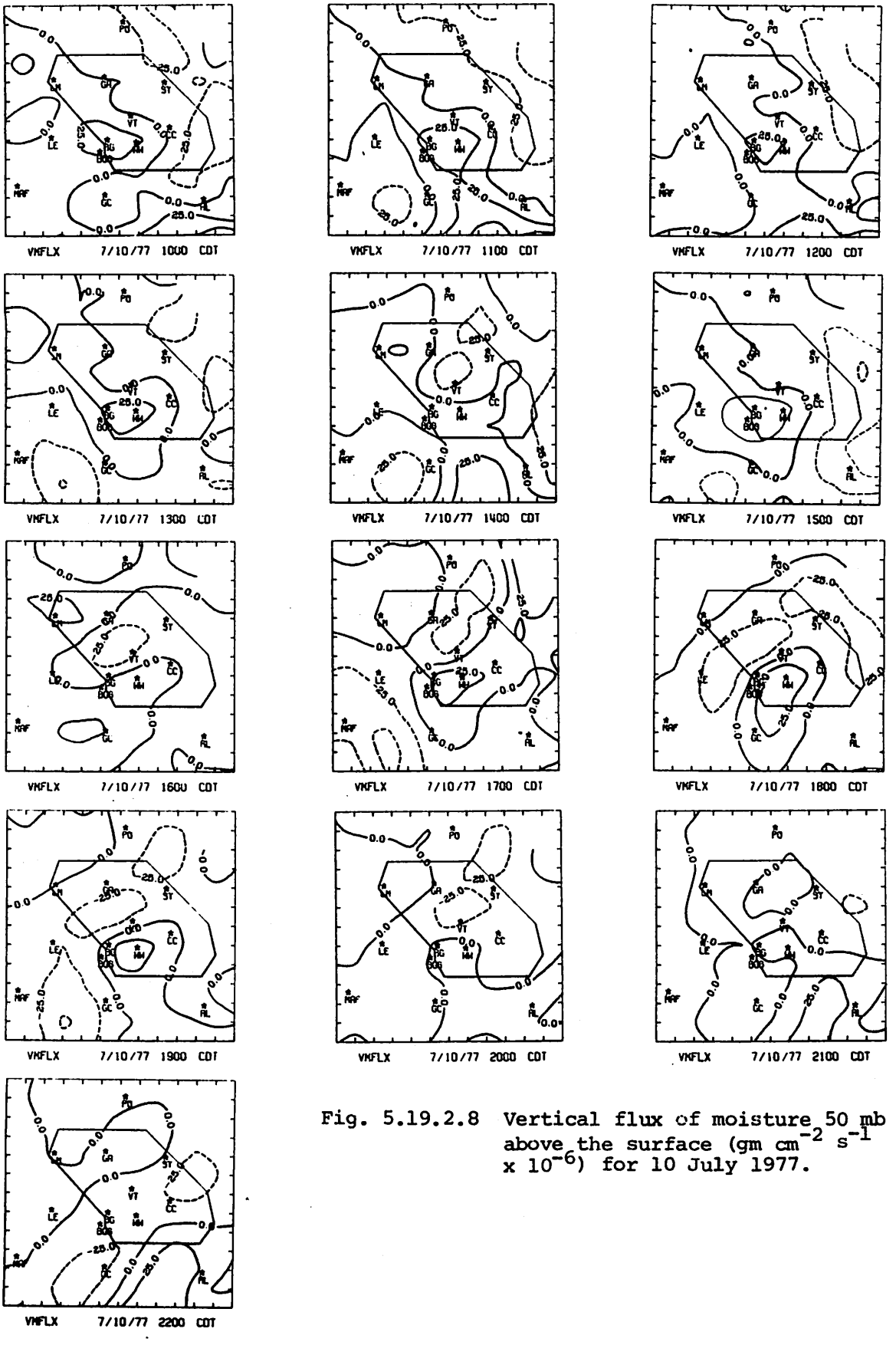

Fig. 5.19.2.8 Vertical flux of moisture 50 mb above the surface (gm cm^{-2} s^{-1} x 10^{-6}) for 10 July 1977.

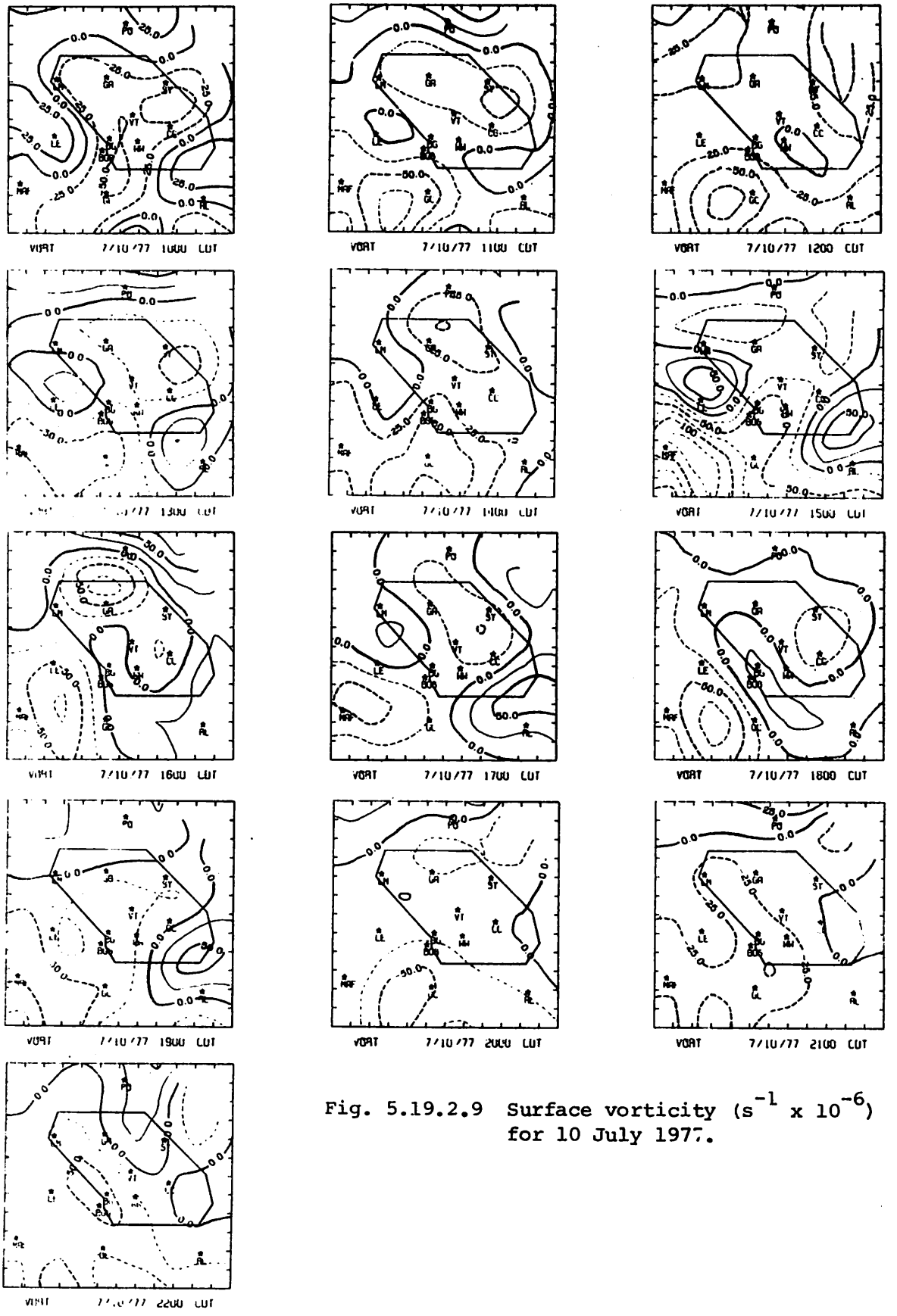

Fig. 5.19.2.9 Surface vorticity (s^{-1} x 10^{-6}) for 10 July 1977.

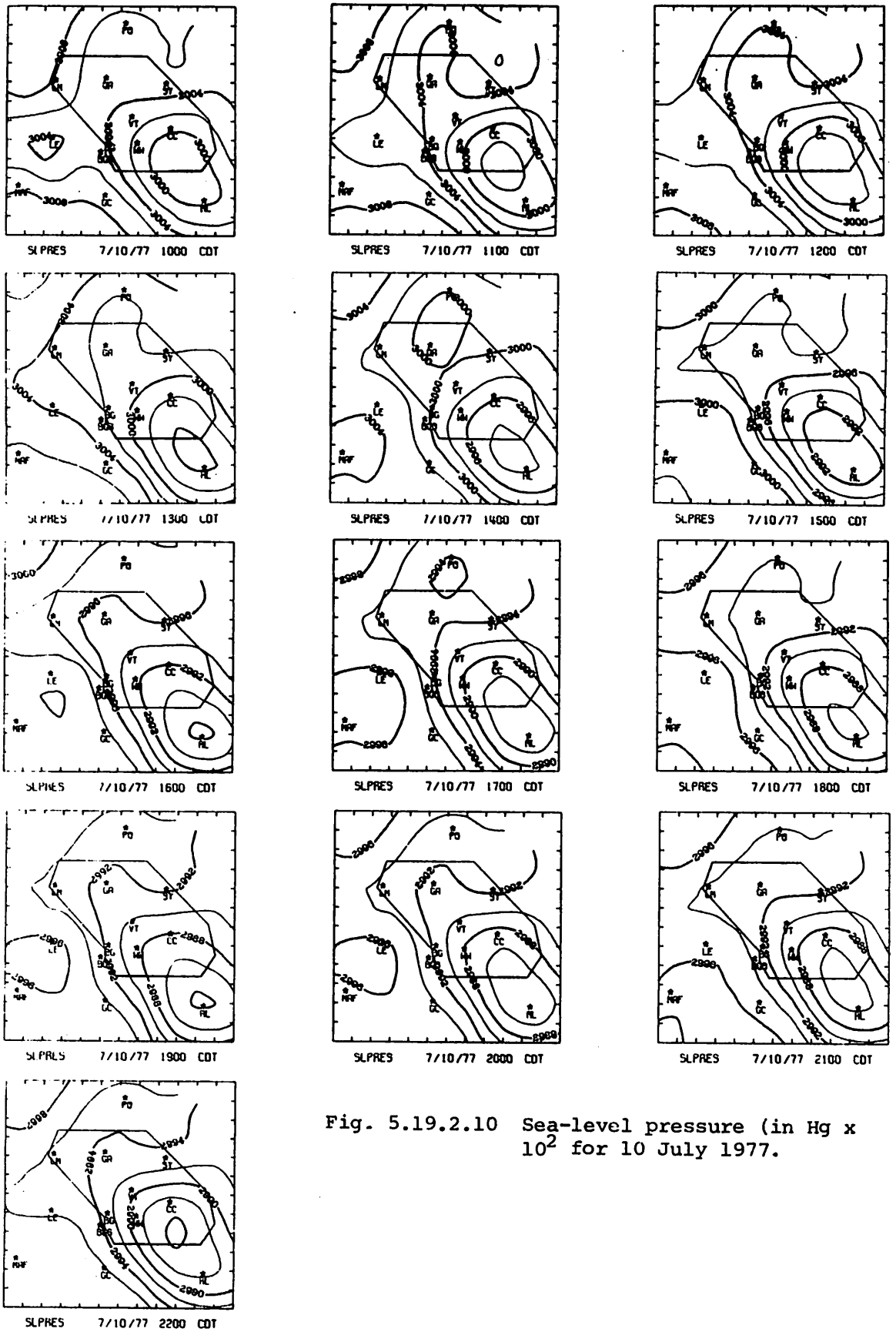

Fig. 5.19.2.10 Sea-level pressure (in Hg x 10^2 for 10 July 1977.

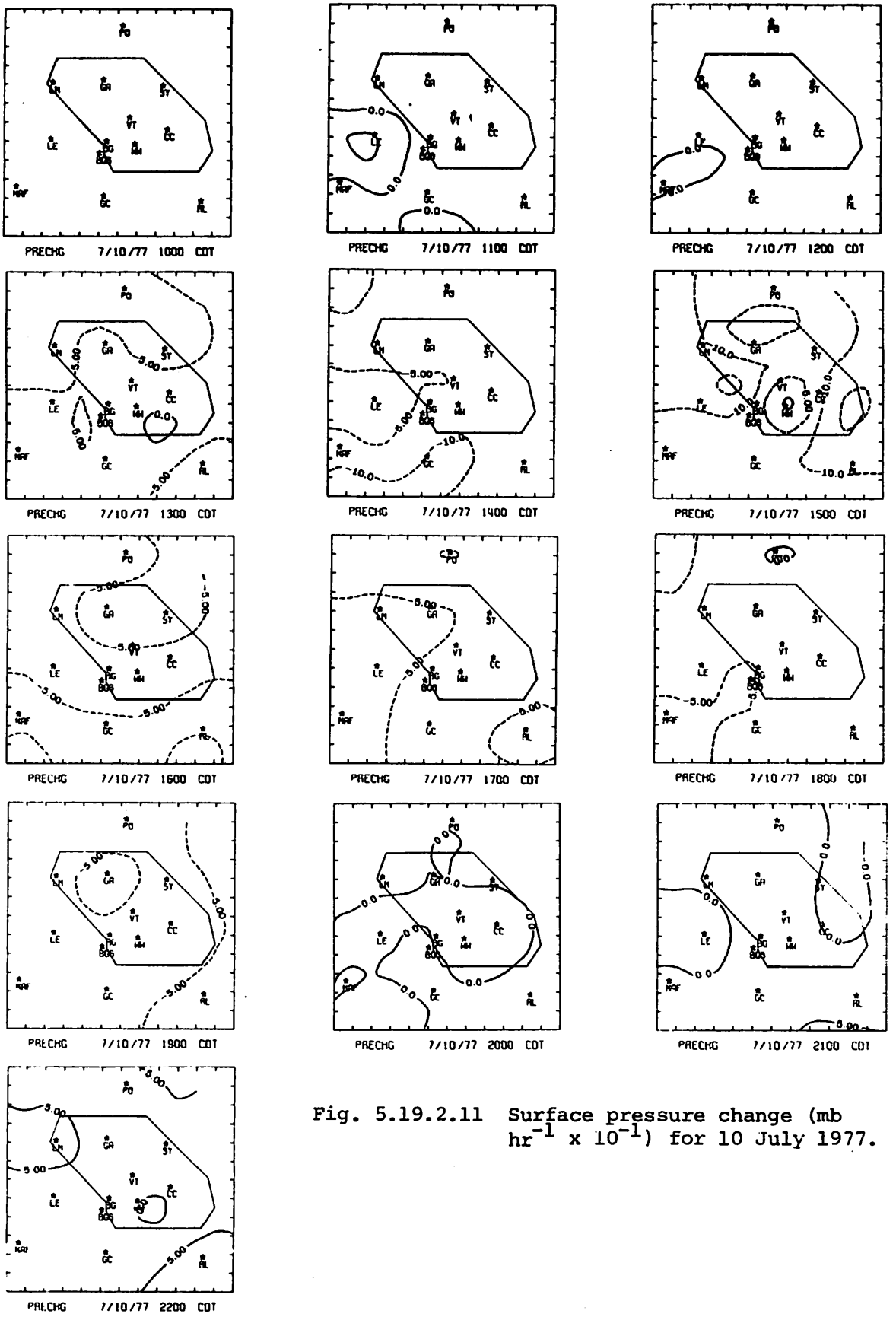

Fig. 5.19.2.11 Surface pressure change (mb hr^{-1} x 10^{-1}) for 10 July 1977.

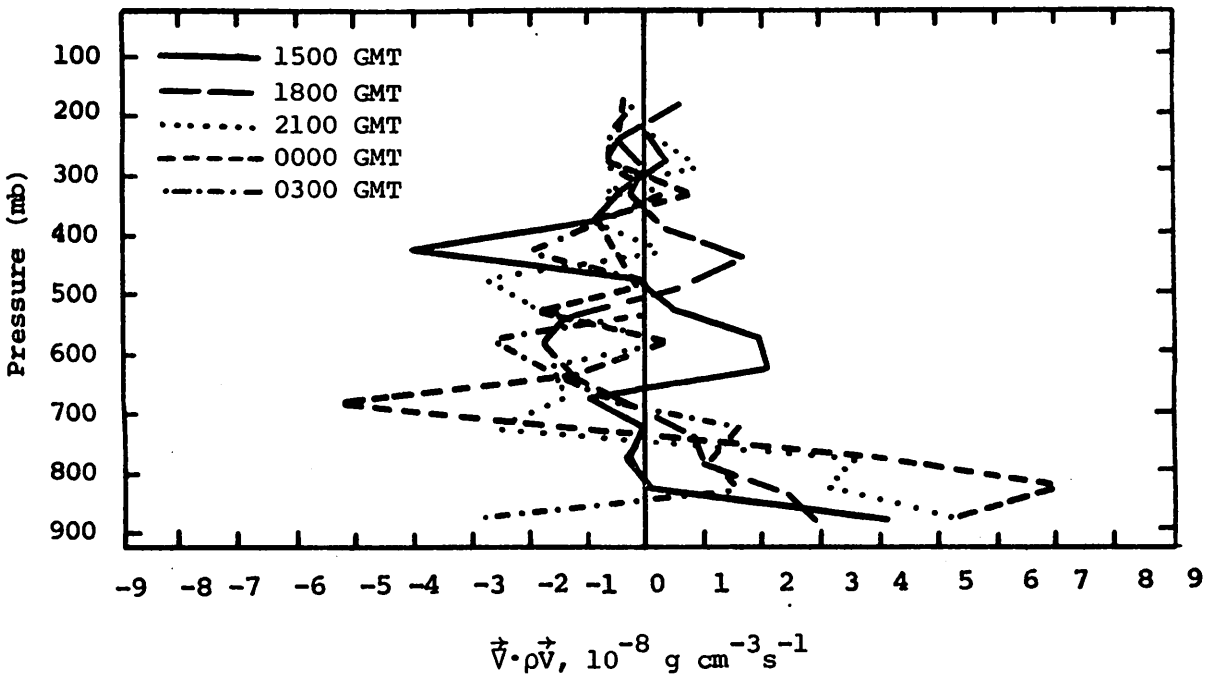

Fig. 5.19.3.1 Vertical profiles of mass divergence on 10 July 1977.

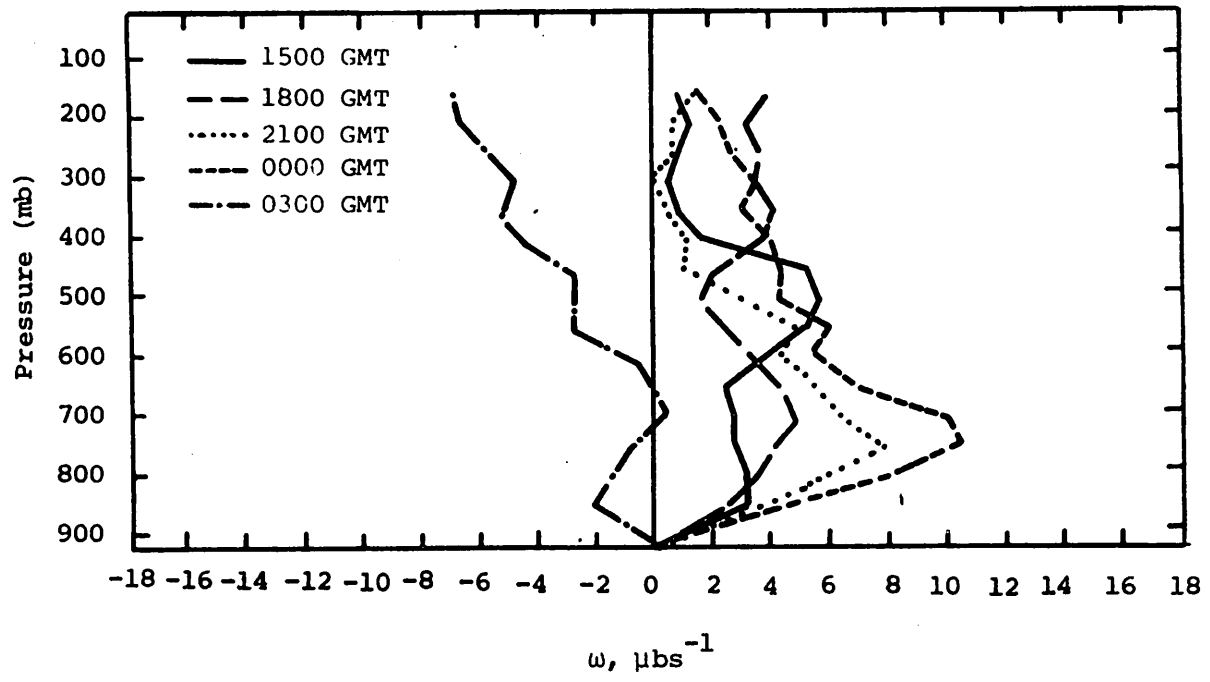

Fig. 5.19.3.2 Vertical profiles of vertical motion on 10 July 1977.

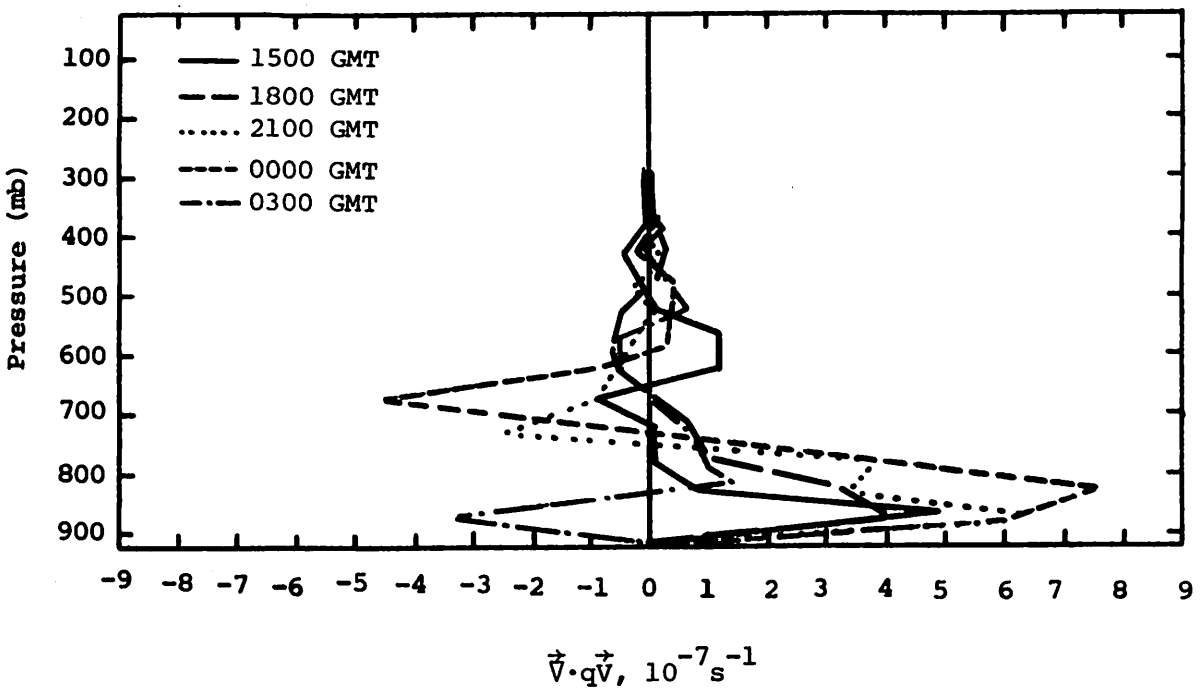

Fig. 5.19.3.3 Vertical profiles of moisture divergence on 10 July 1977.

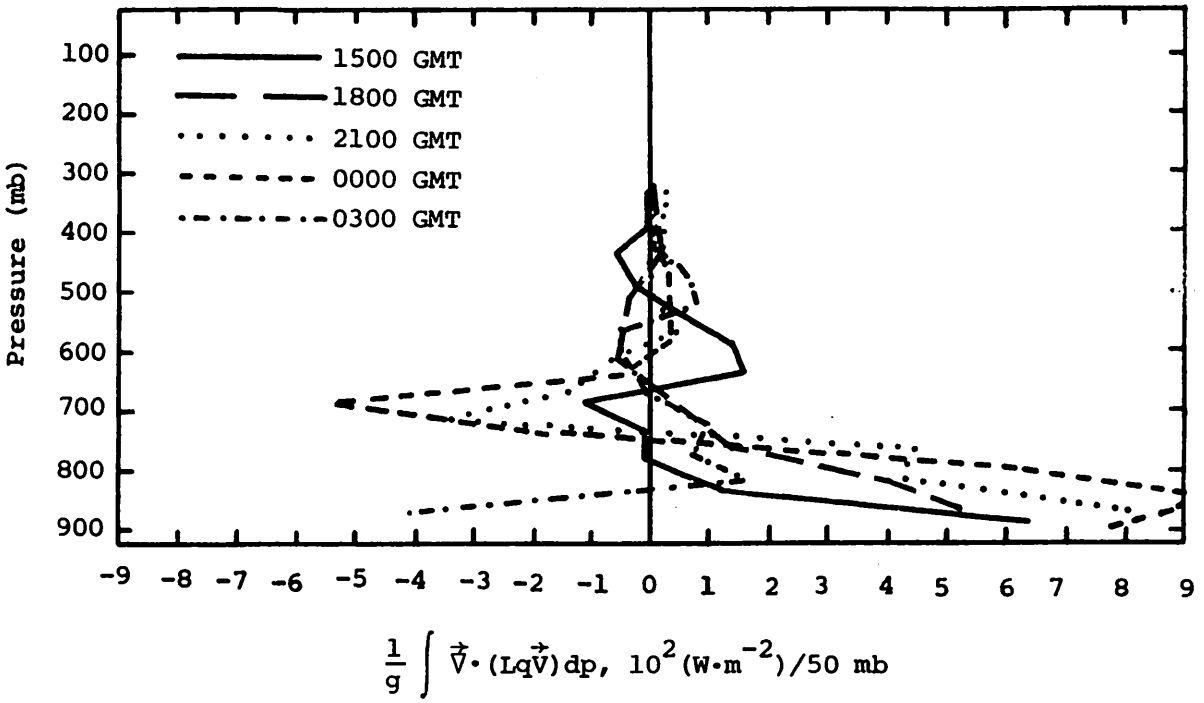

Fig. 5.19.4.1 Vertical profiles of the horizontal flux of latent heat energy on 10 July 1977.

except at 0300 GMT. Vertical flux divergence profiles of latent heat energy showed convergence in low levels and divergence in mid levels as latent heat energy experienced a net downward transport from mid- to low-levels (Fig. 5.19.4.2). Local changes of latent heat energy were small except in low levels where positive values occurred at 1800 and 2100 GMT, and negative values were present at 0000 and 0300 GMT (Fig. 5.19.4.3).

The residual term profiles from the latent heat budget equation (Fig. 5.19.4.4) showed small negative values at 1500 GMT, large negative values at 1800, 2100, and 0000 GMT in mid levels, and positive values at 0300 GMT at most levels. Large mid-level negative values of -R are probably associated with turbulent flux convergence of latent heat energy since no evaporation of clouds or precipitation occurred and lapse rates of temperature were dry adiabatic from the surface up to 700 mb during most times between 1800 and 0000 GMT.

The failure of the diabatic heating profiles (Fig. 5.19.4.5) to show the large cooling at mid levels between 1800 and 0000 GMT gives support to the interpretation given above for the -R profiles since gains of latent heat energy (negative -R values) would have been caused by evaporation of liquid water if environmental cooling were present. Instead, these profiles (dQ/dt) showed relatively small diabatic heating values at low- and mid-levels during a day when activity was absent and evaporation/condensation should be at a minimum. Some positive values at 1500, 1800, and 2100 GMT near the ground are probably associated with radiational heating since surface temperatures went from 22°C (70°F) to 35°C (95°F) during this period.

The horizontal and vertical flux divergence profiles of kinetic energy (Figs. 5.19.4.6 and 5.19.4.7) showed only small values of the terms at all times and levels below 500 mb. Relatively large horizontal flux convergence of kinetic energy occurred around 400 mb at 1500 and 1800 GMT. Vertical flux convergence was present below 400 mb and was followed by flux divergence of kinetic energy around 300 mb at 1500, 1800, and 2100 GMT.

5.19.5 Water Vapor Budget

Figure 5.19.5.1 shows profiles of the net horizontal transport of water vapor. These profiles show a large variation in time but with a net inflow in layers between 750 and 650 mb, and a net outflow aloft.

Figure 5.19.5.2 shows profiles of net vertical transport of water vapor. These profiles generally show a net inflow in layers below 750 mb, and a net outflow aloft. Particularly strong net outflow occurred around 700 mb.

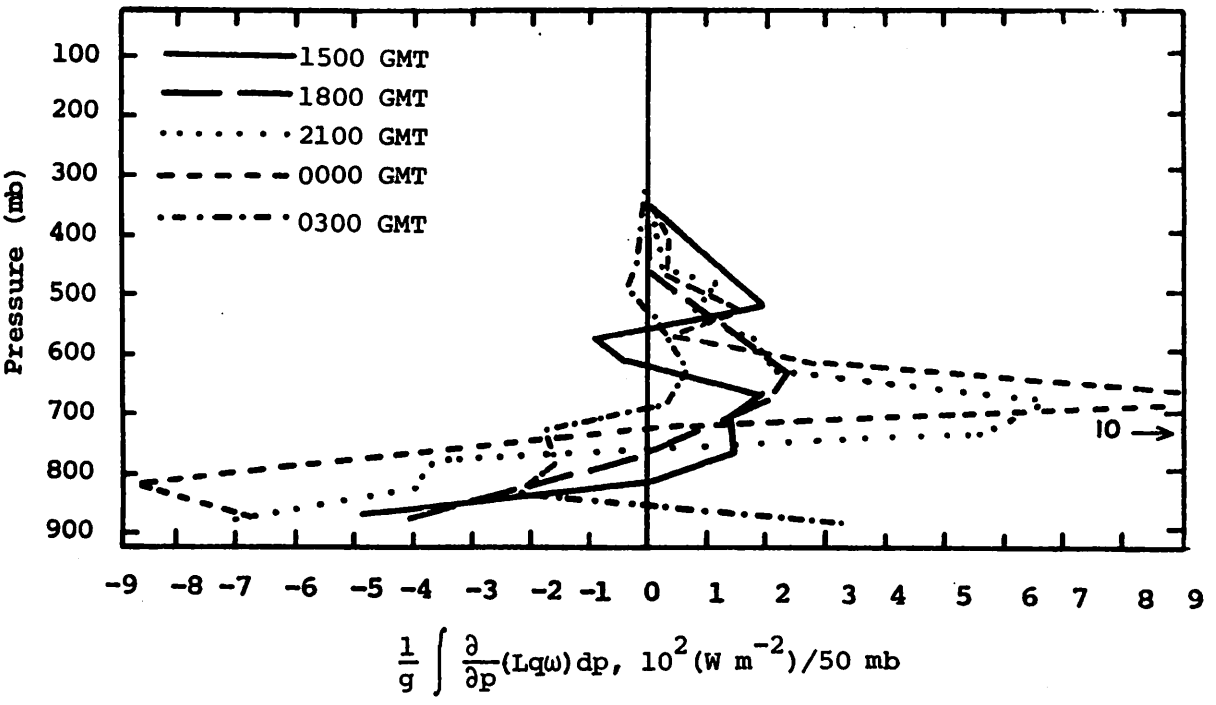

Fig. 5.19.4.2 Vertical profiles of the vertical flux of latent heat energy on 10 July 1977.

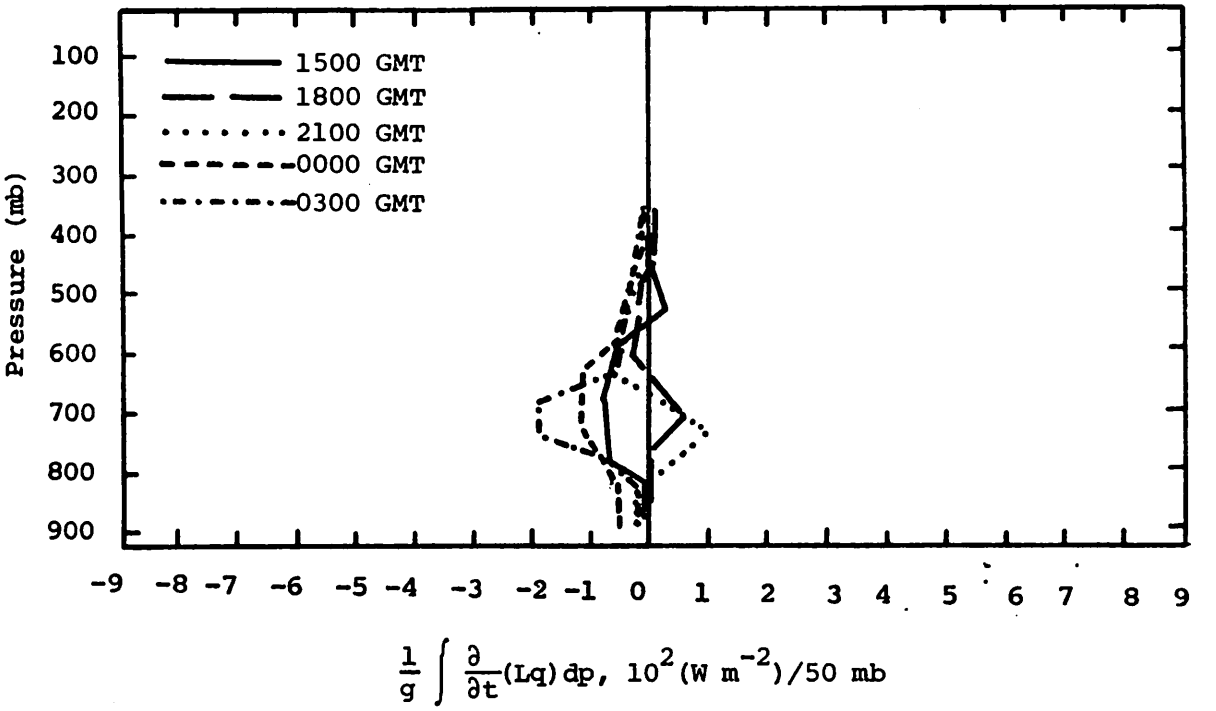

Fig. 5.19.4.3 Vertical profiles of the local change of latent heat energy on 10 July 1977.

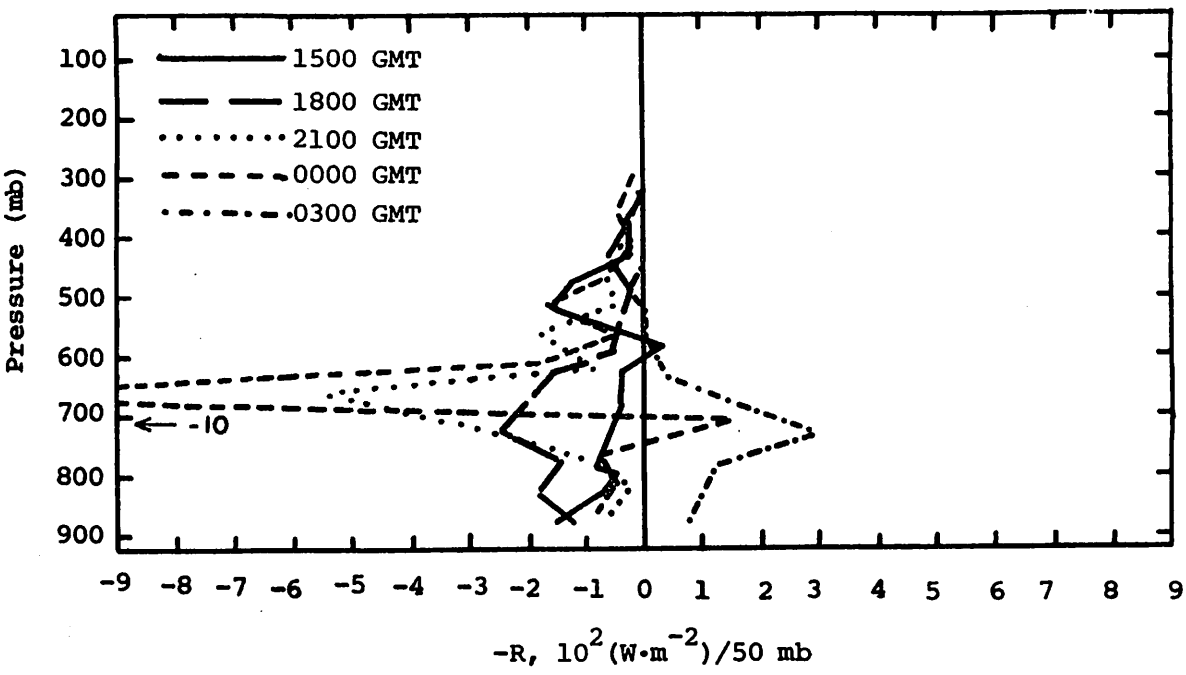

Fig. 5.19.4.4 Vertical profile of the residual of the latent heat energy equation on 10 July 1977.

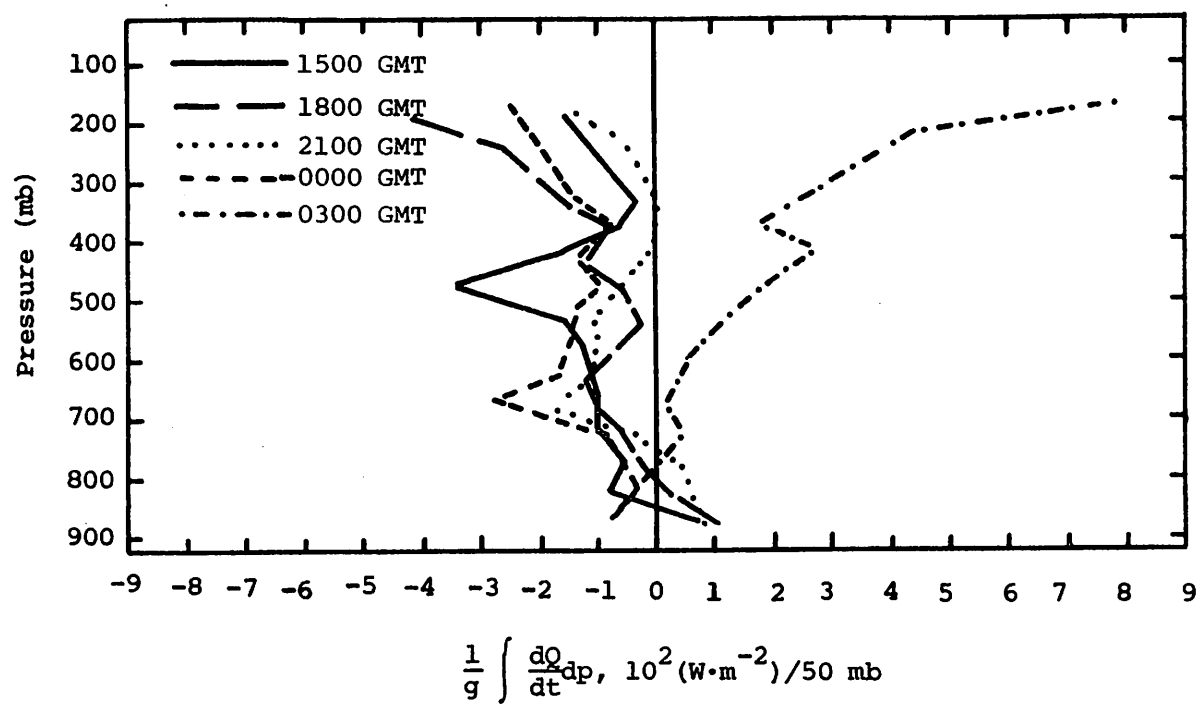

Fig. 5.19.4.5 Vertical profiles of diabatic heating computed from the first law of thermodynamics on 10 July 1977.

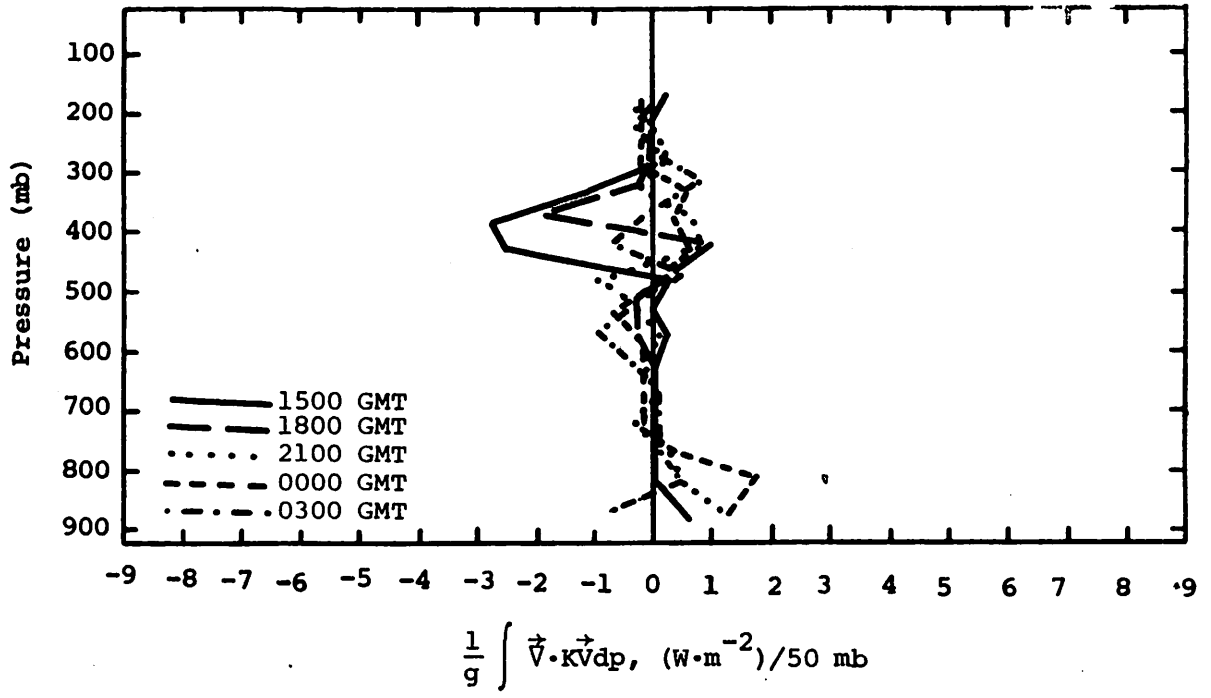

Fig. 5.19.4.6 Vertical profiles of the horizontal flux of kinetic energy on 10 July 1977.

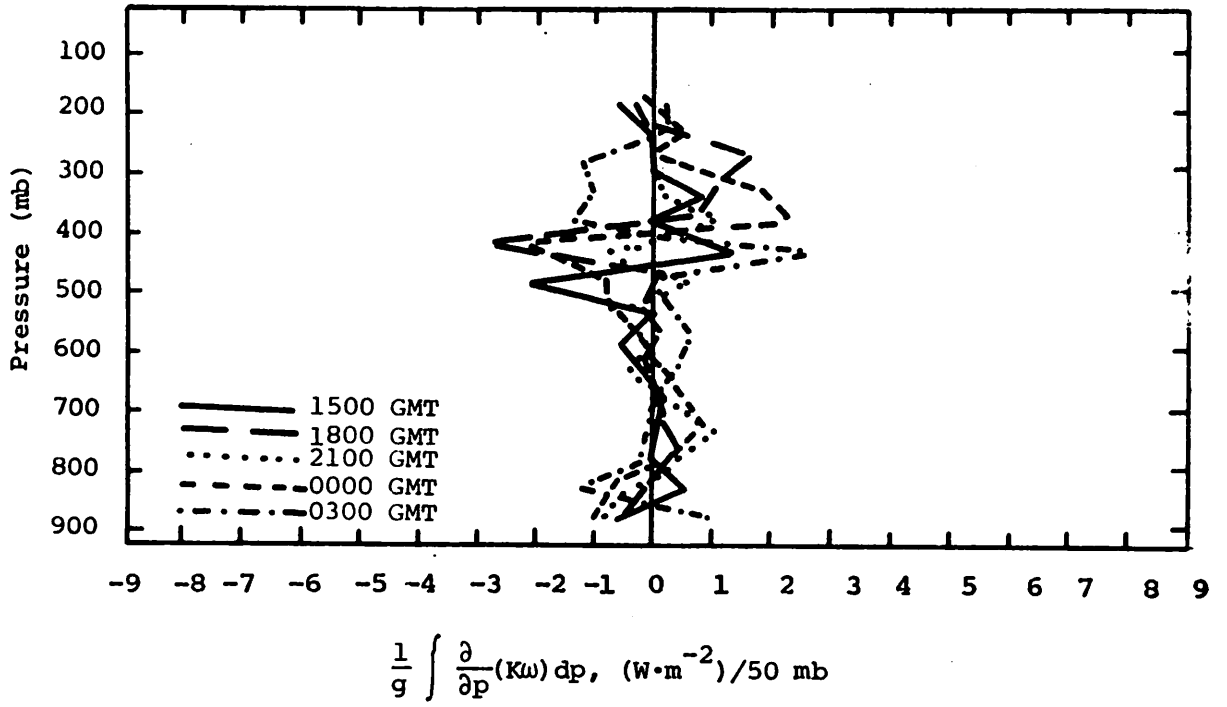

Fig. 5.19.4.7 Vertical profiles of the vertical flux of kinetic energy on 10 July 1977.

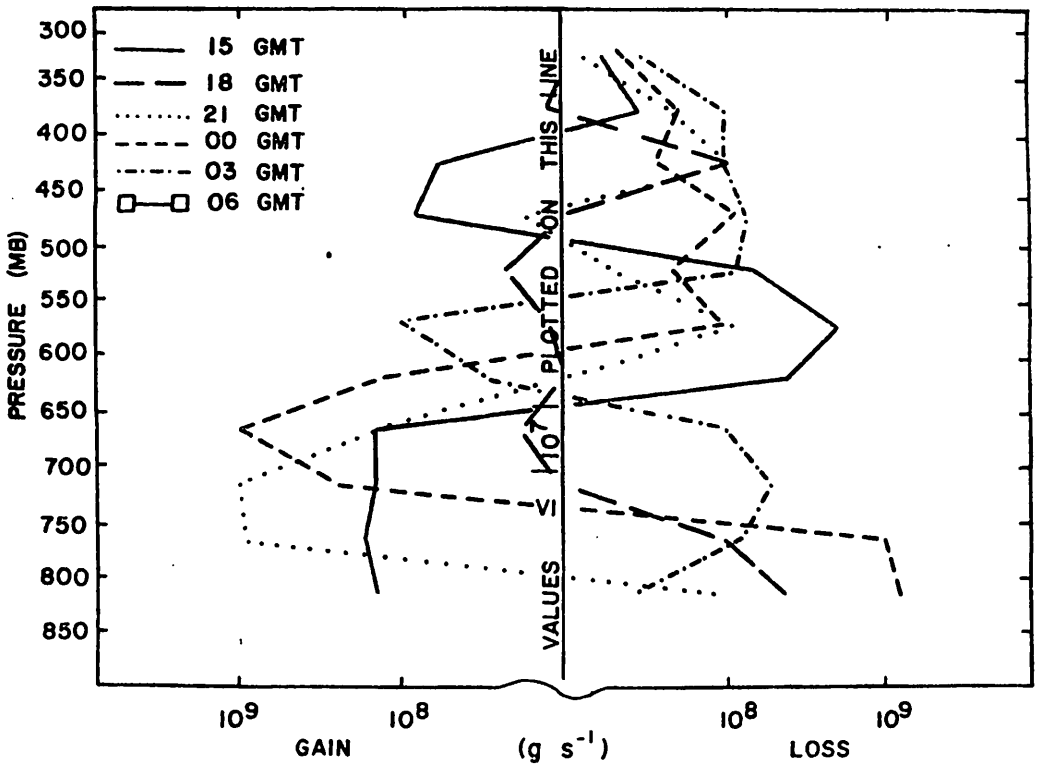

Fig. 5.19.5.1 Net horizontal transport of water vapor through boundaries of 50-mb layers (gm s^{-1}) over the Texas HIPLEX area for 10 July 1977.

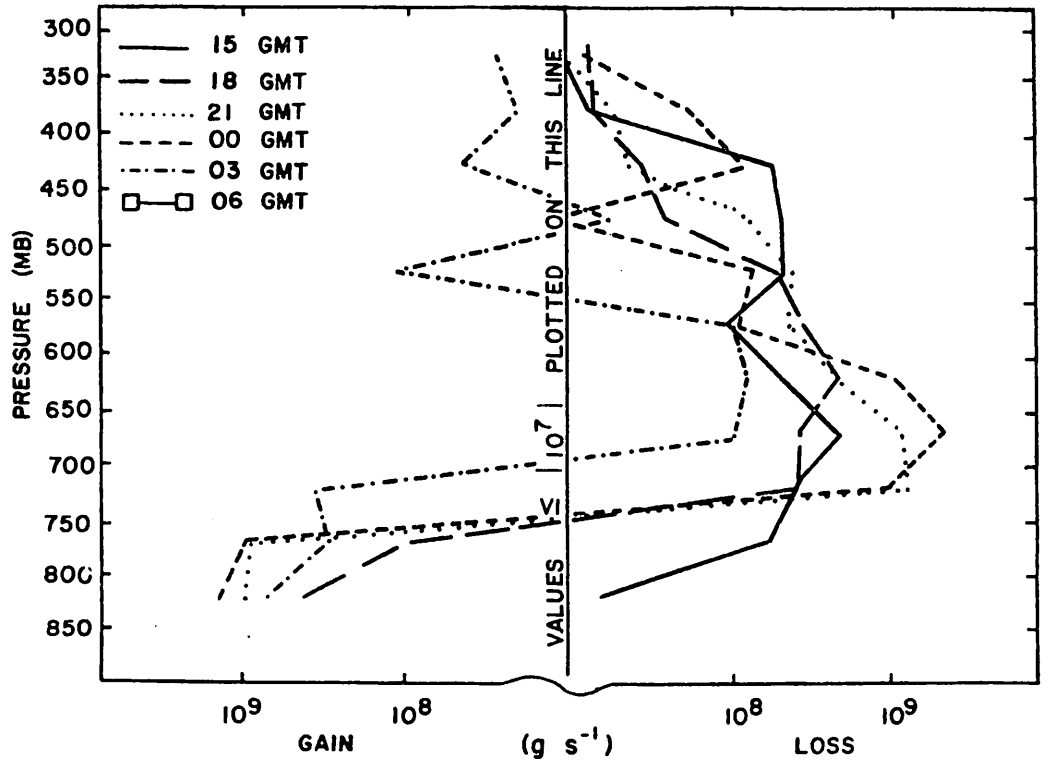

Fig. 5.19.5.2 Net vertical transport of water vapor through boundaries of 50-mb layers (gm s^{-1}) over the Texas HIPLEX area for 10 July 1977.

Figure 5.19.5.3 shows profiles of the vertical transport of water vapor through constant pressure surfaces. These profiles show a strong downward transport for all levels at all times except 0300 GMT.

Figure 5.19.5.4 shows profiles of the combined net horizontal and vertical transport of water vapor. These profiles remain nearly similar with a net inflow in layers below 750 mb, and a strong net outflow in layers above.

Figure 5.19.5.5 shows profiles of the total mass of water vapor. These profiles indicate little variation throughout the day with the largest differences occurring at 550 mb. A general decrease of water vapor occurred with time in this layer.

Figure 5.19.5.6 shows profiles of the local rate-of-change in the total mass of water vapor. These profiles show a net loss for most times especially between 0000 and 0300 GMT. A gain of water vapor occurred in lower layers from 1800 to 0000 GMT which may be attributed to the strong downward transport indicated in Figure 5.19.5.3.

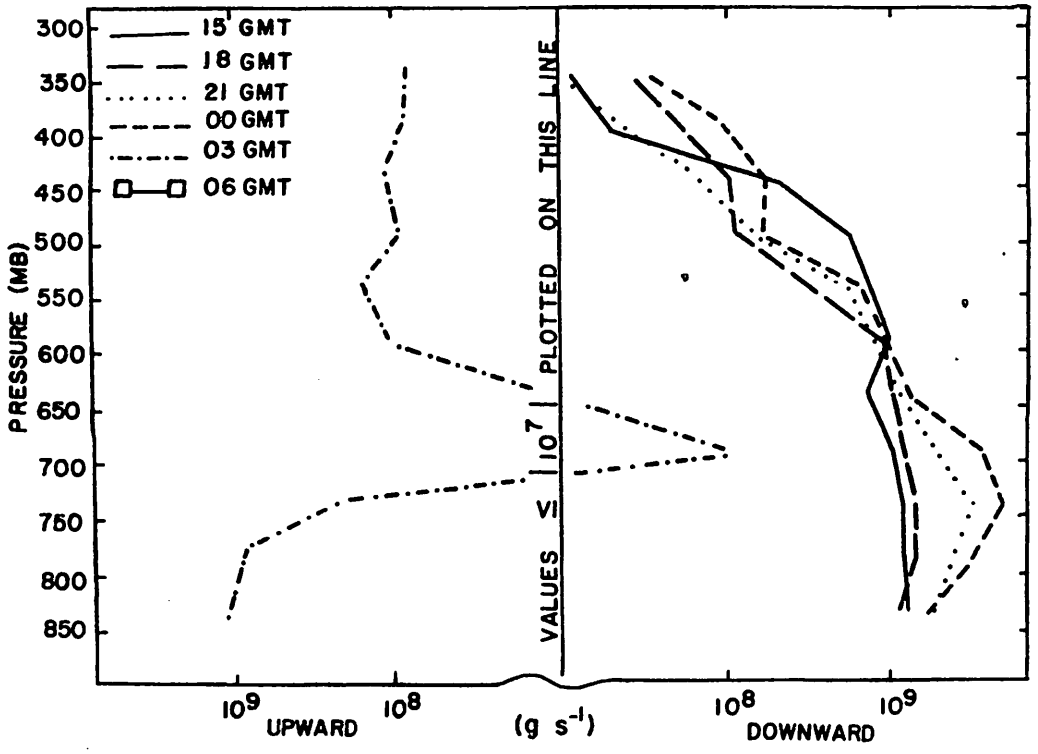

Fig. 5.19.5.3 Vertical transport of water vapor through constant pressure surfaces (gm s^{-1}) over the Texas HIPLEX area for 10 July 1977.

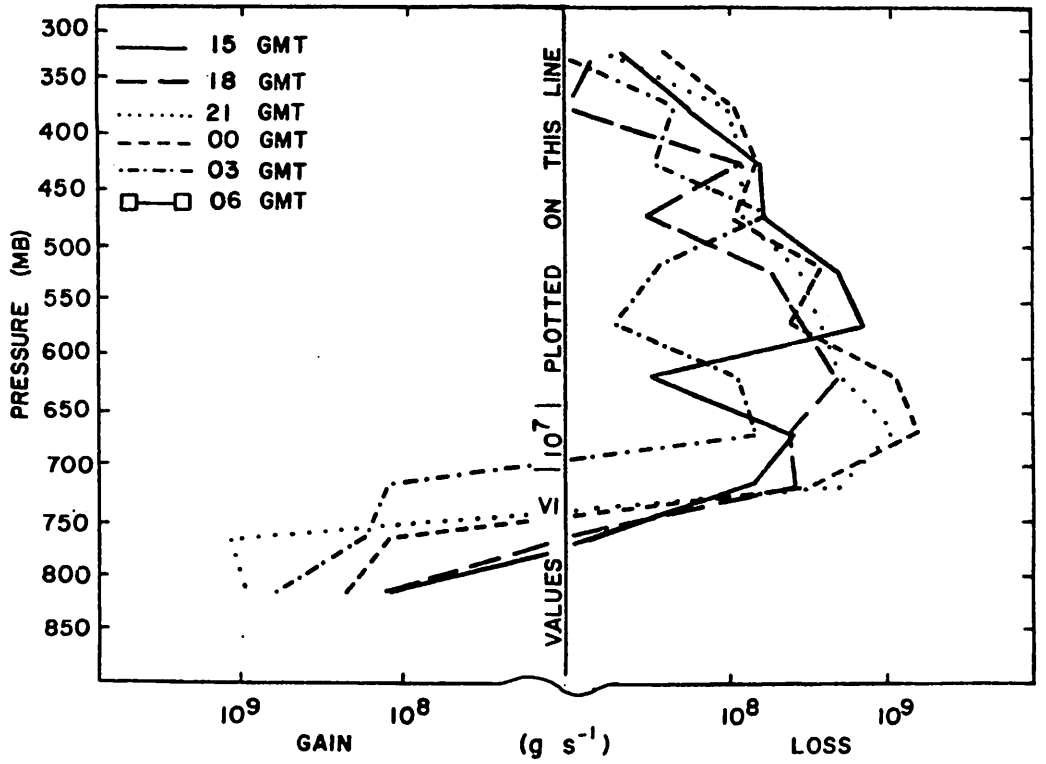

Fig. 5.19.5.4 Combined net horizontal and vertical transport of water vapor through boundaries of 50-mb layers (gm s^{-1}) over the Texas HIPLEX area for 10 July 1977.

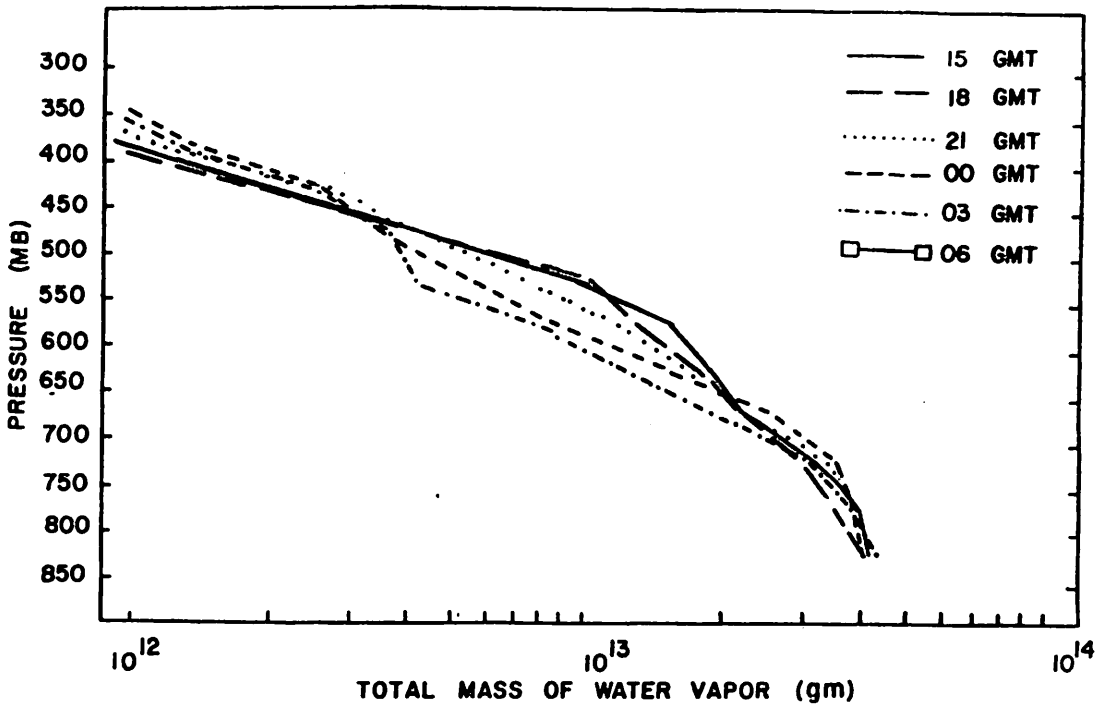

Fig. 5.19.5.5 Total mass of water vapor in layers 50 mb deep (gm) over the Texas HIPLEX area for 10 July 1977.

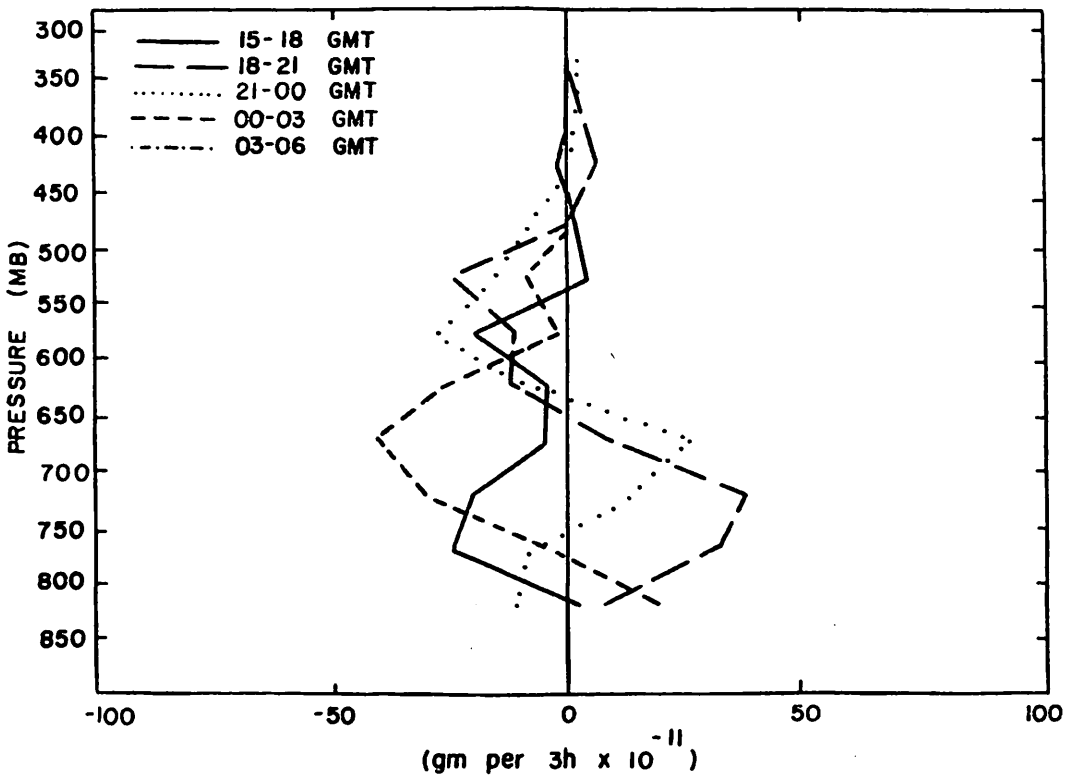

Fig. 5.19.5.6 Local rate-of-change in total mass of water vapor (gm per 3h x 10^{-11}) over the Texas HIPLEX area for 10 July 1977.

5.20 Composite Surface Analysis

Maximum values of velocity and moisture convergence (negative divergence), positive vertical motion ($-\omega$) 50 mb above the surface, and upward flux of moisture ($-\rho q\omega$) 50 mb above the surface observed anywhere in the Texas HIPLEX mesonet were obtained from the computer charts each hour between 1000 and 2200 CDT. The data were grouped for echoes and no echoes. There were 122 observation times when echoes were present, and 96 when they were not present. Percentage frequency distributions were prepared for each variable and are shown in Figs. 5.20.1 through 5.20.4. The value of a variable at the cross-over point represents the value that best distinguishes between the occurrence or nonoccurrence of a radar echo. These values are: velocity divergence, $-10^{-4}s^{-1}$; moisture divergence, -10^{-6} gm $cm^{-1}s^{-1}$, vertical motion 50 mb above the surface (ω), -5 μbars s^{-1}, and vertical flux of moisture 50 mb above the surface ($\rho q\omega$), -5×10^{-5} gm $cm^{-2}s^{-1}$. It is clear from the figures that when the magnitudes of these variables are smaller than the cross-over values, there is a higher percentage of no echoes than when the values are exceeded. Also, the figures show that for each variable the extreme magnitudes are larger when echoes are present than when they are absent.

To aid further in the interpretation of the frequency distributions, contingency tables were prepared using the cross-over values as criteria for distinguishing between echoes and no echoes. The tables are shown in Fig. 5.20.5. These tables confirm in a different way what is shown in Figs. 5.20.1 through 5.20.4. When values of all variables exceed the cross-over values, there usually is more than a 2:1 probability that echoes will be observed than not. The ratios for values below the cross-over values vary between approximately 2:1 and 3:1 in favor of no echoes. In the interpretation of Figs. 5.20.1 through 5.20.5, it should be remembered that the values of the variables chosen at a given time are not necessarily associated with an echo if one was observed.

To gain some idea of how the cross-over values are related to echoes of various types, the echoes were classified as follows.

Lines: Cells organized into a line which exhibits movement.

Clusters: Organized group of 3 or more cells determined by closed contours of radar codes 1, 2, or 3 or any combination of these codes.

Unorganized (A): One or more individual cells the tops of which are under 10 km (codes 1 and 2) and none of which are organized into a line or

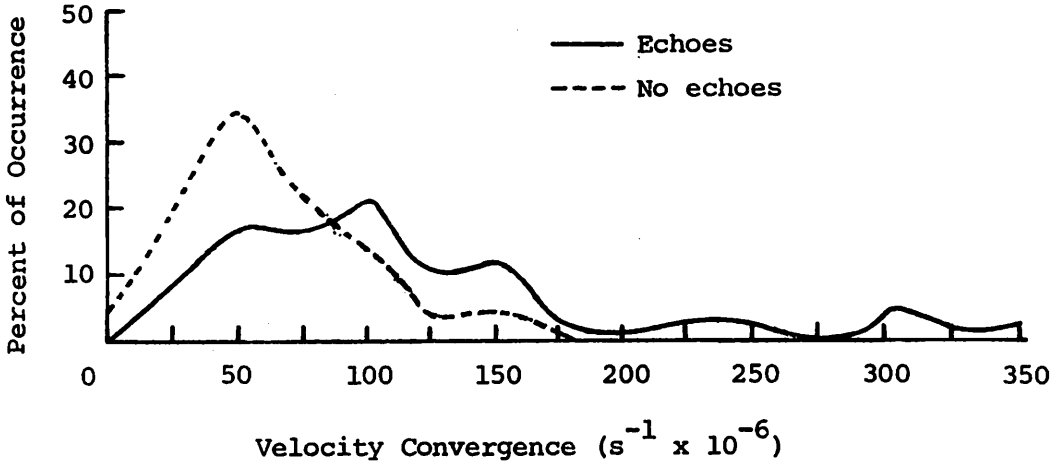

Fig. 5.20.1 Percentage frequency distributions of maximum negative velocity divergence (i.e., convergence) observed anywhere in the mesonetwork when echoes were and were not observed.

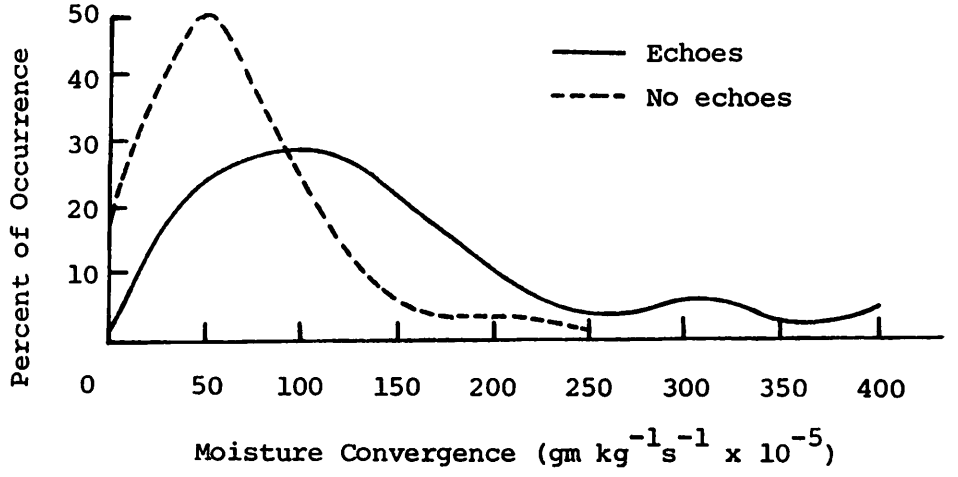

Fig. 5.20.2 Percentage frequency distributions of maximum negative moisture divergence (i.e., convergence) observed anywhere in the mesonetwork when echoes were and were not observed.

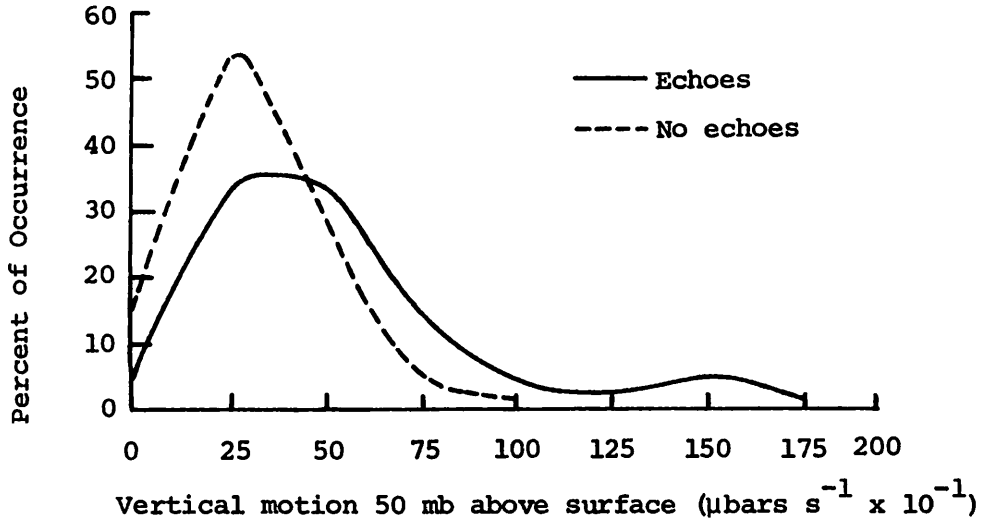

Fig. 5.20.3 Percentage frequency distributions of maximum -ω 50 mb above surface observed anywhere in the mesonetwork when echoes were and were not observed.

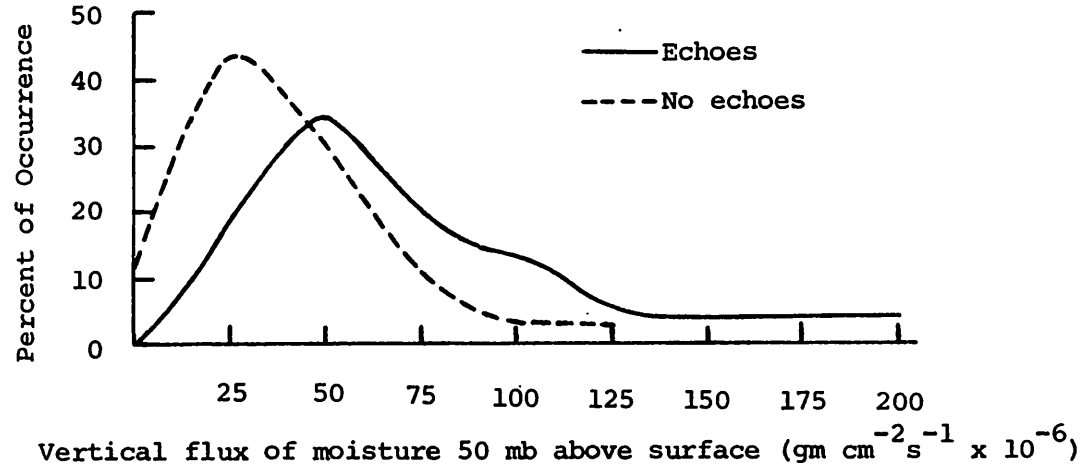

Fig. 5.20.4 Percentage frequency distributions of maximum upward vertical flux of moisture 50 mb above surface observed anywhere in mesonetwork when echoes were and were not observed.

$\vec{\nabla}\cdot\vec{v} < -10^{-4}s^{-1}$

Radar echoes	no	yes
no	73	23
yes	48	74

a. Velocity convergence

$\vec{\nabla}\cdot q\vec{v} < -10^{-3}$gm kg$^{-1}s^{-1}$

Radar echoes	no	yes
no	67	29
yes	33	89

b. Moisture convergence

$\omega_{50} < -5$ µbars s^{-1}

Radar echoes	no	yes
no	63	33
yes	48	74

c. Vertical motion

$\rho q\omega > 5 \times 10^{-5}$gm cm$^{-2}s^{-1}$

Radar echoes	no	yes
no	57	39
yes	24	98

d. Vertical flux of moisture

Fig. 5.20.5 Contingency tables for velocity and moisture convergence, vertical motion 50 mb above the surface, and vertical flux of moisture 50 mb above the surface versus radar echoes.

cluster as defined above. This includes cells that are not entirely on the grid.

Unorganized (B): Same as above except tops exceed 10 km (code 3).

Echo(es) approaching or receding from area: Edge of echo(es) on edge of grid area and there is no cell present in the gridded area. This does not include cases in which there is a complete echo in the grid area at the same time.

No echoes: No echoes observed anywhere in grid area.

The number of occurrences when the magnitudes of the variables were less than or greater than the cross-over values are shown in Table 5.20.1 for each echo classification and when no echoes were present. In all cases, there is a greater probability for echoes when the cross-over values are exceeded than when they are not, but the delineation is defined better for lines and clusters than for the other categories.

Table 5.20.1 Occurrences of echoes as function of echo characteristics and cross-over values for velocity and moisture divergence, vertical motion 50 mb above the surface, and vertical flux of moisture 50 mb above the surface.

Echo Classification	Divergence (s^{-1})		Moisture Divergence ($gm\ kg^{-1}s^{-1}$)		Vert. Moist. Flux ($gm\ cm^{-2}s^{-1}$)		Vertical Motion ($\mu bars\ s^{-1}$)	
	$> -10^{-4}$	$< -10^{-4}$	$> -10^{-3}$	$< -10^{-3}$	$> -5x10^{-5}$	$< -5x10^{-5}$	> -5	< -5
Lines	9	16	4	21	3	22	8	21
Clusters	4	12	2	14	1	15	5	14
Unorganized (A)	15	17	12	20	10	22	16	20
Unorganized (B)	12	16	10	18	7	21	11	18
Receding or Approaching	8	13	5	16	3	18	8	16
No Echoes	73	23	67	29	57	39	63	29

5.21 Average Conditions of Upper-Level Kinematics and Atmospheric Energetics During Times With and Without Convective Activity

The 1976 Texas HIPLEX rawinsonde data (Scoggins and Wilson, 1976), obtained on 14 operational days during June and July, were used to calculate various kinematic parameters aloft from 850 mb to 100 mb at 50 mb intervals. These results were used in the individual case studies to investigate the interactions between convective clouds and their environment for the purpose of determining factors responsible for the initiation, growth, maintenance, and dissipation of convective activity. In summarizing the results of the case studies, average vertical profiles of the kinematic parameters and terms from latent, sensible, kinetic and potential energy budgets were calculated for those time periods with and without thunderstorms over the network (Scoggins et al., 1978). In 1976, the mesoscale kinematics and energetics of the atmosphere were clearly different, at various levels and times, for those periods with and without convective activity. These results indicated that the mesoscale environment exerted a strong controlling influence over thunderstorm development through its three-dimensional circulation and structure. Similar calculations have been made for the 1977 Texas HIPLEX rawinsonde data and are presented in this section.

In 1977, there were 70 time periods that contained the necessary data for kinematic calculations aloft. These time periods were classified as either "convective" or "nonconvective" depending upon whether thunderstorms were present over the network bounded by the PO-RL-MAF triangle. If a radar echo in excess of 6.1 km (20K ft) was observed ±1 hour surrounding a sounding time, the period was termed convective. All other cases were termed non-convective except when balloons were suspected of entering thunderstorms. These cases were considered as not representative of the mesoscale environment in which thunderstorms were present and were excluded from averages presented here. Using this classification, there were 15 and 55 time periods with and without convective activity, respectively.

The primary difference between the convective and nonconvective profiles of horizontal mass divergence (Fig. 5.21.1) is the occurrence in low-levels of strong mass convergence with convective activity and mass divergence during times without convection. Mass convergence was present in both profiles in mid levels, but mass divergence was computed above 600 mb with activity whereas near zero values occurred in upper levels when convective activity was absent.

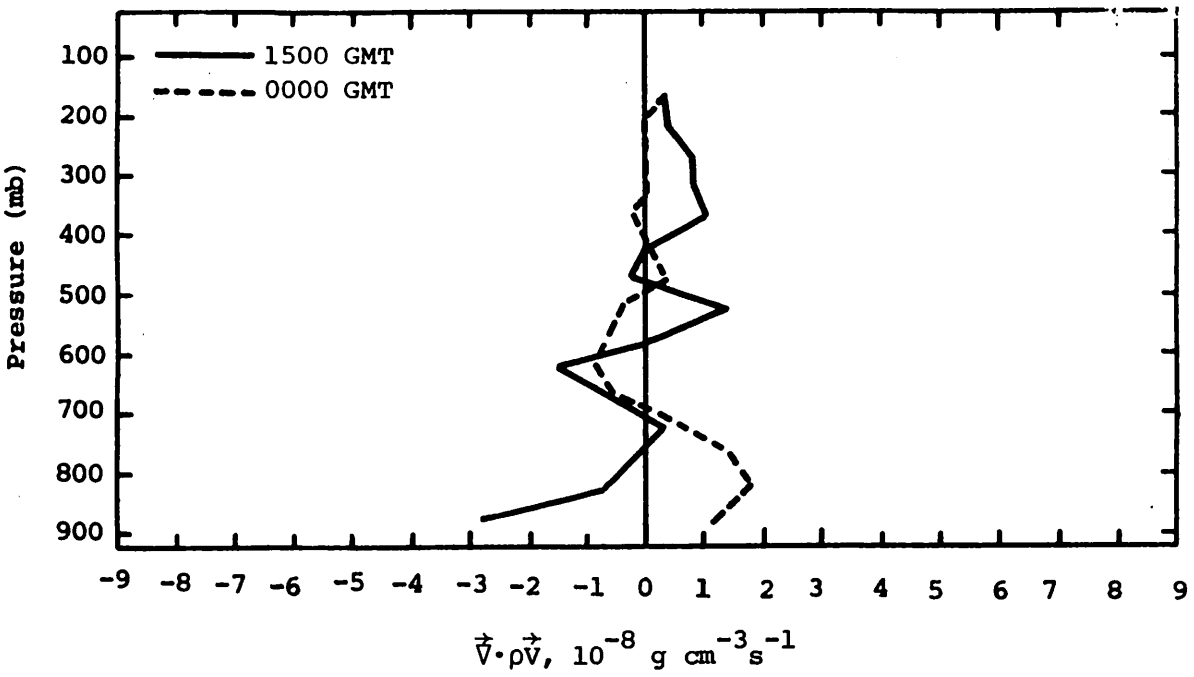

Fig. 5.21.1 Vertical profiles of mass divergence averaged for times of convection and nonconvection.

Vertical velocity profiles were clearly different during times with and without convection (Fig. 5.21.2). Upward vertical velocities, capable of releasing potential instability, were observed at all levels in the convective profile, while subsidence was present at all levels in the non-convective profile, possibly suppressing thunderstorm formation.

Horizontal moisture convergence in low levels was large in the convective profile (Fig. 5.21.3), and large moisture divergence was present in the non-convective curve as water vapor was supplied horizontally during activity times and removed horizontally during periods without activity. This same pattern is found in the horizontal flux divergence profiles of latent heat energy (Fig. 5.21.4) where net inflow in low levels supplies latent heat for storm development and removes it horizontally when convection fails to form.

Vertical flux divergence of latent heat energy occurred in low levels and flux convergence was computed aloft for the convective case (Fig. 5.21.5). This corresponds to a net vertical transport, within the upward vertical velocity field, of latent heat energy and water vapor from low levels to mid levels where cooling and condensation produce convective cloud formation and the release of latent heat. The reverse vertical pattern of convergence/divergence was computed for the nonconvective profile. This indicates that a net downward transport of latent heat energy, within the downward vertical velocity field shown in Fig. 5.21.2, occurs between mid- and low-levels

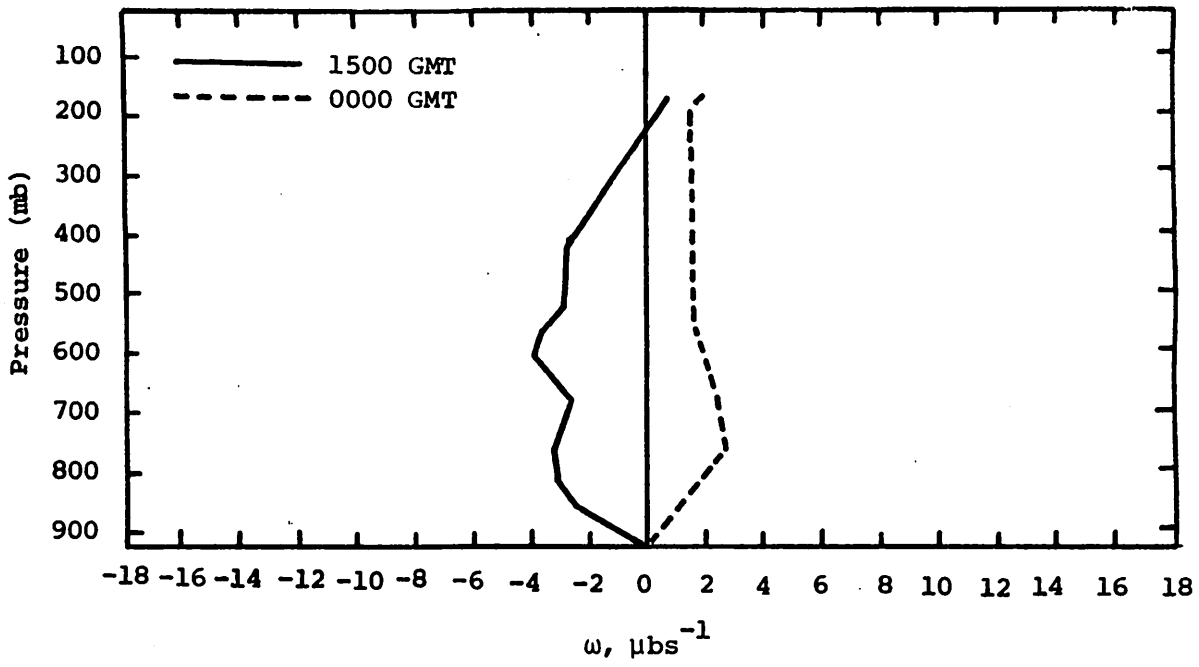

Fig. 5.21.2 Vertical profiles of vertical motion averaged for times of convection and nonconvection.

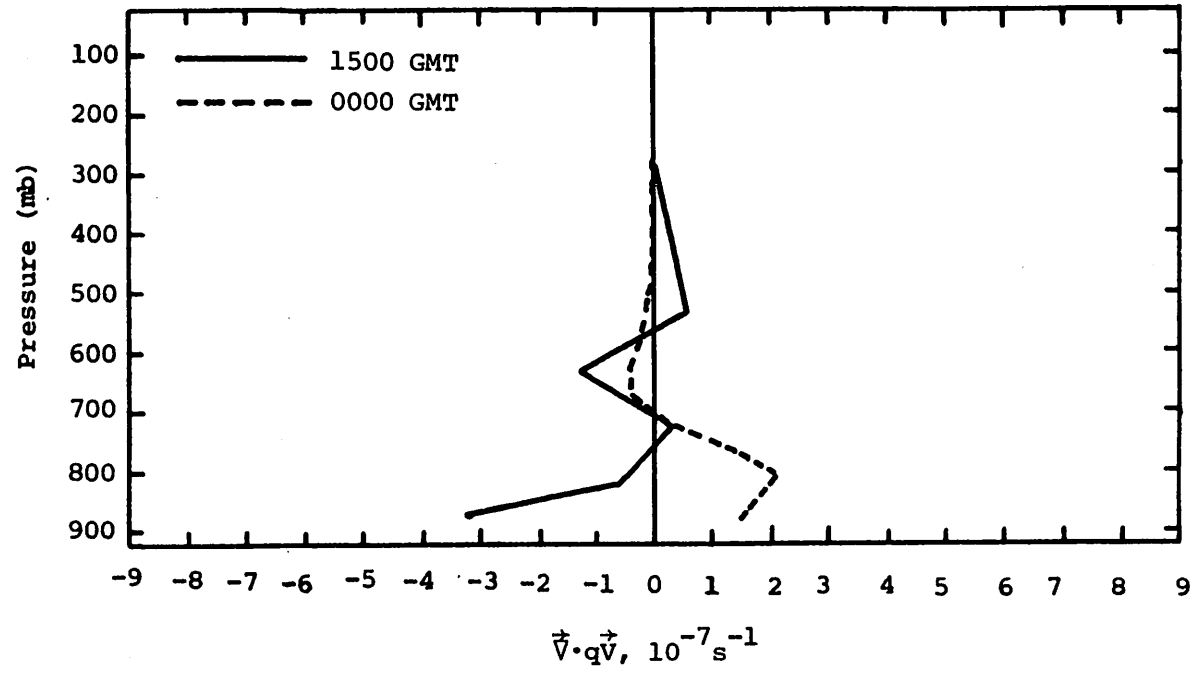

Fig. 5.21.3 Vertical profiles of moisture divergence averaged for times of convection and nonconvection.

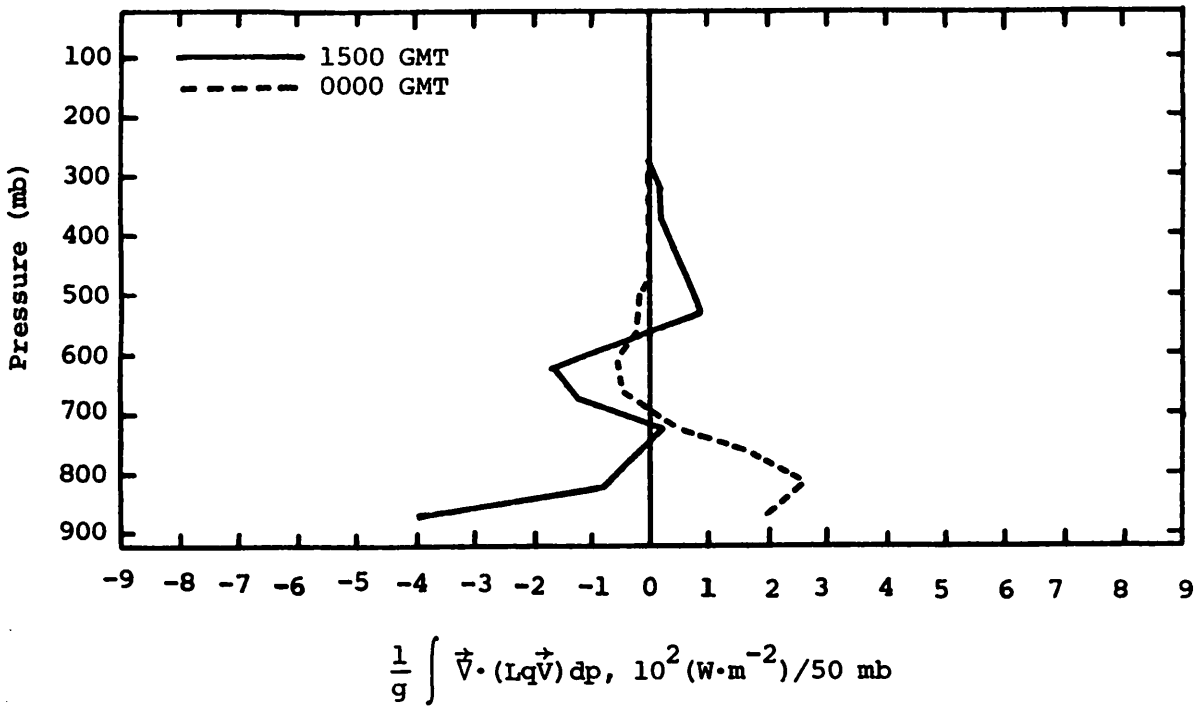

Fig. 5.21.4 Vertical profiles of horizontal flux divergence of latent heat energy averaged for times of convection and nonconvection.

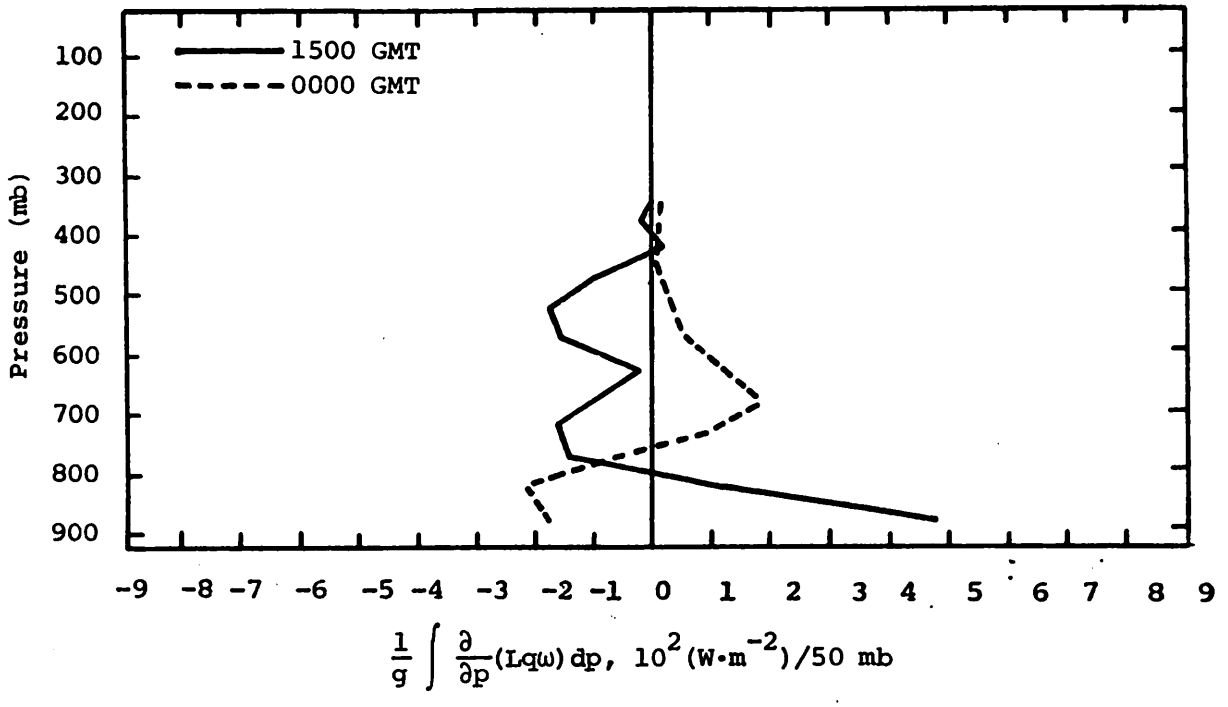

Fig. 5.21.5 Vertical profiles of vertical flux divergence of latent heat energy averaged for times of convection and nonconvection.

which does not promote condensation and cloud formation since adiabatic warming probably lowers relative humidities in mid levels.

The profiles of local changes in latent heat energy (Fig. 5.21.6) are small and positive in the nonconvective profile, indicating that evaporation or turbulent fluxes of latent heat may be important when activity is absent. Negative values in low- and mid-levels during times when activity was present probably reflect the losses of water vapor that occur during condensation.

The residual profiles from the latent heat budget equation (-R) show losses of latent heat energy (positive -R values) in the convective profile that are large in the middle troposphere and gains (negative -R values) of energy at mid levels in the non-convective profile (Fig. 5.21.7). This distribution is consistent with condensation and environmental heating from release of latent heat in convective areas, and evaporation and environmental cooling from losses of sensible heat when activity is not present.

The profiles of diabatic heating (Fig. 5.21.8) support this interpretation since the general shape and sign of the -R profiles in Fig. 5.21.7 closely resemble the diabatic heating profiles below 300 mb. Sensible heating in the convective profile is strongly related to condensation (within an upward vertical velocity field) and cooling in the nonconvective profile relates well with evaporation (within a downward vertical velocity field). However, both the diabatic heating and cooling are somewhat smaller than would result if the latent heat residual profiles were completely responsible for these diabatic effects. Both net radiation and turbulent flux divergence of water vapor and heat may be responsible for the differences.

The nonconvective profiles for both the horizontal and vertical flux divergence of kinetic energy (Figs. 5.21.9 and 5.21.10) are near zero at all levels except above 300 mb when net horizontal inflow of kinetic energy occurred. The convective profiles show net horizontal inflow in low levels and outflow at mid- and upper-levels with vertical flux divergence of kinetic energy in low- and mid-levels and flux convergence aloft. During convective activity, kinetic energy flows inwards in low levels and flow upwards to the high troposphere where it is horizontally exported. As a result, local changes of kinetic energy are small and near zero at all levels during nonconvective periods, and small but slightly negative in the upper-troposphere during times of convection (Fig. 5.21.11).

Horizontal flux convergence of sensible heat energy in low levels and

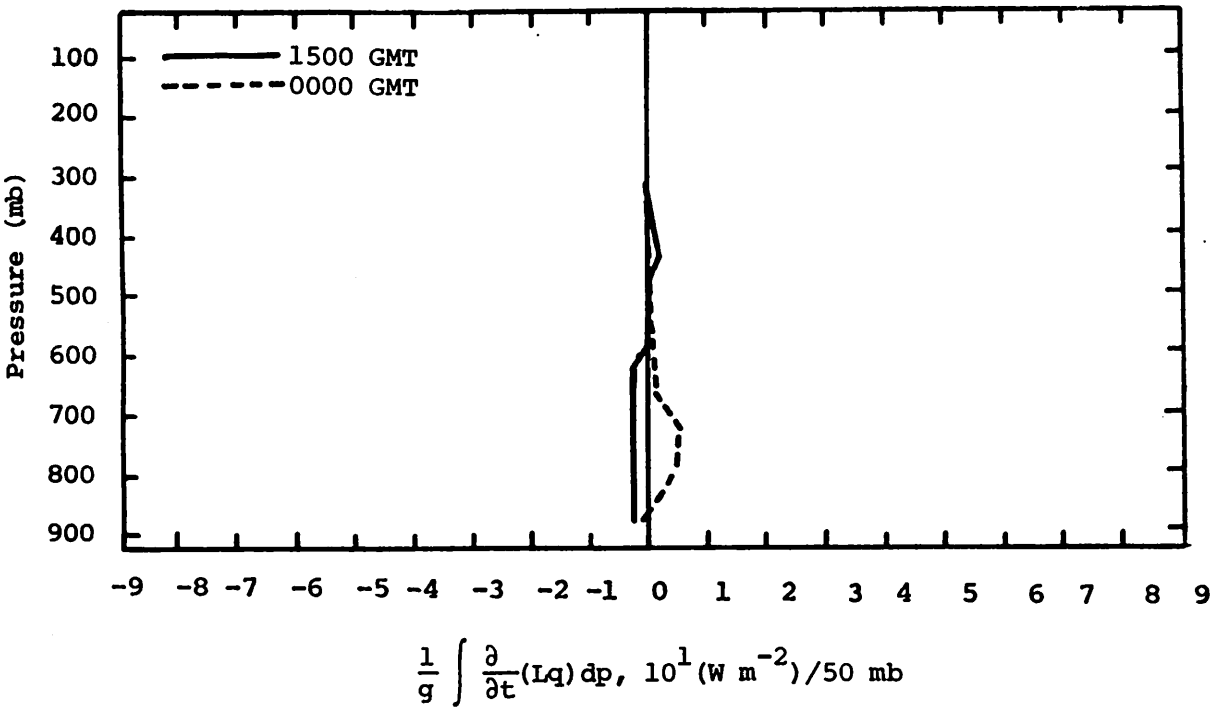

Fig. 5.21.6 Vertical profiles of the local change of latent heat energy averaged for times of convection and nonconvection.

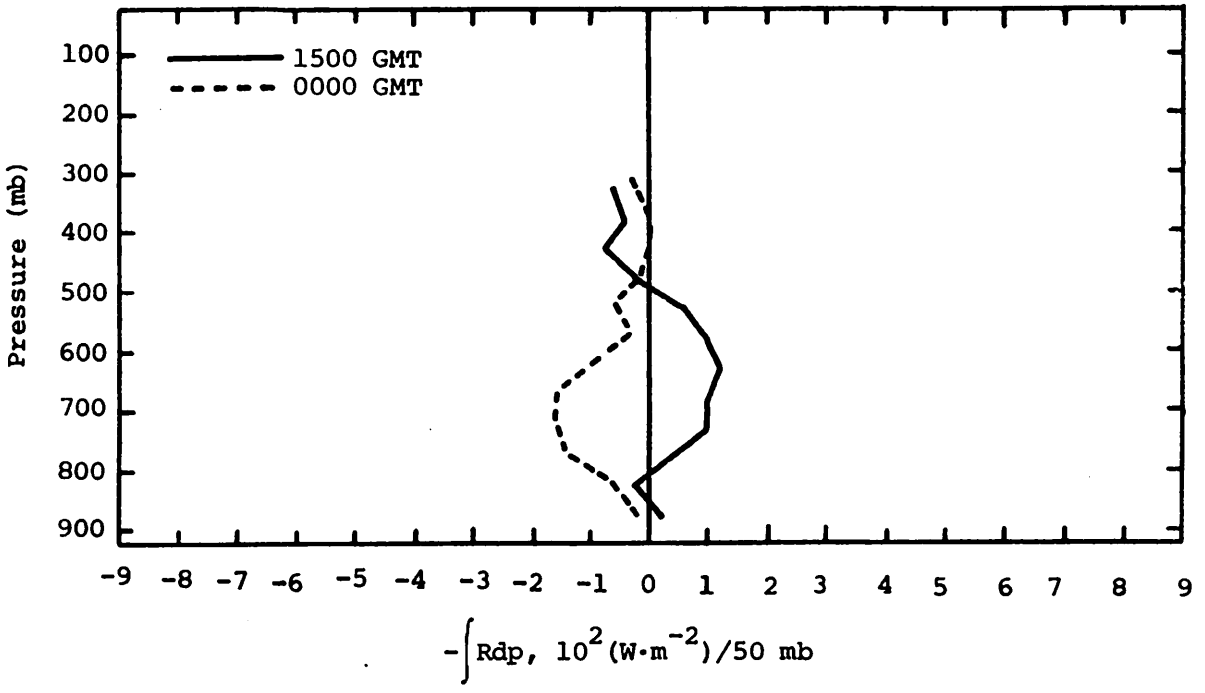

Fig. 5.21.7 Vertical profiles of the residual of the latent heat energy equation averaged for times of convection and nonconvection.

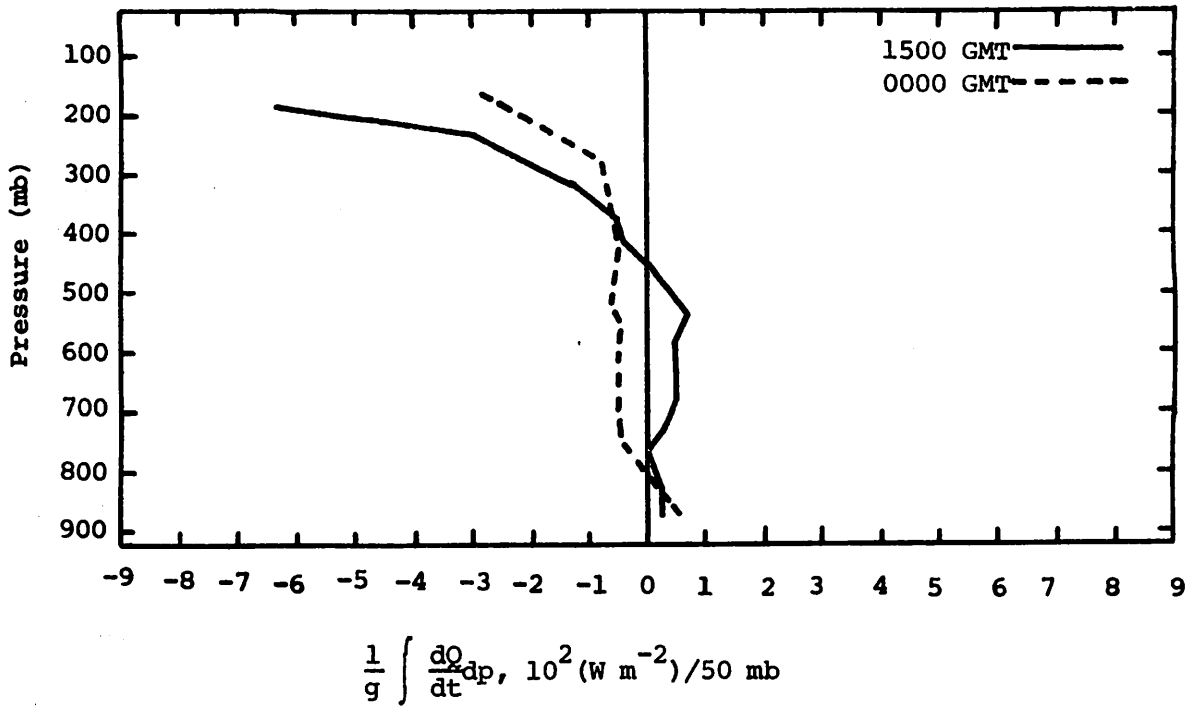

Fig. 5.21.8 Vertical profiles of diabatic heating computed from the first law of thermodynamics averaged for times of convection and nonconvection.

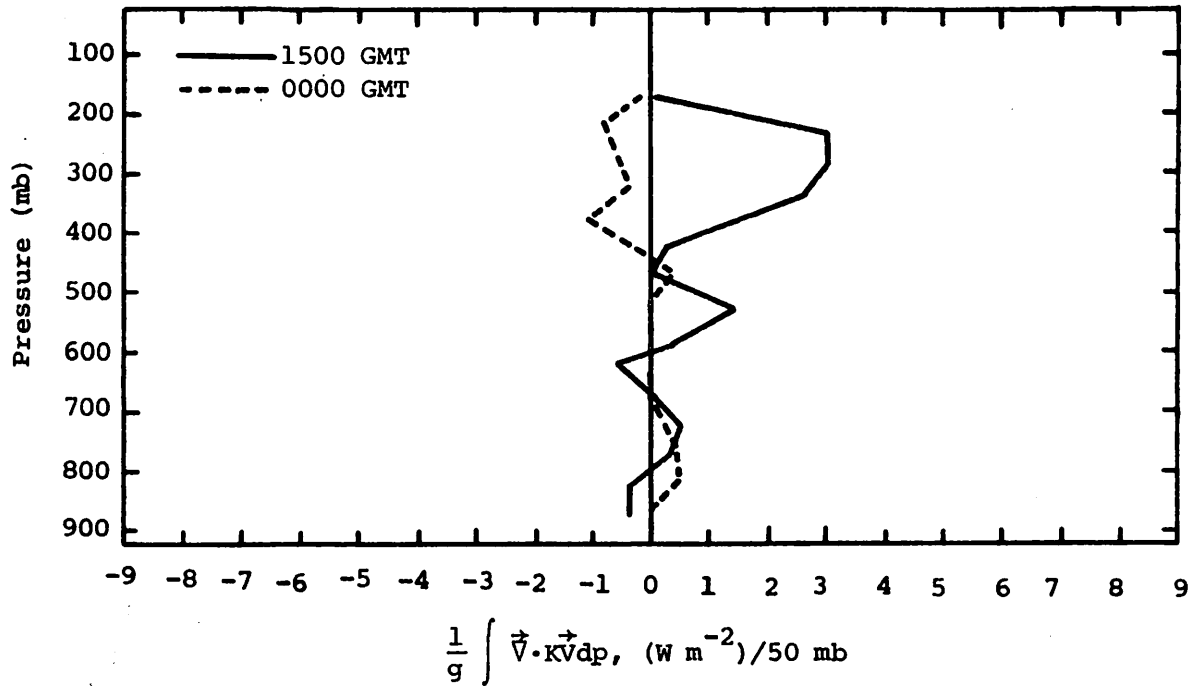

Fig. 5.21.9 Vertical profiles of horizontal flux divergence of energy averaged for times of convection and nonconvection.

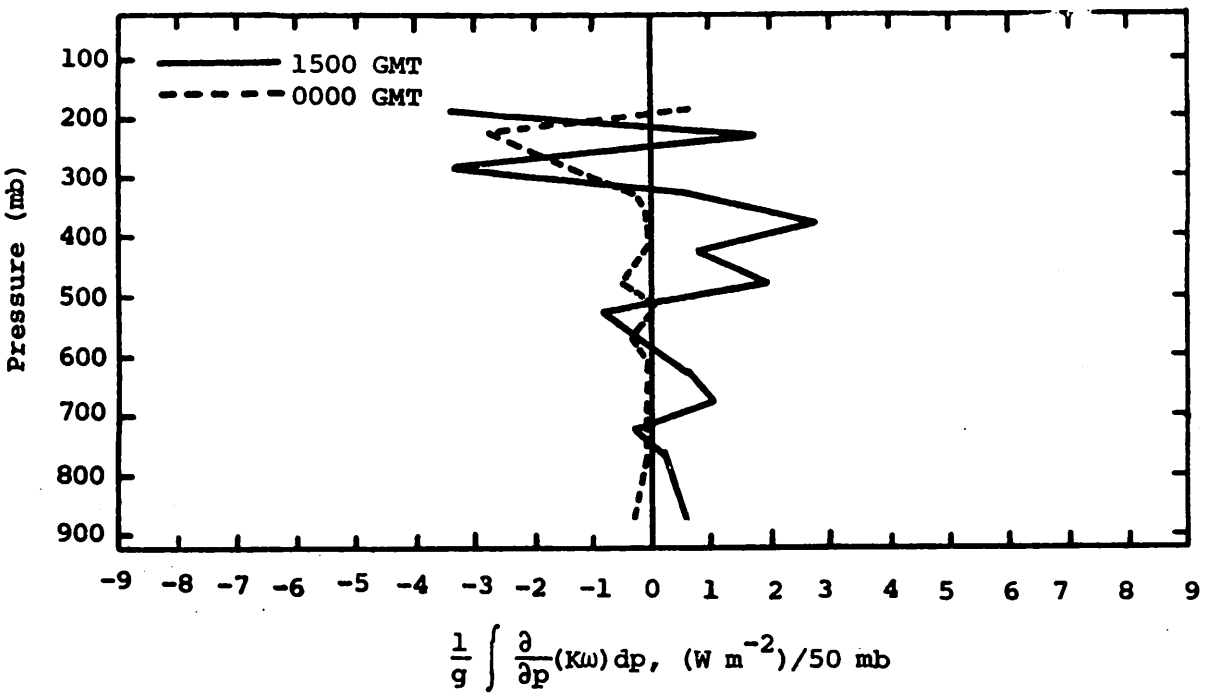

Fig. 5.21.10 Vertical profiles of vertical flux divergence of energy averaged for times of convection and nonconvection.

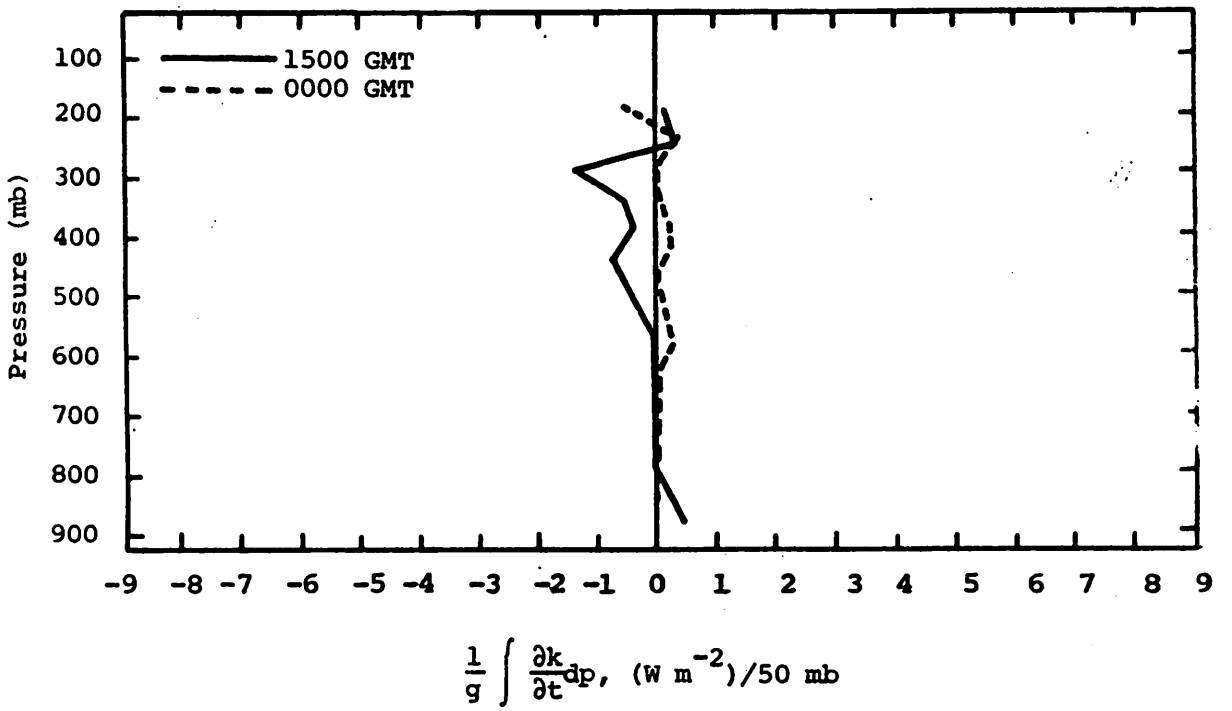

Fig. 5.21.11 Vertical profiles of the local change of kinetic energy averaged for times of convection and nonconvection.

flux divergence in mid- and upper-layers appears in the average convective profile in Fig. 5.21.12. In contrast, net horizontal outflow of sensible heat in low levels and net inflow in mid levels was computed for the nonconvective profile. The pattern contributes to creating increasing low-level temperatures and decreasing upper-level temperatures in the convective profile and visa versa for the nonconvective profile. The static stability is therefore possibly decreased in convective areas and increased in no activity areas, consistent with storm formation and suppression.

Vertical flux divergence of sensible heat in low levels and flux convergence in upper levels in the convective profile (Fig. 5.21.13) is associated with the net vertical transport of sensible heat accomplished by thunderstorms and resulting from upward environmental vertical velocities. The reverse vertical convergence/divergence pattern appears in the nonconvective profile with sensible heat experiencing a net downward transport from mid-to-lower levels in a sinking vertical velocity field. Local changes of sensible heat were generally small at most levels in the nonconvective profile (Fig. 5.21.14) except near the ground where radiational heating probably created large positive values when skies were partially cloud free and summer solar heating was large. However, local changes of sensible heat energy were large and positive in low levels in the convective profile indicating the possible destabilization of the atmosphere during times of convective activity.

The horizontal and vertical flux divergence profiles of potential energy for convective and nonconvective areas in Figs. 5.21.15 and 5.21.16 are generally similar in sign and shape except in low levels where horizontal flux convergence and vertical flux divergence of potential energy were found in the convective areas. Net horizontal outflow and net vertical inflow of potential energy in low levels were computed in the nonconvective areas. Net horizontal outflow of potential energy was very large in upper levels when activity was present.

Local changes in geopotential energy were small and negative in low levels, and small and positive in the upper troposphere in the nonconvective profile (Fig. 5.21.17). However, large negative values were found at all levels especially in the lower and upper troposphere during times of convective activity. This pattern points to the falling geopotential heights that were observed during times of thunderstorms.

In summary, substantial differences occur in energy budget terms and kinematic parameters when averages over times of convection are compared with

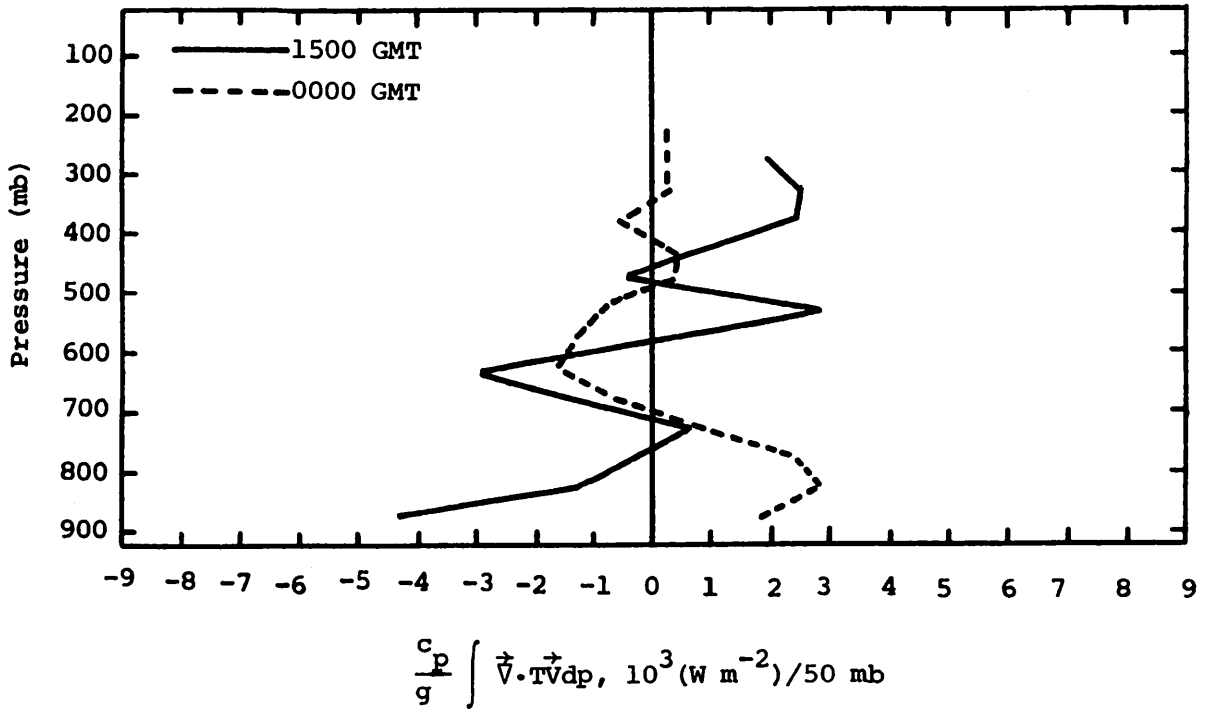

Fig. 5.21.12 Vertical profiles of horizontal flux divergence of sensible heat averaged for times of convection and nonconvection.

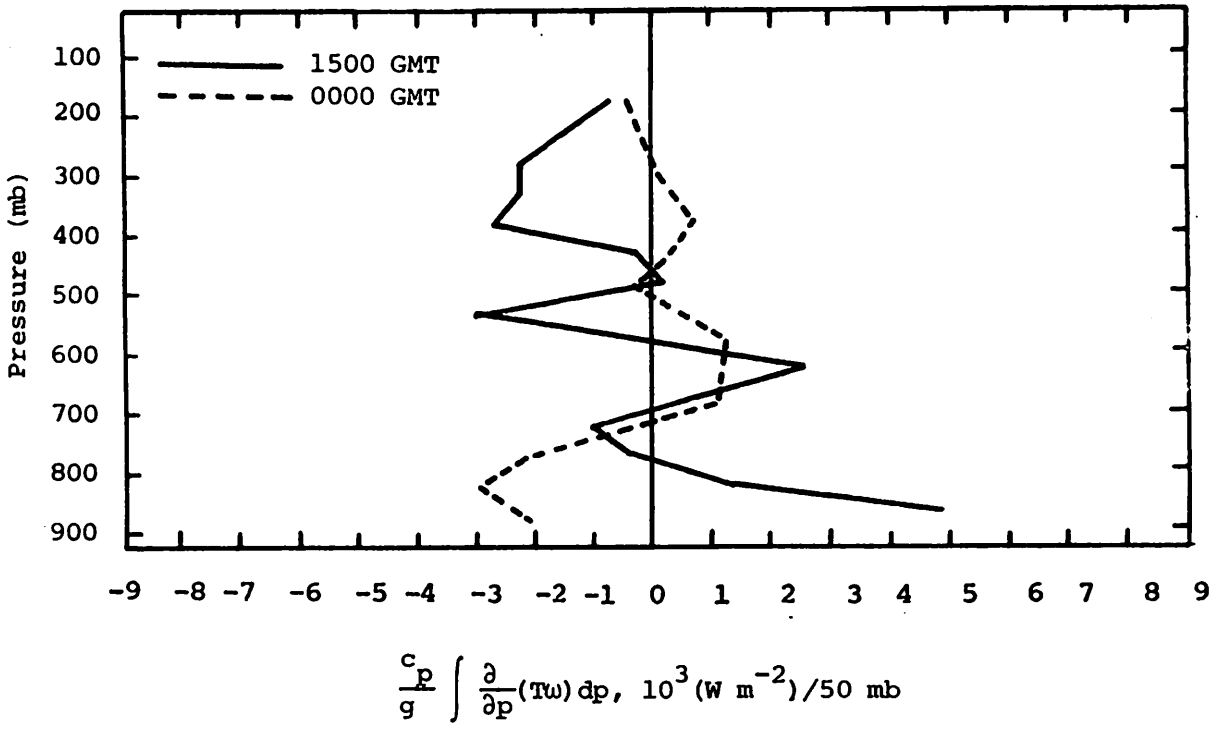

Fig. 5.21.13 Vertical profiles of vertical flux divergence of sensible heat averaged for times of convection and nonconvection.

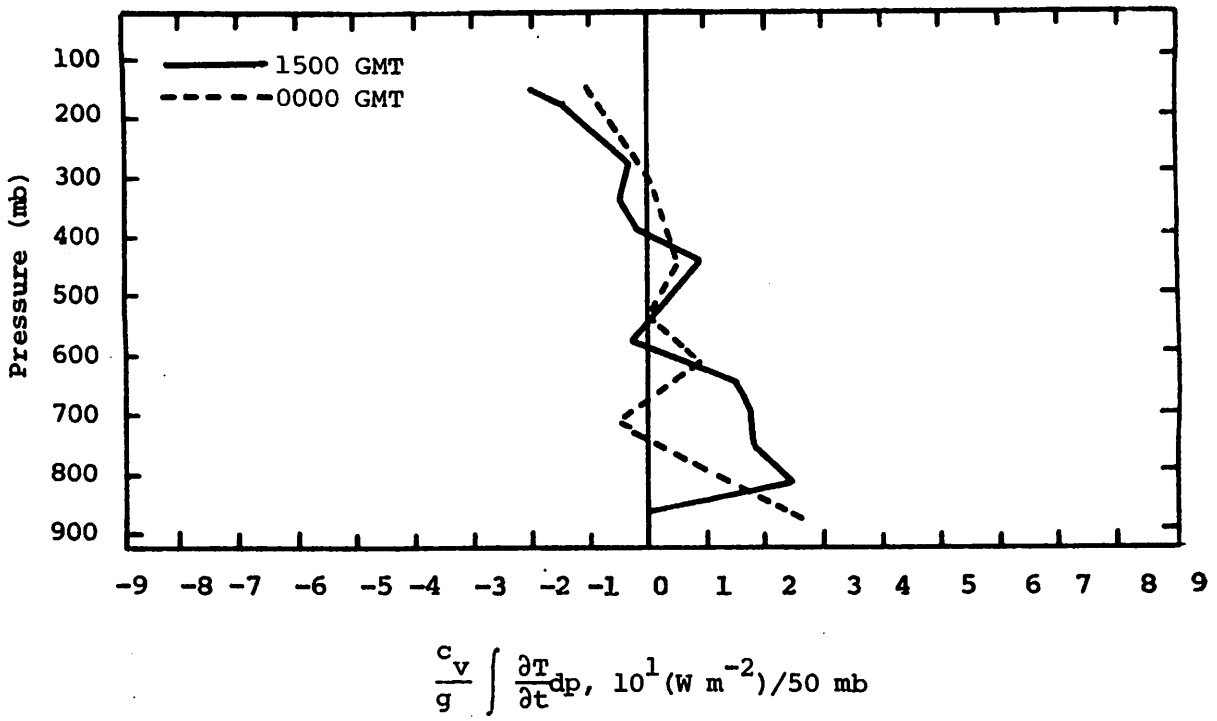

Fig. 5.21.14 Vertical profiles of local change of internal energy averaged for times of convection and nonconvection.

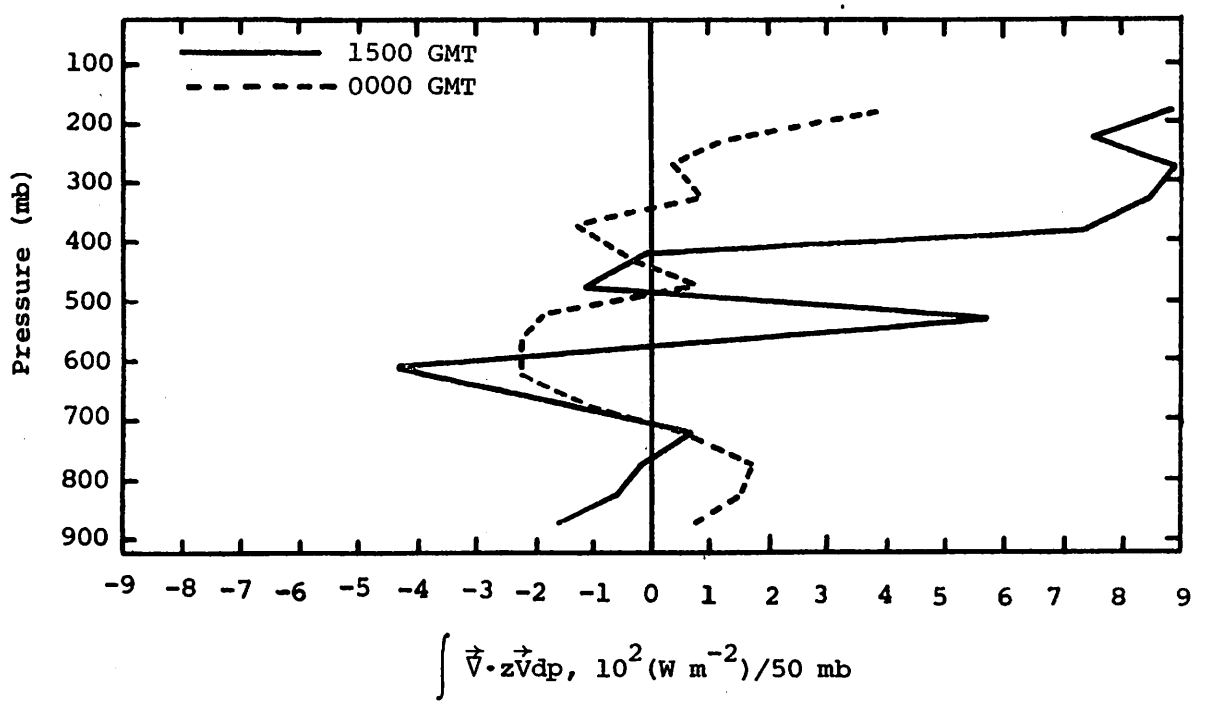

Fig. 5.21.15 Vertical profiles of horizontal flux divergence of potential energy averaged for times of convection and nonconvection.

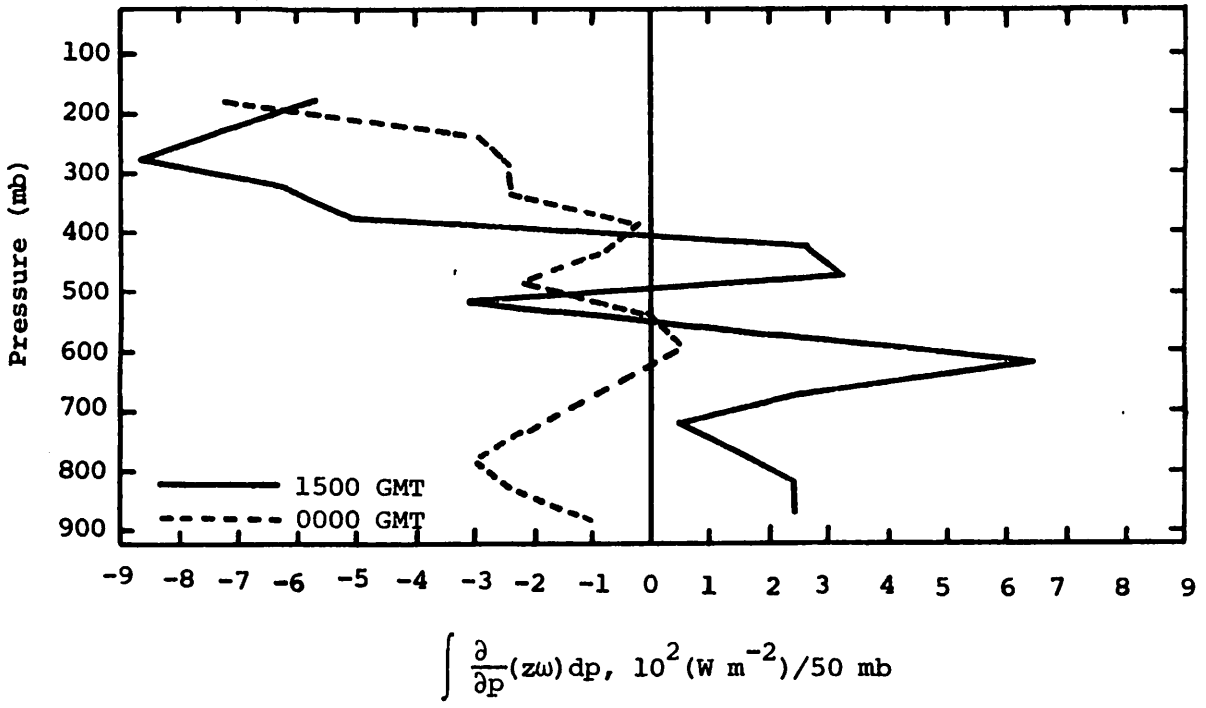

Fig. 5.21.16 Vertical profiles of vertical flux divergence of potential energy averaged for times of convection and nonconvection.

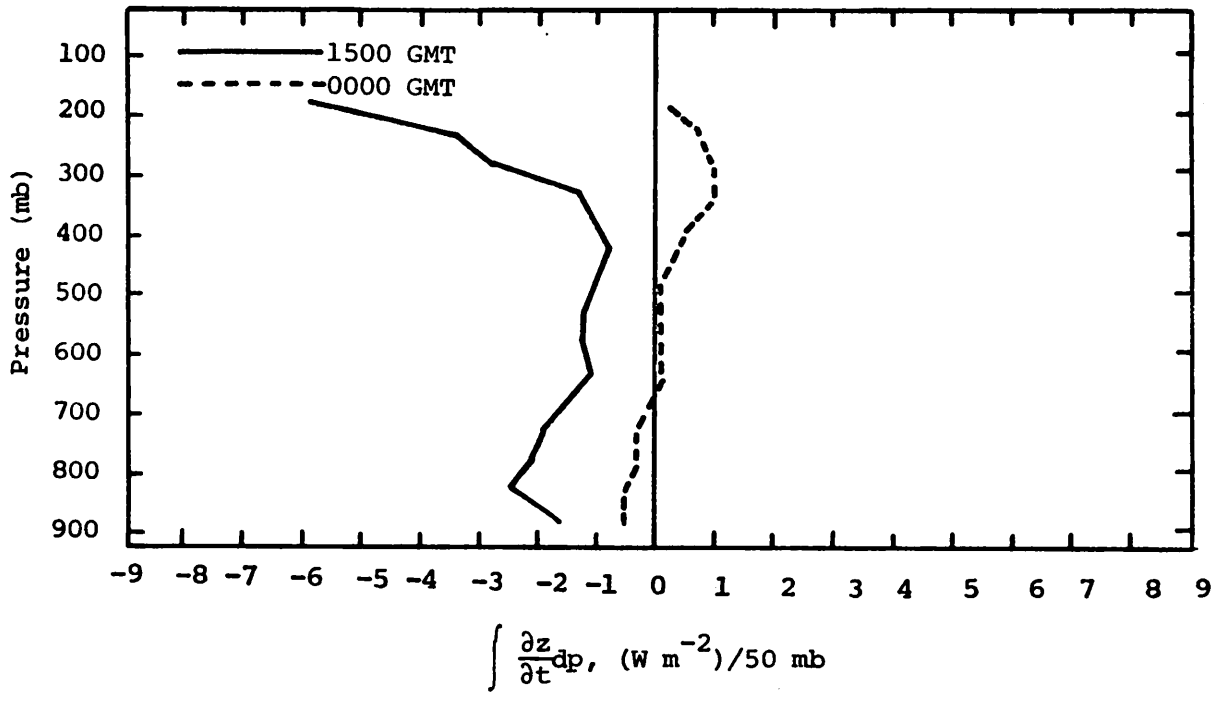

Fig. 5.21.17 Vertical profiles of the local change of potential energy averaged for times of convection and nonconvection.

averages over times of no convection. Low-level net horizontal inflow, net upward transport, and upper-level net horizontal outflow of internal, kinetic, and latent energy are found during times of convection. By contrast, upper- or mid-level net horizontal inflow, net downward transport, and lower-level net outflow of internal, kinetic, and latent energy are found when convective activity is absent.

5.22 Average Moisture Processes as Function of Convective Activity

Terms in the total water budget equation were evaluated for all sounding times for the summer of 1977. The results were divided into 2 groups: (1) times when convective activity was observed over the Texas HIPLEX area; and (2) times when no convective activity was observed over the Texas HIPLEX area. Average profiles were determined for convective and non-convective conditions for each term in the total water budget equation as well as several combinations of terms.

Figure 5.22.1 shows average profiles of net horizontal transport of water vapor. During convective conditions, a net loss occurred in layers below 700 mb and a net gain above. The greatest net inflow occurred between 650 and 550 mb, while for nonconvective conditions, a net outflow occurred in this layer. Both of these profiles show net losses below 700 mb. Between 600 and 700 mb, both profiles show net gains but the magnitude is greater and the layer deeper for convective than nonconvective conditions. These profiles suggest that a primary energy source for the convective activity is horizontal transport of moisture between 700 and 500 mb.

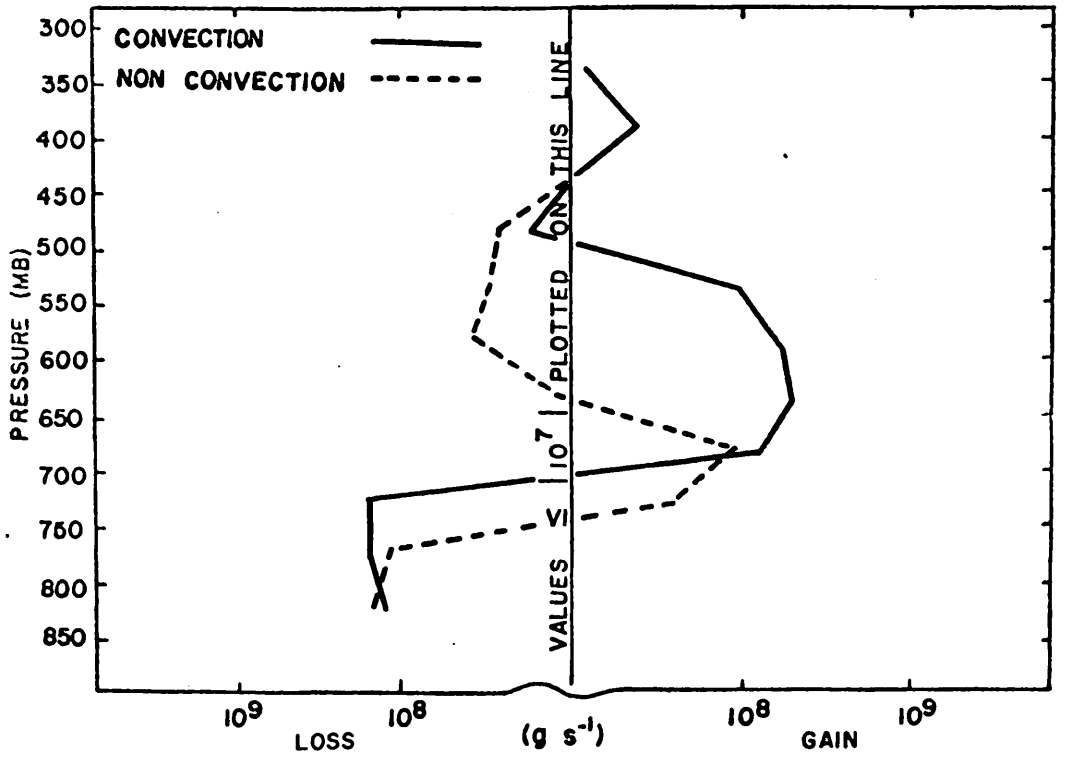

Fig. 5.22.1 Average profiles of net horizontal transport of water vapor through boundaries of 50-mb layers (gm s-1) over the Texas HIPLEX area for convective and nonconvective conditions during 1977.

Figure 5.22.2 shows average profiles of net vertical transport of water vapor. For nonconvective conditions, a net gain occurred below 750 mb and a net loss above 750 mb. For convective conditions, a net inflow occurred at all altitudes except in the layer 550-650 mb where a net loss occurred. This characteristic of net vertical transport of water vapor during convective activity also was observed in the 1976 data.

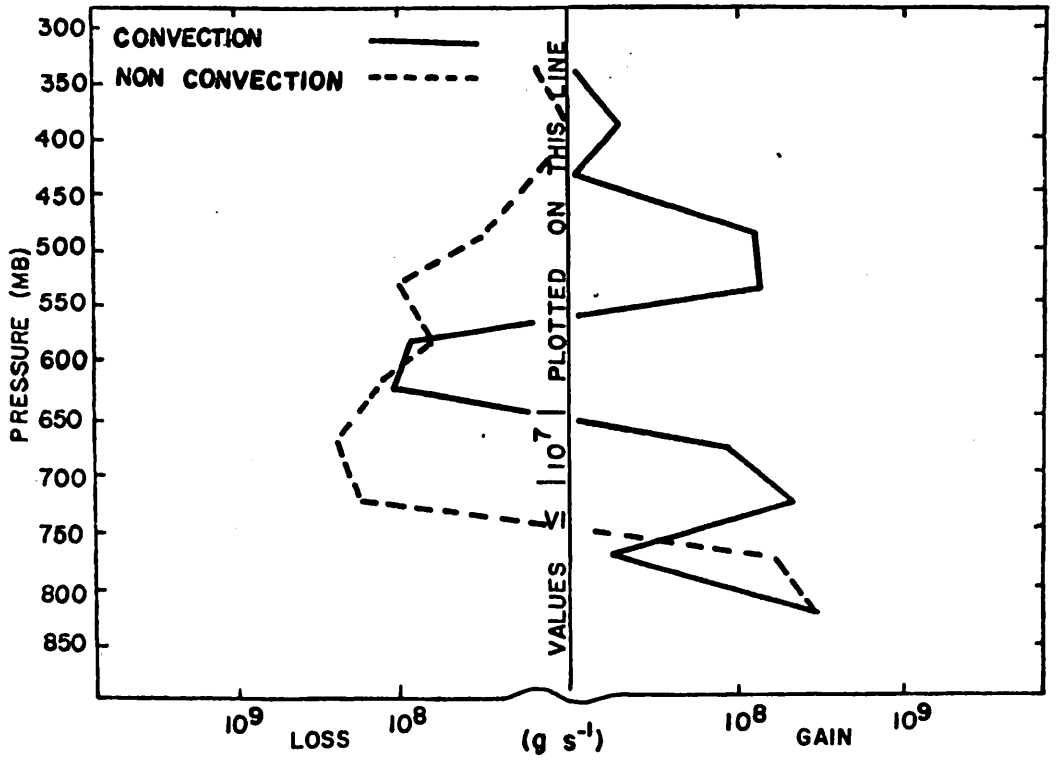

Fig. 5.22.2 Average profiles of net vertical transport of water vapor through boundaries of 50-mb layers (gm s^{-1}) over the Texas HIPLEX area for convective and nonconvective conditions during 1977.

Figure 5.22.3 represents average profiles of vertical transport of water vapor through constant pressure surfaces. These profiles show large upward and downward transports for convective and nonconvective conditions, respectively. For nonconvective conditions, a decrease in the transport of water vapor with height occurred at all levels above 700 mb. However, for convective conditions, an increase with altitude occurred near 550 mb, which is reflected in Fig. 5.22.2 as a net "storage" of water vapor.

Figure 5.22.4 represents average profiles of the combined net horizontal and vertical transport of water vapor. These profiles are nearly mirror images

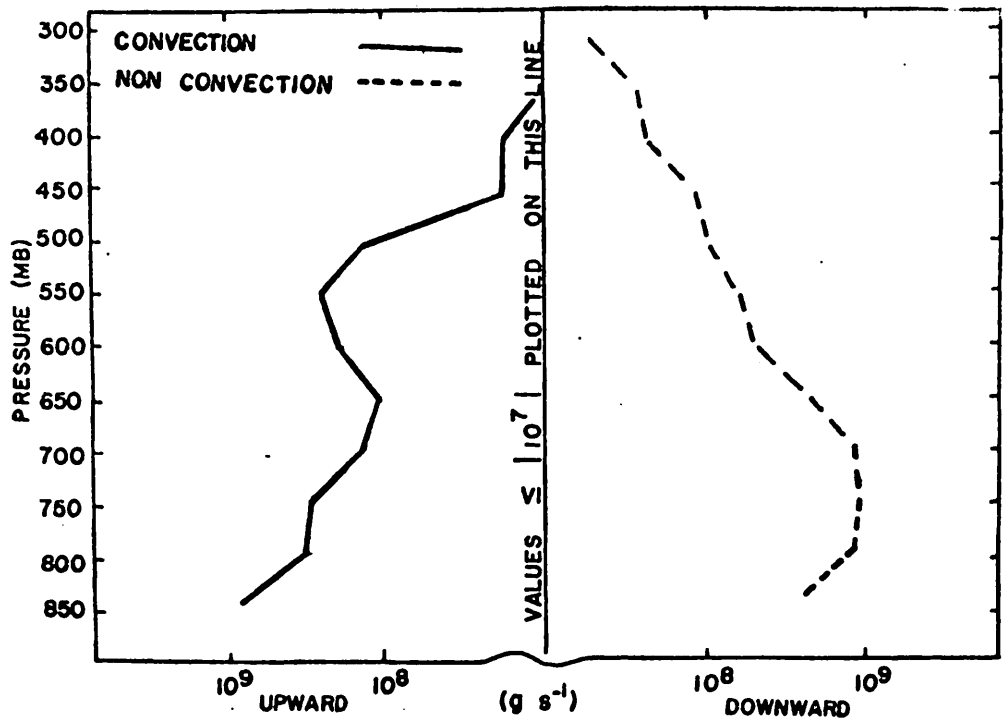

Fig. 5.22.3 Average profiles of the vertical transport of water vapor through constant pressure surfaces (gm s^{-1}) over the Texas HIPLEX area for convective and nonconvective conditions during 1977.

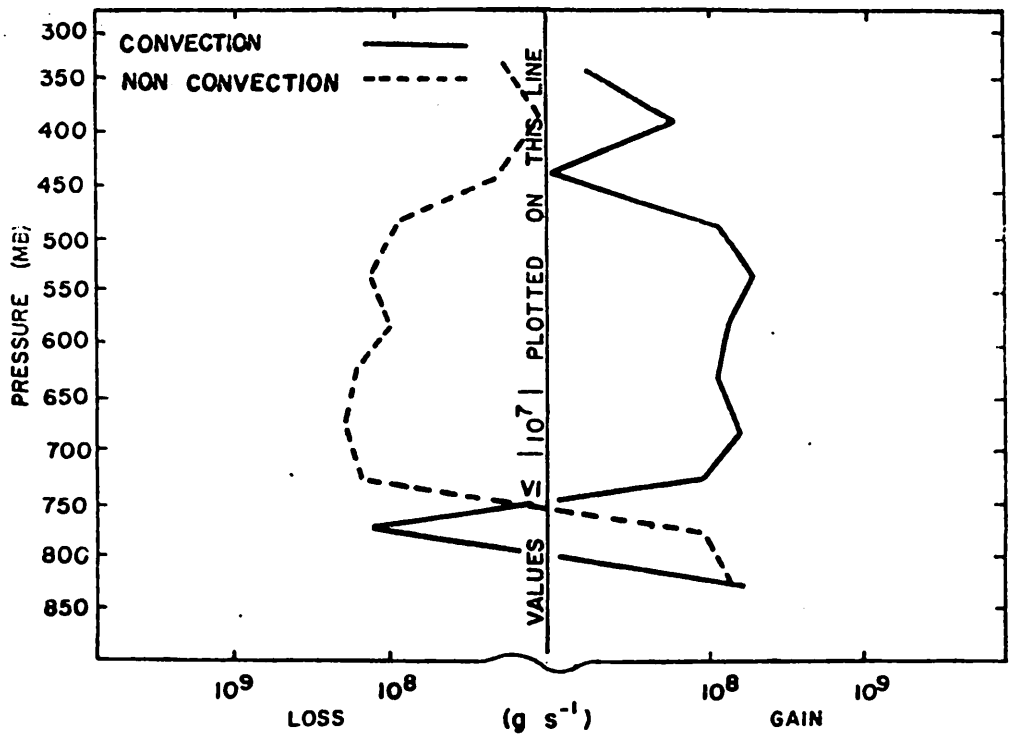

Fig. 5.22.4 Average profiles of combined net horizontal and vertical transport of water vapor through boundaries of 50-mb layers (gm s^{-1}) over the Texas HIPLEX area for convective and nonconvective conditions during 1977.

of one another. They show net inflow during times of convection, and net outflow for times with no convection at all altitudes above 750 mb. These water vapor transports are nearly equal at 825 and 750 mb. These profiles show the importance of moisture processes during convection in the mid to upper troposphere.

Figure 5.22.5 shows average profiles of the local rate-of-change in the total mass of water vapor. During times of nonconvective conditions, a net gain occurred below 600 mb which may be attributed to the downward transport of water vapor shown in Fig. 5.22.3. Also, in layers above 600 mb, a negligible change in water vapor occurred during nonconvective conditions. During convective conditions, a net loss occurred below 650 mb and a net gain above which may be attributed to the upward vertical transports shown in Fig. 5.22.3. The greatest increase in water vapor occurred at 550 mb which is the level where large net horizontal (Fig. 5.22.1) and net vertical transports (Fig. 5.22.2) "store" water vapor.

Figure 5.22.6 shows average profiles of the residual term in the total water budget equation. These profiles resemble those shown in Fig. 5.22.4, and show a net loss during nonconvective conditions and a net gain during convective conditions above 750 mb. For convective conditions, the residual term reaches a maximum at 525 mb. This is the altitude where net horizontal and vertical transports of water vapor, and the local rate-of-change in water vapor show large increases. It has been shown that during convective conditions precipitation becomes a dominant factor in the residual term. Therefore, large increases of the residual in these upper layers might indicate the formation of precipitation during convective activity.

In summary, the average profiles presented above show that the greatest differences between convective and nonconvective conditions occur in layers above approximately 700 mb. For convective conditions, the largest increases occurred between 600 and 450 mb. The profiles also show that water vapor in appreciable amounts is present in these layers during convective conditions.

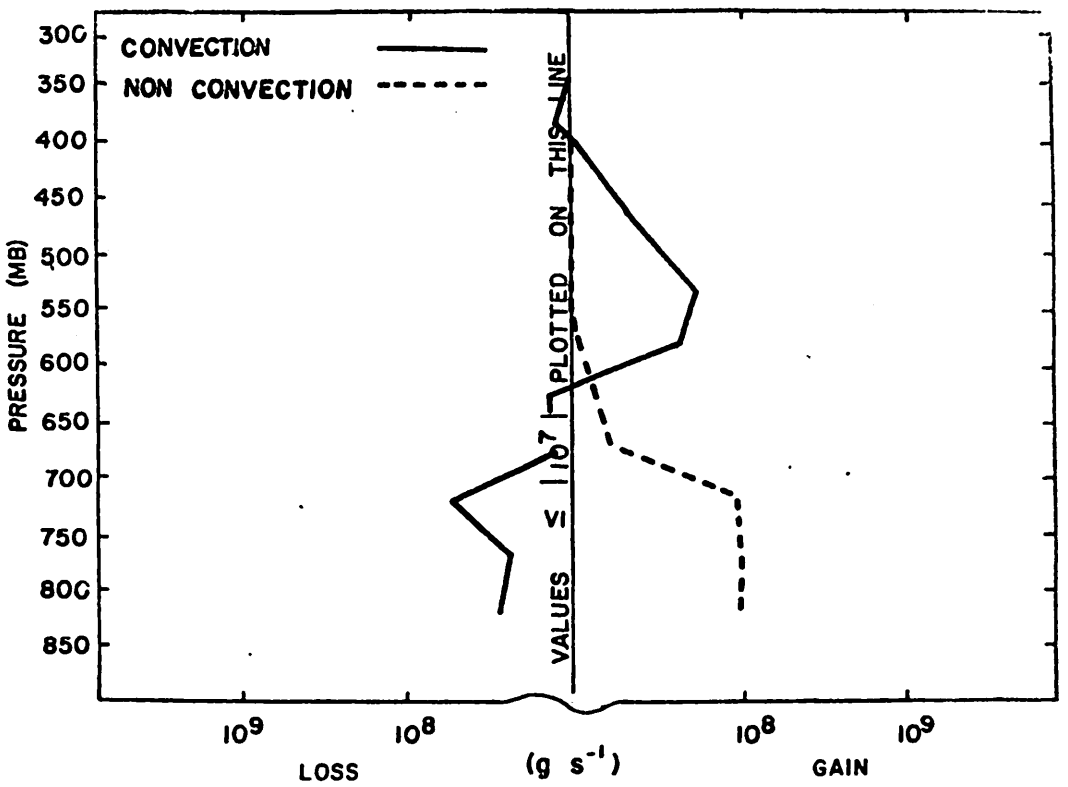

Fig. 5.22.5 Average profiles of the local rate-of-change in total mass of water vapor (gm per 3h x 10^{-11}) over the Texas HIPLEX area for convective and nonconvective conditions during 1977.

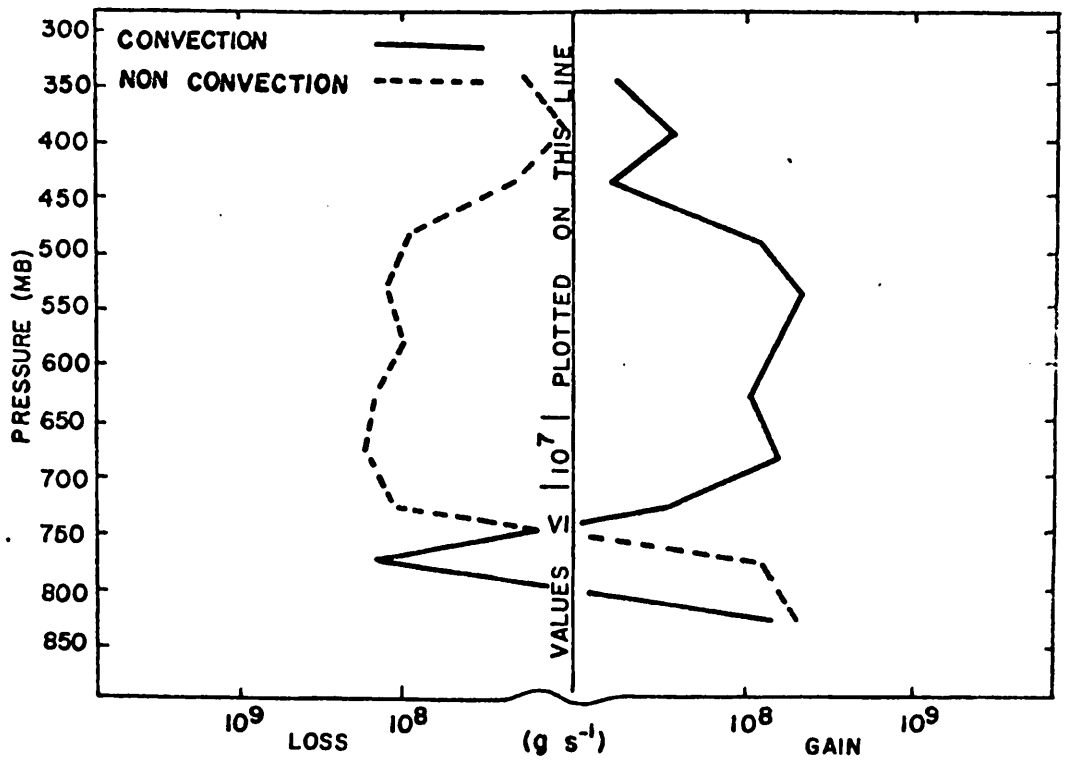

Fig. 5.22.6 Average profiles of the residual in the water budget equation over the Texas HIPLEX area for convective and nonconvective conditions during 1977.

6. SUMMARY AND COMMENTS

This report contains an analysis of Texas HIPLEX mesoscale data for 1977. The approach was to treat each day as a case study, analyze selected surface variables in a composite sense, and establish average conditions of atmospheric energetics and moisture during times with and without convective activity.

A total of 19 days is included in this study. Three of these days consist of surface analyses only, while 16 of the days consist of both surface and upper-air analyses. The surface analyses include radar echoes, temperature, mixing ratio, equivalent potential temperature, terrain-induced vertical motion, velocity divergence, vertical motion 50 mb above the surface, moisture divergence, vertical flux of moisture 50 mb above the surface, and vorticity. The upper-air analyses include mass divergence, vertical motion, moisture divergence, and various terms in budgets of latent heat, total energy, and moisture.

The results confirm those reported for 1976 (Scoggins, et al., 1978) and show that, in most cases, both surface and upper air conditions were altered significantly by convective activity and vice versa. In some cases, pronounced changes in variables such as moisture divergence at all levels including the surface, and vertical motion aloft were associated with the occurrence and extent of convective activity.

Even though the number of days considered in this report is small, the results together with those for 1976, demonstrate conclusively the value and, indeed, the necessity of mesoscale data in the assessment of environmental conditions associated with convective activity, and for determining the interactions of convective clouds with their environment. This type of research is essential in the development of the technology required for rainfall enhancement.

One significant aspect of this research is that it confirms the general results obtained for 1976 data. In addition, these results, combined with those for 1976, form a data set large enough to begin to draw definitive conclusions.

REFERENCES

Barnes, S. L., 1964: A technique for maximizing detail in numerical weather map analysis. J. Appl. Meteor., 3, 396-409.

Kornegay, F. C., and D. G. Vincent, 1976: Kinetic energy budget analysis during interaction of tropical storm Candy (1968) with an extratropical frontal system. Mon. Wea. Rev., 104, 849-859.

Kung, E. C., and T. L. Tsui, 1975: Subsynoptic-scale kinetic energy balance in the storm area. J. Atmos. Sci., 32, 729-740.

Scoggins, J. R., 1977: Texas HIPLEX Mesoscale Experiment - Summer 1977. Final Report, TWDB Contract No. 14-70030, 9 pp. plus 4 Appendices.

Scoggins, J. R., H. E. Fuelberg, B. F. Williams, and M. E. Humbert, 1978: Mesoscale Characteristics of the Texas HIPLEX Area during Summer 1976. Final Report, TWDB Contract No. 14-70020, 343 pp.

Scoggins, J. R., and G. S. Wilson, 1976: Texas HIPLEX Mesoscale Experiment--Summer 1976 Data Tabulations. Final Report, TWDB Contract No. 14-60025, 33 pp.

Vincent, D. G., and L. N. Chang, 1975: Kinetic energy budgets of moving systems: Case studies for an extratropical cyclone and hurricane Celia, 1970. Mon. Wea. Rev., 102, 35-47.